

Journal of
Mechanics of
Materials and Structures

Special issue dedicated to
George J. Simitzes

Volume 4, N° 7-8

September 2009



mathematical sciences publishers

JOURNAL OF MECHANICS OF MATERIALS AND STRUCTURES

<http://www.jomms.org>

Founded by Charles R. Steele and Marie-Louise Steele

EDITORS

CHARLES R. STEELE Stanford University, U.S.A.
DAVIDE BIGONI University of Trento, Italy
IWONA JASIUK University of Illinois at Urbana-Champaign, U.S.A.
YASUhide SHINDO Tohoku University, Japan

EDITORIAL BOARD

H. D. BUI École Polytechnique, France
J. P. CARTER University of Sydney, Australia
R. M. CHRISTENSEN Stanford University, U.S.A.
G. M. L. GLADWELL University of Waterloo, Canada
D. H. HODGES Georgia Institute of Technology, U.S.A.
J. HUTCHINSON Harvard University, U.S.A.
C. HWU National Cheng Kung University, R.O. China
B. L. KARIHALOO University of Wales, U.K.
Y. Y. KIM Seoul National University, Republic of Korea
Z. MROZ Academy of Science, Poland
D. PAMPLONA Universidade Católica do Rio de Janeiro, Brazil
M. B. RUBIN Technion, Haifa, Israel
A. N. SHUPIKOV Ukrainian Academy of Sciences, Ukraine
T. TARNAI University Budapest, Hungary
F. Y. M. WAN University of California, Irvine, U.S.A.
P. WRIGGERS Universität Hannover, Germany
W. YANG Tsinghua University, P.R. China
F. ZIEGLER Technische Universität Wien, Austria

PRODUCTION


PAULO NEY DE SOUZA Production Manager
SHEILA NEWBERY Senior Production Editor
SILVIO LEVY Scientific Editor

See inside back cover or <http://www.jomms.org> for submission guidelines.

Regular subscription rate: \$600 a year (print and electronic); \$460 a year (electronic only).

Subscriptions, requests for back issues, and changes of address should be sent to contact@mathscipub.org or to Mathematical Sciences Publishers, 798 Evans Hall, Department of Mathematics, University of California, Berkeley, CA 94720-3840.

©Copyright 2010. Journal of Mechanics of Materials and Structures. All rights reserved.

 mathematical sciences publishers

DEDICATION



George J. Simitzes was born on 31 July 1932 in Athens, Greece. After receiving his high school diploma, he came to the United States to study engineering. He first attended the University of Tampa (1951–52) and then the Georgia Institute of Technology (1952–56), where he earned the degrees of Bachelor of Aeronautical Engineering and Master of Science in Aerospace Engineering. After a few years, he attended Stanford University (1963–65), where he earned a Ph.D. in Aeronautics and Astronautics. His academic career includes teaching and research at Georgia Tech (Instructor, Assistant Professor, Associate Professor and Professor) in the Schools of Aerospace Engineering and Engineering Science and Mechanics and at the University of Cincinnati (Professor and Department Head of Aerospace Engineering and Engineering Mechanics and Interim Dean of Engineering). He retired in March 2000 from the University of Cincinnati and he is presently Professor Emeritus at both schools.

As a researcher, Professor Simitzes has made pioneering and lasting contributions in the field of Solid and Structural Mechanics. He has written three graduate level text-books and several book chapters. He has authored or coauthored over 160 refereed journal articles in archival engineering journals. He has advised 23 Ph.D. students to completion as well as dozens of M.Sc. students, and he has hosted ten post-doctoral fellows, visiting scholars and faculty from throughout the world during the past three decades. His research publications include works in structural stability, dynamic stability, structural optimization, delamination buckling and growth, analysis of thick composite shells and structural similitude. In his research, he has dealt with beams, bars, plates and shells of various constructions, metallic structures with and without stiffeners, laminated composites, sandwich systems and simple mechanical models.

Professor Simitzes has served and is still serving the scientific and engineering profession through journal editing, organization and participation in professional meetings, membership in professional societal committees and chairing sessions at national and international conferences. He has been invited to deliver Keynote Addresses and Plenary Lectures at several professional meetings. He has also participated in many panels and workshops. He has been a frequent seminar lecturer to many universities and industrial

companies and he has participated in numerous continuing education courses. Professor Simitzes is the recipient of many awards and honors. He is a Fellow of the AIAA, the ASME, and the American Academy of Mechanics, and an Honorary Member of the Hellenic Society of Theoretical and Applied Mechanics and Member of the International Union of Theoretical and Applied Mechanics. He has also been elected Corresponding Member of the Academy of Athens (the Greek equivalent of the US National Academy of Science). Professor Simitzes has been married to Nena Athena Economy for 49 years. They have three children, John, William and Alexandra, and six grandchildren, Michael, Christina, George and Matthew Simitzes, Athena and Marian Zaden, with one more on the way.

We, the guest editors of this volume, have been happy to enjoy collaboration and friendship with Professor Simitzes. Professor Simitzes is renowned for his ability to quickly understand and assess a scientific problem. His vision and readiness to share and discuss ideas are admirable. Both of us immensely benefited from joint research and long conversations, in which we would solicit Professor Simitzes's opinion and advice. Besides our collaboration, it is a real pleasure and honor to associate with Professor Simitzes. His wisdom, erudition, optimism and sincere personal interest have always been an inspiration to us. We are happy to dedicate this volume to Professor Simitzes as a modest token of our appreciation, respect and recognition of his lifetime contributions.

GEORGE KARDOMATEAS: george.kardomateas@aerospace.gatech.edu

Department of Aerospace Engineering, Georgia Institute of Technology, Atlanta, GA 30332-0150, United States

VICTOR BIRMAN: vbirman@mst.edu

Engineering Education Center, Missouri University of Science and Technology, One University Boulevard, St. Louis, MO 63121, United States

BUCKLING AND POSTBUCKLING BEHAVIOR OF LAMINATED COMPOSITE STRINGER STIFFENED CURVED PANELS UNDER AXIAL COMPRESSION: EXPERIMENTS AND DESIGN GUIDELINES

HAIM ABRAMOVICH AND TANCHUM WELLER

An extensive test series on circular cylindrical laminated composite stringer-stiffened panels subjected to axial compression, shear loading introduced by shear and combined axial compression and shear was carried out at the Technion, Israel. The test program was an essential part of an ongoing effort undertaken by the POSICOSS project (improved postbuckling simulation for design of fibre composite stiffened fuselage structures) aiming at design of low cost, low weight airborne structures that was initiated and supported by the Fifth European Initiative Program.

The first part of this test series, dealing with panels PSC1–PSC9 (blade-stiffened), has already been summarized and published. The results of the tests with panels BOX1–BOX4 (blade- and J-stiffened) have also been reported and published. These tests dealt with two identical stiffened panels, combined together by two flat nonstiffened aluminum webs, to form a torsion box, thus enabling application of shear tractions, through introduction of torsion, and combined axial compression and shear. The present manuscript aims at describing test results and relevant numerical studies on the buckling and postbuckling behavior of another set of four panels, AXIAL1–AXIAL4, stiffened by J-type stringers. Based on the experimental studies carried out within the framework of the POSICOSS project and reported in the literature and on the present study design guidelines were formulated and presented. Accompanying supporting calculations were presented as well; they were performed with a “fast” calculation tool developed at the Technion, and based on the effective width method modified to handle laminated circular cylindrical stringer-stiffened composite panels.

1. Introduction

It is well recognized that non-closely stiffened panels can have considerable postbuckling reserve strength, enabling them to carry loads significantly in excess of their initial local skin between stiffeners buckling load [Hutchinson and Koiter 1970]. When appropriately designed, their load carrying capacity appreciably exceed the load corresponding to an equivalent weight unstiffened shell, that is, a shell of identical radius and thicker skin, which is also more sensitive to geometrical imperfections.

The design of aerospace structures places great emphasis on exploiting the behavior under loading and on mass minimization of such panels. An optimum (minimum mass) design approach based on initial buckling, stress or strain, and stiffness constraints typically yields an idealized structural configuration characterized by almost equal critical loads for local and overall buckling. This, of course, results in little

This work was partly supported by the European Commission, Competitive and Sustainable Growth Programme, Contract No. G4RD-CT-1999-00103, project POSICOSS (<http://www.posicoss.de>). The information in this paper is provided as is and no guarantee or warranty is given that the information is fit for any particular purpose. Users thereof use the information at their sole risk and liability.

postbuckling strength capacity and susceptibility to premature failure. However, an alternative optimum design approach can be imposed to achieve lower mass designs for a given loading. This is obtained by requiring the initial local buckling to occur considerably below the design load and allow for the existence of the response characteristics known in postbuckled panels [Lilico et al. 2002], that is, capability to carry loads higher than their initial buckling load. In parallel, to meet the requirements of low structure weight, advanced lightweight laminated composite elements are increasingly being introduced into new designs of modern aerospace structures to enhance both their structural efficiency and performance. In recognition of the numerous advantages that such composites offer, there is also a steady growth in replacement of metallic components by composite ones in other fields of engineering like marine structures, ground transportation, robotics, sports, and others.

Many theoretical and experimental studies have been performed on buckling and postbuckling behavior of flat stiffened composite panels (see for example [Frostig et al. 1991; Segal et al. 1987; Starnes et al. 1985; Vestergren and Knutsson 1978; Romeo 1986; Bucci and Mercuria 1992]). A wide body of descriptions and detailed data on buckling and postbuckling tests was compiled in [Singer et al. 2002] (see chapters 12–14). However, on the other hand studies on cylindrical, unstiffened, and stiffened composite shells and curved unstiffened and stiffened composite panels were quite scarce (see for example [Lei and Cheng 1969; Johnson 1978; Tennyson et al. 1972; Card 1966; Knight and Starnes 1988; Sobel and Agarwal 1976]) at the starting time of the POSICOSS project [Zimmermann and Rolfes 2006] and later its successor, the COCOMAT project [Degenhardt et al. 2006].

In light of the above discussion, in compliance with the demand of the Fifth European Initiative Program to reduce weight without prejudice to cost and structural life in design of next generation aircraft¹, and in recognition of the advantages inherent to post buckled stiffened structures, it has been suggested to assess the introduction of buckled structures and allow buckling in operation of fuselage structures under ultimate load levels. This approach has been adopted and undertaken in the present experimental study, the POSICOSS project. It was particularly aimed at supporting the development of improved, fast and reliable procedures for analysis and simulation of postbuckling behavior of fiber reinforced composite circular cylindrical stiffened panels of future generation fuselage structures and their design.

Within the POSICOSS project, the Aerospace Structures Laboratory (ASL) at the Technion – Israel Institute of Technology performed an extensive test series on the above mentioned type laminated composite stringer-stiffened panels under axial compression, shear loading introduced by torsion, and combined axial compression and shear. The buckling and postbuckling behavior of these panels was recorded till their final collapse and the test results were analyzed and compared with calculated predictions. The first part of this test series, dealing with panels stiffened by blade type stringers (PSC1–PSC9), was summarized in [Abramovich et al. 2003]. The results of the tests with panels stiffened by blade type stringers or J-type stringers (BOX1–BOX4) were reported in [Abramovich et al. 2008]. These tests deal with two identical panels, combined together by two flat nonstiffened aluminum webs, to form a torsion box, thus enabling application of shear tractions through introduction of torsion, as well as combined axial compression and shear. The present manuscript aims at describing and evaluating the buckling

¹This design approach was summarized by the specialists of the European Community in the year 2000 under the name Vision 2020. It can be found at the EU website <http://cordis.europa.eu>

and postbuckling behavior of test results and relevant numerical studies of another set of four panels, AXIAL1–AXIAL4, stiffened by J-type stringers. Based on the results of the experimental study carried out within the framework of the POSICOSS project and reported in [Abramovich et al. 2003; 2008] and the present manuscript, and employing the “fast” tool of [Pevzner et al. 2008] to calculate the collapse loads of the axially compressed panels, design guidelines were formulated and presented.

2. Specimens and test setup

Within the framework of the POSICOSS effort, Israel Aircraft Industries (IAI) has designed and manufactured 21 Hexcel IM7 (12 K)/8552(33%) graphite-epoxy stringer-stiffened composite circular cylindrical panels using a cocuring process. Adhering to the goal of POSICOSS, namely low weight low cost structures, simple blade and J-type stringers were employed to stiffen the panels. The nominal radius of each panel was $R = 938$ mm and its total length $L = 720$ mm (which included two end loading pieces each 30 mm high). The nominal test length was $L_n = 680$ mm and the panel arc-length was $L_{at} = 680$ mm. The skin lay-up was quasiisotropic $(0^\circ, \pm 45^\circ, 90^\circ)_S$. Each layer had a nominal thickness of 0.125 mm. Eight of these panels were used to form 4 torsion boxes. Each box consisted of two curved panels that were connected together by two flat nonstiffened aluminum side plates. Two of the boxes comprised of panels with blade type stringers (Figure 1, top), one box had short-flange J-type stringers (Figure 1, middle) and the fourth box had long-flange J-type stringers (Figure 1, bottom). The dimensions and properties of the different configurations are shown in these figures. The results of the tests experienced with these boxes and corresponding calculations were reported in [Abramovich et al. 2008]. Nine out of these panels, PSC1–PSC9, stiffened by blade type stringers (Figure 1, top) were tested under axial compression and the relevant test results and calculations were reported in [Abramovich et al. 2003]. The last four panels designated as AXIAL1–AXIAL4 with J-type stringers, which are presented in the middle and bottom parts of Figure 1, were tested under axial compression. The test results and numerical studies associated with them are presented in what follows.

It is seen on Table 1 that the two panels AXIAL1 and AXIAL2 were stiffened by five stringers, while AXIAL3 and AXIAL4 had four stringers. The four panels were tested under axial compression only using the 50 tons MTS loading machine at the Aerospace Structures Laboratory, Faculty of Aerospace Engineering, Technion – Israel Institute of Technology, Haifa, Israel (Figure 2).

To visualize the development of displacements and buckling patterns, the Moiré technique has been applied [Abramovich et al. 2003; 2008]. To monitor and record the panel response due to application of axial compression, strain gages were bonded back-to-back, both on the skin and on the stringers. Lateral and axial LVDTs were used to record the out-of-plane deflections and the end-shortening (Figures 3 and 8).

3. Experimental results

The first panel tested was AXIAL1. First buckling occurred at 85 kN near gage #24 close to the upper loading end piece (Figure 3). Increase in axial compression caused the appearance of more buckling waves (see typical behavior in the first three parts of Figure 4). Typical strain gage readings (gages #27 and 28) at panel mid-height close to the panel supported unloaded edge (see Figure 3) are shown in Figure 5, top, where buckling is apparent at about 87 kN. For comparison, readings for strain gages

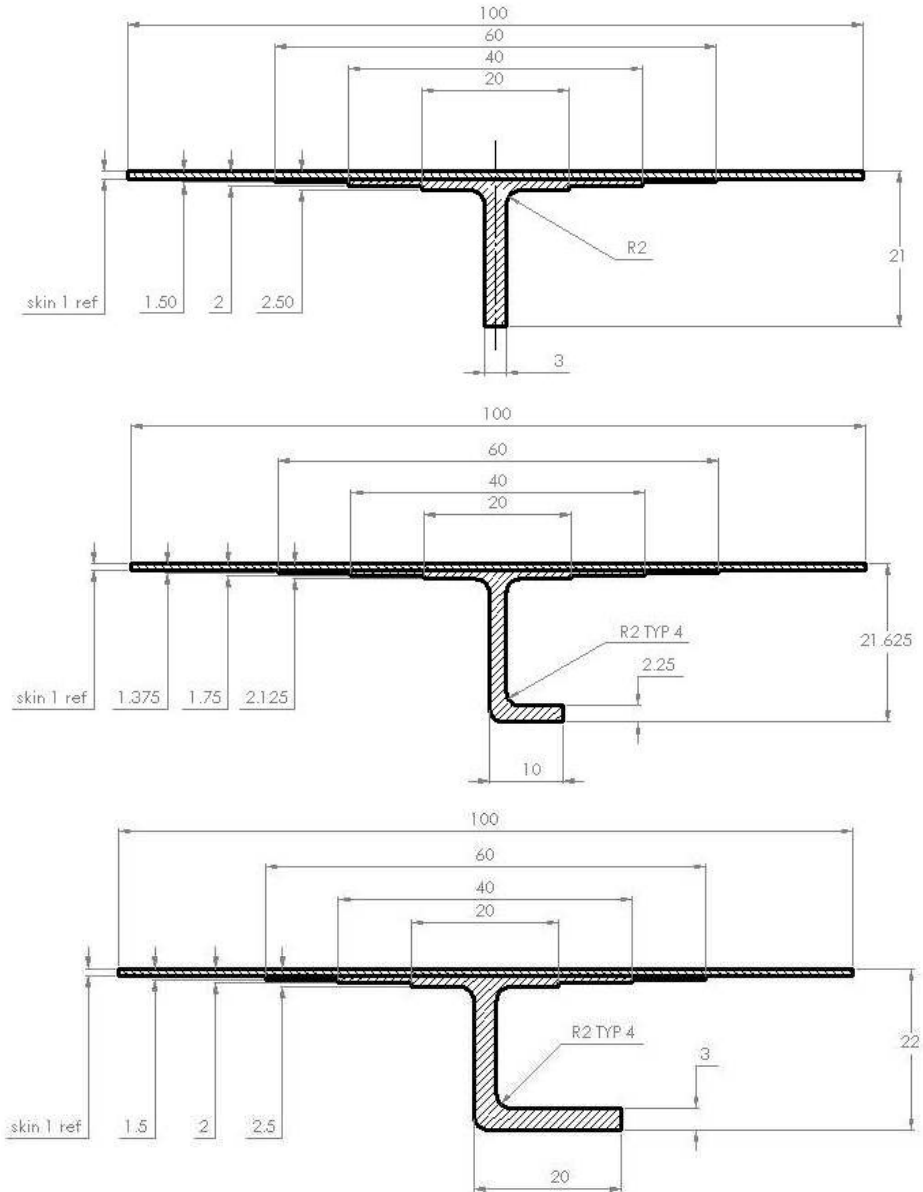


Figure 1. Dimensions, geometry and lay-ups of stiffeners. Top: Panels PSC1–PSC9 [Abramovich et al. 2003], BOX1 and BOX2 [Abramovich et al. 2008]. Middle: Panels AXIAL1, AXIAL2, and BOX 3 [Degenhardt et al. 2006]. Bottom: Panels AXIAL3, AXIAL4, and BOX4 [Abramovich et al. 2008].

#23 and 24 are displayed in Figure 5, bottom. The buckling is observed under slightly a lower load of about 80 kN. A fully developed pattern of buckling waves was obtained under 173 kN. The axial loading was increased till 229.88 kN, when a delamination occurred near strain gage #4 (Figure 3), between the skin and the stringer. Following the occurrence of the delamination, the load dropped to 224.5 kN. The

	Stringer type	
	Short-flange J	Long-flange J
Specimens	AXIAL1, AXIAL2	AXIAL3, AXIAL4
Total panel length	720 mm	720 mm
Free panel length	660 mm	660 mm
Radius	938 mm	938 mm
Arc length	680 mm	680 mm
Number of stringers	5	4
Stringer spacing	136 mm	174 mm
Laminate lay-up of skin	[0, 45, -45, 90] _s	[0, 45, -45, 90] _s
Laminate lay-up of stringer	[45, -45, 0] _{3s}	[45, -45, 0] _{3s}
Ply thickness	0.125 mm	0.125 mm
Type of stringer	J-stringer	J-stringer
Stringer height	20.5 mm	20.5 mm
Stringer feet width	60 mm	60 mm
Stringer flange width	10 mm	20 mm
E_{11}	147300 N/mm ²	147300 N/mm ²
E_{22}	11800 N/mm ²	11800 N/mm ²
G_{12}	6000 N/mm ²	6000 N/mm ²
ν_{12}	0.3	0.3

Table 1. Dimensions, lay-ups and mechanical properties used in calculations of load carrying capacity panels AXIAL1–AXIAL4 (present study).



Figure 2. Panel in loading machine setup used at the Aerospace Structures Laboratory (ASL).

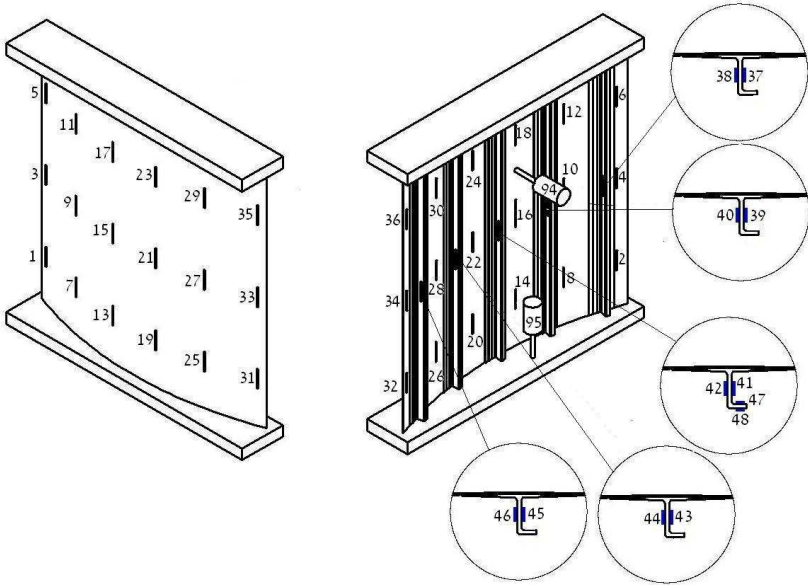


Figure 3. Locations of strain gages and axial and lateral LVDT's for panels AXIAL1 and AXIAL2.

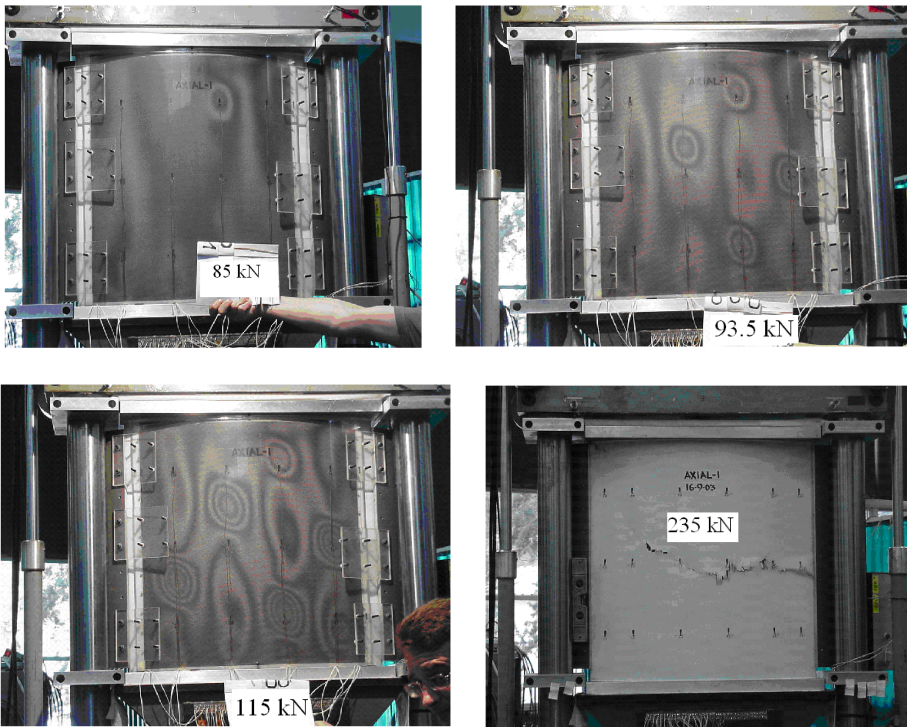


Figure 4. Panel AXIAL1: Development of the buckling pattern as function of axial compression under 85 kN, 93.5 kN, and 115 kN, and after collapse at 235 kN.

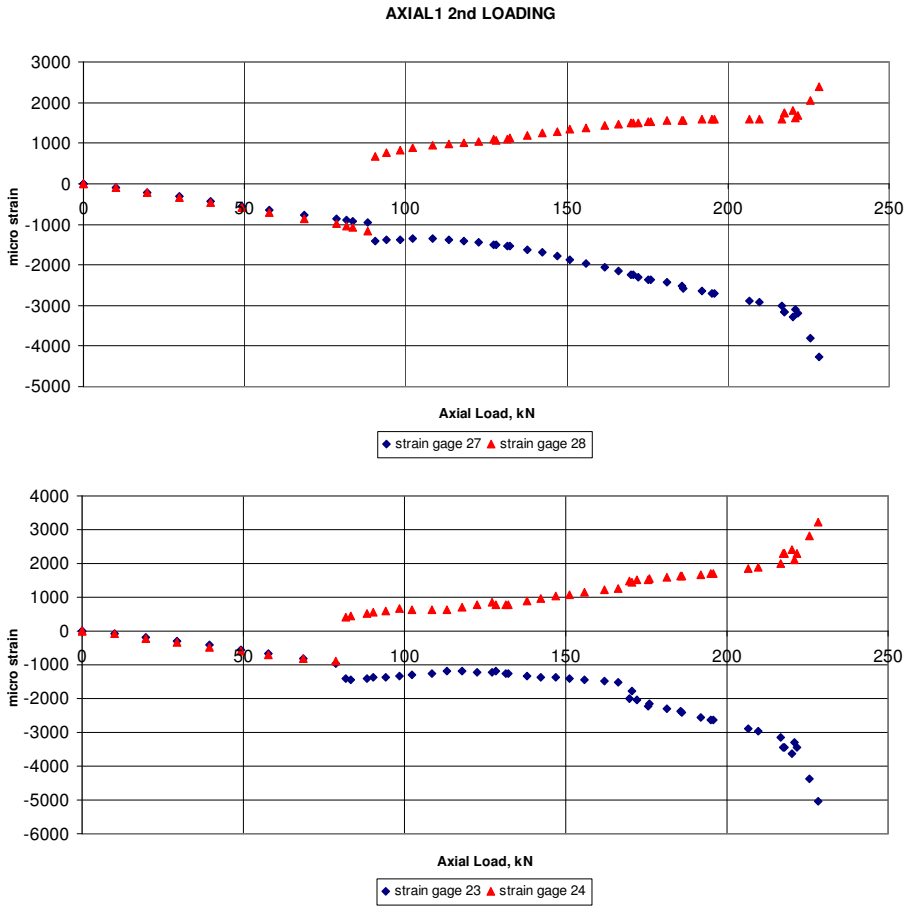


Figure 5. Panel AXIAL1: Strain gage readings versus axial compression.

load was again increased till the panel collapsed at 235.0 kN (Figure 4, bottom right). The collapse was accompanied by breakage of the stringers at mid panel height (across the width of the panel), including the skin.

The second panel tested was AXIAL2. First buckling occurred at 71 kN near gage #19 close to the lower loading end piece (Figure 3). Increase of the axial compression was accompanied by the appearance of more buckling waves (see typical behavior in the first three parts of Figure 6). Typical strain gage readings (gages #15 and 16; see Figure 3) are shown in Figure 7, where the buckling is observed at about 70 kN. The readings of strain gages #27 and 28, at panel mid-height close to the panel supported unloaded edges (see Figure 3), presented in Figure 9, is apparently less definitive. However, careful observation detects local buckling at about 70 kN, in very good agreement with gages 15 and 16. Nine fully developed buckling waves were obtained under 119 kN. The axial loading was increased till 230.5 kN, when collapse occurred (Figure 6, bottom right). Again, collapse was accompanied by breakage of the stringers at the middle of the panel (across the width of the panel), including the skin. Four of the five stringers were broken.



Figure 6. Panel AXIAL2: Development of the buckling pattern as a function of axial compression under 70 kN, 106 kN, 150 kN, and after collapse at 230.5 kN (bottom right).

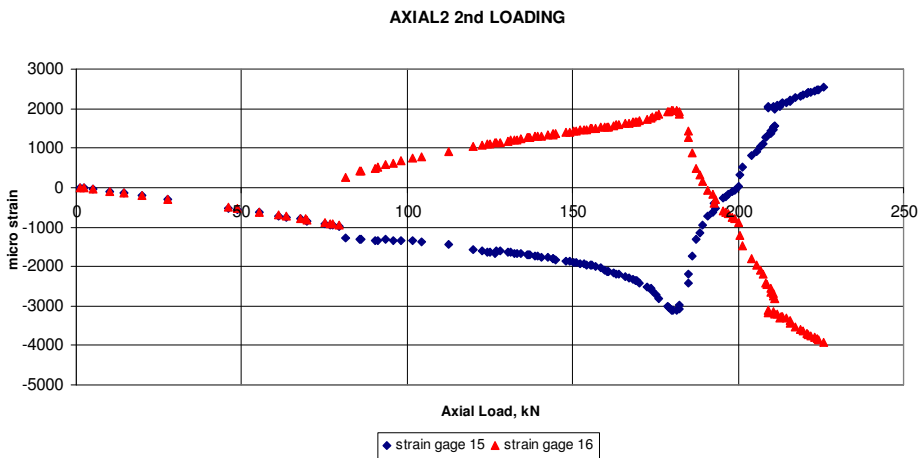


Figure 7a. Panel AXIAL2: Strain gage readings versus axial compression.

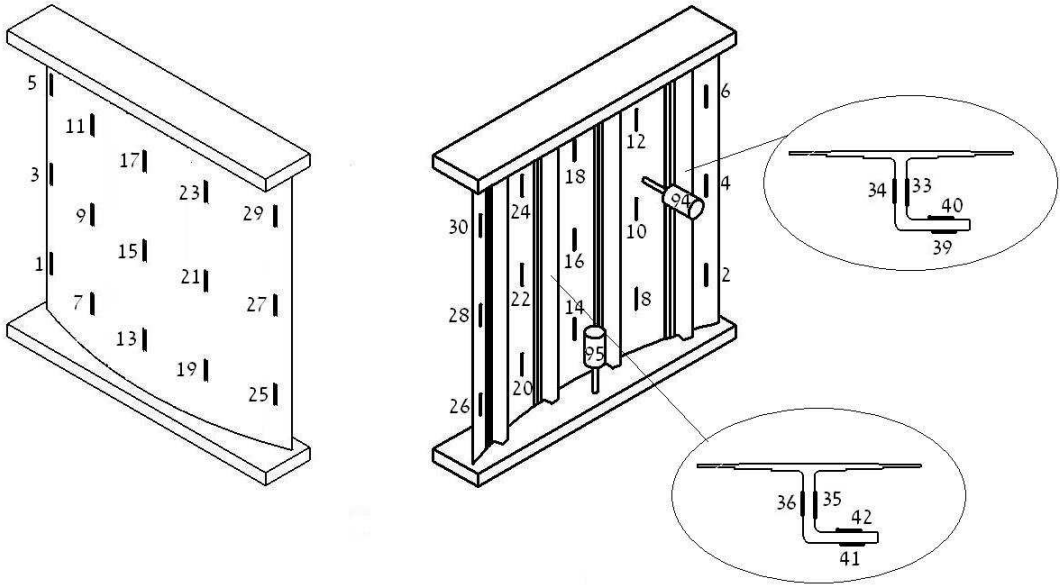


Figure 8. Locations of strain gages and the axial and lateral LVDT's for panels AXIAL3 and AXIAL4.

The third panel tested in the present test series was AXIAL3. It was stiffened by 4 large J-stringers. First buckling occurred at 60 kN with two local waves, one near gage #7, close to the lower loading ,and the other near gage #13, close to the lower loading piece (see [Figure 8](#)) and in the bay adjacent to strain gage #7 ([Figure 8](#)). Increasing the axial compression led to appearance of more buckling waves (see typical behavior in the first three parts of [Figure 9](#)).

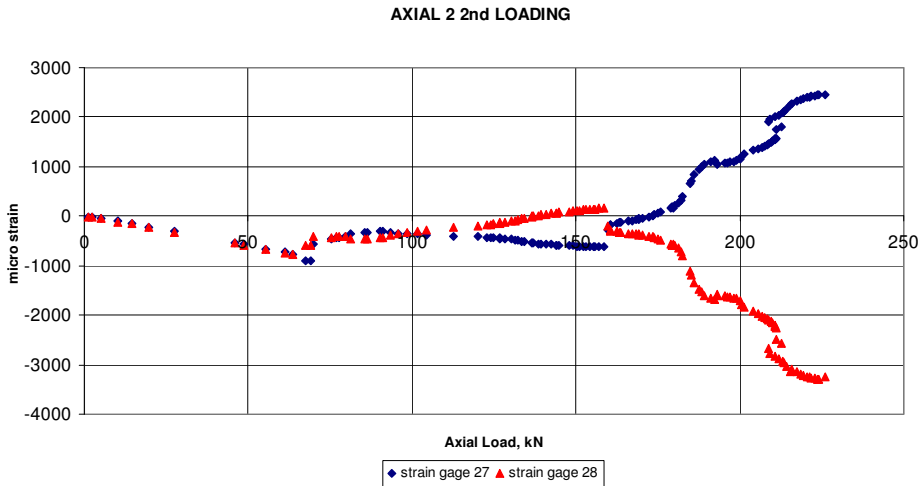


Figure 7b. Panel AXIAL2: Strain gage readings versus axial compression (continued).



Figure 9. Panel AXIAL3: Development of the buckling pattern as a function of axial compression under 65 kN, 125 kN, 190 kN, and after collapse at 295.42 kN (bottom right).

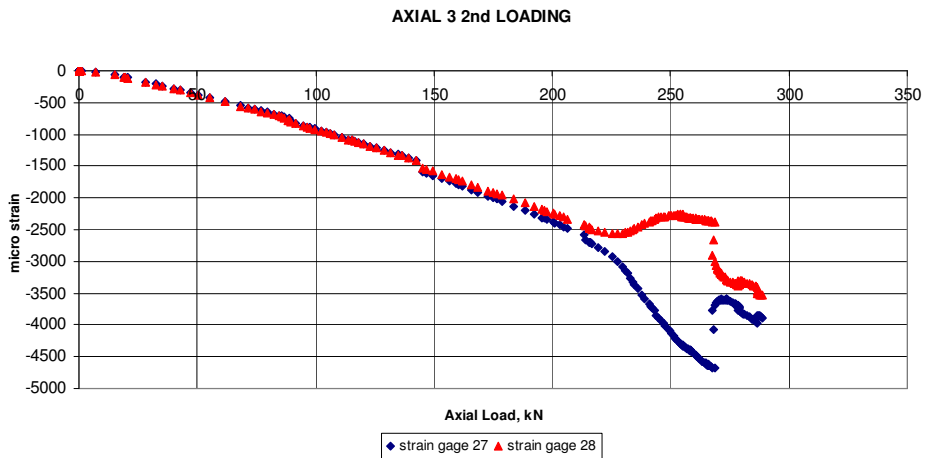


Figure 10. Panel AXIAL3: Strain gages (#27 and 28) readings versus axial compression.

Typical strain gage readings (gages #27 and 28) are shown in Figure 10, where the local buckling load is seen at about 225 kN. Seven fully developed buckling waves were obtained under 164 kN. At a load of 188 kN some noises were noticed, but without visible damage. Noises were also heard under 240 kN and at 280 kN, with the appearance of another wave. The load was further increased till collapse at 295.42 kN (see Figure 9, bottom right) accompanied by a very loud noise. This might indicate a violent failure as compared with a softer failure experienced with the previous panels where such noises were unnoticeable. The collapse was associated with breakage of the stringers in the middle height of the panel (across the width of the panel), separation between the stringers and the skin occurred and the load dropped to 246.0 kN. The panel was held under this load for some time, and then suddenly the load fell again, this time very significantly to 30.0 kN, followed by further damage of the skin.

The last panel tested within the present test series was AXIAL4, a twin of AXIAL3. First buckling occurred at 92.6 kN with two local waves, one near gage #7 close to the lower loading plate and the other near gage #15 at the middle of the panel (Figure 8). Increasing the axial compression caused the appearance of more buckling waves (see typical behavior in the first three parts of Figure 11). Typical strain gage readings (gages #3 and 4) are shown in Figure 12, where local buckling is apparent about

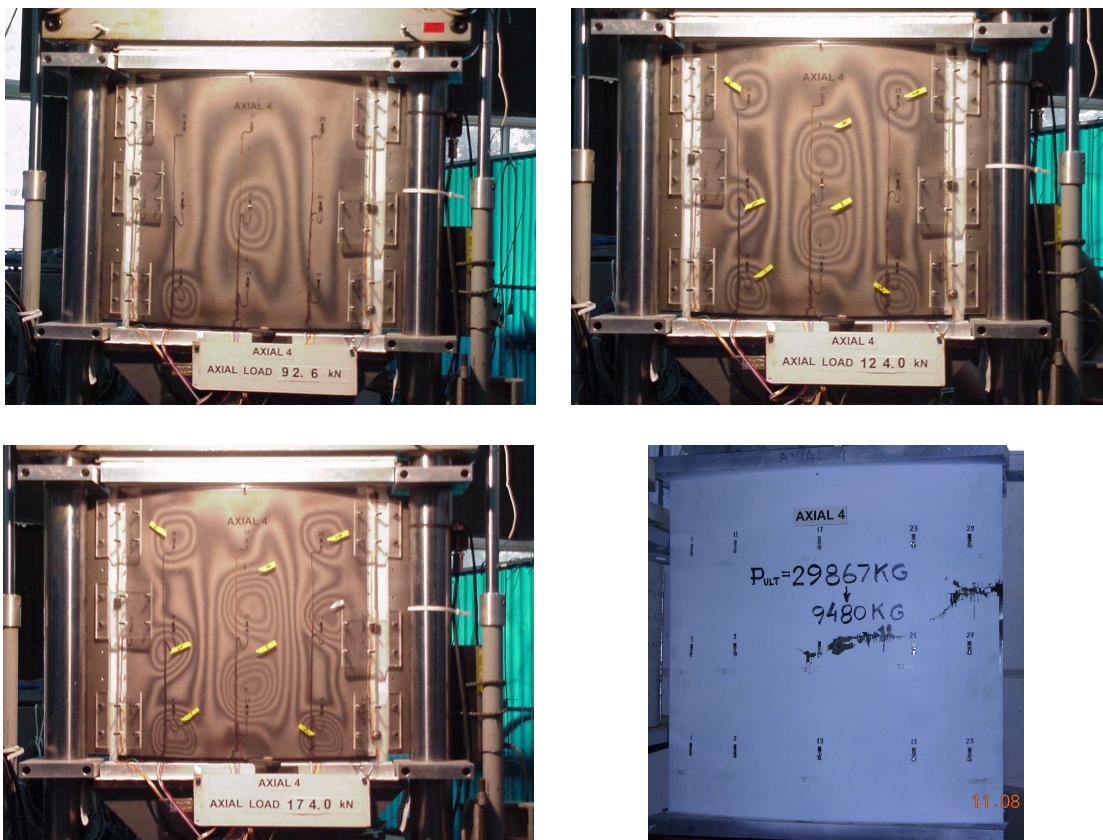


Figure 11. Panel AXIAL4: Development of the buckling pattern as a function of axial compression under 92.6 kN, 124 kN, 174 kN, and after collapse at 298.67 kN.

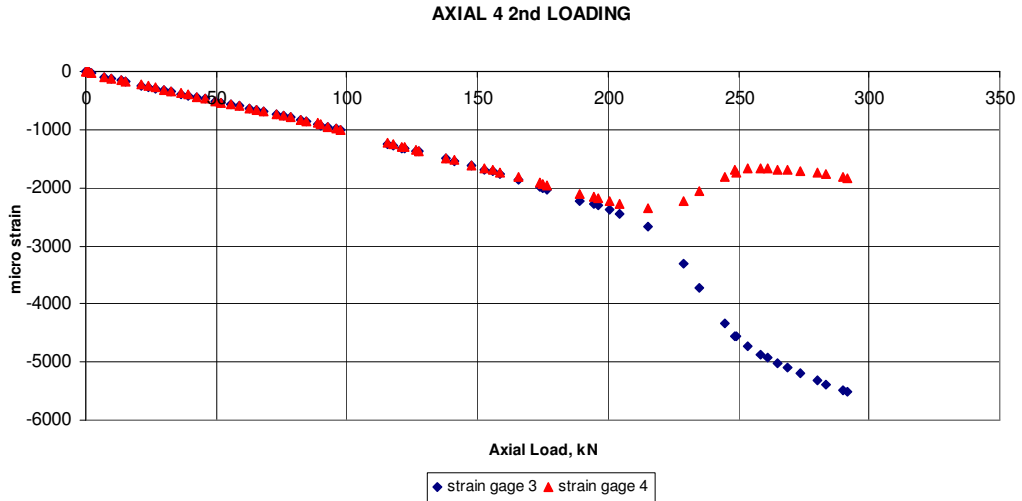


Figure 12. Panel AXIAL4: Strain gages (#3 and 4) readings versus axial compression.

220 kN. Eight fully developed buckling waves were obtained at 174 kN. The load was then increased till collapse of the panel under 298.67 kN (Figure 11, bottom right), again accompanied by a loud noise. The collapse was associated with breakage of the stringers at middle height of the panel (across the width of the panel) including the skin, separation between the stringers and the skin occurred and the axial load dropped to 94.8 kN.

4. Comparisons with calculations

The experimental results obtained in the tests are next compared with numerical analysis using the nonlinear version finite element ABAQUS Explicit [ABAQUS 1998] and the fast tool developed at the Technion, which is based on the effective width method adapted to deal with laminated composite circular cylindrical stringer-stiffened panels [Pevzner et al. 2008].² The results are summarized in Table 2 and Figure 13. (ABAQUS/Explicit is a dynamic analysis program; in this case a quasistatic solution is desired, so the prescribed displacement was increased slowly enough to eliminate any significant inertia effect. The displacement was increased linearly using a smooth amplitude function over a time step period of five to ten times longer than the natural period. The collapse load was found using the Riks method.)

The axial stiffness behavior is presented in Figure 13. It shows fair agreement with ABAQUS predictions in the cases of panels AXIAL1 and AXIAL2 (top half of the figure). It is apparent from this figure that the experimental stiffness of the panels observed in the tests is higher than the predicted one. Very good comparison between the experimental results and the calculated stiffness is found in the bottom half of the figure for panels AXIAL3 and AXIAL4.

Determination of the first experimental buckling load is not simple due to the fact that the appearance of a first single buckle during conduct of a test is usually assumed as the first buckling load, as compared with a fully developed pattern of buckles that is numerically predicted (see also detailed discussion in [Abramovich et al. 2008]). Because of this reason the fast tool also overestimates the first experimental

²The experimental results of panels AXIAL1–AXIAL4 in Table 1 of [Abramovich et al. 2003] were wrongly reported.

Panel	Experimental		ABAQUS		Effective width method	
	FBL [kN]	CL [kN]	FBL [kN]	CL [kN]	FBL [kN]	CL [kN]
AXIAL1	85.0	235.00	95.0	215.0	100.8	202.6
AXIAL2	71.0	230.50	95.0	215.0	100.8	202.6
AXIAL3	60.0	295.42	75.0	330.0	119.3	354.9
AXIAL4	92.6	298.67	75.0	330.0	119.3	354.9

Table 2. First buckling and collapse loads of panels AXIAL1–AXIAL4: numerical and experimental results using the effective width method [Abramovich et al. 2003] and ABAQUS code run under the assumption of quasistatic behavior. FBL = first buckling load; CL = collapse load.

buckling load by 18.6%–42% in case of the first two panels and by 28.8%–98.8% in case of the last two panels when compared with the experimental results in Table 2. The ABAQUS code overestimates the first buckling load by 11.8%–33.8% in the cases of panels AXIAL1 and AXIAL2. In the cases of panels AXIAL3 and AXIAL4 the code over predicts the first experimental buckling load of panel AXIAL3 by 25% and under predicts by 19% for panel AXIAL4. It appears from Table 2 that there is good agreement between ABAQUS predictions and the fast tool ones in the cases AXIAL1 and AXIAL2 whereas very significant differences exists between the predictions by ABAQUS and the fast tool in the cases AXIAL3 and AXIAL4. Furthermore, ABAQUS predictions are lower in all cases. It is also found from Table 2 that using the fast tool, the experimental collapse loads are under estimated by 12.1%–13.8% in the cases of panels AXIAL1 and AXIAL2 and overestimated by 18.8%–20.0% for panels AXIAL3 and AXIAL4. Employing the ABAQUS code, it is seen in Table 2 that the collapse loads are underestimated by 8.5%–6.7% for panels AXIAL1 and AXIAL2, and overestimated by 11.7%–10.5% in the cases AXIAL3 and AXIAL4.

Table 2 reveals good agreement between ABAQUS and the fast tool predictions of the collapse loads. In the cases AXIAL1 and AXIAL2, stiffeners with smaller flange, both codes predict collapse loads that are lower than those experienced in the tests. Also, ABAQUS predictions are higher than those yielded by the fast tool. On the other hand, in the cases AXIAL3 and AXIAL4, stiffeners with larger flanges, both codes predict higher collapse loads than those observed experimentally. However, in this case the ABAQUS predictions are lower than those obtained by the fast tool.

5. Formulation of design rules

Based on the experimental effort carried out within the framework of the POSICOSS project and reported in [Abramovich et al. 2003; 2008], as well as in the present study, and employing the fast tool [Pevzner et al. 2008], design guidelines are next formulated and presented (Table 3).

Figures 14 and 15 present the skin buckling and collapse loads of the tested panels versus the parameter $b/\sqrt{R \cdot s}$, a nondimensional parameter commonly employed in shell analysis to describe the influence of shell radius R , its thickness s , and the distance between the stringers b . It is evident from Figure 14 that as the distance b between two adjacent stringers increases, the first skin buckling load decreases. Panels PSC7–PSC9 demonstrated the highest buckling loads (the panels have 6 blade stringers each),

while as expected, panels AXIAL3 and AXIAL4, each with 4 J-type stringers, experienced the lowest values. The decrease in first buckling is much emphasized in the blade-stiffened panels, whereas in the case of the J-stiffened panels barely exists.

It appears from Figure 15 that either increasing the number of the stringers or their cross-section would yield a higher collapse load of a panel under axial compression. This is apparent for panels AXIAL3 and AXIAL4 (each having 4 J-type stringers with a wide flange) and panels PSC7–PSC9 (each having 6 blade stringers). The parameter $b/\sqrt{R \cdot s}$ does not influence the collapse load in a consistent manner, since there is more than one degree of freedom that can raise the collapse load. Nevertheless, it is observed that in the case of blade-stiffened panels, collapse decreases with increase in $b/\sqrt{R \cdot s}$, whereas the opposite is found for the J-stiffened panels.

The ratio of the collapse load to the corresponding first buckling load, the skin buckling, versus $b/\sqrt{R \cdot s}$ is presented in Figure 15, right. It is seen that the PSC panels, which are stiffened by blade type

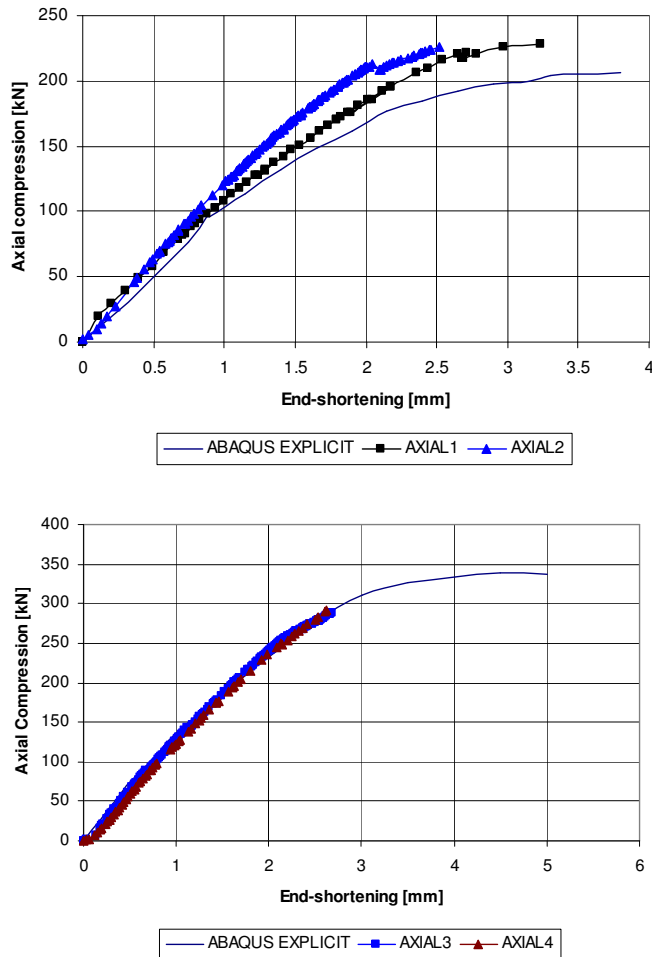


Figure 13. Axial compression versus end shortening: numerical and experimental results. Top: panels with with small J-stiffener; bottom: panels with large J-stiffener.

Panel	h_s [mm]	Stringers	FBL [kN]	CL [kN]	$\sum m_i$ [kg]	$(\sum m_i)/M$
AXIAL1	20.5	5 Small J	85.0	235.00	0.7656	0.516014
AXIAL2	20.5	5 Small J	71.0	230.50	0.7656	0.516014
AXIAL3	20.5	4 Big J	60.0	295.48	0.9293	0.564103
AXIAL4	20.5	4 Big J	92.6	298.67	0.9293	0.564103
BOX1 (panel A)	20	5 Blade	120.3	–	0.8448	0.540541
BOX1 (panel B)	20	5 Blade	134.0	–	0.8448	0.540541
BOX2 (panel A)	20	5 Blade	115.5	–	0.8448	0.540541
BOX2 (panel B)	20	5 Blade	–	–	0.8448	0.540541
BOX3 (panel A)	20.5	5 Small J	79.0	–	0.7656	0.516014
BOX3 (panel B)	20.5	5 Small J	100.0	–	0.7656	0.516014
BOX4 (panel A)	20.5	4 Big J	57.5	–	0.9293	0.564103
BOX4 (panel B)	20.5	4 Big J	57.5	–	0.9293	0.564103
PSC1	20	5 Blade	131.0	212.7	0.8448	0.54054
PSC2	20	5 Blade	150.0	227.0	0.8448	0.54054
PSC4	20	5 Blade	158.5	229.2	0.8448	0.54054
PSC3	15	5 Blade	136.0	162.0	0.6336	0.46875
PSC5	15	5 Blade	113.0	152.6	0.6336	0.46875
PSC6	15	5 Blade	126.0	140.0	0.6336	0.46875
PSC7	20	6 Blade	228.5	228.5	1.0138	0.58537
PSC8	20	6 Blade	240.0	240.0	1.0138	0.58537
PSC9	20	6 Blade	244.0	244.0	1.0138	0.58537

Table 3. First buckling loads (FBL) and collapse loads (CL) found in experimental tests reported in this article and in [Abramovich et al. 2003; 2008].

stringers, experience a consistent and almost constant ratio of 1.125–1.624, whereas the panels AXIAL1–AXIAL4, stiffened by J-type stringers, exhibit significantly higher ratios, in the range of 3.225–4.925, that increase significantly with increase in stiffener cross-section.

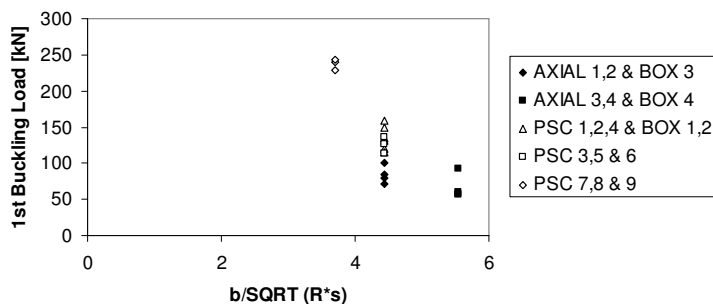


Figure 14. Skin buckling loads of the tested panels versus $b/\sqrt{R \cdot s}$. For all panels, $R = 938$ mm and $s = 1$ mm.

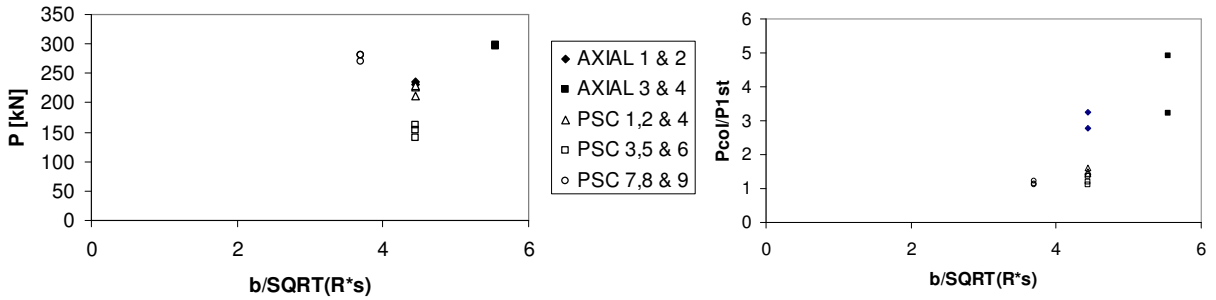


Figure 15. Collapse load (left) and ratio between collapse load and skin buckling load (right) for the tested panels versus $b/\sqrt{R \cdot s}$. Recall that $R = 938$ mm and $s = 1$ mm.

Considering from a design point of view the results presented in Figures 14 and 15 it may be concluded that the simpler and cheaper blade-stiffened panels are superior to the J-type ones when design is based on first skin buckling. However, this argument prevails provided these blade-stiffened panels exhibit a wide enough range to withstand postbuckling. The condition imposed is that the collapse loads corresponding to these type of panels meet the design requirement, namely an ultimate load equal at least to one and a half times the limit load, which according to the present adopted design approach equals the first buckling load. It appears from Table 3 and Figure 15, right, that only the blade stiffened panels PSC1, PSC2, and PSC4 barely meet this condition. On the other hand, when considering the postbuckling capacity of the J-stiffened panels it is apparent from the same table and figure that they possess a very wide range of postbuckling carrying capacity that is associated with collapse loads equal to many times their first skin buckling. It should be noted (see Table 3 and Figure 14), and as already mentioned, that their first skin buckling is low, as a matter of fact the lowest experienced among the panels tested in the present program. Obviously, these observations contradict the low weight low cost demands, the J-stiffened panels are relatively heavy and their manufacturing is complex and more expensive.

In the preceding figures the mass of the panels has been ignored. Obviously, their specific load carrying capacities are the appropriate measures to evaluate their performances. Hence, the panel mass is taken into account and the corresponding results are presented in Figures 16 and 17 for the skin and the collapse loads, respectively. Also in presenting the results, the stringer area is taken into account: instead of using the parameter $b/\sqrt{R \cdot s}$, we use $b/\sqrt{R \cdot s_1}$, where s_1 is defined as

$$s_1 = s \left(1 + \frac{A}{b \cdot s} \right). \quad (1)$$

Here A is the area of the stringer, b is the distance between stringers, and s is the skin thickness. This modified parameter is commonly used when dealing with stringer-stiffened shells and it is therefore also adopted for the present stringer-stiffened panels (it represents a shell/panel with an equivalent uniform skin where the stiffeners are smeared).

Considering the specific first buckling, the behavior observed earlier for both stiffener types in Figure 14 is again exhibited in Figure 16, the highest specific first skin buckling loads are associated with the minimum distance between stringers. As found in Figure 14, the blade stiffened panels (PSC7, PSC8,

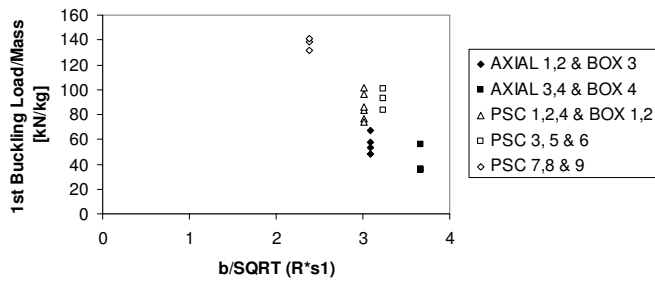


Figure 16. Specific skin buckling loads of the tested panels versus $b/\sqrt{R} \cdot s_1$, where s_1 is given by Equation (1).

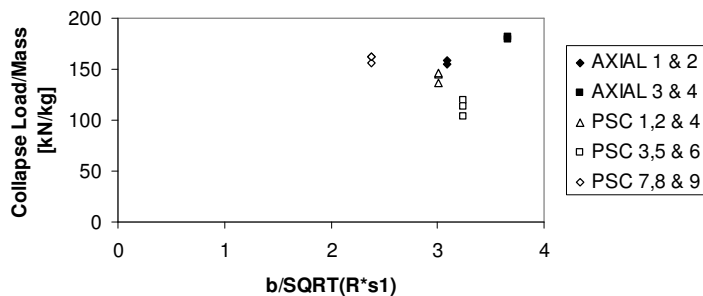


Figure 17. Specific collapse loads of the tested panels versus $b/\sqrt{R} \cdot s_1$.

and PSC9) yield the higher specific first buckling loads. The detailed observations and results shown in Figure 16 are similar to those pertinent to Figure 14; thus the discussion of Figure 14 applies to Figure 16 as well.

Figure 17 shows that when considering specific collapse loads versus $b/\sqrt{R} \cdot s_1$, as in Figure 15, the panels with either the larger stiffeners cross section (AXIAL3 and AXIAL4) or with the larger number of stringers (6 stringers, panels PSC7–PSC9) yield the higher specific collapse values. The worst observation was experienced with panels PSC3, PSC5, and PSC6 (5 stringers with a height of 15 mm). Increasing the blade stiffeners height to $h = 20$ mm (panel PSC1, PSC2, and PSC4) increased the panel specific collapse load, almost to that corresponding to panels AXIAL1 and AXIAL2. It is observed in Figure 17 that the specific collapse loads of panels AXIAL1 and AXIAL2 are almost identical with those of panels PSC7–PSC9. Hence, the specific collapse loads of panels PSC1, PSC2, and PSC4 are quite comparable with those of PSC7–PSC9. Consequently, from a design point of view the simpler and cheaper blade-stiffened configuration presents and provides a much more attractive and favorable configuration for sustaining a prescribed specific collapse load. However, as already discussed above, this holds only when the design meets the required ratio between the limit and ultimate loads.

Next a parametric investigation was performed to calculate the collapse loads of various configurations of panels stiffened by blade and small J-type stringers using the fast tool [Pevzner et al. 2008]. Two J-types of stringers were used, one with 18 layers (thickness of 2.25 mm), and a small flange of 10 mm long and the other having 24 layers (thickness of 3 mm) and a small flange of 10 mm. The height of the stringers was 20.5 mm. The blade type stringers had 24 layers (thickness of 3.0 mm) and two heights 15

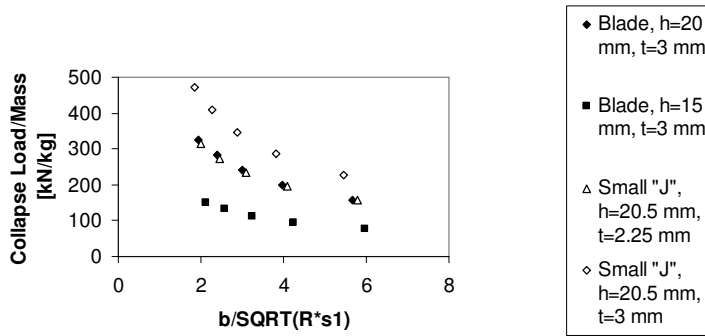


Figure 18. Specific collapse loads predicted by the effective width method for the tested panels, versus $b/\sqrt{R \cdot s_1}$.

and 20 mm. The distances between the stringers, b , were: 226.67, 170.0, 136.0, 113.3, and 97.1 mm, corresponding to 3, 4, 5, 6, and 7 stringers per panel, respectively.

The calculated results are presented in [Figure 18](#). It is observed in this figure that a relatively small increase in J-stiffener dimensions increases significantly their specific collapse load. On the other hand, a more noticeable change in blade stiffeners dimensions is required to achieve a noticeable increase in their specific collapse load capacity. However, by introducing changes in the blades height the specific collapse load capacities of the blade-stiffened panels become equal to those corresponding to the J-stiffened ones. As already discussed above, this makes the blade-stiffened panels more attractive and preferable from a design point of view.

6. Derivation of design guidelines

- Results of analyses show that the influence of panel length on skin buckling load can be neglected within the design space ($400 \text{ mm} \leq l \leq 800 \text{ mm}$).³
- The influence of panel length on the collapse load is significant as long as local instability does not coincide with general instability. Like in a column, the collapse load significantly decreases with increase in panel length. There is a significant influence of the panel length on the ratio of its collapse load to its skin buckling load.
- Assuming that the total length of the structure is fixed, an increase of the collapse load can be achieved by introduction of additional frames. This results in a corresponding increase of the weight of the structure.
- In general, decrease in the stringer spacing leads to increase of skin buckling as well as of the collapse load. Assuming that the total arc-length of a structure is fixed, a decrease in the stringer spacing means more stringers and increase of the collapse load. In this case the weight of the

³Not all of the design guidelines presented herein stem directly from the results presented in the present manuscript but were derived to reflect all the partners' results of the POSICOSS project to enable a wider use. See [[Zimmermann and Rolfes 2006](#); [Bisagni and Cordisco 2006](#); [Zimmermann et al. 2006](#); [Lanzi and Giavotto 2006](#); [Möcker and Reimerdes 2006](#); [Rikards et al. 2006](#)].

structure is increased in proportion to the increase of the number of stiffeners but not the specific collapse load. Regarding the influence of the stringer spacing on the ratio of collapse load to first skin buckling load, no general tendency can be observed from the results of the experimental and parametric studies. Based on the experimental observations reported in Figure 15, right, it appears that almost no effect on the ratio was experienced with blade stiffened panels, whereas a very strong effect was found in the case of J-stiffened panels.

- As a general result of analyses it can be pointed out that skin buckling load per unit length is increased when the panel radius is reduced. Regarding the influence of the radius on the collapse load, an increase of the collapse load was found when reducing the radius. However, in most designs the radius will be fixed and thus the influences of this parameter cannot be exploited to improve the design.
- As a common result of analyses one can summarize that the skin buckling load per unit length is increased when the stringer geometry dimensions are increased. This holds till one reaches values of dimensions of the stringer for which it represents a clamped boundary condition. Therefore, it is not recommended to increase the dimensions of the stringer beyond this value. The collapse load of blade-stiffened panels increases when the stringer height is increased from $h = 14$ mm to $h = 20$ mm, but further increase from $h = 20$ mm to $h = 30$ mm leads to reduction of the collapse load. This is caused by a change of the type of instability experienced when increasing the stringer height. While buckling of the stringers in bending leads to the collapse of the $h = 20$ mm stringers, collapse is caused by torsional buckling in case of the $h = 30$ mm stringers. Furthermore, it should be remembered in design of blade-stiffened panels that an increase of stringer height may lead to decrease of the local buckling load of the stringer. Therefore, it has to be ensured that local buckling of the stringer is avoided before global buckling of the panel. Within the design space that was defined for the present parametric studies this problem was not encountered, but it might be crucial in the case of thin and long stringer blades. Regarding the panel weight, it can be pointed out that increase of the stringer dimensions leads to a relatively small increase (proportional to the additional weight) of the panel weight, provided that the type of the stringer is kept constant.
- Considering the specific collapse load (the ratio of the collapse load over the mass of the panel) versus the modified parameter $b/\sqrt{R * s_1}$ presents a more realistic presentation, because it takes into consideration the cross-section of the stringers, or rather the equivalent skin thickness of the panel.
- There is no advantage in application of J-type stringers over the common practice blade types. There is no gain in local buckling, whereas the significant increase in the collapse load of J-stiffened panels cannot be exploited and thus there is a considerable weight penalty. Due to manufacturing and cost constraints, the blade-stiffener would be the ideal and preferred stringer to stiffen a curved panel.

7. Conclusions

Test results on curved composite panels stiffened by J-stringers were presented and discussed. Test results were compared with predictions yielded by an in-house developed code and the commercial FE code ABAQUS, as well as with test results on blade-stiffened panels that were reported earlier. Design

guidelines have been formulated based on the Technion experimental results and the fast in-house software tool developed within the POSICOSS program. Test results and calculations have demonstrated that from a design point of view, weight reduction, and cost, blade type stringers are more favorable. The design guidelines would allow the designer to better choose a panel configuration to meet prescribed design requirements with various optimisations leading to a higher specific load capacity.

Acknowledgment

We thank Mr. A. Grunwald and Mrs. R. Yaffe, Aerospace Structures Laboratory, Technion, Haifa, Israel for their exceptional assistance in setting up the tests and dedicated assistance in performing them. We also thank Dr. P. Pevzner of the same laboratory for his helpful assistance in carrying out the numerical calculations.

References

- [ABAQUS 1998] *ABAQUS/Explicit: keywords version*, Hibbitt, Karlsson and Sorensen, Pawtucket, RI, 1998.
- [Abramovich et al. 2003] H. Abramovich, A. Grunwald, P. Pevzner, T. Weller, A. David, G. Ghilai, A. Green, and N. Pekker, “Experiments on axial compression postbuckling behavior of stiffened cylindrical composite panels”, in *44th AIAA/ASME/ASCE/AHS/ASC Structures, Structural Dynamics, and Materials Conference* (Norfolk, VA, 2003), AIAA, Reston, VA, 2003. Paper #2003-1793.
- [Abramovich et al. 2008] H. Abramovich, T. Weller, and C. Bisagni, “Buckling behavior of composite laminated stiffened panels under combined shear-axial compression”, *J. Aircraft* **45**:2 (2008), 402–413.
- [Bisagni and Cordisco 2006] C. Bisagni and P. Cordisco, “Post-buckling and collapse experiments of stiffened composite cylindrical shells subjected to axial loading and torque”, *Compos. Struct.* **73**:2 (2006), 138–149.
- [Bucci and Mercuria 1992] A. Bucci and U. Mercuria, “CFRP stiffened-panels under compression”, pp. 12.1–12.14 in *The utilization of advanced composites in military aircraft* (San Diego, CA, 1991), AGARD Report **785**, AGARD/NATO, Neuilly-sur-Seine, 1992.
- [Card 1966] M. F. Card, “Experiments to determine the strength of filament-wound cylinders loaded in axial compression”, Technical Note TN D-3522, NASA, Washington, DC, 1966, Available at <http://hdl.handle.net/2060/19660023039>.
- [Degenhardt et al. 2006] R. Degenhardt, R. Rolfes, R. Zimmermann, and K. Rohwer, “COCOMAT: improved material exploitation at safe design of composite airframe structures by accurate simulation of collapse”, *Compos. Struct.* **73**:2 (2006), 175–178.
- [Frostig et al. 1991] Y. Frostig, G. Siton, A. Segal, I. Sheinman, and T. Weller, “Postbuckling behavior of laminated composite stiffeners and stiffened panels under cyclic loading”, *J. Aircraft* **28**:7 (1991), 471–480.
- [Hutchinson and Koiter 1970] J. W. Hutchinson and W. T. Koiter, “Postbuckling theory”, *Appl. Mech. Rev. (ASME)* **23** (1970), 1353–1366.
- [Johnson 1978] R. Johnson, Jr., “Design and fabrication of a ring-stiffened graphite-epoxy corrugated cylindrical shell”, Contractor Report CR-3026, NASA, Washington, DC, 1978, Available at <http://hdl.handle.net/2060/19780023522>.
- [Knight and Starnes 1988] N. F. Knight, Jr. and J. H. Starnes, Jr., “Postbuckling behavior of selected curved stiffened graphite-epoxy panels loaded in axial compression”, *AIAA J.* **26**:3 (1988), 344–352.
- [Lanzi and Giavotto 2006] L. Lanzi and V. Giavotto, “Post-buckling optimization of composite stiffened panels: computations and experiments”, *Compos. Struct.* **73**:2 (2006), 208–220.
- [Lei and Cheng 1969] M. M. Lei and S. Cheng, “Buckling of composite and homogeneous isotropic cylindrical shells under axial and radial loading”, *J. Appl. Mech. (ASME)* **36** (1969), 791–798.
- [Lilico et al. 2002] M. Lilico, R. Butler, G. W. Hunt, A. Watson, D. Kennedy, and F. W. Williams, “Analysis and testing of a postbuckled stiffened panel”, *AIAA J.* **40**:5 (2002), 996–1000.

- [Möcker and Reimerdes 2006] T. Möcker and H.-G. Reimerdes, “Postbuckling simulation of curved stiffened composite panels by the use of strip elements”, *Compos. Struct.* **73**:2 (2006), 237–243.
- [Pevzner et al. 2008] P. Pevzner, H. Abramovich, and T. Weller, “Calculation of the collapse load of an axially compressed laminated composite stringer-stiffened curved panel: an engineering approach”, *Compos. Struct.* **83** (2008), 341–353.
- [Rikards et al. 2006] R. Rikards, H. Abramovich, K. Kalnins, and J. Auzins, “Surrogate modeling in design optimization of stiffened composite shells”, *Compos. Struct.* **73**:2 (2006), 244–251.
- [Romeo 1986] G. Romeo, “Experimental investigation on advanced composite-stiffened structures under uniaxial compression and bending”, *AIAA J.* **24**:11 (1986), 1823–1830.
- [Segal et al. 1987] A. Segal, G. Sison, and T. Weller, “Durability of graphite-epoxy stiffened panels under cyclic postbuckling compression loading”, pp. 5.69–5.78 in *ICCM and ECCM: 6th International Conference on Composite Materials and 2nd European Conference on Composite Materials* (London, 1987), edited by F. L. Matthews et al., Elsevier, London, 1987.
- [Singer et al. 2002] J. Singer, J. Arboz, and T. Weller, *Buckling experiments: experimental methods in buckling of thin-walled structures*, vol. 2, Wiley, New York, 2002.
- [Sobel and Agarwal 1976] L. H. Sobel and B. L. Agarwal, “Buckling of eccentrically stringer-stiffened cylindrical panels under axial compression”, *Comput. Struct.* **6**:3 (1976), 193–198.
- [Starnes et al. 1985] J. H. Starnes, Jr., N. F. Knight, Jr., and M. Rouse, “Postbuckling behavior of selected flat stiffened graphite-epoxy panels loaded in compression”, *AIAA J.* **23**:8 (1985), 1236–1246.
- [Tennyson et al. 1972] R. C. Tennyson, D. B. Muggeridge, K. H. Chan, and N. S. Khot, “Buckling of fiber-reinforced circular cylinders under axial compression”, Technical Report TR-72-102, Air Force Flight Dynamics Laboratory, Wright-Patterson Air Force Base, OH, 1972.
- [Vestergren and Knutsson 1978] P. Vestergren and L. Knutsson, “Theoretical and experimental investigation of the buckling and postbuckling characteristics of flat carbon fiber reinforced plastic (CFRP) panels subjected to compression or shear loading”, pp. 217–223 in *Proceedings of the 11th Congress of the International Council of the Aeronautical Sciences (ICAS)* (Lisbon, 1978), edited by J. Singer and R. Staufienbiel, Mirandela, Lisbon, 1978.
- [Zimmermann and Rolfes 2006] R. Zimmermann and R. Rolfes, “POSSICOSS: improved postbuckling simulation for design of fibre composite stiffened fuselage structures”, *Compos. Struct.* **73**:2 (2006), 171–174.
- [Zimmermann et al. 2006] R. Zimmermann, H. Klein, and A. Kling, “Buckling and postbuckling of stringer stiffened fibre composite curved panels: tests and computations”, *Compos. Struct.* **73**:2 (2006), 150–161.

Received 15 Nov 2008. Revised 23 Feb 2009. Accepted 24 Feb 2009.

HAIM ABRAMOVICH: haim@aerodyne.technion.ac.il

Faculty of Aerospace Engineering, Technion – Israel Institute of Technology, 32000 Haifa, Israel
<http://ae-www.technion.ac.il/>

TANCHUM WELLER: tanchum@aerodyne.technion.ac.il

Faculty of Aerospace Engineering, Technion – Israel Institute of Technology, 32000 Haifa, Israel
<http://ae-www.technion.ac.il/>

EFFECT OF ELASTIC OR SHAPE MEMORY ALLOY PARTICLES ON THE PROPERTIES OF FIBER-REINFORCED COMPOSITES

VICTOR BIRMAN

The paper presents a comprehensive formulation for the analysis of the stiffness and strength of fiber-reinforced composites with the matrix enhanced by adding elastic or shape memory alloy (SMA) spheroidal particles. The micromechanical model used to evaluate the stiffness tensor of the matrix with embedded particles is based on the Benveniste version of the Mori–Tanaka theory. In the case of a superelastic shape memory alloy particulate matrix, the stiffness of the particles depends on the martensitic fraction that is in turn affected by the state of stress within the particle. In this case an exact solution for the stiffness tensor of the composite material with elastic fibers and matrix and embedded SMA particles is developed combining the recent macromechanical solution for multi-phase composites with the inverse method of the analysis of SMA. In the particular case, this solution results in explicit formulae for the homogeneous material constants of a SMA particulate material subjected to axial loading. Upon the completion of the stiffness analysis the strengths of a fiber-reinforced material with the matrix containing elastic or SMA particles can be analyzed using the Eshelby solution for the stresses. As follows from numerical examples, elastic spherical particles added to the matrix of a fiber-reinforced composite significantly improve the transverse strength and stiffness of the material, even if the volume fraction of such particles is relatively small. The effect of elastic particles on the longitudinal strength and stiffness is less pronounced. It is also illustrated that the stress-induced transformation of superelastic SMA particles results in significant changes of the properties of SMA particulate composites.

1. Introduction

The optimization of composite structures is usually concerned with either increasing their load-carrying capacity without additional weight or reducing weight without sacrificing the load-carrying capacity. In both situations it is necessary to enhance the stiffness and strength of the structure. The straightforward approach to achieving enhanced properties is using a stiffer high-strength material. An alternative approach employs spatially tailored structures with a variable stiffness. Functionally graded structures where the composition of the constituent phases varies in one direction only, that is, through the thickness, have also been extensively studied [Birman and Byrd 2007]. The analysis in the present paper is concerned with improving the performance of composite structures by embedding stiff high-strength elastic or SMA inclusions (particles or fibers) within the matrix of the fiber-reinforced material. The benefits of this approach for the stiffness of fibrous composite materials have recently been demonstrated by Genin and Birman [2009], who considered the effect of spherical glass particles on static and dynamic response of glass/epoxy composites.

Keywords: micromechanics, shape memory alloy composites, stiffness tensor, strength.

This study has been funded by the US Army Research Office under contract W911NF-08-1-0119 (Bruce LaMattina, Project Manager).

Embedding shape memory alloy fibers within a composite material can offer numerous advantages, including improved strength and stiffness, higher buckling loads and desirable dynamic properties. Extensive research on SMA fiber-reinforced composites with fibers that are either bonded to the substrate or embedded within resin sleeves has been reviewed in literature; see, for example, [Birman 1997]. The advantages associated with using SMA are realized through their martensitic and reverse transformations that are triggered by variations of temperature or applied stresses. In particular, the stress-induced transformation of a superelastic SMA represents an interest due to a large hysteresis loop. Accordingly, SMA materials and composites are considered for vibration control in aerospace and civil engineering applications, for example in [Lagoudas 2008; McCormick et al. 2006; Cardone et al. 2004].

The present paper illustrates a two-step micromechanical model for the stiffness and strength analysis of a fiber-reinforced material with particulate elastic or SMA matrix. The properties of the particulate matrix determined at the first step of the analysis are subsequently used to evaluate those of the fiber-reinforced material with the homogeneous matrix. As follows from numerical examples, elastic particles embedded in the matrix can significantly increase both the stiffness and the strength of fiber-reinforced materials.

In addition to the analysis of composites with elastic particulate matrices, the paper presents an exact solution for the strength and stiffness of a fiber-reinforced composite material incorporating superelastic SMA inclusions. The exact solution for the stiffness tensor is obtained by the Genin–Birman generalization of the Benveniste method combined with the three-dimensional formulation for a superelastic SMA. Contrary to available three-dimensional solutions, the present method does not involve assumptions on the law that relates the rate of change in the transformation strain to the rate of change of the martensitic fraction. Instead, the analysis of the matrix with SMA inclusions utilizes the “inverse” method. According to this method, the stresses in SMA inclusions, the applied stresses and the tensor of stiffness of the homogeneous material are determined exactly for the assumed value of the martensitic fraction. Although the inverse solution does not yield the transformation strain in SMA inclusions, this information is not necessary to determine the composite stress-strain relationships and the stiffness tensor. Once the strength and stiffness of a SMA-particulate matrix have been determined, the strength of a fiber-reinforced, SMA-particulate matrix composite can be obtained using standard solutions shown in the paper.

The analysis of SMA reinforced composites developed in the paper is applied to the case of a SMA particulate material. The explicit closed-form solution developed for this case elucidates significant variations in the stiffness of the composite as a result of applied stresses that cause SMA phase transformation.

2. Micromechanics of a fiber-reinforced, particulate-matrix material with elastic constituents

Numerous methodologies of the micromechanical stiffness analysis of composites with inclusions of an arbitrary shape include the Mori–Tanaka model, the double-inclusion method, the models of Ponte Castaneda and Willis, the Kuster–Toksoz model, etc. The bounds for the stiffness tensor have been suggested by Hashin and Shtrikman, Beran, Molyneux and McCoy, Gibiansky and Torquato, etc. A comprehensive review of these techniques is outside the scope of this paper; see for example [Tucker and Liang 1999; Hu and Weng 2000; Torquato 2001; Milton 2002].

Kanaun and Jeulin [2001] and Genin and Birman [2009] proposed the solution for the stiffness tensor of a multi-phase material that is applicable to fiber-reinforced particulate composites. In particular, the latter team found that the stiffness of a cross ply glass/epoxy material evaluated using their approach was within the strict three-point bounds as long as the volume fractions of spherical inclusions and fibers remained relatively small. In the present paper the strength and stiffness analyses of a three-phase reinforced material are conducted in two steps. We begin with the Benveniste version of the Mori–Tanaka solution to specify the stiffness tensor of a particulate matrix that is subsequently applied to evaluate the stiffness of a fiber-reinforced, particulate-matrix material. The strength of the matrix with inclusions (particles) is determined using the heterogeneous matrix stiffness data. In turn, knowing the strength of the matrix enables us to predict the strength of the fiber-reinforced material with a particulate matrix. The principal reason for the two-step stiffness analysis, instead of using the solution for materials with multiple inclusion classes [Kanaun and Jeulin 2001; Genin and Birman 2009], is that the stiffness of the particulate matrix is needed for the subsequent strength analysis of the composite.

2.1. Two-step stiffness analysis. Consider a fiber-reinforced material where the matrix contains uniformly distributed and uniaxially aligned spheroidal inclusions (they are referred to as particles, though the approach could be applied to the case where the inclusions represent short or continuous fibers as long as we use the appropriate Eshelby tensor). It is assumed throughout the paper that the matrix is perfectly bonded to both fibers and particles. The volume fraction of the particles within the matrix remains below 30%, so that the Mori–Tanaka approach is accurate [Genin and Birman 2009]. Then the tensor of stiffness of the particulate matrix can be obtained following [Benveniste 1987] in the form

$$\mathbf{L}_{\text{pm}} = \mathbf{L}_1 + f'_2(\mathbf{L}_2 - \mathbf{L}_1)\mathbf{T}_2(f'_1\mathbf{I} + f'_2\mathbf{T}_2)^{-1}, \quad (1)$$

where the subscripts 1 and 2 identify the matrix and particles, respectively, \mathbf{L}_i is the stiffness tensor of the corresponding phase, \mathbf{I} is the fourth-order identity tensor, f'_i is the volume fraction of the i -th phase, and the prime indicates that these volume fractions are evaluated within the particulate matrix, that is, $f'_1 + f'_2 = 1$. Furthermore,

$$\mathbf{T}_2 = [\mathbf{I} + \mathbf{S}_2\mathbf{L}_1^{-1}(\mathbf{L}_2 - \mathbf{L}_1)]^{-1} \quad (2)$$

is the coefficient tensor in the relation between the strain tensors in the matrix and in the particles

$$\boldsymbol{\varepsilon}_2 = \mathbf{T}_2\boldsymbol{\varepsilon}_1. \quad (3)$$

The elements of the Eshelby tensor \mathbf{S}_2 were obtained for spheroidal inclusions dependent on the aspect ratio by Tandon and Weng [1986].

It is known that the Mori–Tanaka solution for the bulk, elasticity and shear moduli of particulate composites coincides with the Hashin–Shtrikman lower bound. At a high volume fraction of particles the Mori–Tanaka prediction deviates from numerical (FEA) and experimental results. However, the accuracy of the analysis at high particle volume fractions can be improved using the incremental particle-addition approach suggested in the Appendix.

Once the stiffness tensor of the particulate matrix has been evaluated, it is possible to treat the matrix as a homogeneous medium that is isotropic if the particles are isotropic and spherical or if they are randomly oriented. Subsequently, we can apply a similar homogenization procedure to a unidirectional

fiber-reinforced material considering fibers as aligned inclusions with an infinite aspect ratio. Accordingly, the stiffness tensor of such fiber-reinforced, particulate-matrix material is

$$\mathbf{L} = \mathbf{L}_{\text{pm}} + f_3(\mathbf{L}_3 - \mathbf{L}_{\text{pm}})\mathbf{T}_3(f_{\text{pm}}\mathbf{I} + f_3\mathbf{T}_3)^{-1}, \quad (4)$$

where f_3 and f_{pm} are the volume fractions of fibers and particulate matrix, respectively, $f_{\text{pm}} + f_3 = 1$, and

$$\mathbf{T}_3 = [\mathbf{I} + \mathbf{S}_3\mathbf{L}_{\text{pm}}^{-1}(\mathbf{L}_3 - \mathbf{L}_{\text{pm}})]^{-1} \quad (5)$$

The Eshelby tensor for a fiber-reinforced material with an isotropic homogenous matrix, \mathbf{S}_3 , was obtained by [Luo and Weng \[1989\]](#). Alternative micromechanical methods that could be applied to the analysis of a fiber-reinforced material with the isotropic particulate matrix properties determined as shown above include the well-known Halpin–Tsai or mechanics of materials solutions.

2.2. Strength of a particulate matrix. The pioneering study of [Eshelby \[1957\]](#) provided expressions for the stresses just outside a spheroidal inclusion. This work was further continued by [Tandon and Weng \[1986\]](#) and [Kakavas and Kontoni \[2005\]](#) who also illustrated that the analytical results were in a good agreement with the finite element analysis.

Micromechanical strength conditions can be determined by specifying the stress in the matrix, at the particle-matrix interface, and in the particles, and subsequently applying strength criteria to the matrix and particles and at the interface. In this paper, we assume a perfect bond between the matrix and particles. Furthermore, the fracture analysis is not included, though it could be developed based on the knowledge of local stresses and assuming that the crack originates at the particle-matrix interface. The strength of the particles is assumed higher than that of the matrix (as is usually the case in applications), so that failure initiates in the matrix, just outside the particles, where the stresses are elevated due to the stress concentration. Among the strength criteria applicable to the analysis of the isotropic and ductile matrix, we consider the maximum principal stress criterion and the von Mises criterion. In the case of a brittle matrix, these criteria may be inaccurate and the Coulomb–Mohr criterion or the recently suggested Christensen criterion [\[2007\]](#) becomes more appropriate.

Consider a particulate matrix subject to uniaxial tension $\hat{\sigma}_{11}$ (the in-plane coordinates referred to are denoted by 1 and 2). The stresses in the matrix (in the 1-2 plane), just outside a spherical particle, are [\[Tandon and Weng 1986\]](#)

$$\begin{aligned} \sigma_{11,m} &= \hat{\sigma}_{11} \left(1 + \frac{(1-f'_2)(b_1p_1 + 2b_2p_2)}{(1+\nu_1)(1-2\nu_1)} + \frac{p_1 \cos^2 \theta + p_2(\nu_1 + \sin^2 \theta)}{1-\nu_1^2} \cos^2 \theta \right) = F_{11}(\theta)\hat{\sigma}_{11} \\ \sigma_{22,m} &= \hat{\sigma}_{11} \left(\frac{(1-f'_2)(b_3p_1 + (b_4 + b_5)p_2)}{(1+\nu_1)(1-2\nu_1)} + \frac{p_1 \cos^2 \theta + p_2(\nu_1 + \sin^2 \theta)}{1-\nu_1^2} \sin^2 \theta \right) = F_{22}(\theta)\hat{\sigma}_{11} \\ \sigma_{33,m} &= \hat{\sigma}_{11} \left(\frac{(1-f'_2)(b_3p_1 + (b_4 + b_5)p_2)}{(1+\nu_1)(1-2\nu_1)} + \frac{\nu_1 p_1 \cos^2 \theta + p_2(1 + \nu_1 \sin^2 \theta)}{1-\nu_1^2} \right) = F_{33}(\theta)\hat{\sigma}_{11} \\ \sigma_{12,m} &= -\hat{\sigma}_{11} \frac{p_1 \cos^2 \theta + p_2(\nu_1 + \sin^2 \theta)}{1-\nu_1^2} \sin \theta \cos \theta = F_{12}(\theta)\hat{\sigma}_{11} \\ \sigma_{13,m} &= \sigma_{23,m} = 0, \end{aligned} \quad (6)$$

where the coefficients b_j and p_j are specified according to [Tandon and Weng 1986] in terms of the elements of Eshelby's tensor, the particle volume fraction within the particulate matrix f'_2 , and bulk and shear moduli of the matrix and particles.

The principal stresses can now be determined from

$$\begin{vmatrix} \sigma_{11,m} - \sigma & \sigma_{12,m} & 0 \\ \sigma_{12,m} & \sigma_{22,m} - \sigma & 0 \\ 0 & 0 & \sigma_{33,m} - \sigma \end{vmatrix} = 0. \quad (7)$$

Accordingly,

$$\begin{aligned} \sigma_{1,2} &= \hat{\sigma}_{11} \left(\frac{F_{11}(\theta) + F_{22}(\theta)}{2} \pm \sqrt{(F_{11}(\theta) - F_{22}(\theta))^2 + 4F_{12}^2(\theta)} \right) = \hat{\sigma}_{11} F_{1,2}(\theta), \\ \sigma_3 &= \hat{\sigma}_{11} F_{33}(\theta). \end{aligned} \quad (8)$$

The maximum principal stress criterion yields the tensile strength of the particulate matrix:

$$s_{pm,T} = s_{mT} \min\{F_1^{-1}(\theta), F_2^{-1}(\theta), F_{33}^{-1}(\theta)\}, \quad (9)$$

where s_{mT} is the tensile strength of the matrix material.

The von Mises strength criterion predicts the strength

$$s_{pm,T} = \sqrt{2} s_{mT} ([F_1(\theta) - F_2(\theta)]^2 + [F_1(\theta) - F_{33}(\theta)]^2 + [F_2(\theta) - F_{33}(\theta)]^2)^{-1/2}. \quad (10)$$

Either one uses the strength criterion (9) or (10), it is necessary to check all values of $0 \leq \theta \leq \pi/2$ since it is unpractical to analytically determine the angular coordinate corresponding to the onset of failure. Therefore, the strength should be found as the smallest value of the stress given by (9) or (10) obtained by varying the angular coordinate.

The analysis of the axial compressive strength is quite similar: we can use (9) or (10), where $s_{pm,T}$ is replaced with the compressive strength of the particulate matrix $s_{pm,C}$ and s_{mT} is replaced with the compressive strength of the matrix material s_{mC} .

Now consider the shear strength of the particulate matrix subject to the stress $\hat{\sigma}_{12}$. Let

$$R = (1 - f'_2)(1 - 2S_{1212}) - \frac{G_2}{G_2 - G_1} \quad \text{and} \quad S = \frac{(1 - f'_2)(1 - 2S_{1212}) \left(1 - \frac{2G_1}{G_{pm}}\right) - \frac{G_2}{G_2 - G_1}}{(1 - f'_2)(1 - 2S_{1212}) - \frac{G_2}{G_2 - G_1}}, \quad (11)$$

where G_1 and G_2 are the shear moduli of the matrix and particles, respectively, and G_{pm} is the shear modulus of the particulate matrix found using the solution in the previous section. Then the stresses in the matrix adjacent to the particle can be obtained [Tandon and Weng 1986]:

$$\begin{aligned} \sigma_{11,m} &= -\frac{4G_1}{(1 - \nu_1)G_{pm}R} \hat{\sigma}_{12} \sin \theta \cos^3 \theta = \tilde{F}_{11}(\theta) \hat{\sigma}_{12}, \\ \sigma_{22,m} &= -\frac{4G_1}{(1 - \nu_1)G_{pm}R} \hat{\sigma}_{12} \sin^3 \theta \cos \theta = \tilde{F}_{22}(\theta) \hat{\sigma}_{12}, \end{aligned} \quad (12)$$

$$\begin{aligned} \sigma_{33,m} &= -\frac{4G_1\nu_1}{(1-\nu_1)G_{pm}R}\hat{\sigma}_{12}\sin\theta\cos\theta = \tilde{F}_{33}(\theta)\hat{\sigma}_{12}, \\ \sigma_{12,m} &= \hat{\sigma}_{12}\left(S + \frac{4G_1}{(1-\nu_1)G_{pm}R}\sin^2\theta\cos^2\theta\right) = \tilde{F}_{12}(\theta)\hat{\sigma}_{12}, \\ \sigma_{13,m} &= \sigma_{23,m} = 0. \end{aligned}$$

These expressions depend on the shear modulus of the particulate matrix, which is available from the micromechanical solution.

The principal stresses found from (7) are

$$\begin{aligned} \sigma_{1,2} &= \hat{\sigma}_{12}\left(\frac{\tilde{F}_{11}(\theta) + \tilde{F}_{22}(\theta)}{2} \pm \sqrt{(\tilde{F}_{11}(\theta) - \tilde{F}_{22}(\theta))^2 + 4\tilde{F}_{12}^2(\theta)}\right) = \hat{\sigma}_{12}\tilde{F}_{1,2}(\theta), \\ \sigma_3 &= \hat{\sigma}_{12}\tilde{F}_{33}(\theta). \end{aligned} \tag{13}$$

Subsequently, the maximum principal stress criterion or the von Mises criterion yields the shear strength of the particulate matrix in the form (9) and (10), respectively, where F_1 is replaced by \tilde{F}_1 , F_2 by \tilde{F}_2 , F_{33} by \tilde{F}_{33} , $s_{pm,T}$ by $s_{pm,S}$ (the particulate matrix shear strength) and s_{mT} by the matrix shear strength s_{mS} . Similarly to the case for the tensile and compressive strengths, the shear strength of the particulate matrix is found as the smallest stress obtained from the accordingly modified equations (9) or (10) by varying the values of θ .

2.3. Strength of the fiber-reinforced material with a homogenized matrix. The outline of micromechanical solutions for the strengths of a fiber-reinforced material in the axial and transverse directions as well as for the shear strength obtained by assumption that all constituents remain within the linear elastic range and bonding between the fibers and matrix is not violated was given by Daniel and Ishai [2006]. These solutions are outlined here using the properties of fibers and those of the particulate matrix, for completeness. The composite strengths depend on the strength of fibers that we assume known and on the strength, ultimate strain and stiffness of the particulate matrix evaluated using the results shown in the previous sections.

The longitudinal tensile strength s_{1T} depends on the relationship between the ultimate longitudinal tensile strain $\epsilon_{f,l}^u$ of the fibers and the ultimate tensile strain $\epsilon_{pm}^u = s_{pm,T}/E_{pm}$ of the particulate matrix (here E_{pm} is the elastic modulus of the particulate matrix):

$$\begin{aligned} s_{1T} &= s_{fT}\left(f_3 + f_{pm}\frac{E_{pm}}{E_3}\right) \quad \text{if } \epsilon_{f,l}^u < \epsilon_{pm}^u, \\ s_{1T} &= s_{pm,T}\left(f_3\frac{E_3}{E_{pm}} + f_{pm}\right) \quad \text{if } \epsilon_{f,l}^u > \epsilon_{pm}^u, \end{aligned} \tag{14}$$

where s_{fT} is the tensile strength of isotropic fibers and E_3 is their modulus of elasticity.

The modes of failure of a unidirectional fiber-reinforced composite subject to longitudinal compression include fiber microbuckling in either extensional or shear mode and shear failure. The microbuckling

failure modes occur at the following value of the applied compressive stress

$$s'_{1C} = \min \left\{ 2f_3 \sqrt{\frac{E_{pm} E_3 f_3}{3 f_{pm}}}, \frac{G_{pm}}{f_{pm}} \right\}, \quad (15)$$

where G_{pm} is the shear modulus of the particulate matrix.

The shear failure mode of a longitudinally compressed fiber-reinforced material occurs at the stress

$$s''_{1C} = 2s_{fs} \left(f_3 + f_{pm} \frac{E_{pm}}{E_3} \right), \quad (16)$$

where s_{fs} is the shear strength of the fiber.

The longitudinal compressive strength is now found as $s_{1C} = \min\{s'_{1C}, s''_{1C}\}$. The analysis can also account for the effect of fiber misalignment, as discussed by [Daniel and Ishai \[2006\]](#).

The transverse tensile failure of fiber-reinforced composites can be predicted accounting for the stress or strain concentration factor and for residual stresses. For example, the stress concentration factor for a square array of fibers can be obtained in terms of the properties of the particulate matrix and fibers as

$$k = \frac{1 - f_3(1 - E_{pm}/E_3)}{1 - \sqrt{4f_3/\pi}(1 - E_{pm}/E_3)}. \quad (17)$$

Subsequently, the maximum principal stress criterion yields $s_{2T} = (s_{pmT} - \sigma_{pm,res})/k$, where $\sigma_{pm,res}$ is the maximum radial residual stress in the particulate matrix. The latter stress can be found using a concentric cylinder model subject to a uniform temperature, the inner cylinder being the fiber, surrounded with a cylindrical layer of the particulate matrix that is in turn surrounded with the fiber-reinforced medium. A more accurate approach would be based on subdividing the cylindrical layer of the particulate matrix into a thin cylinder of the matrix material encompassed with a cylinder of the particulate matrix material. The radial coordinate of the interface between these two cylinders could be determined from geometric considerations. An alternative formulation employing the maximum principal strain criterion is also available using the properties of the particulate matrix and the maximum residual radial strain.

The compressive strength of a fiber-reinforced composite is the lesser failure stress corresponding to a number of possible scenarios, including interfacial shear failure, debonding and fiber crushing. The typical mode of failure being the compressive matrix failure, the strength is determined as $s_{2C} = (s_{pm,C} + \sigma_{pm,res})/k$.

In-plane shear failure occurs as a result of the interfacial shear stress concentration. The stress concentration factor k_{sh} is available from (17) by replacing the moduli of elasticity with the shear moduli of the corresponding phases. Then the shear strength is $s_{12} = s_{pm,S}/k_{sh}$.

The strengths of the fiber-reinforced material can be specified only upon the conclusion of the micro-mechanical stiffness analysis presented above, since they depend on the stiffness of the particulate matrix.

3. Fiber-reinforced composite material with superelastic shape memory alloy inclusions embedded within the matrix

The total strain in SMA is composed of elastic, transformation and thermal components. The latter components are negligible in the material experiencing superelastic transformations. The increments of the transformation strain are usually evaluated as functions of the increments of the martensitic volume

fraction using an assumption regarding the incremental law; see for example, [Boyd and Lagoudas 1993; Birman et al. 1996; Jonnalagadda et al. 1998; Jiang and Batra 2002]. An alternative theory [Lu and Weng 2000] treated the martensitic phase as a separate class of inclusions within the austenitic metal.

Contrary to the incremental approach referred to above, the present solution is exact, yielding the stiffness and applied stress and strain tensors for a material with superelastic SMA inclusions (spheroidal particles or fibers) corresponding to a prescribed martensitic fraction of SMA (other types of inclusions, besides SMA, can also be present).

The solution follows this sequence:

- (i) The Benveniste version of the Mori–Tanaka formulation for a composite material with multiple classes of inclusions is outlined, following the solution by Genin and Birman [2009].
- (ii) A three-dimensional formulation for the superelastic material is then presented, combining the approaches of [Boyd and Lagoudas 1993] and [Tanaka 1986; Sato and Tanaka 1988].
- (iii) A combination of the micromechanical and superelastic SMA formulations above, together with the inverse method suggested in this paper, is used to obtain the exact solution for the stress-strain response and stiffness of a composite material with multiple inclusions, including superelastic SMA particles or fibers.

The analysis is practical since the knowledge of the transformation strain is not needed in numerous problems concerned with SMA composites. Using the present solution that provides the applied stresses, stiffness and stress-strain relationships corresponding to a prescribed martensitic volume fraction in SMA inclusions, one can also develop a complete hysteresis loop varying this volume fraction to predict the damping capacity of superelastic SMA composites bypassing the evaluation of the transformation strain (this study elucidating a remarkable damping potential of particulate SMA composites is the subject of a separate paper).

3.1. Micromechanics of a composite material with numerous inclusion classes. Consider a representative volume element of a composite material with multiple inclusions of various shapes and properties subject to a remote strain tensor $\bar{\epsilon}_0$. The behavior of SMA undergoing martensitic or reverse transformation is physically nonlinear. However, if the martensitic fraction of SMA is known, we can employ a tangent stiffness tensor of the corresponding inclusions. All inclusions are assumed perfectly bonded to the matrix. The average stress tensor in the element is related to the tensor of the applied average strain via the tangent stiffness tensor by

$$d\sigma_0 = L d\epsilon_0. \quad (18)$$

Following the solution by Genin and Birman [2009], the stiffness tensor is expressed in terms of the corresponding tensors of the matrix ($i = 1$) and inclusions ($i > 1$) by the following equation, which represents an extrapolation of (1):

$$\mathbf{L} = \mathbf{L}_1 + \sum_{i=2}^N f_i (\mathbf{L}_i - \mathbf{L}_1) \mathbf{T}_i (f_1 \mathbf{I} + f_2 \mathbf{T}_2 + \cdots + f_N \mathbf{T}_N)^{-1}, \quad (19)$$

where the number of distinct inclusion classes is $N-1$ and the f_i are the volume fractions of the matrix ($i = 1$) and inclusions ($i \geq 2$). In the following discussion, SMA inclusions are identified by $i = 2$.

Tensors T_i are given by equations similar to (2). Note that the Eshelby tensor S_2 for SMA inclusions is not affected by the martensitic transformation as long as the stiffness of the matrix remains constant [Boyd and Lagoudas 1993].

In the following solution, we employ relationships between the tensor of average applied strain and the tensor of average strain within the inclusions

$$d\boldsymbol{\varepsilon}_i = \mathbf{A}_i(\xi) d\boldsymbol{\varepsilon}_0, \quad (20)$$

where the so-called tensors of concentration factors are given by

$$\mathbf{A}_i = \mathbf{T}_i(f_1\mathbf{I} + f_2\mathbf{T}_2 + \cdots + f_N\mathbf{T}_N)^{-1}. \quad (21)$$

Note that the Genin–Birman solution (19) differs from that using a two-step approach, that is, Equations (1) and (4). A quantitative comparison of the accuracy of these two approaches is outside our scope here.

3.2. Three-dimensional formulation for a shape memory material. The following formulation employs the assumption that the tensor of stiffness of a SMA material during the martensitic or reverse transformation can be represented by the rule of mixtures [Boyd and Lagoudas 1993]

$$\mathbf{L}_2 = \mathbf{L}_2^A + \xi(\mathbf{L}_2^M - \mathbf{L}_2^A), \quad (22)$$

where the superscripts A and M refer to the austenitic and martensitic phase of the material.

Note that the rule of mixtures can also be applied to the strength of the SMA material, so that

$$s_2 = s_2^A + \xi(s_2^M - s_2^A). \quad (23)$$

The three-dimensional constitutive relations for a superelastic shape memory material are

$$d\boldsymbol{\sigma}_2 = d(\mathbf{L}_2(\boldsymbol{\varepsilon}'_2 - \boldsymbol{\varepsilon}^t_2)), \quad (24)$$

where $\boldsymbol{\varepsilon}'_2$ and $\boldsymbol{\varepsilon}^t_2$ are tensors of total and transformation strains, respectively. The rate of change of the tensor $\boldsymbol{\varepsilon}^t_2$ is related to the rate of change of the martensitic volume fraction, using an assumption for the tensor of coefficients in the relationship (called the *transformation tensor*). This approach implies the use of an incremental technique monitoring the changes in the tensors of strain and stress with the changes in the martensitic volume fraction; see, for example, [Birman et al. 1996; Jonnalagadda et al. 1998; Jiang and Batra 2002].

In the present study we discard the assumption regarding the transformation tensor and operate with the average elastic strain tensor within the SMA particle, that is, $\boldsymbol{\varepsilon}_2 = \boldsymbol{\varepsilon}'_2 - \boldsymbol{\varepsilon}^t_2$. This enables us to directly apply linear elastic micromechanical theories, such as the Mori–Tanaka theory and its extrapolation to multi-phase composites outlined in the previous section. While the present approach does not provide tools for a decomposition of the elastic strain and determining the transformation component, it is sufficient in a number of applied problems.

Equation (24) can be replaced with the following incremental relationship utilizing the tangent SMA stiffness tensor:

$$d\boldsymbol{\sigma}_2 = \mathbf{L}_2(\xi) d\boldsymbol{\varepsilon}_2. \quad (25)$$

The martensitic fraction can be related to the effective stress in SMA by extrapolating the solutions for a number of available one-dimensional theories (such as Tanaka's, Liang–Rogers' and Brinson's

theories). As an example, we adopt the Tanaka model [Tanaka 1986; Sato and Tanaka 1988]:

$$\begin{aligned}\zeta &= 1 - \exp[b_M(T_S^M - T) + c_M\sigma_{\text{eff}}] & (A \rightarrow M), \\ \zeta &= \exp[b_A(T_S^A - T) + c_A\sigma_{\text{eff}}] & (M \rightarrow A),\end{aligned}\quad (26)$$

where T is the current temperature, T_S^M and T_S^A are the martensite and austenite phase start temperatures at stress-free conditions, and b_M , b_A , c_M , c_A are constants [Birman et al. 1996].

The effective stress is defined in terms of the components of the deviatoric stress tensor, that is,

$$\sigma_{\text{eff}} = \sqrt{\frac{3}{2}\sigma'_{ij}\sigma'_{ij}}, \quad \sigma'_{ij} = \sigma_{ij} - \frac{1}{3}\sigma_{nn}\delta_{ij}, \quad (27)$$

where $\sigma_{ij} = \sigma_0^{(ij)}$.

3.3. Stiffness of a composite material with SMA particles: exact inverse method. For a composite material where several inclusion classes, including superelastic particles, are embedded within an elastic matrix, we now develop an exact solution to relate the tensor of applied strain to the martensitic fraction in SMA particles and to determine the stiffness tensor corresponding to this applied strain.

Consider the situation where the tensor of applied strain $\boldsymbol{\varepsilon}_0$ is prescribed, except for one component $\varepsilon_0^{(mn)}$ that will be specified from the subsequent solution. We begin by assuming the average martensitic volume fraction ζ in SMA particles (the average per the inclusion class approach to strains and stresses adopted in the Mori–Tanaka micromechanics necessitates the use of the average martensitic volume fraction). The corresponding value of the effective stress σ_{eff} in the particle is immediately available from (26), dependent on the transformation being direct or reversed (temperature is assumed constant). Subsequently, the SMA stiffness tensor \mathbf{L}_2 corresponding to ζ can be determined from (22), and the composite stiffness tensor \mathbf{L} is specified from (19). While these tensors are the ultimate goal of the analysis, the solution cannot stop here since we need to specify the unknown component of the applied strain tensor corresponding to the assumed martensitic volume fraction.

The tensors \mathbf{T}_i for each class of inclusions can be determined from equations similar to (2), where the Eshelby tensor is not affected by the transformation within SMA particles. Subsequently, (21) yields the concentration tensors \mathbf{A}_i .

We have a system of 13 equations obtained from (23), (20) and (27) with respect to twelve unknown components of the SMA stress and strain tensor increments, and the component of applied strain increment $d\varepsilon_0^{(mn)}$. The solution is incremental, starting with the elastic case where SMA particles are in the austenitic phase (in this case the solution is available using [Tandon and Weng 1986]). At each subsequent increment of the martensitic fraction the corresponding effective stress is found from (26). The SMA and composite material tangent stiffness tensors are specified from (22) and (19). Subsequently, equations (20) are used to express all strain components in the SMA inclusions, i.e., $\boldsymbol{\varepsilon}_2 = \boldsymbol{\varepsilon}_2(\varepsilon_0^{(mn)}, \zeta)$. The final phase of the solution is finding the values of $\varepsilon_0^{(mn)}$ and six components of the stress tensor in SMA inclusions from (25) and (27).

The strength of SMA particles corresponding to the prescribed martensitic volume fraction is available from (23). Using the strength and stiffness of the SMA particles corresponding to the applied strain tensor, the strength analysis of a fiber-reinforced, SMA particulate matrix composite can be conducted using the previously illustrated solution.

3.4. Particular case: superelastic SMA particulate composite material. As an example illustrating an application of the inverse method of analysis discussed in the previous section consider the case of an isotropic matrix with spherical SMA particles subject to a uniaxial axial stress $\hat{\sigma}_0^{(11)}$. As shown in [Tandon and Weng 1986], the stresses in a particle subject to a uniaxial loading are

$$\begin{aligned} d\sigma_2^{(11)} &= \left(1 + \frac{1 - f_2'}{(1 + \nu_1)(1 - 2\nu_1)}(b_1 p_1 + 2b_2 p_2)\right) d\hat{\sigma}_0^{(11)}, \\ d\sigma_2^{(22)} &= d\sigma_2^{(33)} = \frac{1 - f_2'}{(1 + \nu_1)(1 - 2\nu_1)}(b_3 p_1 + (b_4 + b_5)p_2) d\hat{\sigma}_0^{(11)}, \\ d\sigma_2^{(mn)} &= 0, \quad m \neq n, \end{aligned} \quad (28)$$

where b_j and p_j are coefficients specified in that reference. These coefficients depend on the stiffness of SMA particles, that is, $b_j = b_j(\zeta)$ and $p_j = p_j(\zeta)$.

The increment of the effective stress in SMA particles can now be explicitly expressed in terms of the increment of the applied stress

$$d\sigma_{\text{eff}} = |d\sigma_2^{(11)} - d\sigma_2^{(22)}| = \left|1 + \frac{1 - f_2'}{(1 + \nu_1)(1 - 2\nu_1)}((b_1 - b_3)p_1 + (2b_2 - b_4 - b_5)p_2)\right| d\hat{\sigma}_0^{(11)}. \quad (29)$$

Explicit expressions for the shear and bulk moduli of a composite material consisting of the matrix with embedded spherical particles, that is, G_{pm} and K_{pm} , are available [Vel and Batra 2004]

$$G_{\text{pm}} = G_1 + \frac{f_2'(G_2 - G_1)}{1 + f_1' \frac{G_2 - G_1}{G_1 + \rho}}, \quad K_{\text{pm}} = K_1 + \frac{f_2'(K_2 - K_1)}{1 + f_1' \frac{G_2 - G_1}{K_1 + 4G_1/3}}, \quad \rho = \frac{G_1(9K_1 + 8G_1)}{6(K_1 + 2G_1)}. \quad (30)$$

The elasticity modulus and the Poisson ratio of the SMA-particulate material can now be determined from $E_{\text{pm}} = 9K_{\text{pm}}G_{\text{pm}}(3K_{\text{pm}} + G_{\text{pm}})^{-1}$ and $\nu_{\text{pm}} = E_{\text{pm}}(2G_{\text{pm}})^{-1} - 1$.

The computational procedure in this case is very simple. The initial step corresponds to the elastic problem with austenitic SMA particles where the solution is available. Then the martensitic fraction is increased incrementally. At each value of ζ one can find the corresponding stiffness characteristics of SMA particles and composite material from (22) and (19), while the effective stress is specified from (26). The coefficients $b_j = b_j(\zeta)$ and $p_j = p_j(\zeta)$ are also calculated at this step. Subsequently, (29) yields the value of the applied stress, while (30) results in the stiffness of the particulate material corresponding to this stress. The strain tensor in the composite material is determined using (18).

4. Numerical examples

The effectiveness of embedding stiff particles within the matrix of a fiber-reinforced composite is shown on the example of a glass/epoxy material with spherical particles within the matrix. The properties of the constituent materials are taken as in [Genin and Birman 2009]: $E_1 = 3.12$ GPa, $\nu_1 = 0.38$, $E_2 = E_3 = 76.0$ GPa, $\nu_2 = \nu_3 = 0.25$. The tensile stress ratio $k_{\text{pm}} = \sigma_{11,m}(\text{max})/\hat{\sigma}_{11}$ as a result of uniaxial tension is shown in Figure 1, left, where the maximum stress in the matrix is normalized with respect to the stress applied to the particulate matrix. The case of $f_2' = 0$ corresponds to a single particle embedded within the matrix, while larger values of the particle volume fraction account for multiple inclusions.

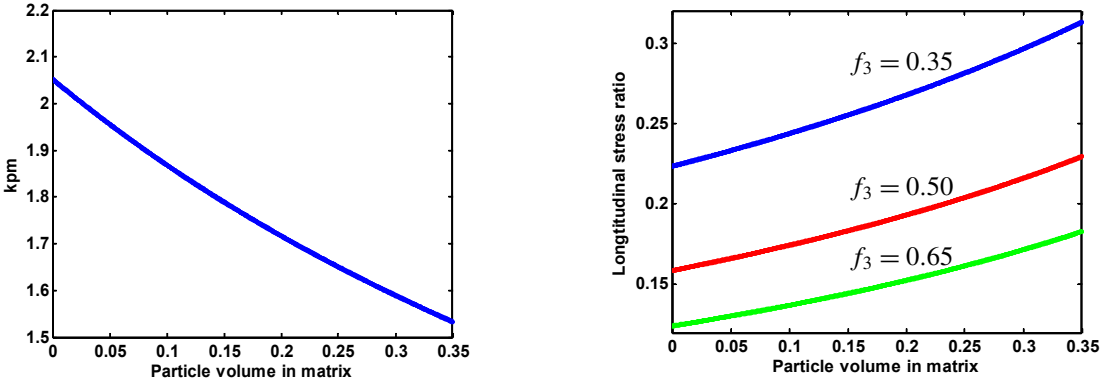


Figure 1. Tensile stress ratio (k_{pm}) in (left) the particulate matrix subject to uniaxial tension, and (right) fiber-reinforced particulate-matrix composite.

The stress ratio reaches a maximum in the case of a single particle as was also observed by Tandon and Weng [1986]. In Figure 1, right, we see the tensile stress concentration ratio at the composite level, that is, the ratio $\sigma_{11,m}(\max)/\sigma_{11}^0$ of the maximum stress in the matrix to the applied composite stress.

The beneficial effect of adding particles on the longitudinal and transverse stiffness of the fiber-reinforced material is reflected in Figure 2. The longitudinal stiffness of the material with a homogeneous

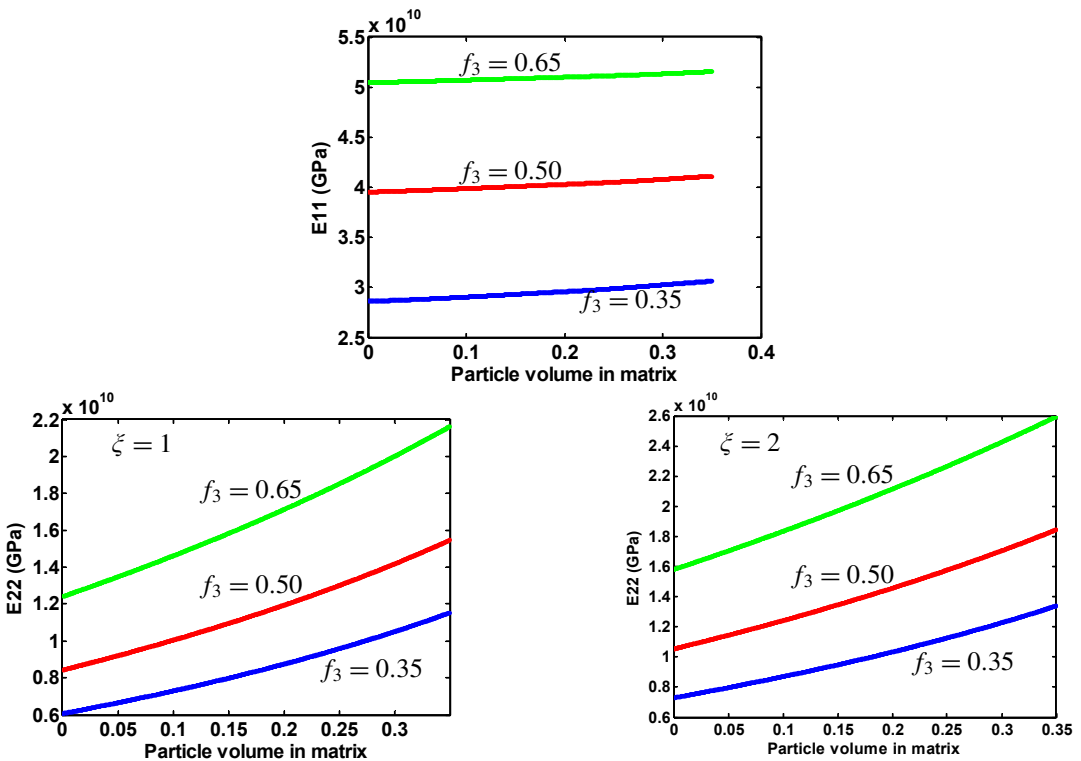


Figure 2. Effect of particle volume fraction in particulate matrix on longitudinal (top) and transverse (bottom) stiffness of fiber-reinforced composite.

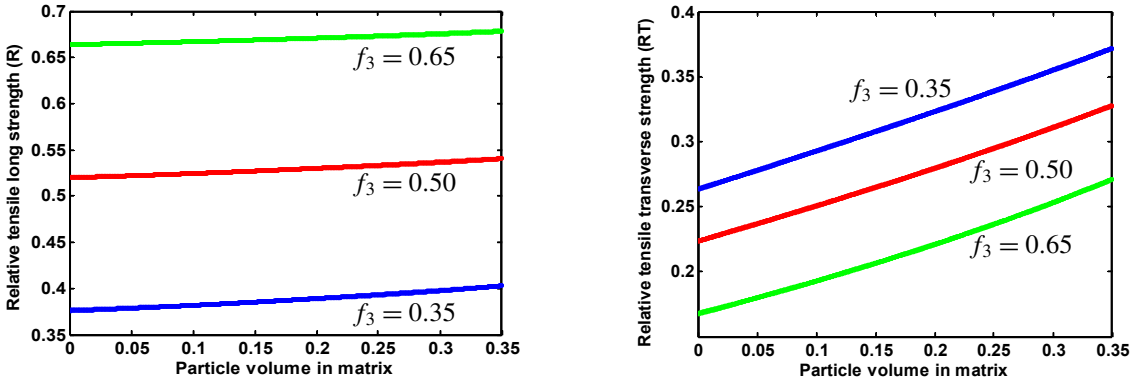


Figure 3. Effect of particles on the tensile longitudinal (left) and transversal (right) strength of fiber-reinforced particulate-matrix composite. ($R = s_{1T}/s_{fT}$)

particulate matrix was determined by the rule of mixtures. The transverse stiffness was determined by the Halpin–Tsai model with the curve fitting parameter equal to $\zeta = 1$ and $\zeta = 2$ (typical range of this parameter). As seen in Figure 2, even a modest amount of particles added to the matrix can significantly enhance the transverse stiffness, although the effect on the longitudinal stiffness is less pronounced.

The effect of particles on the longitudinal tensile strength of the composite material is reflected in Figure 3, left, for the case where $\varepsilon_{f,l}^u < \varepsilon_{pm}^u$. As is obvious from that figure, adding glass particles to the matrix has a relatively small effect on the longitudinal strength of the material. Predictably, the situation is different in the case of transverse strength since it is highly dependent on the strength of the particulate matrix. As is shown in Figure 3, right, the effect of adding particles on the transverse strength of the composite is much more pronounced than that on its longitudinal strength. This is expected since the contribution of the matrix to the transverse strength is higher than that to the longitudinal strength.

Examples of the closed-form solution for composites including SMA Nitinol spherical particles embedded within an epoxy matrix with the properties identical to those in the paper on fibrous SMA composites by Birman et al. [1996] are presented below. Figure 4 shows the shear and elasticity moduli as functions

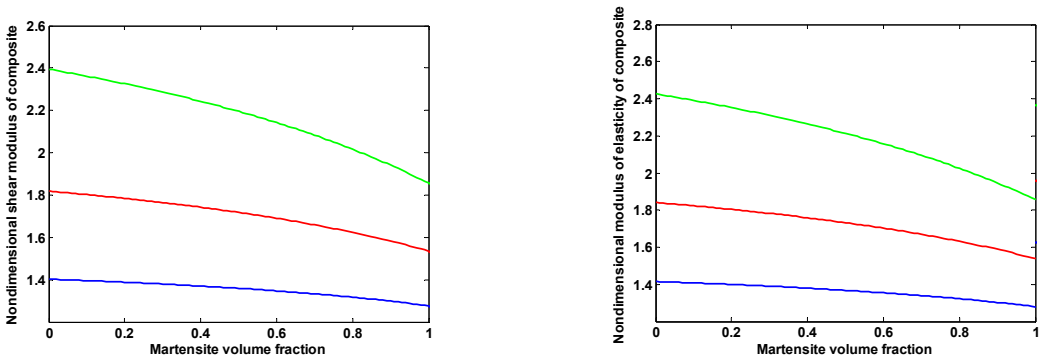


Figure 4. Shear modulus and elasticity modulus of SMA particulate composite (relative to those of epoxy), as functions of the martensitic fraction. The SMA volume fraction is $f_2 = 0.20$ (blue), $f_2 = 0.35$ (red), and $f_2 = 0.50$ (green).

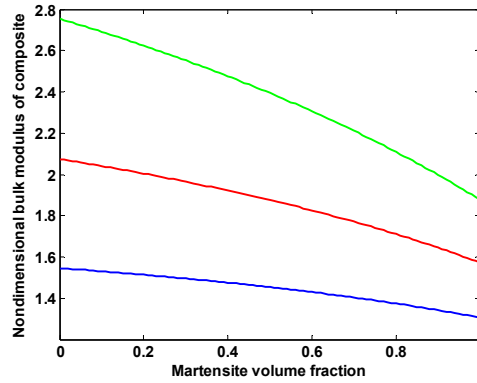


Figure 5. Bulk modulus of SMA particulate composite (relative to that of epoxy), as a function of the martensitic fraction. The SMA volume fraction is $f_2 = 0.20$ (blue), $f_2 = 0.35$ (red), and $f_2 = 0.50$ (green).

of the martensitic volume fraction, for values of the SMA particle volume fraction equal to 20%, 35%, and 50%, while Figure 5 does the same for the bulk modulus. As is evident from these figures, martensitic and reverse phase transformations in SMA particles significantly affect the properties of SMA particulate composites with a high SMA volume fraction. The changes in the case where the volume fraction is relatively low (20%) are noticeable but small (between 10 and 20%).

The effect of applied axial stress on the variation of the martensitic volume fraction in SMA particulate composites is illustrated in Figure 6 for an SMA volume fraction equal to 20% and 50%. Predictably, the range of stresses needed for the transformation loop (from austenite to martensite and back to austenite) is larger if the amount of SMA increases. This reflects a higher stiffness of SMA material, even in the martensitic phase, as compared to the stiffness of the epoxy considered in examples. The results

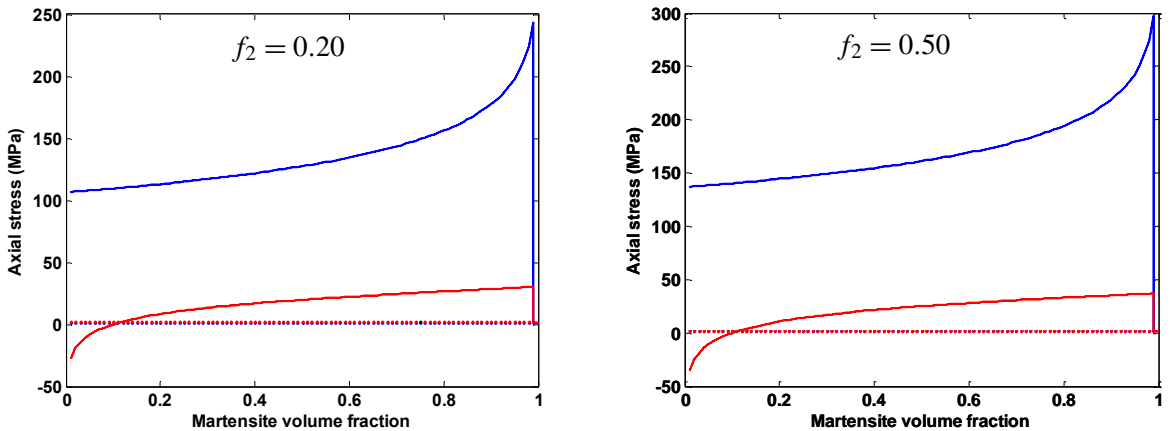


Figure 6. Axial stress that has to be applied to a superelastic shape memory alloy particulate composite to cause martensitic (blue curve) or reverse (red curve) transformation. The SMA volume fraction f_2 is 0.20 (left) and 0.50 (right); the temperature is 40 °C.

illustrated in Figures 5 and 6 can further be employed to develop an exact solution for the hysteresis loop of particulate SMA composites (here the word *exact* refers to the solution within the framework of assumptions employed in the theories of Tanaka for SMA and Mori–Tanaka for composite).

5. Conclusions

The paper illustrates a two-step approach to the strength and stiffness analyses of fiber-reinforced, particulate-matrix composites. The solution is obtained by a generalization of available micromechanical solutions to three-phase materials. The strength and stiffness of the particulate matrix are specified first, followed with the analysis of the properties of a fiber-reinforced material incorporating the already homogenized matrix.

The numerical analysis shows that adding stiff particles to the matrix results in a significant enhancement of the transverse strength and stiffness, but the benefits are less obvious for the longitudinal strength and stiffness. This reflects a relatively larger contribution of the matrix to the transverse properties of the fiber-reinforced material.

The solution is further extrapolated to composites including shape memory alloy (SMA) inclusions. The exact solution is obtained for the stiffness of such composites, eliminating the need to assume a transformation law (a relationship between the increments of the martensitic fraction and the tensor of the transformation strain) and the associated incremental procedure. As follows from numerical examples, the stiffness of particulate SMA composites is significantly influenced by the stress-induced phase transformation.

Appendix: Incremental Mori–Tanaka approach to the homogenization of multi-phase materials

Consider a composite material with a relatively high volume fraction of inclusions $f_i (i = 2, \dots, N)$. The procedure utilizes an incremental homogenization that begins with embedding a low volume fraction of inclusions into the matrix, so $f_1^{(1)} + \sum_{i=2}^N f_i^{(1)} = 1$, where the superscript identifies the step number.

The stiffness of the material at this first step is evaluated using a counterpart of Equation (19):

$$\mathbf{L}^{(1)} = \mathbf{L}_1 + \sum_{i=2}^N f_i^{(1)} (\mathbf{L}_i - \mathbf{L}_1) \mathbf{T}_i (f_1^{(1)} \mathbf{I} + f_2^{(1)} \mathbf{T}_2 + \dots + f_N^{(1)} \mathbf{T}_N)^{-1}, \quad (\text{A1})$$

where

$$\mathbf{T}_i = [\mathbf{I} + \mathbf{S}_i \mathbf{L}_1^{-1} (\mathbf{L}_i - \mathbf{L}_1)]^{-1}. \quad (\text{A2})$$

The Eshelby tensor at the first step is calculated using the properties of the matrix material.

The incremental procedure at the following steps can easily be developed. For example, at the j -th step a prescribed increment of inclusions is added to the matrix that already contains inclusions incorporated at the previous steps, so that $f_1^{(j)} + \sum_{i=2}^N f_i^{(j)} = 1$ and

$$\mathbf{L}^{(j)} = \mathbf{L}^{(j-1)} + \sum_{i=2}^N f_i^{(j)} (\mathbf{L}_i - \mathbf{L}^{(j-1)}) \mathbf{T}_i^{(j)} (f_1^{(j)} \mathbf{I} + f_2^{(j)} \mathbf{T}_2^{(j-1)} + \dots + f_N^{(j)} \mathbf{T}_N^{(j-1)})^{-1} \quad (\text{A3})$$

$$\mathbf{T}_i^j = [\mathbf{I} + \mathbf{S}_i^{(j)} (\mathbf{L}_1^{(j-1)})^{-1} (\mathbf{L}_i - \mathbf{L}^{(j-1)})]^{-1}. \quad (\text{A4})$$

The Eshelby tensor at the j -th step is calculated using the properties of the material evaluated at the $(j-1)$ -st step. The properties of inclusions do not change during the procedure, but the tensor of stiffness of the matrix is continuously updated. The suggested procedure enables us to maintain the volume fraction of additional inclusions at each step below the recommended accuracy limit of the Mori–Tanaka approach. Accordingly, at each step, $\sum_{i=2}^N f_i^{(j)} < r$, where r is prescribed (it could be limited to 0.2 or 0.3, depending on the desirable accuracy).

References

- [Benveniste 1987] Y. Benveniste, “A new approach to the application of Mori–Tanaka’s theory in composite materials”, *Mech. Mater.* **6**:2 (1987), 147–157.
- [Birman 1997] V. Birman, “Review of mechanics of shape memory alloy structures”, *Appl. Mech. Rev. (ASME)* **50** (1997), 629–645.
- [Birman and Byrd 2007] V. Birman and L. W. Byrd, “Modeling and analysis of functionally graded materials and structures”, *Appl. Mech. Rev. (ASME)* **60**:5 (2007), 195–216.
- [Birman et al. 1996] V. Birman, D. A. Saravanos, and D. A. Hopkins, “Micromechanics of composites with shape memory alloy fibers in uniform thermal fields”, *AIAA J.* **34**:9 (1996), 1905–1912.
- [Boyd and Lagoudas 1993] J. G. Boyd and D. C. Lagoudas, “Thermomechanical response of shape memory composites”, *Proc. SPIE* **1917** (1993), 774–790.
- [Cardone et al. 2004] D. Cardone, E. Coelho, M. Dolce, and F. Ponzo, “Experimental behaviour of R/C frames retrofitted with dissipating and re-centering braces”, *J. Earthquake Eng.* **8**:3 (2004), 361–396.
- [Christensen 2007] R. M. Christensen, “A comprehensive theory of yielding and failure for isotropic materials”, *J. Eng. Mater. Technol. (ASME)* **129**:2 (2007), 173–181.
- [Daniel and Ishai 2006] I. M. Daniel and O. Ishai, *Engineering mechanics of composite materials*, 2nd ed., Oxford University Press, New York, 2006.
- [Eshelby 1957] J. D. Eshelby, “The determination of the elastic field of an ellipsoidal inclusion, and related problems”, *Proc. R. Soc. Lond. A* **241**:1226 (1957), 376–396.
- [Genin and Birman 2009] G. M. Genin and V. Birman, “Micromechanics and structural response of functionally graded, particulate-matrix, fiber-reinforced composites”, *Int. J. Solids Struct.* **46**:10 (2009), 2136–2150.
- [Hu and Weng 2000] G. K. Hu and G. J. Weng, “The connections between the double-inclusion model and the Ponte Castaneda–Willis, Mori–Tanaka, and Kuster–Toksoz models”, *Mech. Mater.* **32**:8 (2000), 495–503.
- [Jiang and Batra 2002] B. Jiang and R. C. Batra, “Effective properties of a piezocomposite containing shape memory alloy and inert inclusions”, *Continuum Mech. Therm.* **14**:1 (2002), 87–111.
- [Jonnalagadda et al. 1998] K. D. Jonnalagadda, N. R. Sottos, M. A. Qidwai, and D. C. Lagoudas, “Transformation of embedded shape memory alloy ribbons”, *J. Intell. Mater. Syst. Struct.* **9**:5 (1998), 379–390.
- [Kakavas and Kontoni 2005] P. A. Kakavas and D.-P. N. Kontoni, “Numerical investigation of the stress field of particulate reinforced polymeric composites subjected to tension”, *Int. J. Numer. Methods Eng.* **65**:7 (2005), 1145–1164.
- [Kanaun and Jeulin 2001] S. K. Kanaun and D. Jeulin, “Elastic properties of hybrid composites by the effective field approach”, *J. Mech. Phys. Solids* **49**:10 (2001), 2339–2367.
- [Lagoudas 2008] D. C. Lagoudas (editor), *Shape memory alloys: modeling and engineering applications*, Springer, New York, 2008.
- [Lu and Weng 2000] Z. K. Lu and G. J. Weng, “A two-level micromechanical theory for a shape-memory alloy reinforced composite”, *Int. J. Plast.* **16**:10–11 (2000), 1289–1307.
- [Luo and Weng 1989] H. A. Luo and G. J. Weng, “On Eshelby’s S -tensor in a three-phase cylindrically concentric solid, and the elastic moduli of fiber-reinforced composites”, *Mech. Mater.* **8**:2–3 (1989), 77–88.
- [McCormick et al. 2006] J. McCormick, R. DesRoches, D. Fugazza, and F. Auricchio, “Seismic vibration control using super-elastic shape memory alloys”, *J. Eng. Mater. Technol. (ASME)* **128**:3 (2006), 294–301.

- [Milton 2002] G. W. Milton, *The theory of composites*, Cambridge Monographs on Applied and Computational Mathematics **6**, Cambridge University Press, Cambridge, 2002.
- [Sato and Tanaka 1988] Y. Sato and K. Tanaka, “Estimation of energy dissipation in alloys due to stress-induced martensitic transformation”, *Res Mech.* **23** (1988), 381–393.
- [Tanaka 1986] K. Tanaka, “A thermomechanical sketch of shape memory effect: one dimensional tensile behavior”, *Res Mech.* **18** (1986), 251–263.
- [Tandon and Weng 1986] G. P. Tandon and G. J. Weng, “Stress distribution in and around spheroidal inclusions and voids at finite concentration”, *J. Appl. Mech. (ASME)* **53** (1986), 511–518.
- [Torquato 2001] S. Torquato, *Random heterogeneous materials: microstructure and macroscopic properties*, Interdisciplinary Applied Mathematics **16**, Springer, New York, 2001.
- [Tucker and Liang 1999] C. L. Tucker, III and E. Liang, “Stiffness predictions for unidirectional short-fiber composites: review and evaluation”, *Compos. Sci. Technol.* **59**:5 (1999), 655–671.
- [Vel and Batra 2004] S. S. Vel and R. C. Batra, “Three-dimensional exact solution for the vibration of functionally graded rectangular plates”, *J. Sound Vib.* **272**:3–5 (2004), 703–730.

Received 16 Dec 2008. Revised 9 Feb 2009. Accepted 12 Feb 2009.

VICTOR BIRMAN: vbirman@mst.edu

*Engineering Education Center, Missouri University of Science and Technology, One University Boulevard,
St. Louis, MO 63121, United States*

ON THE DETACHMENT OF PATCHED PANELS UNDER THERMOMECHANICAL LOADING

WILLIAM J. BOTTEGA AND PAMELA M. CARABETTA

The problem of propagation of interfacial failure in patched panels subjected to temperature change and transverse pressure is formulated from first principles as a propagating boundaries problem in the calculus of variations. This is done for both cylindrical and flat structures simultaneously. An appropriate geometrically nonlinear thin structure theory is incorporated for each of the primitive structures (base panel and patch) individually. The variational principle yields the constitutive equations of the composite structure within the patched region and an adjacent contact zone, the corresponding equations of motion within each region of the structure, and the associated matching and boundary conditions for the structure. In addition, the transversality conditions associated with the propagating boundaries of the contact zone and bond zone are obtained directly, the latter giving rise to the energy release rates in self-consistent functional form for configurations in which a contact zone is present as well as when it is absent. A structural scale decomposition of the energy release rates is established by advancing the decomposition introduced in W. J. Bottega, *Int. J. Fract.* **122** (2003), 89–100, to include the effects of temperature. The formulation is utilized to examine the behavior of several representative structures and loadings. These include debonding of unfettered patched structures subjected to temperature change, the effects of temperature on the detachment of beam-plates and arch-shells subjected to three-point loading, and the influence of temperature on damage propagation in patched beam-plates, with both hinged-free and clamped-free support conditions, subjected to transverse pressure. Numerical simulations based on closed form analytical solutions reveal critical phenomena and features of the evolving composite structure. It is shown that temperature change significantly influences critical behavior.

1. Introduction

The role of patched structures has expanded in modern engineering, as uses range from large-scale structural repair to sensors and actuators to small-scale electronic systems. Detachment of the constituent structures is thus an issue of concern as it may influence the effectiveness and integrity of the composite structure. By its nature, the structure possesses a geometrical discontinuity at the edge of the patch. Stress concentrations within the base structure-patch interface at this location (see, for example, [Wang and Rose 2000]) can lead to the initiation of debonding.¹ As a result, a primary mode of failure of such structures under various loading conditions is edge debonding and its propagation. The characterization of edge debonding is thus of critical importance in preserving the useful life of this type of structure.

Keywords: catastrophic, debonding, delamination, doubler, fracture, growth, growth path, interfacial failure, panel, patch, plate, propagation, shell, stable, structure, temperature, thermal, thermomechanical, unstable, variational.

¹For composite repair of structures, the patch edge is often tapered to discourage debond initiation (see, for example, [Duong and Wang 2007, Chapter 7]). The effect of layer-wise step-tapering on damage propagation was studied in [Bottega and Karlsson 1999] and [Karlsson and Bottega 1999a].

The structures of interest are typically subjected to temperature variations from the reference state. Such temperature changes can influence the onset and extent of damage in these structures. In this light, [Duong and Yu \[2002\]](#) examined the thermal effects of curing on the stress intensity factor for an octahedral-shaped composite repair patch bonded to a cracked rectangular plate. A general expression for the stress distribution was calculated analytically by adopting an “equivalent inclusion method” attributed to [Rose \[1981\]](#), assuming a second order polynomial distribution for the strains. The solution is used to analyze a sample problem and is compared with results using FEM. Related work includes that of [Wang et al. \[2000\]](#), who analyzed thermally-induced residual stresses due to curing in plates with circular patches. Structures were restricted to those with identical coaxial circular patches on the upper and lower faces of the plate so as to eliminate bending as an issue. [Moore \[2005\]](#), with an eye towards avoiding detachment of layers due to uniform temperature change, developed an analytical beam type model in the spirit of [Timoshenko \[1925\]](#) to describe peeling of a composite laminate under thermal load. In this context, he calculated the peeling moment that arises from the peel stress at any interface of the structure due to an applied uniform temperature change from the curing temperature. This was done via a force balance approach, where a decomposition of the moments into thermal and mechanical parts was utilized. The results were then applied to three- and four-layer beams. In a similar vein, [Toya et al. \[2005\]](#) employed a force balance based on classical beam theory to evaluate the energy release rate for a bilayer beam possessing an edge delamination when the structure is subjected to different temperatures at the top surface, bottom surface, and interface. They characterized the mode mix using a small-scale decomposition attributed to [Toya \[1992\]](#) which utilizes complex stress intensity factors and the crack closure method to characterize the energy release rate.

In related work, [Karlsson and Bottega \[2000a; 2000b\]](#) studied the effects of a uniform temperature field applied to a patched plate, where the base structure is fixed at both ends with regard to in-plane translation. In that work, the authors uncovered and explained the instability phenomenon they refer to as “slingshot buckling”, whereby, at a critical temperature, the structure “slings” dynamically from an equilibrium configuration possessing deflections in one direction to another equilibrium configuration with deflections in the opposite direction. [Rutgerson and Bottega \[2002\]](#) examined the thermo-elastic buckling of multilayer shell segments. In that study, the layered shells are subjected to an applied transverse pressure in addition to a uniform temperature field. The nonlinear analysis therein showed “slingshot” buckling to occur for thermal loading of these types of structures as well, and at temperatures well below the conventional “limit point” (see also [\[Rutgerson and Bottega 2004\]](#)). The findings on slingshot buckling have since been unified [\[Bottega 2006\]](#). It is concluded that this type of buckling is inherent to many types of composite structures and occurs due to competing mechanical and thermal elements of the loading. Most recently, [Carabetta and Bottega \[2008\]](#) studied the effects of geometric nonlinearities on the debonding of patched beam-plates subjected to transverse pressure. Analyses using both nonlinear and linearized models were conducted and compared. Significant discrepancies were seen to occur between behaviors predicted by the two models, both with respect to the onset of damage propagation and with regard to the stability of the process and to pre-growth behavior, demonstrating the influence of geometric nonlinearities on the phenomena of interest.

In the present work, we examine debonding of both initially flat and initially curved patched structures under uniform temperature alone and in consort with transverse pressure and three-point loading. Toward this end, the problem of propagation of interfacial debonds in patched panels subjected to temperature

change and transverse pressure is formulated from first principles as a propagating boundaries problem in the calculus of variations, in the spirit of [Bottega 1995; Bottega and Loia 1996; 1997; Bottega and Karlsson 1999; Karlsson and Bottega 1999a; 1999b], where various issues, configurations, and loading conditions were studied. For the present study, temperature is accounted for. A region of sliding contact adjacent to the intact region is also considered, and the boundary of the intact region as well as the boundary between the contact zone and a region of separation of the patch and base panel are each allowed to vary along with the displacements within each region. This is done for both cylindrical and flat structures simultaneously. An appropriate geometrically nonlinear thin structure theory is incorporated for each of the primitive structures (base panel and patch) individually. The variational principle then yields the constitutive equations of the composite structure within the patched region and an adjacent contact zone, the corresponding equations of motion within each region of the structure, and the associated matching and boundary conditions for the structure. In addition, the transversality conditions associated with the propagating boundaries of the contact zone and bond zone are obtained directly, the latter giving rise to the energy release rates in self-consistent functional form for configurations in which a contact zone is present as well as when it is not. A structural scale decomposition of the energy release rates is established by advancing the decomposition of [Bottega 2003] to include the effects of temperature. The formulation is then utilized to examine the behavior of several representative structures and loadings. These include debonding of unfettered patched structures subjected to temperature change, the effects of temperature on the detachment of beam-plates and arch-shells subjected to three-point loading, and the influence of temperature on damage propagation in patched beam-plates, with both hinged-free and clamped-free support conditions, subjected to transverse pressure. (The latter is shown in Figure 1.) Numerical simulations based on exact analytical solutions to the aforementioned formulation are performed, the results of which are presented in load-damage size space. Interpretation of the corresponding “growth paths” admits characterization of the separation behavior of the evolving composite structure. It is shown that temperature change significantly influences critical behavior.

2. Formulation

Consider a thin structure (flat or cylindrical) comprised of a base panel (plate or shell) of normalized half-span L to which a patch of half-span $L_p \leq L$ is adhered over the region $S_1 : s \in [0, a]$ (shown in Figure 2 for a flat panel). The coordinate s runs parallel to the reference surface and originates at the centerspan of the structure, as shown. Further, let us consider the debonded portion of the patch to

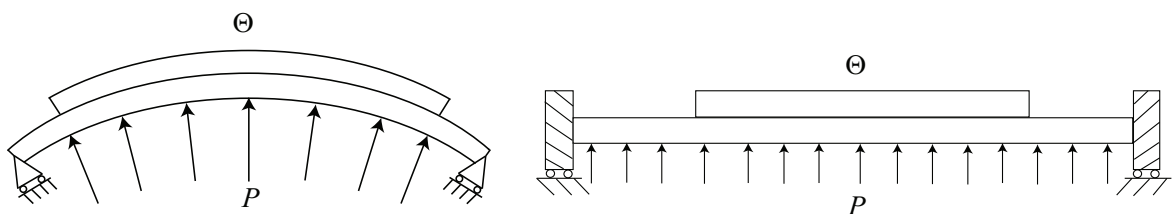


Figure 1. Patched structures subjected to transverse pressure and uniform temperature field. Left: cylindrical panel (arch-shell) with hinged-free supports. Right: flat panel (beam-plate) with clamped-free supports.

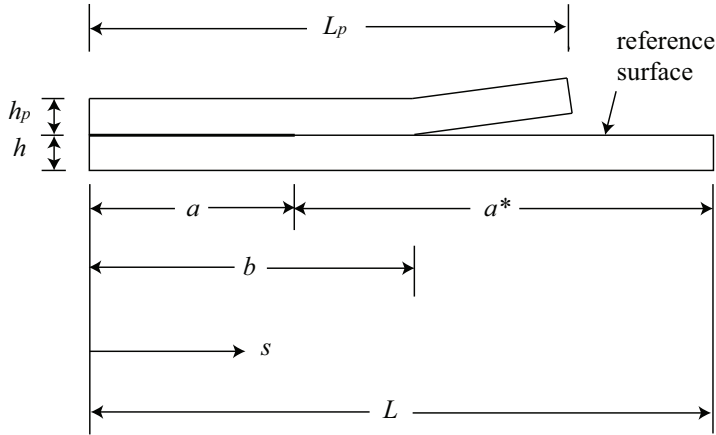


Figure 2. Dimensionless half-span of structure (shown for flat panel).

maintain sliding contact over the region $S_2 : s \in [a, b]$ adjacent to the bonded region, while a portion of the patch defined on $S_3 : s \in [b, L]$ is lifted away from the base structure. These three regions will be referred to as the “bond zone”, “contact zone”, and “lift zone”, respectively. The domain of definition of the portion of the patch within the lift zone is $S_{3p} : s \in [b, L_p]$ such that $S_{3p} \subset S_3$. When referring to the portion of the patch in region S_3 it will be understood that the corresponding subregion is indicated. At this point, let us also define the “conjugate bond zone” $a^* \equiv L - a$ as indicated in the figure. We shall be interested in examining the evolution and response of the composite structure when it is subjected to a uniform temperature increase, Θ , above some reference temperature. In what follows, all length scales are normalized with respect to the dimensional half-span \bar{L} (radius \bar{R}) of the undeformed plate (shell) structure, and the common surface or interface between the patch and base panel, and its extension, will be used as the reference surface. The temperature change, Θ , is normalized with respect to the reference temperature (and the coefficient of thermal expansion of the base structure). The corresponding relations for the normalized (centerline) membrane strains $e_i(s)$ and $e_{pi}(s)$ and the normalized curvature changes $\kappa_i(s)$ and $\kappa_{pi}(s)$ for the base structure and the patch in each region are thus given by

$$\begin{aligned}
 e_i &= u'_i - kw_i + \frac{1}{2}w_i'^2, & \kappa_i &= w_i'' + kw_i, & (s \in S_i) \\
 e_{pi} &= u'_{pi} - kw_{pi} + \frac{1}{2}w_{pi}'^2, & \kappa_{pi} &= w_{pi}'' + kw_{pi}, & (s \in S_{ip})
 \end{aligned}
 \tag{1}$$

where $k = 0$ corresponds to the plate and $k = 1$ corresponds to the shell, and the variables are defined as follows: $u_i = u_i(s)$ (positive in the direction of increasing s) and $w_i = w_i(s)$ (positive downward/inward), respectively, correspond to the axial (circumferential) and transverse (radial) displacements of the centerline of the base panel in region S_i , and $u_{pi} = u_{pi}(s)$ and $w_{pi} = w_{pi}(s)$ correspond to the analogous displacements of the centerline of the patch. The primes indicate total differentiation with respect to s .

The displacements $u_i(s)$ and $u_{pi}(s)$, and the membrane strains $e_i(s)$ and $e_{pi}(s)$ of the substructure centerlines are related to their counterparts $u_i^*(s)$ and $u_{pi}^*(s)$, and $e_i^*(s)$ and $e_{pi}^*(s)$ at the reference

surface, by the relations

$$\begin{aligned} u_i^* &= u_i + \frac{1}{2}hw'_i, & u_{pi}^* &= u_{pi} - \frac{1}{2}h_pw'_{pi} & (i = 1, 2, 3) \\ e_i^* &= e_i + \frac{1}{2}h\kappa_i, & e_{pi}^* &= e_{pi} - \frac{1}{2}h_p\kappa_{pi} & (i = 1, 2, 3) \end{aligned}$$

where $h \ll 1$ is the normalized thickness of the base panel and $h_p \ll 1$ is that of the patch. At this point let us also introduce the normalized membrane stiffness, C , and bending stiffness, D , of the base panel and the corresponding normalized membrane and bending stiffnesses, C_p and D_p , of the patch. The normalization of the stiffnesses of the primitive structures is based on the bending stiffness of the base panel and the half-span \bar{L} (radius \bar{R}) of the system in the undeformed configuration. Hence,

$$C = 12/h^2, \quad D = 1, \quad C_p = CE_0h_0, \quad D_p = E_0h_0^3, \tag{2}$$

where $h_0 = h_p/h$, and

$$E_0 = \bar{E}_p/\bar{E} \quad (\text{plane stress}) \quad \text{or} \quad E_0 = \frac{\bar{E}_p/(1-\nu_p^2)}{\bar{E}/(1-\nu^2)} \quad (\text{plane strain}),$$

where \bar{E} and \bar{E}_p correspond to the (dimensional) elastic moduli of the base panel and patch, respectively, and ν and ν_p are the associated Poisson's ratios.

The nondimensional coefficients of thermal expansion of the base structure and patch, α^0 and α_p^0 , respectively, are the products of the dimensional coefficients and the reference temperature. We correspondingly define, for the present formulation, the augmented coefficients α and α_p such that

$$\begin{aligned} \alpha &= \alpha^0 & \text{and} & & \alpha_p &= \alpha_p^0 & (\text{plane stress}), \\ \alpha &= (1+\nu)\alpha^0 & \text{and} & & \alpha_p &= (1+\nu_p)\alpha_p^0 & (\text{plane strain}). \end{aligned} \tag{3}$$

We next introduce the normalized temperature scale, Θ , such that

$$\tilde{\Theta} = \alpha\Theta = \alpha \frac{\bar{\Theta} - \bar{\Theta}_0}{\bar{\Theta}_0}, \tag{4}$$

where $\bar{\Theta}$ is the dimensional temperature and $\bar{\Theta}_0$ is a reference temperature.

Paralleling the developments in [Bottega 1995], we next formulate an energy functional in terms of (i) the strain energies of each of the individual segments of both the base panel and patch, independently, and expressed in terms of the reference surface variables, (ii) the work done by the applied loading for each case of interest, (iii) constraint functionals which match the transverse displacements in the contact zone and both the transverse (radial) and in-plane (circumferential) displacements in the bond zone², and (iv) a delamination energy functional corresponding to the energy required to create a unit length of new disbond. To complete the formulation, we include a thermal energy functional. We thus formulate the energy functional Π as follows:

$$\Pi = \sum_{i=1}^3 (U_B^{(i)} + U_{Bp}^{(i)} + U_M^{(i)} + U_{Mp}^{(i)} + U_T^{(i)} + U_{Tp}^{(i)}) - \Lambda - \mathcal{W} + \Gamma, \tag{5}$$

²The Lagrange multipliers in this case correspond to the interfacial normal and shear stresses, respectively.

where

$$U_B^{(i)} = \int_{S_i} \frac{1}{2} D \kappa_i^2 ds, \quad \text{and} \quad U_{Bp}^{(i)} = \int_{S_i} \frac{1}{2} D_p \kappa_{pi}^2 ds \quad (i = 1, 2, 3), \tag{6}$$

correspond to the bending energies in the base panel and the patch in region S_i , while

$$U_M^{(i)} = \int_{S_i} \frac{1}{2} C (e_i - \alpha \Theta)^2 ds \quad \text{and} \quad U_{Mp}^{(i)} = \int_{S_i} \frac{1}{2} C_p (e_{pi} - \alpha_p \Theta)^2 ds \quad (i = 1, 2, 3)$$

are the corresponding stretching energies of the base panel and the patch. Further,

$$U_T^{(i)} = \int_{S_i} (c_\sigma - (1 + \Theta)c_e) \Theta ds, \quad U_{Tp}^{(i)} = \int_{S_i} (c_{\sigma p} - (1 + \Theta)c_{ep}) \Theta ds$$

represent the “thermal energies” of the base structure and the patch, respectively, such that the total bracketed expression in (5) corresponds to the (Helmholtz) free energy of the structure, and Θ is the normalized temperature change. The quantities c_σ, c_e ($c_{\sigma p}, c_{ep}$) correspond to the normalized specific heats of the base structure (patch) for constant stress and constant deformation, respectively. These terms are included for completeness. We remark that since we shall consider the normalized temperature change, Θ , as prescribed, the variation of these functionals will vanish identically. (The contribution of the convective type terms of these particular functionals for a given region, associated with the propagation of the interior boundaries $s = a$ and $s = b$, will cancel and hence will have no contribution to the overall variation of Π as well.) Further, if the process is considered to be adiabatic, these terms will vanish identically as the free energy goes to internal energy and may be interpreted as the adiabatic work given by the first four functionals.

The functional Λ appearing in (5) is a constraint functional given by

$$\Lambda = \sum_{i=1}^2 \int_{S_i} \sigma_i (w_{pi} - w_i) ds + \int_{S_i} \tau (u_{p1}^* - u_1^*) ds,$$

where σ_1, σ_2 and τ are Lagrange multipliers (and $\sigma_2 < 0$). Further,

$$\mathcal{W} = - \sum_{i=1}^3 \int_{S_i} p w_i ds$$

is the work done by the applied pressure, and

$$\Gamma = 2\gamma (a^* - a_0^*)$$

is the delamination energy³, where

$$a^* = L - a$$

is the conjugate bond zone half-length as defined earlier, a_0^* corresponds to some initial value of a^* , and γ is the normalized bond energy (bond strength).

The normalized bond energy, γ , is related to its dimensional counterpart, $\bar{\gamma}$, by the relations

$$\gamma = \bar{\gamma} \bar{\ell}^2 / \bar{D},$$

³More generally, γ may be considered to be an implicit function of a^* . In this event, the functional Γ is defined in terms of its first variation, $\delta\Gamma = 2\gamma\delta a^*$ (that is, the virtual work of the generalized force γ).

where \bar{D} is the dimensional bending stiffness of the base panel and $\bar{\ell} = \bar{L}, \bar{R}$ (plate, shell). Likewise, the normalized interfacial stresses σ_1, σ_2 , and τ (the Lagrange multipliers), and the normalized applied pressure p , are related to their dimensional counterparts $\bar{\sigma}_1, \bar{\sigma}_2, \bar{\tau}$, and \bar{p} , respectively, by

$$\sigma_i = \bar{\sigma}_i \bar{\ell}^3 / \bar{D} \quad (i = 1, 2), \quad \tau = \bar{\tau} \bar{\ell}^3 / \bar{D}, \quad p = \bar{p} \bar{\ell}^3 / \bar{D}.$$

We next invoke the principle of stationary potential energy which, in the present context, is stated as

$$\delta \Pi = 0.$$

Taking the appropriate variations, allowing the interior boundaries a and b to vary along with the displacements, we arrive at the corresponding differential equations, boundary and matching conditions, and transversality conditions (the conditions that establish values of the “moveable” interior boundaries a and b to be found as part of the solution, together with the associated displacement field, which correspond to equilibrium conditions of the evolving structure). After eliminating the Lagrange multipliers from the resulting equations, we arrive at a self-consistent set of equations and conditions (including the energy release rates) for the evolving composite structure. We thus have

$$M_i^{*''} + k(M_i^* - N_i^*) - (N_i^* w_i^{*'})' = -p, \quad N_i^{*'} = 0 \quad (s \in S_i; i = 1, 2) \quad (7)$$

$$M_3'' + k(M_3 - N_3) - (N_3 w_3')' = -p, \quad N_3' = 0 \quad (s \in S_3) \quad (8)$$

$$M_{p3}'' + k(M_{p3} - N_{p3}) - (N_{p3} w_{p3}')' = 0, \quad N_{p3}' = 0 \quad (s \in S_{p3}) \quad (9)$$

with

$$w_i^*(s) \equiv w_i(s) = w_{pi}(s) \quad (s \in S_i; i = 1, 2),$$

$$\kappa_i^*(s) \equiv \kappa_i(s) = \kappa_{pi}(s) \quad (s \in S_i; i = 1, 2),$$

$$u_1^*(s) = u_{p1}(s) \quad (s \in S_1).$$

Here

$$N_i(s) = C[e_i(s) - \alpha\Theta], \quad N_{pi}(s) = C_p[e_{pi}(s) - \alpha_p\Theta] \quad (i = 1, 2, 3)$$

are the normalized resultant membrane forces acting on a cross section of the base panel and patch within region S_i ($i = 1, 2, 3$);

$$N_1^*(s) = C^* e_1^*(s) + B^* \kappa_1^*(s) - n^* \Theta = C^* [e_1^*(s) - \alpha^* \Theta] + B^* [\kappa_1^*(s) - \beta^* \Theta], \quad (10)$$

$$M_1^*(s) = A^* \kappa_1^*(s) + B^* e_1^*(s) - \mu^* \Theta = A^* [\kappa_1^*(s) - \beta^* \Theta] + B^* [e_1^*(s) - \alpha^* \Theta] \\ = D^* [\kappa_1^*(s) - \beta^* \Theta] + \rho^* N_1^*, \quad (11)$$

respectively, correspond to the normalized membrane force and normalized bending moment acting on a cross section of the bonded portion of the composite structure;

$$N_2^*(s) = N_2 + N_{p2} \quad \text{and} \quad M_2^*(s) = D_c \kappa_2^*(s) + \frac{1}{2}(h_p N_{p2} - h N_2) \quad (12)$$

correspond to the normalized resultant membrane force and bending moment for the debonded portion of the composite structure within the contact zone; and

$$M_3(s) = D \kappa_3(s) - \frac{1}{2} h N_3 \quad \text{and} \quad M_{p3}(s) = D_p \kappa_{p3}(s) + \frac{1}{2} h_p N_3,$$

correspond to the normalized bending moments in the base panel and patch segments within the region of separation (or lift zone).

The stiffnesses and thermal coefficients of the composite structure defined by (10), (11), and (12) are found in terms of the stiffnesses and thicknesses of the primitive substructures as

$$\begin{aligned} A^* &= D + D_p + (h/2)^2 C + (h_p/2)^2 C_p, & B^* &= (h_p/2)C_p - (h/2)C, \\ C^* &= C + C_p, & D^* &= A^* - \rho^* B^* = D_c + (h^*/2)^2 C_s, \\ \alpha^* &= \alpha_1 - \rho^* \beta^*, & \beta^* &= m^*/D^*, \end{aligned} \quad (13)$$

where

$$\begin{aligned} \rho^* &= B^*/C^*, & D_c &= D + D_p, & h^* &= h + h_p, & C_s &= C C_p / C^*, \\ \mu^* &= \frac{1}{2} h_p C_p \alpha_p - \frac{1}{2} h C \alpha, & n^* &= C_p \alpha_p + C \alpha, & m^* &= \mu^* - \rho^* n^*, & \alpha_1 &= n^*/C^*. \end{aligned} \quad (14)$$

The quantity ρ^* is seen to give the transverse (radial) location of the centroid of the composite structure with respect to the reference surface, D_c is the bending stiffness of the debonded segment of the composite structure in the contact zone, $h^* \ll 1$ is the normalized thickness of the composite structure, and C_s is an effective (series) membrane stiffness. In addition, the parameters α^* and β^* are seen to correspond to the thermal expansion coefficients of the intact portion of the composite structure, and correspond to the thermally-induced membrane strain at the reference surface and the associated curvature change, respectively, per unit normalized temperature change for a free unloaded structure. The thermal expansion coefficient α_1 is seen to be the corresponding strain per unit temperature at the centroid of the intact segment of an unloaded composite structure.

The associated boundary and matching conditions are obtained similarly:

$$u_1^*(0) = 0, \quad w_1^{*'}(0) = 0, \quad [M_1^{*'} - N_1^* w_1^{*'}]_{s=0} = 0 \quad (\text{symmetric deformation}) \quad (15a)$$

$$u_0^*(0) \equiv u_1^*(0) + \rho^* w_1^{*'}(0) = 0, \quad w_1^*(0) = 0, \quad \kappa_1^*(0) = 0 \quad (\text{antisymmetric deformation}) \quad (15b)$$

$$u_1^*(a) = u_2^*(a) = u_{p2}^*(a), \quad N_1^*(a) = N_2^*(a) \quad (a = a_L, -a_R) \quad (16)$$

$$w_1^*(a) = w_2^*(a), \quad w_1^{*'}(a) = w_2^{*'}(a) \quad (a = a_L, -a_R) \quad (17)$$

$$[M_1^{*'} - N_1^* w_1^{*'}]_{s=a} = [M_2^{*'} - N_2^* w_2^{*'}]_{s=a}, \quad M_1^*(a) = M_2^*(a) \quad (a = a_L, -a_R) \quad (18)$$

$$u_2^*(b) = u_3^*(b), \quad N_2(b) = N_3(b) \quad (b = b_L, -b_R) \quad (19)$$

$$u_{p2}^*(b) = u_{p3}^*(b), \quad N_{p2}(b) = N_{p3}(b) \quad (b = b_L, -b_R) \quad (20)$$

$$w_2^*(b) = w_3(b) = w_{p3}(b), \quad w_2^{*'}(b) = w_3^{*'}(b) = w_{p3}^{*'}(b) \quad (b = b_L, -b_R) \quad (21)$$

$$M_2^*(b) = M_3(b) + M_{p3}(b) \quad (b = b_L, -b_R) \quad (22)$$

$$[M_2^{*'} - N_2^* w_2^{*'}]_{s=b} = [M_3^{*'} - N_3 w_3^{*'}]_{s=b} + [M_{p3}^{*'} - N_{p3} w_{p3}^{*'}]_{s=b} \quad (b = b_L, -b_R) \quad (23)$$

$$N_{p3}(\pm L_p) = \kappa_{p3}(\pm L_p) = [M_{p3}^{*'} - N_{p3} w_{p3}^{*'}]_{s=\pm L_p} = 0 \quad (24)$$

$$u_3(\pm L) = 0 \quad \text{or} \quad N_3(\pm L) = 0 \quad (25)$$

$$w_3^{*'}(\pm L) = 0 \quad \text{or} \quad \kappa_3(\pm L) = 0 \quad (26)$$

$$w_3(\pm L) = 0 \quad (27)$$

The transversality condition for the propagating bond zone boundaries, $a = a_L, -a_R$, with the associated propagating contact zone boundaries, $b = b_L, -b_R$, take the following forms depending upon the presence or absence of a contact zone:

$$\mathcal{G}^{(2)}\{a\} = 2\gamma \quad (b > a), \quad \mathcal{G}^{(3)}\{a\} = 2\gamma \quad (b = a). \tag{28}$$

In these expressions, the quantities

$$\mathcal{G}^{(i)}\{a\} \equiv G_{MM}^{(i)} + G_{MT}^{(i)} + G_{TM}^{(i)} + G_{TT} \quad (i = 2, 3)$$

are the energy release rates, whose components are given by

$$G_{MM}^{(2)} \equiv \left[\frac{1}{2} D_c \kappa_2^{*2} + \frac{1}{2C} N_2^2 + \frac{1}{2C_p} N_{p2}^2 \right]_{s=a} - \left[\frac{1}{2} D^* (\kappa_1^* - \beta^* \Theta)^2 + \frac{1}{2C^*} N_1^{*2} \right]_{s=a}, \tag{29}$$

$$G_{MM}^{(3)} \equiv \left[\frac{1}{2} D \kappa_3^2 + \frac{1}{2} D_p \kappa_{p3}^2 + \frac{1}{2C} N_3^2 + \frac{1}{2C_p} N_{p3}^2 \right]_{s=a} - \left[\frac{1}{2} D^* (\kappa_1^* - \beta^* \Theta)^2 + \frac{1}{2C^*} N_1^{*2} \right]_{s=a}, \tag{30}$$

$$G_{MT}^{(i)} \equiv \left[\frac{1}{2} N_i e_T + \frac{1}{2} N_{pi} e_{pT} \right]_{s=a} - \left[\frac{1}{2} N_1^* e_T^* + \frac{1}{2} M_1^* \kappa_T^* \right]_{s=a} \quad (i = 2, 3), \tag{31}$$

$$G_{TM}^{(i)} \equiv \left[\frac{1}{2} N_T e_{pi}^o + \frac{1}{2} N_{pT} e_i^o \right]_{s=a} - \left[\frac{1}{2} N_T^* e_0^* + \frac{1}{2} M_T^* \kappa_0^* \right]_{s=a} \quad (i = 2, 3), \tag{32}$$

$$G_{TT} \equiv \left[\frac{1}{2} N_T e_T + \frac{1}{2} N_{pT} e_{pT} \right]_{s=a} - \left[\frac{1}{2} N_T^* e_T^* + \frac{1}{2} M_T^* \kappa_T^* \right]_{s=a}, \tag{33}$$

where the following measures have been introduced:

$$e_i^o \equiv e_i - \alpha \Theta, \quad e_{pi}^o \equiv e_{pi} - \alpha_p \Theta \quad (i = 2, 3), \tag{34}$$

$$e_T \equiv \alpha \Theta, \quad e_{pT} \equiv \alpha_p \Theta, \quad N_T = C \alpha \Theta, \quad N_{pT} = C_p \alpha_p \Theta, \tag{35}$$

$$e_0^* \equiv e_1^* - \alpha^* \Theta, \quad \kappa_0^* \equiv \kappa_1^* - \beta^* \Theta, \quad e_T^* \equiv \alpha^* \Theta, \quad \kappa_T^* \equiv \beta^* \Theta, \tag{36}$$

$$N_T^* \equiv C^* \alpha_1 \Theta = C^* e_T^* + B^* \kappa_T^*, \quad M_T^* \equiv \mu^* \Theta = D^* \kappa_T^* + \rho^* N_T^*. \tag{37}$$

The conditions established by those equations suggest the following *delamination criterion*:

If, for some initial value $a = a_0$ of the bond zone boundary, the state of the structure is such that $\mathcal{G}^{(i)}\{a\} \geq 2\gamma$, then delamination growth occurs and the system evolves (a decreases, a^ increases) in such a way that the corresponding equality in (28) is satisfied. If $\mathcal{G}^{(i)}\{a\} < 2\gamma$, delamination growth does not occur.*

For a propagating contact zone ($s = b$), the associated transversality condition reduces to the form

$$\kappa_2^*(b) = \kappa_3(b) = \kappa_{p3}(b) \quad (b = b_L < L_p, -b_R > -L_p), \tag{38}$$

to which we add the qualification

$$\kappa_3(b^+) > \kappa_{p3}(b^+) \tag{39}$$

in order to prohibit penetration of the base panel and patch for $s \in S_{3p}$. It is thus seen that such a boundary is defined by the point where the curvature changes of the respective segments of the structure are continuous.

The equations introduced so far define the class of problems of interest.

The boundary conditions (24), together with (9), indicate that the “flap” (the segment of the debonded portion of the patch that is lifted away from the base structure) is unloaded, and hence that

$$N_{p3}(s) = \kappa_{p3}(s) = M'_{p3}(s) = 0 \quad (s \in S_{3p}). \tag{40}$$

Further, integration of (7)₂ and (8)₂, imposition of the associated matching conditions stated by (16)₃, (19)₂, and (20)₂, and incorporation of (40)₁ yield the results that

$$N_1^* = N_2 = N_3 = N_0 = \text{constant}, \quad N_{p2} = 0. \tag{41}$$

The remaining equations are modified accordingly, with the transversality conditions stated in (28) and (38) taking the forms

$$\left. \begin{aligned} \mathcal{G}^{(2)}\{a\} &\longrightarrow \left[\frac{1}{2}D_c\kappa_2^{*2} - \frac{1}{2}D^*\kappa_1^{*2} + \frac{1}{2}N_0^2/C_e + N_0(\alpha - \alpha_1)\Theta + \frac{1}{2}\eta\Theta^2 \right]_{s=a} = 2\gamma \quad (b > a) \\ \mathcal{G}^{(3)}\{a\} &\longrightarrow \left[\frac{1}{2}D\kappa_3^2 - \frac{1}{2}D^*\kappa_1^{*2} + \frac{1}{2}N_0^2/C_e + N_0(\alpha - \alpha_1)\Theta + \frac{1}{2}\eta\Theta^2 \right]_{s=a} = 2\gamma \quad (b = a) \end{aligned} \right\} \tag{42}$$

and

$$\kappa_2^*(b) = \kappa_3(b) = 0, \quad \kappa_3(b^+) > 0 \quad (b < L_p), \tag{43}$$

where

$$\frac{1}{C_e} \equiv \frac{C_p/C}{C^*}, \quad \eta \equiv \alpha^2 C + \alpha_p^2 C_p - \alpha_1^2 C^*. \tag{44}$$

It may be seen from (43) that a propagating or intermediate contact zone boundary may occur only if conditions are such that an inflection point or pseudo-inflection point occurs on the interval $a < s < L_p$. If not, the system will possess either a full contact zone ($b = L_p$), or no contact zone ($b = a$). For the former case, the lifted segment of the flap (region S_{3p}) will not exist and the condition

$$\kappa_2(a^+) < 0 \quad (b = L_p) \tag{45}$$

must be satisfied.

Integrating the strain-displacement relations and imposing the boundary and matching conditions for the axial (circumferential) displacements results in the following *integrability condition*:

$$u_3(L) - u_0 = N_0 \left(\frac{a^*}{C} + \frac{a}{C^*} \right) + (a^*\alpha + a\alpha_1)\Theta - \left(\frac{h}{2} + \rho^* \right) w'(a) + \sum_{i=1}^3 \int_{S_i} (k(1 - \rho^*\delta_{i1})w_i - \frac{1}{2}w_i'^2) ds, \tag{46}$$

where

$$u_0 \equiv [u_1^* + \rho^* w'_1]_{s=0} \tag{47}$$

is the axial (circumferential) deflection of the neutral surface of the composite structure at the origin, and δ_{ij} is Kronecker’s delta. The counterparts of (7)₁ and (8)₁ and the corresponding boundary and matching conditions obtained upon substitution of (38)–(40), together with the transversality conditions stated in (42) and (43), and the integrability condition, (46), transform the problem statement into a *mixed formulation* in terms of the transverse displacements $w_i(s)$ ($i = 1, 2, 3$), the membrane force N_0 , and the moving boundaries a and b .

3. Delamination mode mix

The bond energy (that is, interfacial toughness) is generally dependent upon the mix of “delamination modes”. To assess this influence for the system under consideration, we adopt the structural scale decomposition of the energy release rate for long thin-layered structures established by Bottega [2003] and extend it to include the thermal effects considered for the present study. In the aforementioned reference, the decomposition is established for a general structure and is then applied to selected specific structural configurations, including patched structures. The presence of a contact zone is taken to imply pure mode-II delamination, while the absence of contact is considered to (generally) imply mixed mode-I and mode-II delamination. The mixed mode decomposition is based on the energy release rates for contact and no contact together with a “curvature of contact” defined therein. The decomposition for the present problem follows directly from the aforementioned reference and the inclusion of the thermal terms as follows. The last three terms of the energy release rates given by (42) are seen to constitute the relative thermomechanical membrane energy at the bond zone boundary and thus contribute to the mode-II delamination energy release rate. Incorporating the last two of these (the first is already included in the original) into the resulting partitioning of the energy release rate for the class of patched structures currently under consideration [Bottega 2003, Section 5.3] gives the following decomposition for the present structure:

$$G_I = \frac{1}{2}D_I\kappa_3^2(a), \quad G_{II} = \frac{1}{2}[D_{II}\kappa_3^2 - D^*\kappa_1^{*2}]_{x=a} + \left(\frac{1}{2}N_0^2/C_e + N_0(\alpha - \alpha_1)\Theta + \frac{1}{2}\eta\Theta^2\right), \quad (48)$$

where G_I and G_{II} are, respectively, the mode-I (opening mode) and mode-II (sliding mode) energy release rates, and

$$D_I = D_p D / D_c, \quad D_{II} = D^2 / D_c. \quad (49)$$

The mode ratio G_{II}/G_I can be readily evaluated using (48) for any configuration determined by the formulation established in this section.

4. Analysis

The mixed formulation presented in the previous section admits analytical solutions to within a numerically determined membrane force parameter. (7)–(9) together with the matching conditions, (16)–(23), and the pertinent boundary conditions of (15) and (24)–(27), can be readily solved to yield analytical solutions for the transverse displacement in terms of the membrane force. For given material and geometric properties, the membrane force can be evaluated numerically by substituting the corresponding analytical solutions into the integrability condition, (46), and finding roots (values of N_0) of the resulting transcendental equation using root solving techniques. Each root is associated with an equilibrium configuration of the evolving structure for given values of the temperature, pressure, damage size, and length of the contact zone. Once obtained, these values can be substituted back into the solution for the transverse deflection and the result then substituted into the transversality conditions (42) to generate the delamination growth paths for the evolving structure.⁴ The onset, stability, and extent of propagation can be assessed from these paths. (As a special case, it may be noted from (25)₂ and (41)₁ that when the edges

⁴For computational purposes, it is often convenient to combine the equations of the integrability and transversality conditions in a strategic manner, depending upon the circumstances.

of the base structure are free to translate in the axial (circumferential) direction, the uniform membrane force vanishes identically ($N_0 \equiv 0$). For this case, the analytical solutions may be obtained by direct integration, and substituted into the transversality condition. The corresponding integrability condition will then simply yield the axial (circumferential) displacement of the edge of the base structure.) Finally, the issue of a propagating contact zone may be examined by evaluating a solution for a given value of b (associated with a given value of a) and checking to insure that the resulting displacements satisfy the kinematic inequality (43)₂. The energy release rates for configurations with valid contact zones may then be plotted as a function of the contact zone boundary coordinate, b , for selected values of the bond zone size, a . (It was shown in [Bottega 1995] that for a certain class of problems a propagating contact zone is not possible. Rather, if contact of the detached segment of the patch with the base structure is present it is either in the form of a full contact zone—that is, the entire debonded segment of the patch maintains sliding contact with the base structure—or edge point contact, where only the “free” edge of the patch maintains sliding contact [Karlsson and Bottega 1999b]. If, for this class, neither of these configurations is possible then contact does not occur: a contact zone does not exist.)

For the case of no contact zone, a relatively simple growth path can be determined in the load-bond zone boundary space and the deflection-bond zone boundary space, or equivalently in the load-deflection space. Various scenarios can be predicted from examination of these paths as follows. Consider the generic growth path shown in Figure 3, where λ represents the generalized “load”, say the temperature change or the applied transverse pressure, and a^* corresponds to the size of the damaged region. For a given initial damage size (say point A , C , or F on the horizontal axis), no growth occurs as the load is increased until the load level is such that the growth path is intercepted. At that point growth ensues and may proceed according to several scenarios, depending upon the initial value of a^* . These scenarios include *stable growth* (BEH), where an increment in load produces an increment in damage size; *unstable growth* ($D \rightarrow E$) followed by stable growth (EH), where the damage propagates dynamically (that is, “jumps”) to an alternate stable configuration and then proceeds in a stable manner thereafter; and *unstable, catastrophic growth* ($G \rightarrow H'$), where the damage propagates dynamically through the entire length of the patch, resulting in complete detachment of the patch from the base structure.

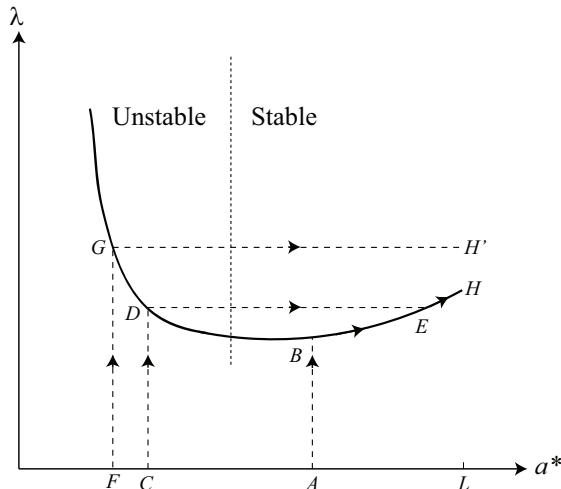


Figure 3. A generic debond growth path.

The formulation discussed in Section 2 and the procedure outlined in the current section are applied to examples of axially (circumferentially) unfettered structures in the next section.

5. Results for axially unfettered structures

In this section, we present results for structures that are completely unfettered and for those whose edges are free to translate in the axial (circumferential) direction. Specifically, in Section 5.1 we consider completely unfettered structures, flat or curved, subjected to temperature change alone. In Section 5.2 we consider the influence of temperature on edge debonding of both flat and curved structures subjected to three-point loading, and in Section 5.3 we examine the effects of temperature on the detachment of axially unfettered patched beam-plates subjected to transverse pressure.

5.1. Unfettered structures in a uniform temperature field. In this section, we examine the behavior of structures, flat or curved, that are completely unfettered (that is, those whose edges are free). The results discussed also hold for the case of pinned-free supports. That is, for structures for which the edges of the base panel are free to translate with regard to axial (circumferential) translation and pinned with regard to rotation.

For this case, a free-body diagram of segments of the structure in each of the regions shows that

$$\kappa_1^* = \beta^* \Theta, \quad \kappa_2^* = \kappa_3 = 0. \tag{50}$$

It follows from earlier discussions that for the present case passive contact occurs ($\kappa_2^* = 0$) for the entire detached segment of the patch, regardless of the sign of the thermally-induced curvature in the bond zone. In this case, the transversality conditions given by (42) reduce to the same form,

$$\mathcal{G} = \frac{1}{2}(\eta/\beta^{*2} - D^*)(\beta^* \Theta)^2 = 2\gamma. \tag{51}$$

Since the bond zone boundary does not appear explicitly in the equation (51) for the growth path, the energy release rate is independent of the location of the bond zone boundary. It follows that when growth occurs it is catastrophic. That is, when the critical temperature change is achieved, the entire patch detaches from the base structure in an unstable manner. Substitution of (44)₂, (13), and (14) into (51) renders the transversality condition for this case to the form

$$(\beta^* \Theta^*)^2 = \frac{2C_s h^{*2}}{D^*(4D^* - C_s h^{*2})}, \tag{52}$$

where

$$\Theta^* \equiv \Theta / \sqrt{2\gamma}. \tag{53}$$

It is seen from (52) that the critical renormed thermal curvature, $\beta^* \Theta^*$, is independent of the coefficients of thermal expansion of the constituent layers. The dependence of the critical thermal moment on the modulus ratio, E_0 , is displayed in Figure 4 for the case $h_p = h = 0.05$. The peak value of the critical curvature occurs for $E_0 \simeq 0.25$. (For later reference, we note that for $E_0 = 1$, $\|\beta^* \Theta^*\|_{cr} = 0.8660$.) We remark that, during the thermal loading, deformation, and evolution processes, the entire debonded segment of the patch maintains sliding contact with the base structure regardless of the sign of the renormed thermal curvature, $\beta^* \Theta^*$.

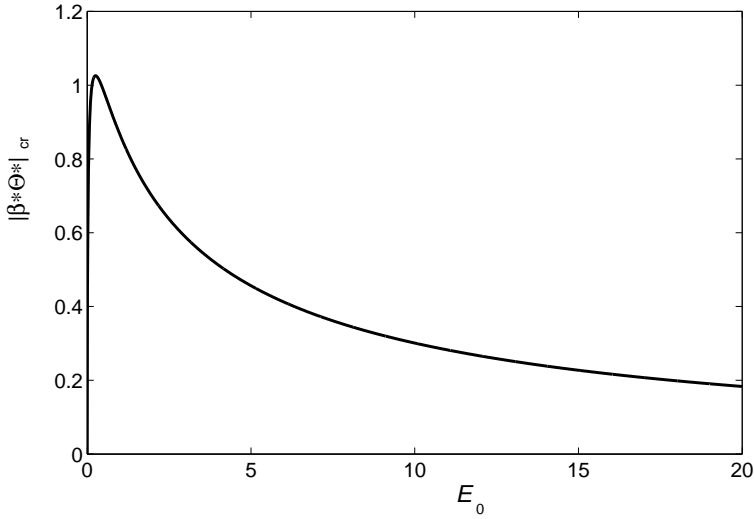


Figure 4. Critical renormed thermal curvature as a function of modulus ratio for a completely unfettered structure subjected to temperature change. ($h_p = h = 0.05$).

5.2. Temperature change and three-point loading. We next consider structures, both flat ($k = 0$) or cylindrical ($k = 1$), that are subjected to three-point loading and a uniform temperature field. For this case, the upwardly directed (normalized) transverse load at the center of the span is taken to be $2Q_0$, and the supports at the edges of the base panel are pinned-free. Equivalently, the edges of the base panel may each be considered to be loaded with a downwardly directed (normalized) transverse load Q_0 and the center of the span considered to be sitting on a knife edge (Figure 5). The normalized load, Q_0 , is related to its dimensional counterpart, \bar{Q}_0 , as follows:

$$Q_0 = \bar{Q}_0 \bar{\ell}^2 / \bar{D}, \tag{54}$$

where, as defined earlier, $\bar{\ell} = \bar{L}, \bar{R}$ (plate, shell). Consideration of the equilibrium of regions 2 and 3 of the structure shows that (43) is violated, and hence that no contact zone is present.

Patched plate. A region-wise moment balance for the patched beam-plate yields

$$\kappa_1^*(a) = \beta^* \Theta + \frac{Q_0}{D^*} (L - a), \quad \kappa_3(a) = \frac{Q_0}{D} (L - a). \tag{55}$$

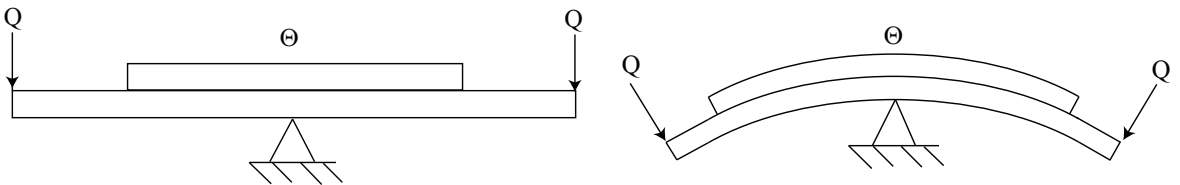


Figure 5. Three-point loading of patched structure. Left: patched beam-plate. Right: patched arch-shell.

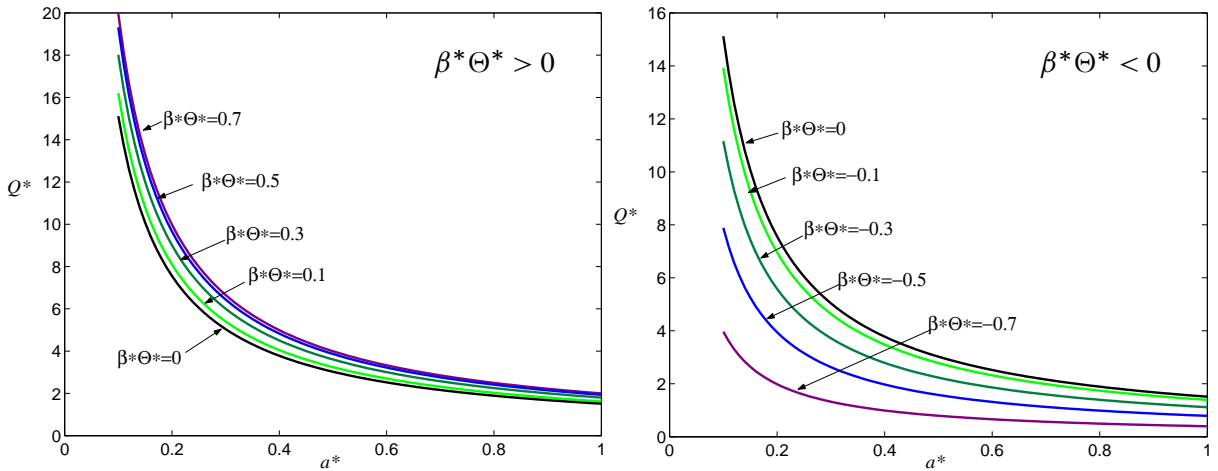


Figure 6. Growth paths for a patched plate subjected to three-point loading for various renormed temperatures (thermal curvatures). $\alpha_p/\alpha = 0.5$ or 2 ; $E_0 = 1$; $h = h_p = 0.05$.

It may be seen from these equations that a pseudo-inflection point may exist at $x = a$ when $\beta^*\Theta < 0$ and $\|\beta^*\Theta\| > Q_0(L - a)/D^*$. Substitution of (55) into (42)₂ reduces the transversality condition for the present case to the form

$$Q^{*2}a^{*2}\left(\frac{1}{D} - \frac{1}{D^*}\right) - 2Q^*a^*(\beta^*\Theta^*) + \left(\frac{\eta}{\beta^{*2}} - D^*\right)(\beta^*\Theta^*)^2 - 2 = 0, \tag{56}$$

where

$$Q^* \equiv Q/\sqrt{2\gamma}, \quad \text{and} \quad \Theta^* \equiv \Theta/\sqrt{2\gamma}. \tag{57}$$

The debond growth paths are easily generated from (56) for any structure of interest. Such paths are displayed in Figure 6 for a structure with the properties $E_0 = 1$, $h_p = h = 0.05$, $\alpha_p/\alpha = 0.5$, and $\alpha_p/\alpha = 2.0$. We note from Figure 4 that, for thermal loading alone, $\|\beta^*\Theta^*\|_{cr} = 0.8660$ when $E_0 = 1$. Thus, propagation will occur due to temperature change alone for this condition. To examine the effects of three-point loading we therefore consider temperature changes for which $\|\beta^*\Theta^*\|_{cr} < 0.8660$.

It may be seen from Figure 6 that, for any initial conjugate bond zone size, once the critical value of Q_0 is achieved it is sufficient for all larger conjugate bond zone sizes. Therefore, growth is catastrophic for all initial damage sizes. That is, once propagation ensues it continues unimpeded, with the patch ultimately completely separated from the base structure. To interpret these results further, we note the following. For the case $\alpha_p/\alpha = 2.0$, $\beta^* > 0$. Thus, for this case, the results displayed in Figure 6, left, correspond to positive temperature changes while those in Figure 6, right, correspond to negative temperature changes. For the case $\alpha_p/\alpha = 0.5$, $\beta^* < 0$, the interpretation is the reverse of that for $\alpha_p/\alpha = 2.0$. That is, for $\alpha_p/\alpha = 0.5$, the results shown on the left are associated with negative temperature changes while those on the right correspond to positive temperature changes. For negative thermally-induced curvature ($\beta^*\Theta^* < 0$), the intact segment of the composite structure is concave up, while the transverse load Q_0 tends to bend the detached segment concave downward thus encouraging “opening”. In this way, the temperature changes are seen to encourage detachment (Figure 6, right), lowering the critical level of the

transverse load well below that for vanishing temperature, with increasing magnitude of the temperature change. In contrast, for positive thermally-induced curvature ($\beta^*\Theta^* > 0$), the intact segment of the composite structure is concave down in the same sense as the curvature change of the detached segment as induced by Q_0 . The thermal effect here is to oppose “opening” and hence to resist detachment. In this sense, the critical level of the transverse load is seen to increase with increasing thermally-induced moment, as seen in [Figure 6](#), left, though these effects are observed to be less dramatic than those associated with negative thermal moments.

Patched shell. We next consider the analogous problem of a patched panel subjected to three-point loading. Recall that for curved structures, length scales are normalized with respect to the *radius* of the undeformed structure. Normalized arc lengths are then angles. Proceeding as for the beam-plate, a region-wise moment balance for the patched panel yields

$$\kappa_1^*(a) = \beta^*\Theta + \frac{Q_0}{D^*}F(a), \quad \kappa_3(a) = \frac{Q_0}{D}F(a), \tag{58}$$

where

$$F(a) = \cos L(\sin L - \sin a) + \sin L(\cos a - \cos L). \tag{59}$$

It is seen from the above equations that a pseudo-inflection point may exist at $x = a$ when $\beta^*\Theta < 0$ and $\|\beta^*\Theta\| > F(a)/D^*$. Substitution of (58) into the second line of (42) reduces the transversality condition for the present case to the form

$$Q^{*2}[F(a)]^2\left(\frac{1}{D} - \frac{1}{D^*}\right) - 2Q^*F(a)(\beta^*\Theta^*) + \left(\frac{\eta}{\beta^{*2}} - D^*\right)(\beta^*\Theta^*)^2 - 2 = 0, \tag{60}$$

where Q^* and Θ^* are defined by (57).

For the purposes of comparison, we shall examine the behavior of a specific structure having the same proportions as those of the beam-plate considered earlier. Toward this end we consider the structure for which $L = 0.4$ radians, $h_p = h = 0.02$ (same thickness to length ratio as the plate), $E_0 = 1$ and $\alpha_p/\alpha = 0.5$ and 2.0 . Corresponding results for a patched shell segment subjected to three-point loading ([Figure 5](#), right) are displayed in [Figure 7](#). It is seen that the behavior is very similar to that of the patched plate. (Recall that the load is normalized via (54).)

5.3. Temperature change and transverse pressure. In this section, we examine symmetric debonding of a patched beam-plate ($k = 0$) for cases where the edges of the base plate are free to translate in the axial direction. It follows from (25)₂ and (41) that, for these support conditions, $N_0 = 0$. This renders the governing differential equations for the transverse displacement $w(s)$, resulting from (7)₁, (8)₁, and (9)₁, linear. The solutions may thus be obtained by direct integration, with the constants of integration evaluated by imposing the boundary and matching conditions for transverse motion given by (15a)_{2,3}, (17), (18), (21)–(23), (24)_{2,3}, (26) and (27). We consider two extreme support conditions at the edges of the base plate: pinned-free and clamped-free. Based on these analytical solutions, numerical simulations are performed for structures possessing the representative properties $h_p = h = 0.05$, $E_0 = 1$, and $2\gamma = 0.1$. The first two properties render $B^* = \beta^* = 0$ and thus eliminate mechanical material bending-stretching coupling within the bonded region. We shall consider two complementary cases of

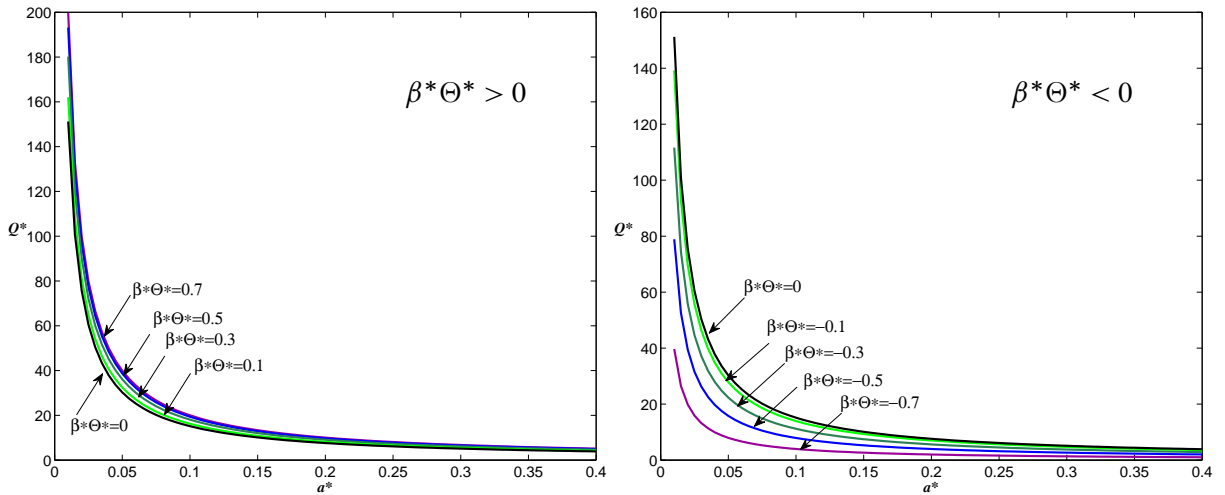


Figure 7. Growth paths for a patched shell subjected to three-point loading for various renormed temperatures (thermal curvatures). $\alpha_p/\alpha = 0.5$ or 2 ; $E_0 = 1$; $h = h_p = 0.02$; $L = 0.4$.

thermal mismatch: $\alpha_p/\alpha = 0.5$ and $\alpha_p/\alpha = 2.0$. For the purposes of presentation and interpretation of results, we introduce the characteristic deflection $\Delta_0 \equiv -w_1(0)$.

Hinged-free supports. We first examine the behavior of a structure with *hinged-free* supports. That is, a beam-plate for which the edges of the base-plate are hinged with respect to rotation and free with respect to in-plane translation (see Figure 1, left). For such support conditions, it may be anticipated that the deformed structure will not exhibit an inflection point or pseudo-inflection point, under the loading considered when deflections are upward. It follows, from the discussion preceding (45), that if a contact zone is present it will be a full contact zone. Moreover, a contact zone may be present only if the deflection of the structure is downward. However, for the supports and loading under consideration, the curvature of the bonded region will be concave upward during negative deflection, but the curvature of the base plate in the unpatched and detached regions will be concave downward regardless of the sign of the deflection. Thus, there will be a pseudo-inflection point at the bond zone boundary for downward deflections of the structure. Since the curvature of the patch in the detached region must be zero or concave upward, a contact zone is not possible.

Debond growth paths for the ratio $\alpha_p/\alpha = 0.5$ are displayed in Figure 8 for various values of the renormalized temperature $\tilde{\Theta} = \alpha\Theta$. The growth paths are presented in $p - a^*$ space (left half of the figure) and in $\Delta_0 - a^*$ space (right half).

For this ratio of thermal expansion coefficients, the influence of the temperature is greater for the base plate than for the patch, which results in a “concave up” curvature ($\beta^* \Theta < 0$) within the bond zone for positive temperature changes. This opposes the concave down curvature induced by the pressure and thus tends to “flatten” the structure within this region. In contrast, since the unbonded and debonded regions of the base plate are bent by the pressure alone, with the temperature change simply extending that segment of the structure, the curvature in these regions is concave downward. When the pressure

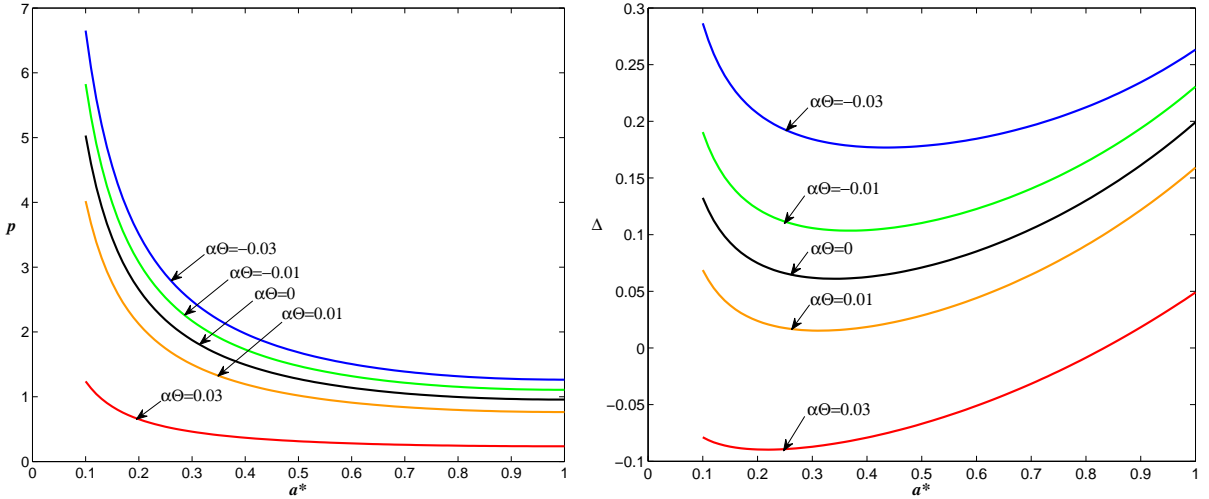


Figure 8. Debond growth paths for structures possessing hinged-free supports, with $\alpha_p/\alpha = 0.5$. Left: p versus a^* . Right: Δ_0 versus a^* .

effect dominates over the thermal moment, the curvature of the bond zone is concave down resulting in an upward deflection of the structure. For pressure-temperature combinations such that the deflection of the structure is upward, the “flattening” of the bond zone (by the temperature change) increases the relative bending of the unpatched segment of the base plate and hence the energy release rate for a given pressure, resulting in a lowering of the threshold pressure with increasing temperature change, as indicated. Moreover, when the temperature is sufficiently large such that the effects of the thermal moments dominate over those due to the pressure, then the curvature within the bond zone will be concave upward and the deflection of the structure will be downward. For these situations, the curvatures of the structure within the bonded and unbonded/debonded regions are of opposite sign, further increasing the relative bending between the detached and bonded segments at the bond zone boundary, and thus increasing the energy release rate at a given pressure level. This, in turn, results in further decreasing of the threshold pressure. Conversely, the threshold pressure increases with decreasing temperature. As the temperature change becomes negative, the thermal moment becomes positive ($\beta^*\Theta > 0$) and reinforces the mechanical moment rendering the curvature of the structure within the bond zone concave down — the same sense as within the detached/unbonded region. As a result, the relative bending at the bond zone boundary is reduced for a given value of the applied pressure and, consequently, the energy release rate. The threshold pressure, therefore, increases accordingly. In this sense, the effect of the thermal moment may be viewed as a reduction of the effective stiffness of the composite structure within the bonded region. At some point, the thermal effect reduces the “effective local stiffness” to the extent that the curvature of the structure within the bond zone is comparable with that of the detached segment of the base plate.

The debond growth paths for a mechanically and geometrically identical structure with $\alpha_p/\alpha = 2.0$ are displayed in Figure 9 for various values of the normalized temperature change. For ratios of the coefficients of thermal expansion greater than one, the thermal moment is positive ($\beta^*\Theta > 0$) for positive temperature changes. The scenarios for structures with this property are therefore the reverse of those for $\alpha_p/\alpha = 0.5$ discussed previously.

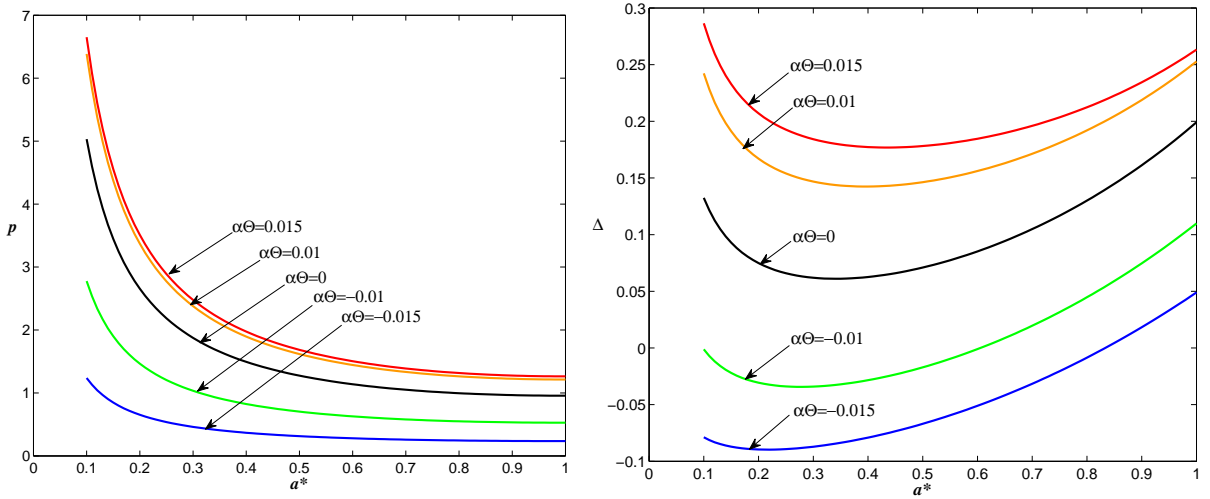


Figure 9. Debond growth paths for structures possessing hinged-free supports, with $\alpha_p/\alpha = 2.0$. Left: p versus a^* . Right: Δ_0 versus a^* .

Clamped-free supports. We next examine the behavior of a structure with *clamped-free* supports. That is, a beam-plate for which the edges of the base-plate are clamped with respect to rotation and free with respect to in-plane translation (see Figure 1, right). The arguments put forth when discussing the previous case, regarding the effects of the competition between the thermal and mechanical moments within the bond zone and their implications regarding curvature of the structure within that region, are paralleled for the present case. However, the constraints imposed on the rotations at the supports for the present case induce a pseudo-inflection point at the bond zone boundary and/or, at least, one inflection point along the half-span $[0, 1]$ for the type of loading considered. For the purposes of the present argument, we consider one inflection or pseudo-inflection point to be present on the half-span. It follows that the curvature of the segment of the structure nearest the support will be concave up when the deflection of the structure is upward. In this light, we deduce the following possible configuration scenarios from (43) and (45). When the deflection is upward, a pseudo-inflection point at the edge of the bonded region or an inflection point within the bond zone will be accompanied by a full contact zone. However, if an inflection point occurs within the unpatched/detached region then it will be accompanied by, at most, contact of the free edge of the patch with the detached segment of the base plate (“edge-point contact”). Conversely, when the deflection is downward, the curvature of the unpatched region will be concave down. For this situation, no contact zone will be present when a pseudo-inflection point is present at the bond zone boundary or an inflection point occurs within the bonded region. A partial propagating contact zone will be present when an inflection point occurs within the detached region and $\Delta_0 < 0$. Situations in which more than one critical point occurs along the span may be considered individually using the criterion established in Section 2 and discussed further in Section 3.

Growth paths for vanishing temperature are presented in Figure 10. Growth paths for structures with the property $\alpha_p/\alpha = 0.5$ are presented in Figure 11, and those for which $\alpha_p/\alpha = 2.0$ are shown in Figure 12, for selected values of the renormed temperature change. It is found, for the geometry and material ratios considered, that a full contact zone is possible for structures for which $L_p \geq 0.79$, depending upon

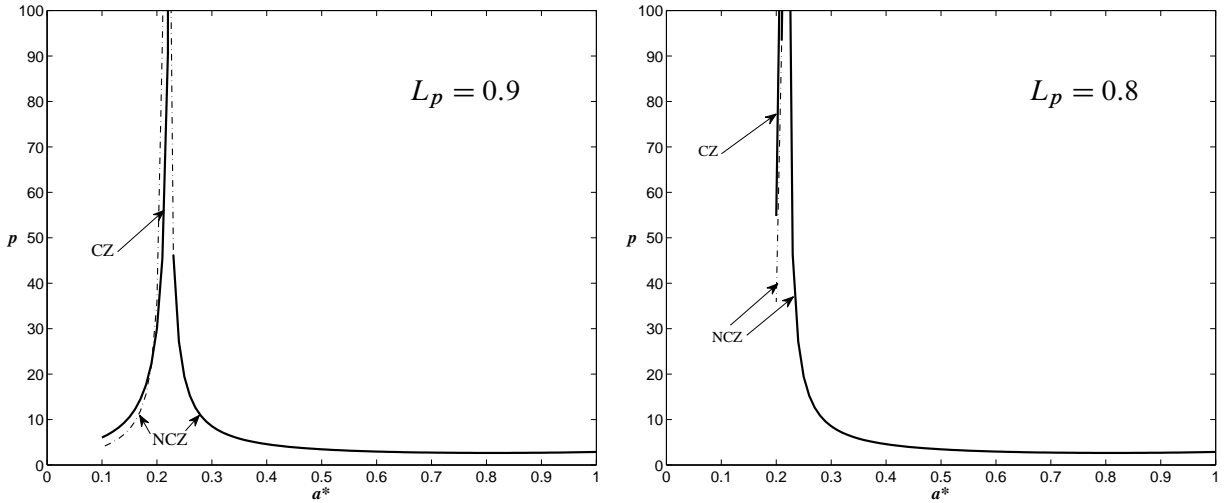


Figure 10. Contact zone (CZ) and no contact zone (NCZ) growth paths for structures subjected to pressure loading only ($\Theta = 0$) and possessing clamped-free supports.

the initial size of the damage. Structures possessing shorter patches have no contact zone regardless of the size of the damage.

Growth paths for a structure possessing a patch of length $L_p = 0.9$ for vanishing temperature change are presented in Figure 10, left. Those for a structure with a patch of length $L_p = 0.8$ are displayed in Figure 10, right. In these figures, the path labeled ‘CZ’ indicates the presence of a contact zone, and paths labeled ‘NCZ’ correspond to configurations with no contact zone. Invalid segments of the no contact zone paths are shown as dashed lines. Both legs of the NCZ path approach an asymptote at $a^* = 0.216$, while the CZ path for $L_p = 0.9$ approaches an asymptote at $a^* = 0.230$. It is seen that, when the contact zone is present, debonding is stable and that growth arrests as the asymptote is approached. It is also seen that the threshold values predicted with a contact zone present are lower than those predicted if it were neglected, for a range of values of a^* . For initial damage size to the right of the asymptote, growth is seen to be catastrophic for relatively small initial conjugate bond zone lengths, unstable followed by stable for intermediate initial damage sizes, and stable for relatively large initial conjugate bond zone sizes and/or patch half-lengths.

The effects of temperature are examined in Figures 11 and 12. The growth paths corresponding to selected temperature changes are displayed in p - a^* space and in Δ_0 - a^* space in Figure 11 for structures where $\alpha_p/\alpha = 0.5$. In each case, dashed segments of the paths correspond to equilibrium configurations for which a contact zone is present, ($L_p = 0.9$), while solid lines indicate configurations with no contact zone. Upon consideration of the figures, it is seen that the qualitative debonding behavior under force-controlled loading for moderate to large flaw sizes is very similar to that previously discussed for structures with hinged-free support conditions, but shows slight stabilization for very large debonds. (This stabilization depends on the temperature, as stable debonding is recovered for smaller flaw sizes as the temperature increases.) For this range, no contact zone is present, $\Delta_0 > 0$, and an inflection point occurs in the unpatched/detached region. For long patches, a contact zone is present, reducing the relative bending at the bond zone boundary and thus raising the threshold pressure, stabilizing the process, and

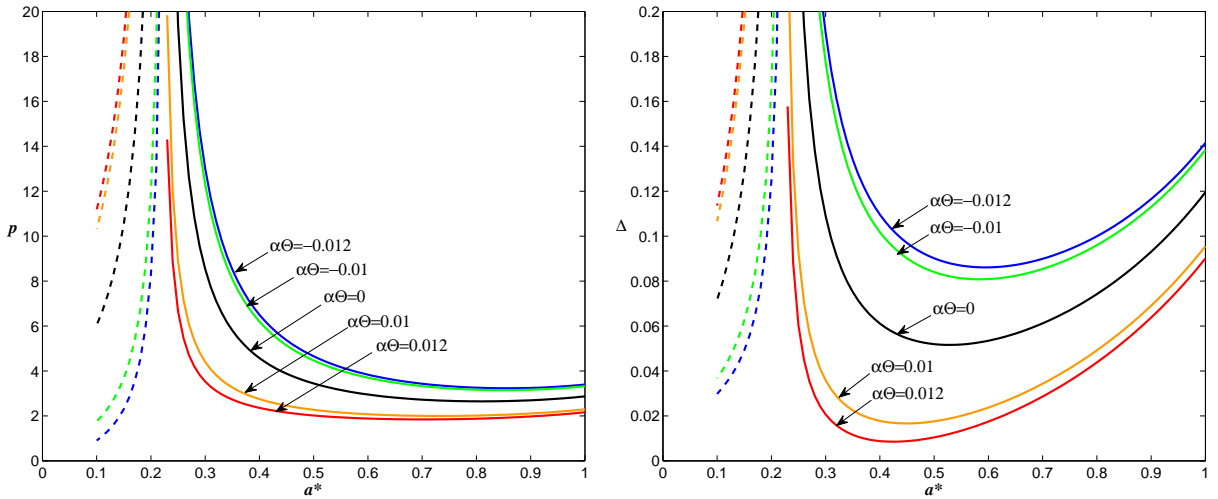


Figure 11. Growth paths corresponding to selected temperatures, for structures with clamped-free supports, with $\alpha_p/\alpha = 0.5$. Dashed lines indicate contact zone configurations for $L_p = 0.9$. Solid lines indicate no contact zone.

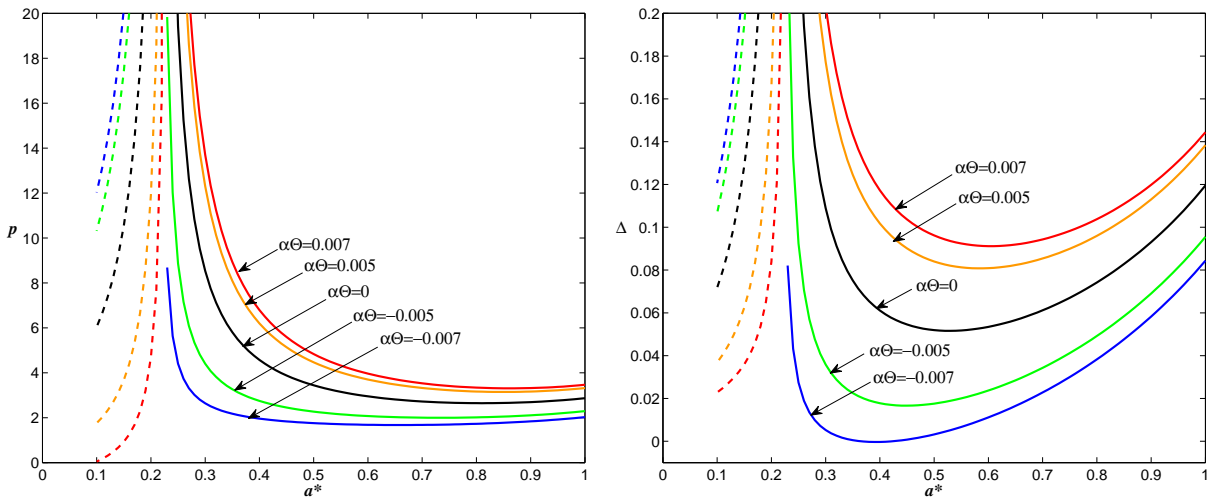


Figure 12. Growth paths corresponding to selected temperatures, for structures with clamped-free supports, with $\alpha_p/\alpha = 2.0$. Dashed lines indicate contact zone configurations for $L_p = 0.9$. Solid lines indicate no contact zone.

leading to eventual (asymptotic) arrest. The scenarios for deflection-controlled loading parallel those discussed for the hinged-free case, for moderate to large disbonds as well. For long patches with small initial debonds, stable growth and asymptotic arrest is indicated as for force-controlled loading. Similar results are shown in Figure 12 for structures with $\alpha_p/\alpha = 2.0$, but the effects of temperature are reversed.

Mode mix. Lastly, we examine the ratio of the mode-II energy release rate to the mode-I energy release rate using the structural scale decomposition presented in Section 3. Configurations for which a contact

Hinged-free support conditions				Clamped-free support conditions			
$\alpha_p/\alpha = 0.5$		$\alpha_p/\alpha = 2$		$\alpha_p/\alpha = 0.5$		$\alpha_p/\alpha = 2$	
$\tilde{\Theta}$	G_{II}/G_I	$\tilde{\Theta}$	G_{II}/G_I	$\tilde{\Theta}$	G_{II}/G_I	$\tilde{\Theta}$	G_{II}/G_I
-0.03	0.0019	-0.015	2.9389	-0.012	0.2488	-0.007	2.5102
-0.01	0.3059	-0.010	4.7497	-0.010	0.3059	-0.005	1.7409
0	0.7500	0	0.7500	0	0.7500	0	0.7500
0.01	1.7409	0.010	0.0870	0.010	1.7409	0.005	0.3059
0.03	27.939	0.015	0.0019	0.012	2.0822	0.007	0.1991

Table 1. Dependence of delamination mode ratio on temperature change for structures with hinged-free and clamped-free support conditions.

zone is present correspond to pure mode-II debonding ($G_{II}/G_I \rightarrow \infty$). For situations in which no contact zone is present, results for both hinged-free and clamped-free support conditions show that the mode partition ratio is independent of the debond size. Therefore, the qualitative debond scenarios for a given temperature discussed earlier are not altered due to the dependence of bond strength on mode mix, the exception being the comparison of contact zone and no contact zone configurations. The threshold levels for contact zone configurations will be relatively higher than indicated for a given temperature, since γ will be higher for pure mode-II. For either support condition considered, it is seen that when $\alpha_p/\alpha = 0.5$, the ratio increases with increasing temperature, and vice versa. The reverse is seen when $\alpha_p/\alpha = 2.0$. The dependence of G_{II}/G_I on $\tilde{\Theta} \equiv \alpha\Theta$ is summarized in [Table 1](#).

6. Concluding remarks

The problem of debonding of patched panels subjected to temperature change and transverse pressure has been formulated from first principles as a propagating boundaries problem in the calculus of variations. This is done for both cylindrical and flat structures simultaneously. An appropriate geometrically nonlinear thin structure theory is incorporated for each of the primitive structures (base panel and patch) individually. The variational principle then yields the constitutive equations of the composite structure within the patched region and an adjacent contact zone, the corresponding equations of motion within each region of the structure, and the associated matching and boundary conditions for the structure. In addition, the transversality conditions associated with the propagating boundaries of the contact zone and bond zone are obtained directly, the latter giving rise to the energy release rates in self-consistent functional form for configurations in which a contact zone is present, as well as when it is absent. Further, a structural scale decomposition of the energy release rates is established by advancing earlier work of the first author to include the effects of temperature. The formulation is utilized to examine the behavior of several representative structures and loadings. These include debonding of completely unfettered patched structures subjected to temperature change, the effects of temperature on the detachment of beam-plates and arch-shells subjected to three-point loading, and the effects of temperature on damage propagation in beam-plates, with both hinged-free and clamped-free support conditions, subjected to transverse pressure. For the unfettered structures subjected to thermal load, the dependence of the critical thermal moment is

found as a function of the ratio of elastic moduli, E_0 , for the patch and base structure. The critical moment is found to increase rapidly as the modulus ratio is increased, to a peak value for a modulus ratio about $E_0 = 0.25$, and then to decrease as the modulus ratio increases beyond this value. Damage propagation for both plate and shell structures subjected to three-point loading is seen to occur in a catastrophic manner once the critical load level is achieved. The critical load level is seen to be significantly influenced by the temperature field, especially for the shell structures. Similar qualitative behavior was seen for force-controlled loading of patched beam-plates subjected to transverse pressure and uniform temperature for the case of hinged-free support conditions. However, for displacement-controlled loading, debond propagation was seen to be stable, unstable followed by stable, or catastrophic, depending on the initial damage size and the temperature. For the case of clamped-free supports, a contact zone is present for very long patches for a limited range of damage sizes. For these situations, growth was seen to be stable, with minor propagation of the damaged region, and to lead to asymptotic arrest. For shorter patches, and for long patches with moderate to large initial damage, no contact zone was present. For these situations, propagation was seen to be catastrophic for moderately small initial damage or moderately large patch size, unstable followed by stable for still larger initial damage and stable for very large initial damage or small patch lengths. The threshold levels of the applied pressure and the stability of debond growth were seen to be strongly influenced by temperature for force-controlled loading. This behavior and its dependence on temperature was accentuated for displacement-controlled loading.

To close, we remark that the membrane force vanishes identically for the axially unfettered structures discussed in [Section 5](#), thus nullifying the contributions of the geometric nonlinearities for these support configurations. It was shown in [\[Carabetta and Bottega 2008\]](#), however, that retention of geometric nonlinearities is essential to adequately model debonding phenomena in thin structures for configurations in which the membrane force does not vanish identically. This is so regardless of whether or not buckling is an issue. In this light, the formulation and analytical procedure developed in the present work (Sections 2–4) is a geometrically nonlinear one, designed to study debonding behavior in structures possessing such configurations. This includes the study of the interaction of thermally-induced buckling and debond propagation as well. Extensive work in this area is currently in progress and will be presented in a forthcoming article by the authors.

Dedication

It is with great pleasure and honor that we contribute this paper to this special issue of JoMMS dedicated to Professor George J. Simitzes, a true gentleman and scholar.

References

- [Bottega 1995] W. J. Bottega, “[Separation failure in a class of bonded plates](#)”, *Compos. Struct.* **30**:3 (1995), 253–269.
- [Bottega 2003] W. J. Bottega, “[Structural scale decomposition of energy release rates for delamination propagation](#)”, *Int. J. Fract.* **122**:1–2 (2003), 89–100.
- [Bottega 2006] W. J. Bottega, “[Sling-shot buckling of composite structures under thermo-mechanical loading](#)”, *Int. J. Mech. Sci.* **48**:5 (2006), 568–578.
- [Bottega and Karlsson 1999] W. J. Bottega and A. M. Karlsson, “[On the detachment of step-tapered doublers, 1: Foundations](#)”, *Int. J. Solids Struct.* **36**:11 (1999), 1597–1623.

- [Bottega and Loia 1996] W. J. Bottega and M. A. Loia, “Edge debonding in patched cylindrical panels”, *Int. J. Solids Struct.* **33**:25 (1996), 3755–3777.
- [Bottega and Loia 1997] W. J. Bottega and M. A. Loia, “Axisymmetric edge debonding in patched plates”, *Int. J. Solids Struct.* **34**:18 (1997), 2255–2289.
- [Carabetta and Bottega 2008] P. M. Carabetta and W. J. Bottega, “Effects of geometric nonlinearities on damage propagation in patched beam-plates subjected to pressure loading”, *Int. J. Fract.* **152**:1 (2008), 51–62.
- [Duong and Wang 2007] C. N. Duong and C. H. Wang, “Bond-line analysis at patch ends”, Chapter 7, pp. 248–279 in *Composite repair: theory and design*, Elsevier, Amsterdam, 2007.
- [Duong and Yu 2002] C. N. Duong and J. Yu, “An analytical estimate of thermal effects in a composite bonded repair: plane stress analysis”, *Int. J. Solids Struct.* **39**:4 (2002), 1003–1014.
- [Karlsson and Bottega 1999a] A. M. Karlsson and W. J. Bottega, “On the detachment of step-tapered doublers, 2: Evolution of pressure loaded structures”, *Int. J. Solids Struct.* **36**:11 (1999), 1625–1651.
- [Karlsson and Bottega 1999b] A. M. Karlsson and W. J. Bottega, “The presence of edge contact and its influence on the debonding of patched panels”, *Int. J. Fract.* **96**:4 (1999), 381–406.
- [Karlsson and Bottega 2000a] A. M. Karlsson and W. J. Bottega, “On thermal buckling of patched beam-plates”, *Int. J. Solids Struct.* **37**:34 (2000), 4655–4690.
- [Karlsson and Bottega 2000b] A. M. Karlsson and W. J. Bottega, “Thermo-mechanical response of patched plates”, *AIAA J.* **38**:6 (2000), 1055–1062.
- [Moore 2005] T. D. Moore, “Thermomechanical peeling in multilayer beams and plates: a solution from first principles”, *Int. J. Solids Struct.* **42**:1 (2005), 271–285.
- [Rose 1981] L. R. F. Rose, “An application of the inclusion analogy for bonded reinforcements”, *Int. J. Solids Struct.* **17**:8 (1981), 827–838.
- [Rutgerson and Bottega 2002] S. E. Rutgerson and W. J. Bottega, “Thermo-elastic buckling of layered shell segments”, *Int. J. Solids Struct.* **39**:19 (2002), 4867–4887.
- [Rutgerson and Bottega 2004] S. E. Rutgerson and W. J. Bottega, “Pre-limit-point buckling of multilayer cylindrical panels under pressure”, *AIAA J.* **42**:6 (2004), 1272–1275.
- [Timoshenko 1925] S. Timoshenko, “Analysis of bi-metal thermostats”, *J. Opt. Soc. Am.* **11**:3 (1925), 233–255.
- [Toya 1992] M. Toya, “On mode I and mode II energy release rates of an interface crack”, *Int. J. Fract.* **56**:4 (1992), 345–352.
- [Toya et al. 2005] M. Toya, M. Oda, A. Kado, and T. Saitoh, “Energy release rates for an edge delamination of a laminated beam subjected to thermal gradient”, *J. Appl. Mech. (ASME)* **72**:5 (2005), 658–665.
- [Wang and Rose 2000] C. H. Wang and L. R. F. Rose, “Compact solutions for the corner singularity in bonded lap joints”, *Int. J. Adhes. Adhes.* **20**:2 (2000), 145–154.
- [Wang et al. 2000] C. H. Wang, L. R. F. Rose, R. Callinan, and A. A. Baker, “Thermal stresses in a plate with circular reinforcement”, *Int. J. Solids Struct.* **37**:33 (2000), 4577–4599.

Received 11 Sep 2008. Revised 23 Dec 2008. Accepted 31 Dec 2008.

WILLIAM J. BOTTEGA: bottega@rci.rutgers.edu

Department of Mechanical and Aerospace Engineering, Rutgers University, 98 Brett Road, Piscataway, NJ 08854-8058, United States

PAMELA M. CARABETTA: pamc@eden.rutgers.edu

Department of Mechanical and Aerospace Engineering, Rutgers University, 98 Brett Road, Piscataway, NJ 08854-8058, United States

EXPONENTIAL SOLUTIONS FOR A LONGITUDINALLY VIBRATING INHOMOGENEOUS ROD

IVO CALIÒ AND ISAAC ELISHAKOFF

A special class of closed form solutions for inhomogeneous rods is investigated, arising from the following problem: for a given distribution of the material density, find the axial rigidity of an inhomogeneous rod so that the *exponential* mode shape serves as the vibration mode. Specifically, for a rod clamped at one end and free at the other, the exponentially varying vibration mode is postulated and the associated semi-inverse problem is solved. This yields distributions of axial rigidity which, together with a specific law of material density, satisfy the governing eigenvalue problem. The results obtained can be used in the context of functionally graded materials for vibration tailoring, that is, for the design of a rod with a given natural frequency according to a postulated vibration mode.

1. Introduction

Recently, several closed-form solutions have been derived by the semi-inverse method [Elishakoff 2005] for the problem of eigenvalues of inhomogeneous structures. In particular Candan and Elishakoff [2001] solved the problem of construction of a bar with a specified mass density and a preselected polynomial mode shape, while Ram and Elishakoff [2004] solved the analogous problem in the discrete setting. It turns out that a bar with a tip mass [Elishakoff and Perez 2005] or with a translational spring [Elishakoff and Yost \geq 2009] can also possess a polynomial mode shape.

In a personal communication to the second author (2007), Dr. A. R. Khvoles posed the question of whether or not an inhomogeneous rod may possess an exponential mode shape. This question is elucidated in the present study. The solution can serve as a benchmark for the validation of various approximate analyses and numerical techniques.

Formulation of problem. Let us consider an inhomogeneous rod of length L , cross-sectional area $A(x)$, varying modulus of elasticity $E(x)$, and varying material density $\rho(x)$. The governing differential equation of the dynamic behavior of such an inhomogeneous rod is given by

$$\frac{\partial}{\partial x} \left[E(x)A(x) \frac{\partial u(x, t)}{\partial x} \right] - \rho(x)A(x) \frac{\partial^2 u(x, t)}{\partial t^2} = 0, \quad (1)$$

where x is the axial coordinate, t the time, and $u(x, t)$ the axial displacement.

For simplicity, the nondimensional coordinate $\zeta = x/L$ is introduced. Harmonic vibration is studied so that the displacement $u(x, t)$ is represented as

$$u(\zeta, t) = U(\zeta)e^{i\omega t}, \quad (2)$$

Keywords: closed form solutions, rod vibration, exponential solutions.

Isaac Elishakoff appreciates the partial financial support of the J.M. Rubín Foundation at Florida Atlantic University.

where $U(\xi)$ is the postulated mode shape and ω the corresponding natural frequency which has to be determined. Upon substitution of Equation (2) into (1), the latter becomes

$$\frac{d}{d\xi} \left[E(\xi)A(\xi) \frac{dU(\xi)}{d\xi} \right] + L^2 \rho(\xi)A(\xi)\omega^2 U(\xi) = 0. \tag{3}$$

The semi-inverse eigenvalue problem is posed as follows: Find an inhomogeneous rod that with reference to a specified exponential mode, $U(\xi)$, satisfies its boundary conditions and the governing dynamic equation of motion. This semi-inverse problem requires the determination of the distribution of axial rigidity, $D(\xi) = E(\xi)A(\xi)$, that together with a prespecified law for the mass distribution, $m(\xi) = A(\xi)\rho(\xi)$, satisfies (3).

We postulate the following form for the mode shape:

$$U(\xi) = A_0 + A_1 \xi \exp(\lambda \xi). \tag{4}$$

In this study, the differential equation (1) will be solved in a closed form for a rod that is clamped at one end and free at the other.

2. Clamped-free rod

We consider an inhomogeneous rod for which the following boundary conditions must be satisfied:

$$U(0) = 0, \quad U'(0) \neq 0, \tag{5}$$

$$U(1) \neq 0, \quad N(1) = 0, \tag{6}$$

where $N(1)$ is the axial force at $\xi = 1$, namely $N(1) = E(1)A(1)U'(1)/L$. Therefore in order to satisfy the boundary condition the mode shape assumes the form

$$U(\xi) = A_1 \xi \exp(-\xi), \quad U'(\xi) = A_1(1 - \xi) \exp(-\xi), \tag{7}$$

whose graph, for $A_1 = 1$, is shown in Figure 1.

Assuming that the mode shape is known, by integrating (3) we obtain

$$E(\xi)A(\xi) \frac{dU(\xi)}{d\xi} = -\omega^2 L^2 \int_0^\xi \rho(\eta)A(\eta)U(\eta) d\eta + N(0)L, \tag{8}$$

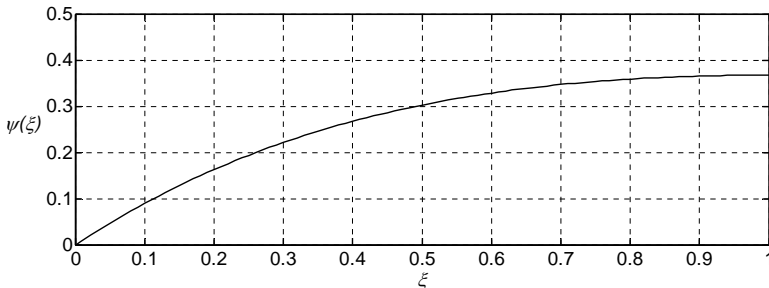


Figure 1. Postulated mode shape, (7).

where $N(0)$ is the amplitude of the axial loading at the cross-section $\zeta = 0$. For the clamped-free bar the boundary conditions (6) become

$$N(1) = \frac{E(1)A(1)}{L} \frac{dU}{d\zeta} \Big|_{\zeta=1} = 0. \tag{9}$$

By evaluating (8) at $\zeta = 1$ and employing the boundary condition (9) the following value of $N(0)$ is obtained:

$$N(0) = \omega^2 L \int_0^1 \rho(\alpha)A(\alpha)U(\alpha) d\alpha. \tag{10}$$

This condition coincides with [Elishakoff et al. 2001, equation 23]. Substitution of (10) into (8) yields

$$E(\zeta)A(\zeta) \frac{dU}{d\zeta} = \omega^2 L^2 \int_{\zeta}^1 \rho(\alpha)A(\alpha)U(\alpha) d\alpha. \tag{11}$$

In the semi-inverse formulation, the mode shape $U(\zeta)$ is a postulated function, that is,

$$U(\zeta) = \psi(\zeta). \tag{12}$$

Substitution into (11) yields the desired axial rigidity

$$D(\zeta) = E(\zeta)A(\zeta) = \frac{\omega^2 L^2}{\psi'(\zeta)} \int_{\zeta}^1 \rho(\alpha)A(\alpha)\psi(\alpha) d\alpha. \tag{13}$$

The candidate mode shape ought to satisfy the boundary conditions. Considering the candidate mode shape $\psi(\zeta) = \zeta \exp(-\zeta)$, the following particular cases arise:

Case 1: Constant cross-sectional area and constant material density. When

$$A(\zeta) = \text{const} = A_0, \quad \rho(\zeta) = \text{const} = \rho_0, \tag{14}$$

then (13) becomes

$$D(\zeta) = A_0 \rho_0 \omega^2 L^2 \frac{e - 2e^{\zeta} + e^{\zeta}}{e(1 - \zeta)}. \tag{15}$$

It is easy to verify that $D(0) > 0$ at $\zeta = 0$. By applying L'Hospital's rule at $\zeta = 1$, we observe that $D(1) > 0$. Therefore, assuming the distribution of axial rigidity reported in Figure 2a,

$$D(\zeta) = D_0 \frac{e - 2e^{\zeta} + e^{\zeta}}{e(1 - \zeta)} \tag{16}$$

in conjunction with the postulated mode shape in (7), shown in Figure 1, and the axial distribution

$$N(\zeta) = D_0 \frac{e - 2e^{\zeta} + e^{\zeta}}{e(1 - \zeta)} \psi'(\zeta), \tag{17}$$

represented in Figure 2b, the following eigenvalue parameter is obtained: $\omega^2 = D_0/A_0\rho_0L^2$.

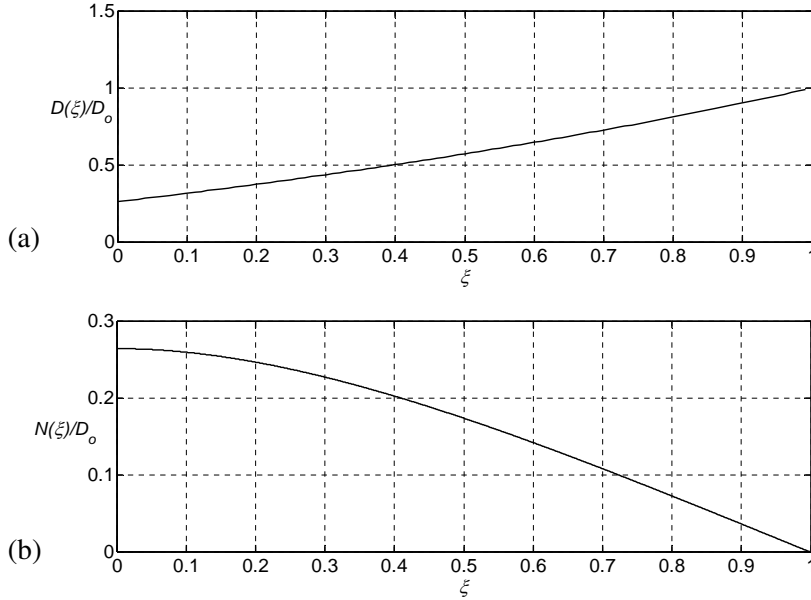


Figure 2. Variation in the axial modulus (a) and axial force (b) in an inhomogeneous bar, corresponding to the mode shape in Figure 1.

Case 2: Variable cross-sectional area and constant material density. When

$$A(\xi) \neq \text{const}, \quad \rho(\xi) = \text{const} = \rho_0, \tag{18}$$

then (13) gives

$$E(\xi) = \frac{\omega^2 L^2}{A(\xi)\psi'(\xi)} \int_{\xi}^1 \rho(\eta)A(\eta)U(\eta) d\eta. \tag{19}$$

As an example we assume the following form for $A(\xi)$:

$$A(\xi) = A_0(1 + \alpha\xi \exp(-\xi)), \tag{20}$$

with $A_0 > 0$ and $\alpha > -1$. Integrating (19), we obtain for the Young’s modulus

$$E(\xi) = \omega^2 L^2 \rho_0 \frac{4e^{1+\xi}(2e^\xi - e(1 + \xi)) + \alpha(5e^{2\xi} - e^2(1 + 2\xi + 2\xi^2))}{4e^2(\xi - 1)(e^\xi + \alpha\xi)}. \tag{21}$$

In view of (20) and (21), the axial stiffness becomes

$$D(\xi) = A_0 \rho_0 \omega^2 L^2 \frac{4 - 8e^{\xi-1} + 4\xi + \alpha e^{-\xi-2}(-5e^{2\xi} + e^2(1 + 2\xi + 2\xi^2))}{4(1 - \xi)}. \tag{22}$$

In Figure 3, the area variability $A(\xi)$, the Young modulus $E(\xi)$, the axial stiffness $D(\xi)$, and the axial force $N(\xi)$ are reported for the case $\alpha = 1$.

It is worth noticing that the solution that has been derived is not reducible to the case where the variation of elastic modulus, density, and cross sectional area are constants.

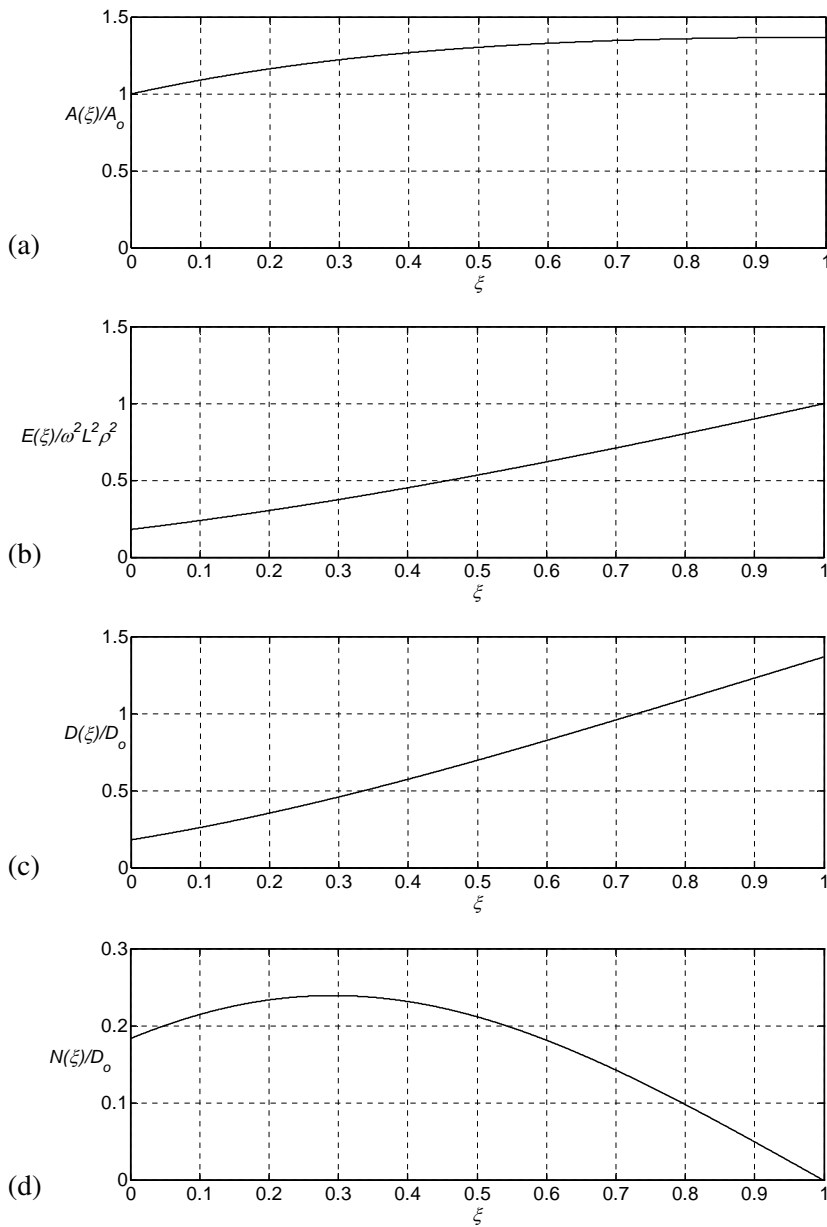


Figure 3. Variation of the cross-sectional area (a), modulus of elasticity (b), axial rigidity (b) and axial force (d) versus a nondimensional coordinate.

3. Conclusion

Apparently for the first time in the literature, it is shown that an inhomogeneous rod can possess an exponential mode shape. The derived closed-form solution can be utilized as a model solution for verification purposes.

References

- [Candan and Elishakoff 2001] S. Candan and I. Elishakoff, “Constructing the axial stiffness of longitudinally vibrating rod from fundamental mode shape”, *Int. J. Solids Struct.* **38**:19 (2001), 3443–3452.
- [Elishakoff 2005] I. Elishakoff, *Eigenvalues of inhomogeneous structures: unusual closed-form solutions*, CRC Press, Boca Raton, FL, 2005.
- [Elishakoff and Perez 2005] I. Elishakoff and A. Perez, “Design of a polynomially inhomogeneous bar with a tip mass for specified mode shape and natural frequency”, *J. Sound Vib.* **287**:4–5 (2005), 1004–1012.
- [Elishakoff and Yost \geq 2009] I. Elishakoff and J. Yost, “Vibration tailoring of a polynomially inhomogeneous bar with a translational spring”. In preparation.
- [Elishakoff et al. 2001] I. Elishakoff, M. Baruch, and R. Becquet, “Turning around a method of successive iterations to yield closed-form solutions for vibrating inhomogeneous bars”, *Meccanica (Milano)* **36**:5 (2001), 573–786.
- [Ram and Elishakoff 2004] Y. M. Ram and I. Elishakoff, “Reconstructing the cross-sectional area of an axially vibrating non-uniform rod from one of its mode shapes”, *Proc. R. Soc. Lond. A* **460**:2046 (2004), 1583–1596.

Received 11 Nov 2008. Revised 18 Jan 2009. Accepted 19 Jan 2009.

IVO CALIÒ: icalio@dica.unict.it

Dipartimento di Ingegneria Civile e Ambientale, Università di Catania, Catania, Italy

ISAAC ELISHAKOFF: elishako@fau.edu

Department of Mechanical Engineering, Florida Atlantic University, P.O. Box 3091, Boca Raton, FL 33431-0991, United States

STABILITY STUDIES FOR CURVED BEAMS

CHONG-SEOK CHANG AND DEWEY H. HODGES

The paper presents a concise framework investigating the stability of curved beams. The governing equations used are both geometrically exact and fully intrinsic; that is, they have no displacement and rotation variables, with a maximum degree of nonlinearity equal to two. The equations of motion are linearized about either the reference state or an equilibrium state. A central difference spatial discretization scheme is applied, and the resulting linearized ordinary differential equations are cast as an eigenvalue problem. The scheme is validated by comparing predicted numerical results for prebuckling deformation and buckling loads for high arches under uniform pressure with published analytical solutions. This is a conservative system of forces despite their being modeled as distributed follower forces. The results show that the stretch-bending coupling term must be included in order to accurately calculate the prebuckling curvature and bending moment of high arches. In addition, the lateral-torsional buckling instability of curved beams under tip moments is investigated. Finally, when a curved beam is loaded with nonconservative forces, resulting dynamic instabilities may be found through the current framework.

1. Introduction

For decades, the vibration of curved beams, rings, and arches has been extensively investigated. About 400 references, which cover the in-plane (i.e., in the plane of the undeformed, initially curved beam), out-of-plane (i.e., out of the plane of the undeformed, initially curved beam), coupled, linear and nonlinear vibrations, have been summarized by in [Chidamparam and Leissa 1993]. While linear theory is adequate for free-vibration analysis of initially curved beams, one must linearize the equations of nonlinear theory about a static equilibrium state, if a beam is brought into a state of high curvature by the loads acting on it. Because of this, the behavior of a beam curved under load may differ substantially from that of an initially curved beam of identical geometry. The geometrically exact and fully intrinsic theory of curved and twisted beams in [Hodges 2003] provides an excellent framework in which to elegantly study the coupled vibration characteristics of curved beams, particularly those curved because they are loaded. This is because of the simplicity of the equations — so simple that each term of every equation can be easily interpreted intuitively. There are no displacement or rotation variables (this is what is meant by “intrinsic” in this context); as a result there are no nonlinearities of degree greater than two. Both finite element and finite difference discretization schemes are easily applied to these equations for numerical computation, and the framework presented herein is simpler than that of other nonlinear beam theories. Because of these observations, we have revisited the topic and broadened the base of cases studied.

This paper provides details of how to make use of the fully intrinsic formulation for calculating vibration frequencies and buckling loads of curved beams. One aspect of these calculations that is substantially different from the usual approach involves the way boundary conditions are enforced. In [Chang and

Keywords: elastic stability, structural stability, buckling, elastica, fully intrinsic.

[Hodges 2009] results from free-vibration analysis of curved beams were compared with those from published work. Chidamparam and Leissa [1995], Tarnopolskaya et al. [1996], and Fung [2004] focused on in-plane vibration; and Irie et al. [1982] and Howson and Jemah [1999] on out-of-plane vibration. The coupled free-vibration frequencies were also presented as part of an investigation of low-frequency mode transition, also referred to as veering [Tarnopolskaya et al. 1999; Chen and Ginsberg 1992].

It was shown analytically by Hodges [1999] and Simitzes and Hodges [2006] that initially curved isotropic beams possess stretch-bending elastic coupling, that this coupling is proportional to initial curvature when the beam reference line is along the locus of cross-sectional centroids, and that this coupling cannot be ignored when calculating the equilibrium state of high circular arches. Although this term does not affect the buckling load, it must be included to calculate the prebuckling state correctly. As a validation exercise, the present formulation is applied to the prebuckling deformation of high arches. Displacement, curvature, bending moment and bifurcation load are compared to the analytical solutions with and without this coupling term.

As a more powerful alternative than analytical treatments for determining cross-sectional elastic constants, one may use VABS (variational asymptotic beam sectional analysis) [Cesnik and Hodges 1997; Yu et al. 2002; Hodges 2006] to numerically calculate all the cross-sectional elastic constants, including the stretch-bending coupling term. Based on results obtained from VABS, it is easy to show that there is another term that depends on initial curvature and reflects shear-twist coupling. This term becomes zero if the beam reference axis is along the locus of sectional shear centers. The location of the sectional shear center depends on the initial curvature, but an analytical expression for that dependence is unknown. Therefore, without a cross-sectional analysis tool such as VABS, which provides accurate cross-sectional elastic constants as a function of initial curvature, certain aspects of the analysis presented herein would be impossible.

2. Intrinsic beam formulation

The geometrically exact, intrinsic governing equations of [Hodges 2003] for the dynamics of an initially curved and twisted, generally anisotropic beam are

$$\begin{aligned}
 F'_B + \widetilde{K}_B F_B + f_B &= \dot{P}_B + \widetilde{\Omega}_B P_B, \\
 M'_B + \widetilde{K}_B M_B + (\widetilde{e}_1 + \widetilde{\gamma}) F_B + m_B &= \dot{H}_B + \widetilde{\Omega}_B H_B + \widetilde{V}_B P_B, \\
 V'_B + \widetilde{K}_B V_B + (\widetilde{e}_1 + \widetilde{\gamma}) \Omega_B &= \dot{\gamma}, \\
 \Omega'_B + \widetilde{K}_B \Omega_B &= \dot{\kappa},
 \end{aligned} \tag{1}$$

where F_B and M_B are the internal force and moment measures, P_B and H_B are the sectional linear and angular momenta, V_B and Ω_B are the velocity and angular velocity measures, γ and κ are the force and moment strain measures, k contains the initial twist and curvature measures of the beam, $K_B = k + \kappa$ contains the total curvature measures, and f_B and m_B are external force and moment measures, where loads such as gravitational, aerodynamic, and mechanical applied loads are taken into account. All quantities are expressed in the basis of the deformed beam cross-sectional frame except k which is in the basis of the undeformed beam cross-sectional frame. The tilde operator as in \widetilde{ab} reflects a matrix form

of the cross product of vectors $\mathbf{a} \times \mathbf{b}$ when both vectors and their cross product are all expressed in a common basis.

A central difference discretization scheme is applied to the intrinsic governing equations in space to obtain a numerical solution. The scheme satisfies both of the space-time conservation laws derived in [Hodges 2003]. This scheme can be viewed as equivalent to a particular finite element discretization, and the intrinsic governing equations are expressed as element and nodal equations. The n -th element equations, which are a spatially discretized form of (1), are

$$\begin{aligned} \frac{\widehat{F}_l^{n+1} - \widehat{F}_r^n}{dl} + (\widetilde{\kappa}^n + \widetilde{k}^n)\overline{F}^n + \overline{f}^n - \dot{\overline{P}}^n - \widetilde{\Omega}^n \overline{P}^n &= 0, \\ \frac{\widehat{M}_l^{n+1} - \widehat{M}_r^n}{dl} + (\widetilde{\kappa}^n + \widetilde{k}^n)\overline{M}^n + (\widetilde{e}_1 + \widetilde{\gamma}^n)\overline{F}^n + \overline{m}^n - \dot{\overline{H}}^n - \widetilde{\Omega}^n \overline{H}^n - \widetilde{V}^n \overline{P}^n &= 0, \\ \frac{\widehat{V}_l^{n+1} - \widehat{V}_r^n}{dl} + (\widetilde{\kappa}^n + \widetilde{k}^n)\overline{V}^n + (\widetilde{e}_1 + \widetilde{\gamma}^n)\overline{\Omega}^n - \dot{\overline{\gamma}}^n &= 0, \\ \frac{\widehat{\Omega}_l^{n+1} - \widehat{\Omega}_r^n}{dl} + (\widetilde{\kappa}^n + \widetilde{k}^n)\overline{\Omega}^n - \dot{\overline{\kappa}}^n &= 0, \end{aligned} \tag{2}$$

where \overline{f}^n and \overline{m}^n include any external forces and moments applied to the n -th element and dl is the length of an element.

The equations for node n need to include possible discontinuities caused by a nodal mass, a nodal force, and a slope discontinuity, so that

$$\begin{aligned} \widehat{F}_r^n - \widehat{C}_{lr}^{nT} \widehat{F}_l^n + \widehat{f}^n - \widehat{P}_r^n - \widetilde{\Omega}_r^n \widehat{P}_r^n &= 0, \\ \widehat{M}_r^n - \widehat{C}_{lr}^{nT} \widehat{M}_l^n + \widehat{m}^n - \widehat{H}_r^n - \widetilde{\Omega}_r^n \widehat{H}_r^n - \widetilde{V}_r^n \widehat{P}_r^n &= 0, \end{aligned} \tag{3}$$

where \widehat{C}_{lr} reflects the slope discontinuity, \widehat{f}^n and \widehat{m}^n are external forces and moments applied at n -th node, and

$$\widehat{V}_l^n = \widehat{C}_{lr}^n \widehat{V}_r^n \quad \text{and} \quad \widehat{\Omega}_l^n = \widehat{C}_{lr}^n \widehat{\Omega}_r^n. \tag{4}$$

One may also include gravitational force in the analysis. When this is done, the formulation needs additional equations to keep track of the vertical direction expressed in the cross-sectional basis vectors of the deformed beam; details may be found in [Patil and Hodges 2006]. This aspect of the analysis is not needed for the problems addressed herein.

3. Boundary conditions

Boundary conditions are needed to complete the formulation. Here, we describe boundary conditions for pinned–pinned and clamped–clamped beams. At each end, for the static case, either natural boundary conditions in terms of \widehat{F} and \widehat{M} or geometric boundary conditions in terms of u and C^{iB} may be prescribed. Here u is a column matrix of displacement measures u_i in the cross-sectional frame of the undeformed beam. Although these geometric boundary conditions are in terms of displacement and rotation variables, they are easily expressed in terms of other variables such as κ , γ , etc., given in (12), keeping the formulation intrinsic.

If displacement and rotation variables appear in the boundary conditions for the free-vibration case, a numerical Jacobian becomes necessary since an analytical determination of it would become intractable. Fortunately, when calculating free-vibration frequencies, one may for convenience replace boundary conditions on displacement and rotation variables with boundary conditions in terms of generalized velocities \widehat{V} and $\widehat{\Omega}$. With the velocity boundary conditions, rigid-body modes will not be eliminated from results.

3.1. Pinned–pinned boundary conditions. A total of 12 boundary conditions is necessary to calculate free-vibration frequencies, given by

$$\widehat{V}_r^1 = \widehat{M}_l^1 = 0, \tag{5}$$

$$\widehat{V}_r^{N+1} = 0 \quad \text{or} \quad \begin{cases} e_1^T C^{iB^{N+1}} \widehat{F}_r^{N+1} = 0, \\ e_2^T \widehat{V}_r^{N+1} = 0, \\ e_3^T C^{iB^{N+1}} \widehat{V}_r^{N+1} = 0, \end{cases} \tag{6}$$

$$\widehat{M}_r^{N+1} = 0, \tag{7}$$

where $C^{iB^{N+1}}$ is the rotation matrix of the beam cross-section at the right end. Equation (5) fixes the left boundary in space but leaves it free to rotate about all three axes. One may either apply a geometric boundary condition of zero displacement at left end or may take advantage of the intrinsic formulation through applying the velocity boundary condition given in (5). The right boundary condition of (6) allows free movement in the axial direction while holding velocity components in the transverse directions to zero, as shown in the right part of Figure 1. When there are no applied loads, one may simply make use of trivial values as reference states.

For a loaded case, however, the reference states should be obtained from a specific static equilibrium. To determine the static equilibrium, six boundary conditions are necessary, given by

$$\widehat{M}_l^1 = 0, \tag{8}$$

$$u_1^{N+1} = 0 \quad \text{or} \quad e_1^T C^{iB^{N+1}} \widehat{F}_r^{N+1} = 0, \quad u_2^{N+1} = u_3^{N+1} = 0. \tag{9}$$

The right end can be chosen either to be fixed in space or free to move in the axial direction, which is described in (9). For static equilibrium, one must apply displacement boundary conditions, which appear in (9), instead of velocity boundary conditions.

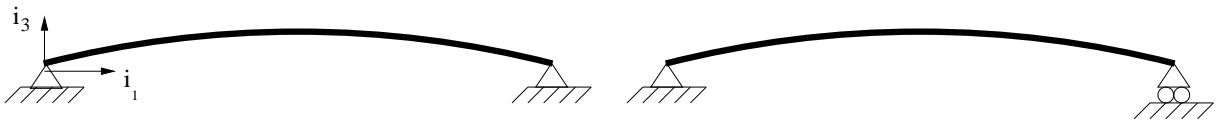


Figure 1. Schematics of initially curved beams with pinned–pinned boundary conditions.



Figure 2. Initially curved beam with clamped–clamped boundary condition.

3.2. Clamped–clamped boundary conditions. The clamped-clamped boundary conditions are

$$\widehat{V}_r^1 = \widehat{\Omega}_r^1 = 0 \quad \text{and} \quad \widehat{V}_r^{N+1} = \widehat{\Omega}_r^{N+1} = 0, \tag{10}$$

describing boundaries fixed in space and with zero rotation about all three axes.

As in the case of the pinned–pinned boundary condition, the boundary conditions for static equilibrium of a loaded case must be written in terms of displacement and rotation, given by

$$u_{\text{def}}^{N+1} = 0 \quad \text{and} \quad \widehat{C}_{\text{undef}}^{iB^{N+1}T} \widehat{C}_{\text{def}}^{iB^{N+1}} = \Delta, \tag{11}$$

where u_{def} is the column matrix of displacement measures at the right end of the beam, $\widehat{C}_{\text{def}}^{iB^{N+1}}$ is the rotation matrix of the beam cross-section at the right end after deformation, and $\widehat{C}_{\text{undef}}^{iB^{N+1}}$ is the rotation matrix of the beam cross-section at the right end in the undeformed state.

The boundary conditions associated with geometric conditions for static equilibrium require displacement and/or rotation to be expressed. These are described by the generalized strain-displacement equations from [Hodges 2003], given by

$$(r + u)' = C^{iB}(\gamma + e_1) \quad \text{and} \quad C^{Bi'} = -(\widetilde{\kappa} + \widetilde{k})C^{Bi}, \tag{12}$$

where r is the column matrix of position vector measures and u is the column matrix of displacement measures, both in the undeformed beam cross-sectional basis, and C^{Bi} is the rotation matrix of the beam cross-sectional reference frame in the deformed configuration. Equation (12) can be discretized as

$$\begin{aligned} r^{n+1} + u^{n+1} &= r^n + u^n + \bar{C}^{iB^n}(\bar{\gamma}^n + e_1)dl, \\ \widehat{C}^{Bi^{n+1}} &= \left(\frac{\Delta}{dl} + \frac{\widetilde{\kappa} + \widetilde{k}^n}{2}\right)^{-1} \left(\frac{\Delta}{dl} - \frac{\widetilde{\kappa} + \widetilde{k}^n}{2}\right) \widehat{C}^{Bi^n}. \end{aligned} \tag{13}$$

4. Linearization

The governing equations in the previous section are linearized about a static equilibrium so that they reduce to an eigenvalue problem to calculate the free-vibration frequencies. First,

$$X = X_{eq} + X^*(t), \tag{14}$$

where X is a state, X_{eq} is a value of the state at a static equilibrium, and X^* is small perturbation about the static value of the state. The linearized element equations from the intrinsic beam formulation are then

$$\begin{aligned} \frac{\widehat{F}_l^{*n+1} - \widehat{F}_r^{*n}}{dl} + (\widetilde{\kappa}_{eq}^n + \widetilde{k}^n)\bar{F}^{*n} + \widetilde{\kappa}^{*n}\bar{F}_{eq}^n + \mu^n \bar{g}^{*n} &= \dot{\bar{P}}^{*n}, \\ \frac{\widehat{M}_l^{*n+1} - \widehat{M}_r^{*n}}{dl} + (\widetilde{\kappa}_{eq}^n + \widetilde{k}^n)\bar{M}^{*n} + \widetilde{\kappa}^{*n}\bar{M}_{eq}^n + (\widetilde{e}_1 + \widetilde{\gamma}_{eq}^n)\bar{F}^{*n} + \widetilde{\gamma}^{*n}\bar{F}_{eq}^n + \mu^n \widetilde{\zeta}^n \bar{g}^{*n} &= \dot{\bar{H}}^{*n}, \\ \frac{\widehat{V}_l^{*n+1} - \widehat{V}_r^{*n}}{dl} + (\widetilde{\kappa}_{eq}^n + \widetilde{k}^n)\bar{V}^{*n} + (\widetilde{e}_1 + \widetilde{\gamma}_{eq}^n)\bar{\Omega}^{*n} &= \dot{\bar{\gamma}}^{*n}, \\ \frac{\widehat{\Omega}_l^{*n+1} - \widehat{\Omega}_r^{*n}}{dl} + (\widetilde{\kappa}_{eq}^n + \widetilde{k}^n)\bar{\Omega}^{*n} &= \dot{\bar{\kappa}}^{*n}. \end{aligned} \tag{15}$$

The linearized nodal equations are

$$\widehat{F}_r^{*n} - \widehat{C}_{lr}^{nT} \widehat{F}_l^{*n} + \widehat{\mu}^n \widehat{g}_r^{*n} - \widehat{P}_r^{*n} = 0 \quad \text{and} \quad \widehat{M}_r^{*n} - \widehat{C}_{lr}^{nT} \widehat{M}_l^{*n} + \widehat{\mu}^n \widehat{\xi}_n \widehat{g}_r^{*n} - \widehat{H}_r^{*n} = 0. \quad (16)$$

These linearized equations of motion can be expressed in a matrix form as $A\dot{X}^* = BX^*$, which is a system of first-order ordinary differential equations. When $X^* = \check{X} \exp(\lambda t)$ is assumed, the system is easily cast as a generalized eigenvalue problem of the form $B\check{X} = A\lambda\check{X}$. When B^{-1} exists, the equations reduce to a standard eigenvalue problem, such that $\lambda^{-1}\check{X} = B^{-1}A\check{X}$. When the eigenvalues are pure imaginary, the motion is simple harmonic.

5. Validation

A typical cross-sectional model for a beam has the form

$$\begin{Bmatrix} \gamma_{11} \\ 2\gamma_{12} \\ 2\gamma_{13} \\ \kappa_1 \\ \kappa_2 \\ \kappa_3 \end{Bmatrix} = \begin{bmatrix} R_{11} & R_{12} & R_{13} & S_{11} & S_{12} & S_{13} \\ R_{12} & R_{22} & R_{23} & S_{21} & S_{22} & S_{23} \\ R_{13} & R_{23} & R_{33} & S_{31} & S_{32} & S_{33} \\ S_{11} & S_{21} & S_{31} & T_{11} & T_{12} & T_{13} \\ S_{12} & S_{22} & S_{32} & T_{12} & T_{22} & T_{23} \\ S_{13} & S_{23} & S_{33} & T_{13} & T_{23} & T_{33} \end{bmatrix} \begin{Bmatrix} F_1 \\ F_2 \\ F_3 \\ M_1 \\ M_2 \\ M_3 \end{Bmatrix} \quad (17)$$

or

$$\begin{Bmatrix} \gamma \\ \kappa \end{Bmatrix} = \begin{bmatrix} R_{3 \times 3} & S_{3 \times 3} \\ S_{3 \times 3}^T & T_{3 \times 3} \end{bmatrix} \begin{Bmatrix} F \\ M \end{Bmatrix}, \quad (18)$$

where the 3×3 submatrices R , S , and T , which make up the cross-sectional flexibility matrix, may be computed by VABS for various initial curvatures [Cesnik and Hodges 1997; Yu et al. 2002; Hodges 2006]. When the reference line of the beam is chosen to be coincident with a cross-section shear center, the shear-torsion elastic couplings S_{21} and S_{31} vanish for that section.

Results in this section are to be compared with the analytical solutions for high arches in [Hodges 1999] and [Simitsev and Hodges 2006]. Hydrostatic pressure is modeled as a distributed follower force with constant magnitude per unit deformed length. When the equations are applied to buckling, the boundaries are allowed (artificially) to move so as to maintain a circular arc in the deformed but prebuckled state. For this case, only the radial displacement u_2 and local stretching strain measure ε are nontrivial and they are given as

$$\bar{u}_2 = \frac{\lambda \rho^2}{1 + \lambda \rho^2} \quad \text{and} \quad \bar{\varepsilon} = -\bar{u}_2, \quad (19)$$

where $\rho^2 = I_3/AR^2$ and $\lambda = f_2 R^3/EI_3$, where $EI_3 = 1/T_{33}$. (Subscript 2 indicates the radial direction along \mathbf{b}_2 and subscript 3 indicates normal to the plane of the undeformed arch. For more details on the definition of parameters see [Hodges 1999] and [Simitsev and Hodges 2006].) Figure 3 shows the excellent agreement between published analytical and present numerical solutions for ε versus λ .

Next, numerical results from the present analysis are compared with published analytical solutions for pinned–pinned and clamped–clamped arches under hydrostatic pressure. When the boundary conditions are not artificially adjusted, the problem is far more interesting. The geometry of the curved beam or arch

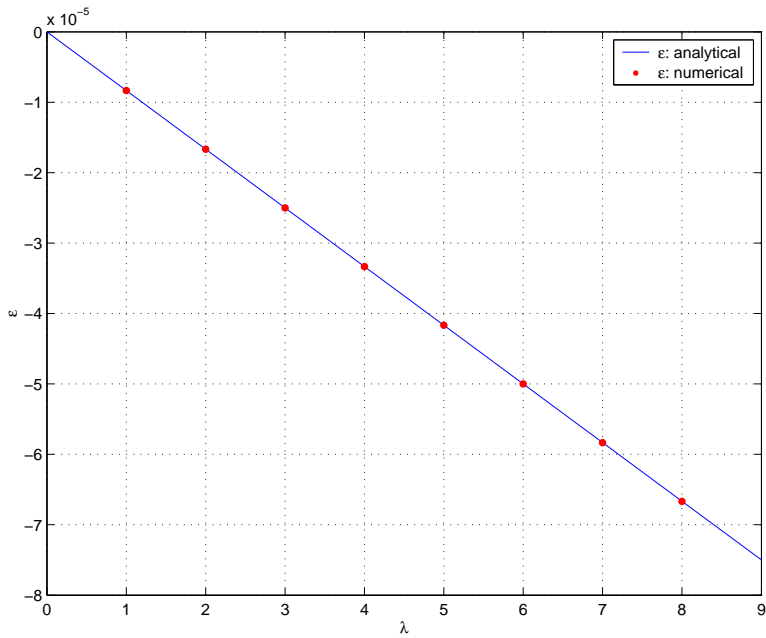


Figure 3. Plot of ε versus λ for $\rho^2 = 8.3333 \times 10^{-6}$, $\alpha = 1$.

used for the results is such that $\ell = 20$ m and $hk_2 = h/R_r = 0.01$, where h is the height of the cross-section, $R_r = 1/k_2$ is the initial radius of curvature, k_2 is the initial curvature, and α is the half-angle ($\ell = 2R_r\alpha$).

The prebuckling tangential and radial displacements u_1 and u_2 , prebuckling curvature κ and bending moment M for the pinned–pinned case are shown in Figures 4 and 5. All quantities are normalized according to the scheme in [Hodges 1999]. The present results agree well with the analytical solutions

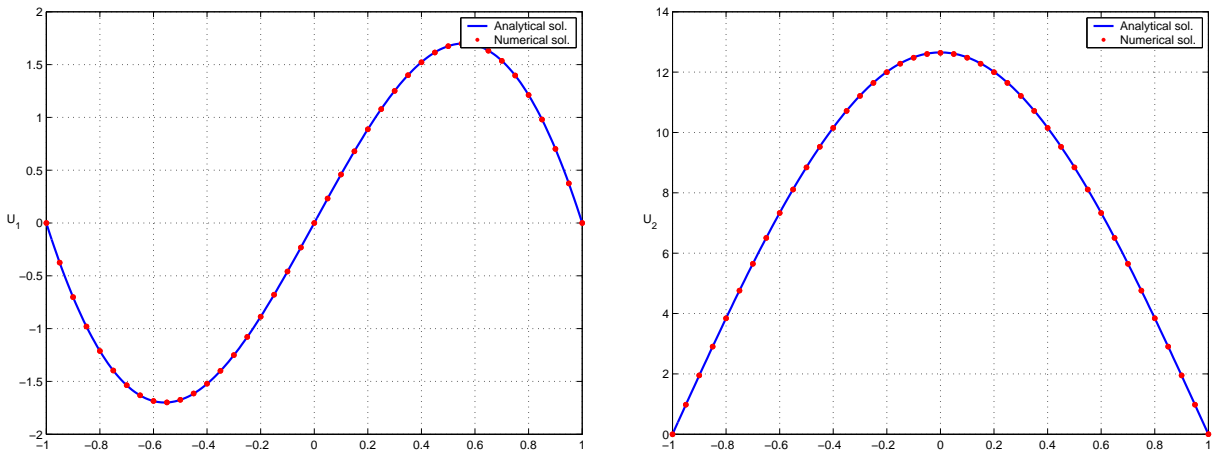


Figure 4. Normalized displacements u_1, u_2 for the pinned-pinned case ($\rho^2 = 8.3333 \times 10^{-6}$, $\lambda = 8$, $\alpha = 1$).

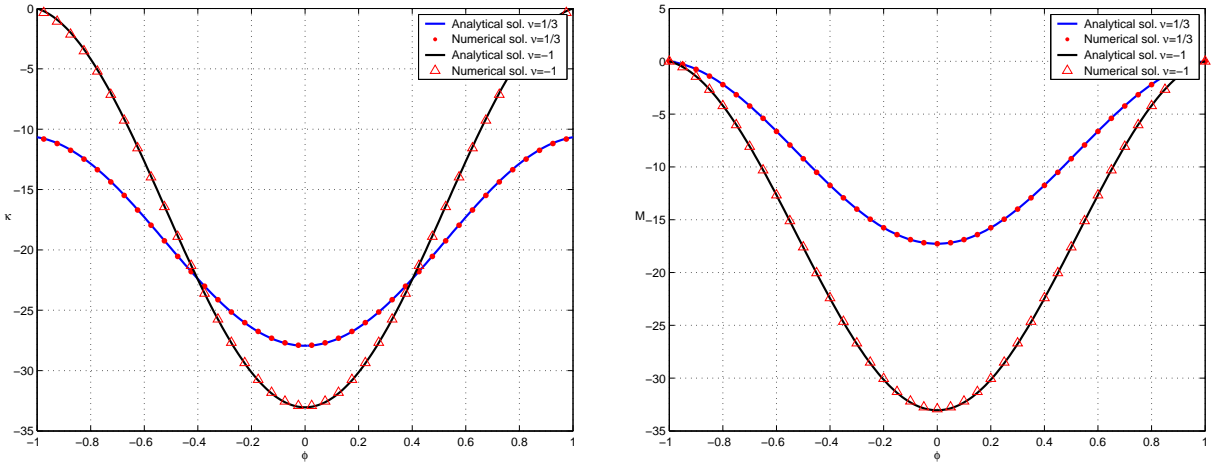


Figure 5. Curvature κ and bending moment M for the pinned-pinned case ($\rho^2 = 8.3333 \times 10^{-6}$, $\lambda = 8$, $\alpha = 1$).

for both $\nu = 1/3$ and $\nu = -1$; note that $\nu = -1$ annihilates the stretch-bending coupling according to both the analytical solution and the cross-sectional flexibility coefficients obtained from VABS. As is the case with the analytical solutions, κ and M depend significantly on whether or not the coupling term is included. Incidentally, there is a typographical error in the captions of Figures 2 and 3 in [Hodges 1999]; the results presented are for $\lambda = 8$, not $\lambda = 5$.

The results for the same beam and same loading but with clamped-clamped boundary conditions are shown in Figure 6 and 7. Only the normalized prebuckling bending moments change with ν , as is the case with the analytical solution in [Hodges 1999].

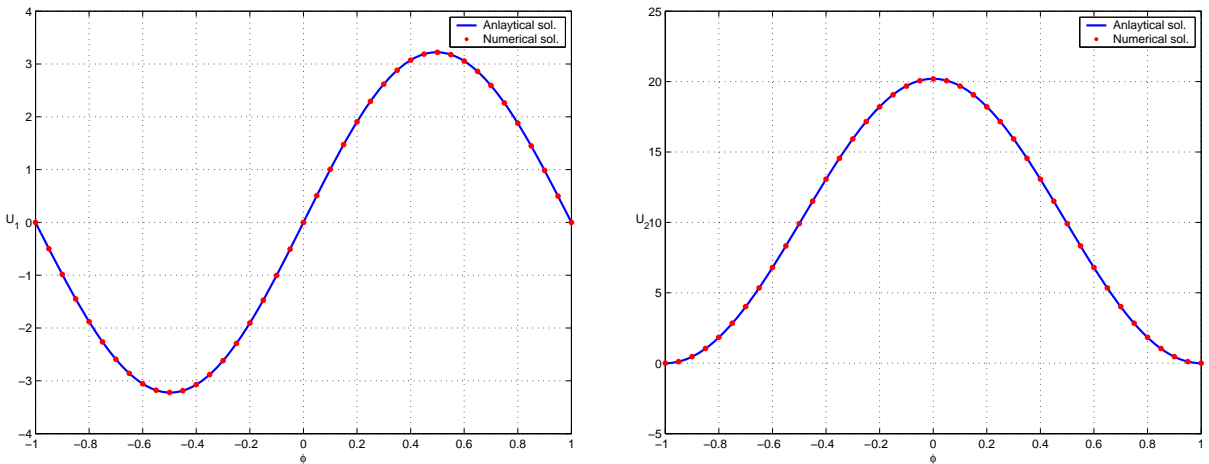


Figure 6. Normalized displacements u_1 , u_2 for the clamped-clamped case ($\rho^2 = 8.3333 \times 10^{-6}$, $\lambda = 8$, $\alpha = 1$).

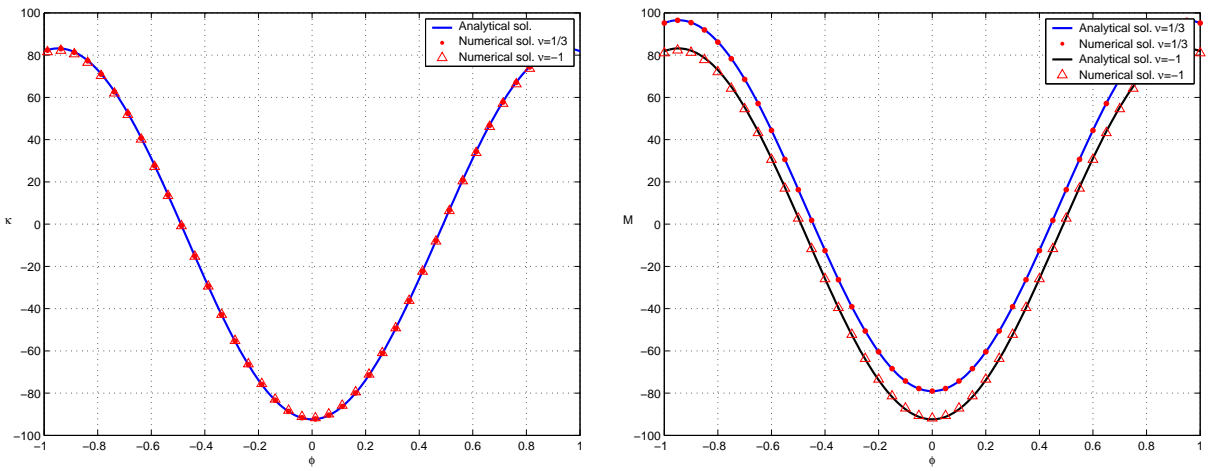


Figure 7. Curvature κ and bending moment M for the clamped-clamped case ($\rho^2 = 8.3333 \times 10^{-6}$, $\lambda = 8$, $\alpha = 1$).

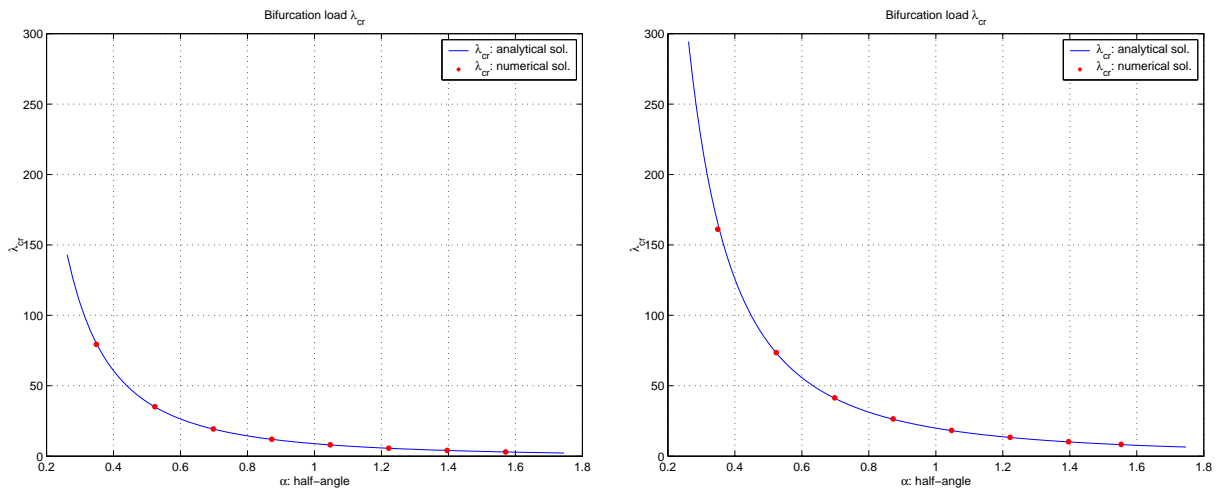


Figure 8. λ_{cr} versus α for $\rho^2 = 8.3333 \times 10^{-6}$ (left for pinned-pinned and right for clamped-clamped cases).

As the distributed follower force increases, the high arch will be buckled. For the pinned-pinned case, the bifurcation load is $\lambda_{cr} = \pi^2/\alpha^2 - 1$ and for the clamped-clamped case, the characteristic equation for the bifurcation load is

$$k \tan \alpha \cot k\alpha = 1,$$

where $k = \sqrt{1 + \lambda}$, as given in [Simitse and Hodges 2006]. For various half-angles, the bifurcation loads are computed and shown in Figure 8. Thus, the present approach is seen to provide an excellent numerical framework to study prebuckled deformation and buckling analysis without ad hoc modeling approximations.

6. Lateral-torsional buckling instability of curved beams under end moments

In this study the stability characteristics of curved beams are considered, including beams both with curvature that is built-in and curvature that occurs because the beam is loaded with end moments. The end moments are applied keeping its original orientation to the beam cross-section in deformation configuration, which are nonconservative. The section properties vary according to the initial curvature. Sample results are given in Table 1. In the general case we consider an curved beam with various initial curvatures k_2 loaded under various equal and opposite values of applied moments at the ends giving rise to a constant value of bending moment \bar{M}_2 . To facilitate this parametric study, the total static equilibrium value of curvature \bar{K}_2 is divided into two parts: the initial curvature k_2 and the curvature caused by the applied end moments \bar{M}_2/EI_2 . The total curvature can then be expressed as

$$\bar{K}_2 = k_2 + \frac{\bar{M}_2}{EI_2}, \tag{20}$$

where EI_2 is the in-plane bending stiffness for bending in the plane of the curved beam. A nondimensional curvature ratio β is then introduced, where β is the ratio of the initial curvature to the final total curvature and defined as

$$\beta = \frac{k_2}{\bar{K}_2} \quad (\bar{K}_2 \neq 0). \tag{21}$$

If $\beta = 0$, the beam has a zero initial curvature. If $\beta = 1$, the beam's initial curvature is the total curvature, which means that no end moments will be applied. If $\beta = -1$, the beam has an opposite initial curvature to the final configuration. The first three parts of Figure 9 show the cases $\beta = -1, 0, 1$. End moments are applied to deform the beam so that $\bar{K}_2 = -0.1$, as shown in the last part of the same figure. A rectangular cross-section is chosen to determine beam properties.

Table 2 and Figure 10 show the vibration frequencies for various β . It shows that the frequencies of modes 2 and 6 change as β changes. The frequency of mode 2, in which the first out-of-plane bending motion dominates, decreases as β decreases, becoming zero when $\beta = -0.0117$. This critical β is named

R_r	1/0.1	1/0.07	1/0.04	1/0.01
R_{11}	$1.4286 \cdot 10^{-9}$	$1.4286 \cdot 10^{-9}$	$1.4286 \cdot 10^{-9}$	$1.4286 \cdot 10^{-9}$
R_{22}	$4.7292 \cdot 10^{-9}$	$4.7291 \cdot 10^{-9}$	$4.7291 \cdot 10^{-9}$	$4.7291 \cdot 10^{-9}$
R_{33}	$4.7291 \cdot 10^{-9}$	$4.7291 \cdot 10^{-9}$	$4.7291 \cdot 10^{-9}$	$4.7291 \cdot 10^{-9}$
S_{12}	$3.4133 \cdot 10^{-10}$	$2.3790 \cdot 10^{-10}$	$1.3619 \cdot 10^{-10}$	$3.4476 \cdot 10^{-11}$
S_{21}	$-1.1431 \cdot 10^{-12}$	$8.6327 \cdot 10^{-13}$	$9.5232 \cdot 10^{-14}$	$-6.7113 \cdot 10^{-13}$
T_{11}	$2.7802 \cdot 10^{-6}$	$2.7803 \cdot 10^{-6}$	$2.7803 \cdot 10^{-6}$	$2.7803 \cdot 10^{-6}$
T_{22}	$1.7143 \cdot 10^{-6}$	$1.7143 \cdot 10^{-6}$	$1.7143 \cdot 10^{-6}$	$1.7143 \cdot 10^{-6}$
T_{33}	$1.7143 \cdot 10^{-6}$	$1.7143 \cdot 10^{-6}$	$1.7143 \cdot 10^{-6}$	$1.7143 \cdot 10^{-6}$
ζ_3	$8.7588 \cdot 10^{-5}$	$6.1310 \cdot 10^{-5}$	$3.5034 \cdot 10^{-5}$	$8.7585 \cdot 10^{-6}$

Table 1. Nonzero cross-sectional constants used for calculation of coupled free-vibration frequencies for initially curved beams: flexibility submatrices R_{ij} , S_{ij} , T_{ij} , radius of curvature R_r , and shear center location ζ_3 .

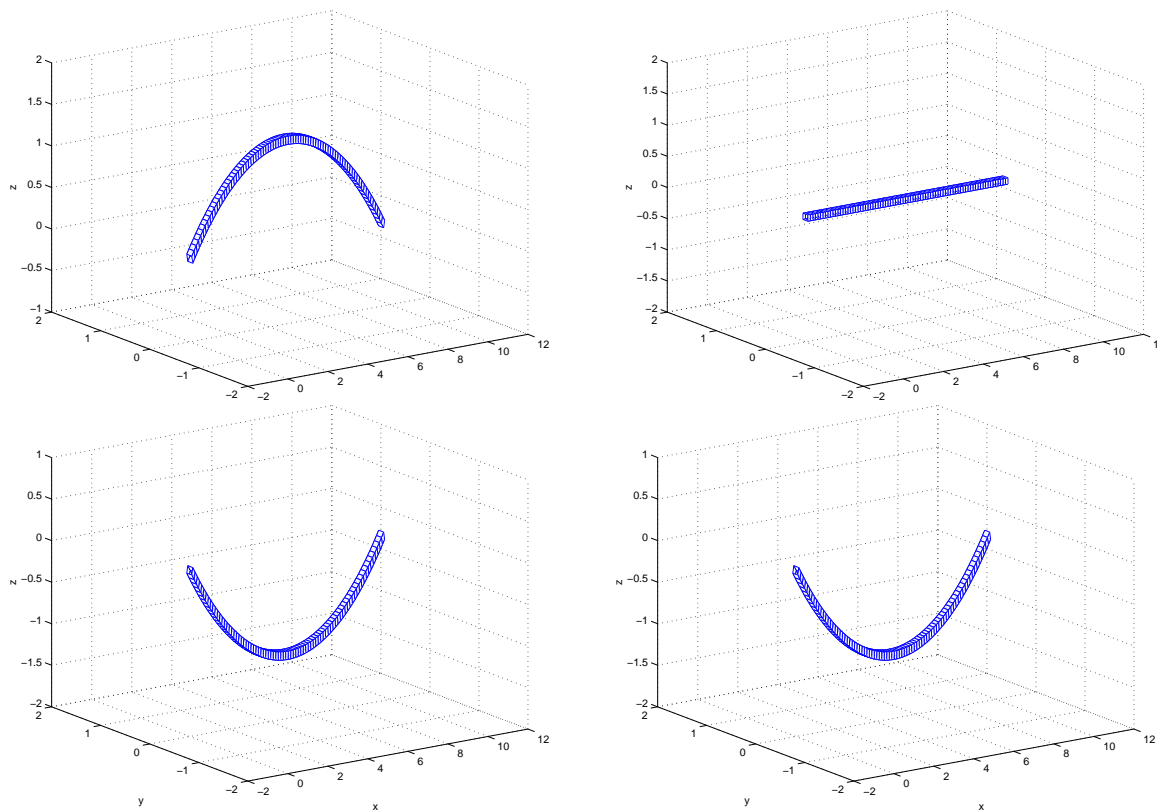


Figure 9. Initial configurations of beams with $\beta = -1$ (top left), $\beta = 0$ (top right), and $\beta = 1$ (bottom left). Bottom right: Final deformed configuration ($\bar{K}_2 = -0.1$) with end moments.

β_{cr} , indicating that this case is at the stability boundary and the lateral-torsional buckling instability will occur if $\beta < \beta_{cr} = -0.0117$.

The lateral-torsional buckling instability depends on the in- and out-of-plane bending stiffnesses and the torsional stiffness, which convey how deep the beam is. For this example with a rectangular cross-section, each stiffness will be determined by the ratio of cross-section $r = h/b$. So various cases for different r and same cross-sectional area $\Omega_{area} = bh/\ell^2$ are studied to determine β_{cr} . β_{cr} indicates that for the

β	mode 1	mode 2	mode 3	mode 4	mode 5	mode 6
0	31.842	32.548	89.567	90.630	177.94	179.13
0.1	31.842	96.606	89.567	90.209	177.94	185.45
0.2	31.842	125.16	89.567	89.776	177.94	199.11
0.3	31.842	140.08	89.332	89.568	177.94	211.83
0.4	31.842	147.61	88.878	89.568	177.94	229.92
0.5	31.842	151.58	88.412	89.568	177.95	248.30

Table 2. Vibration frequencies (ω_{freq}) versus curvature ratio (β).

given cross-section, the instability will occur if the initial curvature k_2 is larger than $-0.1\beta_{cr}$ when the total static equilibrium curvature $\bar{K}_2 = -0.1$. Figure 11 shows the critical values β_{cr} for $\Omega_{area} = 0.01, \sim 0.1,$ and ~ 0.2 . The region above the lines are free of the lateral-torsional buckling instability and the buckling will occur if a case is under the line. As the cross-sectional area gets small and the ratio r increases, that is, the beam gets deeper, the example is prone to the lateral-torsional instability as shown in Figure 11.

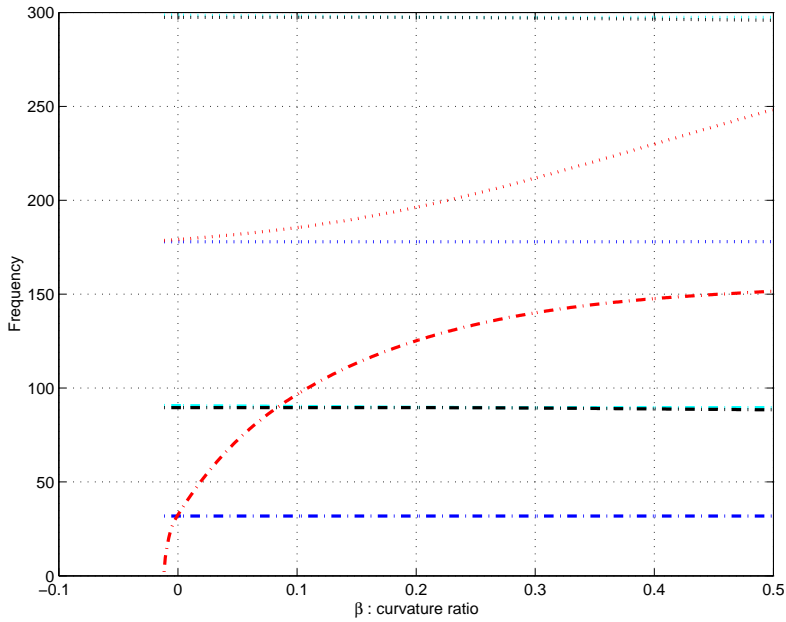


Figure 10. Vibration frequencies (ω_{freq}) versus curvature ratio (β).

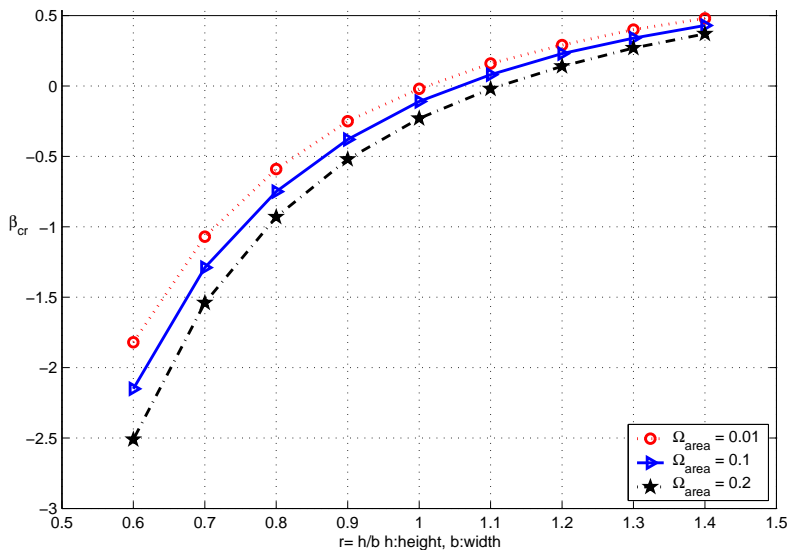


Figure 11. Critical curvature ratio β_{cr} versus $r = h/b$ for the lateral-torsional buckling instability.

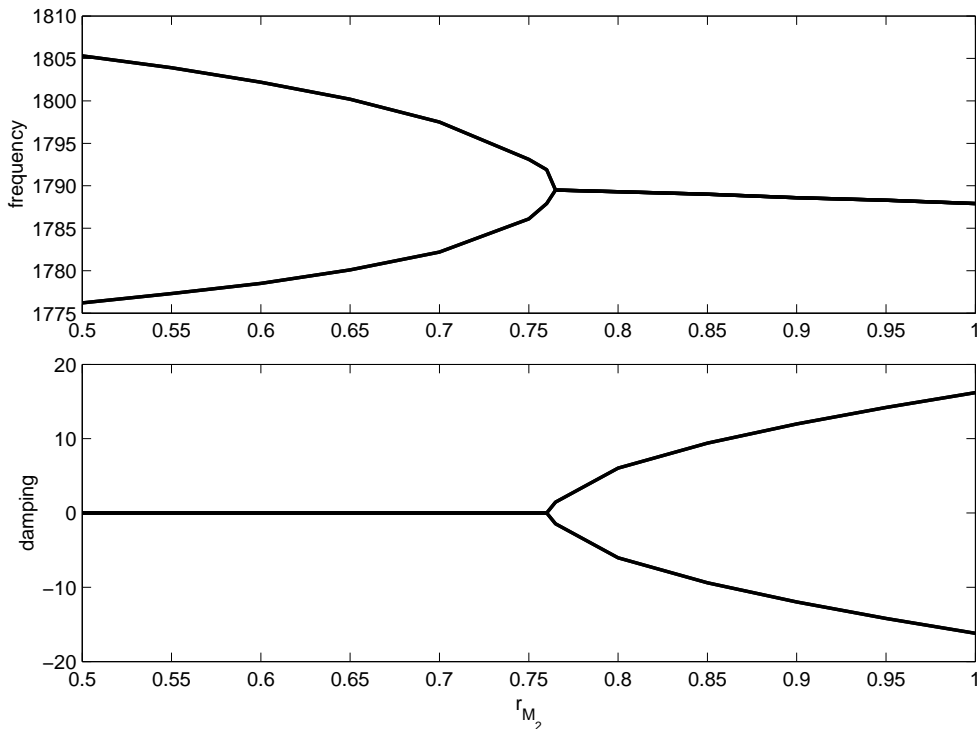


Figure 12. Frequencies and damping for different end moments ($\beta = -0.02$, $r = 1.1$, $\Omega_{\text{area}} = 0.2$).

For deep beams loaded with nonconservative end moments, one may also encounter a lateral-torsional flutter instability. The dynamic instability might occur before the lateral-torsional instability occurs. A further study is done for the case with $\beta = -0.02$, $r = 1.1$, $\Omega_{\text{area}} = 0.2$, which is one case of the lateral-torsional buckling instability boundary curves shown in Figure 11. For this case, the applied tip moment is $\bar{M}_2 = -EI_2(0.1 + k_2) = -0.1002EI_2$, which we denote as the reference value $M_{2,\text{ref}}$. Another instability can be found through lowering the ratio $r_{M_2} = M_2/M_{2,\text{ref}}$. Then, the second torsional and third out-of-plane bending modes shown in Figure 12 become oscillatory with increasing amplitude if $r_{M_2} \geq 0.765$. For this case, the dynamic instability occurs prior to the lateral-torsional instability.

7. Conclusion

The paper describes a numerical procedure of intrinsic beam formulation to study the stability of curved beams under certain types of loading. The linear analysis provides the vibration frequencies about the equilibrium state for given arbitrary configurations undergoing given loads. Present results of prebuckled in-plane deformation and buckling analysis agree well with those from the published paper of high arches. Additional parametric study determines the stability boundaries for the system. For nonconservatively loaded systems, as the example shows, the dynamic instability also can be identified.

The governing equations of the present approach do not require displacement and rotation variables. Even though the displacement and rotation variables appear in the boundary conditions, those variables

are easily recovered from the formulation (i.e. they are secondary variables and can be expressed in terms of the primary variables). This makes the whole analysis quite concise, reducing computational time. Thus, the present approach is an excellent numerical framework to study prebuckled deformation and buckling analysis for curved beams with better understanding.

References

- [Cesnik and Hodges 1997] C. E. S. Cesnik and D. H. Hodges, “VABS: a new concept for composite rotor blade cross-sectional modeling”, *J. Am. Helicopter Soc.* **42**:1 (1997), 27–38.
- [Chang and Hodges 2009] C.-S. Chang and D. H. Hodges, “Coupled vibration characteristics of curved beams”, *J. Mech. Mater. Struct.* **4**:4 (2009), 675–692.
- [Chen and Ginsberg 1992] P.-T. Chen and J. H. Ginsberg, “On the relationship between veering of eigenvalue loci and parameter sensitivity of eigenfunctions”, *J. Vib. Acoust. (ASME)* **114**:2 (1992), 141–148.
- [Chidamparam and Leissa 1993] P. Chidamparam and A. W. Leissa, “Vibrations of planar curved beams, rings, and arches”, *Appl. Mech. Rev. (ASME)* **46**:9 (1993), 467–483.
- [Chidamparam and Leissa 1995] P. Chidamparam and A. W. Leissa, “Influence of centerline extensibility on the in-plane free vibrations of loaded circular arches”, *J. Sound Vib.* **183**:5 (1995), 779–795.
- [Fung 2004] T. C. Fung, “Improved approximate formulas for the natural frequencies of simply supported Bernoulli–Euler beams with rotational restrains at the ends”, *J. Sound Vib.* **273**:1–2 (2004), 451–455.
- [Hodges 1999] D. H. Hodges, “Non-linear inplane deformation and buckling of rings and high arches”, *Int. J. Non-Linear Mech.* **34**:4 (1999), 723–737.
- [Hodges 2003] D. H. Hodges, “Geometrically exact, intrinsic theory for dynamics of curved and twisted anisotropic beams”, *AIAA J.* **41**:6 (2003), 1131–1137.
- [Hodges 2006] D. H. Hodges, *Nonlinear composite beam theory*, Progress in Astronautics and Aeronautics **213**, AIAA, Reston, VA, 2006.
- [Howson and Jemah 1999] W. P. Howson and A. K. Jemah, “Exact out-of-plane natural frequencies of curved Timoshenko beams”, *J. Eng. Mech. (ASCE)* **125**:1 (1999), 19–25.
- [Irie et al. 1982] T. Irie, G. Yamada, and K. Tanaka, “Natural frequencies of out-of-plane vibration of arcs”, *J. Appl. Mech. (ASME)* **49** (1982), 910–913.
- [Patil and Hodges 2006] M. J. Patil and D. H. Hodges, “Flight dynamics of highly flexible flying wings”, *J. Aircraft* **43**:6 (2006), 1790–1798.
- [Simitse and Hodges 2006] G. J. Simitse and D. H. Hodges, *Fundamentals of structural stability*, Elsevier, New York, 2006.
- [Tarnopolskaya et al. 1996] T. Tarnopolskaya, F. R. de Hoog, N. H. Fletcher, and S. Thwaites, “Asymptotic analysis of the free in-plane vibrations of beams with arbitrarily varying curvature and cross-section”, *J. Sound Vib.* **196**:5 (1996), 659–680.
- [Tarnopolskaya et al. 1999] T. Tarnopolskaya, F. R. de Hoog, and N. H. Fletcher, “Low-frequency mode transition in the free in-plane vibration of curved beams”, *J. Sound Vib.* **228**:1 (1999), 69–90.
- [Yu et al. 2002] W. Yu, V. V. Volovoi, D. H. Hodges, and X. Hong, “Validation of the variational asymptotic beam sectional analysis”, *AIAA J.* **40**:10 (2002), 2105–2112.

Received 22 Dec 2008. Revised 31 Dec 2009. Accepted 28 May 2009.

CHONG-SEOK CHANG: juliera324@hotmail.com

Advanced Rotorcraft Technology, 1330 Charleston Road, Mountain View, CA 94043, United States

DEWEY H. HODGES: dhodges@gatech.edu

Georgia Institute of Technology, Daniel Guggenheim School of Aerospace Engineering, 270 Ferst Drive, Atlanta, GA 30332-0150, United States

<http://www.ae.gatech.edu/~dhodges/>

INFLUENCE OF CORE PROPERTIES ON THE FAILURE OF COMPOSITE SANDWICH BEAMS

ISAAC M. DANIEL

The initiation of failure in composite sandwich beams is heavily dependent on properties of the core material. Several core materials, including PVC foams and balsa wood were characterized. The various failure modes occurring in composite sandwich beams are described and their relationship to the relevant core properties is explained and discussed. Under flexural loading of sandwich beams, plastic yielding or cracking of the core occurs when the critical yield stress or strength (usually shear) of the core is reached. Indentation under localized loading depends principally on the square root of the core yield stress. The critical stress for facesheet wrinkling is related to the core Young's and shear moduli in the thickness direction. Experimental mechanics methods were used to illustrate the failure modes and verify analytical predictions.

1. Introduction

The overall performance of sandwich structures depends in general on the properties of the facesheets, the core, the adhesive bonding the core to the skins, and geometric dimensions. Sandwich beams under general bending, shear and in-plane loading display various failure modes. Their initiation, propagation, and interaction depend on the constituent material properties, geometry, and type of loading. Failure modes and their initiation can be predicted by conducting a thorough stress analysis and applying appropriate failure criteria in the critical regions of the beam. This analysis is difficult because of the nonlinear and inelastic behavior of the constituent materials and the complex interactions of failure modes. Possible failure modes include tensile or compressive failure of the facesheets, debonding at the core/facesheet interface, indentation failure under localized loading, core failure, wrinkling of the compression facesheet, and global buckling. Following initiation of a particular failure mode, this mode may trigger and interact with other modes and final failure may follow a different failure path. A general review of failure modes in composite sandwich beams was given in [Daniel et al. 2002]. Individual failure modes in sandwich columns and beams are discussed in [Abot et al. 2002; Gdoutos et al. 2002b; 2003]. Of all the factors influencing failure initiation and mode, the properties of the core material are the most predominant.

Commonly used materials for facesheets are composite laminates and metals, while cores are made of metallic and nonmetallic honeycombs, cellular foams, balsa wood, or truss.

The facesheets carry almost all of the bending and in-plane loads while the core helps to stabilize the facesheets and defines the flexural stiffness and out-of-plane shear and compressive behavior. A number of core materials, including aluminum honeycomb, various types of closed-cell PVC foams,

Keywords: sandwich structures, core materials, experimental methods, characterization, failure modes, strength.

The work discussed in this paper was sponsored by the Office of Naval Research (ONR). The author is grateful to Dr. Y. D. S. Rajapakse of ONR for his encouragement and cooperation.

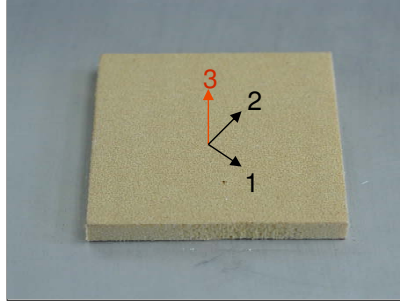


Figure 1. Material coordinate system for sandwich cores.

a polyurethane foam, foam-filled honeycomb and balsa wood, were characterized under uniaxial and biaxial states of stress.

In the present work, failure modes were investigated experimentally in axially loaded composite sandwich columns and sandwich beams under bending. Failure modes observed and studied include indentation failure, core failures, and facesheet wrinkling. The transition from one failure mode to another for varying loading or state of stress and beam dimensions was discussed. Experimental results were compared with analytical predictions.

2. Characterization of core materials

The core materials characterized were four types of a closed-cell PVC foam (Divinycell H80, H100, H160 and H250, with densities of 80, 100, 160 and 250kg/m³, respectively), an aluminum honeycomb (PAMG 8.1-3/16 001-P-5052, Plascore Co.), a polyurethane foam, a foam-filled honeycomb, and balsa wood. Of these, the low density foam cores are quasi-isotropic, while the high density foam cores, the honeycombs, and balsa wood are orthotropic with the 1-2 plane parallel to the facesheets being a plane of isotropy and the through-thickness direction (3-direction) a principal axis of higher stiffness, as shown in [Figure 1](#). All core materials were characterized in uniaxial tension, compression, and shear along the in-plane and through-thickness directions. Typical stress-strain curves are shown in [Figures 2](#) and [3](#). Some

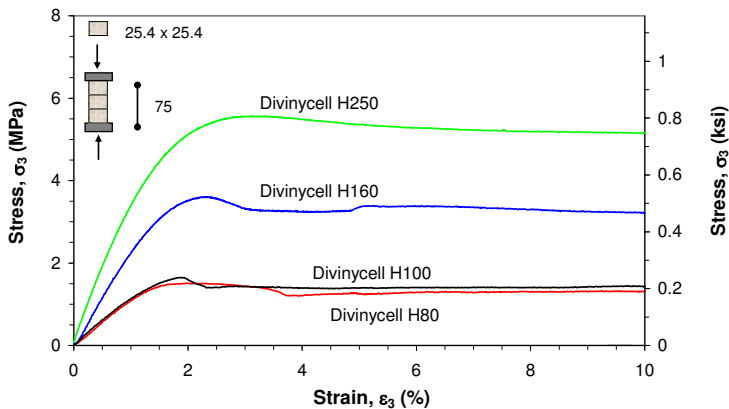


Figure 2. Stress-strain curves of PVC foam cores under compression in the through-thickness direction.

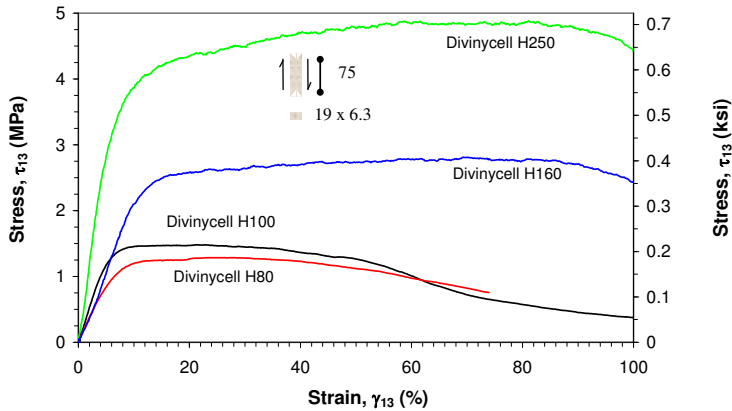


Figure 3. Shear stress-strain curves of PVC foam cores under through-thickness shear.

of their characteristic properties are tabulated in Table 1. The core materials (honeycomb or foam) were provided in the form of 25.4 mm thick plates. The honeycomb core was bonded to the top and bottom facesheets with FM73 M film adhesive and the assembly was cured under pressure in an oven following the recommended curing cycle for the adhesive. The foam cores were bonded to the facesheets using a commercially available epoxy adhesive (Hysol EA 9430) [Daniel and Abot 2000]. Beam specimens 25.4 mm wide and of various lengths were cut from the sandwich plates.

Two core materials, Divinycell H100 and H250 were fully characterized under multiaxial stress conditions [Gdoutos et al. 2002a]. A series of biaxial tests were conducted including constrained strip specimens in tension and compression with the strip axis along the through-thickness and in-plane directions; constrained thin-wall ring specimens in compression and torsion; thin-wall tube specimens in tension and torsion; and thin-wall tube specimens under axial tension, torsion and internal pressure. From these tests and uniaxial results in tension, compression, and shear, failure envelopes were constructed. It

Sandwich core material	ρ	E_1	E_2	E_3	G_{13}	F_{1c}	F_{1t}	F_{2c}	F_{3c}	F_5
Divinycell H80	80	77	77	110	18	1.0	2.3	1.0	1.4	1.1
Divinycell H100	100	95	95	117	25	1.4	2.7	1.4	1.6	1.4
Divinycell H160	160	140	140	250	26	2.5	3.7	2.5	3.6	2.8
Divinycell H250	250	255	245	360	73	4.5	7.2	4.5	5.6	4.9
Balsa Wood CK57	150	110	110	4600	60	0.8	1.2	0.8	9.7	3.7
Aluminum Honeycomb PAMG 5052	130	8.3	6.0	2200	580	0.2	1.2	0.2	11.8	3.5
Foam Filled Honeycomb Style 20	128	25	7.6	240	8.7	0.4	0.5	0.3	1.4	0.75
Polyurethane FR-3708	128	38	38	110	10	1.2	1.1	1.1	1.8	1.4

Table 1. Properties of sandwich core materials: the density, ρ (in units of kg/m^3); and the in-plane moduli, E_1 and E_2 , the out of plane modulus, E_3 , the transverse shear modulus, G_{13} , the in-plane compressive strength, F_{1c} , the in-plane tensile strength, F_{1t} , the in-plane compressive strength, F_{2c} , the out of plane compressive strength, F_{3c} , and the transverse shear strength, F_5 (all in units of MPa).

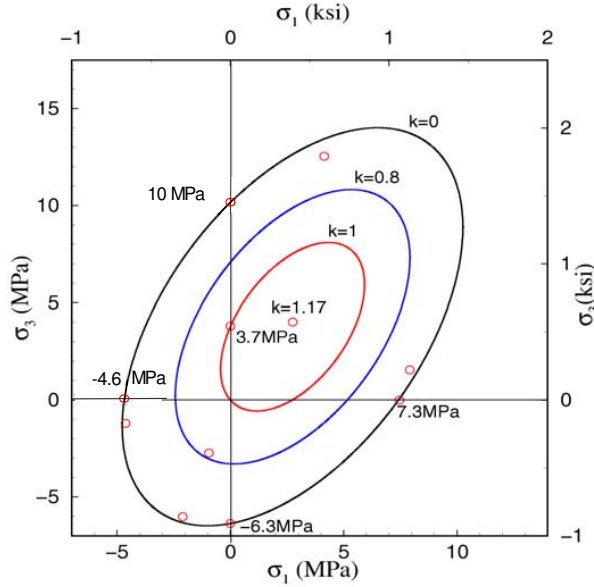


Figure 4. Failure envelopes predicted by the Tsai–Wu failure criterion for PVC foam (Divinycell H250) for $k = 0, 0.8$ and 1 , and experimental results ($k = \tau_{13}/F_{13} = \tau_5/F_5$).

was shown that the failure envelopes were described well by the Tsai–Wu criterion [1971], as shown in Figure 4.

The Tsai–Wu criterion for a general two-dimensional state of stress on the 1-3 plane is expressed as

$$f_1\sigma_1 + f_3\sigma_3 + f_{11}\sigma_1^2 + f_{33}\sigma_3^2 + 2f_{13}\sigma_1\sigma_3 + f_{55}\tau_5^2 = 1, \tag{1}$$

where

$$\begin{aligned} f_1 &= \frac{1}{F_{1t}} - \frac{1}{F_{1c}}, & f_3 &= \frac{1}{F_{3t}} - \frac{1}{F_{3c}}, & f_{11} &= \frac{1}{F_{1t}F_{1c}}, \\ f_{33} &= \frac{1}{F_{3t}F_{3c}}, & f_{13} &= -\frac{1}{2}(f_{11}f_{33})^{1/2}, & f_{55} &= \frac{1}{F_5^2}. \end{aligned}$$

Here F_{1t} , F_{1c} , F_{3t} , and F_{3c} are the tensile and compressive strengths in the in-plane (1, 2) and out-of-plane (3) directions, and F_5 is the shear strength on the 1-3 plane.

Setting $\tau_5 = kF_5$, we can rewrite (1) as

$$f_1\sigma_1 + f_3\sigma_3 + f_{11}\sigma_1^2 + f_{33}\sigma_3^2 + 2f_{13}\sigma_1\sigma_3 = 1 - k^2. \tag{2}$$

It was assumed that the failure behavior of all core materials can be described by the Tsai–Wu criterion. Failure envelopes of all core materials constructed from the values of F_{1t} , F_{1c} and F_5 are shown in Figure 5. Note that the failure envelopes of all Divinycell foams are elongated along the σ_1 -axis, which indicates that these materials are stronger under normal longitudinal stress than in-plane shear stress. Aluminum honeycomb and balsa wood show the opposite behavior. For all materials, the most critical combinations of shear and normal stress fall in the second and third quadrants (the failure envelopes are symmetrical with respect to the σ_1 -axis).

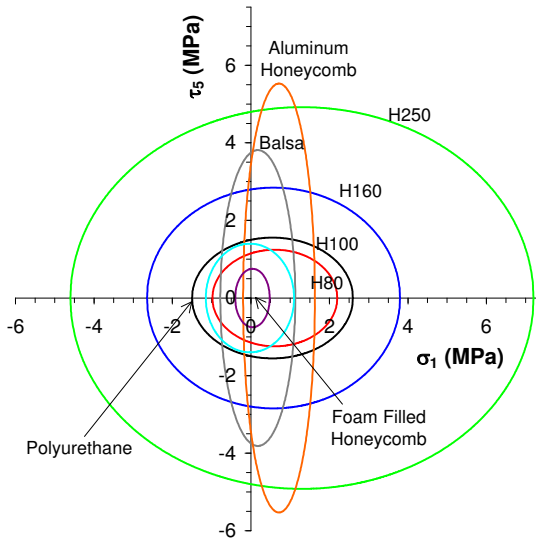


Figure 5. Failure envelopes for various core materials based on the Tsai–Wu failure criterion for interaction of normal and shear stresses.

3. Core failures

The core is primarily selected to carry the shear loading. Core failure by shear is a common failure mode in sandwich construction [Allen 1969; Hall and Robson 1984; Zenkert and Vikström 1992; Zenkert 1995; Daniel et al. 2001a; 2001b; Sha et al. 2006]. In short beams under three-point bending the core is mainly subjected to shear, and failure occurs when the maximum shear stress reaches the critical value (shear strength) of the core material. In long-span beams the normal stresses become of the same order of magnitude as, or even higher than the shear stresses. In this case, the core in the beam is subjected to a biaxial state of stress and fails according to an appropriate failure criterion. It was shown earlier that failure of the PVC foam core Divinycell H250 can be described by the Tsai–Wu failure criterion [Gdoutos et al. 2002a; Bezazi et al. 2007].

For a sandwich beam of rectangular cross section, with facesheets and core materials displaying linear elastic behavior, subjected to a bending moment, M , and shear force, V , the in-plane maximum normal stress, σ , and shear stress, τ , in the core, for a low stiffness core and thin facesheets are given by [Daniel et al. 2001a]

$$\sigma = \frac{PL}{C_1bd^2} \left(\frac{E_c}{E_f} \right) \frac{h_c}{h_f}, \quad \tau = \frac{P}{C_2bh_c}, \quad (3)$$

where

$$M = \frac{PL}{C_1}, \quad V = \frac{P}{C_2}, \quad (4)$$

P being the applied concentrated load, L the length of beam, E_f and E_c the Young’s moduli of the facesheet and core material, h_f and h_c the thicknesses of the facesheets and core, d the distance between the centroids of the facesheets, b the beam width, and C_1 and C_2 constants depending on the loading configuration ($C_1 = 4$, $C_2 = 2$ for three-point bending; $C_1 = C_2 = 1$ for a cantilever beam).

The maximum normal stress, σ , for a beam under three-point bending occurs under the load, while for a cantilever beam under end loading it occurs at the support. The shear stress, τ , is constant along the beam span and through the core thickness, as verified experimentally [Daniel and Abot 2000; Daniel et al. 2002].

When the normal stress in the core is small relative to the shear stress, it can be assumed that core failure occurs when the shear stress reaches a critical value. Furthermore, failure in the facesheets occurs when the normal stress reaches its critical value, usually the facesheet compressive strength. Under such circumstances we obtain from (3) that failure mode transition from shear core failure to compressive facesheet failure occurs when

$$\frac{L}{h_f} = C \frac{F_f}{F_{cs}}, \quad (5)$$

where F_f is the facesheet strength in compression or tension, F_{cs} is the core shear strength, and C is a constant ($C = 2$ for a beam under three-point bending; $C = 1$ for a cantilever beam under an end load).

When the left-hand term of (5) is smaller than the right hand term, failure occurs by core shear, whereas in the reverse case failure occurs by facesheet tension or compression.

The deformation and failure mechanisms in the core of sandwich beams have been studied experimentally by means of moiré gratings and photoelastic coatings [Daniel and Abot 2000; Daniel et al. 2001a; 2001b; Gdoutos et al. 2001; 2002b; Abot and Daniel 2003]. Figure 6 shows moiré fringe patterns in the core of a sandwich beam under three-point bending for an applied load that produces stresses in the core within the linear elastic range. The moiré fringe patterns corresponding to the u (horizontal) and w (through-the-thickness) displacements away from the applied load consist of nearly parallel and equidistant fringes from which it follows that

$$\varepsilon_x = \frac{\partial u}{\partial x} \cong 0, \quad \varepsilon_z = \frac{\partial w}{\partial z} \cong 0, \quad \gamma_{xz} = \frac{\partial u}{\partial z} + \frac{\partial w}{\partial x} = \text{constant}. \quad (6)$$

Thus, the core is under nearly uniform shear stress. This is true only in the linear range, as will be illustrated below.

Figure 7 shows photoelastic coating fringe patterns for a beam under three-point bending. The fringe pattern for a low applied load (2.3 kN) is nearly uniform, indicating that the shear strain (stress) in the

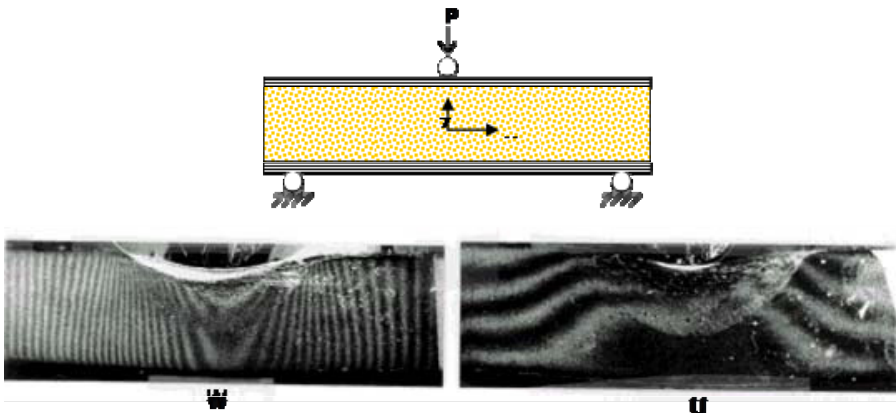


Figure 6. Moiré fringe patterns corresponding to horizontal and vertical displacements in sandwich beam under three-point bending (12 lines/mm, Divinycell H250 core).

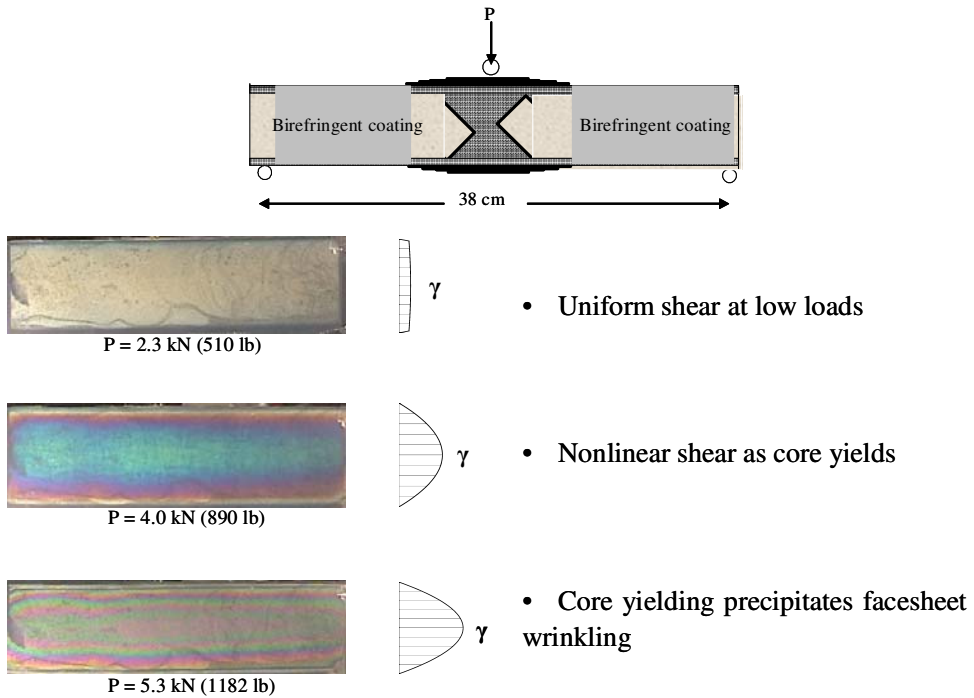


Figure 7. Isochromatic fringe patterns in birefringent coating of sandwich beam under three-point bending (Divinycell H250 core).

core is constant. This pattern remains uniform up to an applied load of 3.3 kN which corresponds to an average shear stress in the core of 2.55 MPa. This is close to the proportional limit of the shear stress-strain curve of the core material (Figure 3). For higher loads, the core begins to yield and the shear strain becomes highly nonuniform peaking at the center and causing plastic flow. The onset of core failure in beams is directly related to the core yield stress in the thickness direction. A critical condition for the core occurs at points where shear stress is combined with compressive stress.

The deformation and failure of the core is obviously dependent on its properties and especially its anisotropy. Honeycomb and balsa wood cores are highly anisotropic with much higher stiffness and strength in the thickness direction, a desirable property. Figure 8 shows isochromatic fringe patterns in the photoelastic coating and the corresponding load deflection curve for a composite sandwich beam under three-point bending. The beam consists of glass/vinylester facesheets and balsa wood core. The fringe patterns indicate that the shear deformation in the core is initially nearly uniform, but it becomes nonuniform and concentrated in a region between the support and the load at a distance of approximately one beam depth from the support. The pattern at the highest load shown is indicative of a vertical crack along the cells of the balsa wood core. The loads corresponding to the fringe patterns are marked on the load deflection curve. It is seen that the onset of nonlinear behavior corresponds to the beginning of fringe concentration and failure initiation in the critical region of the core.

Figure 9 shows the damaged region of the beam. Although the fringe patterns did not show that, it appears that a crack was initiated near the upper facesheet/core interface and propagated parallel to it.

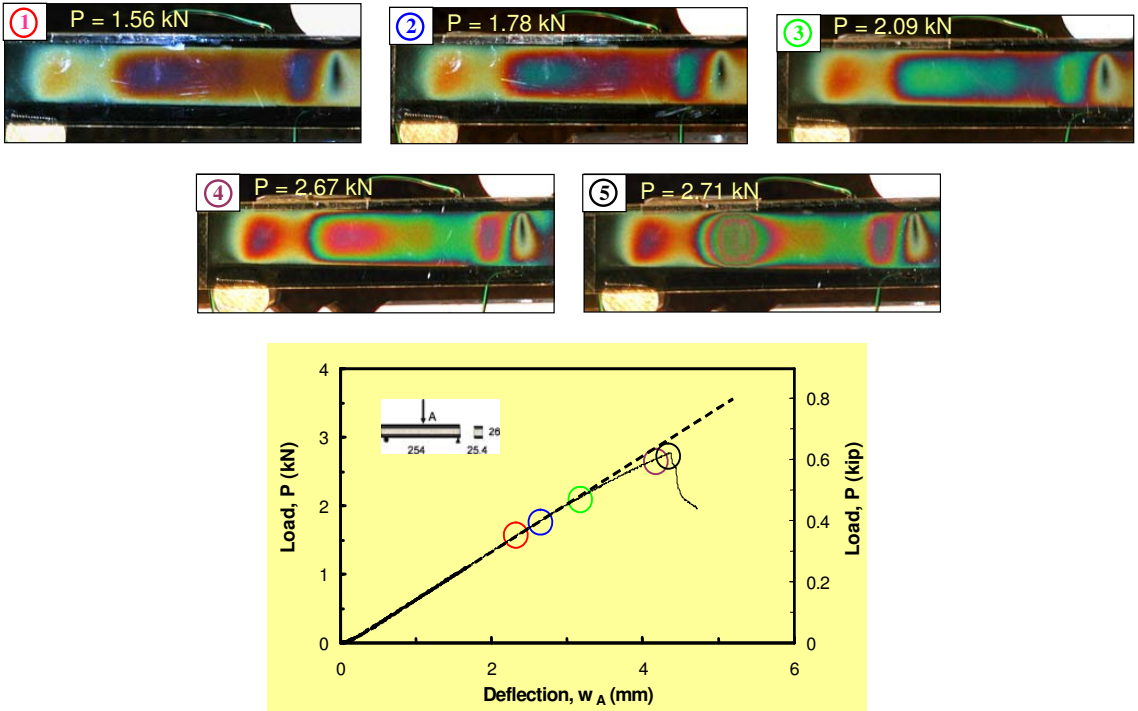


Figure 8. Isochromatic fringe patterns in photoelastic coating and load deflection curve of a composite sandwich beam under three-point bending (glass/vinylester facesheets; balsa wood core).



Figure 9. Cracking in balsa wood core of sandwich beam under three-point bending near support.

The crack traveled for some distance and then turned downwards along the cell walls of the core until it approached the lower interface. It then traveled parallel to the interface towards the support point.

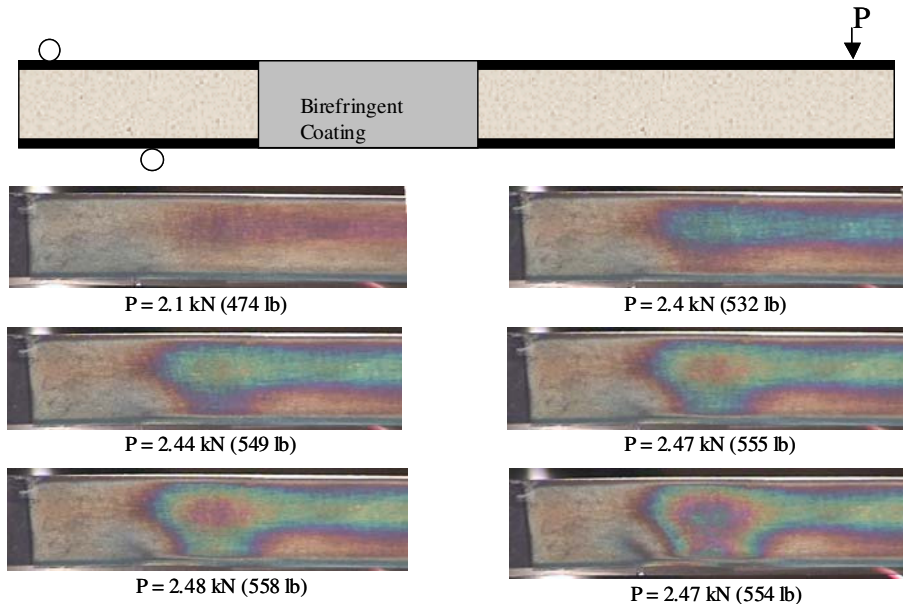


Figure 10. Isochromatic fringe patterns in birefringent coating of cantilever sandwich beam under end loading.

Core failure is accelerated when compressive and shear stresses are combined. This critical combination is evident from the failure envelope of [Figure 4](#). The criticality of the compression/shear stress biaxiality was tested with a cantilever sandwich beam loaded at the free end. The isochromatic fringe patterns of the birefringent coating in [Figure 10](#) show how the peak birefringence moves towards the fixed end of the beam at the bottom where the compressive strain is the highest and superimposed on the shear strain. Plastic deformation of the core, whether due to shear alone or a combination of compression and shear, degrades the supporting role of the core and precipitates other more catastrophic failure modes, such as facesheet wrinkling.

4. Indentation failure

Indentation failure in composite sandwich beams occurs under concentrated loads, especially in the case of soft cores. Under such conditions, significant local deformation takes place of the loaded facesheet into the core, causing high local stress concentrations. The indentation response of sandwich panels was first modeled by [\[Meyer-Piening 1989\]](#) who assumed linear elastic bending of the loaded facesheet resting on a Winkler foundation (core). [Soden \[1996\]](#) modeled the core as a rigid-perfectly plastic foundation, leading to a simple expression for the indentation failure load. [Shuaieb and Soden \[1997\]](#) predicted indentation failure loads for sandwich beams with glass-fiber-reinforced plastic facesheets and thermoplastic foam cores. The problem was modeled as an elastic beam, representing the facesheet, resting on an elastic-plastic foundation representing the core. [Thomsen and Frostig \[1997\]](#) studied the local bending effects in sandwich beams experimentally and analytically. The indentation failure of composite sandwich beams was also studied by [\[Anderson and Madenci 2000; Petras and Sutcliffe 2000; Gdoutos et al. 2002b\]](#).

For linear elastic behavior, the core is modeled as a layer of linear tension/compression springs. The stress at the core/facesheet interface is proportional to the local deflection w , $\sigma = kw$, where the foundation modulus k is given by

$$k = 0.64 \frac{E_c}{h_f} \sqrt[3]{\frac{E_c}{E_f}}, \tag{7}$$

and where E_f and E_c are the facesheet and core moduli, respectively, and h_f is the facesheet thickness. Initiation of indentation failure occurs when the core under the load starts yielding. The load at core yielding was calculated as

$$P_{cy} = 1.70 \sigma_{cy} b h_f \sqrt[3]{\frac{E_f}{E_c}}, \tag{8}$$

where σ_{cy} is the yield stress of the core, and b is the beam width.

Core yielding causes local bending of the facesheet which, combined with global bending of the beam, results in compression failure of the facesheet. The compressive failure stress in the facesheet is related to the critical beam loading P_{cr} by

$$\sigma_f = F_{fc} = \frac{9P_{cr}^2}{16b^2h_f^2F_{cc}} + \frac{P_{cr}L}{4bh_f(h_f + h_c)}, \tag{9}$$

where h_c is the core thickness, L the span length, b the beam width, and F_{cc} , F_{fc} the compressive strengths of the core (in the thickness direction) and facesheet materials, respectively. In the above equation, the first term on the right hand side is due to local bending following core yielding and indentation and the second term is due to global bending.

The onset and progression of indentation failure is illustrated by the moiré pattern for a sandwich beam under three-point bending (Figure 11).

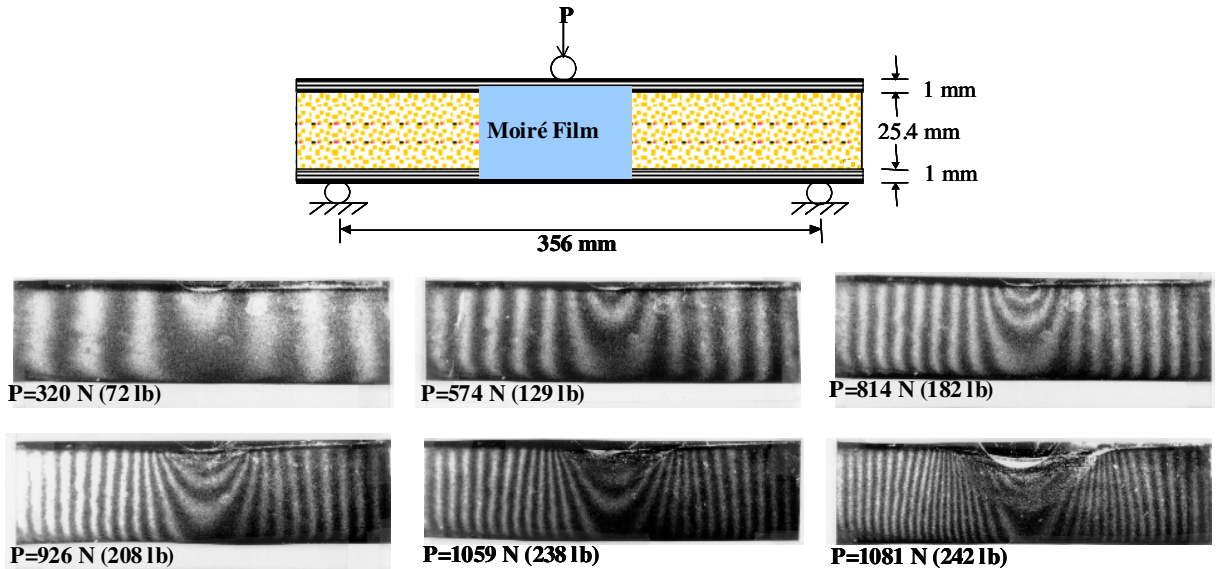


Figure 11. Moiré fringe patterns in sandwich beam with foam core corresponding to vertical displacements at various applied loads (11.8 lines/mm grating; carbon/epoxy facesheets; Divinycell H100 core).

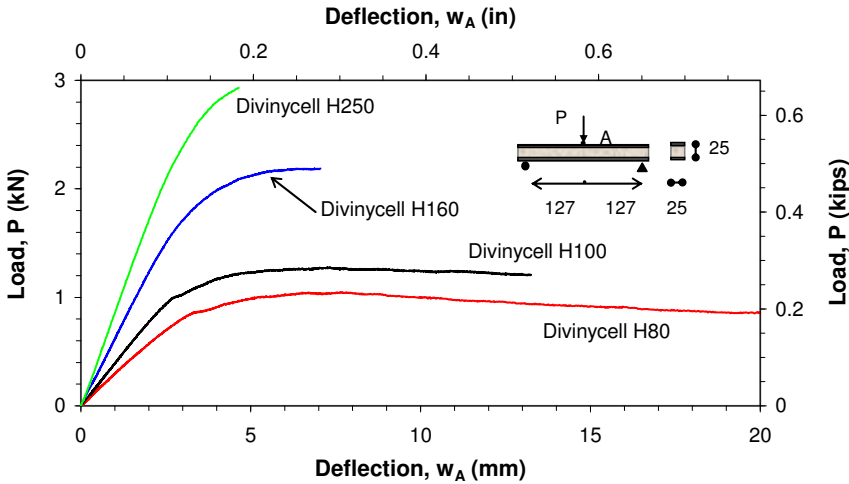


Figure 12. Load versus deflection under load of sandwich beam under three-point bending (carbon/epoxy facesheets, Divinycell cores).

Figure 12 shows load displacement curves for beams of the same dimensions but different cores. The displacement in these curves represents the sum of the global beam deflection and the more dominant local indentation. Therefore, the proportional limit of the load-displacement curves is a good indication of initiation of indentation.

The measured critical indentation loads in Figure 12 were compared with predicted values using (9), which can be approximated as [Soden 1996]

$$P_{cr} \cong \frac{4}{3}bh_f\sqrt{F_{fc}\sigma_{cy}}. \tag{10}$$

Thus, the critical indentation load is proportional to the square root of the core material yield stress. The results obtained are compared in Table 2. The approximate theory with the assumption of rigid-perfectly plastic behavior overestimates the indentation failure load for soft cores, but it underestimates it for stiff cores.

5. Facesheet wrinkling failure

Wrinkling of sandwich beams subjected to compression or bending is defined as a localized short-wave length buckling of the compression facesheet. Wrinkling may be viewed as buckling of the compression facesheet supported on an elastic or elastoplastic continuum [Gdoutos et al. 2003]. It is a common failure mode leading to loss of the beam stiffness. The wrinkling phenomenon is characterized by the interaction

Indentation Load (N)	H80	H100	H160	H250
Measured	1050	1250	2150	2900
Calculated	1370	1500	2000	2380

Table 2. Critical indentation loads for sandwich beams with different cores under three-point bending.

between the core and the facesheet of the sandwich panel. Thus, the critical wrinkling load is a function of the stiffnesses of the core and facesheet, the geometry of the structure, and the applied loading.

A large number of theoretical and experimental investigations has been reported on wrinkling of sandwich structures. Some of the early works were presented and compiled in [Plantema 1966; Allen 1969]. Hoff and Mautner [1945] tested sandwich panels in compression and gave an approximate formula for the wrinkling stress, which depends only on the elastic moduli of the core and facesheet materials. Heath [1960] extended the theory for end loaded plates and proposed a simple expression for facesheet wrinkling in sandwich plates with isotropic components. The theory does not account for shear interaction between the facesheets and the core and thus is more applicable to compressively loaded sandwich columns and to beams under pure bending. Benson and Mayers [1967] developed a unified theory for the study of both general instability and facesheet wrinkling simultaneously for sandwich plates with isotropic facesheets and orthotropic cores. This theory was extended in [Hadi and Matthews 2000] to solve the problem of wrinkling of anisotropic sandwich panels. More studies on the wrinkling of sandwich plates are found in [Vonach and Rammerstorfer 2000; Fagerberg 2004; Birman and Bert 2004; Meyer-Piening 2006; Lopatin and Morozov 2008]. The critical wrinkling stress given in [Hoff and Mautner 1945] is

$$\sigma_{cr} \cong c \sqrt[3]{E_{f1} E_{c3} G_{c13}}, \quad (11)$$

where E_{f1} and E_{c3} are the Young's moduli of facesheet and core, in the axial and through-thickness directions, respectively, G_{c13} is the shear modulus of the core on the 1-3 plane, and c is a coefficient, usually varying in the range of 0.5–0.9.

In the relation above, the core moduli are the initial ones while the material is in the linear range. After the core yields and its stiffnesses degrade (E'_c, G'_c), it does not provide adequate support for the facesheet, thereby precipitating facesheet wrinkling. The reduced critical stress after core degradation is

$$\sigma_{cr} \cong c \sqrt[3]{E_f E'_c G'_c}. \quad (12)$$

Heath's original expression was modified here for a one-dimensional beam and by considering only the facesheet modulus along the axis of the beam and the core modulus in the through-thickness direction. The critical wrinkling stress can then be obtained by

$$\sigma_{cr} = \left[\frac{2}{3} \frac{h_f}{h_c} E_{c3} E_f \right]^{1/2}. \quad (13)$$

Sandwich columns were subjected to end compression and strains were measured on both faces. The stress-strain curves for three columns with aluminum honeycomb, Divinycell H100 and Divinycell H250 cores are shown in Figure 13. Photographs of these columns after failure are shown in Figure 14. The wrinkling stress is defined as the stress at which the strain on the convex side of the panel reaches a maximum value. Note that the column with the honeycomb core failed by facesheet compression and not by wrinkling. The measured failure stress of 1,550 MPa is much lower than the critical wrinkling stresses of 2,850 MPa and 2,899 MPa predicted by (11) and (13), the former for $c = 0.5$. The columns with Divinycell H100 and H250 foam cores failed by facesheet wrinkling, as seen in the stress-strain curves of Figure 13. The measured wrinkling stresses at maximum strain for the Divinycell H100 and H250 cores were 627 MPa and 1,034 MPa, respectively, and are close to the values of 667 MPa and

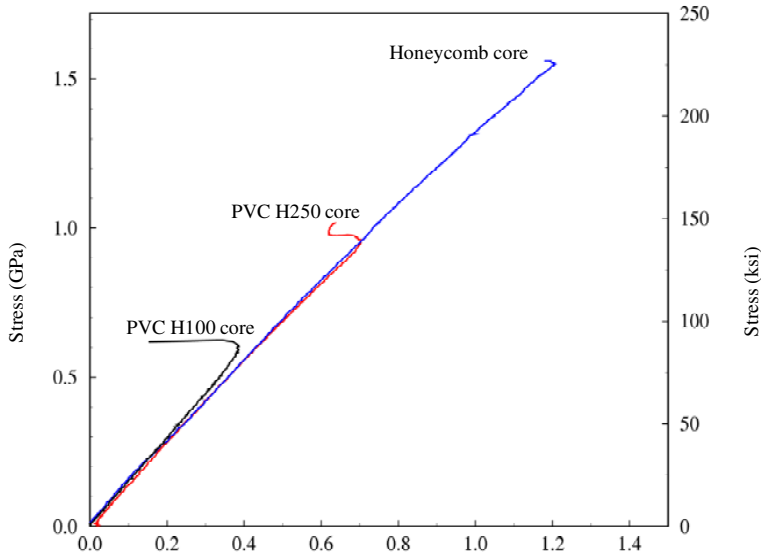


Figure 13. Compressive stress-strain curves for sandwich columns with different cores.

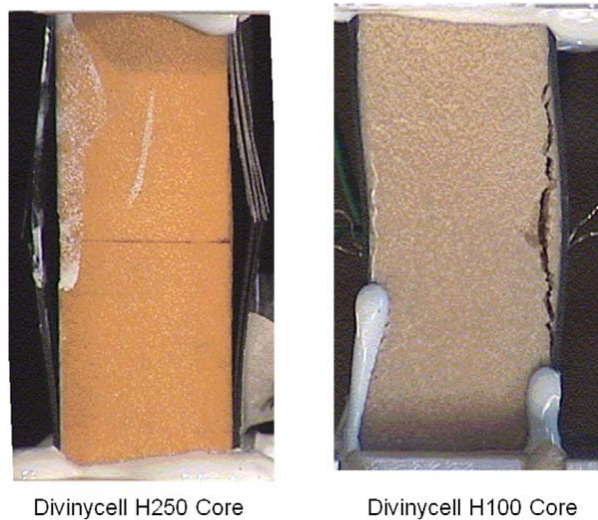


Figure 14. Failure of sandwich columns with two different cores.

1170 MPa predicted by (13). Agreement with the [Hoff and Mautner 1945] prediction would require coefficient values of $c = 0.834$ and $c = 0.662$ in (11).

Figure 15 shows moment versus strain results for two different tests of sandwich beams with Divinycell H100 foam cores under four-point bending. Evidence of wrinkling is shown by the sharp change in recorded strain on the compression facesheet, indicating inward and outward wrinkling in the two tests. In both cases the critical wrinkling stress was $\sigma_{cr} = 673$ MPa. Heath’s relation (13) [Heath 1960] was selected because of the lack of shear interaction due to the pure bending loading. The predicted critical wrinkling stress of 667 MPa is very close to the experimental value.

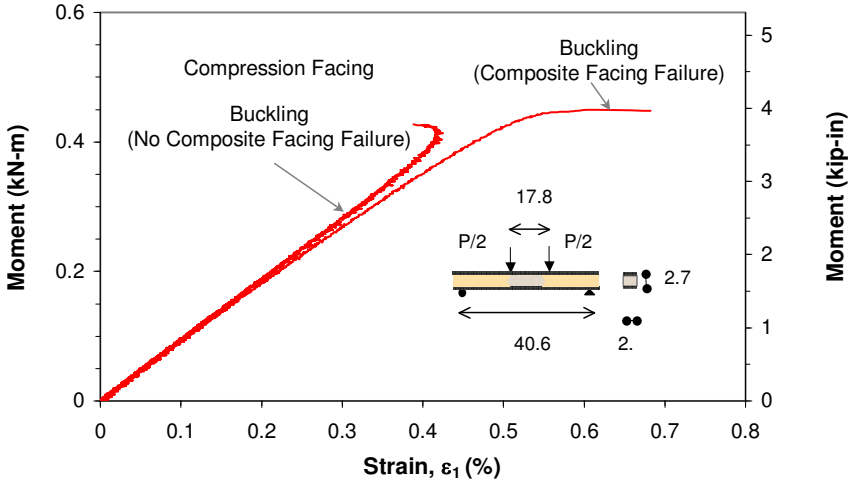


Figure 15. Facesheet wrinkling in sandwich beam under four-point bending (Divinycell H100 foam core; dimensions are in cm).

Sandwich beams were also tested in three-point bending and as cantilever beams. The moment-strain curves shown in Figure 16 illustrate the onset of facesheet wrinkling. Critical stresses obtained from the figure for the maximum moment for specimens 1 and 2 are $\sigma_{cr} = 860$ MPa and 947 MPa, respectively. The predicted value by (11) would agree with the average of the two measurements, 903 MPa, for $c = 0.578$. In the case of the short beam (specimen 3), core failure preceded wrinkling. The measured wrinkling stress was 517 MPa. The core shear stresses at wrinkling for specimens 2 and 3 are 3.2 MPa and 4.55 MPa, respectively. Thus, the core material for specimen 2 is in the linear elastic region, whereas for specimen 3 it is close to the yield point. Equation (14) predicts the measured wrinkling stress with a reduced core shear modulus of $G'_{c13} = 21.2$ MPa for $c = 0.5$.

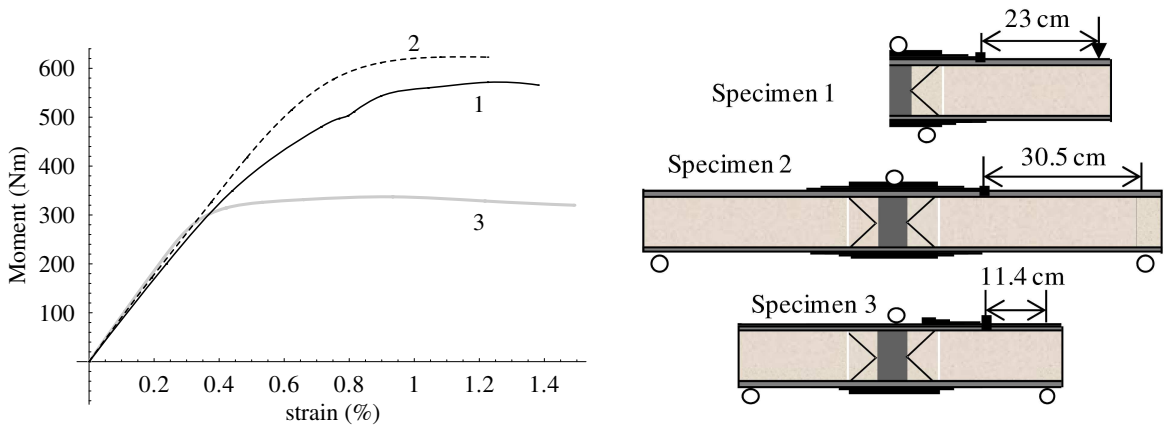


Figure 16. Facesheet wrinkling failure in sandwich beams with Divinycell H250 cores. Curve numbers correspond to specimen numbers on the right.

6. Conclusions

The initiation of failure in composite sandwich beams is heavily dependent on properties of the core material. Plastic yielding or cracking of the core occurs when the critical yield stress or strength (usually shear) of the core is reached. Indentation under localized loading depends principally on the square root of the core yield stress. Available theory predicts indentation failure approximately, overestimating it for soft cores and underestimating it for stiffer ones. The critical facesheet wrinkling stress is predicted fairly closely by Heath's formula for cases not involving shear interaction between the facesheets and the core, such as compressively loaded columns and beams under pure bending. In the case of cantilever beams or beams under three-point bending, entailing shear interaction between the facesheets and core, the Hoff and Mautner formula predicts a value for the critical wrinkling stress which is proportional to the cubic root of the product of the core Young's and shear moduli in the thickness direction. The ideal core should be highly anisotropic with high stiffness and strength in the thickness direction.

References

- [Abot and Daniel 2003] J. L. Abot and I. M. Daniel, "Failure modes in glass/vinylester-balsa wood sandwich beams", pp. 851–859 in *6th International Conference on Sandwich Structures (ICSS-6)* (Fort Lauderdale, FL, 2003), edited by J. R. Vinson et al., CRC Press, Boca Raton, FL, 2003.
- [Abot et al. 2002] J. L. Abot, I. M. Daniel, and E. E. Gdoutos, "Contact law for composite sandwich beams", *J. Sandw. Struct. Mater.* **4**:2 (2002), 157–173.
- [Allen 1969] H. G. Allen, *Analysis and design of structural sandwich panels*, Pergamon, London, 1969.
- [Anderson and Madenci 2000] T. Anderson and E. Madenci, "Graphite/epoxy foam sandwich panels under quasi-static indentation", *Eng. Fract. Mech.* **67**:4 (2000), 329–344.
- [Benson and Mayers 1967] A. S. Benson and J. Mayers, "General instability and face wrinkling of sandwich plates: unified theory and applications", *AIAA J.* **5**:4 (1967), 729–739.
- [Bezazi et al. 2007] A. Bezazi, A. El Mahi, J.-M. Berthelot, and B. Bezzazi, "Experimental analysis of behavior and damage of sandwich composite materials in three-point bending. I: Static tests and stiffness degradation at failure studies", *Strength Mater.* **39**:2 (2007), 170–177.
- [Birman and Bert 2004] V. Birman and C. W. Bert, "Wrinkling of composite-facing sandwich panels under biaxial loading", *J. Sandw. Struct. Mater.* **6**:3 (2004), 217–237.
- [Daniel and Abot 2000] I. M. Daniel and J. L. Abot, "Fabrication, testing and analysis of composite sandwich beams", *Compos. Sci. Technol.* **60**:12–13 (2000), 2455–2463.
- [Daniel et al. 2001a] I. M. Daniel, E. E. Gdoutos, J. L. Abot, and K.-A. Wang, "Core failure modes in composite sandwich beams", pp. 293–303 in *Contemporary research in engineering mechanics* (New York, 2001), edited by G. A. Kardomateas and V. Birman, Aerospace Division/Applied Mechanics Division **65/249**, ASME, New York, 2001.
- [Daniel et al. 2001b] I. M. Daniel, E. E. Gdoutos, J. L. Abot, and K.-A. Wang, "Effect of loading conditions on deformation and failure of composite sandwich structures", pp. 1–17 in *Three-dimensional effects in composite and sandwich structures* (New York, 2001), edited by Y. D. S. Rajapakse, ASME, New York, 2001. Paper # AMD-25412.
- [Daniel et al. 2002] I. M. Daniel, E. E. Gdoutos, K.-A. Wang, and J. L. Abot, "Failure modes of composite sandwich beams", *Int. J. Damage Mech.* **11**:4 (2002), 309–334.
- [Fagerberg 2004] L. Fagerberg, "Wrinkling and compression failure transition in sandwich panels", *J. Sandw. Struct. Mater.* **6**:2 (2004), 129–144.
- [Gdoutos et al. 2001] E. E. Gdoutos, I. M. Daniel, K.-A. Wang, and J. L. Abot, "Nonlinear behavior of composite sandwich beams in three-point bending", *Exp. Mech.* **41**:2 (2001), 182–189.
- [Gdoutos et al. 2002a] E. E. Gdoutos, I. M. Daniel, and K.-A. Wang, "Failure of cellular foams under multiaxial loading", *Compos. A Appl. Sci. Manuf.* **33**:2 (2002), 163–176.

- [Gdoutos et al. 2002b] E. E. Gdoutos, I. M. Daniel, and K.-A. Wang, “Indentation failure in composite sandwich structures”, *Exp. Mech.* **42**:4 (2002), 426–431.
- [Gdoutos et al. 2003] E. E. Gdoutos, I. M. Daniel, and K.-A. Wang, “Compression facing wrinkling of composite sandwich structures”, *Mech. Mater.* **35**:3–6 (2003), 511–522.
- [Hadi and Matthews 2000] B. K. Hadi and F. L. Matthews, “Development of Benson–Mayers theory on the wrinkling of anisotropic sandwich panels”, *Comput. Struct.* **49**:4 (2000), 425–434.
- [Hall and Robson 1984] D. J. Hall and B. L. Robson, “A review of the design and materials evaluation programme for the GRP/foam sandwich composite hull of the RAN minehunter”, *Composites* **15**:4 (1984), 266–276.
- [Heath 1960] W. G. Heath, “Sandwich construction: correlation and extension of existing theory of flat panels subjected to lengthwise compression”, *Aircr. Eng. Aerosp. Technol.* **32**:8 (1960), 230–235.
- [Hoff and Mautner 1945] N. J. Hoff and S. E. Mautner, “The buckling of sandwich-type panels”, *J. Aeronaut. Sci.* **12**:3 (1945), 285–297.
- [Lopatin and Morozov 2008] A. V. Lopatin and E. V. Morozov, “Symmetrical facing wrinkling of composite sandwich panels”, *J. Sandw. Struct. Mater.* **10**:6 (2008), 475–497.
- [Meyer-Piening 1989] H.-R. Meyer-Piening, “Remarks on higher order sandwich stress and deflection analysis”, pp. 107–127 in *Sandwich constructions I: proceedings of the 1st International Conference on Sandwich Construction* (Stockholm, 1989), edited by K.-A. Olsson and R. P. Reichard, Engineering Materials Advisory Services, Cradley Heath, 1989.
- [Meyer-Piening 2006] H.-R. Meyer-Piening, “Sandwich plates: stresses, deflection, buckling and wrinkling loads – a case study”, *J. Sandw. Struct. Mater.* **8**:5 (2006), 381–394.
- [Petras and Sutcliffe 2000] A. Petras and M. P. F. Sutcliffe, “Indentation failure analysis of sandwich beams”, *Compos. Struct.* **50**:3 (2000), 311–318.
- [Plantema 1966] F. J. Plantema, *Sandwich construction: the bending and buckling of sandwich beams, plates, and shells*, Airplane, Missile, and Spacecraft Structures **3**, Wiley, New York, 1966.
- [Sha et al. 2006] J. B. Sha, T. H. Yip, and J. Sun, “Responses of damage and energy of sandwich and multilayer beams composed of metallic face sheets and aluminum foam core under bending loading”, *Metall. Mater. Trans. A* **37**:8 (2006), 2419–2433.
- [Shuaib and Soden 1997] F. M. Shuaib and P. D. Soden, “Indentation failure of composite sandwich beams”, *Compos. Sci. Technol.* **57**:9–10 (1997), 1249–1259.
- [Soden 1996] P. D. Soden, “Indentation of composite sandwich beams”, *J. Strain Anal. Eng. Des.* **31**:5 (1996), 353–360.
- [Thomsen and Frostig 1997] O. T. Thomsen and Y. Frostig, “Localized bending effects in sandwich panels: photoelastic investigation versus high-order sandwich theory results”, *Compos. Struct.* **37**:1 (1997), 97–108.
- [Tsai and Wu 1971] S. W. Tsai and E. M. Wu, “A general theory of strength for anisotropic materials”, *J. Compos. Mater.* **5**:1 (1971), 58–80.
- [Vonach and Rammerstorfer 2000] W. K. Vonach and F. G. Rammerstorfer, “The effects of in-plane core stiffness on the wrinkling behavior of thick sandwiches”, *Acta Mech.* **141**:1–2 (2000), 1–10.
- [Zenkert 1995] D. Zenkert, *An introduction to sandwich construction*, Chameleon, London, 1995.
- [Zenkert and Vikström 1992] D. Zenkert and M. Vikström, “Shear cracks in foam core sandwich panels: nondestructive testing and damage assessment”, *J. Compos. Tech. Res.* **14**:2 (1992), 95–103.

Received 17 Mar 2009. Accepted 18 Jun 2009.

ISAAC M. DANIEL: imdaniel@northwestern.edu

Departments of Civil and Mechanical Engineering, Northwestern University, 2137 Tech Drive, Evanston, IL, 60208-3020, United States

NONLINEAR BEHAVIOR OF THERMALLY LOADED CURVED SANDWICH PANELS WITH A TRANSVERSELY FLEXIBLE CORE

YEOSHUA FROSTIG AND OLE THOMSEN

The nonlinear analysis of a curved sandwich panel with a compliant core subjected to a thermal field and mechanical load is presented. The mathematical formulation is developed first, along with the solution of the stress and displacement fields for the case of a sandwich core with mechanical properties that are independent of the temperature. The nonlinear analysis includes geometrical nonlinearities in the face sheets caused by rotation of the face cross sections and high-order effects due to the transversely flexible core. The mathematical formulation uses the variational principle of minimum energy along with HSAPT (high-order sandwich panel theory) to derive the nonlinear field equations and the boundary conditions. The full displacement and stress fields of the core with uniform temperature-independent mechanical properties and the appropriate governing equations of the sandwich panel are given.

This is followed by the general solution of the core stress and displacement fields when the mechanical core properties are dependent on the radial (through-the-thickness) coordinate. The displacement fields of a core with temperature-dependent mechanical properties are determined explicitly using an equivalent polynomial description of the varying properties.

A numerical study then describes the nonlinear response of curved sandwich panels subjected to concentrated and distributed mechanical loads, thermally induced deformations, and simultaneous thermal and mechanical loads where the mechanical load is below the limit load level of the mechanical response and the imposed temperature field is made to vary. The results reveal that the thermomechanical response is linear when the sandwich panel is heated, but becomes nonlinear with limit point behavior when the panel is cooled down.

Introduction

Curved sandwich structures are increasingly being used in the aerospace, naval and transportation industries, where weight savings combined with high strength and stiffness properties are always in demand. Sandwich structures consist of two thin face sheets, usually metallic or laminated composites, bonded to a core that is often made of honeycomb or a polymer foam with low strength properties. The core usually provides the shear resistance/stiffness to the sandwich structure in the transverse (radial) direction, and a transverse support to the face sheets that is associated to radial normal stresses. Polymer foam or low-strength honeycomb cores are flexible in this (radial/thickness) direction, and this affects both the global and the local response through changes of the core height (compressible core), and a core cross section plane that deforms into a nonlinear pattern.

The manufacture of such sandwich structures often involves elevated temperatures that may be associated with thermally induced deformations. During service, deformations may be induced by elevated

Keywords: sandwich structures, thermal effects, nonlinear geometry, softcore, high-order models.

temperatures, with or without large gradients, which may degrade the properties of the face sheets and the core. In a traditional design process of such structures the thermally induced deformations and the deformations caused by external mechanical loads are considered separately. However, this approach is not necessarily conservative, since the interaction between the external loads and the elevated temperatures, especially when the deformations are large, may lead to unsafe behavior and loss of structural integrity.

The major goal of this work is to investigate under what circumstances the combination of simultaneous thermally induced deformations and mechanical loads applied to curved sandwich structures (panels) may lead to an unstable and thereby potentially disastrous load response.

Outline. After a discussion of earlier work in [Section 1](#) we introduce in [Section 2](#) the mathematical formulation leading to the field and governing equations, the appropriate boundary conditions, the thermal fields within the core, along with the effects of the degradation of the mechanical core properties as a result of elevated temperatures. The full nonlinear governing equations for the temperature-independent (TI) case are derived and presented in [Section 3](#). In [Section 4](#) we turn to the general solution for the core stress and displacement fields when the core properties are coordinate-dependent in the radial (through-the-thickness) direction and display mechanical properties that are temperature-dependent (TD). This is followed in [Section 5](#) by a numerical investigation into the nonlinear response of sandwich panels; the results are described in [Section 5.1](#) for TI cores and in [Section 5.2](#) for TD cores. Further discussion of the numerical study and overall conclusions occupy [Section 6](#).

1. Antecedents

The well known approach for sandwich plates/panels, due to Reissner and Mindlin, replaces the layered sandwich panel by an equivalent single layer (ESL) and takes into the account the relaxed Kirchhoff–Love hypothesis, which assumes that the section plane is not normal to the plate middle surface. This approach has become the foundation for a large group of research works in the field of sandwich structures, including [[Whitney and Pagano 1970](#); [Noor and Burton 1990](#); [Noor et al. 1994](#); [1996](#)], to name a few; see also the references listed in this last paper. [Kollár \[1990\]](#) investigated buckling of generally anisotropic shallow sandwich shells and [Vaswani et al. \[1988\]](#) performed vibration and damping analysis of curved sandwich beams. These last two models used the Flügge shell theory while assuming that the face sheets are membranes and the core is incompressible. A model for shallow cylindrical sandwich panels with orthotropic surfaces suggested in [[Wang and Wang 1989](#)] follows the same relaxed Kirchhoff–Love hypothesis for the core as in references quoted above, but in this work the face sheets are attributed with both in-plane and flexural rigidities. Similarly, using the principle of virtual work along with the Reissner–Mindlin hypothesis and Sanders’ nonlinear stress-displacement relations, a theory for thick shells has been developed [[di Sciuva 1987](#); [di Sciuva and Carrera 1990](#)] that takes into account the shear rotation but assumes that the core is incompressible and linear. A stability analysis for cylindrical sandwich panels with laminated composite faces based on the Reissner hypothesis has been derived [[Rao 1985](#); [Rao and Meyer-Piening 1986](#); [1990](#)]. These authors extended the Reissner–Mindlin theory to derive force-displacement relations of anisotropic sandwich panels with membrane face sheets. As a consequence, local effects, due to localized loads, point supports, presence of load or geometric discontinuities are beyond the capability of these approaches. This well known approach is accurate as long as the core can be considered to be incompressible, i.e., the height of the core remains unchanged so the radial

displacements of the two face sheets are identical. However, compliant core materials such as relatively soft polymer foams are used in many modern sandwich structures. Accordingly it is necessary to relax the Reissner–Mindlin constraints to account for localized effects caused by the change of core height during the deformation of the sandwich structure considered.

A class of high-order theories based on the assumption of cubic and quadratic or trigonometric through-the-thickness distributions for the displacements have been suggested in [Lo et al. 1977; Librescu and Hause 2000; Stein 1986; Reddy 1984a; 1984b]. The results usually include terms that have no physical meaning due to the integration through the thickness. Lo et al. [1977] assumed a cubic shape for the in-plane deformations and a quadratic distribution for the vertical deformation. Stein [1986] used trigonometric series for the displacement distributions. Reddy [1984a; 1984b] also assumed cubic distributions for the in-plane displacements whereas the vertical displacement is assumed to be uniform across the thickness. In addition, the condition of zero shear stresses at the outer fibers of the section was also adopted. All the referenced high-order models use integration through the thickness along with variational principle and in general they are valid for sandwich panels with an incompressible core.

Many investigators have performed numerical analyses of the overall behavior of curved sandwich panels using FEA; see for example [Hildebrand 1991; Hentinen and Hildebrand 1991; Smidt 1995; 1993; Tolf 1983; Kant and Kommineni 1992]. The different analyses, linear or nonlinear, use various types of finite elements along with the limiting Reissner–Mindlin hypothesis, thus ignoring localized effects.

A different approach that includes the effect of the transverse (radial) normal stresses on the overall behavior of sandwich shells has been considered by Kühhorn and Schoop [1992], who introduced geometrically nonlinear kinematic relations along with pre-assumed polynomial deformation patterns for plates and shells. In recent years, the effects of incorporating a vertical flexible core on the local and overall behavior of the flat and curved sandwich panels have been implemented through the use of the high-order theory (HSAPT); see [Frostig et al. 1992] for flat panels, [Bozhevolnaya and Frostig 1997] for nonlinear behavior, [Bozhevolnaya 1998] on shallow sandwich panels, [Karayadi 1998] on cylindrical shells, [Frostig 1999] on the linear behavior of curved sandwich panels, [Bozhevolnaya and Frostig 2001] on the free vibration of curved panels, and [Thomsen and Vinson 2001] on composite sandwich aircraft fuselage structures.

Thermal effects in curved sandwich panels have been considered in [Noor et al. 1997] using a first-order shear deformation computation model with incompressible core. A thermomechanical FE analysis was conducted by Ko [1999], who looked into the peeling stresses involved at the face-core interfaces under cryogenic bending loading conditions. Librescu et al. [1994; 2000] investigated the thermomechanical response of flat and curved panels using a high-order theory that includes transverse (radial) shear flexibility but ignoring the transverse (radial) flexibility of the core. Fernlund [2005] used a simplified sandwich model that ignores the radial stresses as well as the shear deformation in the core in order to determine the spring-in effects of angled sandwich panels.

The thermal and the thermomechanical nonlinear response of a flat sandwich panel with a compressible core has been considered in [Frostig and Thomsen 2008a; 2008b], along with the effect of the thermal degradation of the mechanical properties of the core; see [Frostig and Thomsen 2007]. This series of papers reveals that the transverse flexibility of the core along with its extension and compression as a result of the thermally induced deformation play a major role in the nonlinear response of sandwich panels.

2. Mathematical formulation

The mathematical formulation presented in the paper uses high-order sandwich panel theory (HSAPT) to model the nonlinear response of a curved sandwich panel when subjected to thermally induced deformation along with mechanical loads. The sandwich panel is modeled as two curved faces, with membrane and flexural rigidities following the Euler–Bernoulli hypothesis, that are interconnected through compatibility and equilibrium with a two-dimensional compliant (compressible or extensible) elastic core with shear and radial (through-the-thickness) normal stress resistance. The HSAPT model for the curved panel adopts the following restrictive assumptions:

- The face sheets have in-plane (circumferential) and bending rigidities with small moderate deformations class of kinematic relation [Brush and Almroth 1975; Simites 1976] and negligible shear deformations.
- The core is considered as a two-dimensional linear elastic continuum obeying small deformation kinematic relations; the core height may change and the section planar does not remain plane after deformation.
- The core is assumed to possess shear and radial normal stiffness only, and the in-plane (circumferential) normal stiffness is assumed negligible. Accordingly, the circumferential normal stresses are assumed to be nil.
- Full bonding between the face sheets and the core is assumed and the interfacial layers can resist shear as well as radial normal stresses.
- The loads are applied to the face sheets only.

Field equations and boundary conditions. The field equations and the boundary conditions are derived following the steps of the HSAPT approach for the curved sandwich panel [Frostig 1999; Bozhevolnaya and Frostig 1997]. The field equations are derived using the variational principle of extremum of the total potential energy:

$$\delta(U + V) = 0, \quad (1)$$

where δ is the variational operator, U is in the internal potential strain energy and V is the external potential energy.

The internal potential energy of a fully bonded panel in terms of polar coordinates reads

$$\begin{aligned} \delta U = & \int_0^\alpha \int_{-\frac{1}{2}d_j}^{\frac{1}{2}d_j} \int_{-\frac{1}{2}b_w}^{\frac{1}{2}b_w} \sigma_{sst}(\phi, z_t) \delta \epsilon_{sst}(\phi, z_t) r_t \, dy \, dz_t \, d\phi \\ & + \int_0^\alpha \int_{-\frac{1}{2}d_b}^{\frac{1}{2}d_b} \int_{-\frac{1}{2}b_w}^{\frac{1}{2}b_w} \sigma_{ssb}(\phi, z_b) \delta \epsilon_{ssb}(\phi, z_b) r_b \, dy \, dz_b \, d\phi \\ & + \int_0^\alpha \int_{r_{bc}}^{r_{tc}} \int_{-\frac{1}{2}b_w}^{\frac{1}{2}b_w} (\tau_{rs}(\phi, r_c) \delta \gamma_{rs}(\phi, r_c) + \sigma_{rr}(\phi, r_c) \delta \epsilon_{rr}(\phi, r_c)) r_c \, dy \, dr_c \, d\phi, \end{aligned} \quad (2)$$

where $\sigma_{ssj}(\phi, r_j)$ and $\epsilon_{ssj}(\phi, r_j)$ ($j = t, b$) are the stresses and strains, respectively, in the circumferential directions of the face sheets; $\tau_{rs}(\phi, r_c)$ and $\gamma_{rs}(\phi, r_c)$ are the shear stresses and strains; $\sigma_{rr}(\phi, r_c)$ and $\epsilon_{rr}(\phi, r_c)$ are the radial normal stresses and strains; r and s refer to the radial and circumferential

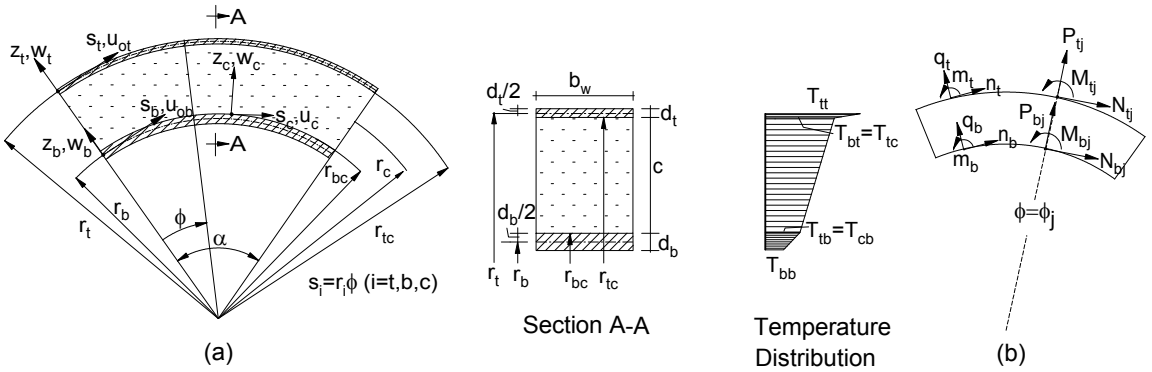


Figure 1. Dimensions, temperature distribution and sign conventions for a curved sandwich panel: (a) geometry; (b) loads at face sheets.

directions of the curved panel; α is the total angle of the curved panel; r_j ($j = t, b, c$) denote the radii of the centroidal lines of the top and both face sheets and the core; $r_{tc} = r_t - d_t/2$ and $r_{bc} = r_b + d_b/2$ refer to the radii of the upper and lower interface line; b_w is the width and d_j ($j = t, b$) are the thicknesses of the face sheets. For geometry, sign conventions, coordinates, deformations and internal resultants, see [Figure 1](#).

The variation of the external energy reads

$$\delta V = - \int_{s=0}^L (n_t \delta u_{ot} + q_t \delta w_t - m_t \delta \beta_t) ds_t - \int_{s=0}^L (n_b \delta u_{ob} + q_b \delta w_{bt} - m_b \delta \beta_b) ds_b - \sum_{j=t,b} \sum_{i=1}^{NC_j} \int_{s=0}^L (N_{ij} \delta u_{oj} + P_{ij} \delta w_j - M_{ij} \delta \beta_j) \delta_d(s_j - s_{ij}) ds_j, \tag{3}$$

where n_j , q_j and m_j ($j = t, b$) are the external distributed loads in the circumferential and radial directions, respectively, and the distributed bending moment applied at the face sheets; u_{oj} and w_j ($j = t, b$) are the circumferential and radial displacements of the face sheets, respectively; β_j is the slope of the section of the face sheet; N_{ejj} , P_{ejj} and M_{ejj} ($j = t, b$) are the concentrated external loads in the circumferential and radial directions, respectively, and the concentrated bending moment applied at either face sheet at $s = s_{ij}$; NC_j ($j = t, b$) is the number of concentrated loads at the top and bottom faces, and $\delta_d(s_j - s_{ji})$ is the Dirac function at the location of the concentrated loads. For sign conventions and definition of loads see [Figure 1](#).

The displacement pattern of the face sheets through their depth follows the Euler–Bernoulli assumptions with negligible shear strain and kinematic relations of small deformation and they read, for $j = t, b$,

$$u_j(\phi, z_j) = u_{oj}(\phi) + z_j \beta_j(\phi), \quad \beta_j(\phi) = \frac{1}{r_j} u_{oj}(\phi) - \frac{1}{r_j} \frac{d}{d\phi} w_j(\phi), \tag{4}$$

where z_j is the radial coordinate measured *upward* from the centroid of each face sheet, r_j is the radius and $s_j = r_j \phi$ is the circumferential coordinate of the face sheets, which have identical radial center, and ϕ is the angle measured from the origin; see [Figure 1](#) for the geometry. Hence, the strain distribution is

also assumed to be linear and it reads

$$\varepsilon_{ssj}(\phi) = \varepsilon_{ossj}(\phi) + z_j \chi_j(\phi), \tag{5}$$

where the mid-plane strain and the curvature equal

$$\varepsilon_{ossj}(\phi) = \frac{d}{d\phi} u_{oj}(\phi) + \frac{w_j(\phi)}{r_j(\phi)} + \frac{1}{2} \beta_j(\phi)^2, \quad \chi_j(\phi) = \frac{1}{r_j} \frac{d}{d\phi} \beta_j(\phi) = \frac{1}{r_j^2} \frac{d}{d\phi} u_{oj}(\phi) - \frac{1}{r_j^2} \frac{d^2}{d\phi^2} w_j(\phi). \tag{6}$$

Notice that thermal strains do not appear in the terms of the strains of the face sheets.

The kinematic relations for the core, under the approximation of small deformations, read

$$\varepsilon_{rrc}(\phi, r) = \frac{\partial}{\partial r} w_c(\phi, r), \quad \gamma_c(\phi, r) = \frac{\partial}{\partial r} u_c(\phi, r) - \frac{u_c(\phi, r)}{r} + \frac{1}{r} \frac{\partial}{\partial \phi} w_c(\phi, r), \tag{7}$$

where $w_c(\phi, r)$ and $u_c(\phi, r)$ are the radial and circumferential displacements of the core, respectively.

The compatibility conditions corresponding to perfect bonding between the face sheets and the core require that

$$u_c(\phi, r = r_{jc}) = u_{oj}(\phi) - \frac{\lambda}{2r_j} d_j(u_{oj}(\phi) - w_j(\phi)_{,\phi}), \quad w_c(\phi, r = r_{jc}) = w_j(\phi), \tag{8}$$

where $\lambda = 1, -1$ for $j = t, b$, respectively; r_{jc} ($j = t, b$) are the radii of the upper and lower face-core interfaces; and $u_c(r = r_{jc}, \phi)$, $w_c(r = r_{jc}, \phi)$ are the displacements of the core in the circumferential and radial directions at the face-core interfaces.

The field equations and the boundary conditions are derived using the variational principle (1), the variational expressions (2) and (3) of the energies, the kinematic relations (5)–(7) of the face sheets and the core, the compatibility requirements (8), and the stress resultants. See Figure 2.

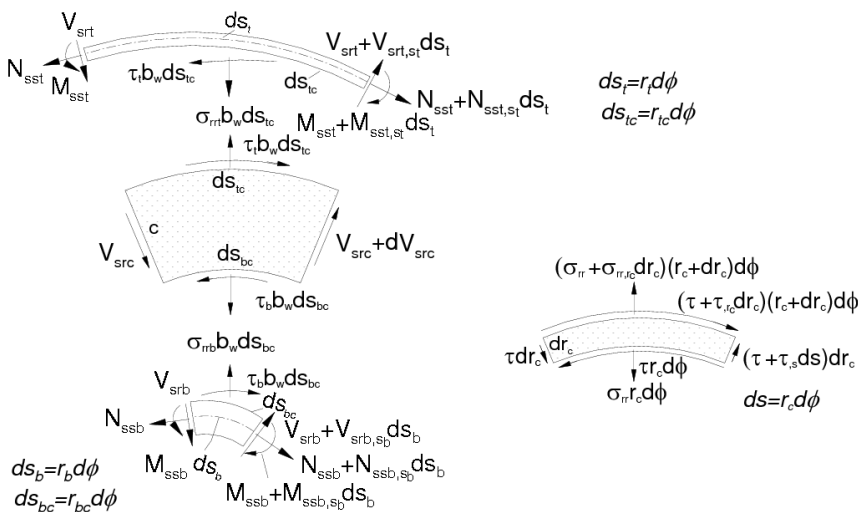


Figure 2. Internal stress resultants and stresses within a curved sandwich panel segment. Left: stress resultants on the deformed shape of the panel. Right: stresses within the core.

The field equations, after integration by parts and some algebraic manipulations, read as follows (notice that since the strains in the core are linear, the field equations of the core coincide with those for the geometrically linear case [Frostig 1999] and are presented here only for convenience):

Face sheets ($j = t, b$):

$$\begin{aligned} & \left(-\frac{d_j}{2r_j} + \lambda\right)b_w r_{jc} \tau_{sr}(\phi, r = r_{jc}) + \frac{1}{r_j} \left(u_{oj}(\phi) - \frac{dw_j(\phi)}{d\phi}\right) N_{ssj}(\phi) - \frac{dN_{ssj}(\phi)}{d\phi} \\ & \qquad \qquad \qquad + m_j(\phi) - \frac{1}{r_j} \frac{dM_{ssj}(\phi)}{d\phi} - r_j n_j = 0, \\ & \left(1 + \frac{1}{r_j} \left(\frac{du_{oj}(\phi)}{d\phi} - \frac{d^2 w_j(\phi)}{d\phi^2}\right)\right) N_{ssj}(\phi) + \frac{1}{r_j} \left(u_{oj}(\phi) - \frac{dw_j(\phi)}{d\phi}\right) \frac{dN_{ssj}(\phi)}{d\phi} \\ & \qquad + \lambda b_w r_{jc} \sigma_{rr}(\phi, r = r_{jc}) - \frac{b_w d_j r_{jc}}{2r_j} \frac{d\tau_{sr}(\phi, r = r_{jc})}{d\phi} - \frac{1}{r_j} \frac{d^2 M_{ssj}(\phi)}{d\phi^2} + \frac{dm_j(\phi)}{d\phi} - r_j q_t = 0. \end{aligned} \tag{9}$$

Core:

$$r_c \frac{\partial \tau_{sr}(\phi, r_c)}{\partial r_c} + 2\tau_{sr}(\phi, r_c) = 0, \qquad r_c \frac{\partial \sigma_{rr}(\phi, r_c)}{\partial r_c} + \sigma_{rr}(\phi, r_c) + \frac{\partial \tau_{sr}(\phi, r_c)}{\partial \phi} = 0. \tag{10}$$

Here N_{ssj} and M_{ssj} ($j = t, b$) are the in-plane and bending moment stress resultants of each face sheet; $\tau_{sr}(\phi, r = r_{jc})$ and $\sigma_{rr}(\phi, r = r_{jc})$ (with $j = t, b$) are the shear and vertical normal stresses, respectively, at the face-core interfaces; and $\lambda = 1, -1$ for $j = t, b$. Notice that here the nonlinear terms involve also in-plane displacements, unlike the case of flat panels. Note also that, due to the geometrical nonlinearities of the face sheets, the equilibrium conditions, which are described by the field equations, correspond to the deformed shape of the face sheets and the undeformed shape of the core; see Figure 2.

Boundary conditions for the curved sandwich panel where the loads and constraints are defined in the circumferential and radial directions of each face sheet and the core independently are called local boundary conditions; see Figure 3(a) on the next page. These conditions at $\phi_e = 0, \alpha$ read as follows:

Face sheets ($j = t, b$):

$$\begin{aligned} & \lambda \left(\frac{M_{ssj}(\phi_e)}{r_j} + N_{ssj}(\phi_e) \right) - N_{ej} + \frac{M_{ej}}{r_j} = 0 \quad \text{or} \quad u_{oj}(\phi_e) = u_{eoj}, \\ & \qquad \qquad \qquad \lambda \frac{M_{ssj}(\phi_e)}{r_j} + \frac{M_{ej}}{r_j} = 0 \quad \text{or} \quad w_{j,\phi}(\phi_e) = Dw_{ej}, \\ & \lambda \left(\frac{D(w_j)(\phi_e) - u_{oj}(\phi_e)}{r_j} N_{ssj}(\phi_e) + \frac{D(M_{ssj})(\phi_e)}{r_j} \right. \\ & \qquad \qquad \qquad \left. - m_j(\phi_e) + \frac{b_w d_j r_{jc} \tau_j(\phi_e)}{2r_j} \right) - P_{ej} = 0 \quad \text{or} \quad w_j(\phi_e) = w_{ej}, \end{aligned} \tag{11}$$

where $\lambda = 1$ for $\phi_e = \alpha$ and $\lambda = -1$ for $\phi_e = 0$, in all three equations; u_{eoj}, w_{ej} are the prescribed circumferential and radial displacements at the edges of the face sheets; Dw_{ej} is the rotation at the same edges; and N_{ej}, P_{ej}, M_{ej} are the imposed external loads. Notice that the circumferential force condition (the first of the three equations above) is actually a combined stress resultant that results from a moment equilibrium about the radial center of the face sheet.

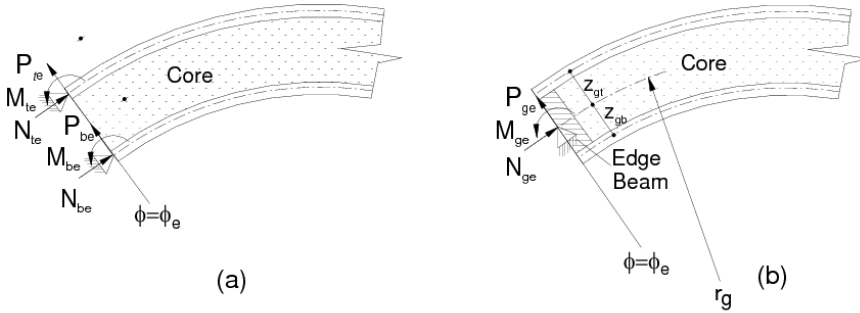


Figure 3. Edge conditions at the edge of a curved sandwich panel: (a) conventional edge with isolated supports; (b) reinforced edge with an edge beam.

Core: The boundary conditions at $\phi_e = 0, \alpha$, through the depth of the core, at $r_{bc} \leq r_c \leq r_{tc}$, read

$$\tau_{rs}(\phi_e, r_c) = 0 \quad \text{or} \quad w_c(\phi_e, r_c) - w_{ec}(r_c) = 0, \tag{12}$$

where $w_{ec}(r)$ denotes the prescribed deformations at the ends of the sandwich panel.

For the case where an edge beam connects the two face sheets and the core, the two face sheets undergo identical displacements and rotations; see Figure 3(b). Thus the distribution of the displacement through the depth of the sandwich panel follows those of a face sheet, given in (4):

$$u_g(\phi_e, z_g) = u_{go}(\phi_e) + \frac{z_g}{r_g} (u_{go}(\phi_e) - D(w_g)(\phi_e)), \tag{13}$$

where $u_{go}(\phi_e)$ denotes the circumferential displacements and $D(w_g)(\phi_e)$ the rotation of the centroid line of the section with the edge beam; see again Figure 3(b). In order to use these displacements, denoted as global displacements, in the variational terms of the boundary conditions that result from the partial integration of the internal and external potential energy terms and the contribution of the loads at the edges of the panel, the global in-plane displacements and rotations must be defined in terms of the displacements and rotation of the face sheets. Hence, these unknowns are determined by imposing the conditions that the global displacements $u_g(\phi_e, z_g)$ at the centroid of the upper and lower face sheets must equal the in-plane displacements $u_{oj}(\phi_e)$ of the face sheets. Thus they read

$$D(w_g)(\phi_e) = \frac{r_t u_{ob}(\phi_e) + r_b u_{ot}(\phi_e)}{c + \frac{1}{2}d_t + \frac{1}{2}d_b}, \quad u_{go}(\phi_e) = \frac{z_{gb} u_{ot}(\phi_e) + z_{gt} u_{ob}(\phi_e)}{c + \frac{1}{2}d_t + \frac{1}{2}d_b}. \tag{14}$$

The existence of the edge beam also imposes relations between the displacements of the face sheets:

$$w_t(\phi_e) = w_b(\phi_e), \quad \beta_t(\phi_e) = \beta_b(\phi_e), \quad \beta_t(\phi_e) = \frac{u_{ot}(\phi_e) - u_{ob}(\phi_e)}{z_{eb} + z_{et}}, \tag{15}$$

where the last equality results from the requirement that the slope of the section of the face sheets and that of the edge beam must be identical.

The global boundary conditions are derived by expressing the displacements and rotations of the face sheets in terms of the global displacements using (14) and (15), and substituting them into the variational

terms at the edges. Hence, by collecting terms with respect to the in-plane displacement and rotation of the edge beam, one obtains for these global conditions

$$\begin{aligned} \frac{r_t N_{sst}(\phi_e) + M_{ssb}(\phi_e) + M_{sst}(\phi_e) + r_b N_{ssb}(\phi_e) + M_{ge}(\phi_e)}{r_g} - N_{ge}(\phi_e) &= 0 \quad \text{or} \quad u_{go}(\phi_e) = u_{geo}, \\ -N_{sst}(\phi_e)z_{gt} - M_{ssb}(\phi_e) - M_{sst}(\phi_e) + N_{ssb}(\phi_e)z_{gb} - M_{ge}(\phi_e) &= 0 \quad \text{or} \quad D(w_g)(\phi_e) = D w_{ge}, \\ V_{srt}(\phi_e) + V_{srb}(\phi_e) + \frac{b_w r_{tc}(r_{tc} - r_{bc})\tau_t(\phi_e)}{r_{bc}} - P_{ge} &= 0 \quad \text{or} \quad w_g(\phi_e) = w_{ge}, \end{aligned} \tag{16}$$

where $V_{srj}(\phi)$ ($j = t, b$) is the radial shear stress resultant in each of the face sheets, which equals

$$V_{srj}(\phi_e) = \frac{D(w_j)(\phi_e) - u_{oj}(\phi_e)}{r_j} N_{ssj}(\phi_e) + \frac{D(M_{ssj})(\phi_e)}{r_j} + \frac{b_w d_j r_{jc} \tau_{sr}(\phi_e, r = r_{jc})}{2r_j} - m_j(\phi_e). \tag{17}$$

Under the assumption of a perfect bond between the edge beam and the core (through the full core depth) the radial displacement field of the core must be uniform through its depth. This is possible only when the upper and lower face sheets have identical displacements; see (15). This is equivalent to a weaker version of the requirement (12)₂, namely

$$w_c(\phi_e) \approx \frac{1}{c} \int_{r_{bc}}^{r_{tc}} w_c(\phi_e, r_c) dr_c = w_{ge}(\phi_e). \tag{18}$$

3. Governing equations in the temperature-independent case

To determine the governing equations we must first define the stress and displacement fields of the core.

Core displacement and stress fields: uniform mechanical properties (TI). The explicit descriptions of the stress and displacement fields of the core are determined through the compatibility conditions (8), applied to the following constitutive relations of an isotropic core:

$$\epsilon_{rr}(\phi, r_c) = \frac{\sigma_{rr}(\phi, r_c)}{E_{rc}} + \alpha_{Tc} T_c(r_c, \phi), \quad \gamma_{sr}(\phi, r_c) = \frac{\tau_{sr}(\phi, r_c)}{G_{src}}, \tag{19}$$

where T_c is the temperature function and E_{rc}, G_{src} are the Young's and shear moduli of the core in the radial direction.

The stress fields within the core are derived through the solution of the field equations (10) of the core, which reads

$$\begin{aligned} \tau_{sr}(\phi, r_c) &= \frac{r_{tc}^2}{r_c^2} \tau_t(\phi), \quad \sigma_{rr}(\phi, r_c) = \frac{r_{tc}^2}{r_c^2} \frac{d\tau_t(\phi)}{d\phi} + \frac{C_{w1}(\phi)}{r_c}, \quad \tau_b(\phi) = \frac{r_{tc}^2}{r_{bc}^2} \tau_t(\phi), \\ \sigma_{rrj}(\phi) &= \frac{r_{tc}^2}{r_{jc}^2} \frac{d}{d\phi} \tau_t(\phi) + \frac{C_{w1}(\phi)}{r_{jc}} \quad (j = t, b), \end{aligned} \tag{20}$$

where $C_{w1}(\phi)$ is a coefficient of integration to be determined through the compatibility conditions (8) at the face-core interfaces; $\tau_j(\phi)$ and $\sigma_{rrj}(\phi)$ ($j = t, b$) are the shear and radial normal stresses, respectively,

at the face-core interfaces. The result for the radial stress field is

$$\sigma_{rr}(\phi, r_c) = \frac{cE_{rc}\alpha_{Tc}}{2r_cL} (T_{ct}(\phi) + T_{cb}(\phi)) - \frac{E_{rc}}{r_cL} (w_t(\phi) - w_b(\phi)) + \left(\frac{r_{tc}c}{r_cr_{bc}L} + \frac{r_{tc}^2}{r_c^2} \right) \frac{d\tau_t(\phi)}{d\phi}, \quad (21)$$

where we have introduced the temperature functions T_{ct} and T_{bt} at the core-face interfaces, as well as the abbreviation

$$L = \ln \frac{r_{bc}}{r_{tc}}.$$

Equation (21) specializes to the vertical normal stresses at the upper and the lower face-core interfaces:

$$\begin{aligned} \sigma_{rri}(\phi) &= \frac{cE_{rc}\alpha_{Tc}}{2r_{tc}L} (T_{ct}(\phi) + T_{cb}(\phi)) - \frac{E_{rc}}{r_{tc}L} (w_t(\phi) - w_b(\phi)) + \left(\frac{c}{r_{bc}L} + 1 \right) \frac{d\tau_t(\phi)}{d(\phi)}, \\ \sigma_{rrb}(\phi) &= \frac{cE_{rc}\alpha_{Tc}}{2r_{bc}L} (T_{ct}(\phi) + T_{cb}(\phi)) - \frac{E_{rc}}{r_{bc}L} (w_t(\phi) - w_b(\phi)) + \left(\frac{r_{tc}c}{r_{bc}^2L} + \frac{r_{tc}^2}{r_{bc}^2} \right) \frac{d\tau_t(\phi)}{d(\phi)}. \end{aligned} \quad (22)$$

The displacement fields of the core in the radial and circumferential directions are determined through the constitutive relations (19) and the three compatibility conditions (8) at the upper face-core interface and the radial compatibility condition at the lower interface. They read as follows:

$$\begin{aligned} w_c(\phi, r_c) &= -\frac{\alpha_{Tc}}{2cL} \left((r_{tc} - r_c)^2 L - c^2 \ln \frac{r_c}{r_{tc}} \right) T_{ct}(\phi) \\ &\quad + \frac{\alpha_{Tc}}{2cL} \left((r_{bc} - r_c)^2 L + c^2 \ln \frac{r_c}{r_{bc}} \right) T_{cb}(\phi) \\ &\quad + \frac{1}{L} \left(w_b(\phi) \ln \frac{r_c}{r_{tc}} - w_t(\phi) \ln \frac{r_c}{r_{bc}} \right) \\ &\quad + \frac{r_{tc}}{E_cr_{bc}r_cL} \left(r_{tc}r_c \ln \frac{r_c}{r_{tc}} - r_{bc}r_c \ln \frac{r_c}{r_{bc}} - r_{tc}r_{bc}L \right) \frac{d\tau_t(\phi)}{d\phi} \end{aligned} \quad (23)$$

$$\begin{aligned} u_c(\phi, r_c) &= -\frac{\alpha_{Tc}}{2r_{tc}cL} \left(Lr_{tc} \left(r_c^2 - r_{tc}^2 - 2r_cr_{bc} \ln \frac{r_c}{r_{tc}} + 2c(r_{tc} - r_c) \right) - c^2 \left(r_{tc} \left(1 + \ln \frac{r_c}{r_{tc}} \right) - r_c \right) \right) \frac{dT_{ct}(\phi)}{d\phi} \\ &\quad + \frac{\alpha_{Tc}}{2r_{tc}cL} \left(Lr_{tc} \left(r_c^2 - r_{tc}^2 - 2r_cr_{tc} \ln \frac{r_c}{r_{tc}} \right) + c^2 \left(r_{tc} - r_c + r_{tc} \ln \frac{r_c}{r_{tc}} \right) \right) \frac{dT_{cb}(\phi)}{d\phi} \\ &\quad - \frac{1}{r_{tc}L} \left(r_{tc} - r_c + r_{tc} \ln \frac{r_c}{r_{bc}} + r_cL \frac{r_{tc}}{r_t} \right) \frac{dw_t(\phi)}{d\phi} \\ &\quad + \frac{1}{r_{tc}L} \left(r_{tc} - r_c + r_{tc} \ln \frac{r_c}{r_{tc}} \right) \frac{dw_b(\phi)}{d\phi} + \frac{r_c^2 - r_{tc}^2}{2r_cG_c} \tau_t(\phi) + \frac{r_c}{r_t} u_{oi}(\phi) \\ &\quad + \frac{1}{2E_cLr_{bc}r_c} \left(2cr_c(r_{tc} - r_c + r_{tc} \ln \frac{r_c}{r_{bc}}) + (2r_{tc}^2r_c - (r_{tc}^2 + r_c^2)r_{bc})L \right) \frac{d^2\tau_t(\phi)}{d\phi^2} \end{aligned} \quad (24)$$

Next we give the fifth of the field equations, which results from the compatibility condition at the lower face-core interface in the circumferential direction, and it derived using (8) and (24) along with a

nonuniform temperature field:

$$\begin{aligned} & \frac{\alpha_{Tc}}{2cr_{tc}L} (c^3 + 2r_{bc}r_{tc}L(c + r_{bc}L)) \frac{dT_{ct}(\phi)}{d\phi} + \frac{\alpha_{Tc}}{2cr_{tc}L} (c^3 - 2r_{bc}r_{tc}L(c + r_{tc}L)) \frac{dT_{cb}(\phi)}{d\phi} \\ & + \frac{r_{bc}}{r_t} u_{ot}(\phi) - \frac{r_{bc}}{r_b} u_{ob}(\phi) + \frac{2c^2 + (r_{tc}^2 - r_{bc}^2)L}{2E_{rc}r_{bc}L} \frac{d^2\tau_t(\phi)}{d\phi^2} - \frac{r_{tc}^2 - r_{bc}^2}{2r_{bc}G_{src}} \tau_t(\phi) \\ & + \left(\frac{c}{r_{tc}L} + \frac{r_{bc}}{r_b} \right) \frac{dw_b(\phi)}{d\phi} - \left(\frac{c}{r_{tc}L} + \frac{r_{bc}}{r_t} \right) \frac{dw_t(\phi)}{d\phi} = 0. \end{aligned} \quad (25)$$

However, when the temperature distribution is uniform through the length of the panel and the elastic constants are uniform, nothing is left of the first line and the compatibility equation becomes identical to the one obtained for the linear case [Frostig 1999]:

$$\begin{aligned} & \frac{r_{bc}}{r_t} u_{ot}(\phi) - \frac{r_{bc}}{r_b} u_{ob}(\phi) + \frac{2c^2 + (r_{tc}^2 - r_{bc}^2)L}{2E_{rc}r_{bc}L} \frac{d^2\tau_t(\phi)}{d\phi^2} - \frac{r_{tc}^2 - r_{bc}^2}{2r_{bc}G_{src}} \tau_t(\phi) \\ & + \left(\frac{c}{r_{tc}L} + \frac{r_{bc}}{r_b} \right) \frac{dw_b(\phi)}{d\phi} - \left(\frac{c}{r_{tc}L} + \frac{r_{bc}}{r_t} \right) \frac{dw_t(\phi)}{d\phi} = 0. \end{aligned} \quad (26)$$

The boundary condition of the core when an edge beam is attached to the end of the panel — see Equation (23) — and the global displacements,

$$w_{ge}(\phi_e) = w_t(\phi_e) = w_b(\phi_e) = 0,$$

require the use of the relaxed condition (18) within the core, which yields

$$\begin{aligned} & \frac{r_{tc}}{E_c r_{bc} L} (-c^2 + r_{bc} r_{tc} L^2) D(\tau_t)(\phi_e) \\ & - \frac{\alpha_{Tc} c}{6L} \left((3c + (3r_{tc} - c)L) T_{ct}(\phi_e) + (3c + (3r_{bc} + c)L) T_{cb}(\phi_e) \right) = 0. \end{aligned} \quad (27)$$

When the temperatures or coefficient of thermal expansion of the core is zero this condition yields $D(\tau_t)(\phi_e) = 0$ for the slope of the stress, which coincides with the linear case of [Frostig 1999].

Governing equations: uniform core (II). The governing equations assume that the face sheets are isotropic. They are defined using the following load-displacement relations ($j = t, b$):

$$\begin{aligned} N_{ssj}(\phi) &= EA_j \left(\frac{1}{r_j} \left(\frac{du_{oj}(\phi)}{d\phi} + w_j(\phi) \right) + \frac{1}{2r_j^2} \left(u_{oj}(\phi) - \frac{dw_j(\phi)}{d\phi} \right)^2 - \frac{\alpha_{Tj}}{2} (T_{jt}(\phi) + T_{jb}(\phi)) \right), \\ M_{ssj}(\phi) &= EI_j \left(\frac{1}{r_j^2} \left(\frac{du_{oj}(\phi)}{d\phi} - \frac{d^2w_j(\phi)}{d\phi^2} \right) - \frac{\alpha_{Tj}}{d_j} (T_{jt}(\phi) - T_{jb}(\phi)) \right). \end{aligned} \quad (28)$$

The governing equations are derived upon substitution of these relations and the shear and radial normal stresses of the core at the upper and lower interfaces, namely (20) and (22), into the equilibrium

equations (9)–(10). This gives

$$\begin{aligned} & \frac{1}{r_t} \left(u_{ot}(\phi) - \frac{dw_t(\phi)}{d\phi} \right) N_{sst}(\phi) + \frac{b_w r_{tc}^2}{r_t} \tau_t(\phi) - r_t n_t + m_t(\phi) - \frac{1}{r_t} \frac{dM_{sst}(\phi)}{d\phi} - \frac{dN_{sst}(\phi)}{d\phi} = 0, \\ & \frac{1}{r_b} \left(u_{ob}(\phi) - \frac{dw_b(\phi)}{d\phi} \right) N_{ssb}(\phi) - \frac{b_w r_{bc}^2}{r_b} \tau_t(\phi) - r_b n_b + m_b(\phi) - \frac{1}{r_b} \frac{dM_{ssb}(\phi)}{d\phi} - \frac{dN_{ssb}(\phi)}{d\phi} = 0, \\ & \frac{b_w E_{rc}}{L} (w_b(\phi) - w_t(\phi)) + \frac{\alpha_{Tc} b_w c E_{rc}}{2L} (T_{ct}(\phi) + T_{cb}(\phi)) \\ & \quad + b_w r_{tc} \left(\frac{r_{tc}}{r_t} + \frac{c}{r_{bc} L} \right) \frac{d\tau_t(\phi)}{d\phi} + \frac{1}{r_t} \left(u_{ot}(\phi) - \frac{dw_t(\phi)}{d\phi} \right) \frac{dN_{sst}(\phi)}{d\phi} \\ & \quad + \left(1 + \frac{1}{r_t} \left(\frac{du_{ot}(\phi)}{d\phi} - \frac{d^2 w_t(\phi)}{d\phi^2} \right) \right) N_{sst}(\phi) - r_t q_t + \frac{d}{d\phi} m_t(\phi) - \frac{1}{r_t} \frac{d^2 M_{sst}(\phi)}{d\phi^2} = 0, \\ & \frac{b_w E_{rc}}{L} (w_t(\phi) - w_b(\phi)) - \frac{\alpha_{Tc} b_w c E_{rc}}{2L} (T_{ct}(\phi) + T_{cb}(\phi)) \\ & \quad - b_w r_{tc} \left(\frac{r_{tc}}{r_b} + \frac{c}{r_{bc} L} \right) \frac{d\tau_t(\phi)}{d\phi} + \frac{1}{r_b} \left(u_{ob}(\phi) - \frac{dw_b(\phi)}{d\phi} \right) \frac{dN_{ssb}(\phi)}{d\phi} \\ & \quad + \left(1 + \frac{1}{r_b} \left(\frac{du_{ob}(\phi)}{d\phi} - \frac{d^2 w_b(\phi)}{d\phi^2} \right) \right) N_{ssb}(\phi) - r_b q_b + \frac{d}{d\phi} m_b(\phi) - \frac{1}{r_b} \frac{d^2 M_{ssb}(\phi)}{d\phi^2} = 0. \end{aligned}$$

To these four equilibrium equations one must add (25) to obtain the full set of governing equations.

4. Temperature dependence: general solution for the core stress and displacement fields

We now take into account the possibility that the mechanical core properties vary with the radial coordinate, as they must if these properties are temperature-dependent and there is a temperature gradient. Specifically, we determine the general solution for the stress and displacement fields within the depth of the core for an isotropic core with the constitutive relations (19), which we copy here adding an explicit dependence of the Young’s and shear moduli of the core (E_{rc} and G_{src}) on the radial coordinate r_c :

$$\begin{aligned} \varepsilon_{rr}(\phi, r_c) &= \frac{\sigma_{rr}(\phi, r_c)}{E_{rc}(r_c)} + \alpha_{Tc} T_c(r_c, \phi), \\ \gamma_{sr}(\phi, r_c) &= \frac{\tau_{sr}(\phi, r_c)}{G_{src}(r_c)}, \end{aligned} \tag{29}$$

The displacement fields are derived using these constitutive relations, the expressions (20) for the stress fields, the kinematic relations (7), the compatibility conditions (8) at the upper face-core interface (that is, with $j = t$), and the compatibility condition (8)₂ in the vertical direction at the lower face-core interface ($j = b$). Hence, the general expression of these fields with the constants of integration where

the temperature distribution through the depth of the core is linear (Figure 1) is

$$w_c(\phi, r_c) = \frac{\alpha_{Tc} r_c}{2c} ((r_c - 2r_{bc})T_{ct}(\phi) - (r_c - 2r_{tc})T_{cb}(\phi)) + \frac{d\tau_t(\phi)}{d\phi} r_{tc}^2 \int \frac{1}{r_c^2 E_{rc}(r_c)} dr_c + C_{w1}(\phi) \int \frac{1}{r_c E_{rc}(r_c)} dr_c + C_{w2}(\phi), \quad (30)$$

$$u_c(r_c, \phi) = \frac{\alpha_{Tc} r_c}{2c} \left((2r_{bc} \ln(r_c) - r_c) \frac{dT_{ct}(\phi)}{d\phi} - (2r_{tc} \ln(r_c) - r_c) \frac{dT_{cb}(\phi)}{d\phi} \right) + \frac{dC_{w2}(\phi)}{d\phi} + r_c C_u(\phi) - r_c r_{tc}^2 \frac{d^2 \tau_t(\phi)}{d\phi^2} \int \int \frac{1}{r_c^2 E_{rc}(r_c)} dr_c - r_c \frac{dC_{w1}(\phi)}{d\phi} \int \int \frac{1}{r_c E_{rc}(r_c)} dr_c + r_c \tau_t(\phi) r_{tc}^2 \int \frac{1}{G_{src}(r_c) r_c^3} dr_c, \quad (31)$$

where $\tau_t(\phi)$ is the shear stress at the upper face-core interface and is used as an unknown, similar to the shear stress unknown in the HSAPT model; C_{w_j} ($i = 1, 2$) are the constants of integration to be determined through the compatibility conditions (8) imposed in the radial directions; and C_u is a constant of integration to be determined by the compatibility requirement (8)₁ for the circumferential displacement at the upper face-core interface.

Nonuniform core moduli. A core with nonuniform mechanical properties occurs when the properties are temperature-dependent (TD), or when it is made of a functionally graded material. In such a case the stress and displacement fields may be determined analytically only when the distribution of the moduli is of the fourth order. However, in order to achieve a general closed-form description of the core fields we describe the moduli, or more precisely their inverses, by a polynomial series:

$$E_{rc}(r_c) = \frac{1}{\sum_{i=0}^{N_e} E_i r_c^i}, \quad G_{src}(r_c) = \frac{1}{\sum_{i=0}^{N_e} G_i r_c^i}, \quad (32)$$

where E_i and G_i are the coefficients of the polynomial description of the elastic moduli functions, and N_e is the number of terms in the polynomial. This polynomial description can be determined through curve fitting procedures or Taylor series. The number of terms depends on the required accuracy to describe of the inverse moduli.

The displacement field of the core is derived through the substitution of the moduli functions (32) into (30) and (31), which yields

$$w_c(\phi, r_c) = r_{tc}^2 \left(-\frac{E_0}{r_c} + E_1 \ln(r_c) + E_2 r_c + \sum_{i=3}^{N_e} \frac{E_i r_c^{i-1}}{i-1} \right) \frac{d\tau_t(\phi)}{d\phi} + \left(E_0 \ln(r_c) + E_1 r_c + \frac{E_2}{2} r_c^2 + \sum_{i=3}^{N_e} \frac{E_i r_c^i}{i} \right) C_{w1}(\phi) + \frac{r_c}{2c} ((r_c - 2r_{bc})T_{ct}(\phi) + (-r_c + 2r_{tc})T_{cb}(\phi)) \alpha_{Tc} + C_{w2}(\phi), \quad (33)$$

$$\begin{aligned}
u_c(\phi, r_c) = & r_{tc}^2 r_c \left(-\frac{E_0}{2r_c^2} + \frac{E_1}{r_c} (\ln(r_c) + 1) - E_2 \ln(r_c) - \sum_{i=3}^{N_e} \frac{E_i r_c^{i-2}}{(i-1)(i-2)} \right) \frac{d^2 \tau_t(\phi)}{d\phi^2} \\
& + r_c \left(\frac{E_0}{r_c} (\ln(r_c) + 1) - E_1 \ln(r_c) - \frac{E_2}{2} r_c - \sum_{i=3}^{N_e} \frac{r_c^{i-1} E_i}{(i-1)i} \right) \frac{dC_{w1}(\phi)}{d\phi} \\
& + \frac{\alpha_{Tc} r_c}{2c} \left((2r_{bc} \ln(r_c) - r_c) \frac{dT_{ct}(\phi)}{d\phi} - (2r_{tc} \ln(r_c) - r_c) \frac{dT_{cb}(\phi)}{d\phi} \right) \\
& + r_{tc}^2 r_c \left(-\frac{G_0}{2r_c^2} + G_2 \ln(r_c) - \frac{G_1}{r_c} + G_3 r_c + \sum_{i=4}^{N_e} \frac{G_i r_c^{i-2}}{i-2} \right) \tau_t(\phi) + \frac{d}{d\phi} C_{w2}(\phi) + r_c C_u(\phi). \quad (34)
\end{aligned}$$

Note that the first three or four terms in the polynomial description are not within the sum terms since they involve integration of $1/r_c$ terms.

The constants of integrations C_{w1} and C_{w2} are determined by applying the compatibility conditions (8)₂ in the vertical direction to the vertical displacement (33) of the core. The third constant of integration, C_u , is determined by imposing the compatibility condition (8)₁ at the upper face-core interface on the displacement (34) in the circumferential direction. The vertical normal stresses within the core and are determined by substitution of the vertical constant of integration in the vertical normal stress distribution, see (20). The fifth governing equation, denoted also as the compatibility equation, which imposes the compatibility condition (8)₁ in the circumferential (in-plane) direction at the lower face-core interface, is determined through substitution of the three constants of integration into the expression (34) for the circumferential displacements of the core. The explicit description of the stress and displacement fields is very lengthy and is not presented herein for brevity.

5. Numerical study

The numerical solution of the nonlinear differential equations can be achieved using numerical schemes such as the multiple-shooting points method [Stoer and Bulirsch 1980] or the finite-difference (FD) approach using trapezoid or mid-point methods with Richardson extrapolation or deferred corrections [Ascher and Petzold 1998], as implemented in Maple, along with parametric or arc-length continuation methods [Keller 1992]. The FD approach as implemented in Maple has been used in this study. It is robust and includes error control along with an arc-length procedure built-in. These solution approaches have been used by the authors in many cases and have been compared also recently with FE nonlinear codes; see for example [Frostig and Thomsen 2008b].

We studied the thermomechanical nonlinear response of a simply supported and clamped shallow curved sandwich panel subjected to a concentrated and distributed load, as shown in Figure 4. The sandwich panel consists of two aluminum face sheets of a thickness of 1 mm and an H60 PVC foam core made by Devinicell with $E_c = 56.7$ MPa and $G_c = 22$ MPa and with a thickness of 25 mm. The geometry of the curved panel is that of an experimental set-up used in [Bozhevolnaya and Frostig 1997; Bozhevolnaya 1998]; see Figure 4. The edges of the curved sandwich panel are reinforced by an edge beam and assumed to be bonded to the adjacent core (Detail A in the figure). The supporting system

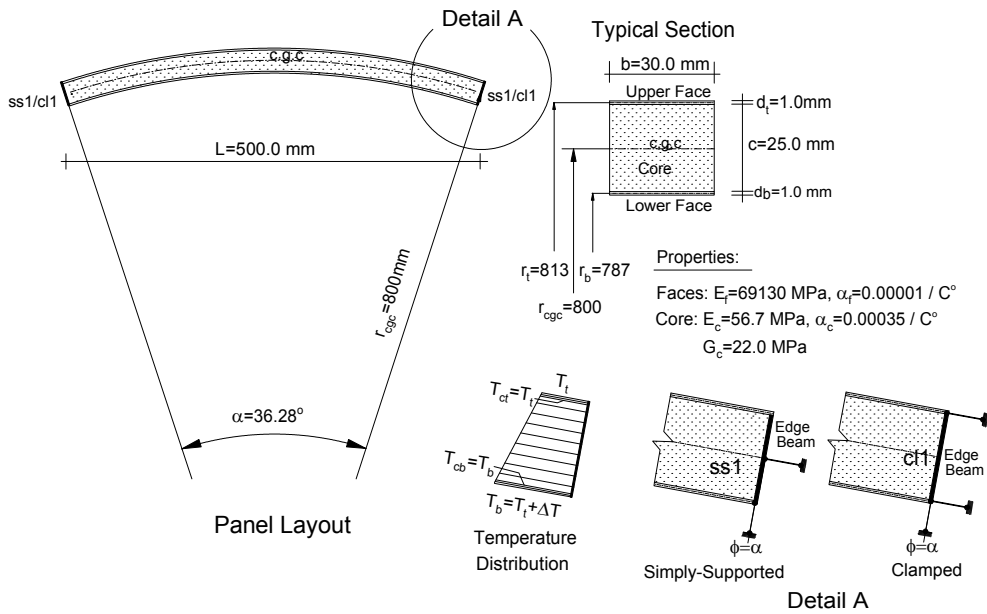


Figure 4. Geometry, dimensions, mechanical properties, temperature distribution and supporting systems of the shallow curved panel under investigation.

prevents circumferential displacement in addition to the other constraints. The simply supporting system is denoted by ss1 and the clamped one by cl1.

Under the assumption of TI core properties, the mechanical response of the curved sandwich panel subjected to a concentrated load at mid-span and a distributed load, and without the response induced by thermal loading, is described first. This is followed by a description of the thermal response without the mechanical loads, and a presentation of the case of simultaneous mechanical and thermal loading.

Finally the effects of the thermal degradation of the core properties with elevated temperature (TD setting) are studied first for thermal loading only, then for combined thermal and mechanical loading.

A symmetric analysis has been considered using symmetry conditions at mid-span.

5.1. Temperature-independent mechanical properties.

Mechanical loading only. The nonlinear mechanical response of a sandwich panel when subjected to a concentrated load that is applied at mid-span to the upper face sheet appears in Figures 5 and 6, with two types of supporting systems. The results include the deformed shape and equilibrium curves of load versus extreme values of selected structural quantities.

The deformed shapes of a simply supported curved sandwich panel appear in Figure 5, left, from which is it seen that prior to the limit point, indicated in Figure 6(a), the panel exhibits indentation at the upper face sheet, which becomes significant as the mid-span displacement increases. In the clamped case, shown in Figure 5, right, the same trends at mid-span as for the first supporting system are observed, while in the vicinity of the clamped support local buckling occurs for large mid-span displacements far beyond the limit point.

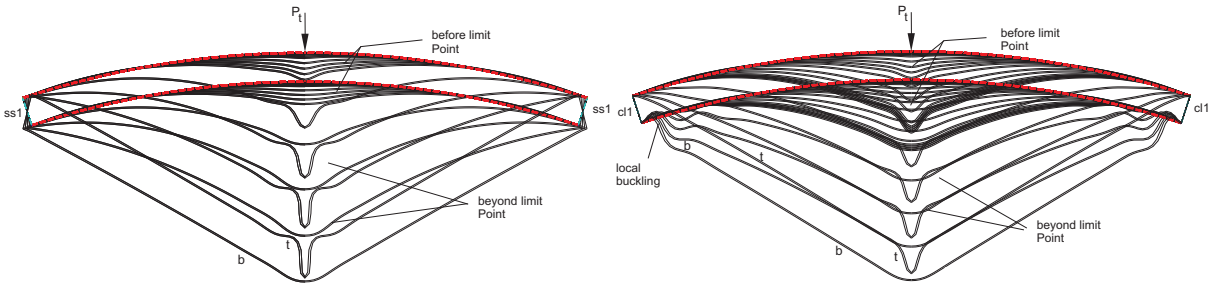


Figure 5. Deformed shapes of the curved panel when loaded by a *concentrated mechanical load* for the two supporting systems. Left: simply supported; right: clamped.

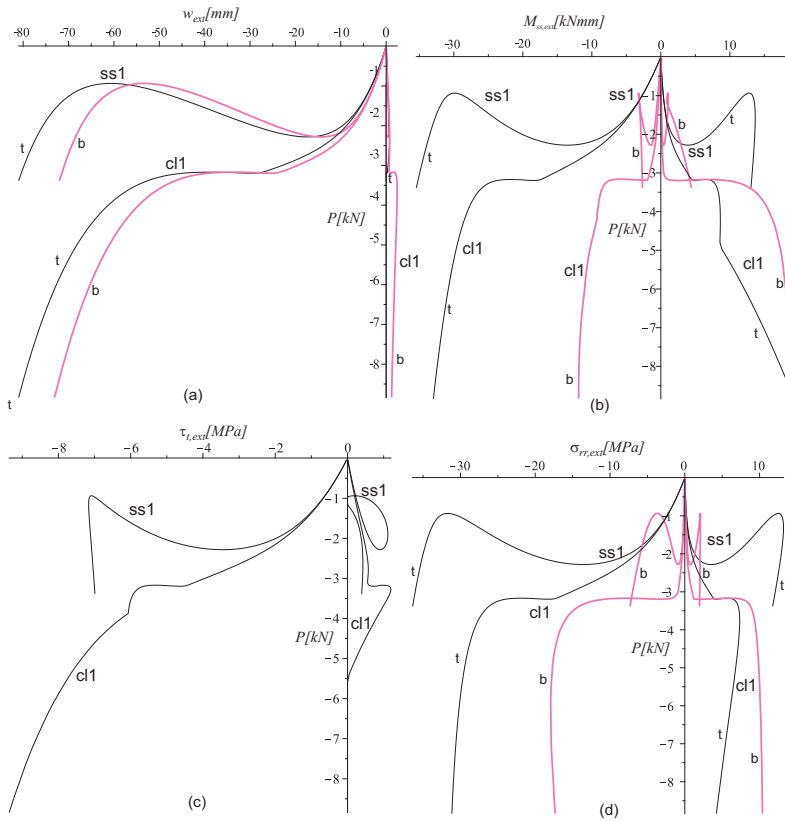


Figure 6. Equilibrium curves of load versus extreme values of (a) vertical displacements of face sheets, (b) bending moments in faces, (c) shear stress in core, and (d) interfacial radial normal stresses at face-core interfaces, all for curved sandwich panel subjected to *concentrated mechanical loading* at mid-span of upper face sheet. Thin black lines (marked t) refer to the upper face sheet; thicker pink lines (marked b) to the lower one.

The equilibrium curves of load versus extreme values of structural quantities of the two supporting systems appear in [Figure 6](#). In part (a) we see the load versus the extreme vertical displacement along the sandwich panel. It reveals that the nonlinear response is characterized by a limit point behavior for

both supporting systems. The limit point load for the simply supporting system is lower than that of the clamped case, and it occurs also at a lower displacement as compared with the clamped case. In the *ss* case there is a decrease in the vertical displacement beyond the limit point value which changes into an increasing branch as the displacement reaches larger values. The trends are different in the clamped case, and they consist of a plateau beyond the limit point displacement followed by an increasing branch. The trends are similar for the upper and lower faces. The plot of load versus extreme bending moments in the face sheets, shown in Figure 6(b), exhibits similar trends for the upper face sheet (thin black curves marked “t”) but quite erratic behavior for the lower one (thicker pink curves marked “b”). Notice that the curves describe the *extreme* values for each load level which do not necessarily occur at the same section. The interfacial shear stresses at the upper face-core interface appear on Figure 6(c), and they exhibit a limit point behavior but with a reduction in their values on the increasing branch for the simply supporting case and an increase for the clamped case. The interfacial radial normal stresses at the upper and lower face-core interfaces appear in Figure 6(d), which reveals trends similar to those observed for the vertical displacements.

The nonlinear mechanical response of the curved sandwich panel due to a fully distributed load exerted at the upper face sheet appears in Figure 7 and 8. The deformed shapes here reveal that at the limit point and beyond it a nonsinusoidal localized local buckling of the mid-span of the upper face sheet occurs. In the clamped case, there is an additional local buckling in the vicinity of the support at the lower face sheet similar to the case with the concentrated load.

The equilibrium curves for this loading scheme appears in Figure 8. The curves of distributed load versus extreme vertical displacement of the face sheets, shown in part (a), reveal a limit point behavior for both supporting systems, where the load at the limit point of the clamped case is a little bit larger than that of the simply supported case, and occurring at similar displacements values. In both cases a very steep descending branch is observed beyond the limit point. The bending moment curves, shown in part (b), exhibit similar trends but with very steep slopes of branches prior to and beyond the limit point. The plot versus upper interfacial shear stresses, in Figure 8(c), exhibits a limit point behavior similar to that of the vertical displacements. The interfacial normal stress curves follow the trends of the bending moments diagram with an abrupt change at the limit point. At the end of the descending branch of the simply supported case the interfacial shear and vertical normal stresses at the upper face-core interface decrease as the vertical displacements increase, as seen in parts (c) and (d) of the figure. Note also that the differences between the simply supporting and the clamped cases are minor.

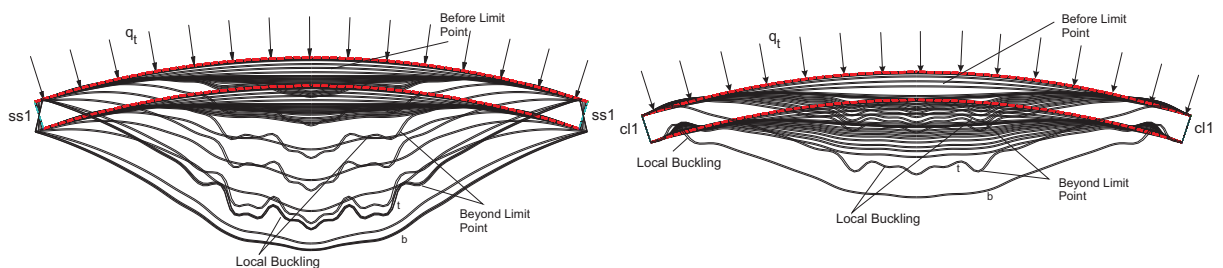


Figure 7. Deformed shapes of the curved panel when loaded by a fully *distributed mechanical load* for the two supporting systems. Left: simply supported; right: clamped.

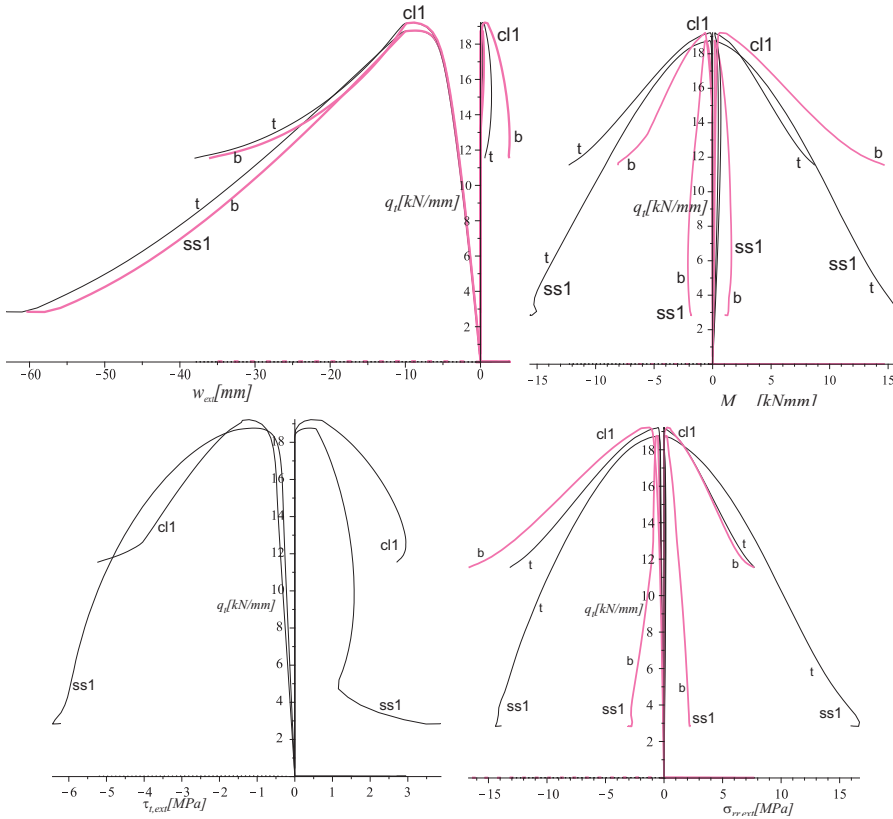


Figure 8. Equilibrium curves of load versus extreme values of (a) vertical displacements of face sheets, (b) bending moments in faces, (c) shear stress in core, and (d) interfacial radial normal stresses at face-core interfaces, all for curved sandwich panel subjected to a *distributed mechanical load* only, applied at the upper face sheet. Thin black lines (marked t) refer to the upper face sheet; thicker pink lines (marked b) to the lower one.

Thermal loading only. The thermal response of a curved sandwich panel subjected to a uniformly distributed temperature through its length and thickness is displayed in Figures 9 and 10. This response is linear throughout the range of temperatures investigated. The deformed shapes for temperatures from 0 to 200°C (heating) appear on the left in Figure 9, and those for temperatures from 0 to -200°C (cooling) on the right. In the case of heating, the two faces move upward around mid-span while in the vicinity of the supports the expansion of the core involves localized changes in the curvature of the two face sheets. By contrast, under cooling the two face sheets move downwards around mid-span while near the

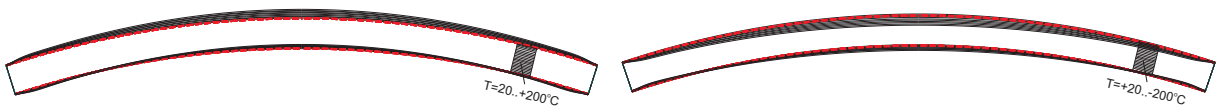


Figure 9. Deformed shapes of the curved sandwich panel subjected to *thermal loading* (left: heating; right: cooling) with no mechanical load.

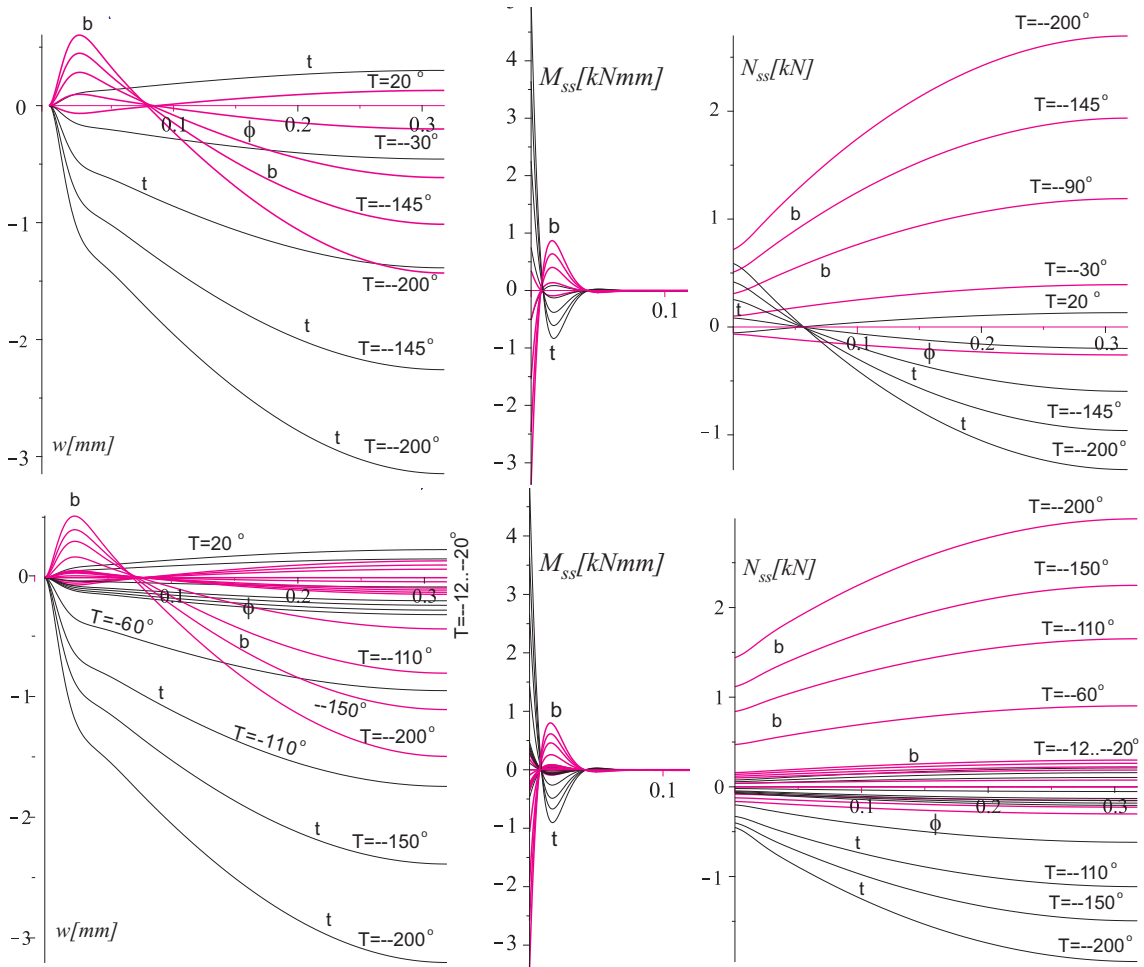


Figure 10. Cooling *thermal loading* results for face sheets along the panel circumference for simply supported (top) and clamped (bottom) systems. The horizontal coordinate is ϕ in all cases; all temperatures in degrees Celsius. Left column: vertical displacements. Middle column: bending moments. Right column: In-plane stress resultant (in core). Thinner black lines marked “t” stand for the upper face or interface; thicker, pink lines marked “b”, for the lower.

supports the core contracts, along with localized bending moments in the face sheets. Notice also that the pattern of displacements is in the opposite direction to that of the external loads (Figures 5 and 7) when heating is considered.

The vertical displacements, the bending moments and the circumferential stress resultants in the faces, along half of the sandwich panel, for the two supporting systems under a cooling temperature pattern appear in Figure 10. The displacement curves for the various temperatures (left column) and the bending moment diagrams (middle column) are almost the same for the two supporting systems. Notice that bending moments occur only in the vicinity of the supports, as a result of the contraction of the core that causes changes in the curvatures of the face sheets. The circumferential forces (normal stress resultants)

in the face sheets (rightmost column of Figure 10) reveal that in the case of a simply supported panel the stress resultants at the edges in the two face sheets are in tension, and around mid-span the upper face sheet is in compression whereas the lower face sheet is in tension. In the case of a clamped support the circumferential stress resultants differs from that of the simply supported case, and the resultants in the upper face sheets are in compression while those of the lower face are in tension. It should be noticed that in the case of elevated temperatures the displacements and the stress resultant patterns in the face sheets and the core are opposite to those observed for the cooling case, which yields that the upper face sheets is in tension while the lower one is in compression. Thus, the heating temperature pattern yields stress resultants that cancel out the stress resultants of the external mechanical loads that appear in Figures 5 and 7. The response is similar when the temperature distribution has a gradient between the two face sheets.

Thermomechanical loading. The thermomechanical response of the curved sandwich panel subjected to a concentrated load applied at mid-span of the upper face sheet along with a circumferentially uniform temperature with a gradient of 40°C between the upper and lower face sheet is considered next; see Figure 11. The study reveals that the combined response is linear when the applied mechanical loads are up to 80% of the load at the limit point. The thermomechanical response when elevated temperatures are considered exhibits a linear behavior since the thermal and mechanical responses act in opposite directions.

A nonlinear thermomechanical response is observed only when cooling temperatures are considered, and the external loads are in the range of 80–90% of the limit point load levels, as shown in Figures 12 and 13. The equilibrium curve of temperature versus the extreme vertical displacement of the face sheets appear in Figure 12a. It reveals that a limit point behavior is observed at about -150°C , when a simply supported panel is considered while in the case of a clamped panel the response is linear within the range of temperatures considered. Note that there is an initial displacement due to the existence of the external load prior to the application of the thermal loading. The bending moment diagrams, the upper interfacial shear stress and the interfacial normal stresses at the two face sheets (Figures 12b, 12c and 12d) exhibit similar trends. Note that the larger vertical normal stresses are in compression (Figure 12d).

The deformed shapes of the combined response for the two supporting systems at different temperature levels appear in Figure 11. The deformed shapes reveal a large indentation at mid-span for both supporting systems which deepens beyond the limit point (Figure 11, left) for the simply supported case and remain linear for the clamped case. Note that the deformed shapes corresponding to the limit point resemble those of the concentrated load only, shown in Figure 5.

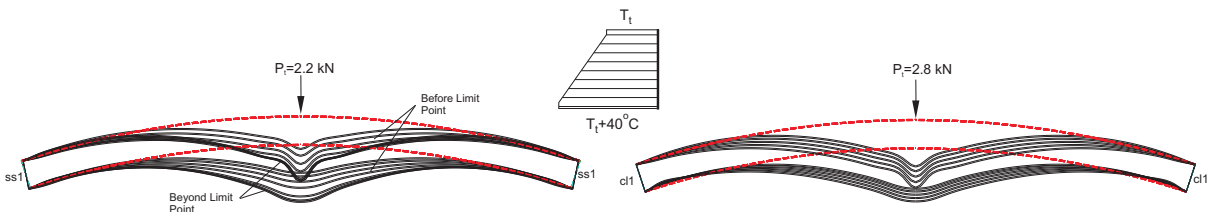


Figure 11. Deformed shapes of curved sandwich panel subjected simultaneously to a *concentrated mechanical load* and *thermal loading*. Left: simply supported; right: clamped.

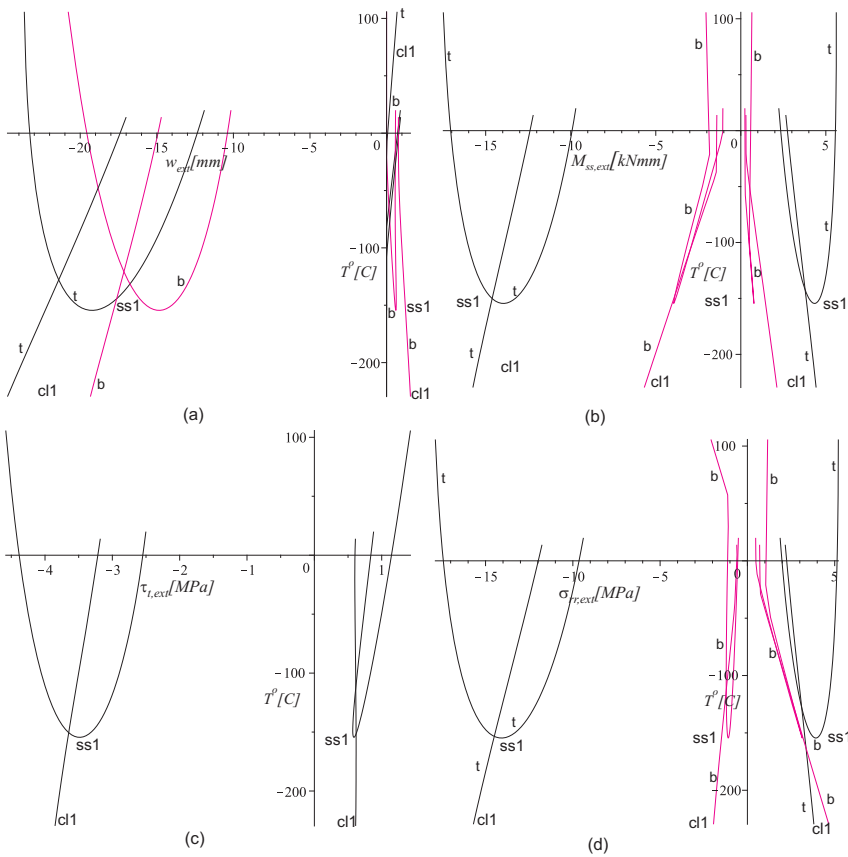


Figure 12. Equilibrium curves of load versus extreme values of (a) vertical displacements of faces sheets, (b) bending moments in faces, (c) shear stress in core, and (d) interfacial radial normal stresses at face-core interfaces, all for curved sandwich panel subjected to a *concentrated mechanical load* applied at mid-span of upper face sheet and *thermal loading* with a *temperature gradient* of 40°C at the lower face sheet. Thin black lines (marked t) refer to the upper face sheet; thicker pink lines (marked b) to the lower one.

The results along half the panel circumference of the combined thermomechanical response for a simply supported sandwich panel at different temperatures appear in Figure 13. The vertical displacements of the upper face sheets (Figure 13a) reveal a deepening indentation as the temperature level drops and the limit point is reached. It is observed that at temperatures above zero (before and beyond the limit point) the two face sheets move upwards in the vicinity of the support as a result of the core expansion, and the indentation disappears as the temperatures are lowered. Significant bending moments in the face sheets are observed in the vicinity of the external load and at the supports (Figure 13b). The magnitude increases as the temperatures are lowered and approach the limit point temperature level. The upper interfacial shear stress diagram reveals high values in the vicinity of the load and the support as well as shear stresses throughout the length of the panel (Figure 13c). The vertical interfacial stresses at both face sheets (Figure 13d), yield compressive as well as tensile stresses in the vicinity of the concentrated

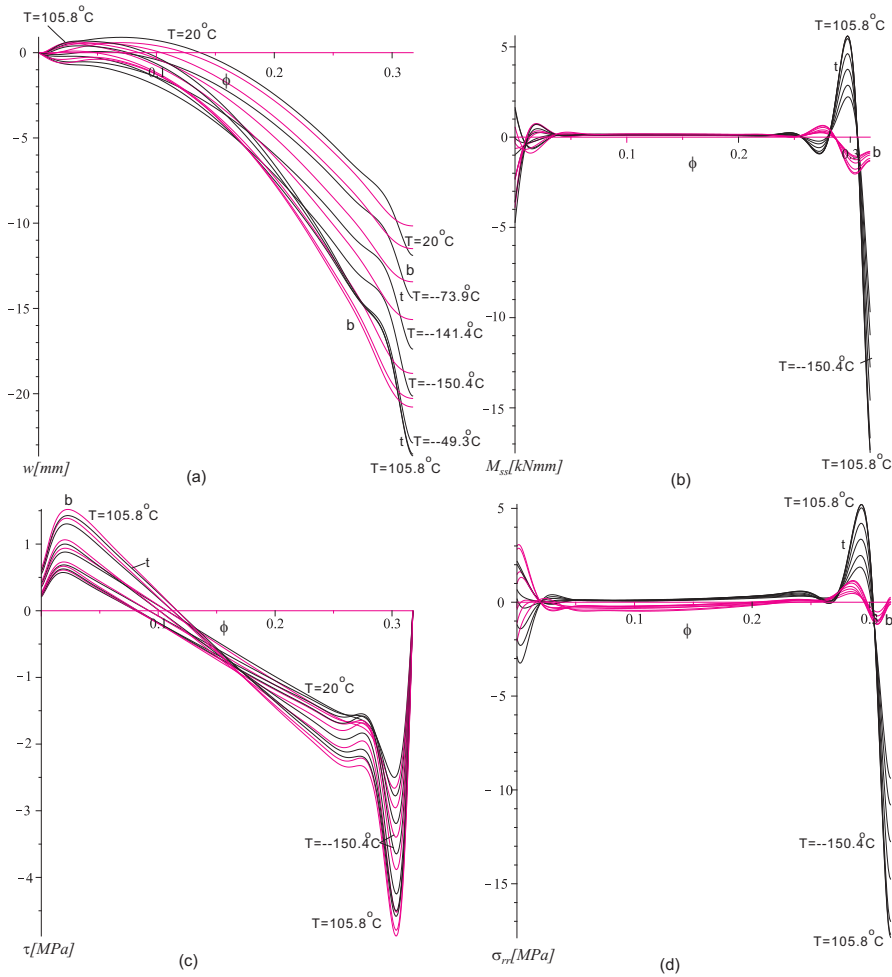


Figure 13. Thermomechanical response results for face sheets along the panel circumference for simply supported system when subjected to a *concentrated mechanical load* applied at mid-span of upper face sheet and *thermal loading* as in the previous figure. Shown are (a) vertical displacements, (b) bending moments, (c) shear stresses in face-core interfaces, and (d) radial normal stresses in same. Thinner black lines marked “t” stand for the upper face or interface; thicker, pink lines marked “b”, for the lower.

load that increase as the temperature approaches low levels. In addition, there is some accumulation of stresses in the vicinity of the support.

The combined thermomechanical response when a distributed load is applied at the upper face sheet and the temperature pattern is uniformly in the circumferential direction and with a gradient through the depth of the panel (Figure 14) is studied next. The combined response is linear as long as the distributed load is below 90% of the level corresponding to the limit point load as well as when the temperatures are above zero. The nonlinear response is presented in Figures 15 and 16 for a distributed load of a 1.7 kN/mm for the simply supported system and 1.741 kN/mm for the clamped case. For both supporting systems the distributed loads are applied at the upper face of the sandwich panel. Note that the applied

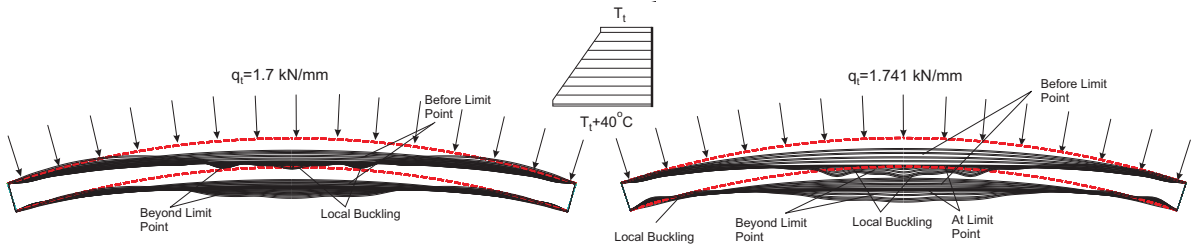


Figure 14. Deformed shapes of curved sandwich panel loaded simultaneously by a distributed load and thermal loading. Left: simply supported; right: clamped.

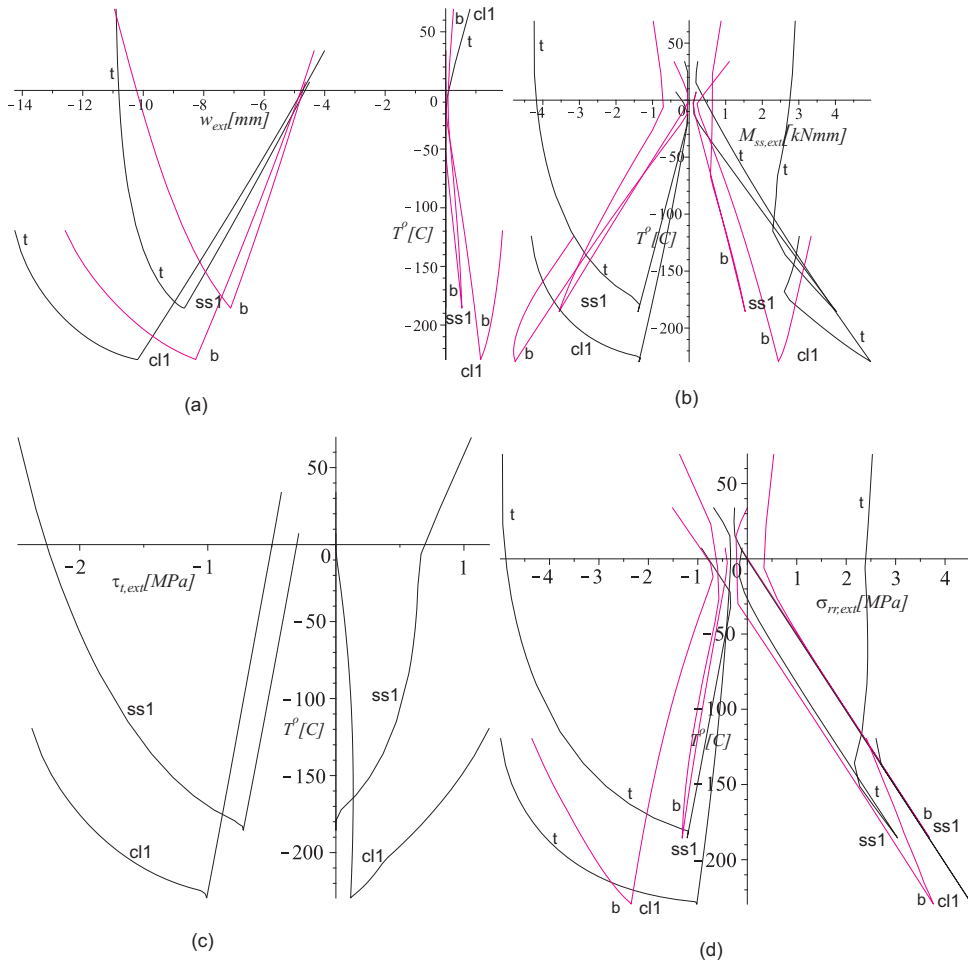


Figure 15. Equilibrium curves of load versus extreme values of (a) vertical displacements of faces sheets, (b) bending moments in faces, (c) shear stress in core, and (d) interfacial radial normal stresses at face-core interfaces, all for curved sandwich panel subjected to a *distributed mechanical load* to the upper face sheet and a *thermal loading* as in the previous figure. Thin black lines (marked t) refer to the upper face sheet; thicker pink lines (marked b) to the lower one.

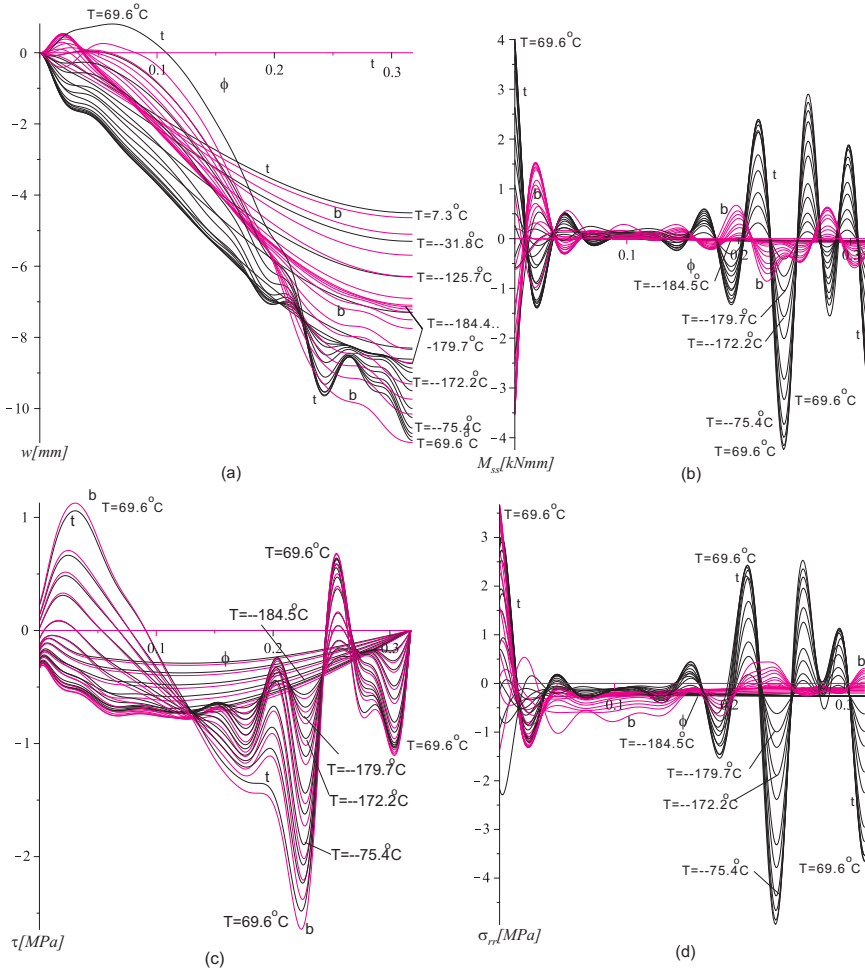


Figure 16. Thermomechanical response results for face sheets along the panel circumference for simply supported system when loaded by a *distributed mechanical load* on the upper face sheet and *thermal loading* as in the figures on the previous page. Shown are (a) vertical displacements, (b) bending moments, (c) shear stresses in face-core interfaces, and (d) radial normal stresses in same. Thinner black lines marked “t” stand for the upper face or interface; thicker, pink lines marked “b”, for the lower.

distributed loads represent 90.5% of the appropriate limit load level with no thermal loading; see [Figure 8](#). For details see [Figure 14](#).

The equilibrium curves of temperature versus extreme values of selected structural quantities reveal a limit point behavior for the two supporting systems with similar trends. The temperature versus the extreme vertical displacement of the face sheets (see [Figure 15a](#)) exhibits a limit point for both supporting systems. In the simply supported case the limit point occurs at -184.5°C , while in the clamped case the limit point is reached at a temperature of -229.47°C . In both cases the descending branches, prior to the limit point, are almost linear while the ascending branch, beyond the limit point, are nonlinear in general. The bending moment curves follow the same trends but with abrupt changes at the limit point

almost like that of a bifurcation behavior (Figure 15b). Note that the lower face sheet exhibits linear branches before and after the limit point, while the second branch, beyond the limit point descends. The upper interfacial shear stresses appear in Figure 15c and follow the trends of the bending moment curves. Similarly, the interfacial normal stresses exhibit a linear behavior prior to the limit point and a nonlinear one beyond that, following the trends of the bending moments.

The deformed shapes of the combined response for the two supporting systems appear in Figure 14. The two supporting systems exhibits a linear response up to the limit point and then they both yield a localized local buckling region around mid-span at temperatures in the vicinity of the limit point temperature level and beyond it. In addition local buckling of the lower face sheet occurs in the vicinity of the support in the case of a clamped panel. The characteristics of the deformed shape at the limit point and above resemble those found for the case of a distributed load and no thermal loading, shown in Figure 7.

The results along half of the panel circumference at different temperatures appear in Figure 16. The vertical displacements of the face sheets (Figure 16a) reveal that at the limit-point displacement local buckling waves appear which deepens on the ascending branch of the equilibrium curve (Figure 15a). This local buckling phenomenon is explicitly observed in the bending moment figure (Figure 16b) and the vertical normal interfacial stresses (Figure 16d). The local buckling affects also the interfacial shear stresses (Figure 16c). In general, the ripple characterization of the local buckling of the upper face sheet affects the response both globally and locally.

5.2. Temperature-dependent mechanical properties. This part of the investigation deals with the response of a curved sandwich panel subjected only to thermal loading, followed by a study of the same panel when subjected to combined thermal and mechanical loading. Both concentrated and distributed mechanical loads are considered, and again both simple support and clamped supporting systems are included in the study. The temperature-dependent core material properties adopted here follow those given by Burmann [2005a; 2005b] for cross-linked PVC Divinycell foams (from DIAB AB, Sweden) for a working range of temperatures between 20°C to 80°C.

The mechanical properties of the Divinycell foams degrade with increasing temperatures. For this study the temperature-dependent mechanical core material properties are defined through curve fitting of the data that appears in the manufacturer's data sheet [DIAB 2003] as follows:

$$E_c(\phi, r_c) = E_{co} f_T(T_c(\phi, r_c)), \quad G_c(\phi, r_c) = G_{co} f_T(T_c(\phi, r_c)),$$

where E_{co} and G_{co} refer to the Young's and shear moduli of the core at $T = 20^\circ\text{C}$, and

$$\begin{aligned} f_T(T) = & 1.1903 + 0.03070734934T - 0.009541812399T^2 + 0.0008705288588T^3 \\ & - 0.00003952259514T^4 + 9.70315767110^{-7}T^5 - 1.32513499810^{-8}T^6 \\ & + 9.52831997110^{-11}T^7 - 2.82196349610^{-13}T^8, \quad (35) \end{aligned}$$

where T is expressed in degrees Celsius. Note that when a thermal gradient is applied to the core the mechanical properties will also be dependent on the radial (through-the-thickness) coordinate. For more details see [Frostig and Thomsen 2008b]. In order to use the polynomial expansion (32) of the inverse of the moduli, the coefficients must be found using Taylor series or curve-fitting tools.

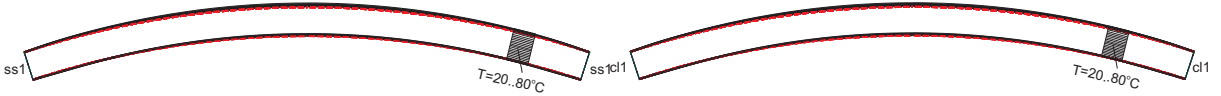


Figure 17. Deformed shapes of curved sandwich panel subjected to uniform *thermal loading* and with *temperature-dependent core properties*. Left: simply supported; right: clamped.

Thermal loading only. The deformed shapes of the curved sandwich panel subjected to thermal loading only appears in Figure 17, and the predicted response in Figures 18 and 19. Figure 17 shows that, for both supporting systems, the panel moves upward as the temperature is increased and the core properties degrade.

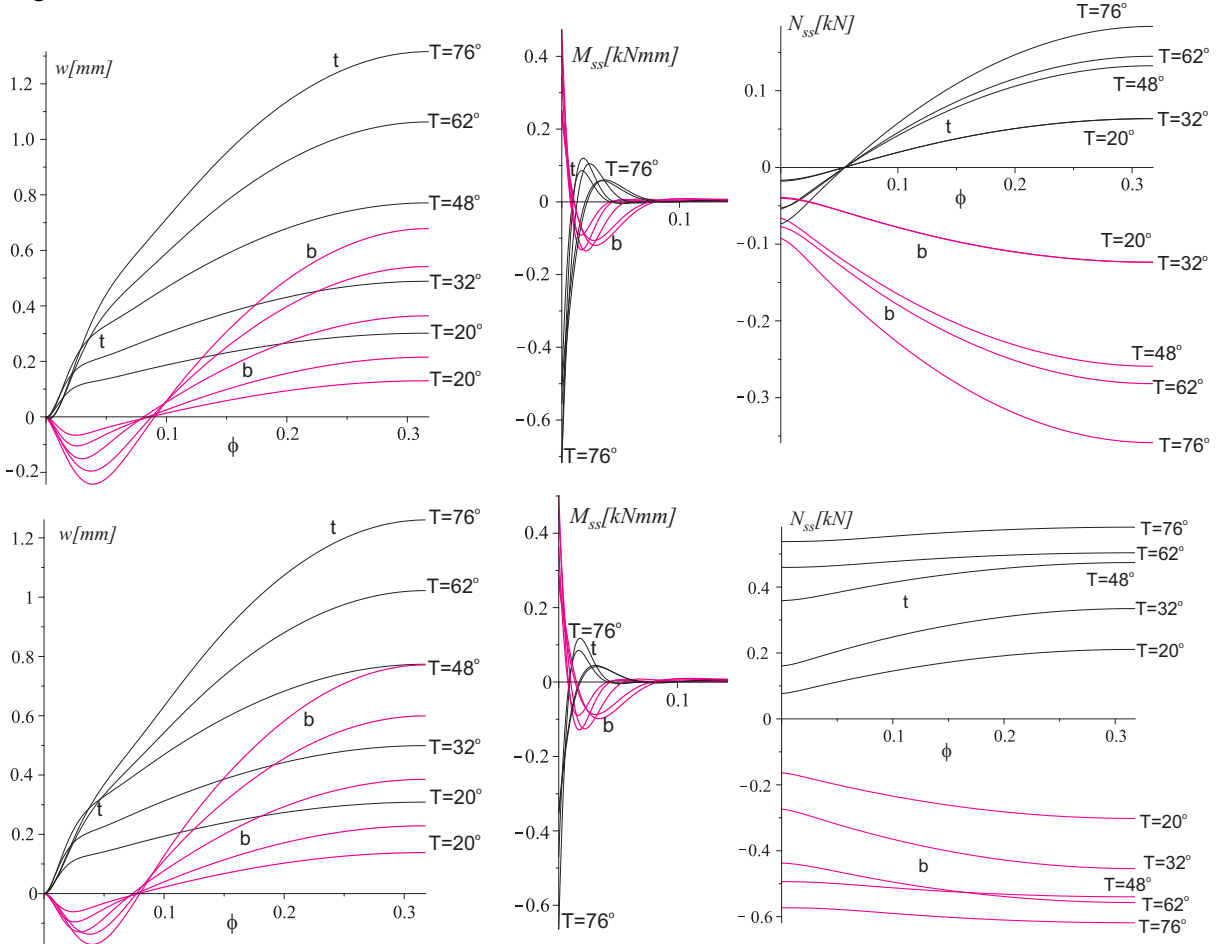


Figure 18. Uniform *thermal loading* results for face sheets along the panel circumference for simply supported (top) and clamped (bottom) systems with *temperature-dependent core properties*. The horizontal coordinate is ϕ ; temperatures in degrees Celsius. Left column: vertical displacements. Middle column: bending moments. Right column: In-plane stress resultant (in core). Thinner black lines marked “t” stand for the upper face or interface; thicker, pink lines marked “b”, for the lower.

The predictions for the face sheets along half of the panel circumference at different temperature levels for the two supporting systems appear in Figure 18. The vertical displacements (Figure 18a) and the bending moments (Figure 18b) of the two supporting systems are almost identical. Also here (see Figure 10 for comparison) the bending moments exist only in the vicinity of the support as a result of the existence of the edge beam. The in-plane stress resultants (Figure 18c) reveal different patterns for the two supporting systems. In the simply supported case the stress resultants of the two face sheets are in compression at near and at the support, and this changes into tension in the upper face sheet and compression in the bottom face sheet away from the supporting region. In the clamped case the upper face sheet is in tension while the lower face sheet is in compression throughout of the length/circumference of

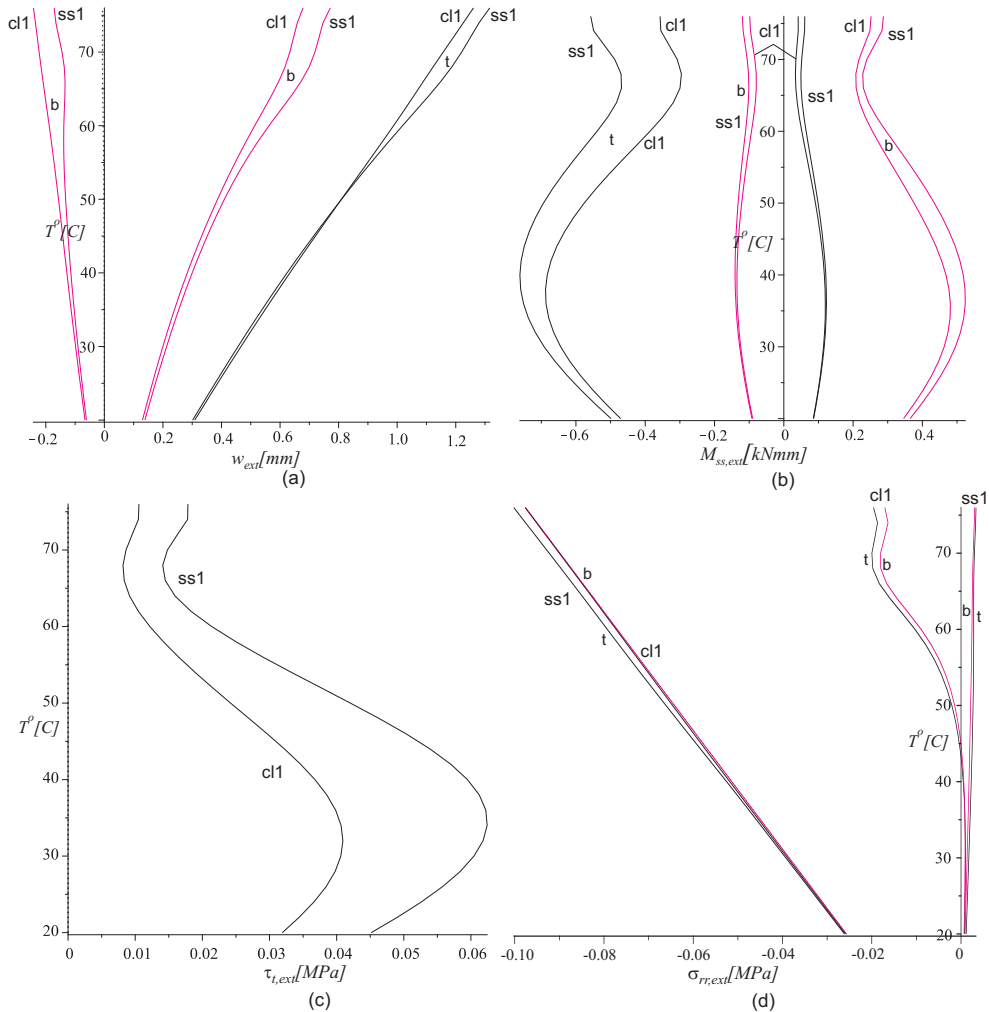


Figure 19. Equilibrium curves of load versus extreme values of (a) vertical displacements of faces sheets, (b) bending moments in faces, (c) shear stress in core, and (d) interfacial radial normal stresses at face-core interfaces, all for curved sandwich panel with *temperature-dependent core properties*, subjected to uniform *thermal loading*. Thin black lines refer to the upper face sheet; thicker pink lines to the lower one.

the panel. The results are very similar to the results obtained for the curved sandwich panel temperature-independent mechanical properties, shown in Figure 10, except for the opposite signs due to the cooling temperatures considered for this example.

The equilibrium curves of temperatures versus extreme values of selected structural quantities for the two supporting systems appear in Figure 19. They reveal a nonlinear behavior which is due to the nonlinearities in the mechanical properties as a result of their temperature dependence. In addition, there are only minor differences between the results of the two supporting systems. The vertical displacement curves (Figure 19a) are almost linear, but they become nonlinear at the upper range of temperatures. The bending moment results (Figure 19b) reveal a nonlinear response in both positive and negative bending moments. The interfacial shear stress results at the upper face core interface (Figure 19c) also reveal a nonlinear response through the range of temperatures. The interfacial radial normal stresses curves, at the upper and lower face core interfaces (Figure 19d) reveal a linear response for the simply supported case and a nonlinear for the clamped case. In both cases the maximum compressive stresses occur in the edge of the panel. However, for the simply supported case there are tensile stresses in the vicinity of the support that do not exist in the clamped system.

Thermomechanical loading. The combined thermal and mechanical loading response study outlines the behavior of the curved sandwich panel when subjected to a concentrated or distributed load below the limit point load levels (see Figures 6 and 8). Again two supporting systems are considered, and the imposed heating temperatures profile change from 20°C to 78°C with and without a gradient between the two face sheets.

We first consider the effects of the thermal degradation of core properties on the response of the simply supported uniformly heated panel with a concentrated load applied at mid-span. The concentrated load is taken as 2.1 kN, which is about 80% of the limit point load without thermal loading (see Figure 6).

The deformed shapes of the panel appear in Figure 20, which reveals an indentation that grows as the temperature is raised. Note here that the thermal loading causes upwards displacements (compare Figure 17), and that the combined thermal and mechanical response yields large indentations as a result of the degrading mechanical core properties.

The vertical displacements along half the circumference of the sandwich panel appear in Figure 21a, where it is observed that quite large values are obtained as the limit point temperature level is reached around $T = 27^\circ\text{C}$ (see Figure 22a). Due to the concentrated load the initial displacement is quite large. The bending moment diagrams (Figure 21b) follow the same trends as obtained when temperature-independent core properties are assumed (see Figure 13), namely, large bending stresses are accumulated in the vicinity of the supports and the load application point. The interfacial shear stresses at the upper

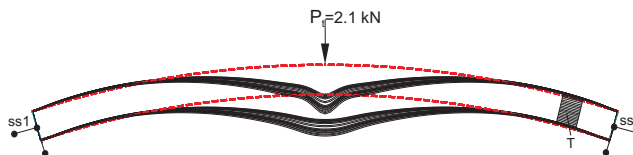


Figure 20. Deformed shapes of the simply supported curved panel subjected to a *concentrated mechanical load* and uniform *thermal loading*, assuming *temperature-dependent core properties*.

and lower face-core interfaces appear in Figure 21c and reveal an attenuation of stresses in the vicinity of the load and the support is observed. The interfacial normal stresses at the top and bottom face-core interfaces (Figure 21d) follow the same trends as found for the bending moments.

The equilibrium curves of temperature versus extreme structural quantities for three loads that lie below the limit point load level when no thermal loading is applied (see Figure 6) appear in Figure 22 for a simply supported curved sandwich panel. In all cases a limit point behavior is observed, and great numerical difficulties that prevent convergence of the solution are encountered.

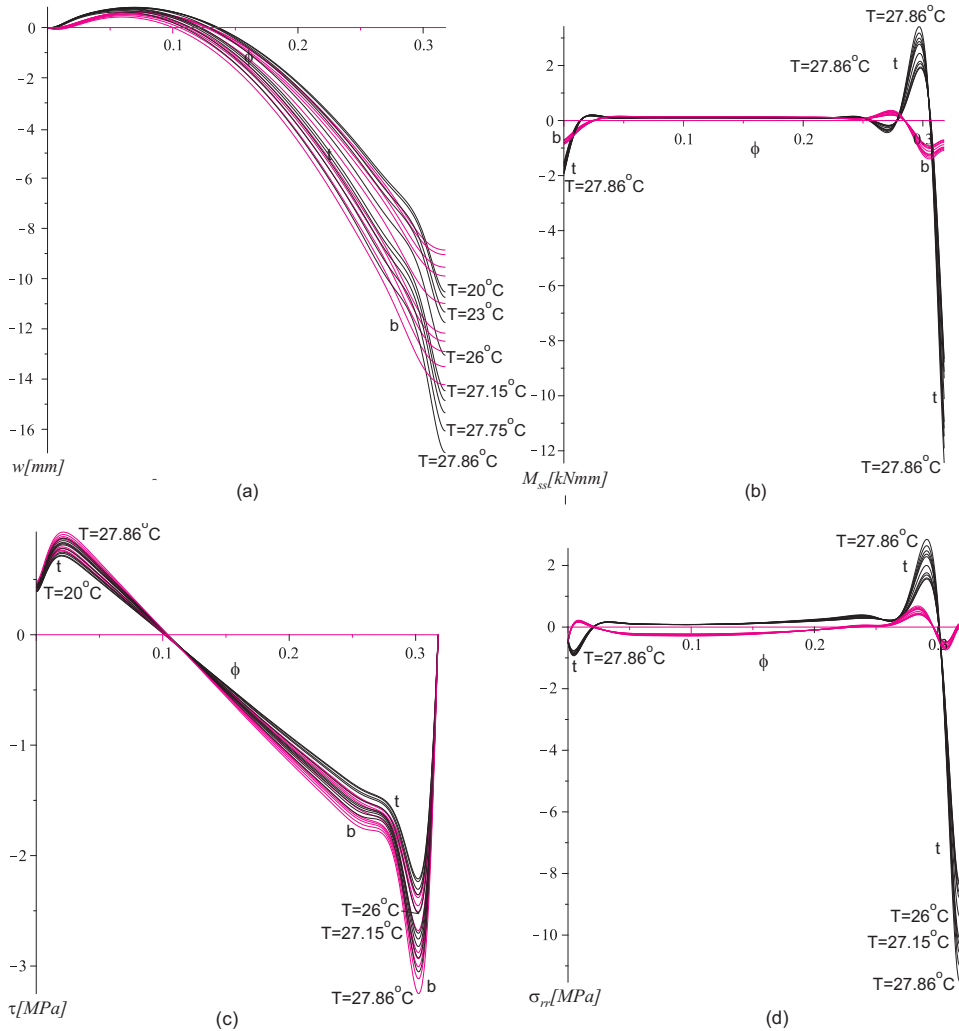


Figure 21. Thermomechanical response results for face sheets along the panel circumference for simply supported panel with *temperature-dependent core properties* when subjected to *concentrated mechanical loading* at mid-span of upper face sheet: (a) vertical displacements, (b) bending moments, (c) shear stresses in face-core interfaces, and (d) radial normal stresses in same. Thinner black lines marked “t” stand for the upper face or interface; thicker, pink lines marked “b”, for the lower.

The temperature versus the vertical displacements curves appear in Figure 22a and they reveal that for the low load level of $P_t = 1.1$ kN the temperature limit point occurs at a temperature of 45.4°C, while for the second load of $P_t = 1.6$ kN the temperature limit point occurs at 37.5°C, and at the higher load of 2.1 kN the critical temperature occurs at 27.86°C. At all load levels the temperature limit point is associated with a zero slope. The bending moment curves (Figure 22b) follow similar trends, but the slope is not zero at the temperature limit point levels. Similar trends are observed in the interfacial shear stresses at the upper face-core interface (Figure 22c) and the interfacial radial (through-the-thickness) normal stresses (Figure 22d).

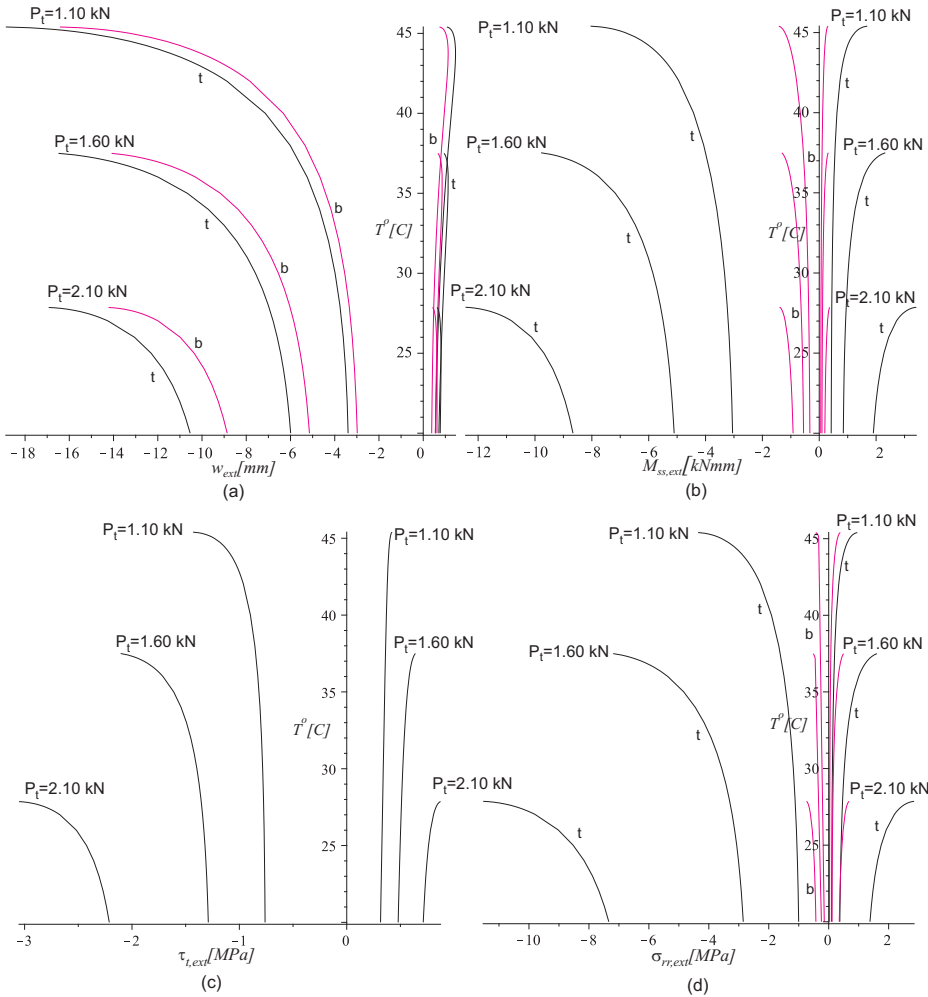


Figure 22. Equilibrium curves of load versus extreme values of (a) vertical displacements of faces sheets, (b) bending moments in faces, (c) shear stress in core, and (d) interfacial radial normal stresses at face-core interfaces, all for simply supported curved sandwich panel with *temperature-dependent core properties*, subjected to various *concentrated mechanical loads*. Thin black lines refer to the upper face sheet; thicker pink lines to the lower one.

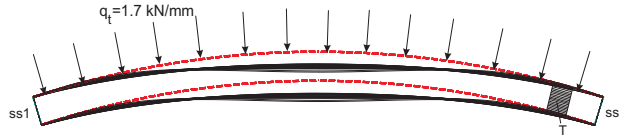


Figure 23. Deformed shapes of the simply supported curved panel when loaded by a fully *distributed mechanical load*, assuming *temperature-dependent core properties*.

The combined thermomechanical response of a simply supported curved sandwich panel with a 1.7 kN/mm distributed load, which is about 90% of the corresponding limit point load level (with no thermal loading), and thermal loadings, at different temperature levels is discussed next. The deformed shapes appear in [Figure 23](#), and reveal quite small deformations (in comparison with the case of a concentrated load) with smooth displacements patterns and no signs of local buckling as observed in the case of temperature-independent properties (see [Figure 7](#)).

The vertical displacements of the face sheets along half the circumference of the panel appear in [Figure 24a](#), where a significant growth of the displacements at the limit point temperature level of 27.72°C is observed. The bending moment diagrams reveal a ripple type patterns in the vicinity of the supports ([Figure 24b](#)). The interfacial shear stresses at the upper and lower face-core interfaces ([Figure 24c](#)) yield significant values in the vicinity of the edge as well at the quarter of the circumference/span. The trends of the interfacial radial normal stresses ([Figure 24d](#)) follow the same trends as those of the bending moments.

The effects of the magnitude of the distributed load level on the equilibrium curves of the combined thermomechanical response of a simply supported curved panel are described in [Figure 25](#). The temperature versus the extreme values of the vertical displacements of the face sheet curves for the different load levels appear in [Figure 25a](#). At all load levels a limit point behavior is detected, and the temperature at which the limit point is reached is lowered as the magnitude of the distributed load is increased. Also, here, the slope of the curves at the limit point approaches zero. Note here that up to the limit point temperature the displacements almost do not change with respect to the initial level (zero temperature), while in the near vicinity of the limit point temperature there is a significant change (increase) of the displacements. With respect to the bending moment curves for the face sheets ([Figure 25b](#)) and the curved of the interfacial radial normal stresses at the face-core interfaces ([Figure 25d](#)) there is a gradual change between the initial values (no thermal loading) and those at the limit point. With respect to the interfacial shear stresses at the upper face-core interface ([Figure 25c](#)) the values prior to the limit point reduce and they are significantly increased at the limit point temperature level.

The effects of a gradient in temperature between the upper and lower face sheets appear in [Figures 26](#) and [27](#), where the high temperature is at the lower face sheet. The combined thermomechanical response of the simply supported and clamped curved sandwich panels includes, in addition to the thermal loading, a concentrated and a distributed load.

The equilibrium curves of the combined thermomechanical response of a concentrated load that is applied at the mid-span of the upper face sheet appear in [Figure 26](#). The results include curves for temperature versus some extreme values of selected structural quantities for the two supporting systems and with a radial thermal gradient across the core thickness between zero to 40°C. The applied loads are 1.1 kN for the simply supported and 1.4 kN for the clamped panel. Both loads are far below the limit

load level with no thermal loading (see Figure 6). The vertical displacement curves of the face sheets appear in Figure 26, top. For the case of a simply supported sandwich panel the response is described by a limit point with almost zero slope at the limit point (Figure 26, top left), which represents an unstable behavior. However, for the clamped case (Figure 26, top right) the curves represent a stable behavior for the low gradients and less stable for the higher gradients (possibly converging towards unstable behavior for very large thermal gradients). The differences between the results of the two supporting systems are much more significant when studying the bending moments curves (see middle row in Figure 26).

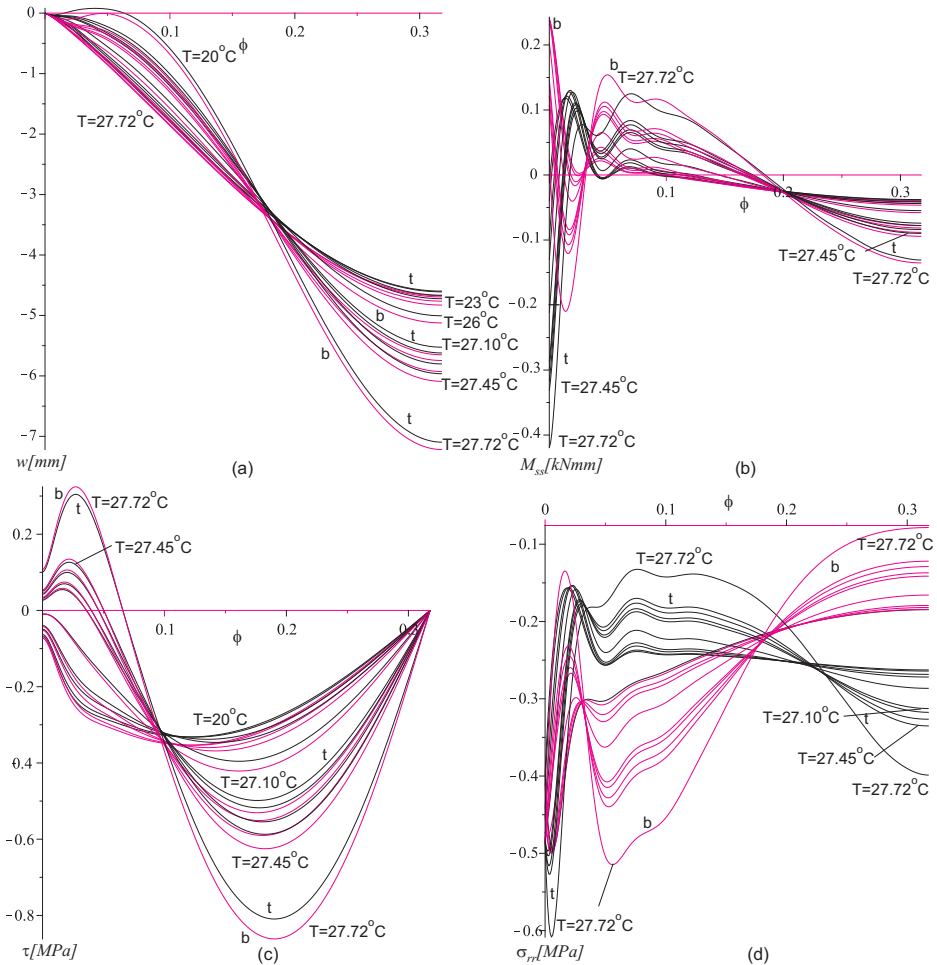


Figure 24. Thermomechanical response results for face sheets along the panel circumference for simply supported panel with *temperature-dependent core properties* when subjected to a fully *distributed mechanical load* applied on upper face sheet and uniform *temperature loading*. Temperatures are in degrees Celsius. Shown are (a) vertical displacements, (b) bending moments, (c) shear stresses in face-core interfaces, and (d) radial normal stresses in same. Thinner black lines marked “t” stand for the upper face or interface; thicker, pink lines marked “b”, for the lower.

The interfacial radial normal stresses (Figure 26, bottom) follow the same trends as those of the bending moments. It should be noticed that in all cases the clamped support conditions yields a more stable behavior as compared with the simply supported sandwich panel.

The combined thermomechanical response for the case of distributed mechanical loads with a thermal gradient between the lower and the upper face sheets appears in Figure 27. Here, the distributed load equals 1.7 kN/mm for the both supporting systems. The equilibrium curves reveal, in all figures, that the differences between the simply supported panel and clamped are minor. Moreover, the equilibrium curves show that responses are generally unstable for any value of the thermal gradient value. The

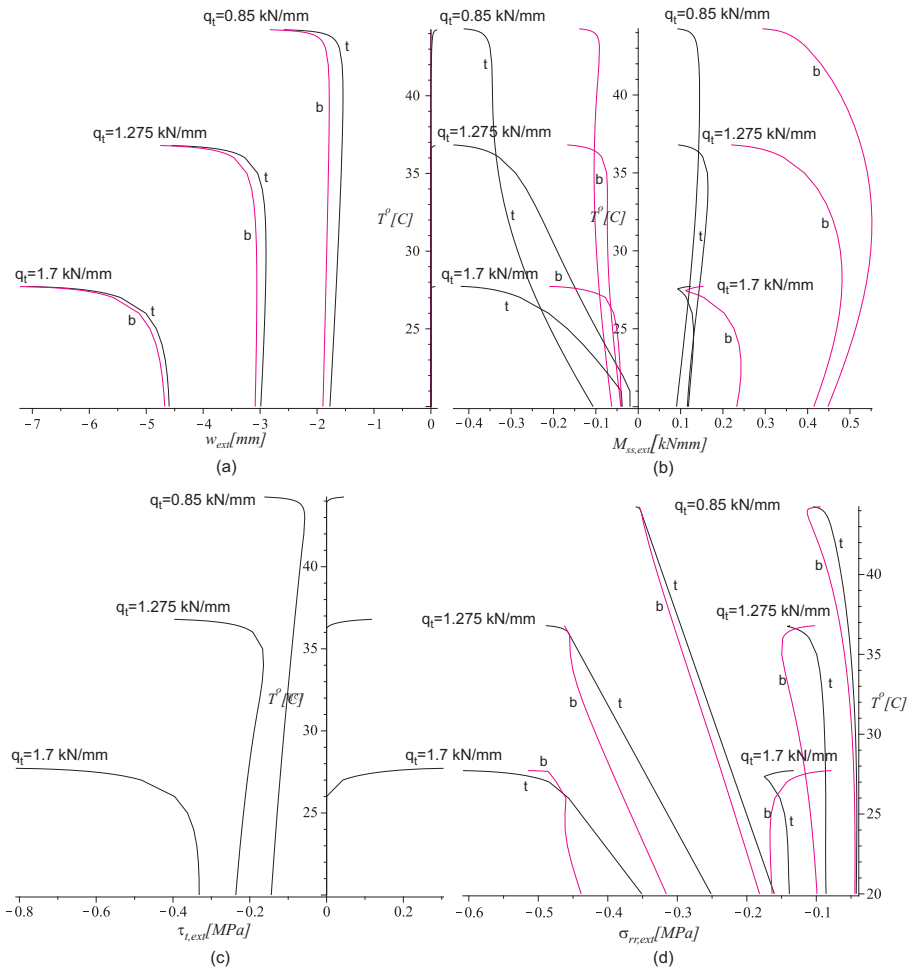


Figure 25. Equilibrium curves of load versus extreme values of (a) vertical displacements of faces sheets, (b) bending moments in faces, (c) shear stress in core, and (d) interfacial radial normal stresses at face-core interfaces, all for simply supported curved sandwich panel with *temperature-dependent core properties*, subjected to a *distributed mechanical load* applied at the upper face sheet and uniform *temperature loading*. Thin black lines refer to the upper face sheet; thicker pink lines to the lower one.

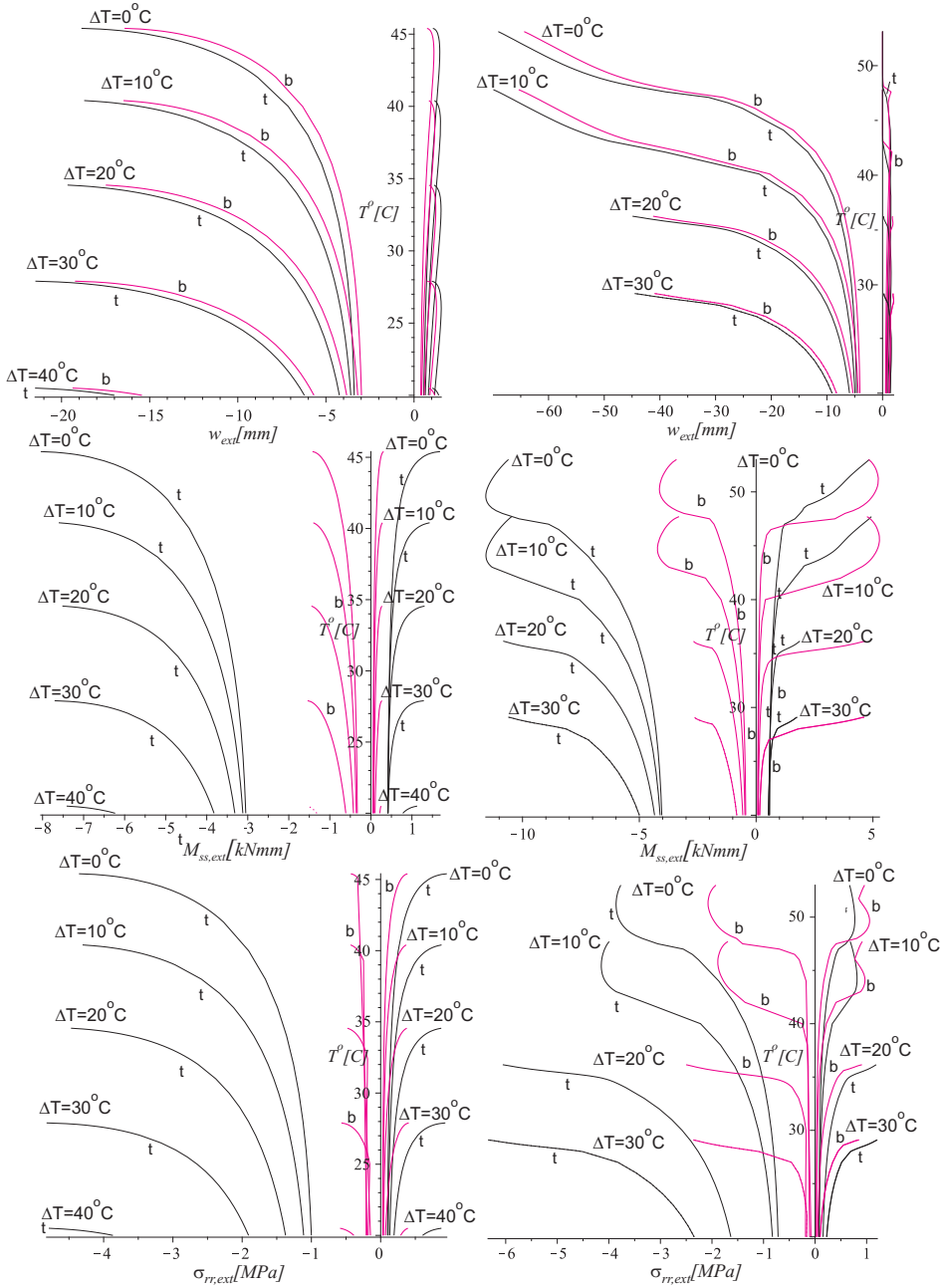


Figure 26. Equilibrium curves of load versus extreme values of vertical displacements of face sheets (top), bending moments in faces (middle), and interfacial radial normal stresses at face-core interfaces (bottom), all for simply supported (left, $P_a = 1.1$ kN) and clamped (right, $P_a = 1.4$ kN) curved sandwich panels with *temperature-dependent core properties*, subjected to a *concentrated mechanical load* P_a applied at mid-span of upper face sheet and *thermal loading* with different *through-the-thickness gradients*. Thin black lines refer to the upper face sheet; thicker pink lines to the lower one.

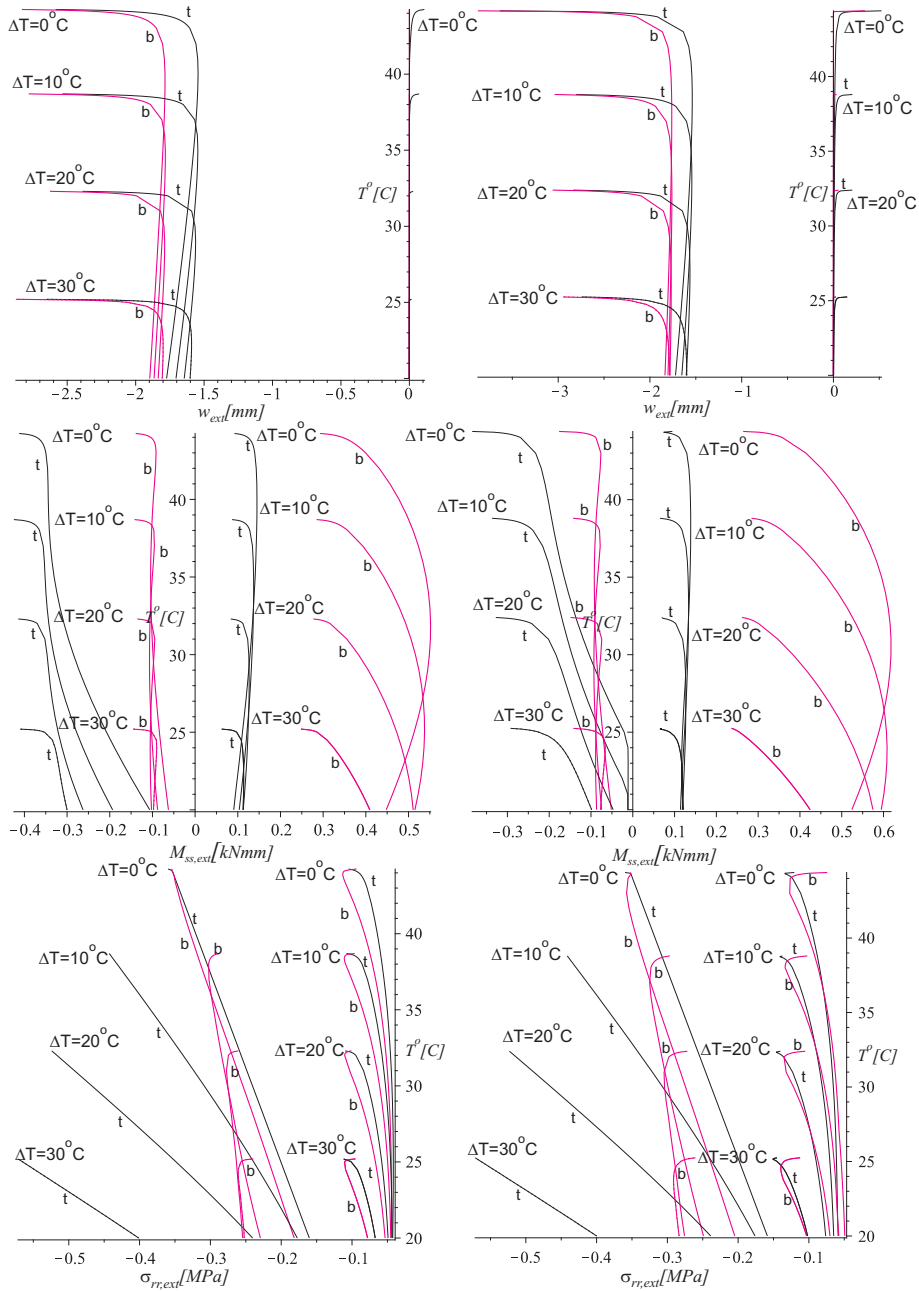


Figure 27. Equilibrium curves of load versus extreme values of vertical displacements of face sheets (top), bending moments in faces (middle), and interfacial radial normal stresses at face-core interfaces (bottom), all for simply supported (left) and clamped (right) curved sandwich panels with *temperature-dependent core properties*, subjected to a *distributed mechanical load* of 0.85 kN/mm applied to upper face sheet and *thermal loading* with different *through-the-thickness gradients*. Thin black lines refer to the upper face sheet; thicker pink lines to the lower one.

curves of extreme values of the vertical displacements of the face sheets versus temperature (Figure 27, top) yield a limit point behavior with a slope of almost zero for both supporting systems. Here it should be noticed that for both cases significant changes of the displacements occur only in the near vicinity of the limit point temperature level. The bending moment curves (Figure 27, middle row) reveal similar trends, with the exception that there is a gradual change between the initial values (corresponding to no thermal loading) and moment values at the limit point. Notice that the negative bending moments of the clamped case are smaller than those of the simply supported case and vice versa with respect to the positive bending moments. The relationship between the radial interfacial normal stresses and the temperature (Figure 27, bottom) is almost linear for the extreme values of the compressive stresses at the upper interface and nonlinear at the lower interface for both supporting systems.

6. Summary and conclusions

The geometrically nonlinear behavior of curved sandwich panels subjected to thermal and mechanical loading was studied, under both temperature-independent (TI) and temperature-dependent (TD) assumptions for the core material properties.

The first half of the paper gives a mathematical formulation for the TI case, based on a variational approach along with high-order sandwich panel theory (HSAPT). The analysis considers the thermal strains of the core along with the effects of its flexibility in the radial (through-the-thickness) direction. The nonlinear field equations of the curved sandwich panel are derived along with the appropriate boundary conditions. The effects of a solid edge beam at the edge of the curved sandwich panel on the boundary conditions are considered. The stress and displacement fields of the core are derived and solved explicitly for the case of a core with uniform mechanical properties. The full nonlinear governing equations are derived and presented.

The second half models thermally induced deformations of curved sandwich panels using the equations previously obtained via HSAPT. The stress and displacement fields of the core are derived and solved explicitly for cores with both TI and TD mechanical properties. The solution for a core with mechanical properties dependent on the radial coordinate is derived and is used to handle the TD case. A polynomial solution is adopted, and a general solution is presented for the stress and displacement fields. The nonlinear response is determined through the solution of the nonlinear equations using a finite-difference scheme along with a natural parametric continuation or a pseudo-arclength or similar procedure.

A numerical study then investigates the response of a shallow curved sandwich panel with a geometry that has been used previously in an experimental study conducted at Aalborg University. The shallow curved sandwich panel is assumed to be subjected to a concentrated or fully distributed load in addition to thermal loading. The panel consists of two aluminum face sheets and a cross-linked PVC H60 Divinacell foam core with mechanical properties that degrade with increasing temperature. The loading system consists of an edge beam at the edges of the curved sandwich panel, resting on a simply supported or clamped system with immovable conditions in the radial direction. The thermal loading consists of heating and cooling temperatures that are uniformly distributed circumferentially, with or without a gradient through the depth of the panel.

The numerical study covers all the combinations of the mechanical-thermal response with TI core properties. The response due to purely mechanical loading is presented first and reveals a typical limit

point behavior for both supporting systems and both types of loads. The study further reveals that under a concentrated load, there is an ascending branch beyond the limit point for the case of a simply supported system. For the case of a distributed load the nonlinear responses are almost identical for the two supporting systems, with insignificant differences in the limit-point load level. For this case local buckling of the upper face sheet is observed for both supporting systems, in addition to local buckling of the lower face sheet in the vicinity of the support when the sandwich panel is clamped at the edges.

Thermal loading with temperature-independent core properties reveals that the response is linear through the entire range from (subzero) cooling to (elevated) heating temperatures, with either uniform or gradient-type distributions through the depth of the sandwich panel. For case of heating the panel expands and changes its circumferential length rather than causing compression, as observed with flat panels. Hence, heating improves the performance of the loaded sandwich panel, since it cancels part of the induced deformations and stresses due to mechanical loading. In the case of cooling the panel contracts, yielding displacements and stress fields similar to those of the mechanical loads.

The thermomechanical response is determined for a mechanical load that is below the limit-point load level where the thermal loading changes from heating to cooling temperatures. For the case of heating, or loads below 85% of the mechanical limit point load, the response is linear for all loading cases and supporting systems. For loads in the range of 90% of the mechanical limit load, the thermomechanical response is nonlinear for the simply supported system for both types of loads. For the case of the clamped supporting system the concentrated load does not yield a limit point within the range of temperatures considered, while for the case of the distributed load a limit point is observed.

The combined response of a distributed load along with cooling temperatures yields a limit point response that is associated with local buckling ripples around mid-span of the upper face sheet and local buckling at the lower face at the support when it is clamped.

The characteristics of the combined response under TI mechanical properties of the core resemble those of the case with mechanical loads only when a limit point behavior is observed. Thus, the thermomechanical response for a curved sandwich panel subjected to both concentrated mechanical load and a thermal load yields similar characteristics to those of case when only a concentrated mechanical load is applied. Hence, the combined mode is actually a nonlinear combination of the mechanical and the thermal loads, and any combination of the two, in terms of magnitude, can yield a response that resembles that obtained for the case when only a mechanical load is applied.

The thermal loading case when the core properties are assumed to be TD follows the same trends as those encountered for the TI case. However, the equilibrium curves of temperature versus extreme values of selected structural quantities are generally nonlinear, due to the nonlinear change of the mechanical core properties with increasing temperature. The effect of the supporting system is minor.

The combined thermomechanical response with TD properties is quite different from that of the TI case and is associated with a limit point behavior at low temperature values. For the TI case only thermal loading in the form of cooling yields a nonlinear responses that are associated with limit point behavior. However, for the TD case the degradation of the core properties governs and yields nonlinear responses with unstable limit point behavior, even though the stress and displacement fields induced by the thermal loads act opposite to those induced by the mechanical loads.

The effects of the load level on the combined thermomechanical response have been investigated for loads below the limit point level for pure mechanical loading case. For the case of a concentrated load,

the response of a simply supported curved sandwich panel is associated with a limit point behavior which is unstable, while that obtained for the clamped case yields a stable behavior that resembles that of a plate sandwich panel structure. Generally, as the load is increased the limit point temperature reduces. For the case of a fully distributed load both the simply supported and the clamped sandwich panels yield unstable limit point responses with very similar limit point temperature values as a result of initiation of local buckling in the compressed face sheet.

For the case where the highest (heated) temperature is on the lower tensile face sheet an unstable limit point behavior of the simply supported panel is observed as the gradient increases, whereas a stable response is obtained for the clamped panel when a concentrated load is considered. For the case of a uniform distributed load an unstable limit point response is observed for both supporting systems with almost identical limit point temperature values. In all cases, an increase of the thermal gradient is associated with a reduction of the limit point temperature.

Acknowledgement

This work was conducted while Frostig was a visiting professor at the Institute of Mechanical Engineering at Aalborg University. The visiting professorship and the research presented herein were sponsored by the US Navy, Office of Naval Research (ONR), Award N000140710227 (“Influence of local effects in sandwich structures under general loading conditions and ballistic impact on advanced composite and sandwich structures”, program manager Dr. Yapa D. S. Rajapakse) and by the Ashtrom Engineering Company, which supports Frostig’s professorship chair at his home institution. The financial support received is gratefully acknowledged. Special thanks to Silvio Levy, the journal’s technical editor, for his accurate and superb work.

References

- [Ascher and Petzold 1998] U. M. Ascher and L. Petzold, *Computer methods for ordinary differential equations and differential-algebraic equations*, SIAM, Philadelphia, 1998.
- [Bozhevolnaya 1998] E. Bozhevolnaya, *A theoretical and experimental study of shallow sandwich panels*, Ph.D. thesis, Institute of Mechanical Engineering, Aalborg University, Aalborg, 1998. Supervisor: A. Kildegaard.
- [Bozhevolnaya and Frostig 1997] E. Bozhevolnaya and Y. Frostig, “Nonlinear closed-form high-order analysis of curved sandwich panels”, *Compos. Struct.* **38**:1–4 (1997), 383–394.
- [Bozhevolnaya and Frostig 2001] E. Bozhevolnaya and Y. Frostig, “Free vibrations of curved sandwich beams with a transversely flexible core”, *J. Sandw. Struct. Mater.* **3**:4 (2001), 311–342.
- [Brush and Almroth 1975] D. O. Brush and B. O. Almroth, *Buckling of bars, plates and shells*, McGraw-Hill, New York, 1975.
- [Burmam 2005a] M. Burmann, “Testing of compressive properties of Divinycell P and HP grades under elevated temperatures”, Department of Aeronautical and Vehicle Engineering, Royal Institute of Technology, 2005, Stockholm. Test Protocol, C2005-05.
- [Burmam 2005b] M. Burmann, “Testing of shear properties of Divinycell P and HP grades under elevated temperatures”, Department of Aeronautical and Vehicle Engineering, Royal Institute of Technology, 2005, Stockholm. Test Protocol, C2005-10.
- [DIAB 2003] DIAB, “Data sheets for Divinycell cross-linked PVC foams”, www.diabgroup.com, 2003.
- [Fernelund 2005] G. Fernelund, “Spring-in angled sandwich panels”, *Compos. Sci. Technol.* **65**:2 (2005), 317–323.
- [Frostig 1999] Y. Frostig, “Bending of curved sandwich panels with a transversely flexible core: closed-form high-order theory”, *J. Sandw. Struct. Mater.* **1**:1 (1999), 4–41.

- [Frostig and Thomsen 2007] Y. Frostig and O. T. Thomsen, “Buckling and nonlinear response of sandwich panels with a compliant core and temperature-dependent mechanical properties”, *J. Mech. Mater. Struct.* **2**:7 (2007), 1355–1380.
- [Frostig and Thomsen 2008a] Y. Frostig and O. T. Thomsen, “Thermal buckling and postbuckling of sandwich panels with a transversely flexible core”, *AIAA J.* **46**:8 (2008), 1976–1989.
- [Frostig and Thomsen 2008b] Y. Frostig and O. T. Thomsen, “Non-linear thermal response of sandwich panels with a flexible core and temperature dependent mechanical properties”, *Compos. B Eng.* **39**:1 (2008), 165–184.
- [Frostig et al. 1992] Y. Frostig, M. Baruch, O. Vilnay, and I. Sheinman, “High-order theory for sandwich-beam bending with transversely flexible core”, *J. Eng. Mech. (ASCE)* **118**:5 (1992), 1026–1043.
- [Hentinen and Hildebrand 1991] M. Hentinen and M. Hildebrand, “Nonlinear behavior of single-skin and sandwich hull panels”, pp. 1039–1063 in *FAST '91: First International Conference on Fast Sea Transportation* (Trondheim, 1991), vol. 2, edited by K. O. Holden et al., Tapir, Trondheim, 1991.
- [Hildebrand 1991] M. Hildebrand, *On the bending and transverse shearing behaviour of curved sandwich panels*, VTT Tiedoteita - Research Notes **1249**, Valtion Teknillinen Tutkimuskeskus, Espoo, 1991.
- [Kant and Kommineni 1992] T. Kant and J. R. Kommineni, “Geometrically non-linear analysis of doubly curved laminated and sandwich fibre reinforced composite shells with a higher order theory and C^0 finite elements”, *J. Reinf. Plast. Compos.* **11**:9 (1992), 1048–1076.
- [Karayadi 1998] E. Karayadi, *Collapse behavior of imperfect sandwich cylindrical shells*, Ph.D. thesis, Delft University of Technology, Faculty of Aerospace Engineering, Delft, 1998. Supervisor: A. Arbocz.
- [Keller 1992] H. B. Keller, *Numerical methods for two-point boundary value problems*, Dover, New York, 1992.
- [Ko 1999] W. L. Ko, “Open-mode debonding analysis of curved sandwich panels subjected to heating and cryogenic cooling on opposite faces”, NASA Technical Publication NASA/TP-1999-206580, Dryden Flight Research Center, Edwards, CA, June 1999, Available at <http://dtrs.dfrc.nasa.gov/archive/00000090>.
- [Kollár 1990] L. P. Kollár, “Buckling of generally anisotropic shallow sandwich shells”, *J. Reinf. Plast. Compos.* **9**:6 (1990), 549–568.
- [Kühhorn and Schoop 1992] A. Kühhorn and H. Schoop, “A nonlinear theory for sandwich shells including the wrinkling phenomenon”, *Arch. Appl. Mech.* **62**:6 (1992), 413–427.
- [Librescu and Hause 2000] L. Librescu and T. Hause, “Recent developments in the modeling and behavior of advanced sandwich constructions: a survey”, *Compos. Struct.* **48**:1–3 (2000), 1–17.
- [Librescu et al. 1994] L. Librescu, W. Lin, M. P. Nemeth, and J. H. Starnes, Jr., “Effects of tangential edge constraints on the postbuckling behavior of flat and curved panels subjected to thermal and mechanical loads”, pp. 55–71 in *Buckling and postbuckling of composite structures: proceedings of the 1994 International Mechanical Engineering Congress* (Chicago, 1994), edited by A. K. Noor, Aerospace Division **41**, ASME, New York, 1994. NASA-TM-111522.
- [Librescu et al. 2000] L. Librescu, M. P. Nemeth, J. H. Starnes, Jr., and W. Lin, “Nonlinear response of flat and curved panels subjected to thermomechanical loads”, *J. Therm. Stresses* **23**:6 (2000), 549–582.
- [Lo et al. 1977] K. H. Lo, R. M. Christensen, and E. M. Wu, “A high-order theory of plate deformation”, *J. Appl. Mech. (ASME)* **44** (1977), 669–676.
- [Noor and Burton 1990] A. K. Noor and W. S. Burton, “Assessment of computational models for multilayered anisotropic plates”, *Compos. Struct.* **14**:3 (1990), 233–265.
- [Noor et al. 1994] A. K. Noor, W. S. Burton, and J. M. Peters, “Hierarchical adaptive modeling of structural sandwiches and multilayered composite panels”, *Appl. Numer. Math.* **14**:1–3 (1994), 69–90.
- [Noor et al. 1996] A. K. Noor, W. S. Burton, and C. W. Bert, “Computational models for sandwich panels and shells”, *Appl. Mech. Rev. (ASME)* **49**:3 (1996), 155–199.
- [Noor et al. 1997] A. K. Noor, J. H. Starnes, Jr., and J. M. Peters, “Curved sandwich panels subjected to temperature gradient and mechanical loads”, *J. Aerosp. Eng. (ASCE)* **10**:4 (1997), 143–161.
- [Rao 1985] K. M. Rao, “Buckling analysis of FRP-faced anisotropic cylindrical sandwich panel”, *J. Eng. Mech. (ASCE)* **111**:4 (1985), 529–544.

- [Rao and Meyer-Piening 1986] K. M. Rao and H. R. Meyer-Piening, “Critical shear loading of curved sandwich panels faced with fiber-reinforced plastic”, *AIAA J.* **24**:9 (1986), 1531–1536.
- [Rao and Meyer-Piening 1990] K. M. Rao and H. R. Meyer-Piening, “Buckling analysis of FRP faced cylindrical sandwich panel under combined loading”, *Compos. Struct.* **14**:1 (1990), 15–34.
- [Reddy 1984a] J. N. Reddy, “A simple higher-order theory for laminated composite shells”, *J. Appl. Mech. (ASME)* **51**:4 (1984), 745–752.
- [Reddy 1984b] J. N. Reddy, “Exact solutions of moderately thick laminated shells”, *J. Eng. Mech. (ASCE)* **110**:5 (1984), 794–809.
- [di Sciua 1987] M. di Sciua, “An improved shear-deformation theory for moderately thick multilayered anisotropic shells and plates”, *J. Appl. Mech. (ASME)* **54**:3 (1987), 589–596.
- [di Sciua and Carrera 1990] M. di Sciua and E. Carrera, “Static buckling of moderately thick, anisotropic, laminated and sandwich cylindrical shell panels”, *AIAA J.* **28**:10 (1990), 1782–1793.
- [Simitses 1976] G. J. Simitses, *An introduction to the elastic stability of structures*, Prentice-Hall, Englewood Cliffs, NJ, 1976.
- [Smidt 1993] S. Smidt, “Curved sandwich beams and panels: theoretical and experimental studies”, Report 93-10, Royal Institute of Technology, Stockholm, 1993.
- [Smidt 1995] S. Smidt, “Bending of curved sandwich beams”, *Compos. Struct.* **33**:4 (1995), 211–225.
- [Stein 1986] M. Stein, “Nonlinear theory for plates and shells including the effects of transverse shearing”, *AIAA J.* **24**:9 (1986), 1537–1544.
- [Stoer and Bulirsch 1980] J. Stoer and R. Bulirsch, *Introduction to numerical analysis*, Springer, New York, 1980.
- [Thomsen and Vinson 2001] O. T. Thomsen and J. R. Vinson, “Analysis and parametric study of non-circular pressurized sandwich fuselage cross section using a high-order sandwich theory formulation”, *J. Sandw. Struct. Mater.* **3**:3 (2001), 220–250.
- [Tolf 1983] G. Tolf, “Stresses in a curved laminated beam”, *Fibre Sci. Technol.* **19**:4 (1983), 243–267.
- [Vaswani et al. 1988] J. Vaswani, N. T. Asnani, and B. C. Nakra, “Vibration and damping analysis of curved sandwich beams with a viscoelastic core”, *Compos. Struct.* **10**:3 (1988), 231–245.
- [Wang and Wang 1989] Y.-J. Wang and Z.-M. Wang, “Nonlinear stability analysis of a sandwich shallow cylindrical panel with orthotropic surfaces”, *Appl. Math. Mech.* **10**:12 (1989), 1119–1130.
- [Whitney and Pagano 1970] J. M. Whitney and N. J. Pagano, “Shear deformation in heterogeneous anisotropic plates”, *J. Appl. Mech. (ASME)* **37**:4 (1970), 1031–1036.

Received 31 Dec 2008. Revised 3 Jun 2009. Accepted 4 Jun 2009.

YEOSHUA FROSTIG: cvrffros@techunix.technion.ac.il

Professor, Ashtrom Engineering Company Chair in Civil Engineering

Technion - Israel Institute of Technology, Faculty of Civil and Environmental Engineering, Haifa, 32000, Israel

OLE THOMSEN: ott@me.aau.dk

Professor, Head of Department

Aalborg University, Department of Mechanical Engineering, Pontoppidanstræde 105, 9220 Aalborg Ø, Denmark

DETERMINATION OF OFFSHORE SPAR STOCHASTIC STRUCTURAL RESPONSE ACCOUNTING FOR NONLINEAR STIFFNESS AND RADIATION DAMPING EFFECTS

RUPAK GHOSH AND POL D. SPANOS

A study of the dynamic behavior of a combined dynamic system comprising a spar structure, a mooring line system, and top tensioned risers (TTR) by buoyancy can is presented. Not only the nonlinear restoring force of the mooring lines, the Coulomb friction at the compliant guides and the spar keel, and the hydrodynamic damping forces are considered, but also the effect of the frequency-dependent radiation damping is readily incorporated in this formulation. The dynamic model is subjected to input force and moment time histories that are compatible with a spectral representation (Jonswap spectrum) of a 100-year hurricane in the Gulf of Mexico. The response of the system is first determined by direct numerical integration of the equations of motion. In this regard, particular caution is exercised to treat properly the frequency-dependent terms which involve convolution transforms in the time domain. Next, a novel approach for determining the system responses is proposed. It is based on the technique of statistical linearization which can accommodate readily and efficiently the frequency-dependent elements of the dynamic system. This is achieved by appropriate modification of the system transfer function and by proper accounting for the system nonlinearities. The time domain analysis results are used to demonstrate the reliability of the statistical linearization solution. Further, the effect of the radiation damping, and the effect of the hydrodynamic forces are investigated.

A list of symbols can be found starting on page 1338.

1. Introduction

Proper concept selection for an oil/gas production facility from various options like spar, semisubmersible, and tension-leg platform (TLP) during the preliminary design phase of a project, is a daunting task since the particular choice affects the overall cost quite significantly. Among the various concepts, the spar structure is often chosen as a deep-water solution, particularly in the Gulf of Mexico. The spar appeal in the Gulf of Mexico is primarily due to its favorable motion performance under hurricane loads. The advantages of a spar structure are also manifested in the use of the dry tree riser systems and the speedy process of its delivery. Operational advantages notwithstanding, the dynamic behavior of a spar structure is a quite complex problem as it has been established by several diverse studies [Agarwal and Jain 2003a; 2003b; Fischer et al. 2004; Koo et al. 2004a; 2004b; Liang et al. 2004; Tao et al. 2004; Low and Langley 2006]. An optimized spar design requires several dynamic analyses [Ran et al. 1996; 1997; 1999] involving a sufficient number of simulations of the expected load cases. These load cases reflect various environmental conditions and operational/functional criteria. In this context, it is also noted that

Keywords: spar offshore structure, sea wave spectrum, nonlinear dynamic analysis, radiation damping, statistical linearization.

the ordinary time domain approach for the analysis of a coupled spar/risers/mooring lines system cannot incorporate conveniently a number of factors in the overall dynamic behavior.

Recognizing these limitations of the time domain analysis in capturing the system response statistics, Spanos et al. [2005] have suggested a computationally efficient approach for obtaining the spar responses based on a frequency domain representation. In this approach, the nonlinearities of a coupled system consisting of spar, top tensioned risers, and mooring lines are treated by using the concept of statistical linearization. Note that the statistical linearization method has already been established as a versatile tool for dynamic analysis of a nonlinear system via an auxiliary linear system, and is discussed in standard references such as [Spanos 1981a; 1981b; Roberts and Spanos 2001]. Further, based on this linearization concept, the studies by Spanos et al. have reported a reasonable agreement between the linearized responses and the nonlinear responses of an associated five-degree-of-freedom (5-DOF) dynamic model. However, these studies did not include the interaction of the hydrodynamic forces in the surge and pitch directions, and the effect of frequency-dependent damping terms. In this paper, the aforementioned linearization approach is extended to account for the interaction of the quadratic damping terms in the surge and pitch directions, and the effect of the frequency-dependent damping terms in the dynamic behavior. The theoretical developments are supplemented by appropriate numerical studies pertaining to a particular spar structure (Figure 1).

2. Spar model

The model considered here is a simplified 5-DOF coupled spar model (Figure 2) representing a truss spar (Figure 1) including fifteen top tensioned risers (TTR), and fifteen mooring lines. The spar consists of a cylindrical hard tank, of three heave plates, and of a soft tank at the bottom. The buoyancy can and stem are in contact with the spar at several preloaded guides in the center well, the heave plates, and the

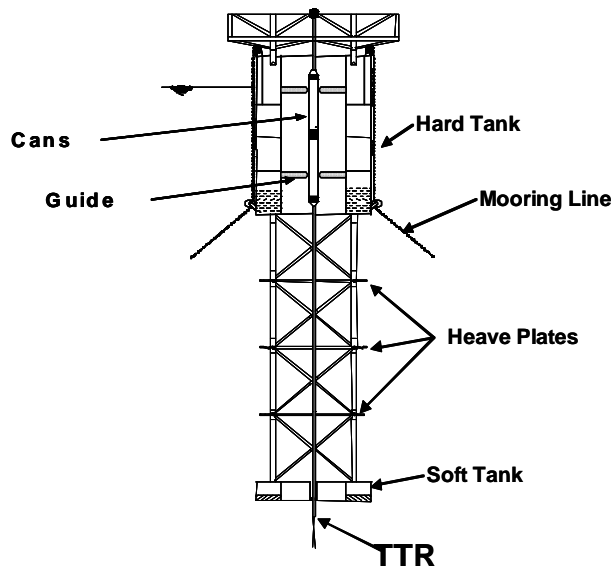


Figure 1. Typical truss spar.

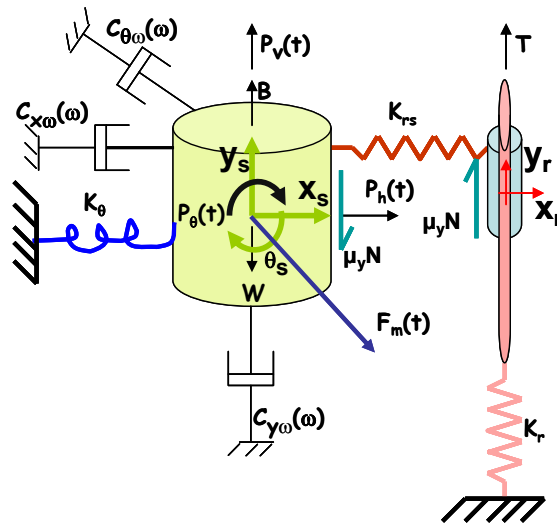


Figure 2. Simplified coupled 5-DOF model.

keel. The reliability of the aforementioned simplified model in capturing the predominant features of the system dynamic behavior has been previously established by comparing its responses to specific loads to those of a full-scale detailed model [Spanos et al. 2003].

Besides the three degrees of freedom in the surge, heave and pitch directions, the riser kinematics in the surge and heave directions is also represented in the coupled model (Figure 2). In the surge direction, the mass of the spar lumped at the center of the gravity is connected to the center of gravity of the buoyancy cans/risers by a linear spring which represents a simplified account of the contact stiffness of the lateral guide. In the vertical direction, the Coulomb friction/traction force acts at the interface of the spar guide and of the buoyancy can, When sliding occurs this force depends on the relative velocity of the spar and of the buoyancy can/riser as shown in (1) and (2). Specifically, for the magnitude

$$F_f = \mu_y N, \tag{1}$$

where “N” is the force normal to the interface, and the coefficient of friction (μ_y) is represented by the equation

$$\mu_y = \mu \operatorname{sgn}(\dot{y}_s - \dot{y}_r); \tag{2}$$

the symbols \dot{y}_s and \dot{y}_r denote the velocities in the vertical direction of the spar and of the risers/buoyancy can, respectively determining the direction of friction when sliding occurs.

The equation of motion in the surge direction (Figure 2) including both the frequency-dependent and hydrodynamic dampings is expressed by

$$M_x^s \ddot{x}_s + M_{x\theta}^s \ddot{\theta}_s + C_{sx} |\dot{x}_s + \alpha \dot{\theta}_s| (\dot{x}_s + \alpha \dot{\theta}_s) + F_{mx}(t) + K_{x\theta} \theta_s + K_{rs} (x_s - x_r) + \int_0^t C_{rx}(\tau) \dot{x}_s(t - \tau) d\tau = P_h(t), \tag{3}$$

where the horizontal component of the mooring lines restoring force $F_m(t)$ is given by the equation

$$F_{mx}(t) = \alpha_1 (x_s)^3 + \alpha_2 (x_s)^2 + \alpha_3 x_s + \beta_1 y_s + C_1. \tag{4}$$

In (3), M_x^s is the mass of the spar, including the added mass in the surge direction; the symbol $K_{x\theta}$ denotes the force in the horizontal direction for unit pitch, and K_{rs} is the linear contact spring between the spar and the buoyancy can; the symbol $C_{s,x}$ is the quadratic damping coefficient; the symbols x_s , x_r and θ_s denote the spar displacement in the surge direction, the riser/buoyancy can displacement in the surge direction and the spar pitch, respectively; α introduces a factor to account for the hydrodynamic force in the horizontal direction due to the pitch motion of spar; the symbol $P_h(t)$ denotes the excitation in the surge direction; the coefficients α_1 , α_2 , α_3 , β_1 and the constant C_1 in the polynomial in (4) have been derived by a regression analysis of the load displacement industrial data for a mooring line. Further, the coefficient C_{rx} is represented using the cosine transform of the frequency-dependent radiation damping function $\lambda_{rx}(\omega)$. That is,

$$C_{rx}(\tau) = \frac{2}{\pi} \int_0^\infty \lambda_{rx}(\omega) \cos \omega\tau d\omega, \tag{5}$$

Similarly, the heave motion of the spar (Figure 2) is governed by the equation

$$M_y^s \ddot{y}_s + F_{my}(t) + K_h y_s + \mu_y N + C_{sy} |\dot{y}_s| \dot{y}_s + W - B + \int_0^t C_{ry}(\tau) \dot{y}_s(t - \tau) d\tau = P_v(t), \tag{6}$$

where the restoring force from the mooring lines in the vertical direction is given by the equation

$$F_{my}(t) = \alpha_4 (x_s)^3 + \alpha_5 (x_s)^2 + \alpha_6 x_s + \beta_2 y_s + C_2, \tag{7}$$

with the symbol M_y^s denoting the mass of the spar including the added mass in the vertical direction. Further, K_h is the hydrodynamic stiffness of the spar in the vertical direction. The symbols W and B denote the weight and buoyancy terms of the spar. The term C_{sy} is the quadratic damping coefficient. As mentioned before the symbol N stands for the total contact preload, y_s is the heave displacement of the spar, and $P_v(t)$ is the excitation in the heave direction. The symbols α_4 , α_5 , α_6 , and β_2 are the coefficients in the polynomial (7) and C_2 is a constant. The damping coefficient C_{ry} is represented using the cosine transform of the frequency-dependent radiation damping function $\lambda_{ry}(\omega)$. That is,

$$C_{ry}(\tau) = \frac{2}{\pi} \int_0^\infty \lambda_{ry}(\omega) \cos \omega\tau d\omega. \tag{8}$$

The pitch motion of the spar (Figure 2) is governed by the equation

$$J_\theta \ddot{\theta}_s + M_{x\theta}^s \ddot{x}_s + (T \overline{GB} + K_\theta) \theta_s + K_{x\theta} x_s + C_{s\theta} |\beta \dot{x}_s + \dot{\theta}_s| (\beta \dot{x}_s + \dot{\theta}_s) + \int_0^t C_{r\theta}(\tau) \dot{\theta}_s(t - \tau) d\tau = P_\theta(t), \tag{9}$$

where J_θ is the mass moment of inertia term, and K_θ is the rotational hydrodynamic stiffness. The symbol T denotes the total top tension accounting for all the risers, and \overline{GB} is the distance between the center of buoyancy and the center of gravity of the spar structure. The symbol θ_s denotes the pitch of the spar, and $P_\theta(t)$ represents the excitation in the pitch direction. The symbol $C_{s\theta}$ is the quadratic damping coefficient. The damping coefficient $C_{r\theta}(\tau)$ is represented by the cosine form of the frequency-dependent radiation damping function $\lambda_{r\theta}(\omega)$. That is,

$$C_{r\theta}(\tau) = \frac{2}{\pi} \int_0^\infty \lambda_{r\theta}(\omega) \cos \omega\tau d\omega. \tag{10}$$

The equations of motion for the buoyancy can including the risers in the surge and heave directions (Figure 2) are

$$M_x^r \ddot{x}_r + K_{rx} x_r - K_{rs}(x_s - x_r) + \zeta_x^r 2\sqrt{K_{rx} M_x^r} \dot{x}_r = 0, \tag{11}$$

and

$$M_y^r \ddot{y}_r + K_{ry} y_r + \zeta_y^r 2\sqrt{K_{ry} M_y^r} \dot{y}_r - \mu_y N = T. \tag{12}$$

In (11) and (12), M_x^r and M_y^r are the effective mass of the risers including the buoyancy can in the horizontal and vertical directions, respectively. The symbols ζ_x^r and ζ_y^r denote the damping ratios for the risers/buoyancy can in the horizontal and the vertical directions, respectively; they are set equal to 0.05; The terms K_{rx} , and K_{ry} are the horizontal and vertical components of the riser stiffness K_r , respectively. The symbols x_r and y_r are the riser displacements in the surge and heave directions, respectively.

Note that the preceding equations of motion involve nonlinear terms, and terms represented via integral transforms. Therefore, the solution of these equations can only be obtained numerically. In this context, a standard algorithm of integrating ordinary differential equation numerically will be required. Further, the convolution integrals in equations (3), (6) and (9) must be treated by a numerical scheme.

3. Equivalent system

Alternatively to the aforementioned approach of direct numerical simulation of the equations of motion, the responses of the system can be determined by resorting to the concept of statistical linearization and pursuing a frequency domain approach.

Specifically, following [Roberts and Spanos 2001], the equivalent linear system is derived from equations (3)–(12) by replacing the nonlinear terms with equivalent linear terms. In matrix form, the equation of motion of this system can be cast in the form

$$\begin{bmatrix} M_x^s & 0 & M_{x\theta}^s & 0 & 0 \\ 0 & M_y^s & 0 & 0 & 0 \\ M_{x\theta}^s & 0 & J_\theta & 0 & 0 \\ 0 & 0 & 0 & M_x^r & 0 \\ 0 & 0 & 0 & 0 & M_y^r \end{bmatrix} \begin{Bmatrix} \hat{\dot{x}}_s \\ \hat{\dot{y}}_s \\ \hat{\dot{\theta}}_s \\ \hat{\dot{x}}_r \\ \hat{\dot{y}}_r \end{Bmatrix} + \begin{bmatrix} C_{lex} + C_{x\omega} & 0 & 0 & 0 & 0 \\ 0 & C_{ley} + C_{y\omega} + C_{ey} & 0 & 0 & -C_{ey} \\ 0 & 0 & C_{le\theta} + C_{\theta\omega} & 0 & 0 \\ 0 & 0 & 0 & C_{dx} & 0 \\ 0 & -C_{ey} & 0 & 0 & C_{dy} + C_{ey} \end{bmatrix} \begin{Bmatrix} \hat{\dot{x}}_s \\ \hat{\dot{y}}_s \\ \hat{\dot{\theta}}_s \\ \hat{\dot{x}}_r \\ \hat{\dot{y}}_r \end{Bmatrix} + \begin{bmatrix} K_{ex} + K_{rs} & 0 & K_{x\theta} & -K_{rs} & 0 \\ 0 & K_{ey} + K_h & 0 & 0 & 0 \\ K_{x\theta} & 0 & T\overline{GB} + K_\theta & 0 & 0 \\ -K_{rs} & 0 & 0 & K_{rex} + K_{rs} & 0 \\ 0 & 0 & 0 & 0 & K_{rey} \end{bmatrix} \begin{Bmatrix} \hat{x}_s \\ y_s \\ \theta_s \\ x_r \\ y_r \end{Bmatrix} = \begin{Bmatrix} P_x(t) \\ P_y(t) \\ P_\theta(t) \\ 0 \\ 0 \end{Bmatrix}. \tag{13}$$

In (13), the coefficients of the frequency-dependent radiation damping are represented by the symbols $C_{x\omega}$, $C_{y\omega}$ and $C_{\theta\omega}$ in the surge, heave and pitch directions. The effect of the static offset (x_o) representing the offset due to a steady current, is included in the analysis by introducing a time-dependent component in the system response denoted by $\hat{x}_s(t)$. That is

$$x_s = x_o + \hat{x}_s. \tag{14}$$

Further, it is required that x_s satisfies the equilibrium of (3) on the average. This leads to the equation

$$\langle \alpha_1(x_o + \hat{x}_s)^3 + \alpha_2(x_o + \hat{x}_s)^2 + \alpha_3x_o + C_1 \rangle = P_{mh}, \quad (15)$$

with the symbol $\langle \rangle$ denoting the operator of the mathematical expectation and the symbol P_{mh} being the mean horizontal force.

Note that the linearized terms in (13) comprise an equivalent damping term to account for the energy dissipated through friction at the interface of the spar and the buoyancy can, an equivalent damping term to represent the quadratic damping, and an equivalent stiffness term to account for the nonlinearity of the mooring lines.

The spar equivalent linear stiffnesses in the horizontal and vertical directions are determined by the equations

$$K_{ex} = \left\langle \frac{\partial F_{mx}}{\partial \hat{x}_s} \right\rangle = 3\alpha_1\sigma_{\hat{x}_s}^2 + 3\alpha_1x_o^2 + 2\alpha_2x_o, \quad (16)$$

and

$$K_{ey} = \left\langle \frac{\partial F_{my}}{\partial y_s} \right\rangle, \quad (17)$$

Furthermore, the linearized component of the riser stiffness in the horizontal and vertical directions are determined by the equations

$$K_{rex} = K_r \left(\frac{8}{\pi} \right)^{1/2} \frac{\sigma_{x_r} + 2x_o}{h} \quad (18)$$

and

$$K_{rey} = K_r \left(1 - \frac{0.5\sigma_{y_r}^2 + 0.5x_o^2}{h^2} \right), \quad (19)$$

where K_r represents the axial stiffness of fifteen TTRs, h represents the height of the spar center of gravity from the seabed, and $\sigma_{x_r}^2$, $\sigma_{y_r}^2$ denote the variances of the riser response in the horizontal and vertical directions, respectively.

Similarly, the nonlinear term of the friction at the compliant guide is approximated by an equivalent dashpot of value

$$C_{ey} = (\mu_y N) \left(\frac{2}{\pi} \right)^{1/2} \frac{1}{\sigma_{\dot{y}}}, \quad (20)$$

where

$$\sigma_{\dot{y}} = (\sigma_{\dot{y}_s}^2 + \sigma_{\dot{y}_r}^2)^{1/2} \quad (21)$$

with $\sigma_{\dot{y}_s}^2$ and $\sigma_{\dot{y}_r}^2$ denoting the variances of the spar and the riser/buoyancy can velocities in the vertical direction. Equations (22)–(24) refer to the quadratic damping in the surge, heave, and pitch directions. The corresponding terms in the surge, heave and pitch directions are expressed in the form

$$C_{lex} = \left(\frac{8}{\pi} \right)^{1/2} C_{sx} ((\sigma_{\dot{x}_s})^2 + \alpha^2(\sigma_{\dot{\theta}_s})^2)^{1/2}, \quad (22)$$

$$C_{ley} = \left(\frac{8}{\pi} \right)^{1/2} C_{sy}\sigma_{\dot{y}_s}, \quad (23)$$

$$C_{le\theta} = \left(\frac{8}{\pi} \right)^{1/2} C_{s\theta} (\beta^2(\sigma_{\dot{x}_s})^2 + (\sigma_{\dot{\theta}_s})^2)^{1/2}. \quad (24)$$

Obviously, the implementation of this formulation requires an iterative procedure, since the equivalent linear parameters depend on the system response, which in turn depends on the parameters. Specifically, equation (13) is recast in the form

$$M\ddot{\underline{u}} + (C + C_e)\dot{\underline{u}} + (K + K_e)\underline{u} = \underline{f}(t), \quad (25)$$

where the vector $\underline{u}(t)$ is defined as

$$\underline{u}^T = (\hat{x}_s, y_s, \theta_s, x_r, y_r) \quad (26)$$

and M , C , C_e , K and K_e represent the mass matrix, damping matrix, equivalent damping matrix, stiffness matrix, and equivalent stiffness matrix, respectively. The symbol \underline{f} represents the excitation vector.

Further, the spectral matrix of the response of the equivalent system is determined from the equation

$$S_r(\omega) = H(j\omega)S_f(\omega)H_c'(j\omega), \quad (27)$$

where $S_r(\omega)$ is the power spectral density matrix of the response; $H(j\omega)$ and $H_c'(j\omega)$ are the transfer functions of responses and its complex conjugate transposed, respectively. The transfer function $H(j\omega)$ is given by the equation

$$H(\omega) = [-\omega^2 M + i\omega(C + C_e) + (K + K_e)]^{-1}. \quad (28)$$

The symbol $S_f(\omega)$ represents the power spectral density of the excitations. Note that in each iteration step, the variances of various response components are determined by using the “generic” equations

$$\sigma_r^2 = \int_{-\infty}^{\infty} S_r(\omega) d\omega \quad \text{and} \quad \sigma_{\dot{r}}^2 = \int_{-\infty}^{\infty} \omega^2 S_r(\omega) d\omega, \quad (29)$$

where σ_r^2 and $\sigma_{\dot{r}}^2$ are generic response displacement and response velocity variances, and $S_r(\omega)$ is the associated spectral density of displacement.

A set of new responses statistics is obtained based on the response from (27) and the iteration continues until convergence in the response statistics is achieved.

4. Numerical results

The preceding two approaches — numerical integration of the governing equation in the time domain and frequency domain solution based on the statistical linearization — are used to study the responses of a coupled system consisting of truss spar, mooring lines, and riser. The total weight of the truss spar is approximately 163,960 t. The radius of hull and draft are 23.8 m and 198.1 m, respectively. Each top tensioned riser is tensioned by using a buoyancy can which transfers tension to the riser at top. The diameter and the height of each buoyancy can are 3.65 m and 73 m, respectively. In this context, the comparison of the nonlinear responses with the responses from the equivalent model is presented for two different load cases. The difference in two load cases is that one of the two load cases includes the effect of the current associated with the 100-year hurricane wave whereas the other load case accounts for the effect due to the 100-year hurricane wave only. As a result of the steady current, the spar in one case will have a static offset from the neutral position. The significant wave height and peak period of the 100-year event are considered as 12.5 m and 14.0 sec. The input excitations for the simplified model

(Figure 2) analysis are specified in the form of force and moment time histories at the center of gravity of the spar. The excitations $P_h(t)$, $P_v(t)$ and $P_\theta(t)$ are obtained from a detailed model analysis [Spanos et al. 2003] by using the motion analysis program MLTSIM [Pauling 1995].

The nonlinear responses are obtained by numerically integrating the equations of motion (3)–(12), which also accounts for the effect of the frequency-dependent radiation damping specified from an industrial data set and plotted in Figure 3.

Step-by-step (0.1 sec) numerical integration is carried out by using the fourth order Runge–Kutta scheme. The linearized responses are determined from the equivalent model by iterations using equations

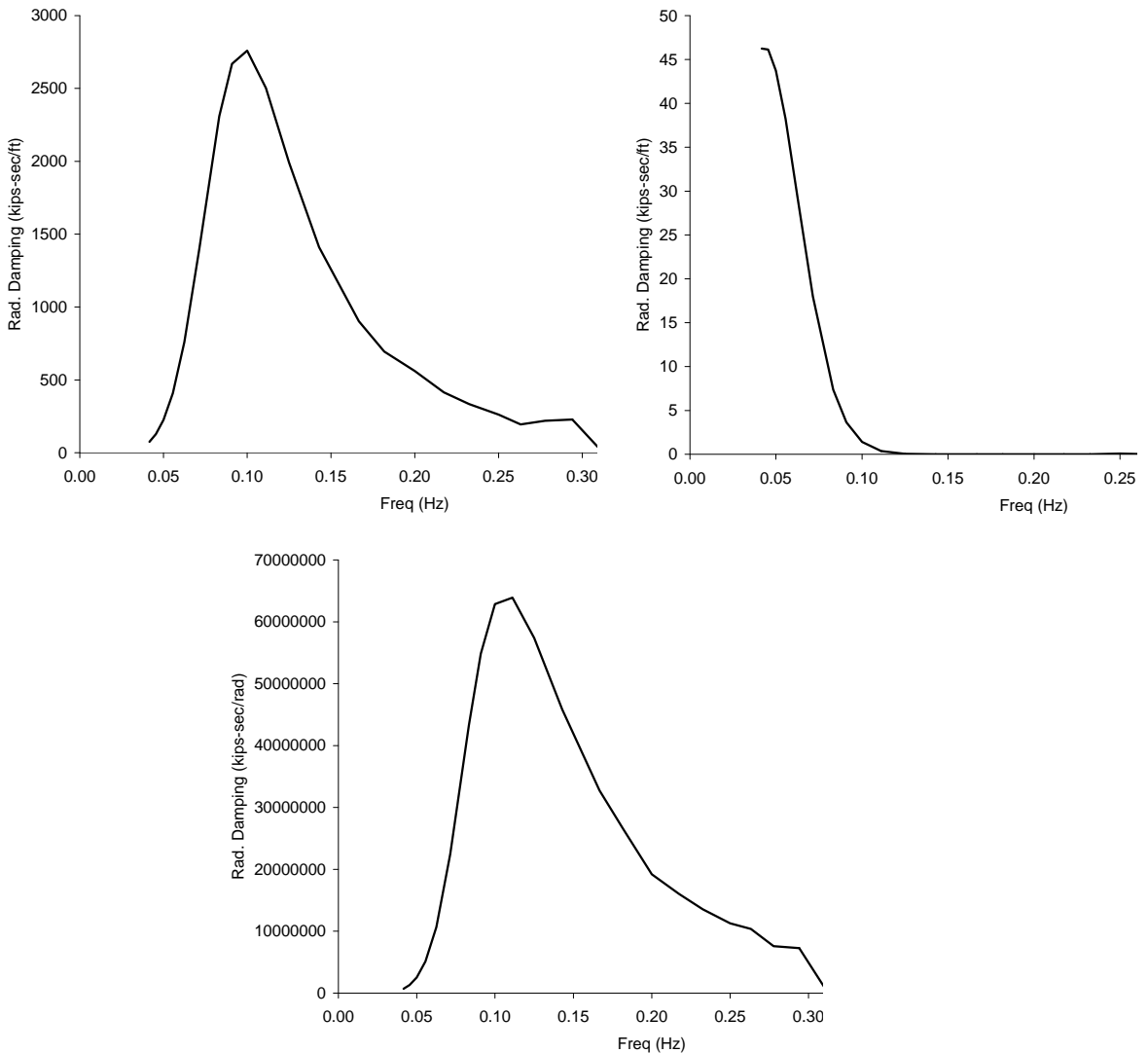


Figure 3. Frequency-dependent damping in the surge direction (top left), in the heave direction (top right), and in the pitch direction (bottom). 1 kips equals 4.447 kN and 1 kips sec/ft equals 14.59 kN sec/m.

Displacement	Wave forces only		Wave forces + Current	
	Nonlinear analysis	Stat. linearization	Nonlinear analysis	Stat. linearization
Surge (m)	1.60	1.64	1.49	1.58
Heave (m)	0.06	0.05	0.05	0.04
Pitch (rad)	0.01	0.01	0.01	0.01

Table 1. Comparison of root mean square responses: nonlinear analysis vs. statistical linearization.

(13)–(29). The root mean square responses in the surge, heave and pitch directions from both analyses are presented in Table 1. The agreement in the response statistics determined by the two approaches is quite reasonable. Clearly, response variances alone do not provide complete insight of the responses in various frequencies ranges. Hence, the power spectral densities of the linear and nonlinear responses are compared to examine the agreement of the responses in the low and wave frequency regions. Figure 4 shows comparisons of the surge, heave and pitch responses for the wave-induced forces only (that is, the effect of currents is not included). It reveals that the linearized surge response is conservative at the natural frequency and peak wave frequency which explains the higher rms surge from the equivalent

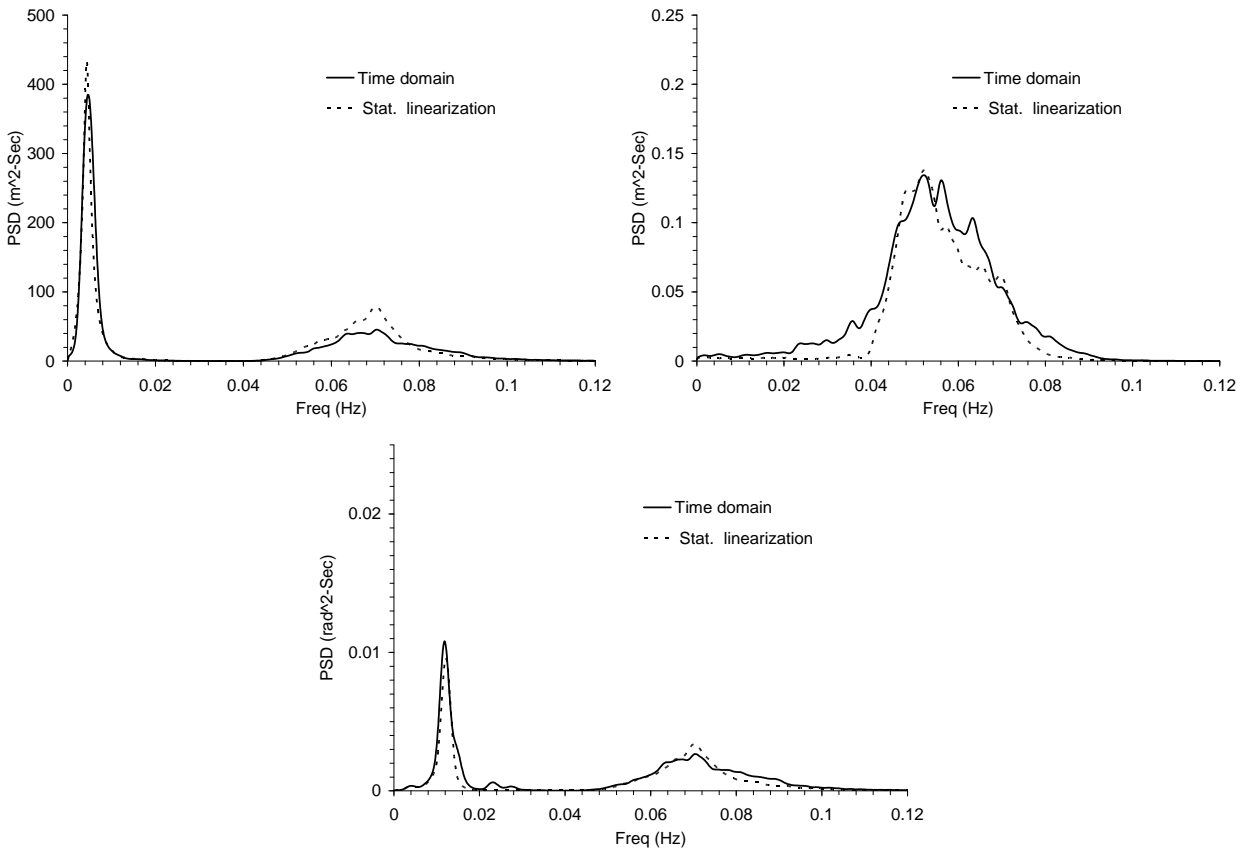


Figure 4. Comparison of the surge (top left), heave (top right) and pitch (bottom) responses for wave-induced forces only (no current).

model analysis. The linearization of Coulomb damping in the equivalent system underpredicts the heave response to an acceptable limit (Figure 4, top right). The pitch response (Figure 4, bottom) exhibits an acceptable agreement at all frequencies.

Next, a comparison of the surge, heave and pitch responses (Figure 5) for the wave-induced forces and current exhibits a trend similar to the one observed in the wave-induced case. The surge and the heave responses (top row in this figure) at the offset position are less than the surge and the heave responses (top row in Figure 4) at the mean position. This trend is persistent irrespective of the analysis methods. The natural frequency of the system in the surge direction is increased due to higher stiffness contribution by the TTRs and mooring lines at the offset position. The heave response comparison (Figure 5, top right) shows that the linearized response is under-predicted at all frequencies to a small extent, and shows similar effect of the Coulomb damping as observed in the previous case. Besides the linearized Coulomb damping, another contributing factor in the reduction of the heave response (top right panels in Figures 4 and 5) at the offset position is the increased stiffness of the mooring lines. Finally, excellent agreement of the pitch responses is obtained in the wave frequency region whereas the equivalent response is conservative in the low frequency region.

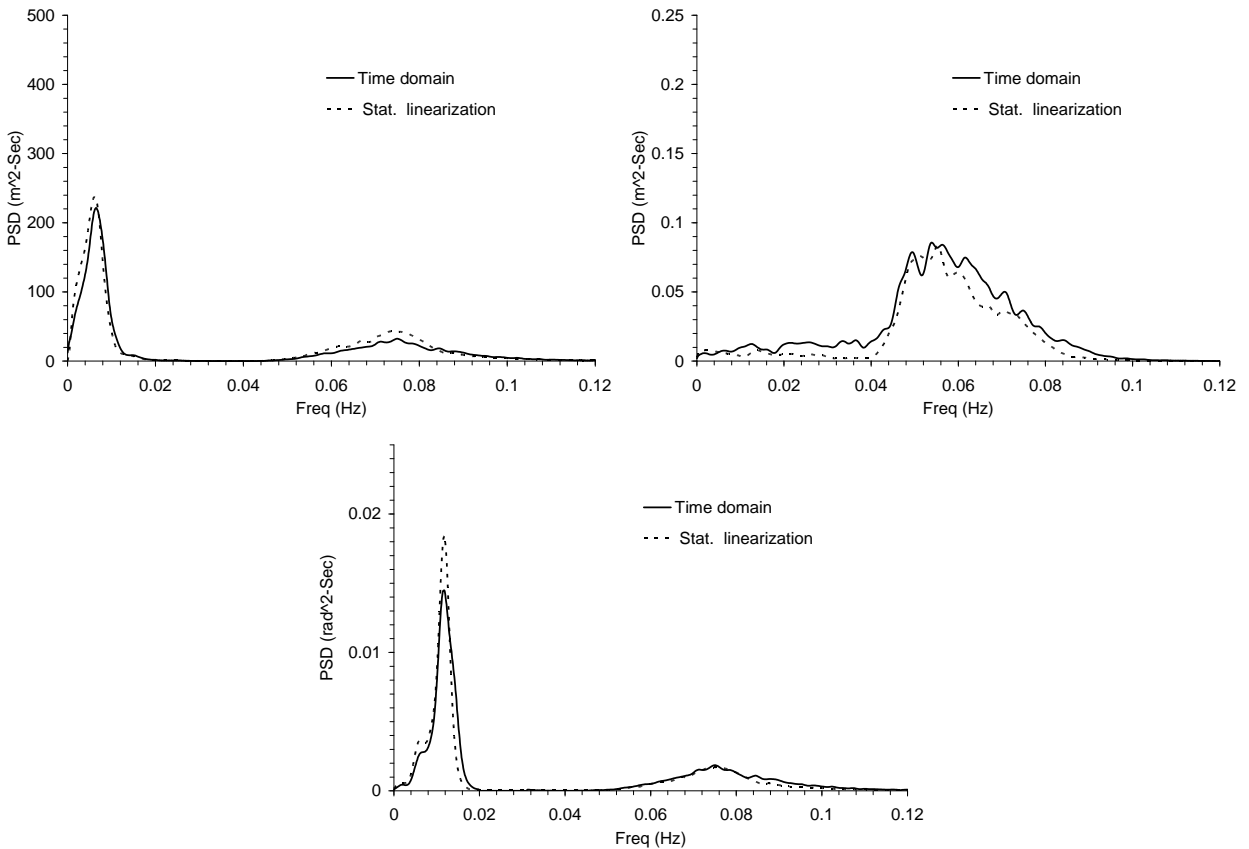


Figure 5. Comparison of the surge (top left), heave (top right) and pitch (bottom) responses for wave- and current-induced forces.

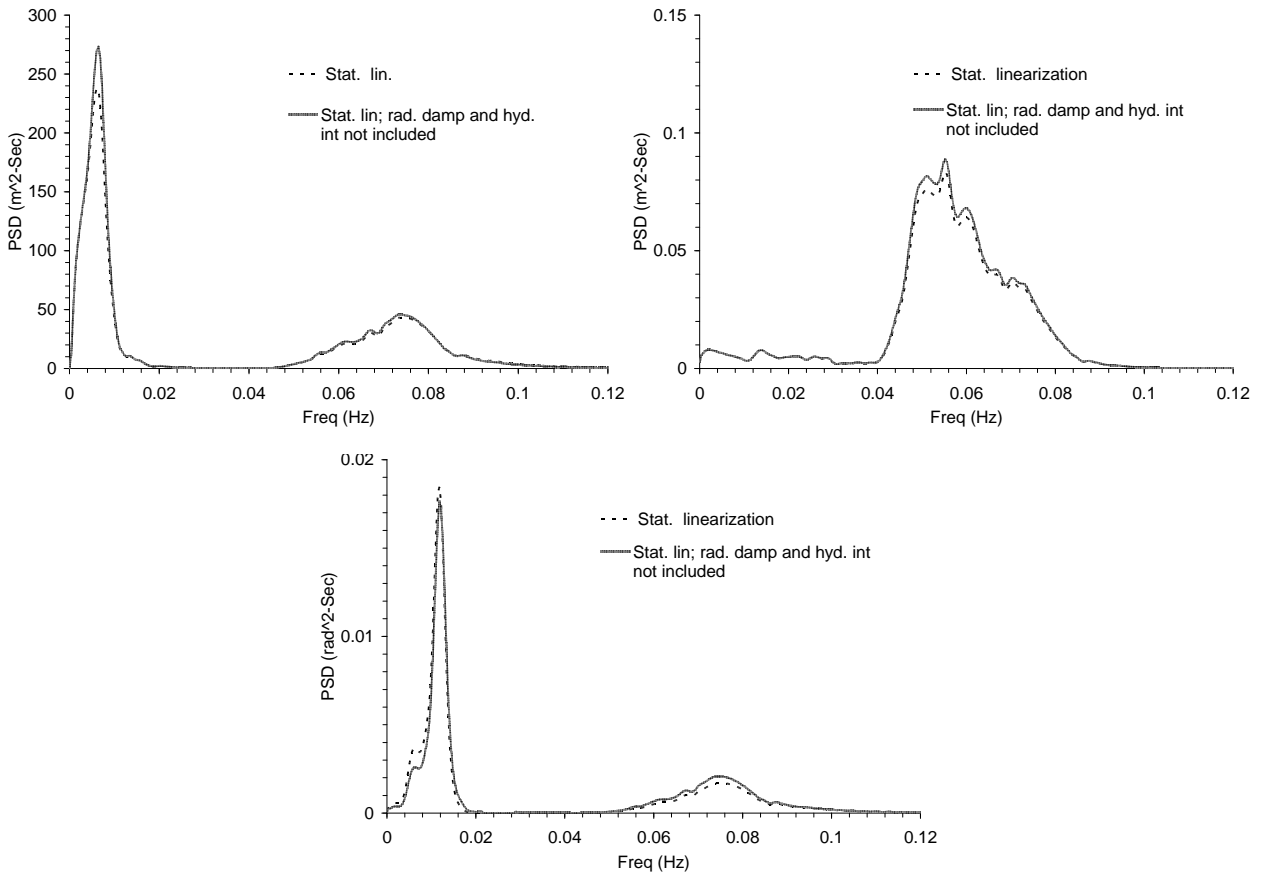


Figure 6. Comparison of the surge (top left), heave (top right) and pitch (bottom) responses, showing effect of hydrodynamic interaction and frequency-dependent damping.

The effect of hydrodynamic interaction and frequency-dependent damping is examined by comparing the linearized responses only. The responses without the effect of frequency-dependent damping and hydrodynamic interaction were earlier reported [Spanos et al. 2005] and included in this paper for comparison study only. This comparison is discussed for the load case consisting of the wave and current only. Figure 6, top left, shows the response comparison in the surge direction. It is apparent that the hydrodynamic interaction and frequency-dependent damping affects the surge response at the natural frequency only. Similarly, the effect on the heave response (Figure 6, top right) is also reflected close to the spar natural period. The spar natural period at the offset position is approximately 18.2 sec assuming the buoyancy can sticks to the hull. The effect in the pitch direction (Figure 6, bottom) is not significant.

5. Concluding remarks

A frequency domain analysis approach for a coupled spar/risers/mooring lines system has been presented. This approach has been used to study the spar dynamic behavior, as well as to assess the effect of the spar/riser/mooring lines interaction on the spar response characteristics. The approach offers the desirable

features of incorporating in the analysis various effects such as that of the nonlinearities of the mooring lines, that of the hydrodynamic damping, and that of frequency-dependent parameters associated with radiation damping. Note that frequency-dependent parameters are ordinarily accounted for in offshore structural dynamics by using elaborate convolution techniques in time domain analyses. However, these parameters have been dealt readily in the frequency domain solution approach presented herein by using the concept of transfer function. Furthermore, the transfer function, appropriately modified, has accounted readily for various nonlinearities of the spar/mooring lines/riser system by using the technique of statistical linearization.

In the studies reported herein it has been found out that the hydrodynamic interaction in the surge and pitch directions and the radiation damping affect considerably the spar responses in the surge and the heave directions; indeed the spectral values at the vicinity of natural frequencies in the surge and the heave directions have been reduced when these parameters were included. Note, however, that this conclusion relates to the particular system and sea-states considered in the present study. Obviously, a qualitatively different conclusion may be derived for other design scenarios.

Clearly a convenient assessment tool can be quite useful for sizing of spar structures as well as for the selection of the number, orientation, and kind of mooring lines (steel wire vs. polyester), in the early stage of any offshore field development. This is also true for the selection of a proper riser system with respect to a spar. This is due to the fact that the characteristics of the spar motion influence the spar-riser interface design. The design options are that of top tensioned riser supported by the buoyancy can (considered herein), and that of a steel catenary riser system; obviously even the latter design option can be readily treated by the herein proposed approach. Note that for a high pressure riser system, the interface load can be significant due to increased wall thickness and associated hull size increases to accommodate higher payloads. In this case the large spar hull size will, of course, influence the riser dynamic responses/fatigue life as well as the hull fabrication and installation cost, and will have a major impact on the total cost of a project. In this regard, a convenient approach like the one presented herein may be used as a reliable tool for a rapid assessment of the merits of the various riser/spar interface scenarios.

Index of notation

- α : A factor to capture the hydrodynamic force in the surge direction due to unit pitch
- $\alpha_1, \alpha_2, \alpha_3, \beta_1$: Coefficients in the polynomial giving the mooring line load-displacement relation; surge direction
- $\alpha_4, \alpha_5, \alpha_6, \beta_2$: Coefficients in the polynomial giving the mooring line load-displacement relation; heave direction
- B : Total buoyancy of the spar
- β : A factor to capture the hydrodynamic force in the pitch direction due to unit surge
- C : Linear damping matrix for the multi-degree-of-freedom system
- C_1/C_2 : Constant in the polynomial representing mooring line load-displacement relation; surge/heave direction
- C_{dx}/C_{dy} : Damping of the risers/buoyancy can in the surge/heave direction
- $C_{sx}/C_{sy}/C_{s\theta}$: Quadratic damping coefficient in the surge/heave/pitch direction
- $C_{x\omega}/C_{y\omega}/C_{\theta\omega}$: Frequency-dependent radiation damping in the surge/heave/pitch direction
- C_e : Equivalent damping matrix for the multi-degree-of-freedom system
- $C_{lex}/C_{ley}/C_{le\theta}$: Equivalent linear damping of the spar in the surge/heave/pitch direction
- C_{ey} : Equivalent Coulomb damping in the heave direction

- $C_{rx}(\tau)/C_{ry}(\tau)/C_{r\theta}(\tau)$: Damping impulse function in the surge/heave/pitch direction
 $\underline{f}(t)$: Force vector representing all excitations
 \underline{F}_f : Friction force at the spar and buoyancy can contact surface
 $F_m(t)$: Restoring force in the mooring lines
 $F_{mx}(t)/F_{my}(t)$: Restoring force in the mooring lines in the surge/heave direction
 \overline{GB} : Distance between center of buoyancy and center of gravity of the spar
 h : Height of the center of gravity of the spar from the seabed
 $H(j\omega)$ and $H'_c(j\omega)$: Frequency response function of the spar and its transpose conjugate
 J_θ : Mass moment inertia in the pitch direction
 K : Linear stiffness matrix for the multi-degree-of-freedom system
 K_e : Equivalent stiffness matrix for the multi-degree-of-freedom system
 K_{ex}/K_{ey} : Equivalent stiffness of the spar in the surge/heave direction
 K_h/K_θ : Hydrodynamic stiffness of the spar in the heave/pitch direction
 $K_{x\theta}$: Force in the surge direction due to unit pitch
 K_{rs} : Contact stiffness of the guide between the buoyancy can and the spar
 K_r : Total axial stiffness of riser system
 K_{rx}/K_{ry} : Riser stiffness in the surge/heave direction
 K_{rex}/K_{rey} : Equivalent riser stiffness in the surge/heave direction
 $\lambda_{rx}(\omega)/\lambda_{ry}(\omega)/\lambda_{r\theta}(\omega)$: Frequency-dependent radiation damping function; surge/heave/pitch direction
 M : Mass matrix for the multi-degree-of-freedom system
 M_x^s, M_y^s : Mass of the spar including the added mass in the surge/heave direction
 M_x^r, M_y^r : Mass of the risers/buoyancy can including the added mass in the surge/heave direction
 $M_{x\theta}^s$: Coupling mass term between surge and pitch direction
 μ : Coefficient of the Coulomb friction at the spar and buoyancy can contact surface
 N : Total preload at the spar/buoyancy can contact guide
 $P_h(t)/P_v(t)/P_\theta(t)$: Excitation in the surge/heave/pitch direction
 P_{mh} : Mean force in the surge direction
 $S_r(\omega)/S_f(\omega)$: Spectral density matrix of the responses/excitations
 $\sigma_{x_r}^2/\sigma_{y_r}^2$: Variance of the riser response in the surge/heave direction
 $\sigma_{x_s}^2/\sigma_{y_s}^2/\sigma_{\theta_s}^2$: Variance of the spar response in the surge/heave/pitch direction
 σ_r^2 : Generic response displacement variance
 σ_f^2 : Generic response velocity variance
 T : Total top tension in the risers
 $\theta_s, \dot{\theta}_s, \ddot{\theta}_s$: Spar rotation/velocity/acceleration in the pitch direction
 \underline{u} : Displacement vector
 W : Total weight of the spar
 x_θ : Static offset of the spar in the surge direction
 x_r/y_r : Risers/buoyancy can displacement in the surge/heave direction
 \dot{x}_r/\dot{y}_r : Risers/buoyancy can velocity in the surge/heave direction
 \ddot{x}_r/\ddot{y}_r : Risers/buoyancy can acceleration in the surge/heave direction
 x_s/y_s : Total spar displacement in the surge/heave direction
 \dot{x}_s/\dot{y}_s : Spar velocity in the surge/heave direction
 \ddot{x}_s/\ddot{y}_s : Spar acceleration in the surge/heave direction
 \hat{x}_s : Time-dependent component of the surge of the spar
 ζ_x^r/ζ_y^r : Damping coefficient for the risers/buoyancy can in the surge/heave direction

References

- [Agarwal and Jain 2003a] A. K. Agarwal and A. K. Jain, “Dynamic behavior of offshore spar platforms under regular sea waves”, *Ocean Eng.* **30**:4 (2003), 487–516.
- [Agarwal and Jain 2003b] A. K. Agarwal and A. K. Jain, “Nonlinear coupled dynamic response of offshore spar platforms under regular sea waves”, *Ocean Eng.* **30**:4 (2003), 517–551.
- [Fischer et al. 2004] F. J. Fischer, S. I. Liapis, and Y. Kallinderis, “Mitigation of current-driven vortex-induced vibrations of a spar platform via “SMART” thrusters”, *J. Offshore Mech. Arct. Eng.* **126**:1 (2004), 96–104.
- [Koo et al. 2004a] B. J. Koo, M. H. Kim, and R. E. Randall, “The effect of nonlinear multi-contact coupling with gap between risers and guide frames on global spar motion analysis”, *Ocean Eng.* **31**:11–12 (2004), 1469–1502.
- [Koo et al. 2004b] B. J. Koo, M. H. Kim, and R. E. Randall, “Mathieu instability of a spar platform with mooring and risers”, *Ocean Eng.* **31**:17–18 (2004), 2175–2208.
- [Liang et al. 2004] N.-K. Liang, J.-S. Huang, and C.-F. Li, “A study of spar buoy floating breakwater”, *Ocean Eng.* **31**:1 (2004), 43–60.
- [Low and Langley 2006] Y. M. Low and R. S. Langley, “Time and frequency domain coupled analysis of deepwater floating production systems”, *Appl. Ocean Res.* **28**:6 (2006), 371–385.
- [Pauling 1995] J. R. Pauling, “MLTSIM: time domain platform simulation for floating platform consisting of multiple interconnected bodies”, 1995.
- [Ran and Kim 1997] Z. Ran and M. H. Kim, “Nonlinear coupled responses of a tethered spar platform in waves”, *Int. J. Offshore Polar Eng.* **7**:2 (1997), 111–118.
- [Ran et al. 1996] Z. Ran, M. H. Kim, J. M. Niedzwecki, and R. P. Johnson, “Responses of a spar platform in random waves and currents: experiment vs. theory”, *Int. J. Offshore Polar Eng.* **6**:1 (1996), 27–34.
- [Ran et al. 1999] Z. Ran, M. H. Kim, and W. Zheng, “Coupled dynamic analysis of a moored spar in random waves and currents: time-domain vs. frequency-domain analysis”, *J. Offshore Mech. Arct. Eng.* **121**:3 (1999), 194–200.
- [Roberts and Spanos 2001] J. B. Roberts and P. D. Spanos, *Random vibrations and statistical linearizations*, Dover, New York, 2001.
- [Spanos 1981a] P. D. Spanos, “Stochastic linearization in structural dynamics”, *Appl. Mech. Rev. (ASME)* **34**:1 (1981), 1–8.
- [Spanos 1981b] P. D. Spanos, “Monte Carlo simulations of responses of non-symmetric dynamic systems to random excitations”, *Comput. Struct.* **13**:1–3 (1981), 371–376.
- [Spanos et al. 2003] P. D. Spanos, R. Ghosh, L. D. Finn, and J. E. Halkyard, “Coupled analysis of a spar structure: Monte Carlo and statistical linearization solutions”, in *Proceedings of the 22nd International Conference of Offshore Mechanics and Arctic Engineering (OMAE 2003)* (Cancun, 2003), edited by S. Chakrabarti and T. Kinoshita, ASME, New York, 2003. Paper # OMAE2003-37414.
- [Spanos et al. 2005] P. D. Spanos, R. Ghosh, L. D. Finn, and J. E. Halkyard, “Coupled analysis of a spar structure: Monte Carlo and statistical linearization solutions”, *J. Offshore Mech. Arct. Eng.* **127**:1 (2005), 11–16.
- [Tao et al. 2004] L. Tao, K. Y. Lim, and K. Thiagarajan, “Heave response of classic spar with variable geometry”, *J. Offshore Mech. Arct. Eng.* **126**:1 (2004), 90–95.

Received 29 Sep 2008. Revised 28 May 2009. Accepted 28 May 2009.

RUPAK GHOSH: Rupak.Ghosh@bp.com

POL D. SPANOS: spanos@rice.edu

Rice University, Departments of Civil and Mechanical Engineering, 6100 Main Street, Mail Stop 321, Houston, TX 77005-1892, United States

THE ELUSIVE AND FICKLE VISCOELASTIC POISSON'S RATIO AND ITS RELATION TO THE ELASTIC-VISCOELASTIC CORRESPONDENCE PRINCIPLE

HARRY H. HILTON

This paper is dedicated to my good friend and colleague Professor Emeritus Georges J. Simitsis.

The conditions for the applicability of the elastic-viscoelastic correspondence principle (analogy) in the presence of any of the five distinct classes of viscoelastic Poisson's ratios (PR) are investigated in detail. It is shown that if Poisson's ratios are time-dependent, no analogy in terms of PRs is possible, except for two of the classes under specifically prescribed highly limited conditions. Separately, the severely restrictive conditions involving time-independent PRs are discussed in detail. Failure to observe all such restrictions leads to ill posed overdeterminate problem formulations. Similarities associated with viscoelastic Timoshenko shear coefficients are also investigated and it is shown that no analogy to equivalent elastic problems can be constructed if these coefficients are time functions. In the final analysis, the PR analogy difficulties can be entirely avoided by characterizing viscoelastic materials in terms of relaxation moduli or creep compliances or creep and relaxation functions without any appeal to PRs.

Introduction

Unlike stress and deformation analyses where approximate solutions are permissible, material characterization must be performed with the highest available degree of precision since thusly defined constitutive relations pervasively impact all subsequent analyses. Consequently, great care must be exercised in modeling material and experimental data and no unnecessary approximations should be introduced¹. A major case in point is the convenient, but fictitious, introduction of the approximation of time-independent viscoelastic PRs to "simplify" material characterization, but which as will be demonstrated results in overdeterminate ill posed problem formulations and thus leads to unreliable material characterizations as well as stress-strain solutions.

Historically, in elasticity Poisson's ratio [Poisson 1829] has found much justifiable favor in analysis and material characterization. When normal strains can be readily measured in two directions, elastic PRs become a most useful universal cornerstone of elastic property description along with shear, bulk and Young's moduli. Much of the PRs' success is due to their simple concept in elasticity, where constitutive relations between stresses and strains are algebraic, with neither energy dissipation nor time-dependent memory.

Keywords: Bernoulli–Euler beams, correspondence principle, material characterization, Poisson's ratio, Timoshenko shear coefficients, viscoelasticity.

¹"Nothing is less real than realism. Details are confusing. It is only by selection, by elimination, by emphasis, that we get at the real meaning of things." —Georgia O'Keeffe

While linear elastic materials have been successfully characterized in terms of moduli and Poisson's ratios (PRs) for almost two centuries [Poisson 1829], the transition to viscoelastic PRs is far less simple than the well established equivalence between elastic moduli and viscoelastic relaxation functions/moduli [Hilton 1996; 2001; 2003; Hilton and Yi 1998; Tschoegl 1997; Tschoegl et al. 2002; Lakes and Wineman 2006; Hilton and El Fouly 2007; Shtark et al. 2007]. There are two overriding issues that need to be precisely and properly addressed when using viscoelastic PRs, namely (i) the time and stress dependencies of PRs and (ii) the inapplicability of the elastic-viscoelastic correspondence principle in terms of PRs. In question is the fundamental nature of PRs as a derived quantity in terms of ratios of perpendicular normal strains as opposed to "pure" material properties such as relaxation moduli, creep compliances, relaxation functions, etc. As such viscoelastic PRs are not universal and are specific to loading, deformation and temperature histories for each viscoelastic material.

On the other hand, in viscoelasticity with its time integral constitutive relations PRs become more complex functions dependent on time and stress histories [Hilton 1996; 2001; Hilton and Yi 1998; Tschoegl 1997; Tschoegl et al. 2002, Hilton and El Fouly 2007, Shtark et al. 2007] behaviorally similar to that of the time-dependent viscoelastic shear center [Hilton and Piechocki 1962]. Even in linear viscoelastic theory, PRs are process dependent nonlinear functions of strains and time and non-universal material properties, whereas linear relaxation and creep functions remain invariant with respect to loading histories. The viscoelastic time dependence has been demonstrated analytically [Hilton 1996; 2001; 2003; Hilton and Yi 1998; Tschoegl 1997; Tschoegl et al. 2002; Lakes and Wineman 2006; Hilton and El Fouly 2007] as well as experimentally [Shtark et al. 2007; Lakes 1991]. Auxetic viscoelastic materials, which have negative elastic PRs, have been treated in [Hilton and El Fouly 2007] where it shown that viscoelastic PRs do not follow the negative elastic patterns.

Consequently, time-independent classical PRs require states of stress and strain where each are defined as distinct temporally and spatially separable functions under inertialess conditions with no mixed boundary conditions. Under these conditions the uniquely admissible PR value is one half, the latter condition being restricted solely to incompressible and isotropic viscoelastic materials. Additionally, material characterization in terms of PRs excludes the applicability of any elastic-viscoelastic correspondence principle. The latter analogy can only be derived in terms of relaxation moduli and/or creep compliances and some very limited PR forms. Therefore, material characterization in terms of relaxation moduli (functions) and/or creep compliances, rather than PRs, remains the method of choice.

It must be remembered that isotropic viscoelastic material properties can only be properly determined through experiments involving simultaneous measurements of two-dimensional strains as summarized in [Hilton 2001] with some additional examples described in [Ravi-Chandar 1998; 2000; Lakes et al. 1979; Qvale and Ravi-Chandar 2004; Giovagnoni 1994; Mead and Joannides 1991; Sim and Kim 1990] or through x-ray evaluations [Hoke et al. 2001].

The original separation of variable analogy was formulated in [Alfrey 1944] and [Alfrey 1948] and the more general and inclusive Fourier transform formulation may be found in [Read 1950]. Viscoelasticity theory including the correspondence principle were place on a rational basis in [Lee 1955]. In [Hilton and Russell 1961] and [Hilton and Clements 1964] the analogy was extended to cover temperature dependent viscoelastic material properties, while in [Hilton and Dong 1965] the correspondence principle was derived for anisotropic materials.

In a number of instances [Gottenberg and Christensen 1963; Olesiak 1966; Paulino and Jin 2001a; 2001b; Jin and Paulino 2002; Jin 2006; Ko et al. 2003; Hilton 1964; Freudenthal and Henry 1960; Bieniek et al. 1981; Librescu and Chandiramani 1989b; 1989a; O'Brien et al. 2001; Zhu 2000; Shrotriya 2000; Shrotriya and Sottos 1998; Zhu et al. 2003; Andrianov et al. 2004; di Bernedetto et al. 2007; Noh and Whitcomb 2003; Klasztorny 2004; Bert 1973; Cowper 1966; Hilton 2009; Therriault 2003], time-independent PR assumptions lead to overdetermined ill-posed problems and cause use of the elastic-viscoelastic correspondence principle to become unjustified. In other analyses [Jin and Paulino 2002; Jin 2006; Ko et al. 2003; Hilton 1964; Freudenthal and Henry 1960; Bieniek et al. 1981; Librescu and Chandiramani 1989b; 1989a; O'Brien et al. 2001; Zhu 2000; Shrotriya 2000; Shrotriya and Sottos 1998; Zhu et al. 2003; Andrianov et al. 2004; di Bernedetto et al. 2007; Noh and Whitcomb 2003; Klasztorny 2004; Bert 1973; Cowper 1966; Hilton 2009; Therriault 2003; Nakao et al. 1985; Singh and Abdelnaser 1993; Chen 1995; Hilton and Vail 1993], the elastic-viscoelastic correspondence principle (analogy) has been applied improperly by extending it to viscoelastic time-dependent PRs. In this paper the applicability and predominant inapplicability of this analogy as it relates to Poisson's ratio in elastic and viscoelastic expressions involving bulk, shear and Young's moduli is examined.

Several illustrative examples consider the effects of viscoelastic PRs, namely one-dimensional relaxation loading, simple bending and Timoshenko beams. The Timoshenko beam in particular brings into play an additional parameter, the shear coefficient, which depends on stresses, material properties, loading histories and paths, cross sectional geometry, and boundary and initial conditions. Its characteristics bear some resemblance to those of the PRs and it also does not generally submit to an elastic-viscoelastic analogy, despite a number of publications to the contrary [Therriault 2003; Nakao et al. 1985; Singh and Abdelnaser 1993; Chen 1995], including one by the present author [Hilton and Vail 1993].

Note that all the viscoelastic Timoshenko beam publications [Nakao et al. 1985; Singh and Abdelnaser 1993; Chen 1995; Hilton and Vail 1993] except [Therriault 2003] preceded [Hilton 1996; 2001; 2003; Hilton and Yi 1998; Tschoegl 1997; Tschoegl et al. 2002] where the viscoelastic PR inconsistencies were derived. On the other hand, [Jin and Paulino 2002] were published after [Hilton 1996; 2001; 2003; Hilton and Yi 1998; Tschoegl 1997; Tschoegl et al. 2002].

1. General concepts

The correspondence principle. The elastic-viscoelastic correspondence principle or analogy comes in two flavors, namely (a) separation of variables and (b) integral transforms. The pertinent references are listed in the introduction. Consider a Cartesian coordinate system $x = \{x_1, x_2, x_3\}$ with Einstein's summation notation and where underlined indices indicate no summation.

The separation of variables analogy states that under proper conditions viscoelastic variables are related to equivalent elastic ones by

$$\sigma_{ij}(x, t) = g(t) \sigma_{ij}^e(x) \quad \epsilon_{ij}(x, t) = h(t) \epsilon_{ij}^e(x) \quad (1)$$

where the superscripts e denote equivalent elastic variables or solutions. The severe restrictions associated with these forms are discussed in Section 3. In particular, it is required that the material be incompressible with PRs $\nu^e(x) = \nu(x, t) = \frac{1}{2}$.

For isotropic materials the integral transform analogy one requires that the Fourier transforms (FT) be

$$\text{elastic} \implies \begin{cases} \bar{\sigma}_{ij}^e(x, \omega) = \bar{\sigma}_{ij}^e(x, \omega, G^e, K^e, \bar{\alpha T}, \bar{X}, \bar{U}) \\ \text{or} \\ \bar{\sigma}_{ij}^e(x, \omega) = \bar{\sigma}_{ij}^e(x, \omega, \mathcal{G}^e, \nu^e, \bar{\alpha T}, \bar{X}, \bar{U}) \end{cases} \quad (2)$$

and

$$\text{viscoelastic} \implies \begin{cases} \bar{\sigma}_{ij}(x, \omega) = \bar{\sigma}_{ij}^e(x, \omega, \bar{G}, \bar{K}, \bar{q}, \bar{\alpha T}, \bar{X}, \bar{U}) \\ \bar{\sigma}_{ij}(x, \omega) \neq \bar{\sigma}_{ij}^e(x, \omega, \bar{\mathcal{G}}, \bar{\nu}, \bar{q}, \bar{\alpha T}, \bar{X}, \bar{U}) \end{cases} \quad (3)$$

(see Table 2), where $X(x, t)$ and $U(x, t)$ are respectively boundary stresses and displacements. The generic symbols \mathcal{G}^e and $\bar{\mathcal{G}}$ refer respectively to G^e, K^e or E^e and \bar{G}, \bar{K} or \bar{E} . The integral transform analogy or correspondence principle then consists of one to one replacements in elastic FT solutions of elastic *moduli* with corresponding viscoelastic *complex moduli*, i.e.,

$$\bar{G} \xrightarrow{\text{for}} G^e, \quad \bar{K} \xrightarrow{\text{for}} K^e, \quad \bar{E} \xrightarrow{\text{for}} E^e, \quad \text{but not } \bar{\nu} \xrightarrow{\text{for}} \nu^e, \text{ except when } \bar{\nu} = \nu^e = \frac{1}{2}. \quad (4)$$

The viscoelastic stresses, strains and displacements are the FT inverses of these modified elastic FTs.

Constitutive relations. Isotropic isothermal nonhomogeneous elastic constitutive relations (Hooke’s law) at constant temperature are then written as

$$\sigma_{ii}^e(x, t) = \sum_{j=1}^3 E_{ii jj}^e(x) \epsilon_{jj}^e(x, t), \quad (5)$$

$$\sigma_{ij}^e(x, t) = 2 G^e(x) \epsilon_{ij}^e(x, t), \quad i \neq j, \quad (6)$$

and with the classical (original) definition of Poisson’s ratio [Poisson 1829] given by

$$\nu_{ij}^e(x, t) = - \frac{\epsilon_{jj}^e(x, t)}{\epsilon_{ii}^e(x, t)}, \quad i \neq j, \quad (7)$$

Thus the elastic PR will be time-dependent whenever the strain components are non-separable functions of space and time or distinct time functions regardless whether the elastic moduli E_{ijkl}^e or G^e are time-dependent.

For a case of one-dimensional stress, where

$$\sigma_{11} \neq 0 \quad \text{and all other } \sigma_{ij} \text{ are } 0, \quad (8)$$

substitution of (7) into (5) in order to eliminate $\epsilon_{22} = \epsilon_{33}$ in favor of ϵ_{11} yields

$$\sigma_{11}^e(x, t) = (E_{1111}^e(x) - 2 \nu_{12}^e(x, t) E_{1122}^e(x)) \epsilon_{11}^e(x, t) = E_0(x, t) \epsilon_{11}^e(x, t), \quad (9)$$

since $E_{1122}^e = E_{1133}^e$ and where E_0 is the Young’s modulus.

Alternately, consider the isotropic constitutive relations in terms of shear and bulk moduli (K^e and G^e):

$$S_{ij}^e(x, t) = 2 G^e(x) E_{ij}^e(x, t), \quad \sigma^e(x, t) = K^e(x) \epsilon^e(x, t), \quad (10)$$

where the stress S_{ij} and strain E_{ij} deviators and mean stresses σ and strains ϵ are

$$S_{ij} = \sigma_{ij} - \delta_{ij} \sigma, \quad \sigma = \frac{\sigma_{ii}}{3}, \quad E_{ij} = \epsilon_{ij} - \delta_{ij} \epsilon, \quad \epsilon = \frac{\epsilon_{ii}}{3}, \quad (11)$$

resulting in

$$\sigma_{11}^e(x, t) = \underbrace{\frac{4G^e + K^e}{3}}_{= E_{1111}^e} \epsilon_{11}^e(x, t) + \underbrace{\frac{K^e - 2G^e}{3}}_{= E_{1122}^e} (\epsilon_{22}^e(x, t) + \epsilon_{33}^e(x, t)), \quad K^e < \infty, \quad (12)$$

and

$$\epsilon_{11}^e(x, t) = \underbrace{\frac{1 + G^e/K^e}{3G^e}}_{= 1/E_0^e = C_0^e} \sigma_{11}^e(x, t), \quad \epsilon_{22}^e(x, t) = \underbrace{\frac{2G^e/K^e - 1}{6G^e}}_{= 1/E_{2211}^e = C_{2211}^e = -\nu_{12}^e/E_0^e} \sigma_{11}^e(x, t), \quad (13)$$

since $\epsilon_{22} = \epsilon_{33}$. Therefore, for any isotropic linear elastic material the PR becomes

$$\nu_{12}^e = \nu^e = \frac{1 - 2G^e/K^e}{2(1 + G^e/K^e)}, \quad (14)$$

with an upper limit of 0.5 for incompressible materials when $K^e \rightarrow \infty$.

The corresponding isotropic nonhomogeneous viscoelastic stress-strain relations at constant temperature are expressable in the form

$$\sigma_{\underline{ii}}(x, t) = \sum_{j=1}^3 \int_{-\infty}^t E_{\underline{ii}jj}(x, t - t') \epsilon_{jj}(x, t') dt', \quad (15)$$

$$\sigma_{ij}(x, t) = 2 \int_{-\infty}^t G(x, t - t') \epsilon_{ij}(x, t') dt', \quad i \neq j. \quad (16)$$

The initial conditions of any viscoelastic problem are

$$\sigma(x, 0) = \sigma^e(x, 0) \quad \text{and} \quad \epsilon_{ij}(x, 0) = \epsilon_{ij}^e(x, 0), \quad (17)$$

with material properties

$$E(x, 0) = E^e(x) \quad G(x, 0) = G^e(x) \quad \nu_{ij}(x, 0) = \nu_{ij}^e(x), \quad (18)$$

and where the superscript e refers to elastic quantities of the corresponding elastic problem (same boundary conditions, geometry, and so on).

In [Hilton 2001] five distinct classes of PR definitions are catalogued:

Class I
[Poisson 1829]

$$\nu_{ij}(x, t) \stackrel{\text{def}}{=} - \frac{\epsilon_{\underline{jj}}(x, t)}{\epsilon_{\underline{ii}}(x, t)}, \quad i \neq j; \quad (19)$$

Class II
[Christensen 1982; Pipkin 1972]

$$\nu_{ij}^{\text{C}}(x, t) \stackrel{\text{def}}{=} - \frac{\epsilon_{\underline{jj}}(x, t)}{\epsilon_{11}(x)}, \quad j \neq 1; \quad \epsilon_{11} = \text{const.}; \quad (20)$$

Class III
[Hilton and Yi 1998]

$$\bar{\nu}_{ij}^{\text{A}}(x, \omega) \stackrel{\text{def}}{=} - \frac{\bar{\bar{\epsilon}}_{\underline{jj}}(x, \omega)}{\bar{\bar{\epsilon}}_{\underline{ii}}(x, \omega)}, \quad i \neq j; \quad (21)$$

Class IV
[Vinogradov and Malkin 1980]

$$v_{ij}^{\mathbf{H}}(x, t) \stackrel{\text{def}}{=} - \frac{\log(1 + \epsilon_{jj}(x, t))}{\log(1 + \epsilon_{ii}(x, t))}, \quad i \neq j; \quad (22)$$

Class V
[Bertilsson et al. 1993]

$$\frac{\partial v_{ij}^{\mathbf{V}}(x, t)}{\partial t} \stackrel{\text{def}}{=} - \frac{\partial \epsilon_{jj}(x, t) / \partial t}{\partial \epsilon_{ii}(x, t) / \partial t}, \quad i \neq j. \quad (23)$$

Consider for instance the original classical Class I definition for isothermal viscoelastic materials, resulting in

$$v_{ij}(x, t) = - \frac{\epsilon_{jj}(x, t)}{\epsilon_{ii}(x, t)} = - \frac{\int_{-\infty}^t C_{jjkl}(x, t - t') \sigma_{kl}(x, t') dt'}{\int_{-\infty}^t C_{iimn}(x, t - t') \sigma_{mn}(x, t') dt'}, \quad i \neq j, \quad (24)$$

with similar expressions for the other PR classes. It can be readily seen that even in linear viscoelasticity the PRs by any definitions are

- (I) nonlinear functions of strains, stresses and their time histories (loading path) and hence process-dependent and not universal material property parameters such as moduli and compliances;
- (II) derived or defined quantities and not fundamental ones such as relaxation moduli or creep compliances;
- (III) material properties determined from one-dimensional normal loading experiments and PRs may not be exportable to other stress fields, unless proper expressions are used to represent these viscoelastic PRs.

Elimination of ϵ_{22} from (15) now results in

$$\sigma_{11}(x, t) = \int_{-\infty}^t (E_{1111}(x, t - t') - 2 \nu_{12}(x, t') E_{1122}(x, t - t')) \epsilon_{11}(x, t') dt'. \quad (25)$$

This isotropic constitutive relation form can be achieved in temporal space only through the use of the Class I PR definition of (19), i.e., Poisson’s original definition [1829], since the strain substitutions must be based on the actual instantaneous strains. Indeed, this viscoelastic protocol is identical to what is employed in the theory of elasticity when Hooke’s law is extended to three dimensions and is the proper approach for formulating general relations between dynamic moduli.

Taking Fourier transforms (FT) of (9) and (25) yields respectively

elastic $\implies \bar{\sigma}_{11}^e(x, \omega) = \bar{E}_{1111}^e(x, \omega) \bar{\epsilon}_{11}^e(x, \omega) - 2 \bar{E}_{1122}^e(x, \omega) \overline{\bar{\nu}_{12} \epsilon_{11}^e}(x, \omega), \quad (26)$

viscoelastic $\implies \bar{\sigma}_{11}(x, \omega) = \bar{E}_{1111}(x, \omega) \bar{\epsilon}_{11}(x, \omega) - 2 \bar{E}_{1122}(x, \omega) \overline{\bar{\nu}_{12} \epsilon_{11}}(x, \omega). \quad (27)$

It can be readily seen that (26) and (27) are not in the proper form for the correspondence principle to be applicable, since they contain the transforms of the Class I PR and strain as opposed to the necessary product of the transforms, i.e. $\overline{\bar{\nu}_{12} \epsilon_{11}} \neq \bar{\nu}_{12} \bar{\epsilon}_{11}$. This inequality can be removed if and only if either the PR or the strain or both are time-independent or if and only if the strains are separable functions as described in (1). Time independent strains are the degenerate case of relations (1). Additional examples are analyzed in detail in the next section.

The relationship between relaxation moduli $G(t)$, compliances $C(t)$ and relaxation and creep functions $\Phi(t)$ and $\Psi(t)$ in the Fourier transform space is

$$\bar{C}(x, \omega) = \frac{1}{\bar{G}(x, \omega)} = i \omega \bar{\Psi}(x, \omega) = \frac{1}{i \omega \bar{\Phi}(x, \omega)}; \tag{28}$$

see [Christensen 1982; Hilton 1964]. The Laplace transform can be obtained from the FT as

$$\text{LT}\{f(x, t)\} = \bar{f}(x, p) = \bar{f}(x, \omega)|_{i \omega = 1/p} \tag{29}$$

These proper definitions then lead to shear viscoelastic constitutive relations

$$\epsilon_S(x, t) = \int_{-\infty}^t C(t-t') \sigma_S(x, t') dt' = \int_{-\infty}^t \Psi(t-t') \frac{\partial \sigma_S(x, t')}{\partial t'} dt' = \int_{-\infty}^t \frac{\partial \Psi(t-t')}{\partial t'} \sigma_S(x, t') dt' \tag{30}$$

and

$$\sigma_S(x, t) = \int_{-\infty}^t G(t-t') \epsilon_S(x, t') dt' = \int_{-\infty}^t \Phi(t-t') \frac{\partial \epsilon_S(x, t')}{\partial t'} dt' = \int_{-\infty}^t \frac{\partial \Phi(t-t')}{\partial t'} \epsilon_S(x, t') dt'. \tag{31}$$

With similar expressions for the normal stresses and strains given by

$$\begin{aligned} \epsilon_{ii}(x, t) &= \sum_{k=1}^3 \int_{-\infty}^t C_{ii kk}^N(x, t-t') \sigma_{kk}(x, t') dt' \\ &= \sum_{k=1}^3 \int_{-\infty}^t \Psi_{ii kk}^N(x, t-t') \frac{\partial \sigma_{kk}(x, t')}{\partial t'} dt' = \sum_{k=1}^3 \int_{-\infty}^t \frac{\partial \Psi_{ii kk}^N(x, t-t')}{\partial t'} \sigma_{kk}(x, t') dt' \end{aligned} \tag{32}$$

and

$$\begin{aligned} \sigma_{ii}(x, t) &= \sum_{k=1}^3 \int_{-\infty}^t E_{ii kk}(x, t-t') \epsilon_{kk}(x, t') dt' \\ &= \sum_{k=1}^3 \int_{-\infty}^t \Phi_{ii kk}^N(x, t-t') \frac{\partial \epsilon_{kk}(x, t')}{\partial t'} dt' = \sum_{k=1}^3 \int_{-\infty}^t \frac{\partial \Phi_{ii kk}^N(x, t-t')}{\partial t'} \epsilon_{kk}(x, t') dt'. \end{aligned} \tag{33}$$

The shear constitutive equations are

$$\sigma_{ij}(x, t) = 2 \int_{-\infty}^t G(x, t-t') \epsilon_{ij}(x, t') dt', \quad i \neq j. \tag{34}$$

Application of Fourier transforms leads to

$$\bar{\sigma}_{ii}(x, \omega) = \sum_{k=1}^3 \bar{E}_{ii kk}(x, \omega) \bar{\epsilon}_{kk}(x, \omega), \tag{35}$$

$$\bar{\sigma}_{ij}(x, \omega) = 2 \bar{G}(x, \omega) \bar{\epsilon}_{ij}(x, \omega), \quad i \neq j, \tag{36}$$

which leads to the proper elastic-viscoelastic correspondence principle in terms of relaxation moduli.

2. The elastic-viscoelastic correspondence principle or analogy

Class I Poisson ratios: original definition. The elastic-viscoelastic analogy cannot be expressed in terms of PRs with classical definitions of (7) and (19) when these elastic or viscoelastic PRs are functions of time, since

$$\begin{aligned} \bar{\bar{\epsilon}}_{22}(x, \omega) &= \overline{\overline{v_{12} \epsilon_{11}}}(x, \omega) = \int_{-\infty}^{\infty} v_{12}(x, t) \epsilon_{11}(x, t) \exp(-i \omega t) dt \\ &\neq \bar{v}_{12}(x, \omega) \bar{\bar{\epsilon}}_{11}(x, \omega) = \int_{-\infty}^{\infty} v_{12}(x, t) \exp(-i \omega t) dt \int_{-\infty}^{\infty} \epsilon_{11}(x, t) \exp(-i \omega t) dt; \end{aligned} \quad (37)$$

the inequality arises because the quantity on the first line of (37) is the transform of the v and ϵ_{11} product, while the one on the second line is a product of their individual transforms. Either elastic and viscoelastic PR will be time independent if and only if all the strains are time-independent or separable functions of space and time with identical time functions [Hilton and Yi 1998; Hilton 2001].

Similarly, the elastic PR relation (14) is not receptive to the application of the elastic-viscoelastic correspondence principle, since, by virtue of (27),

$$\bar{v}_{12}(x, \omega) \neq \frac{1 - 2 \bar{G}(x, \omega) / \bar{K}(x, \omega)}{2(1 + \bar{G}(x, \omega) / \bar{K}(x, \omega))} \quad (38)$$

except for incompressible materials when $K(x, t) \rightarrow \infty$ and $v_{12} \rightarrow 0.5$.

If classical (Class I) Poisson ratios are introduced into the isotropic constitutive relations, then from (19) one obtains their FT as the transform of the products and not the product of the transforms as is required for the correspondence principle [Hilton 1996; 2001; Hilton and Yi 1998]. This can be readily seen by substituting (27) into (36), resulting in

$$\begin{aligned} \bar{\bar{\sigma}}_{ii}(x, \omega) &= \bar{\bar{E}}_{iiii}(x, \omega) \bar{\bar{\epsilon}}_{ii}(x, \omega) - 2 \bar{\bar{E}}_{iikk}(x, \omega) \underbrace{\overline{\overline{v_{ik} \epsilon_{ii}}}}(x, \omega), \quad i \neq k. \\ &= -\bar{\bar{\epsilon}}_{kk}(x, \omega) \end{aligned} \quad (39)$$

This is not the proper form of the elastic-viscoelastic correspondence principle and the analogy, therefore, fails to materialize. Upon inversion one obtains

$$\sigma_{ii}(x, t) = \int_{-\infty}^t \left(E_{iiii}(x, t-t') \epsilon_{ii}(x, t') - 2 E_{iikk}(x, t-t') \underbrace{v_{ik}(x, t') \epsilon_{ii}(x, t')}_{= -\epsilon_{kk}(x, t')} \right) dt', \quad i \neq k. \quad (40)$$

Consequently, the conventional isotropic elastic material property relations

$$G^e = \frac{E^e}{2(1 + \nu^e)} \quad \text{and} \quad K^e = \frac{E^e}{1 - 2\nu^e}, \quad (41)$$

involving the Young's (E^e), shear (G^e) and bulk (K^e) moduli together with PRs, have no counterpart in viscoelasticity except, when PRs are time-independent, because of the inability to arrive at corresponding Laplace or Fourier transforms of ν^e and ν . Therefore

$$\bar{G} \neq \frac{\bar{E}}{2(1 + \bar{\nu})} \quad \text{and} \quad \bar{K} \neq \frac{\bar{E}}{1 - 2\bar{\nu}} \quad \text{and} \quad \bar{\nu} \neq \frac{1 - 2 \bar{G} / \bar{K}}{2(1 + \bar{G} / \bar{K})}, \quad (42)$$

due to (37). Unfortunately, these inequalities prevent conversion by the correspondence principle of the extensive elastic formulas developed in [Hahn 1980] and further amplified in [Whitney and McCullough 1990]. However, relations involving only moduli, such as

$$E^e = \frac{3 G^e}{1 + G^e/K^e}, \tag{43}$$

possess an equivalent viscoelastic integral transform expression of the type

$$\bar{\bar{E}}(x, \omega) = \frac{3 \bar{\bar{G}}(x, \omega)}{1 + \bar{\bar{G}}(x, \omega)/\bar{\bar{K}}(x, \omega)}. \tag{44}$$

Hence, the integral transform elastic-viscoelastic analogy cannot involve Poisson's ratios, except when the viscoelastic PRs are time-independent, with all the attendant severe restrictions outlined above and developed in detail in [Hilton 1996; 2001; Hilton and Yi 1998].

Class II Poisson ratios: one strain component, time-independent. Class II is a special degenerate case of Class I with a time-independent loaded direction strain $\epsilon_{11}(x)$. Taking the FT of (20) leads to

$$\bar{v}_{1j}^C(x, \omega) \epsilon_{11}(x) = \bar{\bar{\epsilon}}_{jj}(x, \omega), \quad j \neq 1, \tag{45}$$

with corresponding constitutive FT relations

$$\bar{\sigma}_{ii}(x, \omega) = (\bar{\bar{E}}_{ii11}(x, \omega) - 2 \bar{\bar{E}}_{iikk}(x, \omega) \bar{v}_{1k}^C(x, \omega)) \epsilon_{11}(x), \quad k \neq i, k \neq 1. \tag{46}$$

which inverts to

$$\sigma_{ii}(x, t) = E_{ii11}(x, t) \epsilon_{11}(x) - 2 \int_{-\infty}^t E_{iikk}(x, t-t') \underbrace{v_{1k}^C(x, t') \epsilon_{11}(x)}_{= -\epsilon_{kk}(x, t')} dt', \quad k \neq i, k \neq 1. \tag{47}$$

This indicates that for this special case, the elastic-viscoelastic analogy is applicable in the FT space even though the PR is time-dependent, but one of the normal strains, $\epsilon_{11}(x)$, must be time-independent. However, (46) cannot be generalized to and are inapplicable for time-dependent strains $\epsilon_{11}(x, t)$, which have to be treated as Class I PRs. (See (25) and (27).)

Class III Poisson ratios: alternate definition based on Fourier transforms. The alternate or transform Poisson ratio [Hilton and Yi 1998] defined by (21) will change the FT of (39) to

$$\bar{\sigma}_{ii}(x, \omega) = (\bar{\bar{E}}_{iiii}(x, \omega) - 2 \underbrace{\bar{\bar{E}}_{iikk}(x, \omega) \bar{v}_{ik}^A(x, \omega)}_{= \bar{\bar{E}}_{iikk}^A(x, \omega)}) \bar{\bar{\epsilon}}_{ii}(x, \omega), \quad k \neq i, \tag{48}$$

with an inverse relation

$$\sigma_{ii}(x, t) = \int_{-\infty}^t (E_{iiii}(x, t-t') - 2 E_{iikk}^A(x, t-t')) \epsilon_{ii}(x, t') dt', \tag{49}$$

where

$$E_{iikk}^A(x, t) = \int_{-\infty}^t E_{iikk}(x, t-t') v_{ik}^A(x, t') dt' = \int_{-\infty}^t E_{iikk}(x, t) v_{ik}^A(x, t-t') dt'. \tag{50}$$

The form (49) restores a format for the correspondence principle in terms of a pseudo relaxation modulus E_{iikk}^A . It must be remembered, however, that neither v_{ij}^A nor \bar{v}_{ij}^A is a physical quantity.

These inherent difficulties associated with viscoelastic PRs stem from the fact that unlike moduli, compliances, relaxation and creep functions, etc., PRs are “derived” rather than fundamental material properties, as seen from (19) and (20)–(23) and discussed in detail in [Hilton 2001]. All but one of these five do not accommodate the elastic-viscoelastic correspondence principle. However, the alternate PR definition based on Fourier transforms [Hilton and Yi 1998], namely

$$\bar{v}_{ij}^A(x, \omega) = - \frac{\bar{\bar{\epsilon}}_{jj}(x, \omega)}{\bar{\bar{\epsilon}}_{ii}(x, \omega)} \quad \text{and} \quad \epsilon_{jj}(x, t) = - \int_{-\infty}^t v_{ij}^A(x, t-t') \epsilon_{ii}(x, t') dt', \quad i \neq j, \quad (51)$$

lends itself to an elastic-viscoelastic analogy in terms of \bar{v}_{ij}^A , but this alternate or transform PR has no physical counter part nor relation to the the classical PR as given by (7) and (37). Furthermore, the Class III PR bears no relation to its classical Class I counterpart

$$v_{ij}^A(x, t) = - \int_{-\infty}^{\infty} \frac{\bar{\bar{\epsilon}}_{jj}(x, \omega)}{\bar{\bar{\epsilon}}_{ii}(x, \omega)} \exp(i \omega t) d\omega \neq v_{ij}(x, t), \quad i \neq j. \quad (52)$$

The viscoelastic PR situation is further aggravated since under many conditions classical (19) and alternate PRs (51) become stress as well as time-dependent for linear viscoelastic materials [Hilton and Yi 1998; Hilton 2001]. Therefore, unlike relaxation moduli and creep compliances which in the linear case are stress independent, viscoelastic PRs in any form are not global material properties which can be used interchangeably among different loading conditions without re-computation to fit each specific set of conditions and time histories.

Class IV Poisson ratios: Hencky definition. The Hencky definition of (22) does not lend itself to any form of the elastic-viscoelastic analogy because of its inherent presence of the logarithmic terms.

Class V Poisson ratios: strain velocity ratios. For this PR class one can use the relaxation form of (33) and substitute the PR from (23) to yield

$$\sigma_{ii}(x, t) = \int_{-\infty}^t \left(\Phi_{iii}^N(x, t-t') - 2 \Phi_{iikk}^N(x, t-t') \frac{\partial v_{ik}^V(x, t')}{\partial t'} \right) \frac{\partial \epsilon_{ii}(x, t')}{\partial t'} dt' \quad k \neq i \quad (53)$$

There are visible similarities between Class I and V definitions and, hence, it is not surprising that the velocity based PR suffers from the same limitations as the Class I representation since

$$\overline{\overline{\frac{\partial v_{ik}^V}{\partial t} \frac{\partial \epsilon_{ii}}{\partial t}}}(x, \omega) = \int_{-\infty}^{\infty} \frac{\partial v_{ik}^V(x, t)}{\partial t} \frac{\partial \epsilon_{ii}(x, t)}{\partial t} \exp(-i \omega t) dt = \overline{\overline{\frac{\partial \epsilon_{kk}}{\partial t}}}(x, \omega) \quad k \neq i \quad (54)$$

This leads to constitutive relations in the FT domain

$$\bar{\bar{\sigma}}_{ii}(x, \omega) = i \omega \bar{\bar{\Phi}}_{iii}^N(x, \omega) \bar{\bar{\epsilon}}_{ii}(x, \omega) - 2 \bar{\bar{\Phi}}_{iikk}^N(x, \omega) \overline{\overline{\frac{\partial v_{ik}^V}{\partial t} \frac{\partial \epsilon_{ii}}{\partial t}}}(x, \omega), \quad k \neq i, \quad (55)$$

and, therefore, is not suited for any form of the elastic-viscoelastic analogy.

3. The seldom time-independent viscoelastic Poisson ratio

In elasticity time-independent strains can be achieved only under time-independent stresses and displacements regardless of boundary conditions. In viscoelasticity time free strains are attainable under considerably more restrictive conditions. (15) can be inverted in order to express strains in terms stress as

$$\epsilon_{ii}(x, t) = \sum_{j=1}^3 \int_{-\infty}^t C_{ii jj}(x, t - t') \sigma_{jj}(x, t') dt', \tag{56}$$

with compliances defined by (28).

As has been pointed out in [Hilton and Yi 1998; Hilton 2001] and as can be seen from (19), the viscoelastic PRs are time-independent if and only if the corresponding viscoelastic solution is separable into products of temporal and spatial parts, such that

$$E_{ijkl}(x, t) = F(t) E_{ijkl}^*(x), \quad C_{ijkl}(x, t) = F_c(t) C_{ijkl}^*(x), \tag{57}$$

$$\epsilon_{ij}(x, t) = h(t) \epsilon_{ij}^e(x), \quad \sigma_{ij}(x, t) = g(t) \sigma_{ij}^e(x), \tag{58}$$

with

$$g(t) = \int_{-\infty}^t F(t - t') h(t') dt' \quad \text{or} \quad h(t) = \int_{-\infty}^t F_c(t - t') g(t') dt' \tag{59}$$

depending on whether $g(t)$ or $h(t)$ is defined *a priori* on the boundary. It must be emphasized that the requirement that the E_{ijkl} and C_{ijkl} all have the same time functions has serious implications. In isotropic viscoelasticity it means that the shear and bulk relaxation moduli all must have identical time functions, which is not the case in real materials. It is not uncommon to witness bulk moduli with relaxation times three to six orders of magnitude larger than those of shear moduli. Therefore, the requirements on the $F(t)$ and $F_c(t)$ functions of (57) are unrealistic means to simply achieve the desired time-independent PRs.

These severe restrictions necessary for the existence of separable variable solutions are discussed in [Hilton 1996; 1964; Alfrey 1944; 1948; Christensen 1982]. Each and every one of the following conditions must be enforced for separation of variable formulations to exist:

- Elastic and viscoelastic materials must be isotropic, homogeneous and incompressible with $\nu^e(t) = \nu(t) = \frac{1}{2}$.
- No dynamic effects and no body forces can be included.
- No moving boundaries, i.e., no penetration or ablation problems, and boundary surface $\Gamma = \Gamma(x)$ only.
- No mixed boundary conditions; only separable stress or separable displacement BCs may be prescribed, i.e.,

$$\sigma_{ij}(x, t) = g(t) \sigma_{ij}^*(x) = g(t) n_i(x) X_j^*(x) \quad \text{on } \Gamma(x) \tag{60}$$

or

$$u_i(x, t) = h(t) U_i^*(x) \quad \text{on } \Gamma(x). \tag{61}$$

- No thermal expansions, i.e. $\alpha T = 0$, except for special cases of stress free boundaries [Hilton and Russell 1961].

- Only separable functions for material properties are permissible (relaxation moduli, compliances, etc.; see (57)).
- Viscoelastic materials must be isotropic [Hilton 1996].
- Relaxation moduli in all directions must have the same separable time function as defined by (57), but $K(x, t) \rightarrow \infty$. An exception occurs when $E(t)$, $G(t)$ and $K(t)$ all obey the same time functions:

$$\frac{E(t)}{E_0} = \frac{G(t)}{G_0} = \frac{K(t)}{K_0} = \mathcal{F}(t), \tag{62}$$

and then $-1 \leq \nu_0 \leq 0.5$. The equal relaxation time function concept was first introduced in [Tsien 1950] and its implications and limitations are discussed in detail in [Hilton 1996]. A time-independent PR other than 0.5 must satisfy the conditions

the special case $\implies \frac{\bar{E}}{\bar{G}} = \frac{E_0}{G_0} = 2(1 + \nu_0) = \frac{3}{1 + G_0/K_0}$ (63)

Having $E(t) \sim G(t)$ is physically achievable, but bulk relaxation moduli generally have relaxation times 3 to 5 orders of magnitude larger than those for $E(t)$ [Hilton 1996; 2001; Hilton and Yi 1998; Qvale and Ravi-Chandar 2004]. (See Figure 1.)

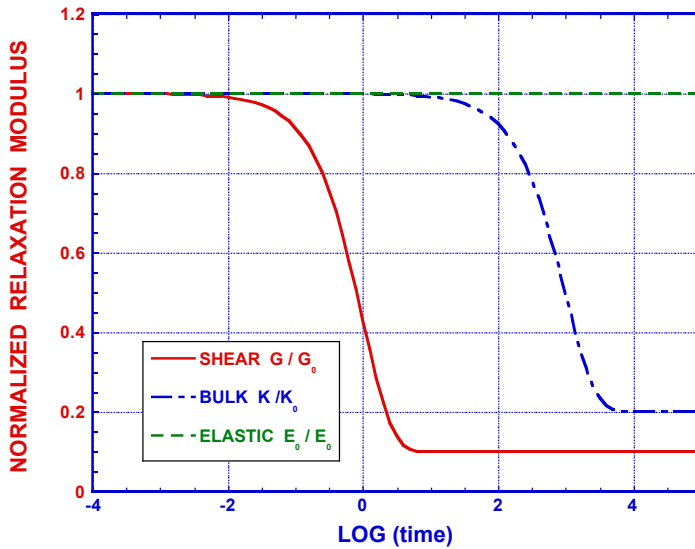


Figure 1. Elastic and viscoelastic relaxation moduli.

One can next ask whether it is possible to obtain a time-independent Class II PR. An examination of (45) indicates that this can only occur if all normal strains are time-independent, i.e., $\epsilon_{jj} = \epsilon_{jj}(x)$.

Consider an isothermal isotropic material with a special 1-D loading in the x_1 direction, such that

$$\epsilon_{11}(x) = \int_{-\infty}^t \overbrace{C_{1111}(x, t-t')}^{= C(x, t-t')} \sigma_{11}(x, t') dt' \tag{64}$$

and

$$\sigma_{11}(x, t) = \int_{-\infty}^t \overbrace{E_{1111}(x, t-t')}^{= E(x, t-t')} \epsilon_{11}(x) dt', \tag{65}$$

indicating that the one-dimensional relaxation stress $\sigma_{11}(x, t)$ necessary to maintain a time-independent strain $\epsilon_{11}(x)$ in the loaded direction must be time-dependent. Similarly, the strains in the other two normal directions are

$$\epsilon_{22}(x, t) = \epsilon_{33}(x, t) = \int_{-\infty}^t \left(C_{2211}(x, t-t') \underbrace{\int_{-\infty}^{t'} E_{1111}(x, t-s) \epsilon_{11}(x) ds}_{= \sigma_{11}(x, t')} \right) dt'. \tag{66}$$

Consequently, these two strains cannot be time-independent in this one-dimensional configuration and a time-independent PR is impossible under this loading. On the other hand, a special three-dimensional loading with all $\sigma_{ii}(x, t)$ necessary to maintain time-independent strains can be imposed. Such a special stress field is material dependent and in a sense is specifically contrived to produce the desired time-independent strains leading to time independent Class II PRs.

4. Error analysis

Consider realistic simulations of a one-dimensional experiment consisting of a prismatic isotropic viscoelastic bar as described above where $\sigma_{11} \neq 0$ and all other $\sigma_{ij} = 0$. One generally measures $\epsilon_{11}(t)$ and $\sigma_{11}(t)$ and determines $C(t)$ or $E(t)$ from (64) or (65). This can be accomplished in either the time or FT or LT spaces by a least square fit of the the coefficients E_n and by using the approximation [Schapery 1962]

$$\tau_n = 10^n \tag{67}$$

such that

$$\text{FT} \implies \frac{\bar{\bar{\sigma}}_{11}(\omega)}{\bar{\bar{\epsilon}}_{11}(\omega)} = \bar{\bar{E}}(\omega) = \frac{E_\infty}{i \omega} + \sum_{n=1}^N \frac{E_n}{i \omega + 1/\tau_n}; \quad \text{LT} \implies \bar{\bar{E}}(p) = \bar{\bar{E}}(\omega)|_{i \omega = p}. \tag{68}$$

If one does not assume values of relaxation times as indicated in (67), then nonlinear algebraic solvers can be used to determine sets of E_n and τ_n from the experimental data. The number of terms N is selected to meet a prescribed accuracy of fit.

The experimental difficulties arise from attempts to simultaneously measure normal strains in the other directions, i.e., $\epsilon_{22}(t)$. Instead, a number of authors have assumed time-independent PRs $\nu_{AS} = \text{constant} \neq 0.5$, obtaining approximate shear and bulk relaxation moduli from

$$\bar{\bar{E}} = \frac{3 \bar{\bar{G}}}{1 + \bar{\bar{G}}/\bar{\bar{K}}} = \frac{1}{\bar{\bar{C}}} \quad \text{and} \quad \bar{\bar{G}}_{AS} \approx \frac{\bar{\bar{E}}}{2(1 + \nu_{AS})}, \tag{69}$$

and thereby creating an ill posed overdetermined problem, resulting in nonuniversal shear and bulk relaxation moduli G_{AS} and K_{AS} . The correct protocol for one-dimensional experiments is formulated in [Shtark et al. 2007].

An error analysis will be undertaken next to evaluate the effects of this PR assumption as part of a computational simulation. Consider a state of one-dimensional stress where σ_{11} and ϵ_{11} produce creep

compliances with $C_0 < C_\infty$ and of the forms

$$C(t) = C_\infty - (C_\infty - C_0) \exp\left(-\frac{t}{\tau_c}\right), \tag{70}$$

$$C_{2211}(t) = -C_{2211\infty} + (C_{2211\infty} - C_{22110}) \exp\left(-\frac{t}{\tau_{2211}}\right). \tag{71}$$

This is equivalent to determining any other two moduli such as $E(t)$, $G(t)$ and the bulk relaxation modulus $K(t)$. Note that as discussed in a previous section $\tau_K > \tau_G$, it follows from (69) and (72) that $\tau_c \neq \tau_{2211}$.

The exact strains for this illustrative example are obtained from the constitutive relations as

$$\bar{\epsilon}_{11} = \frac{\bar{\sigma}_{11}}{\bar{E}} = \frac{1 + \bar{G}/\bar{K}}{3\bar{G}} \bar{\sigma}_{11} = \bar{C} \bar{\sigma}_{11}, \tag{72}$$

$$\bar{\epsilon}_{22} = \frac{2\bar{G}/\bar{K} - 1}{2\bar{E} (1 + \bar{G}/\bar{K})} \bar{\sigma}_{11} = \frac{2\bar{G}/\bar{K} - 1}{6\bar{G}} \bar{\sigma}_{11} = \bar{C}_{2211} \bar{\sigma}_{11}, \tag{73}$$

and the shear and bulk moduli can be determined from (69) and (72) to be

$$\bar{G} = \frac{1}{2(\bar{C} - \bar{C}_{2211})} \quad \text{and} \quad \bar{K} = \frac{1}{\bar{C} + 2\bar{C}_{2211}}, \tag{74}$$

with $C(t) \geq 0$ and $C_{2211}(t) \leq 0$. Note that for $\bar{K}(\omega) \rightarrow \infty$ the compliance $\bar{C}_{2211}(\omega)$ tends to $-\bar{C}(\omega)/2$. As seen from (72) the simulation can also be formulated in terms of G and K instead of the C s above, but the latter approach renders the moduli/compliance relations considerably more involved.

The previously discussed exception of time-independent PRs with $\nu \neq .5$ is evident from (69) and (72) when $G(t) \sim K(t)$ and $\bar{G}/\bar{K} \rightarrow G_0/K_0$. Then

$$\nu_{12}(t) = -\frac{\epsilon_{22}(t)}{\epsilon_{11}(t)} \rightarrow -\frac{2G_0/K_0 - 1}{2(G_0/K_0 + 1)}. \tag{75}$$

On the other hand, it is quite evident from (72) that when $G(t)$ and $K(t)$ respond with different time functions, the isotropic compliances $C(t)$ and $C_{2211}(t)$ obey another set of two distinct time functions.

One can now compare exact $\bar{G}(\omega)$ with approximate $\bar{G}_{AS}(\omega)$ and obtain the error resulting from the introduction of ν_{AS}

$$\bar{G}_{err} = \frac{\bar{G} - \bar{G}_{AS}}{\bar{G}}, \tag{76}$$

where the variables without subscripts AS are exact quantities. Similarly, the error between approximate strains ϵ_{22AS} and correct strains is determined by

$$\epsilon_{22AS}(t) = -\nu_{AS} \epsilon_{11}(t) \quad \text{or} \quad \bar{\epsilon}_{22AS}(\omega) = -\nu_{AS} \bar{\epsilon}_{11}(\omega), \tag{77}$$

and for a one-dimensional loading from (72) one obtains

$$\bar{\epsilon}_{22}(\omega) = \frac{\bar{C}_{2211}(\omega)}{\bar{C}(\omega)} \bar{\epsilon}_{11}(\omega) \quad \text{with} \quad \bar{\epsilon}_{err}(\omega) = \frac{\bar{\epsilon}_{22}(\omega) - \bar{\epsilon}_{22AS}(\omega)}{\bar{\epsilon}_{22}(\omega)}. \tag{78}$$

Typical compliance values and the corresponding viscoelastic PR are displayed in Figure 2.

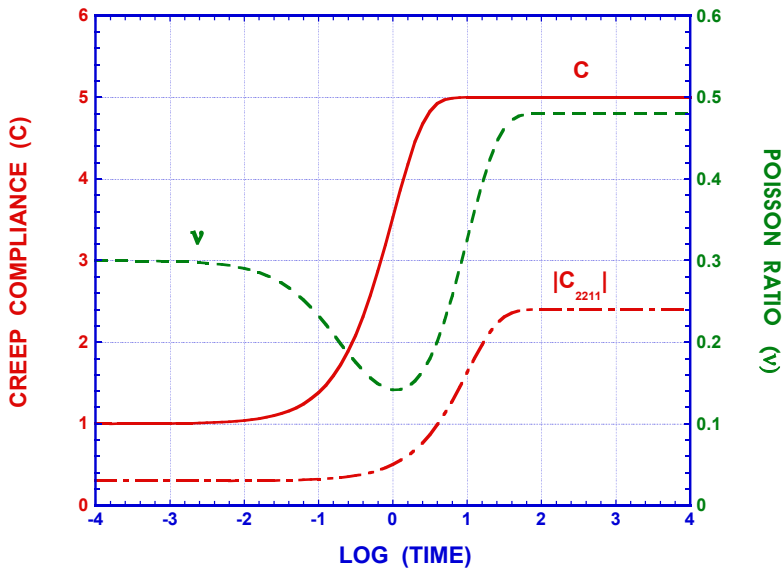


Figure 2. Compliances and PRs.

Note the pattern of initially decreasing from 0.3 and then rising PRs to a long time value of 0.48 for this configuration. Consequently, lower and upper limit estimations based on time-independent initial ν_{AS} and maximum values of 0.5 as was reported in [Therriault 2003] are erroneous and misleading, because they disregard the time history as exemplified by the constitutive relation convolution time integrals. Furthermore, such arbitrarily assumed time-independent PRs ν_{AS} do not even lead to upper and lower bounds which could replace and bracket the experimentally unrecorded relaxation moduli, strains, etc. This fact is further amplified by next examining the experimentally unmeasured shear relaxation moduli and strains in the direction normal to the one-dimensional loading.

Figure 3 depicts the per cent error between the exact LT shear modulus of (74) and the one based on assumed values of the PR ν_{AS} of (69). For this configuration, the estimates for shear moduli based on constant PR values of .3 and .5 lead to maximum errors in shear moduli of 43% and 56% respectively. Errors of such magnitude render the constant PR approach totally unsatisfactory and unacceptable for shear relaxation modulus determination from uniaxial experimental data with only single directional stress and strain measurements.

The errors between the LT of the unmeasured and exact strains ϵ_{22} for $0 \leq p \leq \infty$ or conversely for $\infty \geq t \geq 0$ are shown in Figure 4 based on (72).

It is patent from these graphs that the arbitrary selection of constant Poisson ratios — in the present examples PR values between 0.3 and 0.5 — produces errors in predicted unmeasured strains ϵ_{22} varying from 130% to 270% from the exact values. These errors are so excessive as to make the constant PR approach meaningless. These conclusions should come as no surprise, since earlier (and different) time-independent PR error analyses in [Hilton and Yi 1998] and [Hilton 2001] showed similar undesirable results.

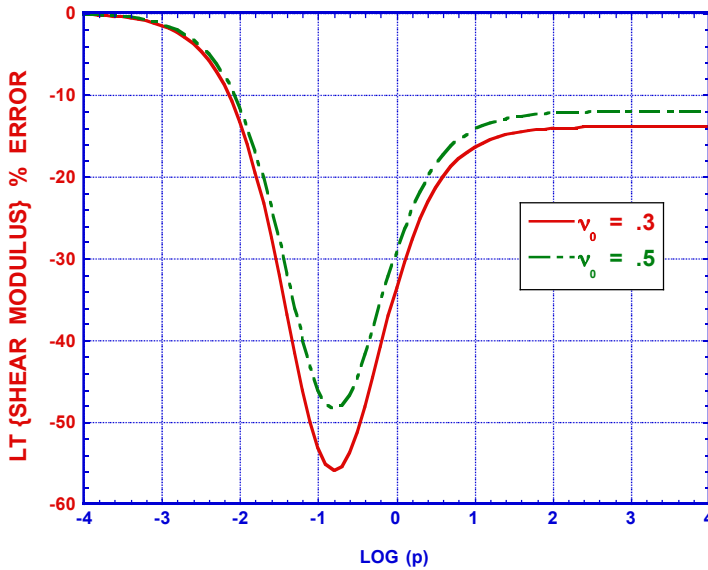


Figure 3. Percent shear modulus error.

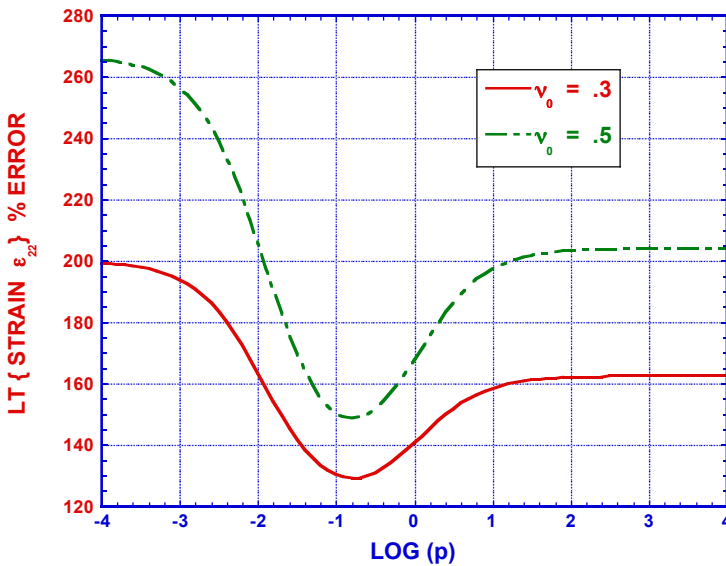


Figure 4. Percent Laplace transform transverse strain errors.

Furthermore, it can be readily seen from (77) and (69) that calculations based solely on the erroneous time-independent PR ν_{as} with values between 0.3 and 0.5 produce unmeasured strains ϵ_{22AS} which differ by 66.7% and corresponding changes in shear moduli G_{AS} of 76.9%. These errors are smaller than the true errors described in the preceding paragraph, but they are much too large to be acceptable in their own right. The generally accepted standard in deviations of elastic moduli is $\pm 3\%$. Although no firm equivalent standards has been established for viscoelastic relaxation moduli, material property characterization protocols based on arbitrarily defined time-independent PRs which yield different relaxation time

histories and maximum errors ranging from 43% to 67% must definitively be rejected as indefensible. (Note that the corresponding maximum strain errors are in excess of 250%.)

Different viscoelastic materials and other temperature conditions would change the specific numerical results, but would not alter the general large discrepancies between exact viscoelastic compliances, strains, PRs, etc. and those based on assumed time-independent values ν_{AS} . While the comparison were conducted in the LT space, the transforms can be inverted analytically or in the presence of complicated transforms by fast Fourier transform (FFT) protocols [van Loan 1992]. In the present simulations the LT results were not inverted into the time plane in order to avoid any additional possible errors resulting from the approximate IFFT.

In summary, the arguments advanced in [O'Brien et al. 2001; Zhu 2000; Shrotriya 2000; Shrotriya and Sottos 1998; Zhu et al. 2003; Andrianov et al. 2004; di Bernedetto et al. 2007; Noh and Whitcomb 2003] to mention a few, that analyses based on time-independent PRs are reasonable approximations to exact solutions — particularly for material characterizations — are disproved by the present simple simulations of exact conditions and their comparison with assumed time-independent PR responses.

5. Some illustrative examples

One-dimensional relaxation loading. The foregoing analysis has direct implications in a number of “simple” problems. Consider a prismatic viscoelastic bar subjected to a one-dimensional loading in the x_1 -direction with $\epsilon_{11}(x)$ only and a relaxation stress $\sigma_{11}(x, t)$ with all other $\sigma_{ij} = 0$. Clearly from (66) the other two normal strains are time-dependent and so is the classical PR, as well as the other PRs of Classes II through V.

Euler–Bernoulli viscoelastic beams. Another case in point is that of a prismatic, isotropic and isothermal Euler-Bernoulli viscoelastic beam of length L , moment of inertia I , height $2c$ and $h(x_2) < c$ the beam thickness or width with static loads $q(x_1)$ and statically determinate boundary conditions (Figure 5).

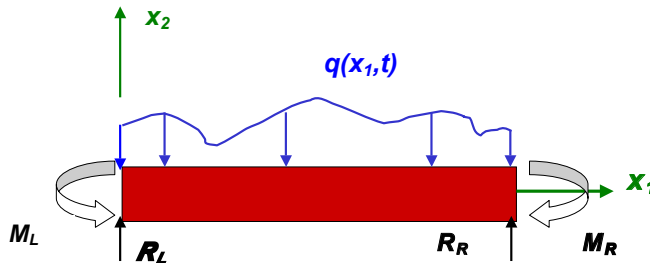


Figure 5. Viscoelastic beam.

Here the self-equilibrating bending and shear stresses are time-independent, but the strains and deflections are not since

$$\int_{-\infty}^t E(t - t') I \frac{\partial^4 w(x_1, t')}{\partial x_1^4} dt' = q(x_1), \quad 0 \leq x_1 \leq L, \tag{79}$$

or, taking the FT,

$$I \frac{\partial^4 \bar{w}(x_1, \omega)}{\partial x_1^4} = \bar{C}(\omega) \frac{q(x_1)}{i \omega}, \quad 0 \leq x_1 \leq L, \tag{80}$$

which upon inversion leads to

$$I \frac{\partial^4 w(x_1, t)}{\partial x_1^4} = q(x_1) \int_{-\infty}^t C(t-t') dt' = h(t) q(x_1), \quad 0 \leq x_1 \leq L, \tag{81}$$

with

$$\sigma_{11}(x_1, x_2) = \frac{M(x_1) x_2}{I} \quad \text{and} \quad \sigma_{12}(x_1, x_2) = \frac{1}{b(x_2)} \int_{x_2}^c \frac{\partial \sigma_{11}(x_1, x_2')}{\partial x_1} b(x_2') dx_2' \tag{82}$$

for $0 \leq x_1 \leq L$ and $-c \leq x_2 \leq c$.

In this special one-dimensional case, the strains are also separable functions by virtue of the constitutive relations (56) and (81), resulting in a time-independent PR with the required value of 0.5 and the mandatory incompressible material ($K \rightarrow \infty$). However, for an anisotropic beam made of say composite materials, no such separation of variables solution is admissible [Hilton 1996] and the corresponding PR for such beams must be time-dependent.

Furthermore, if the applied loads are time-dependent then (79) changes to

$$m \frac{\partial^2 w(x_1, t)}{\partial t^2} + \int_{-\infty}^t E(t-t') I \frac{\partial^4 w(x_1, t')}{\partial x_1^4} dt' = q(x_1, t), \quad 0 \leq x_1 \leq L, \tag{83}$$

and its solution is no longer separable even if the inertia term is neglected, unless the load is limited to the special expression $q(x_1, t) = g(t)f(x_1)$. In general the load can be represented by a Fourier series whose summands are of this form:

$$q(x_1, t) = \sum_{n=1}^{\infty} g_n(t) f_n(x_1), \quad 0 \leq x_1 \leq L, \tag{84}$$

and the deflection $w(x_1, t)$ will also be a sum of separable functions

$$w(x, t) = \sum_{n=1}^{\infty} h_n(t) W_n(x), \tag{85}$$

where each of the the functions $W_n(x)$ individually satisfy all boundary conditions for all $n \geq 1$.

In this case the PRs will be time-dependent regardless of whether or not the inertia term is included. Table 1 summarizes these effects.

Load	Inertia	E	Deflection	PR
$q(x_1)$	Yes or No	$F(t) E_{ijkl}^*(x_1)$	$h(t) w^*(x_1)$	$\nu(x_1) = 0.5$
$q(x_1)$	Yes or No	$E_{ijkl}(x_1, t)$	$w(x_1, t)$	$\nu(x_1, t)$
$g(t) q^*(x_1)$	No	$F(t) E_{ijkl}^*(x_1)$	$h(t) w^*(x_1)$	$\nu(x_1) = 0.5$
$g(t) q^*(x_1)$	Yes	$F(t) E_{ijkl}^*(x_1)$	$w(x_1, t)$	$\nu(x_1, t)$
$g(t) q^*(x_1)$	No	$E_{ijkl}(x_1, t)$	$w(x_1, t)$	$\nu(x_1, t)$
$q(x_1, t)$	Yes or No	$F(t) E_{ijkl}^*(x_1)$	$w(x_1, t)$	$\nu(x_1, t)$
$q(x_1, t)$	Yes or No	$E_{ijkl}(x_1, t)$	$w(x_1, t)$	$\nu(x_1, t)$

Table 1. Euler–Bernoulli bending effects on class I PR.

Viscoelastic Timoshenko beams. Although the definition of the elastic Timoshenko shear coefficient is somewhat arbitrary, in that it is based on equalities of strain energies [Bert 1973] or deformations [Cowper 1966] between exact and approximate solutions to mention a few examples, the concept leads to relatively simple expressions depending only on beam cross sectional geometry and its elastic material properties. However, under either definitions the shear coefficient is dependent on the elastic PR, thus making it impossible to construct an elastic-viscoelastic analogy for this problem [Hilton 2009]. Unfortunately, a number of authors [Therriault 2003; Nakao et al. 1985; Singh and Abdelnaser 1993; Chen 1995] including the present one [Hilton and Vail 1993], have misinterpreted the possibility of the K_{SC} analogy and used it in inappropriate and incorrect settings. Space limitations do not allow to present the correct solution for the viscoelastic Timoshenko beam here; for a complete treatment see [Hilton 2009].

6. Concluding remarks

Poisson ratios are defined quantities and not fundamental material properties such as relaxation moduli and creep compliances which can be derived from first principles through the latter's dependence on thermodynamic derivatives. In linear viscoelasticity PRs are functions of time and stresses as well as their time histories and, therefore, are not universal property parameters such as moduli and compliances. It is, therefore, best to formulate viscoelastic analyses in terms of relaxation moduli or creep compliances without involving Poisson ratios.

The following points emerge from the above analyses:

- (1) The fundamental problem with viscoelastic Poisson's ratios is not so much the diversity of their definitions, i.e. five classes, as it is with their proper use in constructing constitutive relations and correspondence principles involving PRs.
- (2) In general, viscoelastic Poisson ratios can be time-independent if and only if displacements, strains and stresses as well as relaxation moduli and creep compliances are all separable unequal functions in time and space, and then PRs are limited to a single value of 0.5 for incompressible materials.
- (3) A specific exception to the above exists if bulk, shear and Young's relaxation moduli obey identical time functions and stresses, displacements and moduli are separable spatial and temporal functions, then PRs are time-independent and in the elastic range $-1 \leq \nu \leq 0.5$. However, such a phenomenon where changes in shape and in volume exhibit the same time response remain unobserved in nature.
- (4) Linear viscoelastic PRs are not limited to the elastic value range and may exceed it considerably in either direction, because of their dependence on stresses and stress time histories [Shtark et al. 2007; Lakes 1991].
- (5) An assumption of time-independent viscoelastic Poisson ratios $\neq 0.5$ and without enforcement of the above enumerated conditions is not an admissible approximation, because ill posed overdeterminate problems result.
- (6) The conventional elastic-viscoelastic analogy does not apply to expressions involving elastic or viscoelastic PRs based on the classical Poisson and other definitions (Classes I, IV and V), as seen in Table 2.
- (7) Additionally, when the correspondence principle is inapplicable then no relations exist between complex PRs and complex moduli.

- (8) Class II PRs based on one time-independent normal strain are always time-dependent, unless constant volume deformations are maintained.
- (9) An elastic-viscoelastic correspondence principle based on the alternate Fourier transform PR definition (Class III) may be constructed, but these PRs have no physical counterparts.
- (10) Viscoelastic PRs are derived material properties and unlike relaxation moduli are neither universal nor path-independent of loading conditions, since they depend on stress (loading) conditions and relaxation/creep properties as well their time histories.
- (11) In the time space, it is possible to formulate viscoelastic constitutive relations in terms of PRs which bear resemblances to their elastic counterparts (Table 3). However, their forms do not lend themselves to the elastic-viscoelastic correspondence principle, except under very restrictive conditions; see Table 2.
- (12) Simulation study results displayed in Figures 2, 3, and 4 clearly demonstrate that even for a simple time independent loading shear relaxation modulus, PRs and strains based on time-independent PRs are no measure of the exact values of these variables as the former lead to excessively large errors (ranging from 130% to 270% for the strain error in the examples considered), and constitute extremely poor approximations. Furthermore, any such arbitrarily assumed time-independent PRs v_{AS} values do not lead to upper and lower bounds which could replace and bracket the experimentally unrecorded relaxation moduli, strains, etc.
- (13) The time dependence of viscoelastic PRs makes them unsuitable to be characterized from experimental data and measurements in two normal directions must be employed. Alternately, simultaneous loadings, such as tractions and twisting for instance, may be employed on the same specimen.

Class	Name	Viscoelastic Poisson's Ratio $i \neq j$	Eq.	Analogy	Eq.
I	Classical	$v_{ij}(x, t) \stackrel{\text{def}}{=} - \frac{\epsilon_{jj}(x, t)}{\epsilon_{ii}(x, t)}$	(19)	NO	(39)
II	Constant strain	$v_{ij}^C(x, t) \stackrel{\text{def}}{=} - \frac{\epsilon_{jj}(x, t)}{\epsilon_{ii}(x)}$	(20)	YES, but limited to $\epsilon_{11}(x)$ only	(47)
III	Transform	$\bar{v}_{ij}^A(x, \omega) \stackrel{\text{def}}{=} - \frac{\bar{\epsilon}_{jj}(x, \omega)}{\bar{\epsilon}_{ii}(x, \omega)}$	(21)	YES, but \bar{v}_{ij}^A has no physical meaning	(48)
IV	Hencky	$v_{ij}^H(x, t) \stackrel{\text{def}}{=} - \frac{\log(1 + \epsilon_{jj}(x, t))}{\log(1 + \epsilon_{ii}(x, t))}$	(22)	NO	–
V	Velocity	$\frac{\partial v_{ij}^V(x, t)}{\partial t} \stackrel{\text{def}}{=} - \frac{\partial \epsilon_{jj}(x, t) / \partial t}{\partial \epsilon_{ii}(x, t) / \partial t}$	(23)	NO	(54)

Table 2. Poisson ratio elastic-viscoelastic correspondence principle (analogy). See equations (19)–(23) for the bibliographical references for each class.

Class	Constitutive relations
I	$\bar{\sigma}_{ii}(x, \omega) = \bar{E}_{iiii}(x, \omega) \bar{\epsilon}_{ii}(x, \omega) - 2 \bar{E}_{iikk}(x, \omega) \overbrace{\bar{v}_{ik} \bar{\epsilon}_{ii}(x, \omega)}^{= -\bar{\epsilon}_{kk}(x, \omega)}, \quad i \neq k$
I	$\sigma_{ii}(x, t) = \int_{-\infty}^t (E_{iiii}(x, t-t') \epsilon_{ii}(x, t') - 2 E_{iikk}(x, t-t') \underbrace{v_{ik}(x, t') \epsilon_{ii}(x, t')}_{= -\epsilon_{kk}(x, t')}) dt', \quad i \neq k$
II	$\bar{\sigma}_{ii}(x, \omega) = \bar{E}_{ii11}(x, \omega) \epsilon_{11}(x) - 2 \bar{E}_{iikk}(x, \omega) \overbrace{\bar{v}_{1k}^C(x, \omega) \epsilon_{11}(x)}^{= -\bar{\epsilon}_{kk}(x, \omega)}, \quad k \neq i, k \neq 1$
II	$\sigma_{ii}(x, t) = E_{ii11}(x, t) \epsilon_{11}(x) - 2 \int_{-\infty}^t E_{iikk}(x, t-t') \underbrace{v_{1k}^C(x, t') \epsilon_{11}(x)}_{= -\epsilon_{kk}(x, t')} dt', \quad k \neq i, k \neq 1$
III	$\bar{\sigma}_{ii}(x, \omega) = (\bar{E}_{iiii}(x, \omega) - 2 \overbrace{\bar{E}_{iikk}(x, \omega) \bar{v}_{ik}^A(x, \omega)}^{= \bar{E}_{iikk}^A(x, \omega)}) \bar{\epsilon}_{ii}(x, \omega), \quad k \neq i$
III	$\sigma_{ii}(x, t) = \int_{-\infty}^t (E_{iiii}(x, t-t') - 2 E_{iikk}^A(x, t-t')) \epsilon_{ii}(x, t') dt', \quad k \neq i$
V	$\bar{\sigma}_{ii}(x, \omega) = \iota \omega \bar{\Phi}_{iiii}^N(x, \omega) \bar{\epsilon}_{ii}(x, \omega) - 2 \bar{\Phi}_{iikk}^N(x, \omega) \overbrace{\frac{\partial v_{ik}^V}{\partial t} \frac{\partial \epsilon_{ii}}{\partial t}(x, \omega)}^{\overline{\overline{\overline{\quad}}}}, \quad k \neq i$
V	$\sigma_{ii}(x, t) = \int_{-\infty}^t \left(\Phi_{ii11}^N(x, t-t') - 2 \Phi_{iikk}^N(x, t-t') \frac{\partial v_{ik}^V(x, t')}{\partial t'} \right) \frac{\partial \epsilon_{ii}(x, t')}{\partial t'} dt', \quad k \neq i$

Table 3. Linear isotropic constitutive relations with Poisson's ratios.

- (14) In the final analysis, relaxation moduli, compliances, and creep and relaxation functions should be the characterizations of choice since they do not suffer the severe limitations of PRs, such as — even for linear materials — dependence on stress, strain and displacement time histories. Furthermore, they properly allow use of the elastic-viscoelastic correspondence principle without additional constraints.

Acknowledgement

Support by grants from the Technology Research, Education and Commercialization Center (TRECC) of the National Center for Supercomputing Applications (NCSA) at the University of Illinois at Urbana-Champaign (UIUC) is gratefully acknowledged.

plus 1pt

References

- [Alfrey 1944] T. Alfrey, Jr., “Non-homogeneous stress in viscoelastic media”, *Quart. Appl. Math.* **2** (1944), 113–119.
- [Alfrey 1948] T. Alfrey, Jr., *Mechanical behavior of high polymers*, High Polymers **6**, Interscience, New York, 1948.
- [Andrianov et al. 2004] I. V. Andrianov, J. Awrejcewicz, and L. I. Manevich, *Asymptotical mechanics of thin-walled structures: a handbook*, Springer, Berlin, 2004. Pages 244–245.
- [di Bernedetto et al. 2007] H. di Bernedetto, B. Delaporte, and C. Sauzéat, “Three-dimensional linear behavior of bituminous materials: experiments and modeling”, *Int. J. Geomech. (ASCE)* **7**:2 (2007), 149–157.
- [Bert 1973] C. W. Bert, “Simplified analysis of static shear factors for beams of nonhomogeneous cross section”, *J. Compos. Mater.* **7**:4 (1973), 525–529.
- [Bertilsson et al. 1993] H. Bertilsson, M. Delin, J. Kubát, W. R. Rychwalski, and M. J. Kubát, “Strain rates and volume changes during short-term creep of PC and PMMA”, *Rheol. Acta* **32**:4 (1993), 361–369.
- [Bieniek et al. 1981] M. Bieniek, L. A. Henry, and A. M. Freudenthal, “One-dimensional response of linear visco-elastic media”, pp. 155–174 in *Selected papers by Alfred M. Freudenthal: civil engineering classics*, ASCE, New York, 1981.
- [Chen 1995] T.-M. Chen, “The hybrid Laplace transform/finite element method applied to the quasi-static and dynamic analysis of viscoelastic Timoshenko beams”, *Int. J. Numer. Methods Eng.* **38**:3 (1995), 509–522.
- [Christensen 1982] R. M. Christensen, *Theory of viscoelasticity: an introduction*, 2nd ed., Academic Press, New York, 1982.
- [Cowper 1966] G. R. Cowper, “The shear coefficient in Timoshenko’s beam theory”, *J. Appl. Mech. (ASME)* **33** (1966), 335–340.
- [Freudenthal and Henry 1960] A. M. Freudenthal and L. A. Henry, “On Poisson’s ratio in linear viscoelastic propellants”, pp. 33–66 in *Solid propellant rocket research: a selection of technical papers based mainly on a symposium of the American Rocket Society* (Princeton University, 1960), Progress in Astronautics and Rocketry **1**, Academic Press, New York, 1960.
- [Giovagnoni 1994] M. Giovagnoni, “On the direct measurement of the dynamic Poisson’s ratio”, *Mech. Mater.* **17**:1 (1994), 33–46.
- [Gottenberg and Christensen 1963] W. G. Gottenberg and R. M. Christensen, “Some interesting aspects of general linear viscoelastic deformation”, *J. Rheol.* **7**:1 (1963), 171–180.
- [Hahn 1980] H. T. Hahn, “Simplified formulas for elastic moduli of unidirectional continuous fiber composites”, *Compos. Technol. Rev.* **2** (1980), 5–7.
- [Hilton 1964] H. H. Hilton, “An introduction to viscoelastic analysis”, pp. 199–276 in *Engineering design for plastics*, edited by E. Baer, Reinhold, New York, 1964.
- [Hilton 1996] H. H. Hilton, “On the inadmissibility of separation of variables solutions in linear anisotropic viscoelasticity”, *Mech. Compos. Mater. Struct.* **3**:2 (1996), 97–100.
- [Hilton 2001] H. H. Hilton, “Implications and constraints of time-independent Poisson ratios in linear isotropic and anisotropic viscoelasticity”, *J. Elasticity* **63**:3 (2001), 221–251.
- [Hilton 2003] H. H. Hilton, “Comments regarding ‘Viscoelastic properties of an epoxy resin during cure’ by D. J. O’Brien, P. T. Mather and S. R. White”, *J. Compos. Mater.* **37**:1 (2003), 89–94.
- [Hilton 2009] H. H. Hilton, “Viscoelastic Timoshenko beam theory”, *Mech. Time-Depend. Mat.* **13**:1 (2009), 1–10.
- [Hilton and Clements 1964] H. H. Hilton and J. R. Clements, “Formulation and evaluation of approximate analogies for temperature dependent linear viscoelastic media”, pp. 17–24 (Section 6) in *Thermal loading and creep in structures and components* (London, 1964), Proc. Institution of Mechanical Engineers **178**/3L, Inst. Mech. Eng., London, 1964.
- [Hilton and Dong 1965] H. H. Hilton and S. B. Dong, “An analogy for anisotropic, nonhomogeneous, linear viscoelasticity including thermal stresses”, pp. 58–73 in *Developments in mechanics: proceedings of the 8th Midwestern Mechanics Conference* (Case Institute of Technology, 1963), vol. 2, edited by S. Ostrach and R. H. Scanlan, Pergamon, Oxford, 1965.
- [Hilton and El Fouly 2007] H. H. Hilton and A. R. A. El Fouly, “Designer auxetic viscoelastic sandwich column materials tailored to minimize creep buckling failure probabilities and prolong survival times”, in *48th AIAA/ASME/ASCE/AHS Structures, Structural Dynamics and Materials Conference* (Honolulu, HI, 2007), AIAA, Reston, VA, 2007. Paper #2007–2400.

- [Hilton and Piechocki 1962] H. H. Hilton and J. J. Piechocki, "Shear center motion in beams with temperature-dependent linear elastic or viscoelastic properties", pp. 1279–1289 in *Proceedings of the 4th U.S. National Congress of Applied Mechanics* (Berkeley, CA, 1962), vol. 2, edited by R. M. Rosenberg, ASME, New York, 1962.
- [Hilton and Russell 1961] H. H. Hilton and H. G. Russell, "An extension of Alfrey's analogy to thermal stress problems in temperature dependent linear viscoelastic media", *J. Mech. Phys. Solids* **9**:3 (1961), 152–164.
- [Hilton and Vail 1993] H. H. Hilton and C. F. Vail, "Bending-torsion flutter of linear viscoelastic wings including structural damping", pp. 1461–1481 in *34th AIAA/ASME/ASCE/AHS/ASC Structures, Structural Dynamics and Materials Conference* (La Jolla, CA, 1993), vol. 3, AIAA, Reston, VA, 1993. Paper #1993-1475.
- [Hilton and Yi 1998] H. H. Hilton and S. Yi, "The significance of anisotropic viscoelastic Poisson ratio stress and time dependencies", *Int. J. Solids Struct.* **35**:23 (1998), 3081–3095.
- [Hoke et al. 2001] W. E. Hoke, T. D. Kennedy, and A. Torabi, "Simultaneous determination of Poisson ratio, bulk lattice constant, and composition of ternary compounds: $\text{In}_{0.3}\text{Ga}_{0.7}\text{As}$, $\text{In}_{0.3}\text{Al}_{0.7}\text{As}$, $\text{In}_{0.7}\text{Ga}_{0.3}\text{P}$, and $\text{In}_{0.7}\text{Al}_{0.3}\text{P}$ ", *Appl. Phys. Lett.* **79**:25 (2001), 4160–4162.
- [Jin 2006] Z.-H. Jin, "Some notes on the linear viscoelasticity of functionally graded materials", *Math. Mech. Solids* **11**:2 (2006), 216–224.
- [Jin and Paulino 2002] Z.-H. Jin and G. H. Paulino, "A viscoelastic functionally graded strip containing a crack subjected to in-plane loading", *Eng. Fract. Mech.* **69**:14–16 (2002), 1769–1790.
- [Klasztorny 2004] M. Klasztorny, "Constitutive compliance/stiffness equations of viscoelasticity for resins", pp. 245–254 in *Computational methods in materials characterisation* (Santa Fe, NM, 2003), edited by A. A. Mammoli and C. A. Brebbia, High Performance Structures and Materials **6**, WIT, Southampton, 2004.
- [Ko et al. 2003] S.-C. Ko, S. Lee, and C.-H. Hsueh, "Viscoelastic stress relaxation in film/substrate systems: Kelvin model", *J. Appl. Phys.* **93**:5 (2003), 2453–2457.
- [Lakes 1991] R. S. Lakes, "The time dependent Poisson's ratio of viscoelastic cellular materials can increase or decrease", *Cell. Polymers* **10** (1991), 466–469.
- [Lakes and Wineman 2006] R. S. Lakes and A. Wineman, "On Poisson's ratio in linearly viscoelastic solids", *J. Elasticity* **85**:1 (2006), 45–63.
- [Lakes et al. 1979] R. S. Lakes, J. L. Katz, and S. S. Sternstein, "Viscoelastic properties of wet cortex bone, I: Torsional and biaxial studies", *J. Biomech.* **12**:9 (1979), 657–675.
- [Lee 1955] E. H. Lee, "Stress analysis in viscoelastic materials", *Quart. Appl. Math.* **13** (1955), 665–672.
- [Librescu and Chandiramani 1989a] L. Librescu and K. N. Chandiramani, "Recent results concerning the stability of viscoelastic shear deformable plates under compressive edge loads", *Solid Mech. Arch.* **14** (1989), 215–250.
- [Librescu and Chandiramani 1989b] L. Librescu and N. K. Chandiramani, "Dynamic stability of transversely isotropic viscoelastic plates", *J. Sound Vib.* **130**:3 (1989), 467–486.
- [van Loan 1992] C. van Loan, *Computational frameworks for the fast Fourier transform*, Frontiers in Applied Mathematics **10**, SIAM, Philadelphia, 1992.
- [Mead and Joannides 1991] D. J. Mead and R. J. Joannides, "Measurement of the dynamic moduli and Poisson's ratios of a transversely isotropic fibre-reinforced plastics", *Composites* **22**:1 (1991), 15–29.
- [Nakao et al. 1985] T. Nakao, T. Okano, and I. Asano, "Theoretical and experimental analysis of flexural vibration of the viscoelastic Timoshenko beam", *J. Appl. Mech. (ASME)* **52** (1985), 728–736.
- [Noh and Whitcomb 2003] J. Noh and J. Whitcomb, "Effect of transverse matrix cracks on the relaxation moduli of linear viscoelastic laminates", *J. Compos. Mater.* **37**:6 (2003), 543–558.
- [O'Brien et al. 2001] D. J. O'Brien, P. T. Mather, and S. R. White, "Viscoelastic properties of an epoxy resin during cure", *J. Compos. Mater.* **35**:10 (2001), 883–904.
- [Olesiak 1966] Z. Olesiak, "Thermal stresses in thin-walled cylindrical viscoelastic shells with temperature dependent properties", pp. 407–415 in *Theory of plates and shells: selected papers, presented to the Conference on the Theory of Two- and Three-dimensional Structures* (Smolenice, 1963), edited by J. Brilla and J. Balaš, Slovak Academy of Sciences, Bratislava, 1966.
- [Paulino and Jin 2001a] G. H. Paulino and Z.-H. Jin, "Correspondence principle in viscoelastic functionally graded materials", *J. Appl. Mech. (ASME)* **68**:1 (2001), 129–132.

- [Paulino and Jin 2001b] G. H. Paulino and Z.-H. Jin, “Viscoelastic functionally graded materials subjected to antiplane shear fracture”, *J. Appl. Mech. (ASME)* **68**:2 (2001), 284–293.
- [Pipkin 1972] A. C. Pipkin, *Lectures on viscoelasticity theory*, Applied Mathematical Sciences **7**, Springer, New York, 1972.
- [Poisson 1829] S. D. Poisson, “Mémoire sur l’équilibre et le mouvement des corps élastiques”, pp. 357–570 and 623–627 in *Mémoires de l’académie royal des sciences de l’institut de France*, vol. 8, Didot, Paris, 1829.
- [Qvale and Ravi-Chandar 2004] D. Qvale and K. Ravi-Chandar, “Viscoelastic characterization of polymers under multiaxial compression”, *Mech. Time-Depend. Mat.* **8**:3 (2004), 193–214.
- [Ravi-Chandar 1998] K. Ravi-Chandar, “Simultaneous measurement of nonlinear bulk and shear relaxation behavior”, pp. 30–31 in *2nd International Conference on Mechanics of Time Dependent Materials: Proceedings* (Pasadena, CA, 1998), edited by I. Emri and W. G. Knauss, SEM - Center for Time Dependent Materials, Ljubljana, 1998.
- [Ravi-Chandar and Ma 2000] K. Ravi-Chandar and Z. Ma, “Inelastic deformation in polymers under multiaxial compression”, *Mech. Time-Depend. Mat.* **4**:4 (2000), 333–357.
- [Read 1950] W. T. Read, Jr., “Stress analysis for compressible viscoelastic materials”, *J. Appl. Phys.* **21**:7 (1950), 671–674.
- [Schapery 1962] R. A. Schapery, “Approximate methods of transform inversion for viscoelastic stress analysis”, pp. 1075–1085 in *Proceedings of the 4th U.S. National Congress of Applied Mechanics* (Berkeley, CA), vol. 2, edited by R. M. Rosenberg, ASME, New York, 1962.
- [Shrotriya 2000] P. Shrotriya, *Dimensional stability of multilayer circuit boards*, Ph.D. thesis, University of Illinois at Urbana-Champaign, Department of Theoretical and Applied Mechanics, 2000.
- [Shrotriya and Sottos 1998] P. Shrotriya and N. R. Sottos, “Creep and relaxation behavior of woven glass/epoxy substrates for multilayer circuit board applications”, *Polymer Compos.* **19**:5 (1998), 567–578.
- [Shtark et al. 2007] A. Shtark, H. Grozbeyn, G. Sameach, and H. H. Hilton, “An alternate protocol for determining viscoelastic material properties based on tensile tests without use of Poisson’s ratio”, in *Proceedings of the 2007 International Mechanical Engineering Congress and Exposition* (Seattle, WA, 2007), ASME, New York, 2007. Paper #IMECE2007-41068.
- [Sim and Kim 1990] S. Sim and K.-J. Kim, “A method to determine the complex modulus and Poisson’s ratio of viscoelastic materials for FEM applications”, *J. Sound Vib.* **141**:1 (1990), 71–82.
- [Singh and Abdelnaser 1993] M. P. Singh and A. S. Abdelnaser, “Random vibrations of externally damped viscoelastic Timoshenko beams with general boundary conditions”, *J. Appl. Mech. (ASME)* **60**:1 (1993), 149–156.
- [Therriault 2003] D. Therriault, *Directed assembly of three-dimensional microvascular networks*, Ph.D. thesis, University of Illinois at Urbana-Champaign, Department of Aerospace Engineering, 2003.
- [Tschoegl 1997] N. W. Tschoegl, “Time dependence in material properties: an overview”, *Mech. Time-Depend. Mat.* **1**:1 (1997), 3–31.
- [Tschoegl et al. 2002] N. W. Tschoegl, W. G. Knauss, and I. Emri, “Poisson’s ratio in linear viscoelasticity: a critical review”, *Mech. Time-Depend. Mat.* **6**:1 (2002), 3–51.
- [Tsien 1950] H. S. Tsien, “A generalization of Alfrey’s theorem in viscoelastic media”, *Quart. Appl. Math.* **8** (1950), 104–106.
- [Vinogradov and Malkin 1980] G. V. Vinogradov and A. Y. Malkin, *Rheology of polymers: viscoelasticity and flow of polymers*, Mir, Moscow, 1980.
- [Whitney and McCullough 1990] J. M. Whitney and R. L. McCullough, *Delaware composites design encyclopedia, 2: Micromechanical materials modeling*, edited by L. A. Carlsson and J. W. Gillespie, Jr., Technomic, Lancaster, PA, 1990.
- [Zhu 2000] Q. Zhu, *Dimensional accuracy of thermoset polymers composites: process simulation and optimization*, Ph.D. thesis, University of Illinois at Urbana-Champaign, Department of Aerospace Engineering, 2000.
- [Zhu et al. 2003] Q. Zhu, P. Shrotriya, N. R. Sottos, and P. H. Geubelle, “Three-dimensional viscoelastic simulation of woven composite substrates for multilayer circuit boards”, *Compos. Sci. Technol.* **63**:13 (2003), 1971–1983.

Received 1 Oct 2008. Accepted 31 Dec 2008.

HARRY H. HILTON: h-hilton@illinois.edu

Aerospace Engineering Department (AE) and Technology Research, Education and Commercialization Center (TRECC), National Center for Supercomputing Applications (NCSA), University of Illinois at Urbana-Champaign, 104 South Wright Street, MC-236, Urbana, IL 61801-2935, United States

DYNAMIC BUCKLING OF A BEAM ON A NONLINEAR ELASTIC FOUNDATION UNDER STEP LOADING

MAHMOOD JABAREEN AND IZHAK SHEINMAN

An analytical model is presented for the nonlinear behavior of a beam on a nonlinear elastic foundation, subjected to sudden axial compression. Two dynamic buckling criteria, one based on full dynamic analysis (Budiansky–Roth) and the other on static analysis only (Hoff–Simitses), were applied. The effectiveness of the Hoff–Simitses criterion for structures characterized by a limit point was shown.

1. Introduction

Structures on a nonlinear elastic foundation are commonly used in engineering applications. Specifically, beams on such a foundation occupy a prominent place in structural mechanics, and can serve as a simplified model for complex nonlinear systems. The foundation can be characterized as either hardening or softening, the latter type being associated with a limit point behavior instead of bifurcation one.

Most research works on this subject were devoted to static stability, and much less (to the best of the authors' knowledge) to dynamic buckling, in spite of its practical importance. Specifically, [Weitsman \[1969\]](#) and [Kamiya \[1977\]](#) studied beams on a bimodulus and no-tension elastic foundation. The bifurcation-type behavior and the initial postbuckling one were addressed in [[Fraser and Budiansky 1969](#); [Amazigo et al. 1970](#); [Keener 1974](#); [Lee and Wass 1996](#); [Kounadis et al. 2006](#)]. [Sheinman and Adan \[1991\]](#) investigated the imperfection sensitivity of a beam on a nonlinear elastic foundation under static loading, including the effect of transverse shear deformation.

The term “dynamic buckling” refers to stability of a structure under time-dependent loads. It can also be used in a broader sense, covering stability analysis via the equations of motion, irrespective of the type of load. Accordingly, different dynamic buckling/stability criteria have been suggested [[Budiansky and Roth 1962](#); [Hsu 1966](#); [1967](#); [Hoff and Bruce 1954](#); [Simitses 1967](#); [1990](#)], mainly based on the concept of bounded motion as proof of dynamic buckling/stability.

The theory of dynamic buckling of systems with a single degree of freedom subjected to step loading was developed in [[Budiansky and Hutchinson 1966](#); [Hutchinson and Budiansky 1966](#); [Budiansky 1967](#); [Elishakoff 1980](#)]. These authors derived the relationships between the critical step load and the amplitude of the initial imperfection for structures with quadratic, cubic and quadratic-cubic nonlinearities. The effect of Rayleigh's dissipative forces was included in [[Kounadis and Raftoyiannis 1990](#)]. The extension of the aforementioned studies to potential and nonpotential systems with multiple degrees of freedom was developed in [[Kounadis et al. 1991](#); [Kounadis 1997](#); [Kounadis et al. 1997](#); [1999](#); [Raftoyiannis and Kounadis 2000](#); [Gantes et al. 2001](#); [Kounadis et al. 2001](#)]. A comprehensive review on the dynamic

Keywords: dynamic buckling, Hoff–Simitses, Budiansky–Roth, imperfection sensitivity, nonlinear elastic foundation.
The authors are indebted to Ing. E. Goldberg for editorial assistance.

buckling of elastic structures such as frames, arches, and shells can be found in [Simitzes 1990]. Specifically, Birman [1989] studied the dynamic buckling of antisymmetrically laminated angle-ply rectangular plates due to axial step loads. Dube et al. [2000] studied the dynamic buckling of laminated thick shallow spherical cap.

The present study deals jointly with dynamic buckling and imperfection sensitivity. The dynamic buckling load was obtained and examined using the Budiansky–Roth criterion [1962], for which a complex full dynamic analysis is needed, and also for the total potential energy criterion [Hoff and Bruce 1954; Simitzes 1967], where static nonlinear analysis suffices. The purpose of the comparison is to show the advantage in treating dynamic stability problems via the second, purely static, criterion.

The dynamic nonlinear partial differential equations are derived for a general beam on a nonlinear elastic foundation. These partial differential equation were reduced to ordinary nonlinear equations by introducing the Bathe composite method [Bathe and Baig 2005; Bathe 2007]. Then, the Newton–Raphson linearization, and finite difference scheme were used for solving the resulting nonlinear system of ordinary equations. An example of a beam on a softening foundation was considered to study the dynamic buckling and imperfection sensitivity under static and dynamic step loading.

2. Dynamic stability criteria

In the Budiansky and Roth criterion, the dynamic buckling load is defined as the level at which a large increase occurs in the displacement amplitude. In the Hoff–Simitzes criterion, the critical load is defined as the static postlimit load level at which the modified total potential energy is zero. The latter is obtained by subtracting the total potential energy of the unbuckled state from the total potential energy, thus eliminating all trajectories nested in the total potential energy but not leading to buckling. This criterion corresponds to the lower bound of the critical conditions; for example, for an external applied step load, and for autonomous mechanical systems in general.

3. Problem formulation and solution procedure

Figure 1 illustrates a beam on a nonlinear elastic foundation subjected to axial step loading. By Bernoulli–Euler beam theory, the equations of motion (with rotary inertia neglected) read

$$\begin{aligned}
 -\rho A\ddot{u} + N_{,xx,x} + q_u &= 0, \\
 -\rho A\ddot{w} + M_{,xx,xx} + (N_{,xx}(w_{,x} + \bar{w}_{,x}))_{,x} - R(w) + q_w &= 0,
 \end{aligned}
 \tag{3-1}$$

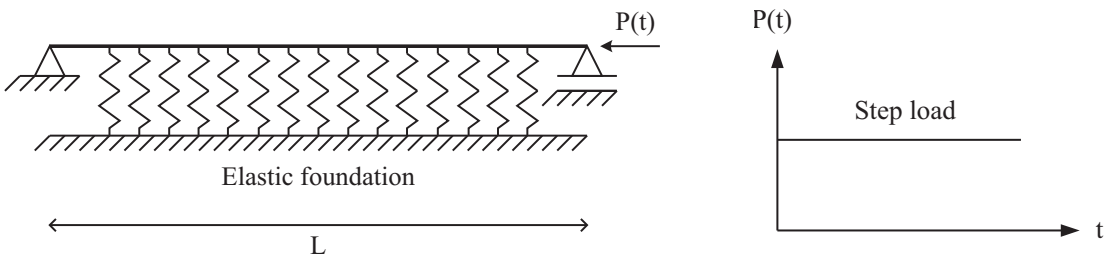


Figure 1. Beam on elastic foundation subjected to axial step load.

where $u = u(x, t)$ and $w = w(x, t)$ are the axial and normal displacements of the beam, respectively; \bar{w}_x is the initial geometrical imperfection; A and I are the cross-section area and moment of inertia; N_{xx} and M_{xx} the resultant axial force and bending moment; q_u and q_w the external applied loads in the axial and normal directions, respectively. The superior dot ($\dot{}$), denotes the derivative with respect to time, and $()_{,x}$ the derivative with respect to the axial coordinate. The response of the foundation is characterized by two parameters $\{K_1, K_3\}$ (see [Sheinman and Adan 1991]) and described by the function

$$R(w) = K_1 w + K_3 w^3. \tag{3-2}$$

The nonlinear kinematic relations for the beam entail the assumption of large displacements, moderate rotations, and small strains. Thus the constitutive relations (resultant axial force and bending moment) and the kinematic relations (axial strain and change of curvature) read:

$$\begin{Bmatrix} N_{xx} \\ M_{xx} \end{Bmatrix} = \begin{bmatrix} A_{11} & 0 \\ 0 & D_{11} \end{bmatrix} \begin{Bmatrix} \varepsilon_{xx} \\ \kappa_{xx} \end{Bmatrix}, \quad \begin{Bmatrix} \varepsilon_{xx} \\ \kappa_{xx} \end{Bmatrix} = \begin{Bmatrix} u_{,x} + \frac{1}{2}(w_{,x} + 2\bar{w}_{,x})w_{,x} \\ -w_{,xx} \end{Bmatrix}, \tag{3-3}$$

A_{11} and D_{11} being the axial and flexural rigidities. Specifically, for isotropic materials the rigidities are given by $A_{11} = EA$, and $D_{11} = EI$.

This sixth-order set of nonlinear partial differential equations is converted into an equivalent set of six first-order ones by recourse to the following variables:

$$z = \{u, w, \phi_x, N_{xx}, Q_{xz}, M_{xx}\}^T \tag{3-4}$$

The equivalent set, $\psi = \{\psi_1, \psi_2, \psi_3, \psi_4, \psi_5, \psi_6\}^T$, reads

$$\psi = \begin{Bmatrix} \psi_1 \\ \psi_2 \\ \psi_3 \\ \psi_4 \\ \psi_5 \\ \psi_6 \end{Bmatrix} = \begin{Bmatrix} -\rho A \ddot{u} + N_{xx,x} + q_u \\ -\rho A \ddot{w} + Q_{xz,x} - R(w) + q_w \\ M_{xx,x} - Q_{xz} - N_{xx}(\phi_x - \bar{w}_{,x}) \\ N_{xx} - A_{11}u_{,x} - \frac{1}{2}A_{11}(\phi_x - 2\bar{w}_{,x})\phi_x \\ \phi_x + w_{,x} \\ M_{xx} - D_{11}\phi_{x,x} \end{Bmatrix} = \mathbf{0}, \tag{3-5}$$

with the following boundary conditions at $x = 0$ and $x = L$:

$$\begin{aligned} N_{xx} = \bar{N}_{xx} \quad or \quad u = \bar{u}, \\ Q_{xz} = \bar{Q}_{xz} \quad or \quad w = \bar{w}, \\ M_{xx} = \bar{M}_{xx} \quad or \quad \phi_x = \bar{\phi}_x, \end{aligned} \tag{3-6}$$

where the bar denotes an applied force or displacement at the boundaries.

No unconditionally stable time integration procedure exists for the dynamic solution of nonlinear equations. Here, the composite implicit time integration procedure [Bathe and Baig 2005; Bathe 2007] was chosen for solving (3-5) in the time space. Assuming that the dynamic solution at time t (i.e. z_t, \dot{z}_t and \ddot{z}_t) is completely known, the solution at time $t + \Delta t$ is computed by introducing the substep at time $t + \theta \Delta t$, where $\theta \in \{0, 1\}$ (for instance, $\theta = 1/2$). Specifically, using Newmark’s scheme [1959], the

velocity and acceleration fields are explicitly given in terms of the displacement field at time $t + \theta \Delta t$, and the displacement, velocity and acceleration fields at t :

$$\begin{aligned} \dot{z}^{t+\theta\Delta t} &= \frac{\gamma}{\beta(\theta\Delta t)}(z^{t+\theta\Delta t} - z^t) + \left(1 - \frac{\gamma}{\beta}\right)\dot{z}^t + \left(1 - \frac{\gamma}{2\beta}\right)(\theta\Delta t)\ddot{z}^t \\ \ddot{z}^{t+\theta\Delta t} &= \frac{1}{\beta(\theta\Delta t)^2}(z^{t+\theta\Delta t} - z^t) - \frac{1}{\beta(\theta\Delta t)}\dot{z}^t - \left(\frac{1}{2\beta} - 1\right)\ddot{z}^t \end{aligned} \tag{3-7}$$

The solution of z at $t + \theta \Delta t$, (i.e., $z^{t+\theta\Delta t}$), was obtained, after substitution of (3-7) in (3-5), by linearizing the latter via the Newton–Raphson method:

$$\begin{aligned} \psi^{t+\theta\Delta t} &= \psi^{t+\theta\Delta t}(z^{t+\theta\Delta t}, z_{,x}^{t+\theta\Delta t}; z^t, \dot{z}^t, \ddot{z}^t) = \mathbf{0}, \\ \frac{\partial \psi^{t+\theta\Delta t}}{\partial z^{t+\theta\Delta t}} \Delta z^{t+\theta\Delta t} + \frac{\partial \psi^{t+\theta\Delta t}}{\partial z_{,x}^{t+\theta\Delta t}} \Delta z_{,x}^{t+\theta\Delta t} + \psi^{t+\theta\Delta t} &= \mathbf{0}. \end{aligned} \tag{3-8}$$

Finally, equations (3-8) were solved by means of a finite-difference scheme. Once convergence was reached, the complete dynamic solution (of the first substep) was obtained using (3-7). Then in the second substep, the velocity and acceleration fields were approximated according to [Collatz 1966] by

$$\begin{aligned} \dot{z}^{t+\Delta t} &= c_1 z^t + c_2 z^{t+\theta\Delta t} + c_3 z^{t+\Delta t}, \\ \ddot{z}^{t+\Delta t} &= c_1 \dot{z}^t + c_2 \dot{z}^{t+\theta\Delta t} + c_3 \dot{z}^{t+\Delta t}, \end{aligned} \tag{3-9}$$

where the constant coefficients are given by

$$c_1 = \frac{1 - \theta}{\theta \Delta t}, \quad c_2 = \frac{-1}{(1 - \theta)\theta \Delta t}, \quad c_3 = \frac{2 - \theta}{(1 - \theta)\Delta t} \tag{3-10}$$

Substitution of (3-9) in (3-5) yielded the equations needed to obtain the solution for z at time $t + \Delta t$ (i.e., $z^{t+\Delta t}$), which were treated in the same manner as above:

$$\begin{aligned} \psi^{t+\Delta t} &= \psi^{t+\Delta t}(z^{t+\Delta t}, z_{,x}^{t+\Delta t}; z^t, \dot{z}^t, \ddot{z}^t, z^{t+\theta\Delta t}, \dot{z}^{t+\theta\Delta t}, \ddot{z}^{t+\theta\Delta t}) = \mathbf{0}, \\ \frac{\partial \psi^{t+\Delta t}}{\partial z^{t+\Delta t}} \Delta z^{t+\Delta t} + \frac{\partial \psi^{t+\Delta t}}{\partial z_{,x}^{t+\Delta t}} \Delta z_{,x}^{t+\Delta t} + \psi^{t+\Delta t} &= \mathbf{0}. \end{aligned} \tag{3-11}$$

Once convergence of the solution ($z^{t+\Delta t}$) was achieved, the complete dynamic solution could be obtained using (3-9).

4. Results and discussion

The beam and the softening foundation used as an example in demonstrating the effectiveness of the Hoff–Simitses criterion had the following properties [Sheinman and Adan 1991]: Beam-length $L = 4.0\text{ m}$; rectangular cross-section with width $b = 0.04\text{ m}$ and depth $h = 0.08\text{ m}$; mass density $\rho = 7850\text{ kg/m}^3$; modulus of elasticity $E = 2.1 \times 10^{11}\text{ Nm}^{-2}$. The elastic foundation parameters are: $K_1 = 1000\text{ kNm}^{-2}$ and $K_3 = -100\text{ MNm}^{-4}$. The imperfection shape was taken as

$$\bar{w}(x) = \xi h \sin(\pi x / L), \quad \xi = 0.01. \tag{4-1}$$

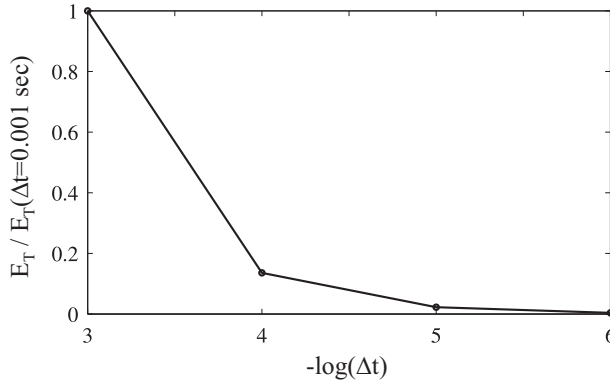


Figure 2. Convergence curve; normalized total energy versus time step Δt .

Of the examined criteria for convergence of the time-history solution with respect to the time step Δt (in seconds), the one of vanishing (beam at rest at $t = 0$) the total energy, $E_T =$ kinetic energy + total potential energy, was found to be the most representative. An example of this convergence is illustrated in Figure 2. The small time step was chosen on view of the high frequency of the characteristic behavior in the axial direction.

Figure 3 shows the time history of the vertical midspan displacement of the beam, $w(x = L/2)$, under three levels of axial-load ($\bar{N}_{xx} = 0.80 N_{xx,bif}$, $\bar{N}_{xx} = 0.85 N_{xx,bif}$ and $\bar{N}_{xx} = 0.85125 N_{xx,bif}$, where $N_{xx,bif} = 222.7 \text{ kN}$ is the buckling load of the perfect beam). It is seen that under the first two load levels the beam undergoes simple oscillations about the near static stable equilibrium position. By contrast, the third level is associated with large oscillations and a jump to postbuckling. Since the postbuckling equilibrium solution is unstable (see Figure 6), the dynamic solution is unbounded. Figure 4 shows the phase-plane curves of the vertical midspan displacement. It is seen that the two stable dynamic solutions form closed curves, while for the unstable one the curve diverges. It should be emphasized that the fluctuations in the phase-plane curves (Figure 4) are due to the high axial frequencies.

Figure 5 illustrates the Budiansky–Roth criterion showing the maximum vertical midspan displacement versus the applied load. Again, the equations of motion were solved for several values of the

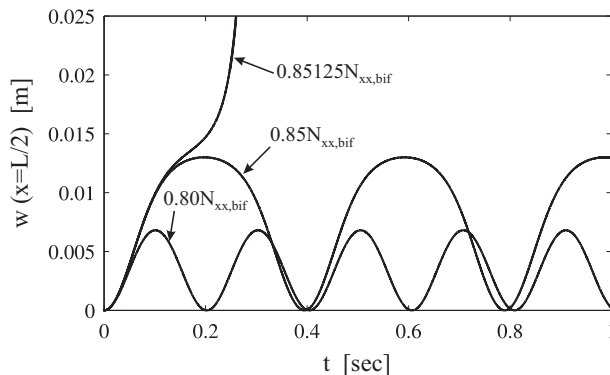


Figure 3. Vertical displacement versus time for three different load levels.

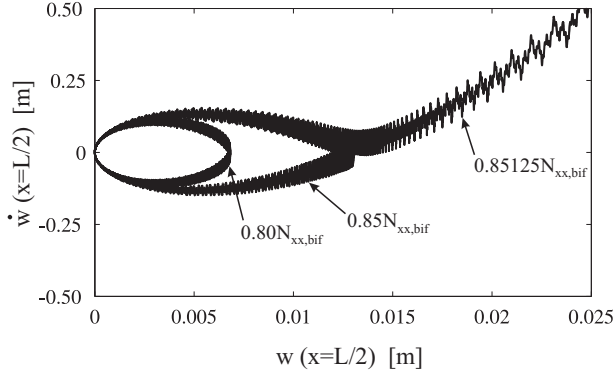


Figure 4. Phase-plane curves for three different load levels.

applied axial-load, starting from a small value and increasing it. The maximum displacement is seen to increase smoothly with the load, and culminates in a large jump (unbounded motion) at the highest level. Trail and error locates the dynamic buckling load at $N_{xx,d} = 0.85123 N_{xx,bif}$.

Figure 6 shows the nonlinear static equilibrium path used for the Hoff–Simites criterion [Simites 1990]. Specifically, the total potential energy, U_T , defined by

$$U_T = \frac{1}{2} \int_0^L (N_{xx}\epsilon_{xx} + M_{xx}\kappa_{xx}) dx + \int_0^L \int R(w)dw dx - \int_0^L (q_u u + q_w w) dx - \left[\bar{N}_{xx}\bar{u} + \bar{Q}_{xz}\bar{w} + \bar{M}_{xx}\bar{\phi}_x \right]_0^L, \quad (4-2)$$

was modified by introducing a constant C that eliminates all trajectories that are represented in U_T but that do not lead to a buckling mode:

$$U_{T,mod} = U_T - C. \quad (4-3)$$

For the case of an axially loaded beam at $x = L$ the constant C reads

$$C = -\frac{\bar{N}_{xx}^2(L) L}{2A_{11}}. \quad (4-4)$$

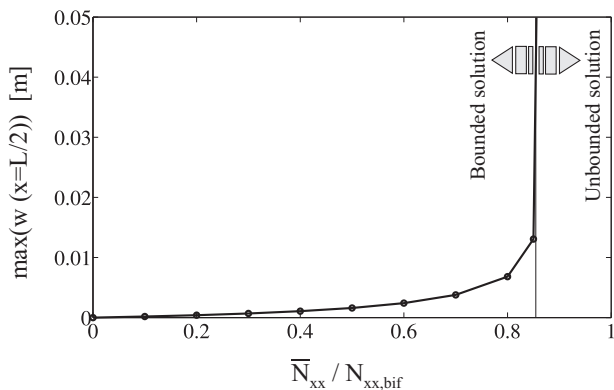


Figure 5. Maximum vertical midspan displacement versus applied load.

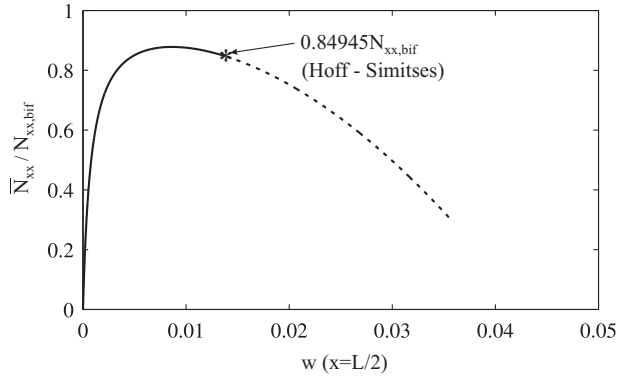


Figure 6. Applied load versus vertical midspan displacement.

Here, once the static solution is obtained (by solving (3-5) with neglecting the inertia terms), the modified total potential energy — see (4-3) — was calculated at every point of the path. The solid stretch in Figure 6 representing the path with negative modified total potential energy (bounded motion), and the dotted stretch with positive one (unbounded). It was found that this criterion (whereby the modified total potential energy is zero) yields a slightly lower dynamic buckling load ($N_{xx,d} = 0.84945 N_{xx,bif}$) than its Budiansky–Roth counterpart.

Figure 7 summarizes The dynamic sensitivity to imperfection according to the different criteria. The results are seen to be quite close (less than 1% divergence). The curve for the static buckling load (limit-point) is also plotted in this figure, and serves as an upper bound for the dynamic buckling load.

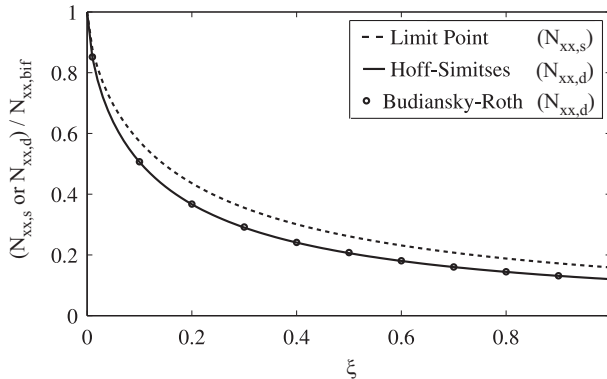


Figure 7. Imperfection sensitivity under static and dynamic step loads.

5. Summary and conclusions

A solution procedure for dynamic buckling of a beam on a nonlinear elastic foundation under dynamic step loading is presented. Two criteria (Hoff–Simitses and Budiansky–Roth) were applied and studied. It was found that the Hoff–Simitses criterion, for which static analysis suffices, is fully adequate and most effective for structures characterized by limit-point behavior. Its generalization for any dynamic loading is still a challenge.

References

- [Amazigo et al. 1970] J. C. Amazigo, B. Budiansky, and G. F. Carrier, “Asymptotic analyses of the buckling of imperfect columns on nonlinear elastic foundations”, *Int. J. Solids Struct.* **6**:10 (1970), 1341–1356.
- [Bathe 2007] K.-J. Bathe, “Conserving energy and momentum in nonlinear dynamics: a simple implicit time integration scheme”, *Comput. Struct.* **85**:7–8 (2007), 437–445.
- [Bathe and Baig 2005] K.-J. Bathe and M. M. I. Baig, “On a composite implicit time integration procedure for nonlinear dynamics”, *Comput. Struct.* **83**:31–32 (2005), 2513–2524.
- [Birman 1989] V. Birman, “Problems of dynamic buckling of antisymmetric rectangular laminates”, *Compos. Struct.* **12**:1 (1989), 1–15.
- [Budiansky 1967] B. Budiansky, “Dynamic buckling of elastic structures: criteria and estimates”, pp. 83–106 in *Dynamic stability of structures*, edited by G. Hermann, Pergamon, Oxford, 1967.
- [Budiansky and Hutchinson 1966] B. Budiansky and J. W. Hutchinson, “Dynamic buckling of imperfection sensitive structures”, pp. 636–651 in *Proceedings of the 11th International Congress of Applied Mechanics* (Munich, 1964), edited by H. Görtler, Springer, Berlin, 1966.
- [Budiansky and Roth 1962] B. Budiansky and R. S. Roth, “Axisymmetric dynamic buckling of clamped shallow spherical shells in *Collected papers on instability of shell structures*”, Technical Note NASA TN D-1510, Langley Research Center, Langley Station, VA, 1962, Available at <http://hdl.handle.net/2060/19630000930>.
- [Collatz 1966] L. Collatz, *The numerical treatment of differential equations*, 3rd ed., Springer, New York, 1966.
- [Dube et al. 2000] G. P. Dube, P. C. Dumir, and A. Mallick, “Dynamic buckling of laminated thick shallow spherical cap based on a static analysis”, *Mech. Res. Commun.* **27**:5 (2000), 561–566.
- [Elishakoff 1980] I. Elishakoff, “Remarks on the static and dynamic imperfection-sensitivity of nonsymmetric structures”, *J. Appl. Mech. (ASME)* **47**:1 (1980), 111–115.
- [Fraser and Budiansky 1969] W. B. Fraser and B. Budiansky, “The buckling of a column with random initial deflections”, *J. Appl. Mech. (ASME)* **36**:2 (1969), 232–240.
- [Gantes et al. 2001] C. J. Gantes, A. N. Kounadis, J. Raftoyiannis, and V. V. Bolotin, “A dynamic buckling geometric approach of 2-DOF autonomous potential lumped-mass systems under impact loading”, *Int. J. Solids Struct.* **38**:22–23 (2001), 4071–4089.
- [Hoff and Bruce 1954] N. J. Hoff and V. G. Bruce, “Dynamic analysis of the buckling of laterally loaded flat arches”, *J. Math. Phys. (Cambridge)* **32**:4 (1954), 276–288.
- [Hsu 1966] C. S. Hsu, “On dynamic stability of elastic bodies with prescribed initial conditions”, *Int. J. Eng. Sci.* **4**:1 (1966), 1–21.
- [Hsu 1967] C. S. Hsu, “The effect of various parameters on the dynamic stability of a shallow arch”, *J. Appl. Mech. (ASME)* **34**:2 (1967), 349–358.
- [Hutchinson and Budiansky 1966] J. W. Hutchinson and B. Budiansky, “Dynamic buckling estimates”, *AIAA J.* **4**:3 (1966), 525–530.
- [Kamiya 1977] N. Kamiya, “Circular plates resting on bimodulus and no-tension foundations”, *J. Eng. Mech. (ASCE)* **103**:6 (1977), 1161–1164.
- [Keener 1974] J. P. Keener, “Buckling imperfection sensitivity of columns and spherical caps”, *Quart. Appl. Math.* **32**:2 (1974), 173–188.
- [Kounadis 1997] A. N. Kounadis, “Non-potential dissipative systems exhibiting periodic attractors in regions of divergence”, *Chaos Solitons Fract.* **8**:4 (1997), 583–612.
- [Kounadis and Raftoyiannis 1990] A. N. Kounadis and J. Raftoyiannis, “Dynamic stability criteria of nonlinear elastic damped/undamped systems under step loading”, *AIAA J.* **28**:7 (1990), 1217–1223.
- [Kounadis et al. 1991] A. N. Kounadis, J. Mallis, and J. Raftoyiannis, “Dynamic buckling estimates for discrete systems under step loading”, *Z. Angew. Math. Mech.* **71**:10 (1991), 391–402.

- [Kounadis et al. 1997] A. N. Kounadis, C. Gantes, and G. Simitzes, “Nonlinear dynamic buckling of multi-DOF structural dissipative systems under impact loading”, *Int. J. Impact Eng.* **19**:1 (1997), 63–80.
- [Kounadis et al. 1999] A. N. Kounadis, C. J. Gantes, and V. V. Bolotin, “Dynamic buckling loads of autonomous potential systems based on the geometry of the energy surface”, *Int. J. Eng. Sci.* **37**:12 (1999), 1611–1628.
- [Kounadis et al. 2001] A. N. Kounadis, C. J. Gantes, and V. V. Bolotin, “An improved energy criterion for dynamic buckling of imperfection sensitive nonconservative systems”, *Int. J. Solids Struct.* **38**:42–43 (2001), 7487–7500.
- [Kounadis et al. 2006] A. N. Kounadis, J. Mallis, and A. Sbarounis, “Postbuckling analysis of columns resting on an elastic foundation”, *Arch. Appl. Mech.* **75**:6–7 (2006), 395–404.
- [Lee and Wass 1996] S. H. Lee and A. M. Wass, “Initial post-buckling behavior of a finite beam on an elastic foundation”, *Int. J. Non-Linear Mech.* **31**:3 (1996), 313–328.
- [Newmark 1959] N. M. Newmark, “A method of computation for structural dynamics”, *J. Eng. Mech. (ASCE)* **85**:3 (1959), 67–94.
- [Raftoyiannis and Kounadis 2000] I. G. Raftoyiannis and A. N. Kounadis, “Dynamic buckling of 2-DOF systems with mode interaction under step loading”, *Int. J. Non-Linear Mech.* **35**:3 (2000), 531–542.
- [Sheinman and Adan 1991] I. Sheinman and M. Adan, “Imperfection sensitivity of a beam on a nonlinear elastic foundation”, *Int. J. Mech. Sci.* **33**:9 (1991), 753–760.
- [Simitzes 1967] G. J. Simitzes, “Axisymmetric dynamic snap-through buckling of shallow spherical caps”, *AIAA J.* **5**:5 (1967), 1019–1021.
- [Simitzes 1990] G. J. Simitzes, *Dynamic stability of suddenly loaded structures*, Springer, New York, 1990.
- [Weitsman 1969] Y. Weitsman, “On the unbonded contact between plates and an elastic half space”, *J. Appl. Mech. (ASME)* **36**:2 (1969), 198–202.

Received 25 Jun 2009. Revised 30 Jul 2009. Accepted 20 Aug 2009.

MAHMOOD JABAREEN: cvjmah@tx.technion.ac.il

Faculty of Civil and Environmental Engineering, Technion – Israel Institute of Technology, Haifa, 32000, Israel

IZHAK SHEINMAN: cvrnrsh@tx.technion.ac.il

Faculty of Civil and Environmental Engineering, Technion – Israel Institute of Technology, Haifa, 32000, Israel

DIRECT DAMAGE-CONTROLLED DESIGN OF PLANE STEEL MOMENT-RESISTING FRAMES USING STATIC INELASTIC ANALYSIS

GEORGE S. KAMARIS, GEORGE D. HATZIGEORGIU AND DIMITRI E. BESKOS

A new direct damage-controlled design method for plane steel frames under static loading is presented. Seismic loading can be handled statically in the framework of a push-over analysis. This method, in contrast to existing steel design methods, is capable of directly controlling damage, both local and global, by incorporating continuum damage mechanics for ductile materials in the analysis. The design process is accomplished with the aid of a two-dimensional finite element program, which takes into account material and geometric nonlinearities by using a nonlinear stress-strain relation through the beam-column fiber modeling and including $P-\delta$ and $P-\Delta$ effects, respectively. Simple expressions relating damage to the plastic hinge rotation of member sections and the interstorey drift ratio for three performance limit states are derived by conducting extensive parametric studies involving plane steel moment-resisting frames under static loading. Thus, a quantitative damage scale for design purposes is established. Using the proposed design method one can either determine damage for a given structure and loading, or dimension a structure for a target damage and given loading, or determine the maximum loading for a given structure and a target damage level. Several numerical examples serve to illustrate the proposed design method and demonstrate its advantages in practical applications.

1. Introduction

Current steel design codes, such as [AISC \[1998\]](#) and [EC3 \[2005\]](#), are based on ultimate strength and the associated failure load. In both codes, member design loads are usually determined by global elastic analysis and inelasticity is taken into account indirectly through the interaction equations involving design loads and resistances defined for every kind of member deformation. Instability effects are also taken in an indirect and approximate manner through the use of the effective length buckling factor, while displacements are checked for serviceability at the end of the design process. Seismic design loads are obtained with the aid of seismic codes, such as [AISC \[2005\]](#) and [EC8 \[2004\]](#). In this case the global analysis can be elastostatic as before, spectral dynamic, static inelastic (push-over) or nonlinear dynamic.

Damage of materials, members, and structures is defined as their mechanical degradation under loading. Control of damage is always desirable by design engineers. Even though current methods of design [[AISC 1998](#); [EC3 2005](#); [AISC 2005](#); [EC8 2004](#)] are associated with ultimate strength and consider inelastic material behavior indirectly or directly, they are force-based and cannot achieve an effective control of damage, which is much better related to displacements than forces. For example, the percentage of the interstorey drift ratio (IDR) of seismically excited buildings is considered a solid basic

Keywords: continuum damage mechanics, damage control, steel structures, design methods, beam-column, finite element method, second order effects, elastoplastic behavior.

indicator of the level of damage, as suggested by the HAZUS99-SR2 User's Manual [FEMA 2001]. Even the displacement-based seismic design method [Priestley et al. 2007], in which displacements play the fundamental role in design and are held at a permissible level (target displacements), does not lead into a direct and transparent control of damage.

To be sure, there are many works in the literature dealing with the determination of damage in members and structures, especially in connection with the seismic design of reinforced concrete structures. More specifically, damage determination of framed buildings at the local and global level can be done with the aid of damage indices computed on the basis of deformation and/or energy dissipation, as shown by Park and Ang [1985] and Powell and Allahabadi [1988], for example. On the other hand, the finite element method has been employed in the analysis of steel and reinforced concrete structures in conjunction with a concentrated inelasticity (plasticity and damage) beam element in [Florez-Lopez 1998]. Damage determination in reinforced concrete and masonry structures has also been done by employing continuum theories of distributed damage in the framework of the finite element method [Cervera et al. 1995; Hatzigeorgiou et al. 2001; Hanganu et al. 2002]. Note that in all these references, the approach is to determine damage as additional structural design information, and cannot lead to a structural design with controlled damage.

Here we extend the direct damage-controlled design (DDCD) method, first proposed in Hatzigeorgiou and Beskos [2007] for concrete structures, to structural steel design. The basic advantage of DDCD is the dimensioning of structures with damage directly controlled at both local and global levels. In other words, the designer can select a priori the desired level of damage in a structural member or a whole structure and direct his design in order to achieve this preselected level of damage. Thus, while the DDCD deals directly with damage, inelastic design approaches, such as [AISC 1998; EC3 2005; AISC 2005; EC8 2004; Priestley et al. 2007] are concerned indirectly with damage. Furthermore, the a priori knowledge of damage, as it is the case with DDCD, ensures a controlled safety level, not only in strength but also in deflection terms. Thus, the present work, unlike all previous works on damage of steel structures, develops for the first time a direct damage-controlled steel design method, which is not just restricted to damage determination as an additional structural design information.

More specifically, the present work develops a design method for plane steel moment-resisting frames under static monotonic loading capable of directly controlling damage, both at local and global level. Seismic loading can be handled statically in the framework of a push-over analysis. Local damage is defined pointwise and expressed as a function of deformation on the basis of continuum damage mechanics theory for ductile materials [Lemaitre 1992]. On the other hand, global damage definition is based on the demand-and-capacity-factor design format as well as on various member damage combination rules. The method is carried out with the aid of the two-dimensional finite element program DRAIN-2DX [Prakash et al. 1993], which takes into account material and geometric nonlinearities, modified by the authors to employ damage as a design criterion in conjunction with appropriate damage levels. Material nonlinearities are implemented in the program by combining a nonlinear stress-strain relation for steel with the beam-column fibered plastic hinge modeling. Geometric nonlinearities involve P - δ and P - Δ effects. Thus, the proposed method belongs to the category of design methods using advanced methods of analysis [Chen and Kim 1997; Kappos and Manafpour 2001; Vasilopoulos and Beskos 2006; 2009], which presents significant advantages over the code-based methods. Local buckling can be avoided by using only class 1 European steel sections, something which is compatible with the inelastic analysis

employed herein. Furthermore, all structural members are assumed enough laterally braced in order to avoid lateral-torsional buckling phenomena. Using the proposed design method one can either determine damage for a given structure and loading, or dimension a structure for a target damage and given loading, or determine the maximum loading for a given structure and a target damage level.

2. Stress-strain relations for steel

Essential features of a steel constitutive model applicable to practical problems should be, on the one hand the accurate simulation of the actual steel behavior and on the other hand the simplicity in formulation and efficiency in implementation in a robust and stable nonlinear algorithmic manner. In this work, a multilinear stress-strain relation for steel characterized by a good compromise between simplicity and accuracy and a compatibility with experimental results, is adopted. The stress-strain (σ , ε) relation in tension for this steel model is of the form

$$\sigma = E\varepsilon \text{ for } \varepsilon \leq \varepsilon_y, \quad \sigma = \sigma_y + E_h(\varepsilon - \varepsilon_y) \text{ for } \varepsilon_y < \varepsilon \leq \varepsilon_u, \quad \sigma = \sigma_u \text{ for } \varepsilon_u < \varepsilon. \quad (1)$$

Equation (1) describes a trilinear stress-strain relation representing elastoplastic behavior with hardening, as shown in Figure 1, with E and E_h being the elastic and the inelastic moduli, respectively, ε_y and ε_u the yield and the ultimate strains, respectively and σ_y and σ_u the yield and ultimate stress, respectively. The negative counterpart to (1) can be adopted for the compression stress state, as shown in Figure 1. Similar stress-strain curves have been proposed earlier by, for example, [Gioncu and Mazzolani 2002]; European and American steels exhibit a stress-strain behavior similar to that of Figure 1. Thus, the model (1) can effectively depict the true behavior of structural steel.

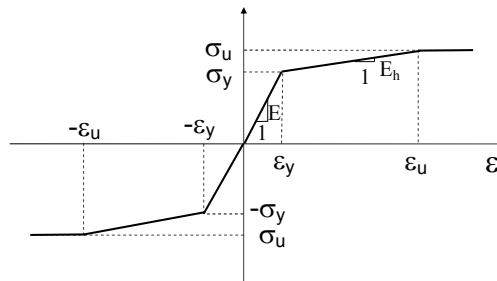


Figure 1. Stress-strain relation for steel.

3. Local damage

Local damage is usually referred to a point or a part of a structure and is one of the most appropriate indicators about their loading capacity. In the framework of continuum damage mechanics, the term “local” is associated with damage indices describing the state of the material at particular points of the structure, and the term “global” with damage indices describing the state of any finite material volume of the structure. Thus, global damage indices can be referred to any individual section, member, substructure, or the whole structure. This categorization of damage in agreement with continuum mechanics principles stipulating that constitutive models are defined at point level and all other quantities are obtained by integrating pointwise information.

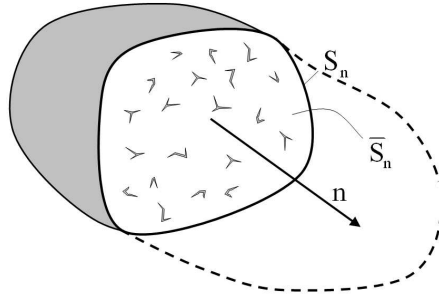


Figure 2. Cross section of a damaged material.

Continuum damage mechanics has been established for materials with brittle or ductile behavior and attempts to model macroscopically the progressive mechanical degradation of materials under different stages of loading. For structural steel, damage results from the nucleation of cavities due to decohesions between inclusions and the matrix followed by their growth and their coalescence through the phenomenon of plastic instability. The theory assumes that the material degradation process is governed by a damage variable d , the local damage index, which is defined pointwise, following [Lemaitre \[1992\]](#), as

$$d = \lim_{S_n \rightarrow 0} \frac{S_n - \bar{S}_n}{S_n}, \tag{2}$$

where S_n stands for the overall section in a damage material volume, \bar{S}_n for the effective or undamaged area, while $(S_n - \bar{S}_n)$ denotes the inactive area of defects, cracks, and voids ([Figure 2](#)). This index corresponds to the density of material defects and voids and has a zero value when the material is in the undamaged state and a value of unity at material rupture or failure.

The main goal of continuum damage mechanics is the determination of initiation and evolution of the damage index d during the deformation process. [Lemaitre \[1992\]](#), by assuming that damage evolution takes place only during plastic loading (plasticity induced damage) was able to propose a simple damage evolution law, as shown in [Figure 3](#), which can successfully simulate the behavior of steel or other ductile materials. Damage index d is represented by a straight line in damage-strain space, with end points at $d = 0$ for $\varepsilon = \varepsilon_y$, and $d = 1$ for $\varepsilon = \varepsilon_u$, where strain values are assumed to be absolute. This damage evolution law can be expressed as

$$d = 0 \text{ for } \varepsilon \leq \varepsilon_y, \quad d = \frac{\varepsilon - \varepsilon_y}{\varepsilon_u - \varepsilon_y} \text{ for } \varepsilon_y < \varepsilon \leq \varepsilon_u. \tag{3}$$

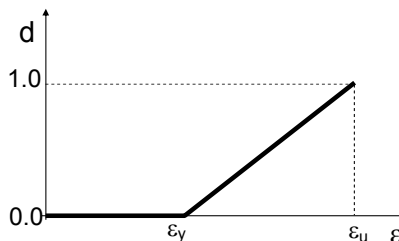


Figure 3. Damage-strain curve for steel.

A similar linear damage evolution law was proposed in [Florez-Lopez 1998]. Both laws are supported by experiments. One can observe that while the damage evolution law for concrete [Hatzigeorgiou and Beskos 2007] was derived by appropriately combining basic concepts of damage mechanics and a nonlinear stress-strain equation for plain concrete, the damage evolution law (3) for steel was taken directly from the literature [Lemaitre 1992].

4. Global damage

Global damage is referred to a section of a member, a member, a substructure, or a whole structure and constitutes one of the most suitable indicators about their loading capacity. Several methods to determine an indicator of damage at the global level have been presented in the literature. In general, these methods can be divided into four categories involving the following structural demand parameters: stiffness degradation, ductility demands, energy dissipation, and strength demands. According to the first approach, one of the most popular ways is to relate damage to stiffness degradation indirectly, that is, to the variation of the fundamental frequency of the structure during deformation [DiPasquale and Cakmak 1990]. However, this approach is inappropriate for the evaluation of the global damage of a substructure or its impact on the overall behavior. Furthermore, in order to evaluate the complete evolution of global damage with loading, a vast computational effort is needed due to the required eigenvalue analysis at every loading step. An alternative way to determine global damage is by computing the variation of the structural stiffness during deformation, as in [Ghobarah et al. 1999]; but again, evaluation of the global damage evolution requires heavy computations at every loading step. Many researchers determine damage in terms of the IDR. Whereas macroscopic quantities such as IDRs are good indicators of global damage in regular structures, this is not generally the case in more complex and/or irregular structures. Damage determination has also been done with the aid of damage indices computed on the basis of ductility (defined in terms of displacements, rotations or curvatures) and/or energy dissipation, as is evident in the method of [Park and Ang 1985] for framed concrete buildings or in the review article [Powell and Allahabadi 1988]. For the computation of damage in steel structures under seismic loading, one can mention [Vasilopoulos and Beskos 2006; Benavent-Climent 2007]. Note that all these indices are appropriate for seismic analyses only. They are not applicable to other types of problems, such as static ones; see [Hanganu et al. 2002].

In this work, for the section damage index D_S of a steel member, the following expression is proposed

$$D_S = \frac{c}{d} = \frac{\sqrt{(M_S - M_A)^2 + (N_S - N_A)^2}}{\sqrt{(M_B - M_A)^2 + (N_B - N_A)^2}}. \quad (4)$$

In the above, the bending moments M_A , M_S , and M_B and the axial forces N_A , N_S , and N_B as well as the distances c and d are those shown in the moment M – axial force N interaction diagram of Figure 4 for a plane beam-column element. The bending moment M_S and axial force N_S are design loads incorporating the appropriate load factors in agreement with EC3 [2005].

Figure 4 includes a lower bound damage curve, the limit between elastic and inelastic material behavior and an upper bound damage curve, the limit between inelastic behavior and complete failure. Thus, damage at the former curve is zero, while at the latter curve is one. Equation (4) is based on the assumption that damage evolution varies linearly between the above two damage bounds. These

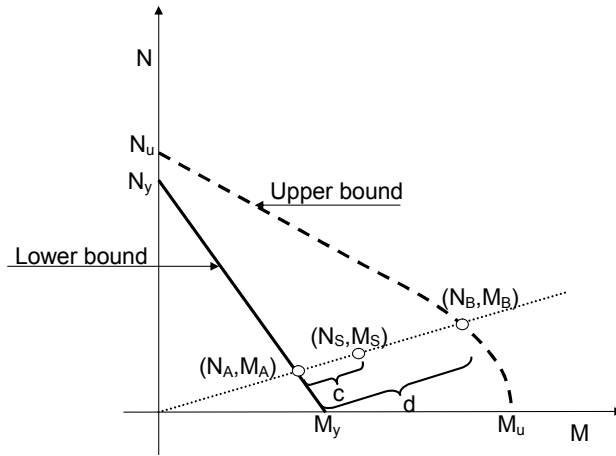


Figure 4. Section damage definition.

lower and upper bound curves can be determined accurately with the aid of the beam-column fibered plastic hinge modeling described in the next section. For their determination, the resistance safety factors are taken into account in agreement with EC3. The bound curves of Figure 4 can also be determined approximately by code type of formulae. Thus, the lower bound curve can be expressed as

$$\frac{M}{M_y} + \frac{N}{N_y} = 1, \tag{5}$$

where N_y and M_y are the minimum axial force and bending moment, respectively, which cause yielding, while the upper bound curve can be expressed as

$$\frac{M}{M_u} + \left(\frac{N}{N_u}\right)^2 = 1, \tag{6}$$

where N_u and M_u are the ultimate axial force and bending moment, respectively, which cause failure of the section. Equations (5) and (6) can be used for the construction of the bounding curves of Figure 4. The provisions in EC3 give a M-N interaction formula similar to (6), with the hardening effect not taken into account, that is, with $\sigma_u = \sigma_y$ or equivalently, $N_u = N_y$. Furthermore, since EC3 allows inelastic analysis only for section class 1, the proposed method is limited to sections of that class.

The section damage index proposed in (4) represents an extension of (3) from strains (or stresses) to forces and moments, i.e., stress resultants. Expressions for damage in terms of stress resultants are also mentioned in [Lemaitre 1992]. By contrast, Florez-Lopez [1998] uses *generalized effective stress*, which corresponds to bending moment, by analogy with the definition of *effective stress*, which corresponds to inelastic stress. His formulation, however, includes only bending moments, without any interaction with axial forces.

It should be noted that the proposed section damage index corresponds to the aforementioned fourth type of damage indicators, which are related to the strength demand approach. More specifically, this index is based on the demand-and-capacity-factor design format. There is an analogy or correspondence between the capacity ratio of interaction equations of EC3 and the proposed damage index; see Figure 4. This format is similar to the one implemented for performance evaluation of new and existing steel

moment-resisting structures in the FEMA standards 350 and 351, respectively [FEMA 2000a; 2000b]. The member damage index D_M is taken as the largest section damage index, along the member. This is a traditional and effective assumption in structural design; see [Kappos and Manafpour 2001].

Therefore,

$$D_M = \max(D_S). \quad (7)$$

To provide an overall damage index that is representative of the damage state of a complex structure, the member damage indices must be combined in a rational manner to reflect both the severity of the member damage and the geometric distribution of damage within the overall structure. Various weighted-average procedures have been proposed for combining the member damage indices into an overall damage index. Thus, for a structure composed of m members, the overall damage index, D_O , has the form

$$D_O = \left(\frac{\sum_{i=1}^m D_{M,i}^2 W_i}{\sum_{i=1}^m W_i} \right)^{1/2}, \quad (8)$$

where $D_{M,i}$ and W_i denote the damage and weighting factor of the i -th member. This expression is in agreement with the fact that the most damaged members affect the overall damage much more than the undamaged (elastic) members. Park and Ang [1985], assuming that the distribution of damage is correlated with the distribution of plastic strain energy dissipation, applied (8) with the weighting factors to correspond to the amount of plastic strain energy dissipation. Similar assumptions have been proposed elsewhere; e.g., in [Powell and Allahabadi 1988]. However, all these approaches are exclusively applied to seismic problems where the external loads have a cyclic form. It is evident that the amount of plastic strain energy dissipation is an inappropriate measure for static monotonic problems. For this reason, the overall damage index D_O is assumed here to be of the form [Cervera et al. 1995]

$$D_O = \left(\frac{\sum_{i=1}^m D_{M,i}^2 \Omega_i}{\sum_{i=1}^m \Omega_i} \right)^{1/2}, \quad (9)$$

where Ω_i denotes the volume of the i -th member. This relation reflects both the severity of the member damage and the geometric distribution of damage within the structure.

5. Global damage levels

5.1. Introduction. Damage is used here as a design criterion. Thus, the designer, in addition to a method for determining damage, also needs a scale of damage in order to decide which level of damage is acceptable for his design. Many damage scales can be proposed in order to select desired damage levels associated with the strength degradation and capacity of a structure to resist further loadings. Table 1 provides the three performance levels, immediate occupancy (IO), life safety (LS), and collapse prevention (CP), associated with modern performance-based seismic design with the corresponding limit response values (performance objectives) in terms of interstorey drift ratio (IDR), θ_{pl} (plastic rotation at member end), μ_θ (local ductility), and d (damage) as well as the relevant references. The selection of the appropriate damage level depends on various factors, such as the importance factor or the “weak beams – strong columns” rule in seismic design of structures. Thus, for example, nuclear power plants should be designed with zero damage and plane frames with 60% and 30% maximum damage in beams and columns, respectively. The proposed design method uses the damage level scale that has been derived

Index	Source	Performance level		
		IO	LS	CP
IDR (transient) (permanent)	[Leelataviwat et al. 1999]	1–2%	2–3%	3–4%
	[SEAOC 1999]	1.5%	3.2%	3.8%
	[Vasilopoulos and Beskos 2006]	0.5%	1.5%	3%
	[FEMA 1997]	0.7%	2.5%	5%
	[FEMA 1997]	negligible	1%	5%
θ_{pl}/θ_y	[FEMA 1997]	≤ 1	≤ 6	≤ 8
μ_θ	[FEMA 1997]	2	7	9
damage	[Vasilopoulos and Beskos 2006]	$\leq 5\%$	$\leq 20\%$	$\leq 50\%$
	[ATC 1985]	0.1–10%	10–30%	30–60%

Table 1. Performance levels and corresponding limit response values given by several sources.

with the aid of extensive parametric studies on plane frames and corresponds to the three performance levels of the FEMA 273 code [FEMA 1997]. It should be noted that damage characterizations (such as minor and major) given by modern seismic codes are qualitative and very general, and hence inappropriate for use in practical design. In contrast to them, the proposed values of damage indices can be easily used in practical design.

The following subsections provide details concerning the parametric studies conducted herein for the derivation of simple expressions relating damage to the plastic hinge rotation of the member sections and the IDR of the plane steel frames considered to be used for the construction of a practical quantitative damage scale.

5.2. Frame geometry and loading. A set of 36 plane steel moment-resisting frames was employed for the parametric studies. These frames are regular and orthogonal with storey heights and bay widths equal to 3 m and 5 m, respectively. Furthermore, they are characterized by a number of storeys n_s with values 3, 6, 9, 12, 15, and 20 and a number of bays n_b with values 3 and 6. The frames were subjected to constant uniform vertical loads $1.35G + 1.5Q = 30$ kN/m and horizontal variable loads $1.35W$, where G , Q , and W correspond to dead, live, and wind loads, respectively. The material properties taken from structural steel grade S235, were divided by a factor of 1.10 for compatibility with EC3 provisions. The frames were designed in accordance with EC3 [2005] and EC8 [2004].

Data for the frames, including values for n_s , n_b , beam and column sections, and first and second natural periods, are presented in the table on the next two pages, taken from [Karavasilis et al. 2007].

5.3. Proposed global damage level values. The previously described plane steel frames were analyzed by the computer program DRAIN-2DX [Prakash et al. 1993]. Use was made of its beam-column element with two possible plastic hinges at its ends modeled by fibers. During the analyses, the vertical loads of the frames remained constant, while the horizontal ones were progressively increased in order to identify the damage corresponding to each performance level of Table 1. Damage was calculated at section and structural levels by using expressions (4), (7), and (9). In addition, the interstorey drift ratio and the plastic hinge rotation at the end of each member were computed. The latter was computed in the form

#	n_s	n_b	columns and beams (see caption on next page)	T_1 /sec	T_2 /sec
1	3	3	240-330(1-3)	0.73	0.26
2	3	3	260-330(1-3)	0.69	0.21
3	3	3	280-330(1-3)	0.65	0.19
4	3	6	240-330(1-3)	0.75	0.23
5	3	6	260-330(1-3)	0.70	0.21
6	3	6	280-330(1-3)	0.66	0.20
7	6	3	280-360(1-4) 260-330(5-6)	1.22	0.41
8	6	3	300-360(1-4) 280-330(5-6)	1.17	0.38
9	6	3	320-360(1-4) 300-330(5-6)	1.13	0.37
10	6	6	280-360(1-4) 260-330(5-6)	1.25	0.42
11	6	6	300-360(1-4) 280-330(5-6)	1.19	0.40
12	6	6	320-360(1-4) 300-330(5-6)	1.15	0.38
13	9	3	340-360(1) 340-400(2-5) 320-360(6-7) 300-330(8-9)	1.55	0.54
14	9	3	360-360(1) 360-400(2-5) 340-360(6-7) 320-330(8-9)	1.52	0.53
15	9	3	400-360(1) 400-400(2-5) 360-360(6-7) 340-330(8-9)	1.46	0.51
16	9	6	340-360(1) 340-400(2-5) 320-360(6-7) 300-330(8-9)	1.57	0.55
17	9	6	360-360(1) 360-400(2-5) 340-360(6-7) 320-330(8-9)	1.53	0.53
18	9	6	400-360(1) 400-400(2-5) 360-360(6-7) 340-330(8-9)	1.47	0.51
19	12	3	400-360(1) 400-400(2-3) 400-450(4-5) 360-400(6-7) 340-400(8-9) 340-360(10) 340-330(11-12)	1.90	0.66
20	12	3	450-360(1) 450-400(2-3) 450-450(4-5) 400-450(6-7) 360-400(8-9) 360-360(10) 360-330(11-12)	1.78	0.62
21	12	3	500-360(1) 500-400(2-3) 500-450(4-5) 450-450(6-7) 400-400(8-9) 400-360(10-11) 400-330(12)	1.72	0.60
22	12	6	400-360(1) 400-400(2-3) 400-450(4-5) 360-400(6-7) 340-400(8-9) 340-360(10) 340-330(11-12)	1.90	0.67
23	12	6	450-360(1) 450-400(2-3) 450-450(4-5) 400-450(6-7) 360-400(8-9) 360-360(10) 360-330(11-12)	1.78	0.63
24	12	6	500-360(1) 500-400(2-3) 500-450(4-5) 450-450(6-7) 400-400(8-9) 400-360(10-11) 400-330(12)	1.72	0.61
25	15	3	500-300(1) 500-400(2-3) 500-450(4-5) 450-400(6-7) 400-400(8-12) 400-360(13-14) 400-330(15)	2.29	0.78
26	15	3	550-300(1) 550-400(2-3) 550-450(4-5) 500-400(6-7) 450-400(8-12) 450-360(13-14) 450-330(15)	2.22	0.75
27	15	3	600-300(1) 600-400(2-3) 600-450(4-5) 550-450(6-7) 500-450(8-9) 500-400(10-12) 500-360(13-14) 500-330(15)	2.10	0.72
28	15	6	500-300(1) 500-400(2-3) 500-450(4-5) 450-400(6-7) 400-400(8-12) 400-360(13-14) 400-330(15)	2.30	0.78
29	15	6	550-300(1) 550-400(2-3) 550-450(4-5) 500-400(6-7) 450-400(8-12) 450-360(13-14) 450-330(15)	2.21	0.75
30	15	6	600-300(1) 600-400(2-3) 600-450(4-5) 550-450(6-7) 500-450(8-9) 500-400(10-12) 500-360(13-14) 500-330(15)	2.10	0.72

#	n_s	n_b	columns and beams (see caption)	T_1/s	T_2/s
31	20	3	600-300(1) 600-400(2-3) 600-450(4-5) 550-450(6-10) 500-450(11-13) 500-400(14-16) 450-400(17) 450-360(18-19) 450-330(20)	2.82	0.97
32	20	3	650-300(1) 650-400(2-3) 650-450(4-5) 600-450(6-10) 550-450(11-13) 550-400(14-16) 500-400(17) 500-360(18-19) 500-330(20)	2.76	0.94
33	20	3	700-300(1) 700-360(2) 700-400(3) 700-450(4-5) 650-450(6-10) 600-450(11-13) 600-400(14-16) 550-400(17) 550-360(18-19) 550-330(20)	2.73	0.93
34	20	6	600-300(1) 600-400(2-3) 600-450(4-5) 550-450(6-10) 500-450(11-13) 500-400(14-16) 450-400(17) 450-360(18-19) 450-330(20)	2.75	0.96
35	20	6	650-300(1) 650-400(2-3) 650-450(4-5) 600-450(6-10) 550-450(11-13) 550-400(14-16) 500-400(17) 500-360(18-19) 500-330(20)	2.70	0.93
36	20	6	700-300(1) 700-360(2) 700-400(3) 700-450(4-5) 650-450(6-10) 600-450(11-13) 600-400(14-16) 550-400(17) 550-360(18-19) 550-330(20)	2.67	0.92

Table 2. Steel moment-resisting frames considered in parametric studies. In the central column, the expression 240-330(1-3) means that the first three storeys have columns with HEB240 sections and beams with IPE330 sections. The numbers in parentheses always refer to a range of storeys or single storey.

θ_{pl}/θ_y , where θ_y is the rotation at yielding expressed in FEMA [1997] as

$$\theta_y = \frac{M_{pl}L}{6EI}, \tag{10}$$

where L is the member length, E is the modulus of elasticity of the material and I is the moment of inertia of the section. When members, such as columns, are subjected to an axial compressive force P , the right-hand side of (10) is multiplied by the factor $1 - (P/P_y)$, where P_y is the axial yield force of the member.

This subsection presents the results of the parametric studies. Figure 5 shows the variation of the section damage index D_s versus the ratio θ_{pl}/θ_y for low-rise (3 and 6 storeys) and high-rise (9, 12, 15 and 20 storeys) frames, respectively. Figure 6 shows the variation of the overall damage index D_o versus IDR for low- and high-rise frames respectively. Using the method of least squares the mean values of these variations were determined and plotted as straight line segments in Figures 5–6. The analytical expressions of these lines are of the following form

For the low rise frames:

$$D_s = 12.526 \cdot \left(\frac{\theta_{pl}}{\theta_y}\right) \text{ for } \frac{\theta_{pl}}{\theta_y} \leq 2.2 \quad \text{and} \quad D_s = 3.54 \cdot \left(\frac{\theta_{pl}}{\theta_y}\right) + 20.14 \text{ for } \frac{\theta_{pl}}{\theta_y} > 2.2 \tag{11}$$

$$D_o = 4.67 \cdot IDR. \tag{12}$$

For the high rise frames:

$$D_s = 2.42 \cdot \left(\frac{\theta_{pl}}{\theta_y}\right) \tag{13}$$

$$D_o = 0.94 \cdot IDR. \tag{14}$$

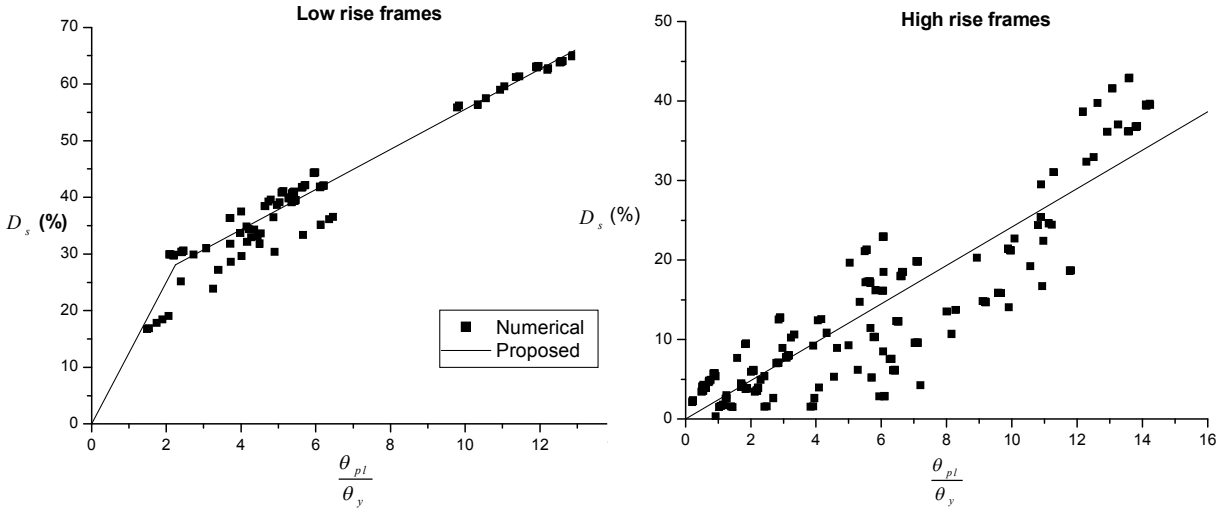


Figure 5. D_s versus θ_{pl}/θ_y curves for low- and high-rise frames.

The coefficient of determination R^2 in (11) and (13) is 0.96 and 0.79 respectively, showing that there is good correlation between the section damage and the plastic hinge rotation. On the contrary, the correlation between structure damage and the IDR is not so good as the coefficient of determination is 0.53 and 0.72 for (12) and (14), respectively.

Using the values of θ_{pl} and IDR given in FEMA [1997] for the three performance levels of Table 1 into (11)–(14), a section and overall damage scale is constructed for low- and high-rise frames and given in Table 4. The low values of damage in the high rise frames in that table can be explained by the instabilities caused in the analyses due to the concentration of damage in one or two sections and the $P-\delta$ and $P-\Delta$ effects. In the case of structural damage, this concentration combined with the definition of D_o in (9) explains these very small values. It is apparent from (9) that even if one has large values of

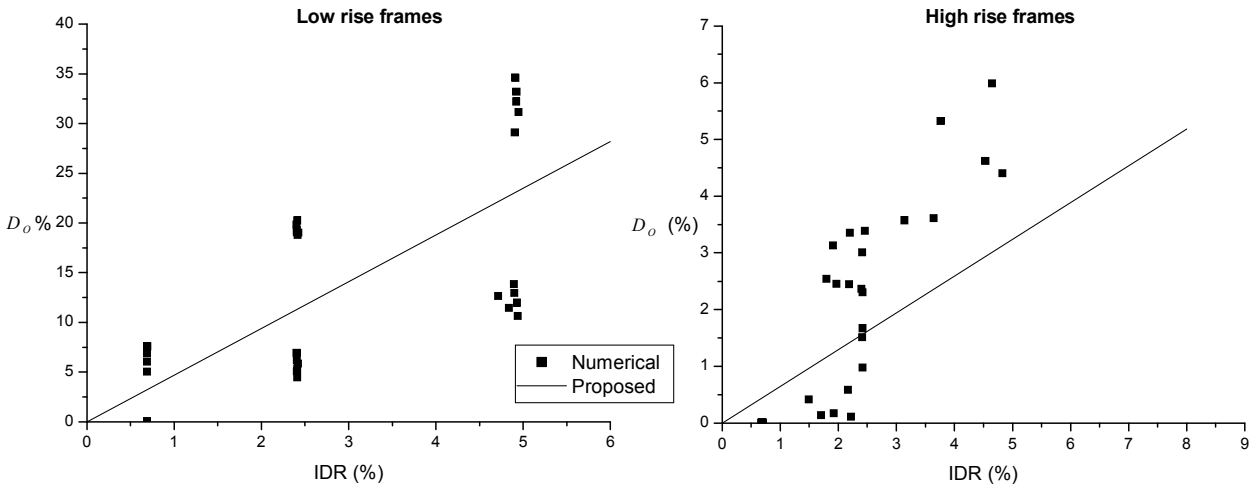


Figure 6. D_o versus IDR curves for low- and high-rise frames.

section damage in a few sections, the overall damage will have a small value because of the small or zero values in other sections. For this reason, the overall damage index is not considered as a representative one, and the section damage index is used in the applications.

6. Direct damage-controlled steel design

The application of the proposed DDCD method to plane steel members and framed steel structures is done with the aid of the DRAIN-2DX [Prakash et al. 1993] computer program, modified properly by the authors to perform both analysis and design. This program can statically analyze with the aid of the finite element method plane beam structures taking into account material and geometric nonlinearities. Material nonlinearities are accounted for through fiber modeling of plastic hinges in a concentrated plasticity theory (element 15 of DRAIN-2DX). Geometric nonlinearities include the P - δ effect (influence of axial force acting through displacements associated with member bending) and the P - Δ effect (influence of vertical load acting through lateral structural displacements), which are accounted for by utilizing the geometric stiffness matrix.

The beam-column section is subdivided in a user-defined number of steel fibers (Figure 7). Sensitivity studies have been undertaken to define the appropriate number of fibers for various types of sections. For example, for an I-section under axial force and uniaxial bending moment one can have satisfactory accuracy by dividing that section into 30 fibers (layers). Thus, for every structural steel member, selected sections are divided into steel fibers and the stress-strain relationship of (1) is used for tension and compression.

In the analysis, every member of the structure needs to be subdivided into several elements (usually three or four) along its length to model the inelastic behavior more accurately. The analysis leads to highly accurate results, but is, in general, computationally intensive for large and complex structures. Figure 8 shows the flow chart of the modified DRAIN-2DX for damage-controlled steel design.

Using this modified DRAIN-2DX, the user has three design options at his disposal in connection with damage-controlled steel design:

- (i) determine damage for a given structure under given loading,
- (ii) dimension a structure for given loading and given target damage, or
- (iii) determine the maximum loading a given structure can sustain for a given target damage.

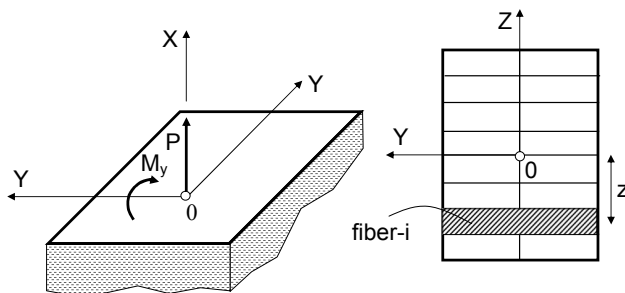


Figure 7. Fiber modeling of a general section.

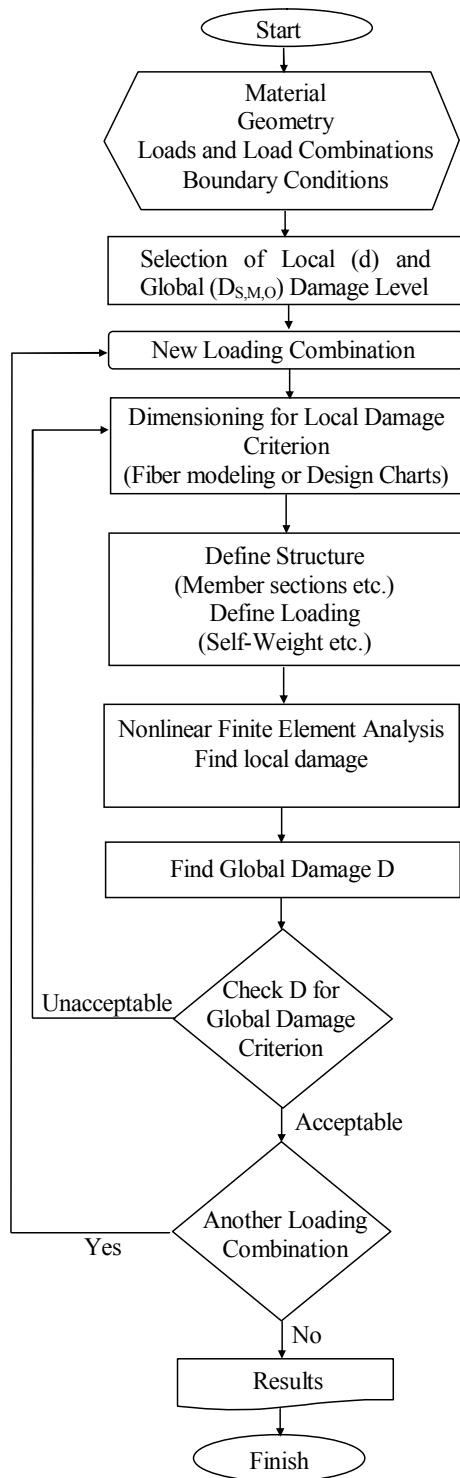


Figure 8. Flowchart of the modified program DRAIN-2DX [Prakash et al. 1993].

The first option is the one usually chosen in current practice. The other two options are the ones which actually make the proposed design method a direct damage-controlled one.

7. Examples of application

This section describes two numerical examples to illustrate the use of the proposed design method and demonstrate its advantages.

7.1. Static design of a plane steel frame. A plane two bay – two storey steel frame is examined in this example. Figure 9 shows the geometry and loading of the frame. Columns consist of standard HEB sections, while beams of standard IPE sections. The beams are subjected to uniform vertical loads $G = 15.0 \text{ kN/m}$ and $Q = 20.0 \text{ kN/m}$, where G and Q correspond to permanent and live loads, respectively. Additionally, the frame is subjected to horizontal wind loads $W = 12.6 \text{ kN}$ at the first floor level and $W = 22.2 \text{ kN}$ at the second. Steel is assumed to follow the material properties of steel grade S235 with trilinear stress-strain curve. Without loss of generality, only one loading combination of EC3 is examined here, that corresponding to $1.35(G + Q + W)$.

In the following, the frame is studied for the three design options of the proposed design method. Initially, the first design option, related to the determination of damage for a given structure and known loading, is examined. In this case, the structure is designed according to the EC3 method. In order to design this frame, four different member sections are determined, as shown in Figure 9: (a) columns of the first floor, (b) columns of the second floor, (c) beams of the first floor, and (d) beams of the second floor.

The most appropriate standard sections have been found to be those in Table 3. These sections have been obtained on the basis of a first order elastic analysis according to EC3. In order to determine the damage level, the structure is analyzed by the modified DRAIN-2DX program [Prakash et al. 1993], taking into account inelasticity and second order phenomena. The damage determined in all the members was found equal to zero (Table 3) indicating linear elastic behavior of the structure.

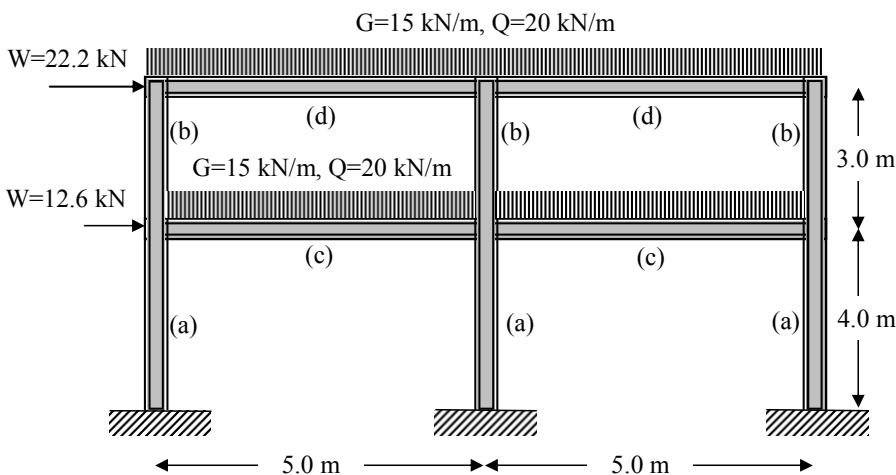


Figure 9. Geometry and loads for the frame of Section 7.1.

Member		EC3			Proposed method – DDCD	
		Sections	Capacity ratio	Damage	Sections	Damage
columns	(a)	HEB-180	0.742	0.0%	HEB-160	0.0%
	(b)	HEB-140	0.821	0.0%	HEB-140	24.3%
beams	(c)	IPE-360	0.686	0.0%	IPE-240	73.7%
	(d)	IPE-330	0.842	0.0%	IPE-270	20.0%

Table 3. Design of two-dimensional frame for the structure of [Figure 9](#).

The second design option has to do with member dimensioning for a preselected target damage level and known loading. Thus, using the modified DRAIN–2DX program, one can determine the most appropriate sections in order to have the selected target (maximum) damage at members, for the same loading combination as above. Two different damage levels are considered by setting the maximum member damage equal to 25% and 75% for columns and beams, respectively. The sections found appear in [Table 3](#). For those sections, the computed values of maximum member damage D_S become 24.2% and 73.7% for columns and beams, very close from below to the preselected (target) values of 25% and 75%. It is evident that the acceptance of greater damage levels decreases the sizes of the sections.

Finally, the third design option associated with the determination of maximum loading for a given structure and preselected target damage is examined. Use is made again of the modified DRAIN–2DX program. The examined structure is assumed to consist of the standard sections obtained in the second design option (see [Table 3](#)). In this case, vertical (permanent and live) loads are assumed to remain the same. Thus, allowing maximum values of damage $D_S = 30%$ and $0%$ for beams and columns, respectively, one can determine the maximum wind load. The allowable maximum wind load is found to be 11.5 and 20.2 kN for the first and second floor, respectively.

7.2. Seismic design of a plane steel frame by push-over. Consider an S235 plane steel moment-resisting frame of three bays and three storeys. The bay width is assumed to be 5 m and the storey height 3 m. The load combination $G + 0.3Q$ on beams is equal to 27.5 kN/m. HEB profiles are used for the columns and IPE profiles for the beams. The frame was designed according to [EC3 \[2005\]](#) and [EC8 \[2004\]](#) for a peak ground acceleration equal to 0.4 g, a soil class D and a behaviour factor $q = 4$ with the aid of the SAP2000 program [\[2005\]](#) in conjunction with the capacity design requirements of EC8. Thus, for a design base shear of 355 kN, the following column and beam sections were obtained for the three storeys: (HEB280-IPE360) + (HEB260-IPE330) + (HEB240-IPE300). The maximum elastic top floor displacement was found equal to 0.0465 m. Thus, according to EC8, the corresponding inelastic displacement will be $0.0465q = 0.186$ m, following the well known equal displacement rule.

The frame is subsequently analyzed using static inelastic push-over analysis with an inverted triangle type of profile of horizontal forces. The forces are progressively increased until the maximum inelastic displacement of the frame reaches the previously computed one of 0.186 m.

The damage distribution in the frame is shown in [Figure 10](#). It is observed that plastic hinges are formed both in beams and columns, which implies that in reality the capacity design requirement is not satisfied. Damage values are up to about 47% in the beams and up to 26% in columns (44% at their

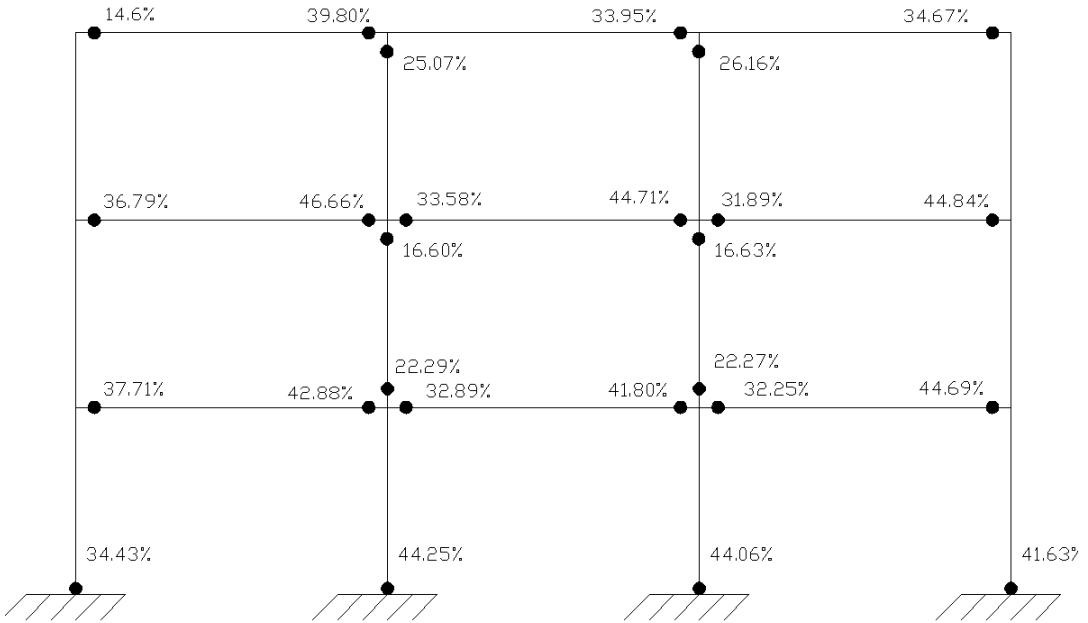


Figure 10. Damage distribution in the frame of Section 7.2 designed according to EC3 and EC8.

bases). The DDCD can overcome this drawback of formation of plastic hinges in the columns, because it can directly control damage and plastic hinge formation in the frame. Indeed, this frame is designed for the CP performance level of Table 4 by assuming target damage of 45% in the beams and 0% in all columns except those of the first floor where the target damage at their bases is 40%. For this target damage distribution and design base shear computed with the aid of the EC8 spectrum, the sections of the frame are obtained. For the resulting frame the push-over curve is used to determine the elastic displacement for the aforementioned base shear. This displacement is multiplied by q in order to find the maximum inelastic one and hence the corresponding base shear from the push-over curve. For this base shear the distribution of damage is obtained. If this distribution is in accordance with the target one, the selected sections are acceptable. Otherwise, the sections are changed and the previous procedure is repeated. Thus, for the damage distribution of Figure 11 with damage values up to about 44% in the beams and up to 37% in column bases, the column and beam sections for the three storeys of the frame were found to be (HEB300-IPE330) + (HEB300-IPE330) + (HEB280-IPE300). This selection results in a global collapse mechanism satisfying completely the capacity design requirement.

Performance level	Low rise frames		High rise frames	
	D_s	D_O	D_s	D_O
IO	$\leq 13\%$	$\leq 3\%$	$\leq 3\%$	$\leq 1\%$
LS	$\leq 40\%$	$\leq 12\%$	$\leq 15\%$	$\leq 2\%$
CP	$\leq 50\%$	$\leq 24\%$	$\leq 20\%$	$\leq 5\%$

Table 4. Performance levels and corresponding section and structural damage.

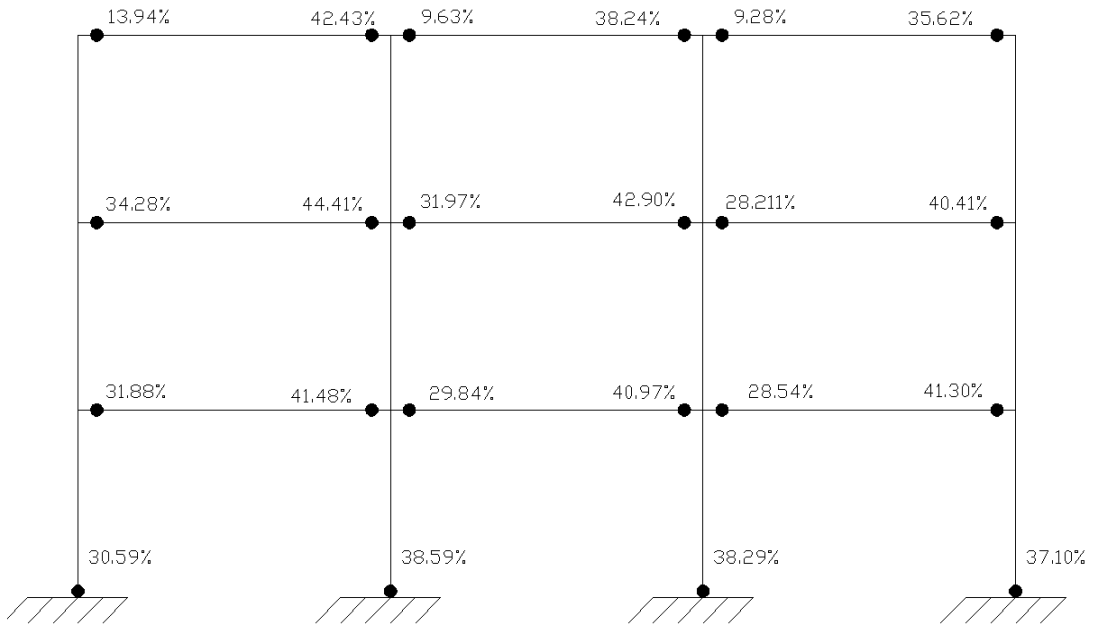


Figure 11. Damage distribution in the frame of [Section 7.2](#) designed according to DDCD.

8. Conclusions

This paper introduced the direct damage-controlled design (DDCD) method for structural steel design. The method

- works with the aid of the finite element method incorporating material and geometric nonlinearities, a continuum mechanics definition of damage and a damage scale derived on the basis of extensive parametric studies;
- allows the designer to either determine the damage level for a given structure and known loading, or dimension a structure for a target damage level and known loading, or determine the maximum loading for a given structure and a target damage level;
- can also be used for the case of seismic loading in the framework of the static inelastic (push-over) analysis providing a reliable way for achieving seismic capacity design.

References

- [AISC 1998] “Load and resistance factor design: structural members, specifications and codes”, 2nd revision of the 2nd ed., American Institute of Steel Construction, Chicago, 1998.
- [AISC 2005] “Seismic provisions for structural steel buildings”, standard AISC 341-05, American Institute of Steel Construction, Chicago, 2005.
- [ATC 1985] “Earthquake damage evaluation data for California”, standard ATC-13, Applied Technology Council, Redwood City, CA, 1985.
- [Benavent-Climent 2007] A. Benavent-Climent, “An energy-based damage model for seismic response of steel structures”, *Earthquake Eng. Struct. Dyn.* **36**:8 (2007), 1049–1064.

- [Cervera et al. 1995] M. Cervera, J. Oliver, and R. Faria, “Seismic evaluation of concrete dams via continuum damage models”, *Earthquake Eng. Struct. Dyn.* **24**:9 (1995), 1225–1245.
- [Chen and Kim 1997] W. F. Chen and S. E. Kim, *LFRD steel design using advanced analysis*, CRC Press, Boca Raton, FL, 1997.
- [DiPasquale and Cakmak 1990] E. DiPasquale and A. S. Cakmak, “Detection of seismic structural damage using parameter-based global damage indices”, *Probab. Eng. Mech.* **5**:2 (1990), 60–65.
- [EC3 2005] “Eurocode 3: Design of steel structures, part 1-1: general rules for buildings”, standard EN 1993-1-1, European Committee on Standardization (CEN), Brussels, 2005.
- [EC8 2004] European Committee for Standardization (CEN), “Eurocode 8: design of structures for earthquake resistance, part 1: general rules, seismic actions and rules for buildings”, standard EN 1998-1, Brussels, 2004.
- [FEMA 1997] “NEHRP guidelines for the seismic rehabilitation of buildings”, standard FEMA-273, Building Seismic Safety Council, Federal Emergency Management Agency (FEMA), Washington, D.C., 1997, Available at <http://www.wbdg.org/ccb/FEMA/ARCHIVES/fema273.pdf>.
- [FEMA 2000a] FEMA, “Recommended seismic design criteria for new steel moment-frame buildings”, standard FEMA-350, Federal Emergency Management Agency (FEMA), Sacramento, CA, 2000, Available at <http://www.fema.gov/plan/prevent/earthquake/pdf/fema-350.pdf>.
- [FEMA 2000b] FEMA, “Recommended seismic evaluation and upgrade criteria for existing welded steel moment-frame buildings”, standard FEMA-351, Federal Emergency Management Agency (FEMA), Washington, D.C., 2000, Available at <http://www.fema.gov/plan/prevent/earthquake/pdf/fema-351.pdf>.
- [FEMA 2001] “HAZUS99 User’s manual”, Service Release 2, Federal Emergency Management Agency (FEMA), Washington, D.C., 2001.
- [Florez-Lopez 1998] J. Florez-Lopez, “Frame analysis and continuum damage mechanics”, *Eur. J. Mech. A Solids* **17**:2 (1998), 269–283.
- [Ghobarah et al. 1999] A. Ghobarah, H. Abou-Elfath, and A. Biddah, “Response-based damage assessment of structures”, *Earthquake Eng. Struct. Dyn.* **28**:1 (1999), 79–104.
- [Gioncu and Mazzolani 2002] V. Gioncu and F. M. Mazzolani, *Ductility of seismic resistant steel structures*, Spon Press, London, 2002.
- [Hanganu et al. 2002] A. D. Hanganu, E. Onate, and A. H. Barbat, “A finite element methodology for local/global damage evaluation in civil engineering structures”, *Comput. Struct.* **80**:20-21 (2002), 1667–1687.
- [Hatzigeorgiou and Beskos 2007] G. D. Hatzigeorgiou and D. E. Beskos, “Direct damage-controlled design of concrete structures”, *J. Struct. Eng. (ASCE)* **133**:2 (2007), 205–215.
- [Hatzigeorgiou et al. 2001] G. D. Hatzigeorgiou, D. E. Beskos, D. D. Theodorakopoulos, and M. Sfakianakis, “A simple concrete damage model for dynamic FEM applications”, *Int. J. Comput. Eng. Sci.* **2**:2 (2001), 267–286.
- [Kappos and Manafpour 2001] A. J. Kappos and A. Manafpour, “Seismic design of R/C buildings with the aid of advanced analytical techniques”, *Eng. Struct.* **23**:4 (2001), 319–332.
- [Karavasilis et al. 2007] T. L. Karavasilis, N. Bazeos, and D. E. Beskos, “Behavior factor for performance-based seismic design of plane steel moment resisting frames”, *J. Earthq. Eng.* **11**:4 (2007), 531–559.
- [Leelataviwat et al. 1999] S. Leelataviwat, S. C. Goel, and B. Stojadinović, “Toward performance-based seismic design of structures”, *Earthquake Spectra* **15**:3 (1999), 435–461.
- [Lemaitre 1992] J. Lemaitre, *A course on damage mechanics*, Springer-Verlag, Berlin, 1992.
- [Park and Ang 1985] Y. J. Park and A. H. S. Ang, “Mechanistic seismic damage model for reinforced concrete”, *J. Struct. Eng. (ASCE)* **111**:4 (1985), 722–739.
- [Powell and Allahabadi 1988] G. H. Powell and R. Allahabadi, “Seismic damage prediction by deterministic methods: concepts and procedures”, *Earthquake Eng. Struct. Dyn.* **16**:5 (1988), 719–734.
- [Prakash et al. 1993] V. Prakash, G. H. Powell, and S. Campbell, *DRAIN-2DX base program description and user guide*, version 1.10, University of California, Berkeley, CA, 1993.

- [Priestley et al. 2007] M. J. N. Priestley, G. M. Calvi, and M. J. Kowalsky, *Displacement-based seismic design of structures*, IUSS Press, Pavia, Italy, 2007.
- [SAP2000 2005] *SAP2000: Static and dynamic finite element analysis of structures*, version 9.1.4, Computers and Structures, Inc., Berkeley, CA, 2005.
- [SEAOC 1999] “Recommended lateral force requirements and commentary”, known as the *SEAOC Blue Book*, 7th ed., Seismology Committee, Structural Engineers Association of California, Sacramento, CA, 1999.
- [Vasilopoulos and Beskos 2006] A. A. Vasilopoulos and D. E. Beskos, “Seismic design of plane steel frames using advanced methods of analysis”, *Soil Dyn. Earthq. Eng.* **26**:12 (2006), 1077–1100. Corrigendum in **27**:2 (2007), 189.
- [Vasilopoulos and Beskos 2009] A. A. Vasilopoulos and D. E. Beskos, “Seismic design of space steel frames using advanced methods of analysis”, *Soil Dyn. Earthq. Eng.* **29**:1 (2009), 194–218.

Received 8 Dec 2008. Accepted 13 Mar 2009.

GEORGE S. KAMARIS: kamaris@upatras.gr
Department of Civil Engineering, University of Patras, 26500 Patras, Greece

GEORGE D. HATZIGEORGIU: gchatzig@env.duth.gr
Department of Environmental Engineering, Democritus University of Thrace, 67100 Xanthi, Greece

DIMITRI E. BESKOS: d.e.beskos@upatras.gr
Department of Civil Engineering, University of Patras, 26500 Patras, Greece

NONLINEAR FLUTTER INSTABILITY OF THIN DAMPED PLATES: A SOLUTION BY THE ANALOG EQUATION METHOD

JOHN T. KATSIKADELIS AND NICK G. BABOUSKOS

We investigate the nonlinear flutter instability of thin elastic plates of arbitrary geometry subjected to a combined action of conservative and nonconservative loads in the presence of both internal and external damping and for any type of boundary conditions. The response of the plate is described in terms of the displacement field by three coupled nonlinear partial differential equations (PDEs) derived from Hamilton's principle. Solution of these PDEs is achieved by the analog equation method (AEM), which uncouples the original equations into linear, quasistatic PDEs. Specifically, these are a biharmonic equation for the transverse deflection of the plate, that is, the bending action, plus two linear Poisson's equations for the accompanying in-plane deformation, that is, the membrane action, under time-dependent fictitious loads. The fictitious loads themselves are established using the domain boundary element method (D/BEM). The resulting system for the semidiscretized nonlinear equations of motion is first transformed into a reduced problem using the aeroelastic modes as Ritz vectors and then solved by a new AEM employing a time-integration algorithm. A series of numerical examples is subsequently presented so as to demonstrate the efficiency of the proposed methodology and to validate the accuracy of the results. In sum, the AEM developed herein provides an efficient computational tool for realistic analysis of the admittedly complex phenomenon of flutter instability of thin plates, leading to better understanding of the underlying physical problem.

1. Introduction

The stability of thin plates subjected to conservative as well as nonconservative loads is of great importance in many fields of engineering such as aircrafts, space structures, mechanical, and civil engineering applications. The combined action of conservative and nonconservative loads, such as follower forces and aerodynamic pressure, initiate flutter instability in the plate that manifests itself in the form of vibrations with ever-increasing amplitude as time goes. Basically, flutter is a self-excited oscillation which occurs in systems which are not subjected to periodic forces. Linear plate theory indicates that there is a critical value of load above which the plate becomes unstable and the displacements grow exponentially with time. However, as the deflection of the plate increases, the membrane stresses pick up considerably in magnitude and limit the motion to a bounded value with increasing amplitude as the load level increases. Hence, we have to consider the nonlinear plate problem in order to have a better insight to this type of instability. In presence of damping, be it internal or external, the plate becomes unstable at the critical value of the nonconservative forces and reaches a periodic motion, known as limit cycle oscillation, which is independent of the initial displacements.

Keywords: nonlinear flutter, plates, aeroelasticity, instability, follower forces, boundary elements, analog equation method, aerodynamic loads.

The linear flutter of plates has been examined by many authors who used analytic and approximate techniques. [Leipholz and Pfenndt \[1983\]](#) studied the flutter instability of rectangular plates with various types of boundary conditions under uniformly distributed follower forces. [Adali \[1982\]](#) investigated the flutter and divergence instability of a rectangular plate on an elastic foundation where he found that the type of instability depends on the combination of the conservative and nonconservative loads, the Poisson's ratio, the foundation moduli and the plate aspect ratio. [Higuchi and Dowell \[1992\]](#) were among the first researchers to investigate the destabilizing effect of structural damping on flutter instability of plates. [Zuo and Schreyer \[1996\]](#) studied the flutter and divergence instability of beams and thin rectangular plates under the combined action of conservative and nonconservative loads. [Kim and Kim \[2000\]](#) used the finite element method (FEM) to analyze Kirchhoff and Mindlin type of plates under follower forces.

The linear and nonlinear flutter of plates subjected to aerodynamic pressure has been also the subject of many investigators due to the importance of this type of instability in flight vehicles traveling at supersonic Mach numbers. For instance, [Dowell \[1966\]](#) studied the nonlinear oscillations of a plate that is subjected to in-plane loads and aerodynamic pressure according to quasisteady supersonic flow theory. Next, [Mei \[1977\]](#) also studied this problem using the FEM, while [Shiau and Lu \[1990\]](#) investigated the nonlinear flutter of composite laminated plates. The limit cycle oscillations of a thin isotropic rectangular plate exposed to supersonic air flow has been also investigated by many authors [[Weiliang and Dowell 1991](#); [Guo and Mei 2003](#); [Chen et al. 2008](#)]. Due to the complexity of the governing equations, only approximate and numerical techniques such as the Rayleigh–Ritz method and the FEM have been used, which however treat plates with relatively simple geometry (rectangular, triangular) under simple load distributions and boundary (support) conditions. Finally, the linear flutter and divergence instability of a plate of arbitrary geometry with any type of boundary conditions has been investigated recently by [Babouskos and Katsikadelis \[2009\]](#).

In this paper the problem of nonlinear flutter instability of plates of any type of geometry subjected to arbitrary boundary conditions under interior and edge conservative and nonconservative loads of follower type is solved in presence of internal (structural) and external (viscous) damping. The equations of the plate are derived by using Hamilton's principle and considering nonlinear kinematic relations resulting from the von Kármán assumption. The resulting initial-boundary value problem consisting of three coupled nonlinear hyperbolic PDEs in terms of displacements with nonlinear boundary conditions is solved using the AEM developed in [[Katsikadelis 1994](#); [2002](#)], which converts the original equations into three linear uncoupled quasistatic PDEs, namely a linear plate (biharmonic) equation for the transverse deflection and two linear (Poisson) membrane equations for the membrane (in-plane) deformation. The new problem employs time-dependent fictitious loads that are established using the D/BEM, under the original boundary conditions. This procedure results in an initial value problem of nonlinear equations of motion for the discretized fictitious sources, whose solution is achieved by transformation to a reduced problem using Ritz vectors. The aeroelastic modes, namely the eigenmodes of the linear flutter plate problem near the critical point and in absence of damping, are selected as Ritz vectors [[Guo and Mei 2003](#)]. The reduced initial value problem is solved using a new AEM time step integration algorithm [[Katsikadelis 2009](#)]. Finally, the response of the plate is established from the integral representation of the substitute problems. In terms of examples, the vibration of plates under a given initial disturbance plus the action of the conservative and nonconservative forces and the ensuing postcritical behavior

is examined. These numerical examples demonstrate the efficiency and validate the accuracy of the methodology. Useful conclusions are drawn, which validate also the findings of earlier investigators. In sum, the present method provides a computational tool for a realistic analysis and better understanding of the complex phenomenon of nonlinear flutter instability of plates in the presence of damping. Although the membrane inertia forces were ignored here, the solution procedure permits their inclusion and their influence will be the subject of a forthcoming paper.

2. Governing equations

2.1. The nonlinear plate problem. Consider a thin elastic plate of uniform thickness h occupying the two dimensional multiply connected domain Ω of the xy plane with boundary $\Gamma = \bigcup_{i=0}^K \Gamma_i$ (Figure 1). The curves Γ_i ($i = 0, 1, 2, \dots, K$) may be piecewise smooth. The boundary may be simply supported, clamped, free, or elastically supported with transverse stiffness $k_T(x)$ and rotational stiffness $k_R(x)\mathbf{x} : (x, y) \in \Gamma$, respectively. The plate is subjected to in-plane conservative n_x, n_y , and/or nonconservative loads p_x, p_y (body forces) as well as to aerodynamic pressure Δp due to air flow. Moreover, along the movable edges conservative N_n^*, N_t^* and nonconservative P_n^*, P_t^* forces may be applied. The von Kármán assumption for the kinematic relation is adopted:

$$\varepsilon_x = u_{,x} + \frac{1}{2}w_{,x}^2, \quad \varepsilon_y = v_{,y} + \frac{1}{2}w_{,y}^2, \quad \gamma_{xy} = u_{,y} + v_{,x} + w_{,x}w_{,y}, \quad (2-1)$$

where $u = u(x, y, t)$ and $v = v(x, y, t)$ are the membrane displacements and $w = w(x, y, t)$ the transverse displacement.

Quasisteady supersonic first-order piston theory is employed for the aerodynamic pressure; it gives a good approximation for high supersonic Mach numbers [Dowell 1966; Mei 1977; Guo and Mei 2003].

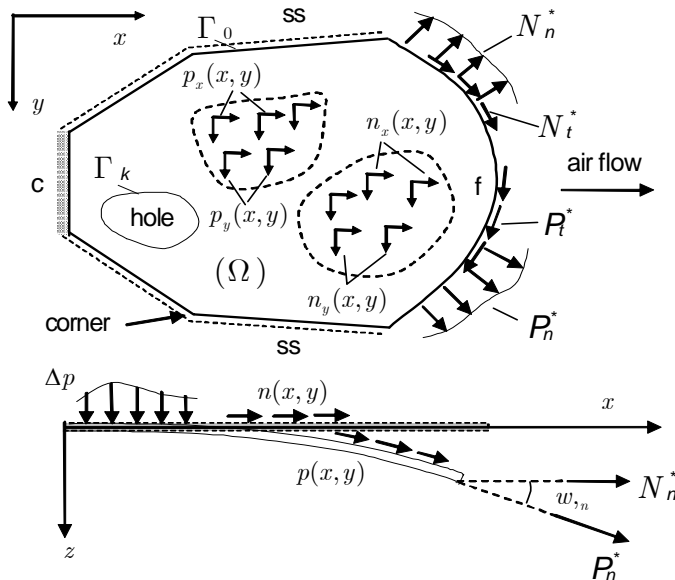


Figure 1. Plate geometry and supports (c = clamped, ss = simply supported, f = free).

In this case the pressure is

$$\Delta p = -(q_x w_{,x} + q_y w_{,y} + c \dot{w}), \tag{2-2}$$

where q_x , q_y , and c are parameters depending on the density, the velocity and the direction of the air flow and are given in [Guo and Mei 2003]. Neglecting in-plane inertia and damping forces, the governing equations and the boundary conditions of the problem are obtained from Hamilton’s principle, which in this case reads

$$\int_{t_1}^{t_2} (\delta T - \delta U + \delta V + \delta W_{nc}) dt = 0, \tag{2-3}$$

where T , U are the kinetic and elastic energy and V the potential of the external forces:

$$T = \frac{1}{2} \int_{\Omega} \rho h \dot{w}^2 d\Omega, \tag{2-4}$$

$$U = \frac{D}{2} \int_{\Omega} (w_{,xx}^2 + w_{,yy}^2 + 2\nu w_{,xx} w_{,yy} + 2(1 - \nu) w_{,xy}^2) d\Omega + \frac{1}{2} \int_{\Gamma} (k_T w^2 + k_R w_{,n}^2) ds \tag{2-5}$$

$$+ \frac{C}{2} \int_{\Omega} \left((u_{,x} + \frac{1}{2} w_{,x}^2)^2 + (v_{,y} + \frac{1}{2} w_{,y}^2)^2 + 2\nu (u_{,x} + \frac{1}{2} w_{,x}^2) (v_{,y} + \frac{1}{2} w_{,y}^2) + \frac{1-\nu}{2} (u_{,y} + v_{,x} + w_{,x} w_{,y})^2 \right) d\Omega,$$

$$V = - \int_{\Omega} [(n_x + p_x)u + (n_y + p_y)v] d\Omega - \int_{\Gamma} ((N_n^* + P_n^*)u_n + (N_t^* + P_t^*)u_t) ds. \tag{2-6}$$

Here δW_{nc} is the virtual work of the nonconservative loads and the external and internal damping forces, written as

$$\delta W_{nc} = \int_{\Omega} ((p_x - q_x)w_{,x} + (p_y - q_y)w_{,y}) \delta w d\Omega + \int_{\Gamma} (P_n^* w_{,n} + P_t^* w_{,t}) \delta w ds - \int_{\Omega} c \dot{w} \delta w d\Omega$$

$$- \int_{\Omega} \eta D ((\dot{w}_{,xx} + \nu \dot{w}_{,yy}) \delta w_{,xx} + (\dot{w}_{,yy} + \nu \dot{w}_{,xx}) \delta w_{,yy} + 2(1 - \nu) \dot{w}_{,xy} \delta w_{,xy}) d\Omega, \tag{2-7}$$

where $c = c(x, y)$ and $\eta = \eta(x, y)$ are the external damping and internal damping coefficients, $\rho = \rho(x, y)$ is the material density of the plate, $D = Eh^3/12(1 - \nu^2)$ is the flexural rigidity with E , ν being the Young’s modulus and Poisson’s ratio, respectively, and $C = Eh/(1 - \nu^2)$ is the membrane stiffness of the plate.

Introducing (2-4)–(2-7) into (2-3), using the calculus of variations, performing the necessary integrations by parts, and ignoring the time-dependent terms in the boundary conditions, we obtain the following initial and boundary value problems:

(i) For the transverse deflection,

$$D \nabla^4 w - (N_x w_{,xx} + 2N_{xy} w_{,xy} + N_y w_{,yy}) + (q_x + n_x) w_{,x} + (q_y + n_y) w_{,y} + \rho h \ddot{w} + c \dot{w} + \eta D \nabla^4 \dot{w} = 0$$

in Ω , $\tag{2-8}$

$$w(\mathbf{x}, 0) = g_1(\mathbf{x}), \quad \dot{w}(\mathbf{x}, 0) = g_2(\mathbf{x}) \tag{2-9}$$

in Ω ,

$$Vw + N_n^* w_{,n} + N_t^* w_{,t} + k_T w = 0 \quad \text{or} \quad w = 0 \quad \text{on } \Gamma, \tag{2-10a}$$

$$Mw - k_R w_{,n} = 0 \quad \text{or} \quad w_{,n} = 0 \quad \text{on } \Gamma, \tag{2-10b}$$

$$k_T^{(k)} w^{(k)} - \llbracket Tw \rrbracket_k = 0 \quad \text{or} \quad w^{(k)} = 0 \quad \text{at corner point } k, \tag{2-10c}$$

(ii) For the in-plane deformation,

$$\left. \begin{aligned} \nabla^2 u + \frac{1+\nu}{1-\nu} (u_{,x} + v_{,y})_{,x} + w_{,x} \left(\frac{2}{1-\nu} w_{,xx} + w_{,yy} \right) + \frac{1+\nu}{1-\nu} w_{,xy} w_{,y} + \frac{n_x + p_x}{Gh} = 0 \\ \nabla^2 v + \frac{1+\nu}{1-\nu} (u_{,x} + v_{,y})_{,y} + w_{,y} \left(\frac{2}{1-\nu} w_{,yy} + w_{,xx} \right) + \frac{1+\nu}{1-\nu} w_{,xy} w_{,x} + \frac{n_y + p_y}{Gh} = 0 \end{aligned} \right\} \text{ in } \Omega, \tag{2-11}$$

$$\left. \begin{aligned} N_n = N_n^* + P_n^* \quad \text{or} \quad u_n = u_n^* \\ N_t = N_t^* + P_t^* \quad \text{or} \quad u_t = u_t^* \end{aligned} \right\} \text{ on } \Gamma, \tag{2-12}$$

where $G = E/2(1 + \nu)$ is the shear modulus, Vw is the equivalent shear force, Mw is the normal bending moment, Tw is the twisting moment along the boundary, while $\llbracket Tw \rrbracket_k$ is its discontinuity jump at corner k . The operators producing these quantities are given as

$$V = -D \left(\frac{\partial}{\partial n} \nabla^2 + (1 - \nu) \frac{\partial}{\partial s} \left(\frac{\partial^2}{\partial s \partial n} - \kappa \frac{\partial}{\partial s} \right) \right), \tag{2-13a}$$

$$M = -D \left(\nabla^2 - (1 - \nu) \left(\frac{\partial^2}{\partial s^2} + \kappa \frac{\partial}{\partial n} \right) \right), \tag{2-13b}$$

$$T = D(1 - \nu) \left(\frac{\partial^2}{\partial s \partial n} - \kappa \frac{\partial}{\partial s} \right), \tag{2-13c}$$

where $\kappa = \kappa(s)$ is the curvature of the boundary and n, s are the intrinsic boundary coordinates. Finally, the quantities N_x, N_y, N_{xy} represent the in-plane membrane forces given as

$$N_x = C(\varepsilon_x + \nu \varepsilon_y), \quad N_y = C(\varepsilon_y + \nu \varepsilon_x), \quad N_{xy} = C \frac{1 - \nu}{2} \gamma_{xy}. \tag{2-14}$$

2.2. The linear plate problem. The plate problem is linearized if the stretching of the middle surface due to bending is neglected, that is if it is set $w_{,x}^4 = w_{,y}^4 = w_{,x}^2 w_{,y}^2 \simeq 0$ in (2-5). This implies that although the in-plane forces contribute to bending they are not influenced by it. Thus the nonlinear terms in (2-11) vanish. The boundary conditions are the same for both problems. Apparently, in this case the two problems are uncoupled. Therefore, the in-plane forces N_x, N_y, N_{xy} are obtained from the linearized equations (2-11), which are solved independently. The solution of the linear problem is required because the eigenmodes of the resulting eigenvalue problem are employed for the solution of the nonlinear equations of motion (Section 3.4).

3. The AEM solution

3.1. The plate problem. The initial boundary value problem (2-8)–(2-10) for the dynamic response of the plate is solved using the AEM [Katsikadelis 1994]. The analog equation for the problem at hand is

$$\nabla^4 w = b(\mathbf{x}, t), \quad \mathbf{x} = \{x, y\} \in \Omega, \tag{3-1}$$

where $b(\mathbf{x}, t)$ represents the time-dependent fictitious load. Equation (3-1) is a quasistatic equation, that is, the time appears as a parameter, and it can be solved with the boundary conditions (2-10) at any instant t using the BEM. Thus, the solution at a point $\mathbf{x} \in \Omega$ is obtained in integral form as

$$w(\mathbf{x}, t) = \int_{\Omega} w^* b d\Omega + \int_{\Gamma} (w^* V w + w_{,n} M w^* - w_{,n}^* M w - w V w^*) ds - \sum_k (w^* \llbracket T w \rrbracket - w \llbracket T w^* \rrbracket)_k, \quad (3-2)$$

which for $\mathbf{x} \in \Gamma$ yields the following two boundary integral equations for points where the boundary is smooth:

$$\frac{1}{2} w(\mathbf{x}, t) = \int_{\Omega} w^* b d\Omega + \int_{\Gamma} (w^* V w + w_{,n} M w^* - w_{,n}^* M w - w V w^*) ds - \sum_k (w^* \llbracket T w \rrbracket - w \llbracket T w^* \rrbracket)_k, \quad (3-3)$$

$$\frac{1}{2} w_{,v}(\mathbf{x}, t) = \int_{\Omega} \omega^* b d\Omega + \int_{\Gamma} (\omega^* V w + w_{,n} M \omega^* - \omega_{,n}^* M w - w V \omega^*) ds - \sum_k (\omega^* \llbracket T w \rrbracket - w \llbracket T \omega^* \rrbracket)_k, \quad (3-4)$$

in which $w^* = w^*(\mathbf{x}, \mathbf{y})$, for $\mathbf{x}, \mathbf{y} \in \Gamma$, is the fundamental solution and ω^* its normal derivative at point $\mathbf{x} \in \Gamma$:

$$w^* = \frac{1}{8\pi} r^2 \ln r, \quad \omega^* = \left(\frac{1}{8\pi} r^2 \ln r \right)_{,v} = \frac{1}{8\pi} r r_{,v} (2 \ln r + 1). \quad (3-5)$$

\mathbf{v} being the unit normal vector to the boundary at point \mathbf{x} , whereas \mathbf{n} is the unit normal vector to the boundary at the integration point \mathbf{y} , and $r = \|\mathbf{x} - \mathbf{y}\|$ (Figure 2, left).

Equations (3-3) and (3-4) can be used to establish the boundary quantities not specified. They are solved numerically using the BEM. The boundary integrals are approximated using N constant boundary elements, whereas the domain integrals are approximated using M linear triangular elements. The domain discretization is performed automatically using the Delaunay triangulation. Since the fictitious source is not defined on the boundary, the nodal points of the triangles adjacent to the boundary are placed on their sides (Figure 2, right).

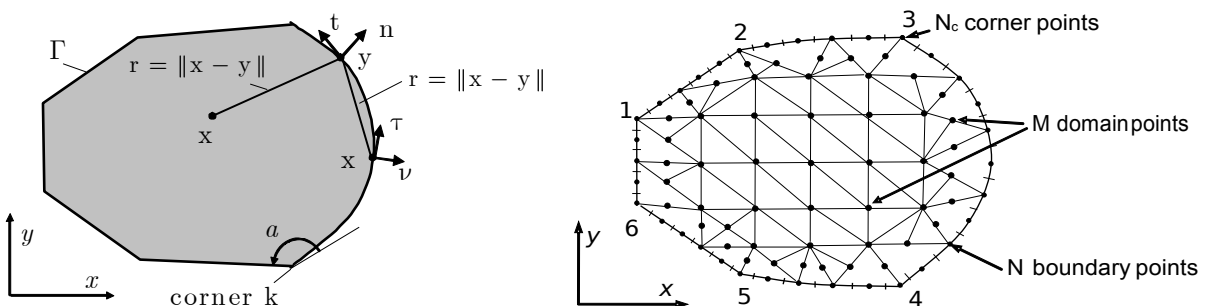


Figure 2. Left: BEM notation. Right: Boundary and domain discretization.

Thus, after discretization and application of the boundary integral equations (3-3) and (3-4) at the N boundary nodal points and (3-3) at the N_c corner points we obtain

$$H \begin{Bmatrix} \mathbf{w} \\ \mathbf{w}_c \\ \mathbf{w}_{,n} \end{Bmatrix} = G \begin{Bmatrix} \mathbf{V} \\ \mathbf{R} \\ \mathbf{M} \end{Bmatrix} + \mathbf{A}\mathbf{b}, \tag{3-6}$$

where H, G are $N \times N$ known coefficient matrices originating from the integration of the kernel functions on the boundary elements, A is an $N \times M$ coefficient matrix originating from the integration of the kernel function on the domain elements, $\mathbf{w}, \mathbf{w}_c, \mathbf{w}_{,n}$ are the vectors of the N boundary nodal displacements, N_c corner displacements and N boundary nodal normal slopes, respectively, $\mathbf{V}, \mathbf{R}, \mathbf{M}$ are the vectors of the N nodal values of effective shear force, N_c concentrated corner forces, and N nodal values of the normal bending moment, and \mathbf{b} is the vector of the M nodal values of the fictitious source.

Equation (3-6) constitutes a system of $2N + N_c$ equations for $4N + 2N_c + M$ unknowns. Additional $2N + N_c$ equations are obtained from the boundary conditions. Thus, the boundary conditions (2-10), when applied at the N boundary nodal points and the N_c corner points yield the equations

$$\alpha_1 \mathbf{w} + \alpha_2 \mathbf{w}_{,n} + \alpha_3 \mathbf{V} = \mathbf{0}, \quad \beta_1 \mathbf{w}_{,n} + \beta_2 \mathbf{M} = \mathbf{0}, \quad \mathbf{c}_1 \mathbf{w}_c + \mathbf{c}_2 \mathbf{R} = \mathbf{0}, \tag{3-7}$$

where $\alpha_1, \alpha_2, \alpha_3, \beta_1, \beta_2, \mathbf{c}_1, \mathbf{c}_2$ are known coefficient matrices. Note that the first equation in (3-7) has resulted after approximating the derivative $w_{,r}$ in (2-10a) with a finite difference scheme.

Equations (3-6) and (3-7) can be combined and solved for the boundary quantities $\mathbf{w}, \mathbf{w}_c, \mathbf{w}_{,n}, \mathbf{V}, \mathbf{R}, \mathbf{M}$ in terms of the fictitious load \mathbf{b} . Subsequently, these expressions are used to eliminate the boundary quantities from the discretized counterpart of (3-2). Thus we obtain the following representation for the deflection

$$w(\mathbf{x}, t) = \sum_{k=1}^M b_k(t) W_k(\mathbf{x}), \quad \mathbf{x} \in \Omega. \tag{3-8}$$

The derivatives of $w(\mathbf{x})$ at points \mathbf{x} inside Ω are obtained by direct differentiation of (3-2). Thus, we obtain after elimination of the boundary quantities

$$w_{,pqr}(\mathbf{x}, t) = \sum_{k=1}^M b_k(t) W_{k,pqr}(\mathbf{x}), \quad p, q, r \in \{0, x, y\}, \quad \mathbf{x} \in \Omega, \tag{3-9}$$

3.2. The plane stress problem. Noting that Equations (2-11) are of the second order their analog equations are obtained using the Laplace operator. This yields

$$\nabla^2 u = b_1(\mathbf{x}, t), \quad \nabla^2 v = b_2(\mathbf{x}, t). \tag{3-10}$$

Setting $q = u_{,n}$, the integral representation of the solution of the first of these equations is

$$\varepsilon u(\mathbf{x}, t) = \int_{\Omega} v^* b_1 d\Omega - \int_{\Gamma} (v^* q - q^* u) ds \quad \mathbf{x} \in \Omega \cup \Gamma \tag{3-11}$$

in which $v^* = \ell nr/2\pi$ is the fundamental solution to $\nabla^2 u = b_1(\mathbf{x}, t)$ and $q^* = v^*_{,n}$ its derivative normal to the boundary, $r = \|\mathbf{y} - \mathbf{x}\|$ $\mathbf{x} \in \Omega \cup \Gamma$ and $\mathbf{y} \in \Gamma$, ε is the free term coefficient ($\varepsilon = 1$ if $\mathbf{x} \in \Omega$, $\varepsilon = \frac{1}{2}$ if $\mathbf{x} \in \Gamma$ and $\varepsilon = 0$ if $\mathbf{x} \notin \Omega \cup \Gamma$).

Using the BEM with constant boundary elements and linear triangular domain elements and following the same procedure applied for the plate equation, we obtain the following representation for the in-plane displacement u and its derivatives:

$$u_{,pq}(\mathbf{x}, t) = \sum_{k=1}^M b_k^{(1)}(t)U_{k,pq}^{(1)}(\mathbf{x}) + \sum_{k=1}^M b_k^{(2)}(t)U_{k,pq}^{(2)}(\mathbf{x}) + U_{0,pq}(\mathbf{x}), \quad p, q \in \{0, x, y\}, \mathbf{x} \in \Omega. \quad (3-12)$$

Similarly, we obtain for the displacement v

$$v_{,pq}(\mathbf{x}, t) = \sum_{k=1}^M b_k^{(1)}(t)V_{k,pq}^{(1)}(\mathbf{x}) + \sum_{k=1}^M b_k^{(2)}(t)V_{k,pq}^{(2)}(\mathbf{x}) + V_{0,pq}(\mathbf{x}), \quad p, q \in \{0, x, y\}, \mathbf{x} \in \Omega. \quad (3-13)$$

where $U_k^{(1)}, U_k^{(2)}, V_k^{(1)}, V_k^{(2)}, U_0, V_0$ are known functions. Note that U_0, V_0 result from the nonhomogeneous boundary conditions.

3.3. The final step of the AEM. Equations (3-9), (3-12) and (3-13) give the displacements $w(x, t), u(x, t), v(x, t)$ and their derivatives provided that the three fictitious sources $\mathbf{b}(t), \mathbf{b}^{(1)}(t), \mathbf{b}^{(2)}(t)$ are first established. This is achieved by working as following.

Collocating the PDEs (2-8) and (2-11) at the M internal nodal points and substituting the expressions (3-9) for the transverse deflection and the values (3-12), (3-13) for the membrane displacements, we obtain the following system of $3M$ nonlinear equations for $b_k(t), b_k^{(1)}(t), b_k^{(2)}(t), (k = 1, \dots, M)$

$$M\ddot{\mathbf{b}} + C\dot{\mathbf{b}} + \mathbf{H}(\mathbf{b}, \mathbf{b}^{(1)}, \mathbf{b}^{(2)}) = \mathbf{0}, \quad (3-14a)$$

$$\mathbf{A}_1\mathbf{b}^{(1)} + \mathbf{B}_1\mathbf{b}^{(2)} + \mathbf{H}_1(\mathbf{b}) = \mathbf{G}_1, \quad (3-14b)$$

$$\mathbf{A}_2\mathbf{b}^{(1)} + \mathbf{B}_2\mathbf{b}^{(2)} + \mathbf{H}_2(\mathbf{b}) = \mathbf{G}_2, \quad (3-14c)$$

where \mathbf{M}, \mathbf{C} are $M \times M$ known generalized mass and damping matrices, \mathbf{H} is a generalized stiffness vector depending nonlinearly on the $\mathbf{b}, \mathbf{b}^{(1)}, \mathbf{b}^{(2)}$ and originates from the nonlinear terms of (2-8), $\mathbf{H}_1(\mathbf{b}), \mathbf{H}_2(\mathbf{b})$ are generalized stiffness vectors depending nonlinearly on \mathbf{b} and originate from the nonlinear terms of (2-11), $\mathbf{A}_1, \mathbf{A}_2, \mathbf{B}_1, \mathbf{B}_2$ are $M \times M$ known matrices and originate from the linear terms of (2-11), and $\mathbf{G}_1, \mathbf{G}_2$ are vectors containing the in-plane loads. The expressions of these quantities are given in the Appendix.

Equation (3-14a) represents the semidiscretized equation of motion of the plate. The associated initial conditions are obtained by substituting (3-8) into (2-9):

$$\mathbf{b}(0) = \mathbf{W}^{-1}\mathbf{g}_1, \quad \dot{\mathbf{b}}(0) = \mathbf{W}^{-1}\mathbf{g}_2, \quad (3-15)$$

where \mathbf{W} is $M \times M$ known matrix and $\mathbf{g}_1, \mathbf{g}_2$ are vectors originating from (2-9).

3.4. The solution of the nonlinear equations of motion. Equations (3-14b) and (3-14c) are quasistatic and linear with respect to $\mathbf{b}^{(1)}$ and $\mathbf{b}^{(2)}$. Thus solving for these vectors and substituting in (3-14a) yields the equation of motion

$$M\ddot{\mathbf{b}} + C\dot{\mathbf{b}} + \mathbf{S}(\mathbf{b}) = \mathbf{0}. \quad (3-16)$$

A time step integration for nonlinear equations can be employed to solve (3-16) with the initial conditions (3-15). The use however, of all the degrees of freedom may be computationally costly and in some

cases be inefficient due to the large number of coefficients $b_k(t)$. To overcome this difficulty in this investigation, the number of degrees of freedom is reduced using the Ritz transformation

$$\mathbf{b} = \Psi \mathbf{z}, \tag{3-17}$$

where $z_i(t)$ ($i = 1, \dots, L < M$) are new time-dependent parameters and Ψ is the $M \times L$ transformation matrix. Using this transformation, (3-16) and (3-15) are transformed into the reduced nonlinear initial value problem

$$\tilde{\mathbf{M}}\ddot{\mathbf{z}} + \tilde{\mathbf{C}}\dot{\mathbf{z}} + \tilde{\mathbf{S}}(\mathbf{z}) = \mathbf{0}, \tag{3-18a}$$

$$\mathbf{z}(0) = (\Psi^T \Psi)^{-1} \Psi^T \mathbf{W}^{-1} \mathbf{g}_1, \quad \dot{\mathbf{z}}(0) = (\Psi^T \Psi)^{-1} \Psi^T \mathbf{W}^{-1} \mathbf{g}_2, \tag{3-18b}$$

where $\tilde{\mathbf{M}} = \Psi^T \mathbf{M} \Psi$, $\tilde{\mathbf{C}} = \Psi^T \mathbf{C} \Psi$, and $\tilde{\mathbf{S}}(\mathbf{z}) = \Psi^T \mathbf{S}(\mathbf{b})$.

In this investigation the eigenmodes of the linear flutter plate problem near the critical load in absence of damping are selected as Ritz vectors [Guo and Mei 2003]. Equation (3-18a) under any specified initial conditions, say $g_1(\mathbf{x}) \neq 0$, $g_2(\mathbf{x}) = 0$, is solved and the postcritical response of the plate is studied by increasing the conservative and nonconservative loads. It is convenient to take the first mode of the linear problem as $g_1(\mathbf{x})$. The new AEM time step integration method developed for multiterm fractional differential equations [Katsikadelis 2009] has been employed to solve (3-18), because the modified Newton–Raphson method was not successful in all cases.

For the linear problem the nonlinear terms $\mathbf{H}_1(\mathbf{b})$, $\mathbf{H}_2(\mathbf{b})$ vanish and Equations (3-14b), (3-14c) can be solved independently to obtain the fictitious sources \mathbf{b}_1 , \mathbf{b}_2 . Moreover, (3-14a) becomes linear:

$$\mathbf{M}\ddot{\mathbf{b}} + \mathbf{C}\dot{\mathbf{b}} + (\mathbf{K} + \mathbf{F})\mathbf{b} = \mathbf{0}, \tag{3-19}$$

where \mathbf{K} and \mathbf{F} are linear generalized stiffness matrices given as

$$K_{ik} = D\delta_{ik}, \tag{3-20}$$

$$F_{ik} = (q_x^i + n_x^i)W_{ik,x} + (q_y^i + n_y^i)W_{ik,y} - N_x^i W_{ik,xx} - 2N_{xy}^i W_{ik,xy} - N_y^i W_{ik,yy}, \tag{3-21}$$

where $i, k = 1, \dots, M$ and δ_{ik} the Kronecker delta.

This problem is solved by assuming a time harmonic solution

$$b_k(t) = \beta_k e^{i\lambda t}, \tag{3-22}$$

where β_k are parameters which do not depend on time and λ is the frequency of the vibration.

Substituting (3-22) into (3-19) we obtain the quadratic eigenvalue problem

$$(-\lambda^2 \mathbf{M} + \lambda i \mathbf{C} + \mathbf{K} + \mathbf{F})\boldsymbol{\beta} = \mathbf{0}, \tag{3-23}$$

where $\boldsymbol{\beta}$ is the vector containing the elements β_k . By increasing the conservative and nonconservative loads the imaginary part of frequency λ becomes negative and the plate becomes unstable. The obtained eigenmodes from the eigenvalue problem (3-23) in absence of damping and near the critical value are employed as Ritz vectors in (3-17).

4. Examples

On the base of the previously described procedure a FORTRAN code has been written for solving the nonlinear flutter instability problem for plates. The efficiency and accuracy of the method is demonstrated by the following examples.

Example 1. We study the stability of the square plate of Figure 3. The plate is subjected to a follower uniform in-plane line load along the free edge. The boundary conditions are also shown in the figure. Two types of in-plane boundary conditions, designated as case (i) and case (ii), are considered along the edges $x = 0$ and $y = 0, 4$. Case (i), though not realistic, has been studied because there are results in the literature for comparison. It should be noted that in this case the distribution of the membrane forces is uniform ($N_x = P, N_y = N_{xy} = 0$). In case (ii) the distribution of the membrane forces is nonuniform and it results from the simultaneous solution of the nonlinear plane stress problem. This is an advantage of the presented solution method, since it permits the investigation of the influence of the in-plane boundary conditions on the nonlinear flutter instability. The parameters used are

$$E = 30 \text{ GPa}, \quad h = 0.1 \text{ m}, \quad \nu = 0.3, \quad \rho = 10^4 \text{ kg/m}^3.$$

The results were obtained with $N = 276$ boundary elements and $M = 133$ internal collocation points (Figure 4, left).

Figure 4, right, shows the first two eigenfrequencies of the linear plate problem without damping as the follower load increases. Flutter instability occurs when two real frequencies coalesce and become complex conjugate. The linear flutter loads are for case (i) $P_{cr} = 8917 \text{ kN}$ (8868 kN [Adali 1982]) and for case (ii) $P_{cr} = 10400 \text{ kN}$. The modes of the linear eigenproblem obtained at (i) $P = 8800 \text{ kN}$ and (ii) $P = 10000 \text{ kN}$ were employed as Ritz vectors. Figure 5 shows the dependence of the maximum deflection at point A of the undamped plate on the follower force using different number of the linear modes. The use of more than 10 modes does not change the results considerably. Figure 6 shows the amplitude of the oscillations when external and internal damping is considered. Figure 7, left, shows the

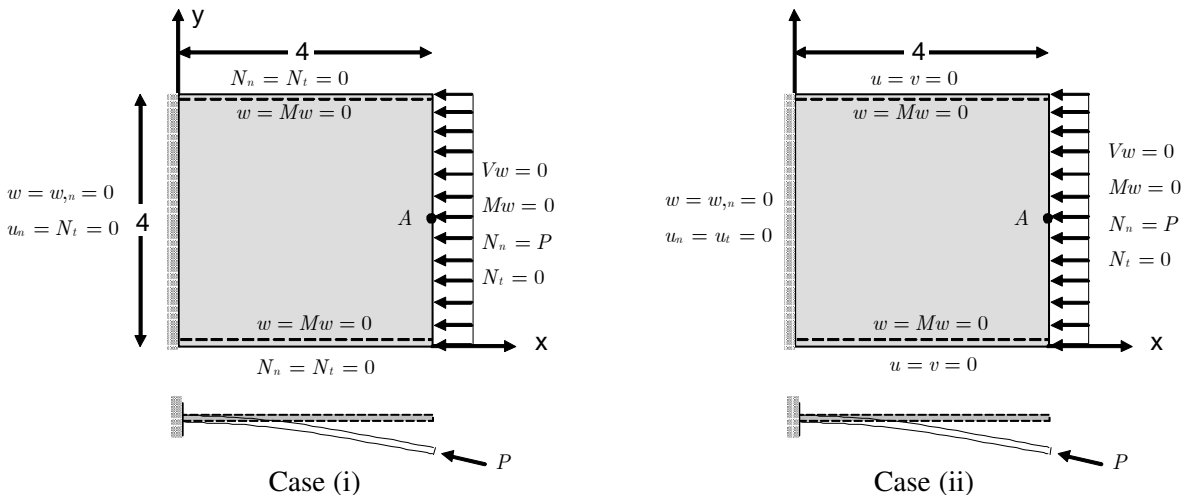


Figure 3. Geometry and boundary conditions of the plate in Example 1.

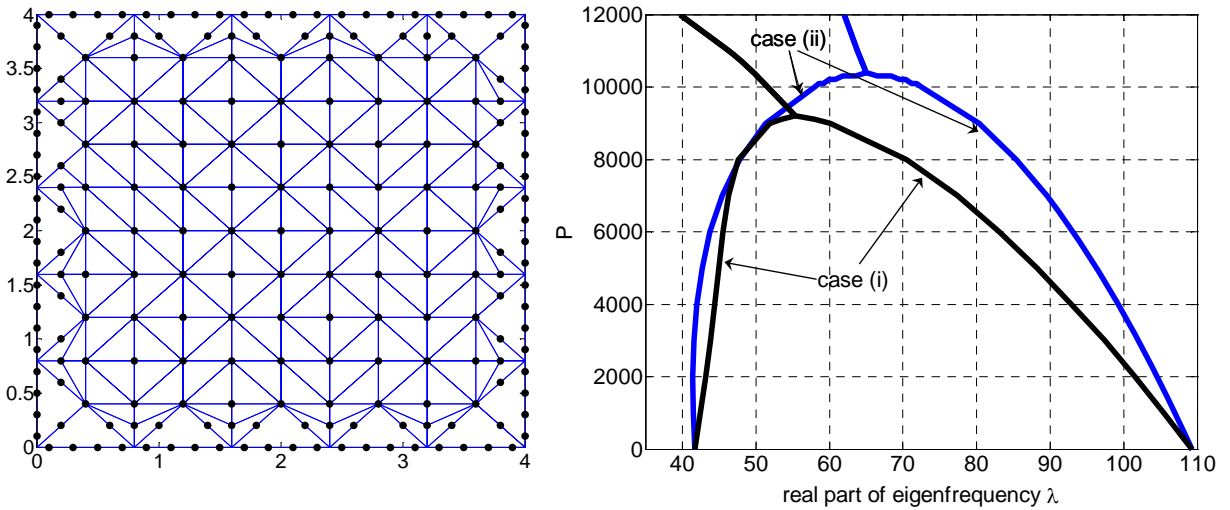


Figure 4. In reference to Example 1. Left: Boundary and domain nodal points. Right: Frequencies versus load.

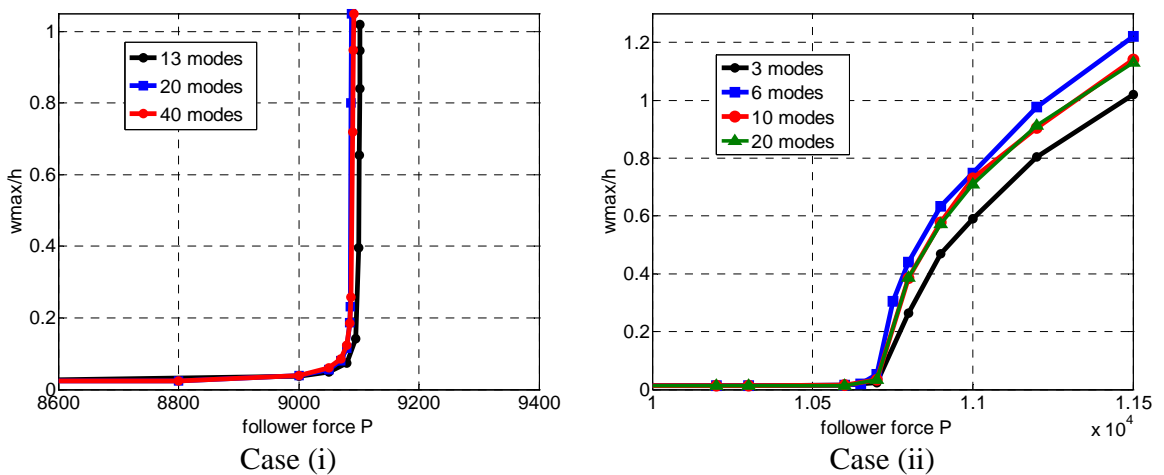


Figure 5. Maximum deflection at point A with different number of the linear modes employed for reduction of the degrees of freedom in the undamped plate in Example 1.

time history of the deflection at A on the free edge in case (ii) without ($c = 0$) and with external damping ($c = 2$). In the presence of damping (external or internal) the plate reaches a limit cycle oscillation. It is observed that viscous damping has a stabilizing effect while the structural damping destabilizes the plate. This result is in accordance with that reported by other researchers [Higuchi and Dowell 1992; Mei 1977]. Finally, Figure 7, right, shows the limit cycle of the deflection at point (3.2, 2); note that it is a Lamé curve with $n = 2.1$.

Example 2. The stability of the simply supported plate of Figure 8 is investigated. The plate is subjected to aerodynamic pressure due to steady supersonic air flow $q_x = 0.307\mu$, $q_y = 0$ and aerodynamic damping

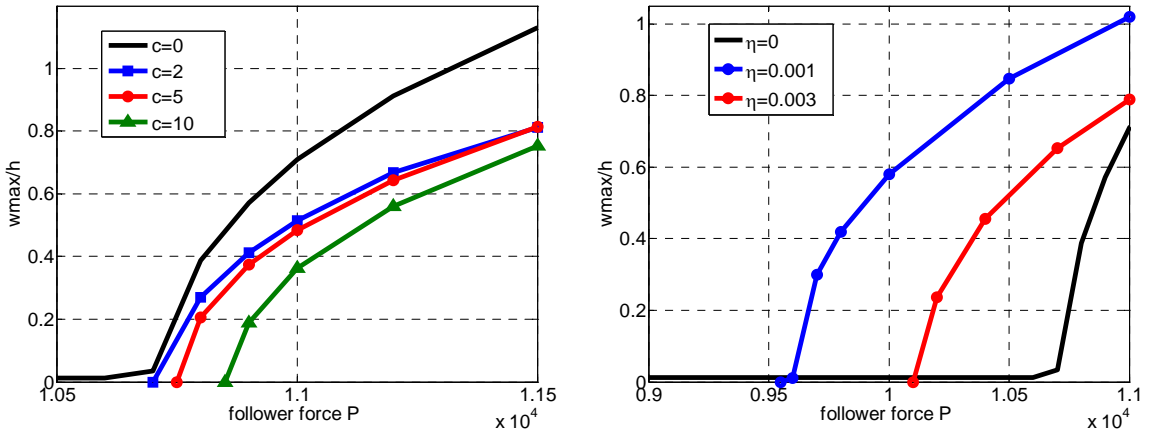


Figure 6. Amplitude of the limit cycle oscillation at point A for case (ii) (10 Ritz modes), with viscous damping (left) and with structural damping (right).

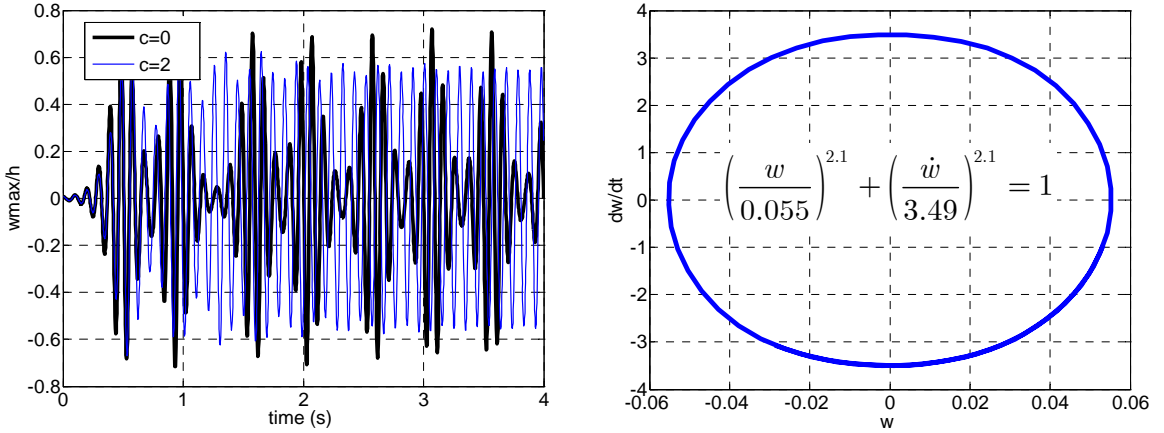


Figure 7. Left: Time history of the deflection at point (3.2, 2) with and without external damping. Right: Phase plane plot at point (3.2, 2) for external damping $c = 2$ for $t > 7$ sec ($P = 11500$ kN/m, 10 Ritz modes, case (ii)).

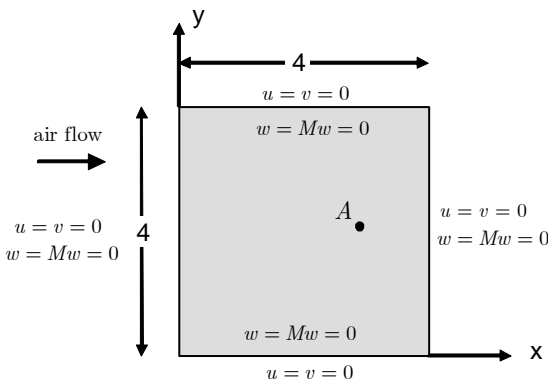


Figure 8. Simply supported immovable plate of Example 2.

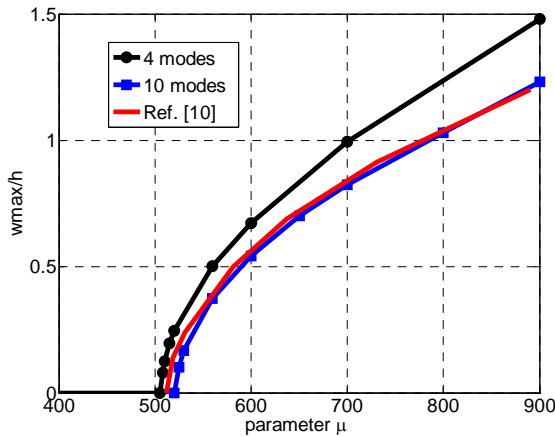


Figure 9. Amplitude of the limit cycles versus parameter μ at point $A(3, 2)$.

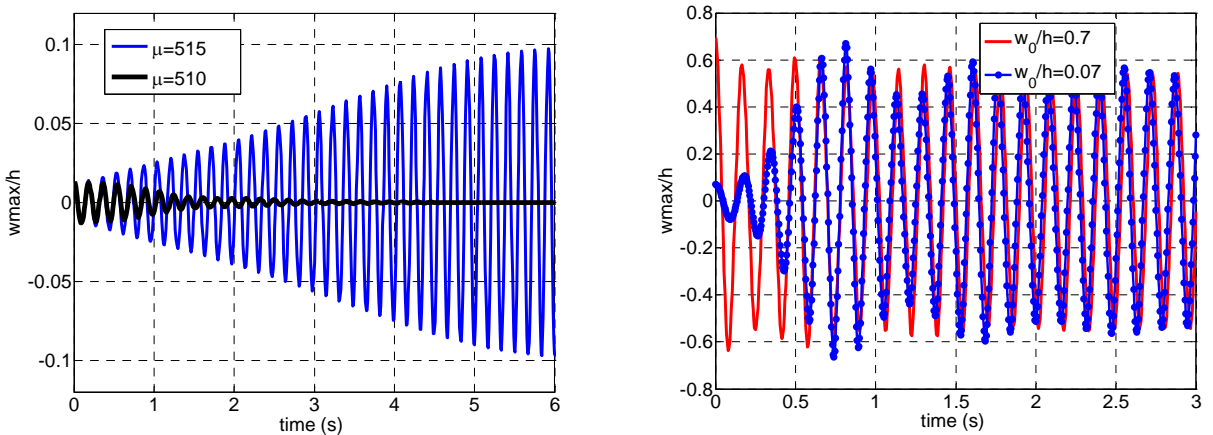


Figure 10. Left: Time history of the deflection at point A for two values of μ . Right: The effect of the initial conditions on limit cycle oscillations, for $\mu = 600$.

$c = 0.00857\sqrt{\mu}$, where μ is a nondimensional parameter which depends on the air flow velocity [Guo and Mei 2003]. The other parameters are

$$E = 210 \text{ GPa}, \quad h = 0.01 \text{ m}, \quad \nu = 0.33, \quad \rho = 10^4 \text{ kg/m}^3.$$

For the linear problem the critical value was found $\mu_{cr} = 519$ ($\mu_{cr} = 512$ in [Guo and Mei 2003]). Figure 9 shows the amplitude of the limit cycle oscillation at point $A(3, 2)$ with increasing parameter μ using 4 and 10 Ritz modes and a FEM solution [Guo and Mei 2003]. Figure 10 shows the time history of the deflection at point A for two values of μ , and then for two different initial conditions; from the graph on the right it is clear that the limit cycle oscillation is independent of the initial displacements. Figure 11 depicts the time history of the bending moment m_x and the membrane force N_x at point A for $\mu = 890$. Finally, in Figure 12 we see the phase plane plot at point A for $\mu = 890$, and the limit cycle, which is again a Lamé curve with $n = 2.8$.

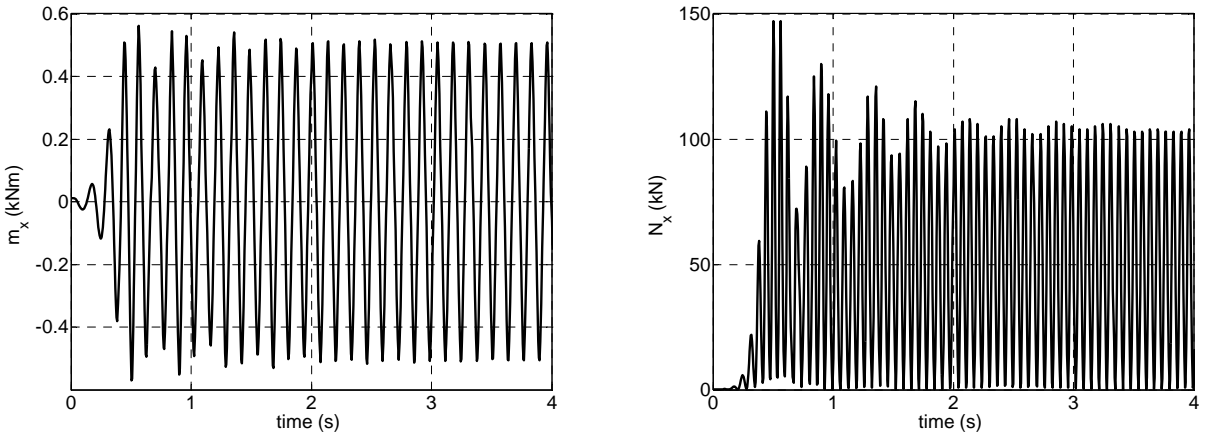


Figure 11. Time history of the bending moment m_x (left) and of the membrane force N_x (right) at point A, for $\mu = 890$.

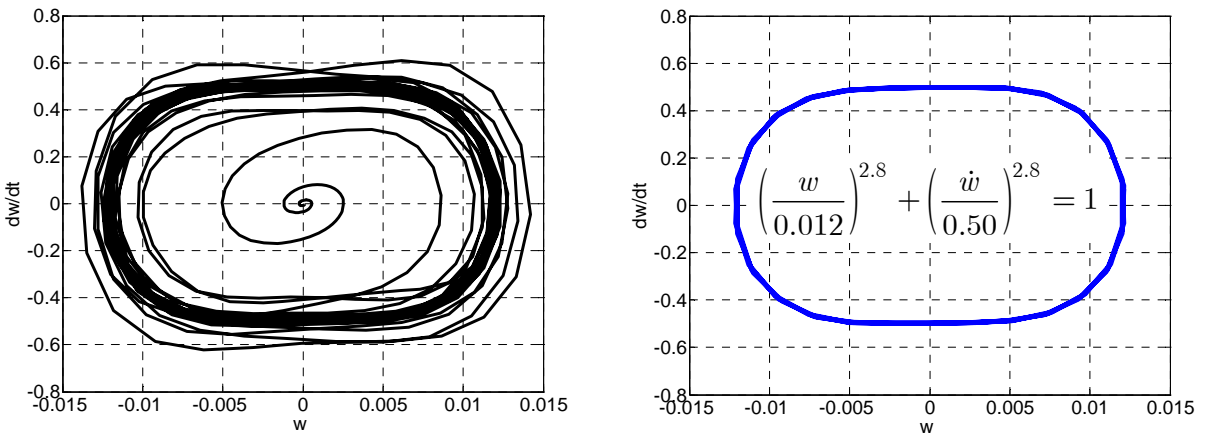


Figure 12. Phase plane plot at point A for $\mu = 890$ (10 modes) for $0 < t < 5$ (left) and $t > 4$ (right).

Example 3. The rectangular plate of [Figure 13](#) is subjected to the combined action of aerodynamic pressure due to steady supersonic air flow $q_x = \mu$, $q_y = 0$ and a conservative in-plane line load along two opposite edges. The aerodynamic damping is $c = 0.1$. The other parameters used are

$$E = 210 \text{ GPa}, \quad h = 0.01 \text{ m}, \quad \nu = 0.3, \quad \rho = 7550 \text{ kg/m}^3.$$

The results were obtained with $N = 300$ boundary elements and $M = 253$ internal collocation points and 20 eigenmodes as Ritz vectors for reduction of the degrees of freedom. [Figure 14](#) presents the stability regions with increasing aerodynamic pressure (nonconservative) and in-plane load (conservative). [Figure 15](#) presents the time history of the deflection at the center of the plate in the case of divergence type of instability. In this case the plate buckles but remains in dynamic stable situation. [Figure 16](#) shows the time history of the deflection of point A(1.5, 2) in the case of flutter instability.

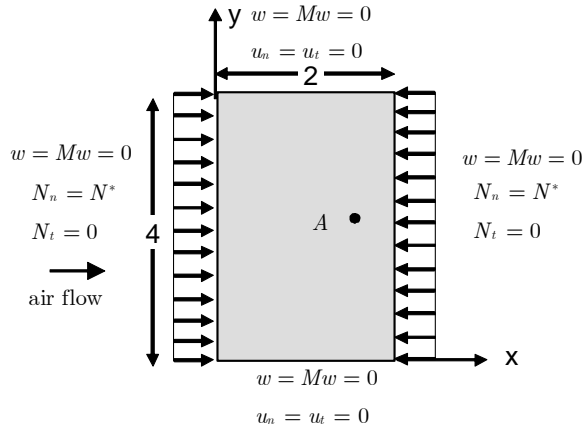


Figure 13. Geometry and boundary conditions of the plate in Example 3.

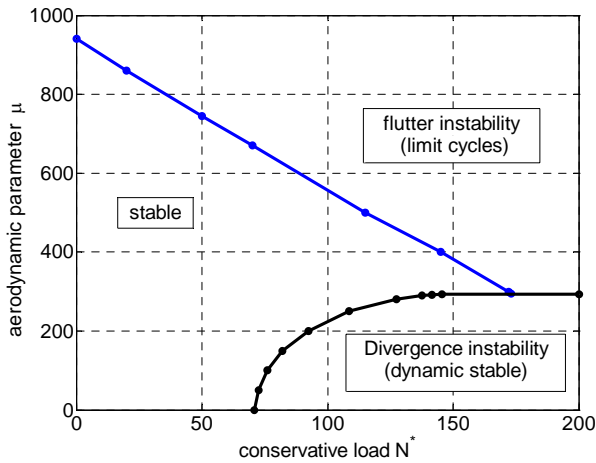


Figure 14. Stability regions for the combined action of nonconservative (aerodynamic pressure) and conservative loads.

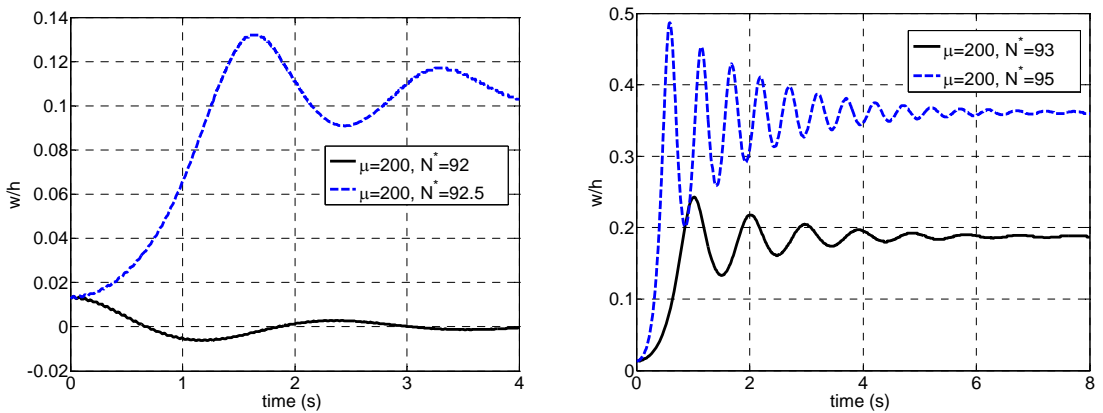


Figure 15. Time history of the deflection at the center of the plate ($\mu = 200$) for $N^* = 92, 92.5$ (left) and $N^* = 93, 95$ (right).

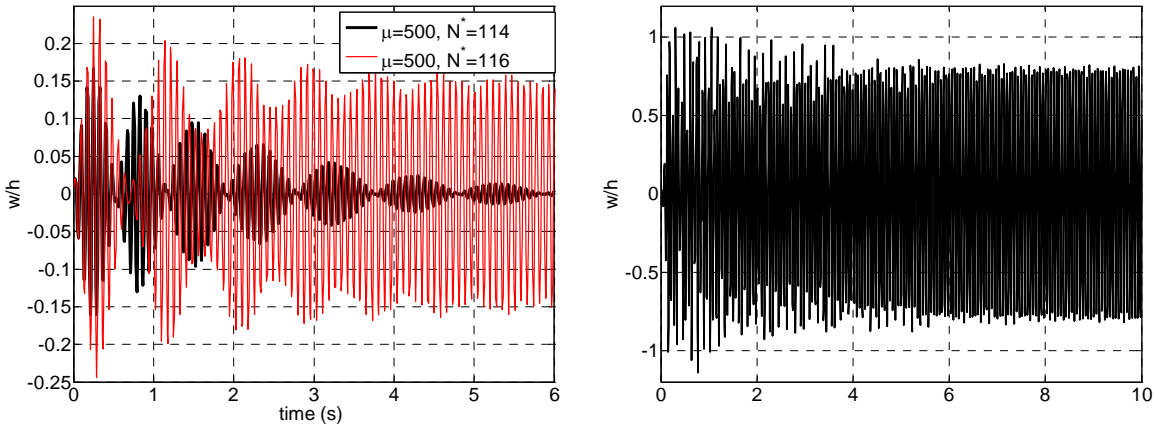


Figure 16. Time history of the deflection at point A for $\mu = 500$, $N^* = 114$, 116 (left) and $\mu = 700$, $N^* = 100$ (right).

Example 4. The cantilever plate of Figure 17, left, is subjected to aerodynamic pressure due to steady supersonic air flow $q_x = 0$, $q_y = 0.031v^2$, where v is the air velocity. The other parameters used are $E = 210$ GPa, $h = 0.01$ m, $\nu = 0.3$, $\rho = 7550$ kg/m³. The results were obtained with $N = 385$ boundary elements and $M = 125$ internal collocation points and 20 eigenmodes as Ritz vectors for reduction of the degrees of freedom. Figure 18 on the preceding page presents the frequencies of the linear plate

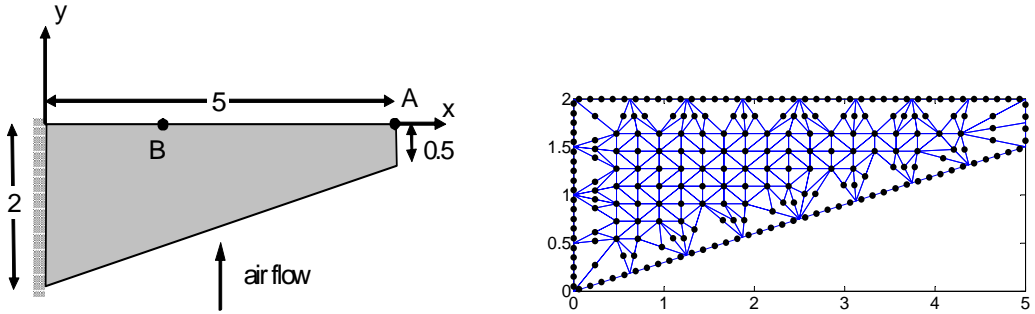


Figure 17. Left: Cantilever plate of Example 4. Right: Boundary and domain nodal points.

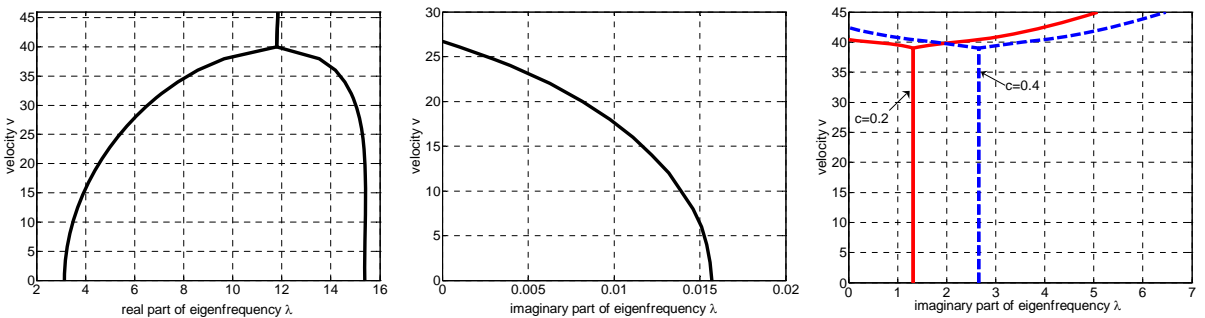


Figure 18. Frequency vs. air velocity for the linear plate problem with no damping (left), structural damping $\eta = 0.01$ (middle), and viscous damping $c = 0.2, 0.4$ (right).

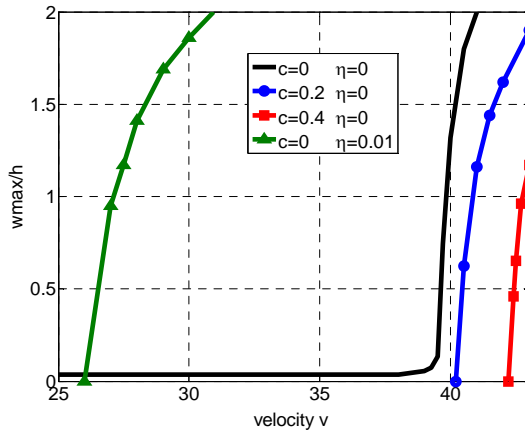


Figure 19. Maximum deflection in absence of damping and amplitude of the limit cycles in presence of damping versus air velocity v at corner point A.

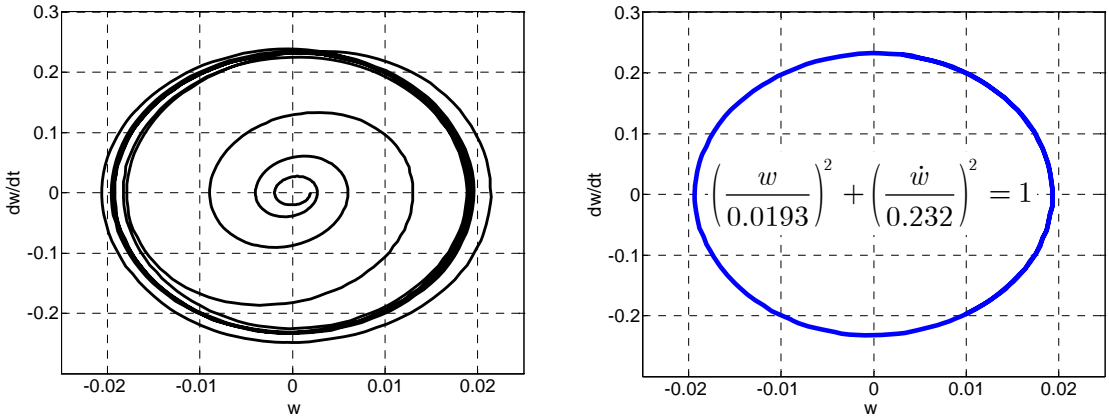


Figure 20. Phase plane plot at point (5, 2) with external damping $c = 0.2$ for $0 < t < 8$ sec (left) and $t > 7$ sec (right), with $v = 43$ m/s and 20 Ritz modes.

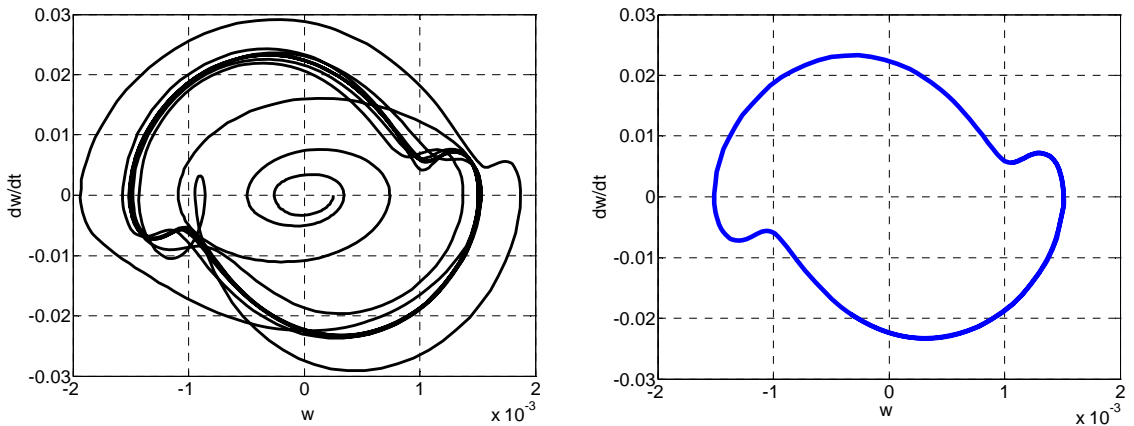


Figure 21. Phase plane plot at point (2, 2) with external damping $c = 0.2$ for $0 < t < 8$ sec (left) and $t > 7$ sec (right), with $v = 43$ m/s and 20 Ritz modes.

problem as the air velocity increases in absence of damping and for various values of external (viscous) and internal (structural) damping. The linear flutter velocity is $v_{cr} = 38.9$ m/s in absence of damping, $v_{cr} = 40.5$ m/s with external damping $c = 0.2$, $v_{cr} = 42.3$ m/s with external damping $c = 0.4$ and $v_{cr} = 26.7$ m/s with internal damping $\eta = 0.01$. Figure 19 presents the maximum deflection at point A in absence of damping and the amplitude of the limit cycles in presence of internal or external damping for various values of the flow velocity. Figures 20 and 21 show the phase plot at points A and B respectively when $v = 43$ m/s and $c = 0.2$. At point A the limit cycle is a Lamé curve with $n = 2$ (ellipse).

5. Conclusions

Nonlinear flutter instability of thin plates of arbitrary geometry subjected to general types of boundary conditions, under both interior as well as edge conservative and nonconservative loads, and in the presence of external and internal damping, has been investigated in this work. Solution of this problem is achieved by the AEM, an integral equation method that converts coupled nonlinear PDEs describing the response of the plate into uncoupled, linear PDEs that are subsequently treated by the D/BEM. More specifically, the semidiscretized nonlinear equations of motion give rise to an initial-value problem that is efficiently solved using a small set of modes near the critical point as Ritz vectors in conjunction with a novel time stepping algorithm.

As far as numerical implementation was concerned, the influence of in-plane boundary conditions that appears in realistic formulations of plate aeroelasticity problems on flutter instability was investigated. Certain findings on the nonlinear flutter instability reported earlier by other researchers that were based on simple engineering models were validated. Among them is the stabilizing effect of external (viscous) damping in contrast to the destabilizing effect of internal (structural) damping. Also, the combined action of conservative and nonconservative loads was studied, which may lead to divergence or flutter instability in the plate. In closing, the methodology presented herein yields an efficient computational tool for studying complex problems stemming from the nonlinear dynamic response of thin plates subjected to conservative and nonconservative loads.

Appendix: Expressions for the matrices (3-14)

The indices i and k range from 1 to M .

$$\begin{aligned}
 M_{ik} &= \rho_i h W_{ik}, & C_{ik} &= c_i W_{ik}, \\
 H^i &= -N_x^i \sum_{k=1}^M W_{ik,xx} b_k - 2N_{xy}^i \sum_{k=1}^M W_{ik,xy} b_k - N_y^i \sum_{k=1}^M W_{ik,yy} b_k \\
 & & & + (q_x^i + n_x^i) \sum_{k=1}^M W_{ik,x} b_k + (q_y^i + n_y^i) \sum_{k=1}^M W_{ik,y} b_k, \\
 A_{1ik} &= \delta_{ik} + \frac{1+\nu}{1-\nu} (U_{ik,xx}^{(1)} + V_{ik,xy}^{(1)}), & B_{1ik} &= \frac{1+\nu}{1-\nu} (U_{ik,xx}^{(2)} + V_{ik,xy}^{(2)}), \\
 A_{2ik} &= \frac{1+\nu}{1-\nu} (U_{ik,xy}^{(1)} + V_{ik,yy}^{(1)}), & B_{2ik} &= \delta_{ik} + \frac{1+\nu}{1-\nu} (U_{ik,xy}^{(2)} + V_{ik,yy}^{(2)}),
 \end{aligned}$$

$$G_1^i = -\frac{n_x^i + p_x^i}{Gh} - \frac{1 + \nu}{1 - \nu} (U_{0i,xx} + V_{0i,xy}), \quad G_2^i = -\frac{n_y^i + p_y^i}{Gh} - \frac{1 + \nu}{1 - \nu} (U_{0i,xy} + V_{0i,yy}),$$

$$H_1^i = \left(\frac{2}{1 - \nu} \sum_{k=1}^M W_{ik,xx} b_k + \sum_{k=1}^M W_{ik,yy} b_k \right) \sum_{k=1}^M W_{ik,x} b_k + \frac{1 + \nu}{1 - \nu} \sum_{k=1}^M W_{ik,xy} b_k \sum_{k=1}^M W_{ik,y} b_k,$$

$$H_2^i = \left(\frac{2}{1 - \nu} \sum_{k=1}^M W_{ik,yy} b_k + \sum_{k=1}^M W_{ik,xx} b_k \right) \sum_{k=1}^M W_{ik,y} b_k + \frac{1 + \nu}{1 - \nu} \sum_{k=1}^M W_{ik,xy} b_k \sum_{k=1}^M W_{ik,x} b_k,$$

where

$$N_x^i = C \left(\sum_{k=1}^M (U_{ik,x}^{(1)} + \nu V_{ik,y}^{(1)}) b_k^{(1)} + \sum_{k=1}^M (U_{ik,x}^{(2)} + \nu V_{ik,y}^{(2)}) b_k^{(2)} + U_{0i,x} + \nu V_{0i,y} \right. \\ \left. + \frac{1}{2} \left(\sum_{k=1}^M W_{ik,x} b_k \right)^2 + \frac{1}{2} \nu \left(\sum_{k=1}^M W_{ik,y} b_k \right)^2 \right),$$

$$N_y^i = C \left(\sum_{k=1}^M (\nu U_{ik,x}^{(1)} + V_{ik,y}^{(1)}) b_k^{(1)} + \sum_{k=1}^M (\nu U_{ik,x}^{(2)} + V_{ik,y}^{(2)}) b_k^{(2)} + \nu U_{0i,x} + V_{0i,y} \right. \\ \left. + \frac{1}{2} \nu \left(\sum_{k=1}^M W_{ik,x} b_k \right)^2 + \frac{1}{2} \left(\sum_{k=1}^M W_{ik,y} b_k \right)^2 \right),$$

$$N_{xy}^i = C \frac{1 - \nu}{2} \left(\sum_{k=1}^M (U_{ik,y}^{(1)} + V_{ik,x}^{(1)}) b_k^{(1)} + \sum_{k=1}^M (U_{ik,y}^{(2)} + V_{ik,x}^{(2)}) b_k^{(2)} + U_{0i,y} + V_{0i,x} + \sum_{k=1}^M W_{ik,x} b_k \sum_{k=1}^M W_{ik,y} b_k \right).$$

References

[Adali 1982] S. Adali, “Stability of a rectangular plate under nonconservative and conservative forces”, *Int. J. Solids Struct.* **18**:12 (1982), 1043–1052.

[Babouskos and Katsikadelis 2009] N. Babouskos and J. T. Katsikadelis, “Flutter instability of damped plates under combined conservative and nonconservative loads”, *Arch. Appl. Mech.* **79**:6–7 (2009), 541–556.

[Chen et al. 2008] D. Chen, Y. Yang, and C. Fan, “Nonlinear flutter of a two-dimension thin plate subjected to aerodynamic heating by differential quadrature method”, *Acta Mech. Sinica* **24**:1 (2008), 45–50.

[Dowell 1966] E. H. Dowell, “Nonlinear oscillations of a fluttering plate”, *AIAA J.* **4**:7 (1966), 1267–1275.

[Guo and Mei 2003] X. Guo and C. Mei, “Using aeroelastic modes for nonlinear panel flutter at arbitrary supersonic yawed angle”, *AIAA J.* **41**:2 (2003), 272–279.

[Higuchi and Dowell 1992] K. Higuchi and E. H. Dowell, “Effect of structural damping on flutter of plates with a follower force”, *AIAA J.* **30**:3 (1992), 820–825.

[Katsikadelis 1994] J. T. Katsikadelis, “The analog equation method: a powerful BEM-based solution technique for solving linear and nonlinear engineering problems”, pp. 167–182 in *Boundary element method XVI* (Southampton, 1994), edited by C. A. Brebbia, Computational Mechanics Publications, Southampton, 1994.

[Katsikadelis 2002] J. T. Katsikadelis, “The analog boundary integral equation method for nonlinear static and dynamic problems in continuum mechanics”, *J. Theor. Appl. Mech. (Warsaw)* **40** (2002), 961–984.

[Katsikadelis 2009] J. T. Katsikadelis, “Numerical solution of multi-term fractional differential equations”, *Z. Angew. Math. Mech.* **89**:7 (2009), 593–608.

[Kim and Kim 2000] J. H. Kim and H. S. Kim, “A study on the dynamic stability of plates under a follower force”, *Comput. Struct.* **74**:3 (2000), 351–363.

- [Leipholz and Pfenndt 1983] H. Leipholz and F. Pfenndt, “Application of extended equations of Galerkin to stability problems of rectangular plates with free edges and subjected to uniformly distributed follower forces”, *Comput. Methods Appl. Mech. Eng.* **37**:3 (1983), 341–365.
- [Mei 1977] C. Mei, “A finite-element approach for nonlinear panel flutter”, *AIAA J.* **15**:8 (1977), 1107–1110.
- [Shiau and Lu 1990] L. C. Shiau and L. T. Lu, “Nonlinear flutter of composite laminated plates”, *Math. Comput. Model.* **14** (1990), 983–988.
- [Weiliang and Dowell 1991] Y. Weiliang and E. Dowell, “Limit cycle oscillation of a fluttering cantilever plate”, *AIAA J.* **29**:11 (1991), 1929–1936.
- [Zuo and Schreyer 1996] Q. H. Zuo and H. L. Schreyer, “Flutter and divergence instability of nonconservative beams and plates”, *Int. J. Solids Struct.* **33**:9 (1996), 1355–1367.

Received 10 Oct 2008. Revised 7 Mar 2009. Accepted 9 Mar 2009.

JOHN T. KATSIKADELIS: jkats@central.ntua.gr

Academy of Athens, Office of Theoretical and Applied Mechanics, 4 Soranou Efessiou,, 11527 Athens, Greece

and

National Technical University of Athens, School of Civil Engineering, Heroon Polytechniou 9, 15780 Athens, Greece

NICK G. BABOUSKOS: babouskosn@yahoo.gr

National Technical University of Athens, School of Civil Engineering, Heroon Polytechniou 9, 15773 Athens, Greece

THE EFFECT OF INFINITESIMAL DAMPING ON NONCONSERVATIVE DIVERGENCE INSTABILITY SYSTEMS

ANTHONY N. KOUNADIS

The present work discuss the local dynamic asymptotic stability of 2-DOF weakly damped nonconservative systems under follower compressive loading in regions of divergence, using the Liénard–Chipart stability criterion. Individual and coupling effects of the mass and stiffness distributions on the local dynamic asymptotic stability in the case of infinitesimal damping are examined. These autonomous systems may either be subjected to compressive loading of constant magnitude and varying direction (follower) with infinite duration or be completely unloaded. Attention is focused on regions of divergence (static) instability of systems with positive definite damping matrices. The aforementioned mass and stiffness parameters combined with the algebraic structure of positive definite damping matrices may have under certain conditions a tremendous effect on the Jacobian eigenvalues and thereafter on the local dynamic asymptotic stability of these autonomous systems. It is also found that contrary to conservative systems local dynamic asymptotic instability may occur, strangely enough, for positive definite damping matrices before divergence instability, even in the case of infinitesimal damping (failure of Ziegler’s kinetic criterion).

1. Introduction

The importance of damping on the local dynamic asymptotic stability of nonconservative systems was recognized long ago [Ziegler 1952; Nemat-Nasser and Herrmann 1966; Crandall 1970]. Particular attention was given to nonconservative discrete systems under follower load (autonomous systems) which may lose their stability either via flutter (vibrations of continuously increasing amplitude) or via divergence (static) instability depending on the region of variation of the nonconservativeness loading parameter.

The local dynamic stability of such autonomous nonconservative damped systems is governed by the *matrix-vector* differential equation [Kounadis 2006; 2007]

$$\mathbf{M}\ddot{\mathbf{q}} + \mathbf{C}\dot{\mathbf{q}} + \mathbf{V}\mathbf{q} = 0, \quad (1)$$

where the dot denotes differentiation with respect to time t , $\mathbf{q}(t)$ is an n -dimensional state vector with coordinates $q_i(t)$ ($i = 1, \dots, n$), and \mathbf{M} and \mathbf{C} are $n \times n$ real symmetric matrices, while \mathbf{V} is an asymmetric matrix if the nonconservativeness loading parameter η is different from one ($\eta = 1$ corresponds to a conservative load). Specifically, the matrix \mathbf{M} , associated with the total kinetic energy of the system, is a function of the concentrated masses m_i ($i = 1, \dots, n$), and is always positive definite; \mathbf{C} , whose elements are the damping coefficients c_{ij} ($i, j = 1, \dots, n$), may be positive definite, positive semidefinite, as in the case of pervasive damping [Zajac 1964; 1965], or indefinite [Laneville and Mazouzi 1996; Sygulski

Keywords: nonconservative divergence, follower load, infinitesimal damping mass, Liénard–Chipart criterion, asymptotic instability.

1996]; V is a generalized stiffness matrix with coefficients k_{ij} ($i, j = 1, \dots, n$), whose elements V_{ij} are also linear functions of η and of a suddenly applied external load λ of constant magnitude with varying direction (partial follower load defined by η) and infinite duration [Kounadis 1999], that is, $V_{ij} = V_{ij}(\lambda; k_{ij}, \eta)$. Apparently, due to this type of loading the system under discussion is autonomous. The static instability or buckling loads λ_i^c ($i = 1, \dots, n$) are obtained by setting to zero the determinant of the stiffness asymmetric ($\eta \neq 1$) matrix $V(\lambda; k_{ij}, \eta)$:

$$V = |V(\lambda; k_{ij}, \eta)| = 0. \quad (2)$$

This clearly yields an n -th degree algebraic equation in λ for given values of k_{ij} and η . Assuming distinct critical states the determinant of the matrix $V(\lambda; k_{ij}, \eta)$ is positive for $\lambda < \lambda_1^c$, zero for $\lambda = \lambda_1^c$, and negative for $\lambda > \lambda_1^c$.

The boundary between flutter and divergence instability is obtained by solving with respect to λ and η the system of algebraic equations [Kounadis 1997]

$$V = \frac{\partial V}{\partial \lambda} = 0 \quad (3)$$

for given stiffness parameters k_{ij} ($i, j = 1, \dots, n$).

We established in [Kounadis 2006; 2007] the conditions under which the above autonomous dissipative systems under step loading of constant magnitude and direction (conservative load) with infinite duration may exhibit dynamic bifurcation modes of instability before divergence, that is, for $\lambda < \lambda_1^c$, when infinitesimal damping is included. These dynamic bifurcational modes may occur through either a degenerate Hopf bifurcation (leading to periodic motion around centers) or a generic Hopf bifurcation (leading to periodic attractors or to flutter). These unexpected findings (implying failure of Ziegler's kinetic criterion and other singularity phenomena) may occur for a certain combination of values of the mass (primarily) and stiffness distributions of the system in connection with a positive semidefinite or an indefinite damping matrix [Kounadis 2006; 2007].

The question now arises whether there are combinations of values of these parameters (the mass and stiffness distributions) which, in connection with positive definite damping matrices, may lead to dynamic bifurcational modes of instability when the system is nonconservative due to a partial follower compressive load associated with the nonconservativeness parameter η . Only cases of divergence instability occurring for suitable values of η are considered. Namely, pseudoconservative systems are considered which are subjected to nonconservative circulatory forces, being therefore essentially nonconservative systems [Huseyin 1978]. Systems exhibiting flutter are called Ziegler circulatory, although in this terminology pseudoconservative systems are not distinguished [Ziegler 1952]. Attention is focused mainly on infinitesimal damping which may have a tremendous effect on the system's divergence instability. Such local dynamic instability will be sought through Liénard–Chipart's set of asymptotic stability criteria [Gantmacher 1959; 1970] which are elegant and more readily employed than the well known Routh–Hurwitz stability criteria. The local dynamic asymptotic stability of these systems using the above criteria is also discussed if there is no loading ($\lambda = 0$).

In addition to the above main objective of this work, some new cases when the above autonomous systems are loaded by the aforementioned type of step follower compressive load will be also discussed by

analyzing 2-degree of freedom (DOF) systems for which a lot of numerical results are available. Finally, the conditions for the existence of a double purely imaginary root (eigenvalue) are properly discussed.

2. Basic equations

The solution of (1) can be sought in the form

$$\mathbf{q} = \mathbf{r} e^{\rho t}, \quad (4)$$

where ρ is in general a complex number (eigenvalue) and \mathbf{r} is a complex vector independent of time t .

Introducing \mathbf{q} from (4) into (1) we get

$$(\rho^2 \mathbf{M} + \rho \mathbf{C} + \mathbf{V}) \mathbf{r} = 0. \quad (5)$$

For given matrices \mathbf{M} , \mathbf{C} , and \mathbf{V} solutions of (5) are related to the Jacobian eigenvalues $\rho = \rho(\lambda)$ obtained by setting the determinant to zero, so

$$|\rho^2 \mathbf{M} + \rho \mathbf{C} + \mathbf{V}| = 0; \quad (6)$$

expansion of the determinant gives the characteristic (secular) equation for an n -DOF system

$$\rho^{2n} + \alpha_1 \rho^{2n-1} + \cdots + \alpha_{2n-1} \rho + \alpha_{2n} = 0, \quad (7)$$

where the real coefficients α_i ($i = 1, \dots, 2n$) are determined by means of the Bôcher formula [Pipes and Harvill 1970]. The eigenvalues ρ_j ($j = 1, \dots, 2n$) of (7) are, in general, complex conjugate pairs $\rho_j = v_j \pm \mu_j i$ (where v_j and μ_j are real numbers and $i = \sqrt{-1}$), with corresponding complex conjugate eigenvectors \mathbf{r}_j and $\bar{\mathbf{r}}_j$ ($j = 1, \dots, n$). Since $\rho_j = \rho_j(\lambda)$, clearly $v_j = v_j(\lambda)$, $\mu_j = \mu_j(\lambda)$, $\mathbf{r}_j = \mathbf{r}_j(\lambda)$, and $\bar{\mathbf{r}}_j = \bar{\mathbf{r}}_j(\lambda)$. Thus, the solutions of (1) are of the form

$$A e^{v_j t} \cos \mu_j t, \quad B e^{v_j t} \sin \mu_j t, \quad (8)$$

where constants A and B are determined from the initial conditions. Solutions (7) are bounded, tending to zero as $t \rightarrow \infty$, if all eigenvalues of (7) have negative real parts, that is, when $v_j < 0$ for all j . In this case the algebraic polynomial (7) is called a Hurwitz polynomial (since all its roots have negative real parts) and the origin ($\mathbf{q} = \dot{\mathbf{q}} = 0$) of the system is asymptotically stable.

Regarding the criteria for asymptotic stability it is worth mentioning the following. Consider the more general case of a polynomial in z with real coefficients α_i ($i = 0, 1, \dots, n$)

$$f(z) = \alpha_0 z^n + \alpha_1 z^{n-1} + \cdots + \alpha_{n-1} z + \alpha_n = 0 \quad (\alpha_0 > 0), \quad (9)$$

for which we will seek the necessary and sufficient conditions so that all its roots have negative real parts.

Denoting by z_κ ($\kappa = 1, \dots, m$) the real and by $r_j \pm i s_j$ ($j = 1, \dots, (n-m)/2$; $i = \sqrt{-1}$) the complex roots of (9) we can arrange for all these complex roots to lie to the left of the imaginary axis:

$$z_\kappa < 0, \quad r_j < 0 \quad (\kappa = 1, \dots, m; j = 1, \dots, \frac{n-m}{2}). \quad (10)$$

Then one can write

$$f(z) = \alpha_0 \prod_{\kappa=1}^m (z - z_\kappa) \prod_{j=1}^{\frac{n-m}{2}} (z^2 - 2r_j z + r_j^2 + s_j^2). \quad (11)$$

Since due to inequality (10) each term in the last part of (11) has positive coefficients, it is deduced that all coefficients of (9) are also positive. However, this (meaning $\alpha_i > 0$ for all i with $\alpha_0 > 0$) is a necessary but by no means sufficient condition for all roots of (9) to lie in the left half-plane ($\text{Re}(z) < 0$).

The Routh–Hurwitz criterion [Gantmacher 1959; 1970] gives necessary and sufficient conditions for asymptotic stability, that is, for all roots of (9) to have negative real parts; the conditions are

$$\Delta_1 > 0, \quad \Delta_2 > 0, \quad \dots, \quad \Delta_n > 0, \tag{12}$$

where

$$\Delta_1 = \alpha_1, \quad \Delta_2 = \begin{bmatrix} \alpha_1 & \alpha_3 \\ \alpha_0 & \alpha_2 \end{bmatrix}, \quad \Delta_3 = \begin{bmatrix} \alpha_1 & \alpha_3 & 0 \\ \alpha_0 & \alpha_2 & \alpha_4 \\ 0 & \alpha_1 & \alpha_3 \end{bmatrix}, \quad \dots, \quad \Delta_n = \begin{bmatrix} \alpha_1 & \alpha_3 & \alpha_5 & \dots \\ \alpha_0 & \alpha_2 & \alpha_4 & \dots \\ 0 & \alpha_1 & \alpha_3 & \dots \\ 0 & \alpha_0 & \alpha_2 & \alpha_4 & \dots \\ \vdots & \vdots & \vdots & \vdots & \ddots \\ & & & & \alpha_i \end{bmatrix} \tag{13}$$

with $\alpha_\kappa = 0$ for $\kappa > n$. The last equality yields $\Delta_n = \alpha_n \Delta_{n-1}$.

Note that when the necessary conditions $\alpha_i > 0$ (for all i) hold, the inequalities (17) are *not* independent. For instance, for $n = 4$ the Routh–Hurwitz conditions reduce to the single inequality $\Delta_3 > 0$, for $n = 5$ they reduce to $\Delta_2 > 0$ and $\Delta_4 > 0$, while for $n = 6$ they reduce again to two inequalities, $\Delta_3 > 0$ and $\Delta_5 > 0$. This case was discussed by Liénard and Chipart who established the following elegant criterion for asymptotic stability [Gantmacher 1970].

The Liénard–Chipart stability criterion. Necessary and sufficient conditions for all roots of the real polynomial $f(z) = \alpha_0 z^n + \alpha_1 z^{n-1} + \dots + \alpha_{n-1} z + \alpha_n = 0$ ($\alpha_0 > 0$) to have negative real parts can be given in any one of the following forms:

$$\alpha_n > 0, \quad \alpha_{n-2} > 0, \quad \dots, \quad \text{with} \begin{cases} \text{either} & \Delta_1 > 0, \quad \Delta_3 > 0, \quad \dots, \\ \text{or} & \Delta_2 > 0, \quad \Delta_4 > 0, \quad \dots, \end{cases} \tag{14}$$

or

$$\alpha_n > 0, \quad \alpha_{n-1} > 0, \quad \alpha_{n-3} > 0, \quad \dots, \quad \text{with} \begin{cases} \text{either} & \Delta_1 > 0, \quad \Delta_3 > 0, \quad \dots, \\ \text{or} & \Delta_2 > 0, \quad \Delta_4 > 0, \quad \dots \end{cases} \tag{15}$$

This stability criterion was rediscovered by Fuller [1968].

In this study attention is focused on 2-DOF nonconservative (due to partial follower compressive loading) dissipative systems, whose characteristic equation (7) is written as follows:

$$\rho^4 + \alpha_1 \rho^3 + \alpha_2 \rho^2 + \alpha_3 \rho + \alpha_4 = 0 \quad (\alpha_0 = 1). \tag{16}$$

According to the last criterion all roots of (16) have negative real parts provided that $\alpha_4 > 0$, $\alpha_2 > 0$, and $\Delta_3 = \alpha_3(\alpha_1 \alpha_2 - \alpha_3) - \alpha_1^2 \alpha_4 > 0$. Clearly, from the last inequality it follows that $\alpha_3 > 0$. Hence, the positivity of α_1 and α_3 was assured via the above conditions ($\alpha_4 > 0$, $\alpha_2 > 0$, $\Delta_1 > 0$, and $\Delta_3 > 0$).

3. Mathematical analysis

Consider the cantilevered dissipative spring model with 2 DOFs under a partial follower compressive tip load which is shown on the next page. Subsequently we will examine in detail the effect of a violation of one or more of the conditions of the Liénard–Chipart criterion on its local dynamic asymptotic stability. The response of this dynamic model carrying two concentrated masses is studied when it is either loaded under a suddenly applied load of constant magnitude and varying direction with infinite duration or completely unloaded. Such autonomous dissipative systems with positive definite damping matrices and particularly with infinitesimal damping are properly investigated. If at least one root of the secular equation (16) has a positive real part the corresponding solution — see (8) — will contain an exponentially increasing function with time, and the system will become dynamically asymptotically unstable.

The seeking of an imaginary root of the secular equation (16) which represents a borderline between dynamic stability and instability is a first, important step in our discussion. Clearly, an imaginary root gives rise to an oscillatory motion of the form $e^{i\mu t}$ ($i = \sqrt{-1}$, μ real number) around the trivial state. However, the existence of at least one multiple imaginary root of the κ -th order of multiplicity leads to a solution containing functions of the form $e^{i\mu t}$, $t e^{i\mu t}$, \dots , $t^{\kappa-1} e^{i\mu t}$, which increase with time. Hence, the multiple imaginary root on the imaginary axis denotes local dynamic instability. The discussion of such a situation is also another objective of this study.

The nonlinear equations of motion for the 2-DOF nonconservative model of the figure with rigid links of equal length ℓ are given by [Kounadis 1997]

$$\begin{aligned} (1+m)\ddot{\theta}_1 + \ddot{\theta}_2 \cos(\theta_1 + \theta_2) - \dot{\theta}_2^2 \sin(\theta_1 - \theta_2) + c_{11}\dot{\theta}_1 + c_{12}\dot{\theta}_2 + V_1 &= 0, \\ \ddot{\theta}_2 + \ddot{\theta}_1 \cos(\theta_1 - \theta_2) - \dot{\theta}_1^2 \sin(\theta_1 - \theta_2) + c_{22}\dot{\theta}_2 + c_{12}\dot{\theta}_1 + V_2 &= 0, \end{aligned} \quad (17)$$

where

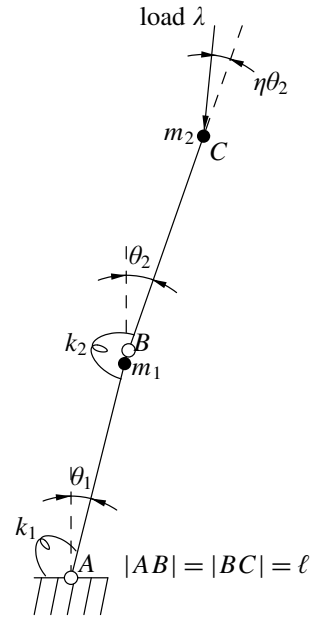
$$V_1 = (1+k)\theta_1 - \theta_2 - \lambda \sin(\theta_1 + (\eta-1)\theta_2), \quad V_2 = \theta_2 - \theta_1 - \lambda \sin \eta\theta_2,$$

η is the nonconservativeness loading parameter, and

$$m = \frac{m_1}{m_2}, \quad k = \frac{k_1}{k_2}, \quad \lambda = \frac{P\ell}{k_2}.$$

Linearization of Equation (17) after setting

$$\Theta = \begin{bmatrix} \theta_1 \\ \theta_2 \end{bmatrix} = e^{\rho t} \begin{bmatrix} \varphi_1 \\ \varphi_2 \end{bmatrix} = e^{\rho t} \phi$$



gives $(\rho^2 \mathbf{M} + \rho \mathbf{C} + \mathbf{V})\phi = 0$, where

$$\begin{aligned}
 \mathbf{M} &= \begin{bmatrix} m_{11} & m_{12} \\ m_{12} & m_{22} \end{bmatrix} = \begin{bmatrix} 1+m & 1 \\ & 1 \end{bmatrix}, & \mathbf{C} &= \begin{bmatrix} c_{11} & c_{12} \\ c_{12} & c_{22} \end{bmatrix}, \\
 \mathbf{V} &= \begin{bmatrix} V_{11} & V_{12} \\ V_{21} & V_{22} \end{bmatrix} = \begin{bmatrix} k+1-\lambda & -1-\lambda(\eta-1) \\ & -1 \quad 1-\lambda\eta \end{bmatrix}.
 \end{aligned} \tag{18}$$

In the case of a positive definite damping matrix of Rayleigh viscous type $c_{11} = c_1 + c_2$, $c_{12} = -c_2$, and $c_{22} = c_2$, where c_i ($i = 1, 2$) is the damping coefficient of the i -th bar.

The static buckling equation, $\det V = 0$, leads to

$$\eta\lambda^2 - \eta(k+2)\lambda + k = 0, \tag{19}$$

whose lowest root is the first buckling load λ_1^c equal to

$$\lambda_1^c = \frac{1}{2}(k+2 - \sqrt{(k+2)^2 - 4k/\eta}) \quad (\eta \neq 0). \tag{20}$$

For real roots the discriminant Δ of (19) must be greater or equal to zero ($\Delta \geq 0$) which yields

$$\eta \geq \frac{4k}{(k+2)^2}. \tag{21}$$

For instance, for $k = 1$ it follows that static instability occurs for $\eta \geq 4/9$ and flutter instability for $\eta < 4/9$. The coefficients of the characteristic equation (16) are given by

$$\begin{aligned}
 \alpha_1 &= \frac{1}{m}[(1+m)c_{22} + c_{11} - 2c_{12}], \\
 \alpha_2 &= \frac{1}{m}[(1+m)(1-\lambda\eta) + 3 + k - \lambda + \lambda(\eta-1) + |c|], \\
 \alpha_3 &= \frac{1}{m}\{c_{11}(1-\lambda\eta) + c_{22}(1+k-\lambda) + [2 + \lambda(\eta-1)]c_{12}\}, \\
 \alpha_4 &= \frac{1}{m}[\eta\lambda^2 - \eta(k+2)\lambda + k] = \frac{1}{m} \det V,
 \end{aligned} \tag{22}$$

where $|c| = \det C$.

The region of existence of adjacent equilibria (region of divergence instability) is related to static bifurcations with two distinct critical loads obtained via $\alpha_4 = 0$ or (19). The boundary between the region of existence and nonexistence of adjacent equilibria is defined by

$$\alpha_4 = \frac{d\alpha_4}{d\lambda} = 0, \tag{23}$$

which due to relations (22) gives

$$\eta_0 = \frac{4k}{(k+2)^2}, \quad \lambda_0 = \frac{k+2}{2}. \tag{24}$$

This is a double (compound) branching point related to a double root of (19) with respect to λ . Considering the function $\eta = \eta(\lambda, k)$ the necessary condition for an extremum $\partial\eta/\partial\lambda = \partial\eta/\partial k = 0$ yields $\lambda_0 = 2$ and $k_0 = 2$ implying $\eta_0 = \frac{1}{2}$. Note that η_0 is the maximum distance of the double branching point from the λ^c -axis (curve η versus λ^c). Two characteristic curves are considered, $k < 2$ and $k > 2$. It is clear that

$\lambda_0^c \rightarrow 1$ and $\eta_0 \rightarrow 0$ as $k \rightarrow 0$, whereas for $k > 2\lambda_0^c \rightarrow \infty$, $\eta_0 \rightarrow 0$ as $k \rightarrow \infty$. It is easy now to establish the locus of the double branching points in the plane of $\eta - \lambda^c$ (see Figure 1), being independent of m . Note that for $k \rightarrow 0$ or $k \rightarrow \infty$ the region of flutter instability disappears.

Subsequently, the Liénard–Chipart criterion for asymptotic stability is used, which is more simple and efficient than that of Routh–Hurwitz. Clearly, if one of the conditions (15a, b) is violated there is no asymptotic stability. We will apply this criterion for the above 2-DOF cantilevered model ($n = 4$, $\alpha_0 = 1$) in the case of a positive definite damping matrix for which one can show that $m > 0$ always implies $\alpha_1 > 0$. Now consider the case of the Rayleigh positive definite viscous damping matrix in the region of divergence stability, that is, for $\eta \geq \eta_0 = 4k(k + 2)^2$. Then $c_{11} = c_1 + c_2$, $c_{12} = c_{21} = -c_2$, and $c_{22} = c_2$

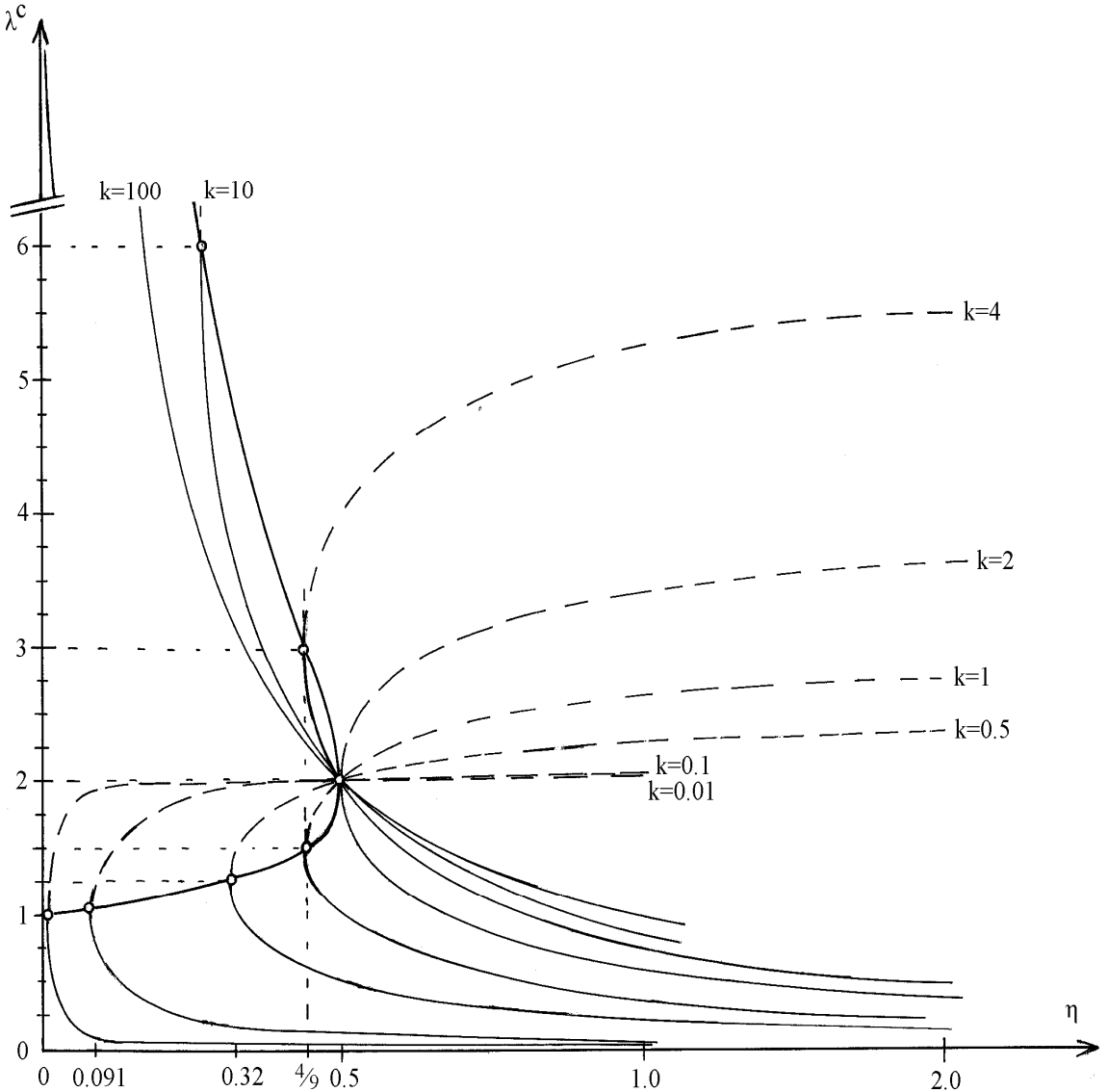


Figure 1. Locus of double branching points (λ_0^c, η_0).

($c_i > 0, i = 1, 2$), and relations (22) become

$$\begin{aligned} \alpha_1 &= \frac{1}{m}[c_1 + (4 + m)c_2], & \alpha_2 &= \frac{1}{m}[m + k + 4 + c_1c_2 - \lambda(\eta m + 2)] \\ \alpha_3 &= \frac{1}{m}[c_1(1 - \lambda\eta) + c_2(k - 2\lambda\eta)], & \alpha_4 &= \frac{1}{m}[\eta\lambda^2 - \eta(k + 2)\lambda + k]. \end{aligned} \tag{25}$$

According to the first set of conditions (14) we have

$$\alpha_4 > 0, \quad \alpha_2 > 0, \quad \Delta_1 = \alpha_1 > 0, \quad \Delta_3 > 0, \tag{26}$$

where

$$\Delta_3 = \begin{vmatrix} \alpha_1 & \alpha_3 & 0 \\ 1 & \alpha_2 & \alpha_4 \\ 0 & \alpha_1 & \alpha_3 \end{vmatrix} = \alpha_3(\alpha_1\alpha_2 - \alpha_3) - \alpha_1^2\alpha_4. \tag{27}$$

From (25) it follows that $\alpha_1 > 0$. Since $\alpha_4 = \det(V/m)$ ($m > 0$) one may consider the following cases regarding the interval of variation of λ :

$$\left. \begin{aligned} \text{For } \lambda < \lambda_1^c &\Rightarrow \det V > 0 \text{ and hence } \alpha_4 > 0, \\ \text{For } \lambda_1^c < \lambda < \lambda_2^c &\Rightarrow \det V < 0 \text{ and hence } \alpha_4 < 0, \\ \text{For } \lambda \geq \lambda_2^c &\Rightarrow \det V > 0 \text{ and hence } \alpha_4 > 0. \end{aligned} \right\} \tag{28}$$

Considering always the region of divergence instability, $\eta \geq 4k/(k + 2)^2$, and keeping in mind the interval of values of λ the following cases of violation of conditions (26) are discussed:

First case: $\alpha_4 > 0$ (for $\lambda < \lambda_1^c$), $\alpha_2 < 0$, and $\Delta_3 > 0$. In view of (27), clearly $\Delta_3 > 0$ implies $\alpha_3 < 0$ (since always $\alpha_1 > 0$) or due to relation (25)

$$c_1(1 - \lambda\eta) + c_2(k - 2\lambda\eta) < 0. \tag{29}$$

Since $c_1, c_2 > 0$ the quantities $1 - \lambda\eta$ and $k - 2\lambda\eta$ must be of opposite sign. Inequality (29) can always be satisfied for suitable values of $c_i > 0$ ($i = 1, 2$). Subsequently one can find suitable values for k, η , and m for which

$$\lambda < \lambda_1^c = \frac{1}{2}(k + 2 - \sqrt{(k + 2)^2 - 4k/\eta})$$

is also consistent with $\alpha_2 < 0$. The important conclusion which then can be drawn is that a local dynamic asymptotic instability in regions of divergence (for λ less than the first buckling load) may occur in the case of a positive definite damping matrix. This is excluded in the case of conservative loading ($\eta = 1$), as shown in [Kounadis 2006; 2007].

More specifically one can establish to the following proof: In view of (25), the condition $\alpha_2 < 0$ implies

$$\lambda > \frac{m + k + 4 + c_1c_2}{\eta m + 2}, \tag{30}$$

which must be consistent with (20),

$$\lambda < \frac{1}{2}(k + 2 - \sqrt{(k + 2)^2 - 4k/\eta}). \tag{31}$$

One can show that there are values of λ for which both inequalities (30) and (31) are satisfied for $\eta \geq 4k/(k+2)^2$, $m > 0$, $k > 0$, and $c_i > 0$ ($i = 1, 2$). For example for $k = 5$, $m = 8$, $c_1 = 0.001$, and $c_2 = 0.00013$ we get $\eta \geq 4k/(k+2)^2 = 20/49 = 0.408163265$. Choosing $\eta = 0.41$ we obtain $\lambda_1^c = 3.26574$, as well as

$$\lambda > \frac{m+k+4+c_1c_2}{\eta m+2} = 3.219697.$$

For $\lambda = 3.26 < \lambda_1^c = 3.26574$, we find: $\alpha_1 = 0.00032$, $\alpha_2 = -0.0266$, $\alpha_3 = -4.26 \times 10^{-6}$, $\alpha_4 = 0.0001395$, and $m^3 \Delta_3 = 1.96 \times 10^{-9} \approx 0$. Figure 2 shows, for these values of parameters α_i ($i = 1, \dots, 4$), a large amplitude chaotic-like response in the $(\theta_2, \dot{\theta}_2)$ phase plane. Hence, for $3.26 \leq \lambda \leq 3.26574$, the damped autonomous system exhibits local asymptotic instability before divergence for a positive definite damping matrix (with coefficients practically zero) of the Rayleigh viscous type. This is an unexpected finding which does not occur for the same system under conservative ($\eta = 1$) tip load [Kounadis 2006; 2007].

Second case: $\alpha_4 < 0$ (for $\lambda_1^c < \lambda < \lambda_2^c$), $\alpha_2 > 0$, and $\Delta_3 > 0$. In view of (25), the condition $\alpha_2 > 0$ implies

$$\lambda < \frac{m+k+4+c_1c_2}{\eta m+2}, \quad \text{and hence} \quad \lambda_1^c < \frac{m+k+4+c_1c_2}{\eta m+2} < \lambda_2^c, \quad (32)$$

or, due to (19),

$$\frac{1}{2}(k+2 - \sqrt{(k+2)^2 - 4k/\eta}) < \frac{m+k+4+c_1c_2}{\eta m+2} < \frac{1}{2}(k+2 + \sqrt{(k+2)^2 - 4k/\eta}). \quad (33)$$

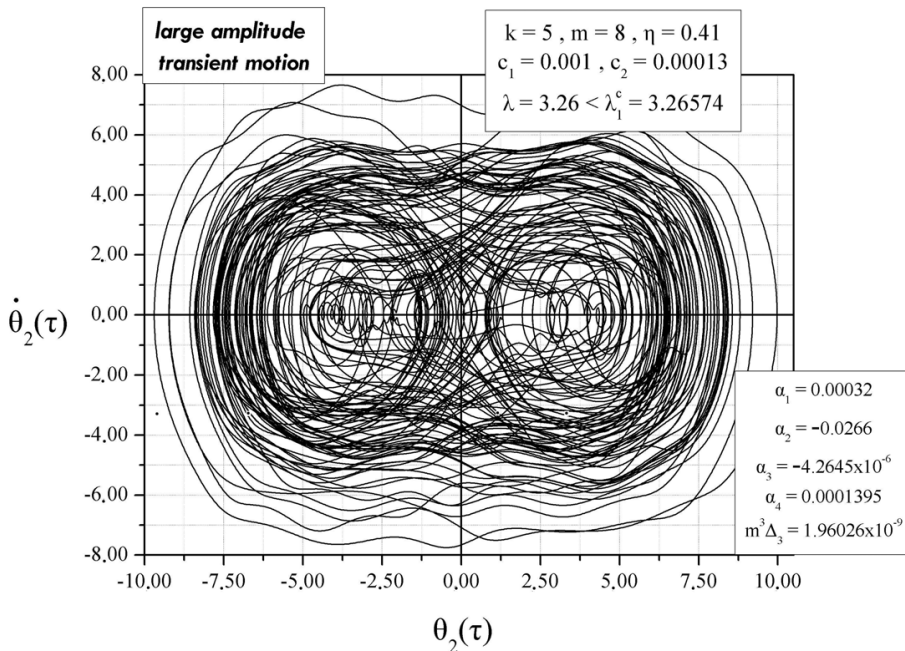


Figure 2. Phase-plane response $(\theta_2(\tau)$ versus $\dot{\theta}_2(\tau)$) for a cantilever with parameters $k = 5$, $\eta = 0.41$, $m = 8$, $c_1 = 0.001$, $c_2 = 0.00013$, and $\lambda = 3.26 < \lambda_1^c = 3.26574$. The model is locally dynamically unstable exhibiting large amplitude chaotic motion.

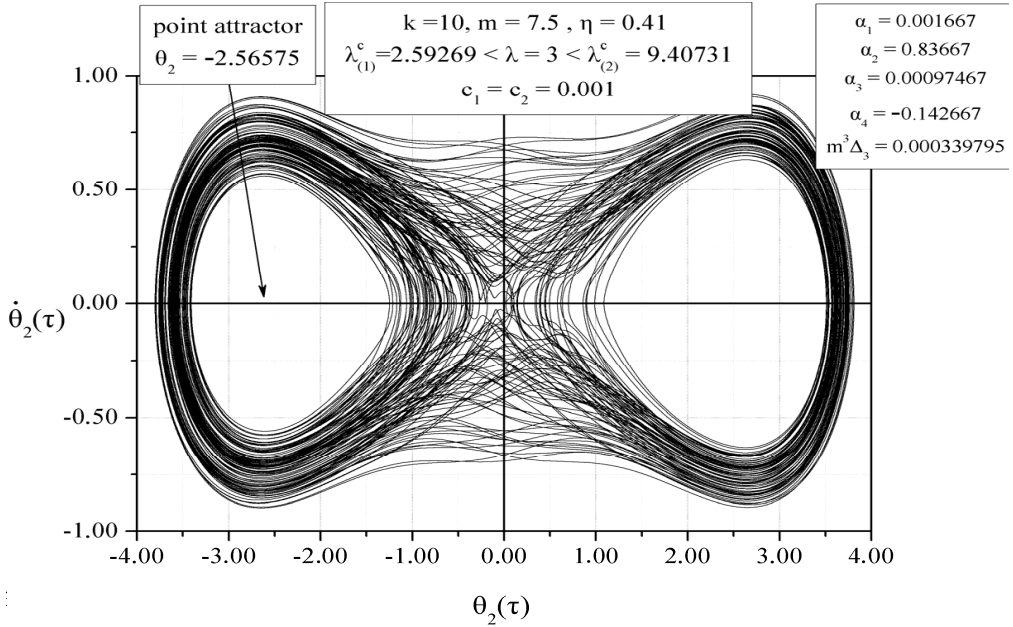


Figure 3. Phase-plane response ($\theta_2(\tau)$ versus $\dot{\theta}_2(\tau)$) for a cantilever with parameters $k = 10, \eta = 0.41, m = 7.5, c_1 = c_2 = 0.001$, and $\lambda_1^c = 2.59269 < \lambda = 3 < \lambda_2^c = 9.40731$. The model exhibits large amplitude chaotic motion which is finally captured by the left stable equilibrium point acting as an attractor.

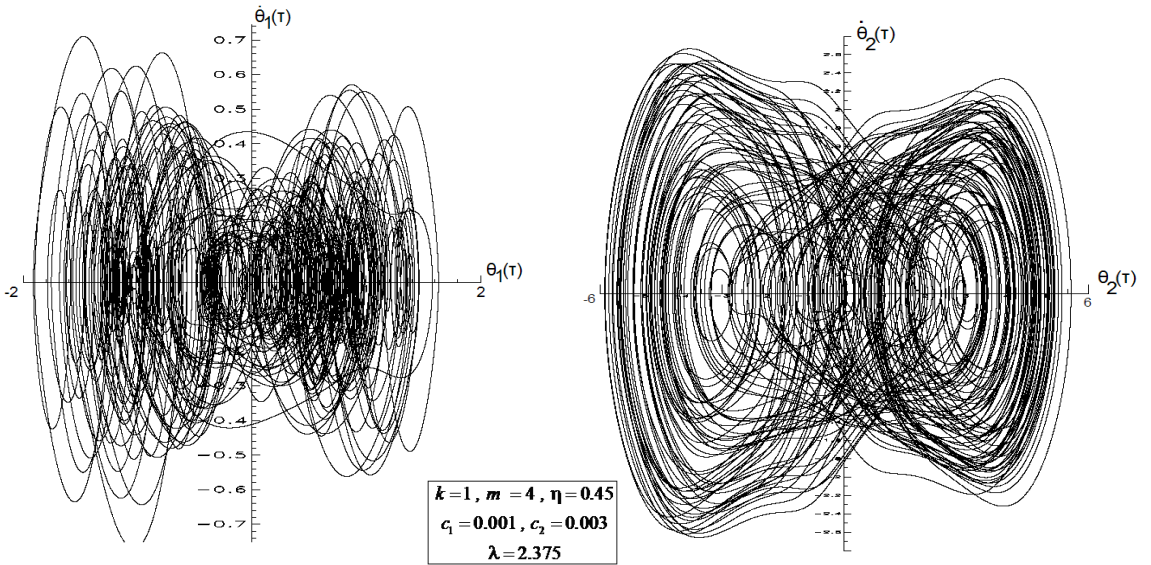


Figure 4. Phase-plane response ($\theta_i(\tau)$ versus $\dot{\theta}_i(\tau), i = 1, 2$) for a cantilever with parameters $k = 1, \eta = 0.45, m = 4, c_1 = 0.001, c_2 = 0.003$, and $\lambda = 2.37 > (k + m + 4 + c_1 c_2) / (\eta m + 2) = 2.36842$. The model is locally dynamically unstable exhibiting large amplitude chaotic motion.

For instance, if $k = 10$ then $\eta \geq 4k/(k + 2)^2 = 0.27777777$. Choosing $\eta = 0.41$, $c_1 = c_2 = 0.001$, and $m = 7.5$ inequality (33) yields $2.59269 < 4.23645 < 9.40731$. For $\lambda = 3$ we get: $\alpha_1 = 0.001667$, $\alpha_2 = 0.83667$, $\alpha_3 = 0.00097467$, $\alpha_4 = -0.142667$, and $m^3 \Delta^3 = 3.39795 \times 10^{-4}$.

As was anticipated the system is locally dynamically asymptotically unstable. However, a nonlinear dynamic analysis will show that the system is globally stable. This is so, because the cantilever under statically applied load exhibits postbuckling strength and hence the postbuckling stable equilibria act as point attractors. Figure 3 shows, corresponding to the given parameters α_i ($i = 1, \dots, 4$), the motion in the $(\theta_2, \dot{\theta}_2)$ phase plane, which after large amplitude vibrations is finally captured by the left stable equilibrium point (of the cantilever) acting as point attractor.

Third case: $\alpha_4 > 0$ (for $\lambda > \lambda_2^c$), $\alpha_2 < 0$, and $\Delta_3 > 0$. Clearly $\alpha_2 < 0$ and $\Delta_3 > 0$ imply $\alpha_3 < 0$. Inequality $\alpha_2 < 0$ due to relations (25) yields

$$\lambda > \frac{k+m+4+c_1c_2}{\eta m+2}. \quad (34)$$

We must also have

$$\lambda > \lambda_2^c = \frac{1}{2}(k+2 + \sqrt{(k+2)^2 - 4k/\eta}). \quad (35)$$

One can readily show that both (34) and (35) can be satisfied for various values of λ and of the parameters $m > 0$, $k > 0$, $c_i > 0$ ($i = 1, 2$), and $\eta \geq 4k/(k+2)^2$.

For instance, for $m = 4$, $c_1 = 0.001$, $c_2 = 0.003$, and $k = 1$ implying $\eta = 4/9$, after choosing $\eta = 0.45$ we obtain $\lambda \geq (k+m+4+c_1c_2)/(\eta m+2) = 2.36842$ and $\lambda_2^c = 1.66666$. Hence, for $\lambda = 2.375$ we have local asymptotic instability. Figure 4 shows, corresponding to these values of the parameters, the $(\theta_1, \dot{\theta}_1)$ and $(\theta_2, \dot{\theta}_2)$ phase plane responses similar to those presented by Sophianopoulos et al. [2002] using the same cantilever model.

Fourth case. $\alpha_4 > 0$ for $\lambda < \lambda_1^c$, $\alpha_2 > 0$, and $\Delta_3 \leq 0$. The condition $\Delta_3 = 0$ (being necessary for a Hopf bifurcation) yields

$$\alpha_3(\alpha_1\alpha_2 - \alpha_3) - \alpha_1^2\alpha_4 = 0, \quad (36)$$

which due to $\alpha_1 > 0$ implies also $\alpha_3 > 0$. For instance, if $k = 1$ then $\eta = 4k/(k+2)^2 = 4/9$. Subsequently choosing $\eta = 0.45$ we obtain $\lambda_1^c = \frac{1}{2}(k+2 - \sqrt{(k+2)^2 - 4k/\eta}) = 1.3333$. Take $\lambda = 1.2$, $m = 1$, $c_1 = 0.001$, and $c_2 = 0.0036$, which yield $\alpha_1 = 0.019$, $\alpha_2 = 3.06$, $\alpha_3 = 0.000172$, $\alpha_4 = 0.028$, and $\Delta_3 = -1.3749 \times 10^{-7}$. Figure 5, on the basis of these values of parameters α_i ($i = 1, \dots, 4$), shows periodic motion around centers in the $(\theta_1, \dot{\theta}_1)$, whose final amplitude depends on the initial conditions.

Equation (36) is the necessary condition for the existence of a pair of purely imaginary roots of the characteristic equation (16). This case is associated either with a degenerate Hopf bifurcation or with a generic Hopf bifurcation [Kounadis 2006; 2007].

Using (22), we reduce (36) to a second-degree algebraic equation in λ :

$$A\lambda^2 + B\lambda + \Gamma = 0, \quad (37)$$

where

$$\begin{aligned}
 A &= m[\eta c_{11} + c_{22} - c_{12}(\eta - 1)]^2 + \eta[(1 + m)c_{22} + c_{11} - 2c_{12}]^2 \\
 &\quad - (\eta m + 2)[(1 + m)c_{22} + c_{11} - 2c_{12}][\eta c_{11} + c_{22} - c_{12}(\eta - 1)], \\
 B &= [(1 + m)c_{22} + c_{11} - 2c_{12}]\{(\eta m + 2)[c_{11} + c_{22}(1 + k) + 2c_{12}] + (4m + k + |c|)[\eta c_{11} + c_{22} - c_{12}(\eta - 1)]\} \\
 &\quad - 2m[c_{11} + c_{12}(1 + k) + 2c_{12}][\eta c_{11} + c_{22} - c_{12}(\eta - 1)] - \eta(k + 2)[(1 + m)c_{22} + c_{11} - 2c_{12}]^2, \\
 \Gamma &= m[c_{11} + c_{22}(1 + k) + 2c_{12}]^2 + k[(1 + m)c_{22} + c_{11} - 2c_{12}]^2 \\
 &\quad - [(1 + m)c_{22} + c_{11} - 2c_{12}](4 + m + k + |c|)[c_{11} + c_{22}(1 + k) + 2c_{12}].
 \end{aligned}
 \tag{38}$$

Unlike A and B , the coefficient Γ is independent of η .

For λ to be real the discriminant $\mathcal{D} = B^2 - 4A\Gamma$ of (37) must be nonnegative. If $\mathcal{D} > 0$, the quadratic equation has two unequal roots; if $\mathcal{D} = 0$, it has a double root, equal to $\lambda_H = -B/2A$. Note also that the intersection between the curve of (37) and the curve of the first static load λ_1^c , corresponds to a dynamic coupled flutter-divergence bifurcation.

The case $\lambda = 0$. The most important particular case is when $\lambda = 0$, implying $\Gamma = \Gamma(k, m, c_{ij}) = 0$; then all the coefficients of the characteristic equation (16) given in relations (22) or (25) are independent of

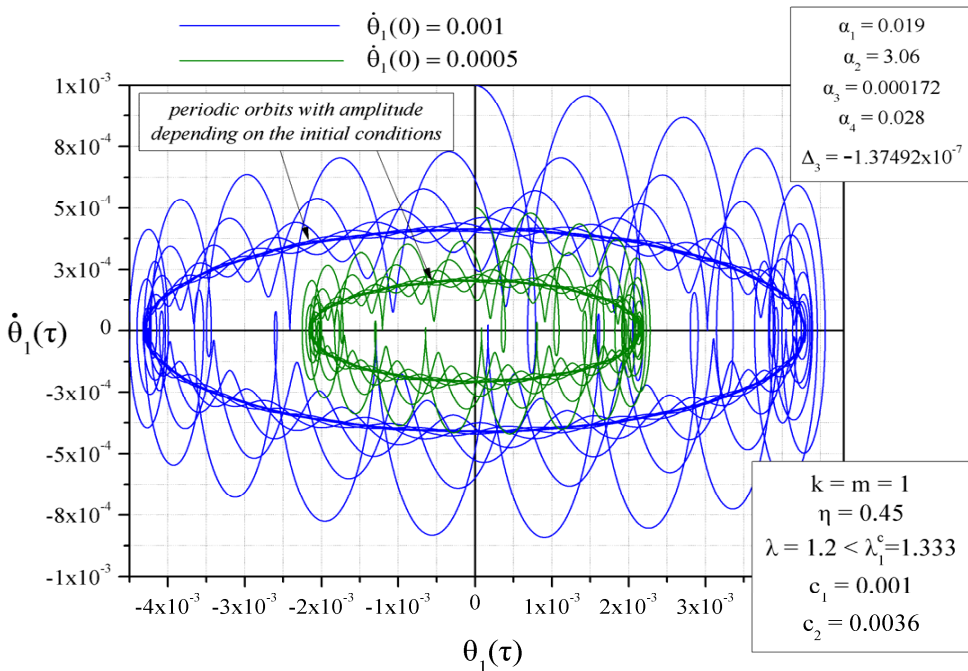


Figure 5. Phase-plane response $(\theta_1(\tau)$ versus $\dot{\theta}_1(\tau))$ for a cantilever with parameters $k = 1$, $\eta = 0.45$, $m = 1$, $c_1 = 0.001$, $c_2 = 0.0036$, and $\lambda = 1.2 < \lambda_1^c = 1.33333$. The model is locally dynamically unstable exhibiting periodic motion around centers, whose final amplitude depends on the initial conditions.

η . Thus Γ is the same as for a conservative load ($\eta = 1$). Strangely enough, the unloaded cantilever, although statically stable, is dynamically locally unstable under any small disturbances!

Conditions for a double imaginary root. For a double imaginary root the first derivative of the secular equation (16) must also be zero, which yields $4\rho^3 + 3\alpha_1\rho^2 + 2\alpha_2\rho + \alpha_3 = 0$. Inserting $\rho = \mu i$ into this equation, where μ is real, yields $\mu^2 = \frac{1}{2}\alpha_2 = \alpha_3/3\alpha_1$ and thus $\alpha_3 = \frac{3}{2}\alpha_1\alpha_2$. Since $\rho = \mu i$ must also be a root of (16) we obtain $\mu^2 = \alpha_3/\alpha_1$, which implies $\alpha_3 = \frac{1}{2}\alpha_1\alpha_2$. This is consistent with the previous expression $\alpha_3 = \frac{3}{2}\alpha_1\alpha_2$ only when $\alpha_3 = 0$ due to either $\alpha_1 = 0$ (which is excluded for a positive definite damping matrix) or $\alpha_2 = 0$ (which is also excluded since it implies $\mu = 0$). Hence, if the damping matrix C is positive definite and of Rayleigh viscous type ($c_{11} = c_1 + c_2$, $c_{12} = c_{21} = -c_2$ and $c_{22} = c_2$ with c_1 and c_2 both positive) then the case of a double imaginary root is excluded [Sophianopoulos et al. 2008]. Note also that in this case the expressions of A , B , and Γ are simplified as follows:

$$\begin{aligned} A &= \eta[m\eta(c_1 + 2c_2)]^2 + [c_1 + (m + 4)c_2]^2 - (c_1 + 2c_2)(2 + \eta m)[c_1 + (m + 4)c_2], \\ B &= [c_1 + (m + 4)c_2]\{(\eta m + 2)(c_1 + c_2k) + \eta(4 + m + k + c_1c_2)(c_1 + 2c_2)\} \\ &\quad - 2m\eta(c_1 + c_2k)(c_1 + 2c_2) - \eta(k + 2)[c_1 + (m + 4)c_2]^2, \\ \Gamma &= m(c_1 + c_2k)^2 + k[c_1 + (m + 4)c_2]^2 - [c_1 + (m + 4)c_2](4 + m + k + c_1c_2)(c_1 + kc_2). \end{aligned} \quad (39)$$

4. Conclusions

The coupling effect of the mass and stiffness distributions of a 2-DOF cantilevered model under partial follower compressive load at its tip in connection with (mainly) infinitesimal positive definite damping is discussed in detail in regions of divergence stability. For the local dynamic asymptotic stability of such autonomous systems attention is focused on the violation of the Liénard–Chipart asymptotic stability criterion. The most important findings of this study are:

- The geometric locus of the double branching points (η_0, λ_0^c) corresponding to various values of k is established via the relations η versus λ^c . The locus is independent of the mass m , whose effect on dynamic instability is of paramount importance. Note that for $k \rightarrow 0$ or $k \rightarrow \infty$ the region of flutter tends to zero. The intersection between the curve (37) and curve λ_1^c corresponds with a coupled fluttered-divergence instability bifurcation.
- The Liénard–Chipart, a more elegant and readily employed stability criterion than that of Routh–Hurwitz, brought into light new types of dynamic bifurcations.
- The mass and stiffness distributions combined with a positive definite negligibly small damping matrix, strangely enough, may have a considerable effect on the local dynamic asymptotic stability prior to divergence. Similar phenomena may occur in conservative systems, but only in the cases of positive semidefinite or indefinite damping matrices [Kounadis 2006; 2007].
- The model under partial follower tip load (step load of constant-magnitude and varying direction with infinite duration) under certain conditions may exhibit a divergent (unbounded) motion before divergence in the case of a positive definite negligibly small damping matrix at a certain value of the external load. This is a completely unexpected result.

- The cantilevered model when unloaded (although being statically stable) under certain conditions becomes dynamically locally unstable to any small disturbance which is also an unexpected finding.
- The case of a double imaginary root in the case of a positive definite damping matrix is excluded.

References

- [Crandall 1970] S. H. Crandall, “The role of damping in vibration theory”, *J. Sound Vib.* **11**:1 (1970), 3–18.
- [Fuller 1968] A. T. Fuller, “Conditions for a matrix to have only characteristic roots with negative real parts”, *J. Math. Anal. Appl.* **23**:1 (1968), 71–98.
- [Gantmacher 1959] F. R. Gantmacher, *The theory of matrices*, Chelsea, New York, 1959.
- [Gantmacher 1970] F. R. Gantmacher, *Lectures in analytical mechanics*, vol. 231, Mir, Moscow, 1970.
- [Huseyin 1978] K. Huseyin, *Vibrations and stability of multiple-parameter systems*, Noordhoff, Alphen aan den Rijn, 1978.
- [Kounadis 1997] A. N. Kounadis, “Non-potential dissipative systems exhibiting periodic attractors in region of divergence”, *Chaos Solitons Fract.* **8**:4 (1997), 583–612.
- [Kounadis 1999] A. N. Kounadis, “A geometric approach for establishing dynamic buckling loads of autonomous potential two-degree-of-freedom systems”, *J. Appl. Mech. (ASME)* **66**:1 (1999), 55–61.
- [Kounadis 2006] A. N. Kounadis, “Hamiltonian weakly damped autonomous systems exhibiting periodic attractors”, *Z. Angew. Math. Phys.* **57**:2 (2006), 324–349.
- [Kounadis 2007] A. N. Kounadis, “Flutter instability and other singularity phenomena in symmetric systems via combination of mass distribution and weak damping”, *Int. J. Non-Linear Mech.* **42**:1 (2007), 24–35.
- [Laneville and Mazouzi 1996] A. Laneville and A. Mazouzi, “Wind-induced ovaling oscillations of cylindrical shells: critical onset velocity and mode prediction”, *J. Fluid. Struct.* **10**:7 (1996), 691–704.
- [Nemat-Nasser and Herrmann 1966] S. Nemat-Nasser and G. Herrmann, “Some general considerations concerning the destabilizing effect in nonconservative systems”, *Z. Angew. Math. Phys.* **17**:2 (1966), 305–313.
- [Pipes and Harvill 1970] L. A. Pipes and L. R. Harvill, *Applied mathematics for engineers and physicists*, 3rd ed., McGraw-Hill/Kogakusha, Tokyo, 1970. International Student Edition.
- [Sophianopoulos et al. 2002] D. S. Sophianopoulos, A. N. Kounadis, and A. F. Vakakis, “Complex dynamics of perfect discrete systems under partial follower forces”, *Int. J. Non-Linear Mech.* **37**:7 (2002), 1121–1138.
- [Sophianopoulos et al. 2008] D. S. Sophianopoulos, G. T. Michaltsos, and A. N. Kounadis, “The effect of infinitesimal damping on the dynamic instability mechanism of conservative systems”, *Math. Probl. Eng.* **2008** (2008). Special issue on Uncertainties in nonlinear structural dynamics, Article ID 471080.
- [Sygulski 1996] R. Sygulski, “Dynamic stability of pneumatic structures in wind: theory and experiment”, *J. Fluid. Struct.* **10**:8 (1996), 945–963.
- [Zajac 1964] E. E. Zajac, “The Kelvin–Tait–Chetaev theorem and extensions”, *J. Astronaut. Sci.* **11** (1964), 46–49.
- [Zajac 1965] E. E. Zajac, “Comments on ‘Stability of damped mechanical systems, and a further extension’”, *AIAA J.* **3**:9 (1965), 1749–1750.
- [Ziegler 1952] H. Ziegler, “Die Stabilitätskriterien der Elastomechanik”, *Ing. Arch.* **20**:1 (1952), 49–56.

Received 12 Sep 2008. Revised 27 Jan 2009. Accepted 5 Feb 2009.

ANTHONY N. KOUNADIS: kounadis@bioacademy.gr

Foundation for Biomedical Research, Academy of Athens, Soranou Efessiou 4, 11527 Athens, Greece

PROPERTY ESTIMATION IN FGM PLATES SUBJECT TO LOW-VELOCITY IMPACT LOADING

REID A. LARSON AND ANTHONY N. PALAZOTTO

A property estimation sequence is presented for determining local elastic properties of a two-phased, two-constituent functionally graded material (FGM) plate subject to impact loading. The property estimation sequence combines the use of experimentally determined strain histories, finite element simulations of the experimental impact events, and an analytical model of the impact tests. The experimental, computational, and analytical models are incorporated into a parameter estimation framework, based on optimization theory, to solve for material properties of individual graded layers in the FGM plate specimens. The property estimation sequence was demonstrated using impact tests performed on a titanium-titanium boride (Ti-TiB) FGM plate system. The estimated material properties of the Ti-TiB FGM from the sequence were shown to correlate well with published material properties for the titanium-titanium boride FGM system. The estimated properties were further input into a finite element model of the impact events and were shown to approximate the experimental strain histories well. This property estimation framework is formulated to apply to virtually any two-phase FGM system and is thus an invaluable tool for research engineers studying the response of FGMs under load.

1. Introduction

Functionally graded materials (FGMs) are advanced composites with mechanical properties that vary continuously through a given dimension. The property variation, in the context of this article, is accomplished by varying the volume fraction ratio of two constituents along a given dimension. FGMs have generated a great deal of interest in recent years due to their flexibility for use in a wide variety of environments, including those structural applications where extreme thermal and corrosion resistance are required.

Most research into FGMs has occurred over the previous two decades. Suresh and Mortensen [1998] provided a comprehensive literature review of the state of the art in FGMs then prevalent, and Birman and Byrd [2007] compiled another extensive literature review covering FGM research from 1997 to 2007. Selected works pertinent to this investigation, specifically those of FGM plate statics and dynamics, will be highlighted here. J. N. Reddy and his colleagues [Reddy et al. 1999; Loy et al. 1999; Reddy 2000; Pradhan et al. 2000; Reddy and Cheng 2001; 2002] have studied the behavior of a wide variety of FGM plate configurations under static and dynamic loading, as have others in the field [Woo and Meguid 2001; Yang and Shen 2001; Yang and Shen 2002; Vel and Batra 2002; Prakash and Ganapathi 2006]. To date, only a few researchers have given consideration to studying impact response and wave propagation in functionally graded composites. Gong et al. [1999] studied low-velocity impact of FGM cylinders with various grading configurations. Bruck [2000] developed a technique to manage stress waves in discrete

Keywords: functionally graded materials, parameter estimation, impact testing.

and continuously graded FGMs in one-dimension. Li et al. [2001] first studied FGM circular plates under dynamic pressures simulating an impact load with a specific metal-ceramic system and using a rate-dependent constitutive relation they developed. Banks-Sills et al. [2002] also studied an FGM system under dynamic pressures of various temporal application. Larson et al. [2009] performed impact tests on titanium-titanium boride monolithic and functionally graded specimens and further developed finite element simulations that approximated the impact tests with a strong degree of correlation. With the exception of the last reference, all of these works were performed using analytical and computational techniques, but none of them were compared to physical or experimental data given the fact that very little test data of any kind associated with functionally graded composites can be found in the literature. This is due to (a) the difficulty to manufacture FGMs, (b) the limited availability of such materials in industry and academia, and (c) the high cost associated with producing them.

Local property estimation and accurate material models for use in FGMs present another set of unique challenges with multiphased functionally graded composites for many of the same reasons that little test data is available in the literature. To date, most investigators assume that common material models used to estimate properties in polymer-matrix fibrous composites apply in general to functionally graded materials, including those where metal and ceramic constituents are used. In this work, local elastic properties will be estimated in two-phase metal-ceramic functionally graded plates subject to impact loading using three common material models applied in a novel parameter estimation sequence. The estimation sequence combines the use of experimentally determined strain histories, finite element simulations of the experimental impact events, and an analytical model of the impact tests. The experimental, computational, and analytical models are incorporated into a parameter estimation framework, based on optimization theory, to solve for material properties of individual graded layers in the FGM plate specimens. The estimates of the local material properties can be used to study the dynamic behavior of FGM plates.

The *major contribution* of this work is a property estimation sequence that can be applied to virtually any two-phase FGM plate system under impact loading where strain data has been experimentally collected over the course of an impact event. The *key objectives* necessary to construct and validate the property estimation sequence are: (a) obtain an analytical model that reasonably approximates the conditions and results of a series of FGM plate impact tests; (b) construct a finite element model that can be used to study the FGM plate impact experiments; (c) outline the parameter estimation framework that determines FGM properties from impact data using the analytical and finite element models of the tests; and (d) correlate the FEM and experimental results using the estimated FGM properties in the finite element models for the plate specimens.

This article is organized as follows. First, an overview of FGM plate impact experiments conducted and documented in previous work by the authors is presented. Next, an analytical treatment of the impact tests is discussed based on development from previous work in the field. A finite element model of the impact tests was developed using two material models. Next, the analytical treatment and finite element model of the impact tests are used directly in a parameter estimation sequence that simultaneously determines FGM properties while matching FEM and experimental strain histories from the impact tests. Lastly, the parameter estimation sequence is demonstrated by comparing estimated material properties from an FGM system to those published in the field and comparing FEM and experimental strain histories. The article concludes with a discussion to aid future investigators in this field.

2. FGM plate impact experiments

A series of FGM plate impact tests were conducted in [Larson et al. 2009]. The results of these tests play a central role in this study, and a brief summary of the tests is presented here. The FGM system used in the tests was a titanium-titanium boride (Ti-TiB) system developed by BAE Systems – Advanced Ceramics in Vista, California. BAE Systems uses a proprietary “reaction sintering” process to produce Ti-TiB FGMs. Commercially pure titanium (Ti) and titanium diboride (TiB_2) are combined in powder form in a graphite die according to prescribed volume fractions through the plate thickness. A catalyzing agent is applied to the construction, and the powders are subjected to extreme temperature (near the melting point of titanium) and pressure in a vacuum or inert gas environment. The catalyzing agent reacts with the titanium and titanium diboride powders to form titanium boride (TiB) that crystallizes in a needle morphology. In the reaction process, almost no residual TiB_2 remains in the FGM. Through the sintering process, the powders adhere together and the Ti-TiB FGM is the final product. The change in composition of the constituents along a dimension is discrete and not truly continuous, although the distance over which a discrete change occurs can be very small and can closely approximate a continuous function over a larger distance. The FGM plates used in testing were graded over seven discrete layers of equal thickness with Ti/TiB compositions ranging from 15%/85% to 100%/0% as shown in Figure 1.

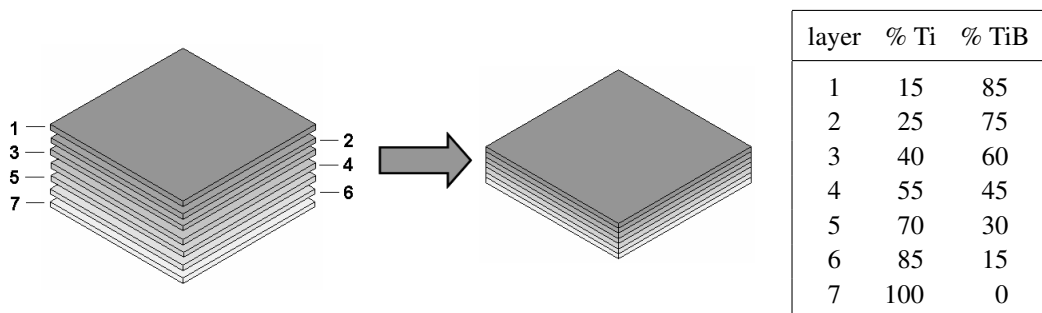


Figure 1. BAE Systems Ti-TiB FGM through-the-thickness configuration of the plate specimens. The thickness of each layer is 0.181 cm.

The impact tests were conducted using the Dynatup apparatus owned by the Air Force Research Laboratory, Wright-Patterson AFB, OH. The Dynatup apparatus delivers a controlled impact load to a specimen by storing a known potential energy and converting that energy to kinetic energy prior to impact. Here, a known mass was raised above each plate specimen to a specified height and released from rest. The velocity at impact is measured by the system and can be compared to the velocity that would occur under frictionless conditions. These were the conditions for each of the four tests performed:

test	sample	crosshead/tup		velocity, actual (m/s)	impact energy (J)
		mass (kg)	height (m)		
1	7-Layer Ti-TiB FGM	13.06	0.508	3.040	60.35
2	7-Layer Ti-TiB FGM	13.06	0.635	3.412	76.02
3	7-Layer Ti-TiB FGM	13.06	0.762	3.765	92.56
4	7-Layer Ti-TiB FGM	13.06	0.889	4.078	108.6

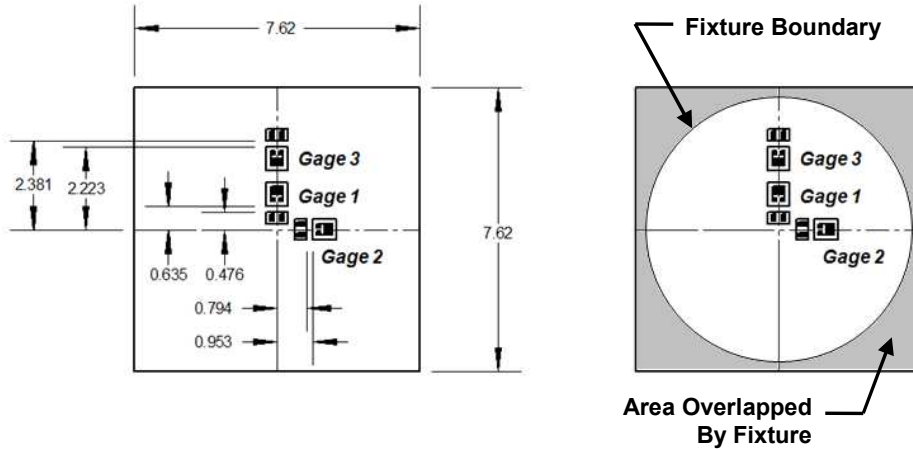


Figure 2. Specimen plate with location of three strain gages in FGM impact tests. The gages are installed on the bottom surface of the plate, opposite the surface impacted by the Dynatup. All dimensions are in centimeters.

Each of the four plates was 7.62 cm \times 7.62 cm and 1.27 cm thick. The specimen plates were placed in a specially designed fixture that configured the plates so that they behaved very closely to a circular plate 6.99 cm in diameter with a *simply supported boundary condition*. Each of the four FGM specimen plates in the Dynatup were impacted on the TiB-rich surface (layer 1 in Figure 1) directly in the center of the plate with a 2.54 cm diameter tup with hemispherical tip. The opposite surface of the plate was instrumented with three strain gages as shown in Figure 2. The strain gages collected strain histories over the course of the impact events. The strain histories from each gage can be used to trace the local and global deflection of the plate using analytical and computational techniques. Strain histories from gages 2 and 3 are plotted for each of the tests in Figure 5 and will be discussed later in this article. The maximum strains from each gage and each test are shown in the table below. The FGM plate in test 4 failed midway through the test, and it is not certain whether it failed at the maximum strain level attainable had the plate not failed.

test	sample	maximum strain		
		gage 1	gage 2	gage 3
1	7-Layer Ti-TiB FGM	0.0014595	0.0013910	0.0006638
2	7-Layer Ti-TiB FGM	0.0017830	0.0014677	0.0007573
3	7-Layer Ti-TiB FGM	0.0018890	0.0017203	0.0007016
4	7-Layer Ti-TiB FGM	Failed	Failed	Failed

3. Analytical treatment of plate impacts

The first objective in constructing the property estimation sequence was to obtain an analytical model that reasonably approximates the conditions and results of the FGM plate impact tests. This section will describe the analytical model chosen for this very task. Larson [2008] demonstrated through extensive analysis of the test results that the period of impact loading in each of the FGM plate impact tests

was significantly larger than the period of the specimen plate-fixtured's first natural mode. Under these conditions, the global response of the FGM plates subject to impact can be approximated by applying quasistatic analytical theory [Zukas et al. 1982; Goldsmith 1960]. Reddy et al. [1999] developed a theory for axisymmetric circular FGM plates relating classic plate theory to first-order shear deformable theory under quasistatic conditions. The mid-surface deflection of a homogeneous, axisymmetric circular plate with simply supported boundary and concentrated central load P from classical plate theory is given by (see [Ugural 1999]):

$$w_0^C(r) = \frac{P}{16\pi D} \left[2r^2 \ln \frac{r}{a} + \frac{3+\nu}{1+\nu} (a^2 - r^2) \right] \quad (3-1)$$

where r is the radial coordinate, a is the radius of the plate, and D is the flexural rigidity. The mid-surface deflection of a functionally graded plate that is first-order shear deformable is given by [Reddy et al. 1999] as

$$w_0^{\text{FST}}(r) = \frac{D}{\Omega_1} w_0^C(r) + \frac{\mathcal{M}^C(r) - \mathcal{M}^C(a)}{A_{55}} + \frac{1}{4} \frac{c_2}{\Omega_1} (a^2 - r^2). \quad (3-2)$$

The radial strain at a radial coordinate r and thickness coordinate z (note $z = 0$ is the plate mid-surface) in the FGM plate can be determined from the theory of elasticity:

$$\epsilon_{rr}^{\text{FST}}(r, z) = \left[z - \frac{B_{11}}{A_{11}} \right] \left\{ -\frac{P}{16\pi \Omega_1} \left[4 \ln \frac{r}{a} + 6 - 2 \left(\frac{3+\nu}{1+\nu} \right) \right] + \frac{c_2}{2\Omega_1} \right\} + \frac{k_1}{2}. \quad (3-3)$$

The moment sum \mathcal{M}^C in (3-2) is given by

$$\mathcal{M}^C = \frac{M_{rr}^C + M_{\theta\theta}^C}{1+\nu}, \quad (3-4)$$

where the radial and angular moment loads M within the plate from classical plate theory are

$$M_{rr}^C = -D_{11} \frac{d^2 w_0^C}{dr^2} - D_{12} \frac{1}{r} \frac{dw_0^C}{dr}, \quad M_{\theta\theta}^C = -D_{12} \frac{d^2 w_0^C}{dr^2} - D_{11} \frac{1}{r} \frac{dw_0^C}{dr}. \quad (3-5)$$

The constants in (3-2) and (3-3) from application of the boundary conditions are

$$c_2 = -\frac{2D}{a} \left(\frac{\nu - \Omega_2/\Omega_1 - \Omega_9}{\nu + \Omega_2/\Omega_1 + \Omega_9} \right) \frac{dw_0^C(a)}{dr}, \quad k_1 = \frac{2B_{11}}{aA_{11}} \left(-\frac{D}{\Omega_1} \frac{dw_0^C(a)}{dr} + \frac{c_2}{\Omega_1} \frac{a}{2} \right), \quad (3-6)$$

where the Ω_i are constants defined by

$$\Omega_1 = D_{11} - \frac{B_{11}^2}{A_{11}}, \quad \Omega_2 = D_{12} - \frac{B_{11}B_{12}}{A_{11}}, \quad \Omega_3 = B_{11} + B_{12}, \quad \Omega_9 = \frac{\Omega_3}{\Omega_1} \frac{B_{11}}{A_{11}} \quad (3-7)$$

in terms of material properties: A_{ij} , B_{ij} , and D_{ij} , the in-plane, bending-extension coupling, and bending stiffnesses from classic composite laminate theory (see [Daniel and Ishai 2006]); and A_{55} , the transverse shear stiffness, also from classic composite laminate theory. For brevity, the equations for the stiffnesses are not reproduced but note that the stiffnesses are direct functions of the elastic material properties (elastic modulus and Poisson's ratio) assumed for the FGM layers. Models for the elastic properties will be the focus of the next subsection.

The relation for strain in the FGM plates in (3-3) can be used to tie the test results to analytical theory. Knowing the radial location of the strain gages in each test from Figure 2 and the maximum strain values

for each gage in each test (see table on page 1432), the maximum contact force P can be solved for in (3-3) using known material properties. The value for the contact force P is then substituted into (3-2) to solve for the transverse deflection of the FGM plate's midsurface. This is a key aspect of estimating material properties in the FGM and will be discussed again subsequently.

A very important note on the displacement and strain of the plate is in order before proceeding. For a concentrated load, at or very near $r = 0$ the displacement and strains are unbounded. Westergaard [1926] proposed that the problem can be alleviated by using an equivalent radius r_e in place of r in these equations at the center of the plate, meaning the concentrated load is assumed to be applied over a very small area given by

$$r_e = \sqrt{1.6 r_c^2 + h^2} - 0.675 h, \quad r_c \leq 0.5 h. \quad (3-8)$$

Here r_c is a small radius that defines a small circular area over which the concentrated load is assumed to be distributed and h is the thickness of the plate. One can set r_c to zero for a concentrated load, if desired, in which case r_e is equal to $0.325h$. For r less than or equal to r_e , r_e is substituted for r as a constant in the equations for displacement and strain, (3-2) and (3-3) respectively. This has the effect of bounding the solutions near the plate center, although it is only an approximation to the exact solution.

3A. Material models. Material properties such as elastic modulus, Poisson's ratio, and density must be assumed for local mixtures of Ti-TiB. In the case of the seven-layer FGM, the material properties vary in discrete jumps; in a truly continuous FGM, the material properties vary in a continuous fashion as a function of the distribution of constituents. Here, three material models that estimate properties of local mixtures of constituents are presented where the "average" properties of the composite are based on functions of the volume fractions and individual properties of the constituents.

First, the classical rule-of-mixtures (ROM) directly relates the net material properties of multiphase materials to the ratio of volume fractions (V^f) of the constituents. If \mathcal{P} is an arbitrary property of a two-phase mixture and \mathcal{P}_1 and \mathcal{P}_2 are arbitrary properties of the two constituents, then the relation

$$\mathcal{P} = V_1^f \mathcal{P}_1 + V_2^f \mathcal{P}_2 \quad (3-9)$$

is assumed to describe the local properties of the FGM under the classical rule-of-mixtures. Equation (3-9) is based on the Voigt model for determining longitudinal stiffnesses if both FGM phases are in a state of equal strain [Suresh and Mortensen 1998; Daniel and Ishai 2006]. The assumption that the two phases in the FGM are in a state of equal strain can be thought of as analogous to (two) springs acting in parallel to resist a longitudinal force. A force extends or compresses two springs in parallel an equal distance (i.e., equal strain) and the springs exert forces based on their appropriate spring constants (i.e., elastic moduli adjusted by volume fractions). For this reason, the Voigt model is often referred to as a "parallel" model in composite theory.

The second material model was developed by Hill [1965]. His so-called self-consistent (SC) material model was developed specifically for two-phase composite materials. The model is general enough to be assumed applicable to FGMs. Hill showed that if a series of randomly dispersed isotropic spheres served as inclusions in a homogeneous matrix and if the matrix-inclusion composite bulk material displayed statistical isotropy (that is, a significant percentage of the composite behaves isotropically and can be reasonably assumed to behave as such), then the net bulk modulus K and shear modulus G for the

composite are given by the relations

$$\frac{\delta}{K} = \frac{V_1^f}{K - K_2} + \frac{V_2^f}{K - K_1}, \quad \frac{\eta}{G} = \frac{V_1^f}{G - G_2} + \frac{V_2^f}{G - G_1} \quad (3-10)$$

where $\delta = 3 - 5\eta = K/(K + 4G/3)$, and the subscripts 1 and 2 refer to the individual phases. Equations (3-10) must be solved for K and G simultaneously. The bulk and shear moduli are related to the elastic modulus E and Poisson ratio ν by

$$K = \frac{E}{3(1 - 2\nu)}, \quad G = \frac{E}{2(1 + \nu)}. \quad (3-11)$$

The third model was formulated by Mori and Tanaka [1973]. They demonstrated that in two-phase composites, i.e., a matrix with randomly distributed misfitting inclusions, the average internal stress in the matrix is uniform throughout the material and independent of the position of the domain where the average is obtained. They also showed that the actual stress in the matrix is the average stress in the composite plus a locally varying stress, the average of which is zero in the matrix phase. Benveniste [1987] used their analysis as the basis for developing equations that can be used to determine bulk and shear moduli for the composite material as a whole:

$$\frac{K - K_1}{K_2 - K_1} = \frac{V_2^f \Psi_1}{(1 - V_2^f) + V_2^f \Psi_1}, \quad \frac{G - G_1}{G_2 - G_1} = \frac{V_2^f \Psi_2}{(1 - V_2^f) + V_2^f \Psi_2}. \quad (3-12)$$

Ψ_1 and Ψ_2 are constants, based on the geometry of the inclusions. Berryman [1980a; 1980b] provides a formulation for inclusions with (1) spherical and (2) ellipsoid geometries. General ellipsoids can be complicated, but spherical inclusions are special cases with simple formulas for Ψ_1 and Ψ_2 :

$$\Psi_1 = \frac{K_1 + (4/3)G_1}{K_2 + (4/3)G_1}, \quad \Psi_2 = \frac{G_1 + f_1}{G_2 + f_1}, \quad f_1 = \frac{G_1(9K_1 + 8G_1)}{6(K_1 + 2G_1)}. \quad (3-13)$$

Another special case of ellipsoid inclusions is that of needle-shaped inclusions; the constants Ψ_1 and Ψ_2 are given by

$$\Psi_1 = \frac{K_1 + G_1 + G_2/3}{K_2 + G_1 + G_2/3}, \quad \Psi_2 = \frac{1}{5} \left(\frac{4G_1}{G_1 + G_2} + 2 \frac{G_1 + f_1'}{G_2 + f_1'} + \frac{K_2 + 4G_1/3}{K_2 + G_1 + G_2/3} \right), \quad (3-14)$$

with $f_1' = G_1(3K_1 + G_1)/(3K_1 + 7G_1)$. The Mori–Tanaka (MT) material model will be used for both cases of spherical (MT-S) and needle-shaped (MT-N) inclusions in this study.

Each of the three material models (rule-of-mixtures, self-consistent, and Mori–Tanaka) are important because the elastic modulus and Poisson's ratio for local mixtures of the constituents must be used to determine the A_{ij} , B_{ij} , and D_{ij} stiffnesses for the FGM plates necessary to evaluate the displacement and strains associated with the impact tests. Note that for a given set of elastic properties and set of volume fractions of the constituents in a mixture, each of the three material models will yield different properties for the mixture. This fact will be important later in the article as the property estimation sequence is applied in practice.

4. Finite element model

The second objective necessary to implement the property estimation sequence is constructing a finite element model that can be used to study the FGM plate impact experiments. A finite element model (FEM) of the plate impact tests was developed extensively [Larson et al. 2009] to study the plate impact tests in and is discussed in this section. The commercial code ABAQUS was used for this study. The model is composed of two major components: (a) the FGM specimen plate and (b) the Dynatup fixture and tup. Each of these portions has interesting features that will be briefly discussed in the following paragraphs.

4A. FGM plates FEM. Two plate finite element models were constructed to study the FGM impact tests. The first model is a two-phase representation of the FGM where elements containing only Ti or TiB properties are randomly distributed according to local volume fraction constraints in the FGM. The two-phase finite element representation of the FGM plates is shown in Figure 3. In the figure, black elements represent TiB and white elements are Ti. The material properties for commercially pure titanium [Oberg et al. 2000] are

$$\text{elastic modulus } E = 110 \text{ GPa}, \quad \text{Poisson ratio } \nu = 0.340, \quad \text{density } \rho = 4510 \text{ kg/m}^3.$$

The material properties for titanium boride [BAE 2007] are

$$\text{elastic modulus } E = 370 \text{ GPa}, \quad \text{Poisson ratio } \nu = 0.140, \quad \text{density } \rho = 4630 \text{ kg/m}^3.$$

The second model of the FGM plates is the homogenized-layers model, also shown in Figure 3. In this model, homogenized material properties are assigned to elements based on the properties of Ti and TiB and their local volume fraction ratio using one of the three material models outlined in the previous section. *The material properties in each layer of the FGM are constant.* In the figure, the layers of the FGM are shaded based on the local volume fractions of the constituents; darker layers are TiB-rich and lighter areas are Ti-rich.

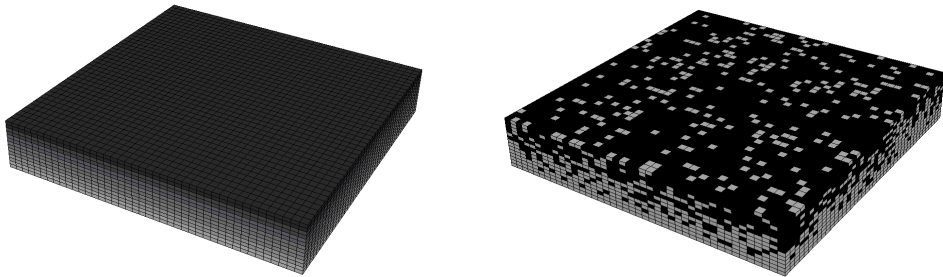


Figure 3. Schematic of specimen plate FEMs: left, homogenized-layers FEM; right, two-phase FEM.

The plates were meshed with eight-noded linear brick elements in a $42 \times 42 \times 14$ -element mesh (27735 nodes and 24696 elements). The nodal grid and mesh were built using a separate mathematical script and this grid and mesh was exported to ABAQUS. The script was designed to quickly and efficiently build each grid and mesh for both the two-phase and homogenized-layers FEM of each plate.

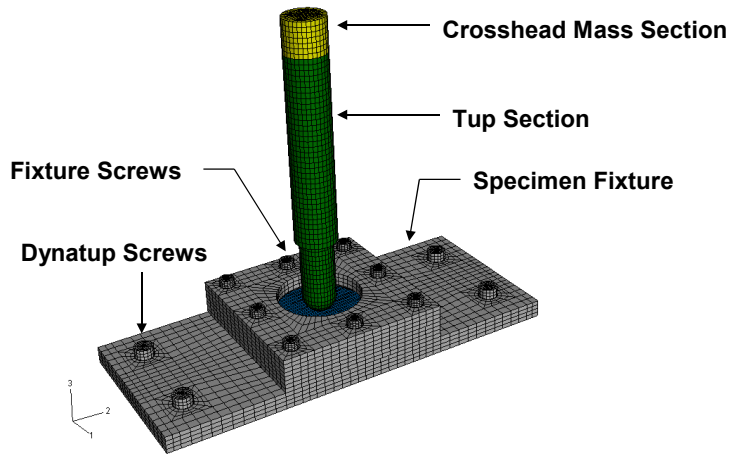


Figure 4. Finite element mesh and model for the plate impact experiments.

4B. Dynatup, fixture FEM. The second major portion of the finite element model is the Dynatup and plate fixture FEM. The plate fixture and tup FEM is shown with a specimen plate installed in [Figure 4](#). The fixture essentially provides a boundary condition for the specimen plates very close to the actual tests (despite the fact the fixture was shown to configure the plate specimens as circular plates with simply supported boundary conditions [[Larson 2008](#)]). The specific details surrounding the plate fixture can be found in [[Larson 2008](#); [2009](#)]. The fixture and attachment screws were composed of 18-8 grade stainless steel and were assigned properties (1) elastic modulus, $E = 193$ GPa; (2) Poisson ratio, $\nu = 0.290$; and (3) density, $\rho = 8030$ kg/m³. The same linear eight-noded brick elements as used to model the plate specimens.

The tup delivers the impact load to the plate specimens. In the FEM, the tup model stores the entire mass of the crosshead-tup assembly and a velocity field is applied to the model with the same magnitude as the impact velocity in the FGM plate tests (see table at the bottom of page [1431](#)). The tup is meshed with eight-noded linear brick elements.

The FGM plate, fixture, and Dynatup assembly employ contact algorithms in ABAQUS to ensure the boundary conditions of the system are properly enforced. The FGM plate is in contact with the fixture components, the fixture components are in contact with each other, and the tup and FGM plate are in contact for the duration of the impact event. Additional constraints and boundary conditions were applied throughout the model as necessary to ensure the FEM reached a solution that closely emulated the conditions of the Dynatup impact tests.

5. Parameter estimation sequence

This section presents the theory and implementation of the parameter estimation sequence used to estimate FGM properties from the impact test data. This is the third objective of this work and the estimation sequence is the major contribution of this study. The section begins with an overview of general parameter estimation theory, followed by a mathematical model used to predict the plate deflection from an impact load, and then concludes with a formulated estimation sequence and its implementation.

5A. Overview of parameter estimation theory. The parameter estimation theory presented in this section is taken from standard textbooks [Arora 1989; Haftka et al. 1990; Dennis Jr. and Schnabel 1983]. The parameter estimation sequence is posed as a *constrained minimization problem*, generally defined as

$$\begin{aligned} \min f(\mathbf{x}) &= f(x_1, \dots, x_n) \\ \text{subject to } \mathbf{h}(\mathbf{x}) &= 0 \\ \text{and } \mathbf{g}(\mathbf{x}) &\leq 0. \end{aligned} \quad (5-1)$$

The *objective function* f , the *equality constraint functions* $\mathbf{h} = (h_1, \dots, h_p)$ and the *inequality constraint functions* $\mathbf{g} = (g_1, \dots, g_m)$ all depend on the design variable $\mathbf{x} = (x_1, \dots, x_n)$. These functions can be combined into the *Lagrange function* \mathcal{L} , defined as

$$\mathcal{L}(\mathbf{x}, \boldsymbol{\lambda}, \boldsymbol{\mu}) = f(\mathbf{x}) + \boldsymbol{\lambda}^T \mathbf{h}(\mathbf{x}) + \boldsymbol{\mu}^T \mathbf{g}(\mathbf{x}) \quad (5-2)$$

in terms of two vectors of *Lagrange multipliers*: a vector $\boldsymbol{\lambda}$ for the p equality constraints and a vector $\boldsymbol{\mu}$ for the m inequality constraints. (The Lagrange multipliers are not functions of the design variable \mathbf{x} .)

Now recall from multivariate calculus that a *necessary* condition for a differentiable function $F(\mathbf{x})$ to have a local extremum (maximum or minimum) at \mathbf{x}^\bullet is that the gradient of F be zero at \mathbf{x}^\bullet :

$$\nabla F(\mathbf{x}^\bullet) = \mathbf{0}. \quad (5-3)$$

If that condition is satisfied, a *necessary* condition for \mathbf{x}^\bullet to be a local *minimum* of F is that the Hessian matrix

$$\mathbf{H} = \left[\frac{\partial^2 F}{\partial x_i \partial x_j} \right]_{i,j=1,\dots,n} \quad (5-4)$$

evaluated at \mathbf{x}^\bullet be positive semidefinite. The stronger condition that the Hessian be positive definite at \mathbf{x}^\bullet is also *sufficient* for \mathbf{x}^\bullet to be a local minimum. Replacing “positive” by “negative” gives conditions for maximization. An indefinite Hessian implies neither a maximum nor a minimum of F .

William Karush, in his 1939 master’s thesis, gave necessary conditions for a point \mathbf{x}^\bullet to satisfy the constrained minimization problem (5-1). These conditions, often called the Kuhn–Tucker conditions, are obtained by applying the gradient criterion (5-3) to the Lagrange function (5-2) and dualizing the inequality constraints. (In the absence of inequality constraints, of course, the problem had been solved by Lagrange.) The Kuhn–Tucker necessary conditions are

$$\begin{aligned} \frac{\partial \mathcal{L}}{\partial x_j} &\equiv \frac{\partial f}{\partial x_j} + \sum_{i=1}^p \lambda_i^\bullet \frac{\partial h_i}{\partial x_j} + \sum_{i=1}^m \mu_i^\bullet \frac{\partial g_i}{\partial x_j} = 0 \quad \text{for } j = 1, \dots, n, \\ h_i(\mathbf{x}^\bullet) &= 0 \quad \text{for } i = 1, \dots, p, \\ g_i(\mathbf{x}^\bullet) &\leq 0 \quad \text{for } i = 1, \dots, m, \\ \mu_i^\bullet g_i(\mathbf{x}^\bullet) &= 0 \quad \text{for } i = 1, \dots, m, \\ \mu_i^\bullet &\geq 0 \quad \text{for } i = 1, \dots, m. \end{aligned} \quad (5-5)$$

We will apply them directly to the FGM property estimation problem in [Section 5C](#).

5B. Mathematical model for plate deflection. A series of simulations with the two-phase FGM plate FEM were run in order to estimate the maximum center deflection of the plate from impact by fitting a second-order polynomial to the FEM results using the method of least squares (such techniques are well documented in the literature; see for example [Myers and Montgomery 1995; Lawson and Erjavec 2001]). The second-order polynomial has the form

$$\hat{y} = b_0 + \sum_{i=1}^k b_i x_i + \sum_{i=1}^k \sum_{j=i}^k b_{ij} x_i x_j, \quad (5-6)$$

where \hat{y} is the dependent variable being estimated, x_i ($i = 1, \dots, k$) are the independent variables, or “factors,” of the second-order polynomial, and b_0 , b_{ii} , and b_{ij} are the coefficients of the terms containing independent variables.

The math model is constructed by determining the b -coefficients. The equations for doing so can be posed in matrix and vector form by setting

$$\mathbf{X} = \begin{bmatrix} 1 & x_1 & x_2 & x_3 & x_4 & x_1^2 & x_2^2 & x_3^2 & x_4^2 & x_1 x_2 & x_1 x_3 & x_1 x_4 & x_2 x_3 & x_2 x_4 & x_3 x_4 \end{bmatrix}, \quad (5-7)$$

for a response variable with four independent variables x_i , $i = 1, \dots, 4$. Each of the column-vector elements of \mathbf{X} contains the values or cross-multiplied values of the independent variables for each simulation where an individual \hat{y} was determined. The response variable \hat{y} results of each simulation are assembled into a vector and denoted \mathbf{Y} . The response variable \hat{y} in this case corresponds to the mid-surface transverse center deflection of the FGM plate from impact, w_0^{FEM} , collected in each FEM simulation. The mid-surface transverse center deflection is a function of four independent variables (discussed momentarily). The vector of coefficients \mathbf{b} for the second-order model in (5-6) is given by

$$\mathbf{b} = (\mathbf{X}^T \mathbf{X})^{-1} \mathbf{X}^T \mathbf{Y}. \quad (5-8)$$

The transverse deflection of the FGM plates subject to impact is dependent on the material properties and the impact velocity of the tup (understanding that the plate geometry, configuration, and boundary condition do not change). The relevant material properties are three: elastic modulus, Poisson’s ratio, and density. As discussed earlier, the FGM plates behaved elastically in impact tests at room temperature, so restricting the study to these three parameters is valid.

The material properties and behavior of the titanium constituent are well documented in the literature and are assumed to be accurate. The TiB constituent, on the other hand, is not well understood and the limited available literature shows a wide range of estimated properties [Sahay et al. 1999; Atri et al. 1999; Panda and Ravichandran 2003; 2006; Ravichandran et al. 2004]. These properties with uncertain values are variables over which to optimize. It is convenient to let the design variables be ratios rather than the property values themselves. That is, we write

$$x_1 = C_1 \equiv \frac{E_{\text{TiB}}}{E_{\text{Ti}}}, \quad x_2 = C_2 \equiv \frac{\nu_{\text{TiB}}}{\nu_{\text{Ti}}}, \quad x_3 = C_3 \equiv \frac{\rho_{\text{TiB}}}{\rho_{\text{Ti}}}.$$

These coefficients C_i are allowed to take values over a given range of magnitudes, corresponding to the minimum and maximum predicted values for these properties. Table 1 shows each coefficient and

variable	meaning	values:		
		maximum (coded +1)	midrange (coded 0)	minimum (coded -1)
$x_1 = C_1$	elastic modulus coefficient	4.20	3.40	2.60
$x_2 = C_2$	Poisson's ratio coefficient	0.50	0.40	0.30
$x_3 = C_3$	density coefficient	1.10	1.00	0.90
$x_4 = v_{\text{tup}}$	tup velocity	4.128 m/s	3.493 m/s	2.858 m/s

Table 1. Factors used in Box–Behnken designed experiment.

the range of values it can assume, based on data from [Sahay et al. 1999; Atri et al. 1999; Panda and Ravichandran 2003; Ravichandran et al. 2004; Panda and Ravichandran 2006; Hill and Lin 2002]. The fourth design variable, the tup impact velocity, is also assumed to be limited to certain magnitudes based on the settings for the impact tests. These four independent variables can then be coded to range from values -1 to $+1$, indicating minimum value and maximum value, respectively, and a midpoint value 0 .

An efficient method for generating the b -coefficients in (5-6) has been developed by Box and Behnken [1960]. The series of tests necessary to determine the b -coefficients (15 b -coefficients in all for the four factors x_i) in (5-6) are shown in Table 2. According to the Box–Behnken designed experiments, 27 tests must be conducted where \hat{y} is measured (again, \hat{y} is the maximum center deflection of the FGM plate denoted w_0^{FEM}) using the combination of variables and associated levels shown in Table 2. The results from the two-phase FGM plate FEM according to the prescribed simulation parameters are shown in the Table 2.

Assembling the 27×1 vector Y with the results from the tests and the 27×15 array X in (5-7) and applying the vector and array to (5-8), the b -coefficients for this set of tests is determined. The b -coefficients are then used in (5-6) and the resulting mathematical model for predicting the mid-surface transverse deflection of the FGM plate at the center ($r = 0$) is

$$\begin{aligned}
 w_0^{\text{FEM}} = \hat{y} = & -258.34 \times 10^{-6} \\
 & + 22.57 \times 10^{-6}x_1 + 1.21 \times 10^{-6}x_2 + 9.25 \times 10^{-9}x_3 - 37.77 \times 10^{-6}x_4 \\
 & - 3.39 \times 10^{-6}x_1^2 + 420.46 \times 10^{-9}x_2^2 - 42.04 \times 10^{-9}x_3^2 - 4.26 \times 10^{-6}x_4^2 \\
 & + 142.00 \times 10^{-9}x_1x_2 - 148.50 \times 10^{-9}x_1x_3 + 3.60 \times 10^{-6}x_1x_4 \\
 & - 55.50 \times 10^{-9}x_2x_3 - 90.75 \times 10^{-9}x_2x_4 - 45.25 \times 10^{-9}x_3x_4
 \end{aligned} \tag{5-9}$$

where $-1 \leq x_i \leq +1$. The units of w_0^{FEM} are meters. Since the coded variables for the TiB property coefficients and tup velocity are unitless, all the b -coefficients in (5-9) are in units of meters as well.

The mathematical model was then used to predict the plate deflection at each of the 27 simulations using the coded x_i values and the results are shown in Table 2. It is easily seen that the mathematical model predicts the results from the FEM simulations very closely. This mathematical model is a key component of the parameter estimation sequence described in the following paragraphs.

The two-phase FEM was used to develop the math model (5-9) to harness effects of the random distribution of constituents. In the homogenized-layers model, localized effects from adjacent phases of materials are averaged out through the use of material models that specify constant properties for

test	coded variable				w_0^{FEM} , mm	
	x_1	x_2	x_3	x_4	result	predicted
1	-1	-1	0	0	0.2849	0.2849
2	+1	-1	0	0	0.2401	0.2401
3	-1	+1	0	0	0.2827	0.2828
4	+1	+1	0	0	0.2374	0.2374
5	0	0	-1	-1	0.2250	0.2249
6	0	0	+1	-1	0.2248	0.2248
7	0	0	-1	+1	0.3003	0.3004
8	0	0	+1	+1	0.3003	0.3004
9	0	0	0	0	0.2583	0.2583
10	-1	0	0	-1	0.2466	0.2472
11	+1	0	0	-1	0.2084	0.2093
12	-1	0	0	+1	0.3310	0.3299
13	+1	0	0	+1	0.2784	0.2776
14	0	-1	-1	0	0.2592	0.2592
15	0	+1	-1	0	0.2564	0.2567
16	0	-1	+1	0	0.2597	0.2591
17	0	+1	+1	0	0.2570	0.2568
18	0	0	0	0	0.2583	0.2583
19	0	-1	0	-1	0.2262	0.2257
20	0	+1	0	-1	0.2240	0.2231
21	0	-1	0	+1	0.3001	0.3011
22	0	+1	0	+1	0.2981	0.2988
23	-1	0	-1	0	0.2845	0.2845
24	+1	0	-1	0	0.2393	0.2391
25	-1	0	+1	0	0.2838	0.2842
26	+1	0	+1	0	0.2391	0.2393
27	0	0	0	0	0.2583	0.2583

Table 2. Box–Behnken designed experiment for four factors (see [Table 1](#)), with results from FEM (maximum transverse displacement at center of plate w_0^{FEM}) and predicted values from mathematical model.

the mixture. Thus, the transverse deflection of an FGM plate under the conditions of the impact tests discussed is much easier to predict using conventional techniques—such as through the analytical model of the FGM plate impacts discussed previously. Most FGMs tend to exhibit statistical distributions of constituents that can produce localized effects that are nearly impossible to predict without simulation tools or over-simplified assumptions. In this case, the statistical effects to the transverse deflection of the plate in a two-phase mixture are generally accounted for through the use of the least squares fit to the simulation data in (5-9).

5C. Material property estimation. The property estimation sequence is posed as the following minimization problem: minimize the error between the analytical prediction for the transverse deflection of the FGM plate mid-surface (w_0^{FST}) and the prediction for the same transverse deflection of the mid-surface predicted by the math model from the FEM simulations (w_0^{FEM}) by adjusting the material properties for the TiB constituent (adjust the vector of property coefficients \mathbf{C}) subject to bounds on the values the TiB properties can assume. Mathematically, the minimization problem from (5-1) is thus formulated as

$$\begin{aligned} \min f(\mathbf{C}) &= (w_0^{\text{FST}}(\mathbf{C}_1, \mathbf{C}_2) - w_0^{\text{FEM}}(\mathbf{C}_1, \mathbf{C}_2, \mathbf{C}_3))^2 \\ \text{subject to } g_1(\mathbf{C}) &= C_1^{\min} - C_1 \leq 0, \\ g_2(\mathbf{C}) &= C_1 - C_1^{\max} \leq 0, \\ g_3(\mathbf{C}) &= C_2^{\min} - C_2 \leq 0, \\ g_4(\mathbf{C}) &= C_2 - C_2^{\max} \leq 0, \\ g_5(\mathbf{C}) &= C_3^{\min} - C_3 \leq 0, \\ g_6(\mathbf{C}) &= C_3 - C_3^{\max} \leq 0. \end{aligned} \tag{5-10}$$

$f(\mathbf{C})$ is the objective function and the equations $g_i(\mathbf{C})$ in (5-10) are the *inequality* constraint equations. Essentially, by minimizing the error between w_0^{FEM} and w_0^{FST} , the error is being minimized between a model that accounts for a statistical distribution of constituents and one that homogenizes material properties in each FGM layer. This process incorporates the test data (necessary to determine w_0^{FST}), an analytical model describing w_0^{FST} , and the results of FEM simulations under the same conditions (through w_0^{FEM}). This problem can be posed for each of the FGM impact tests individually. Note that w_0^{FEM} is really a function of the TiB coefficients \mathbf{C} and the velocity of the tup. In the w_0^{FEM} term from (5-10), the velocity of the tup at impact for an individual test is already known and is therefore a constant. Thus, only the TiB properties \mathbf{C} need to be adjusted to evaluate w_0^{FEM} . Similarly, the velocity of the tup in the w_0^{FST} analytical term is accounted for through the strain data in the tests by solving for the maximum force applied during the impact event. The analytical model does not require the density term to evaluate w_0^{FST} because of the quasistatic assumptions. Thus, w_0^{FST} is evaluated by adjusting only the TiB coefficients associated with the elastic modulus and Poisson's ratio (C_1 and C_2). Given this information, it is therefore intuitive why w_0^{FEM} is a function of only C_1 , C_2 , and C_3 and w_0^{FST} is a function of only C_1 , C_2 in the minimization problem (5-10).

The objective function and the constraint equations are combined into the Lagrange equation,

$$\mathcal{L} = f(\mathbf{C}) + \boldsymbol{\mu}^T \mathbf{g}(\mathbf{C}) \tag{5-11}$$

where $\boldsymbol{\mu}$ is the vector of Lagrange multipliers, one for each of the six inequality constraints. The minimum point of $\mathcal{L}(\mathbf{C})$ occurs at $[\mathbf{C}^\bullet, \boldsymbol{\mu}^\bullet]$, subject to the Kuhn–Tucker necessary conditions in (5-5). If the point $[\mathbf{C}^\bullet, \boldsymbol{\mu}^\bullet]$ is truly a minimizer of \mathcal{L} , then the Hessian of \mathcal{L} will be at least positive semidefinite and at best positive definite to satisfy the necessary and sufficient conditions for a minimum point.

The minimization problem is solved numerically. The mathematical model (5-9) for the two-phase FEM is rather straightforward; however the analytical prediction for w_0^{FST} is very difficult to evaluate into a simple closed-form relationship because of the dependence of the stiffness terms on (potentially) complicated material models. All partial derivatives were evaluated numerically and the solution to find

the minimizer of \mathcal{L} was conducted using modified Newton's method [Dennis Jr. and Schnabel 1983]. The choice of numerical solver is not unique; any appropriate numerical technique for solving for zeros to a series of equations could be used.

5D. Implementation. The following is a summary of the steps to implement the parameter estimation sequence. This sequence is demonstrated using the Ti-TiB FGM, but the steps to carry out the estimation can be used with any two-constituent material system evaluated in the manner the Ti-TiB FGM plates have been. It is assumed that a mathematical model for the finite element response of the FGM such as that in (5-9) has already been determined.

- (1) Set the material properties of one constituent to be held constant, named constituent 1 here (Ti for this study). The properties of constituent 2 (TiB) will be a set of constants multiplied by the set of material properties for the first constituent:

$$\text{FGM Constituent 1: } \mathcal{P}_1, \mathcal{P}_2, \dots, \mathcal{P}_n$$

$$\text{FGM Constituent 2: } C_1\mathcal{P}_1, C_2\mathcal{P}_2, \dots, C_n\mathcal{P}_n$$

- (2) Determine limits for the constants as constraints on the solution.
- (3) Assemble the objective function and constraints into a minimization problem (5-10). Form the Lagrange function by augmenting the objective function with the constraint relations multiplied by the set of Lagrange multipliers.
- (4) Choose a set of constants C_1, \dots, C_n as an initial estimate for the properties of constituent 2 within the constraints of the set. Set the vectors of Lagrange multipliers to zero. Assemble the vector $\bar{\mathbf{C}}_k = [\mathbf{C}_k, \boldsymbol{\mu}_k]$. At this initial estimate, $k = 0$. Choose a numerical step-size (fixed or variable) appropriate for the numerical algorithm used to solve the equations.
- (5) Evaluate the gradient and Hessian of \mathcal{L} at $\bar{\mathbf{C}}_k$.
- (6) Use the current properties for constituents 1 and 2 to solve for the transverse displacement of the FGM plate at the center with the mathematical model for the finite element tests, w_0^{FEM} .
- (7) Using the strain gage test data (maximum radial strains) from the nominal radial plate locations and the current estimate for the material properties of constituents 1 and 2, solve for the maximum impact load P from the impact event using (3-3).
- (8) The P load and the current estimate for the material properties of constituents 1 and 2 are used to solve for the maximum transverse displacement w_0^{FST} at the center of the plate using (3-2).
- (9) Solve for the current estimate of \mathcal{L} using the solutions of w_0^{FST} , w_0^{FEM} , and the current estimate for $\bar{\mathbf{C}}_k$.
- (10) Perform an iteration of the numerical solver (modified Newton's method was used in this work) to solve for $\bar{\mathbf{C}}_{k+1}$.
- (11) Evaluate the gradient and Hessian of \mathcal{L} at the updated $\bar{\mathbf{C}}_{k+1}$.
- (12) Compare the norm of $\nabla\mathcal{L}(\bar{\mathbf{C}}_k)$ to the norm of $\nabla\mathcal{L}(\bar{\mathbf{C}}_{k+1})$. If the absolute value of the difference of the two norms is less than a predefined tolerance, terminate solution and go to the next step. (Another appropriate termination criterion may be used in place of that used in this work.) Else, set $k + 1 = k$ and go to step (6).

- (13) If the Hessian of \mathcal{L} at the updated \bar{C}_{k+1} is positive definite and the gradient $\nabla\mathcal{L}$ at the updated \bar{C}_{k+1} is sufficiently close to zero (determined by a user-defined metric), terminate solution and analyze minimum point. If minimum point is determined to be not acceptable, adjust initial choice of \bar{C}_0 and repeat process.

6. Results

The final objective of this study is to correlate the FEM and experimental results using the estimated FGM properties in the finite element models for the plate specimens. To accomplish this, the property estimation sequence must be implemented and the outputs analyzed. These tasks will be the focus of this section.

The parameter estimation sequence was conducted as described in this paper using the three material models to estimate the analytical prediction of w_0^{FST} . These models were the classic rule-of-mixtures (ROM), the self-consistent model (SC), the Mori–Tanaka estimates (needles, MT-N, and spheres, MT-S). The initial estimates for the material parameters published in this section were $C_1 = 3.40$, $C_2 = 0.40$, and $C_3 = 1.00$; essentially the center points from the Box–Behnken tests in [Table 1](#). The choice of these initial values here was merely for conceptual convenience only and the choice of initial values is more or less arbitrary in the region of interest. The minimum and maximum constraints on the parameters are the minimum and maximum levels for each parameter shown in [Table 1](#) relaxed by 20% in each direction. Given the high degree of correlation in the second-order math model for the two-phase FEM, it was felt that this range would be accurate to the two-phase FEM without running further simulations in the Box–Behnken FEM tests. Note that while the results published in this section may not represent global minimums of \mathcal{L} (the convexity of the objective function was not evaluated because of the complex nature of the objective function) for the region of interest here, various initial estimates were taken throughout the region, including points on the boundary from the inequality constraints, and in all cases the algorithm converged to the same solution for the material parameters. The solutions found for these parameters are shown in [Table 3](#) as tested for the three primary material models and experimental tests 1–3 (the FGM plate in Test 4 failed so data was not used in the estimation sequence from that test). When the FEM mathematical model was used to estimate w_0^{FEM} for iterations of the parameter estimation sequence, the velocity from the Dynatup experiment was used for v_{tup} and held constant. Thus, w_0^{FEM} for each estimation sequence was reduced to a function of C_1 , C_2 , and C_3 .

The estimates for the coefficients C_1 , C_2 , and C_3 in [Table 3](#) show that in general all models estimated similar results for the three parameters. The difference in results is associated directly with the material models themselves and their estimates for material properties in each layer of the FGM. To illustrate this, consider the transverse displacements at the center of the plates at the minimization of \mathcal{L} summarized in [Table 4](#). In all cases the parameter estimation sequence virtually estimated the same plate deflections at the center regardless of material model. Recall the estimation sequence was tied directly to the results of the plate experiments for all material models. Since the Ti–TiB plates should ideally have the same composition through the thickness and the plates should have the same average behavior in each layer regardless of the material model chosen, it should be expected that the parameter estimation sequence would converge to very similar material properties for each layer and adjust C_i so that the material model reflects this. In [Table 6](#), it is evident that this is indeed the case. The material property estimates (E

test	coeff.	material model			
		ROM	SC	MT-S	MT-N
1	C_1	2.549	2.468	2.494	2.486
	C_2	0.3478	0.3583	0.3594	0.3602
	C_3	0.9458	0.9414	0.9409	0.9408
2	C_1	2.309	2.239	2.256	2.250
	C_2	0.3468	0.3551	0.3573	0.3572
	C_3	0.9325	0.9298	0.9277	0.9281
3	C_1	2.442	2.367	2.389	2.381
	C_2	0.3355	0.3424	0.3439	0.3441
	C_3	0.9540	0.9508	0.9501	0.9501

Table 3. Comparison of predicted coefficients for TiB material properties using the parameter estimation technique and three material models. The initial estimates for the material parameters were $C_1 = 3.40$, $C_2 = 0.40$, $C_3 = 1.00$.

test	method	material model			
		ROM	SC	MT-S	MT-N
1	plate theory, w_0^{FST}	0.25926	0.26197	0.26107	0.26136
	math model, w_0^{FEM}	0.25927	0.26198	0.26108	0.26137
2	plate theory, w_0^{FST}	0.29064	0.29336	0.29268	0.29291
	math model, w_0^{FEM}	0.29065	0.29337	0.29269	0.29292
3	plate theory, w_0^{FST}	0.30959	0.31261	0.31170	0.31199
	math model, w_0^{FEM}	0.30960	0.31262	0.31171	0.31200

Table 4. Predicted maximum center displacement of plate at center of bottom surface using the predicted TiB coefficients in Table 3. All units in millimeters.

coeff.	material model			
	ROM	SC	MT-S	MT-N
C_1	2.433	2.358	2.380	2.372
C_2	0.3434	0.3519	0.3535	0.3538
C_3	0.9441	0.9407	0.9396	0.9397

Table 5. Comparison of predicted coefficients for TiB material properties based on an average of the results shown in Table 3.

and ν only) in each layer, based on the average results for C_i in Table 5, show a very strong degree of correlation between the layers. Further, the estimates for these layers based on C_i correlate well with the published results determined experimentally. The correlation between the published results is strongest

%Ti / %TiB	elastic modulus E , GPa					Poisson ratio ν				
	Literature	ROM	SC	MT-S	MT-N	Literature	ROM	SC	MT-S	MT-N
15 / 85	274.3	244.0	231.7	234.3	232.7	0.170	0.150	0.161	0.160	0.161
25 / 75	247.6	228.2	213.9	217.0	215.2	0.182	0.173	0.187	0.185	0.187
40 / 60	193.7	204.6	188.4	192.6	190.8	0.216	0.206	0.225	0.220	0.222
55 / 45	162.2	180.9	165.1	169.9	168.2	0.246	0.240	0.259	0.253	0.255
70 / 30	139.4	157.3	144.1	148.6	147.4	0.276	0.273	0.290	0.284	0.286
85 / 15	120.1	133.6	125.8	128.7	128.0	0.310	0.307	0.317	0.313	0.314
100 / 0	106.9	110.0	110.0	110.0	110.0	0.340	0.340	0.340	0.340	0.340

Table 6. Elastic property data from parameter estimation scheme for Ti-TiB volume ratios using the (averaged) predicted values from the four material models in the estimation sequence, compared to experimental values reported in [Hill and Lin 2002].

at low to medium volume fractions of TiB and weakest (but still pretty good) at higher volume fractions of TiB. This is likely a consequence of residual titanium diboride known to be present at higher volume fractions of TiB affecting the predictions from the estimation sequence.

The maximum impact force P in each test was related to the maximum radial strains at points on the plate. Since the force data was not collected during the tests, the strain histories from the plates were used to estimate P . The predictions of load P are affected by the material properties through the FGM plates. In Table 7, the estimated force P based on the strain histories in each test at each location are compared with the different material models used to predict C_i . The average predicted load

test	method	material model			
		ROM	SC	MT-S	MT-N
1	strain gage 1	96.24	92.57	93.61	93.22
	strain gage 2	131.75	126.82	128.16	127.61
	strain gage 3	96.35	92.88	93.73	93.32
	Average Load	108.11	104.09	105.16	104.72
2	strain gage 1	111.15	107.91	108.81	108.46
	strain gage 2	130.31	126.58	127.58	127.16
	strain gage 3	101.52	98.72	99.42	99.09
	Average Load	114.33	111.07	111.94	111.57
3	strain gage 1	121.29	117.18	118.36	117.91
	strain gage 2	157.87	152.63	154.07	153.47
	strain gage 3	97.924	94.78	95.57	95.19
	Average Load	125.70	121.53	122.67	122.19

Table 7. Predicted maximum force (kN) applied to the plate at instant of maximum center displacement using the predicted TiB coefficients in Table 3.

was calculated at each iteration of the parameter estimation sequence. The data in Table 7 yields some interesting results. First, the average P for each test matches well regardless of material model. This is another verification of the statement that the estimation sequence attempts to match the properties in each layer to the actual FGM within the framework of the material model used in the sequence. Secondly, the results show the trend that the force increases as the velocity/energy increases for each test. Lastly, the P loads individually calculated at each position vary somewhat in each test, implying variability occurred in strain gage placement on each plate.

Figure 5 show the strain histories from the homogenized-layers FEMs using the Mori–Tanaka needles (MT-N) material model results compared to the experimental strain histories for FGM plate tests 1–4 (C_i per Table 5). The other models were not plotted simply because the results were virtually the same (as demonstrated through the correlation of layer-by-layer material properties). The FEM results match the test data very well for the most part. Some of the peculiarities observed in the experimental strain histories are not captured with the optimized FEMs. These minor discrepancies can be attributed to any number of causes, including but not limited to FEM boundary conditions, strain gage-adhesive-plate interactions, and tup impacts slightly off center. The FEM determined through this process, however, correlates well with published results and was developed through a process directly tied to the physics and results of the Dynatup impact tests.

Lastly, a comment on the ability of the three material models to accurately represent the physical properties of the Ti-TiB mixtures is in order. The three material models were specifically chosen for use in the parameter estimation sequence for several important reasons. First, these models have been commonly used in the literature to analytically predict properties for a wide variety of composite materials. Second, the models are relatively easy to implement in mathematical equations and simulation computer code while simultaneously providing a reasonable estimate of property variation as the volume-fraction ratio of a two-phase mixture varies. Third, each of the models was formulated under different assumptions with respect to the geometry, configurations, and behavior of the mixtures under loading conditions. Using

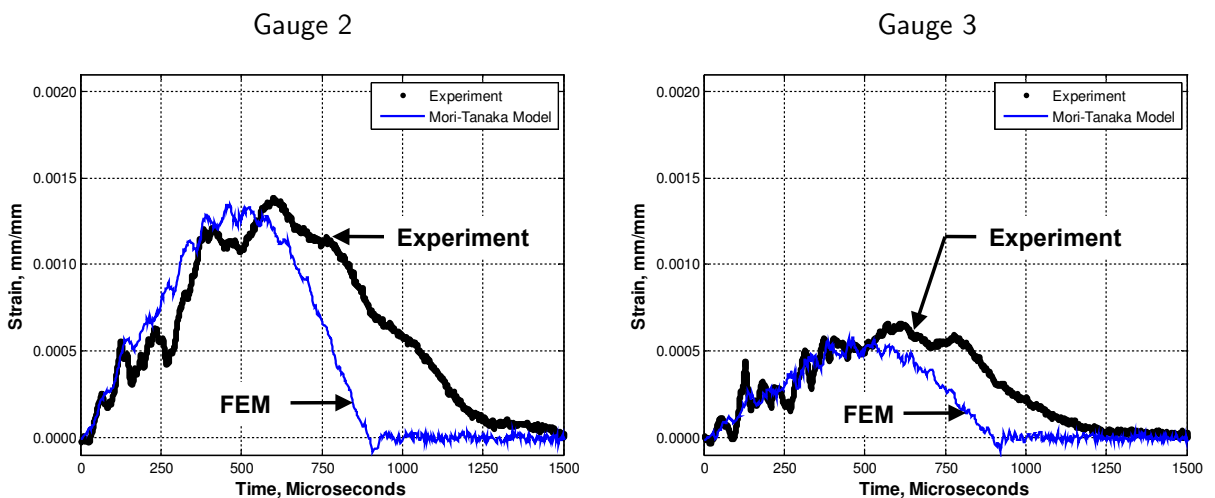


Figure 5. Experimental strain histories and FEM comparison using optimized Mori–Tanaka needles plate models, for test 1. (Continued on next page.)

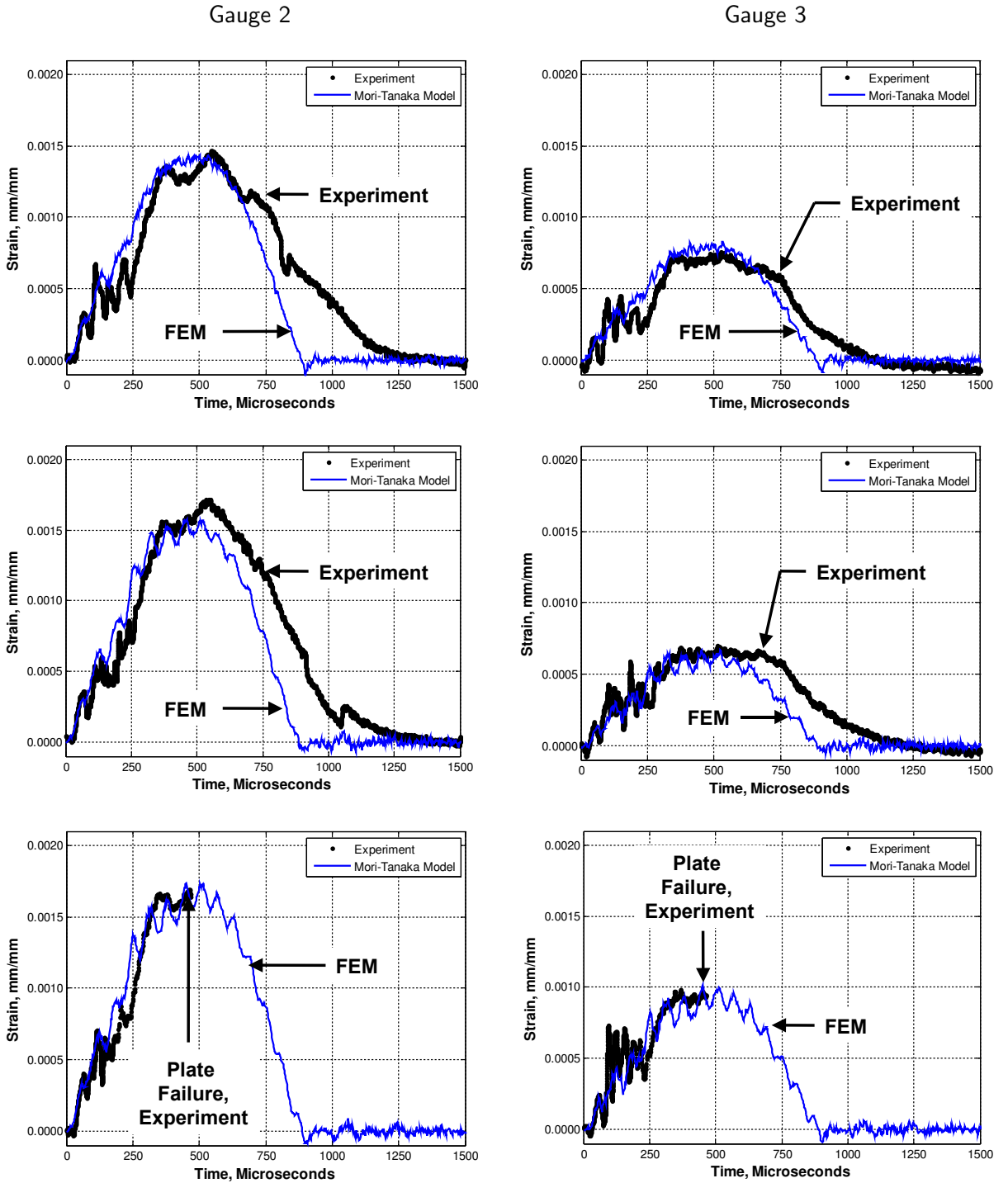


Figure 5 (continued). Experimental strain histories and FEM comparison using optimized Mori–Tanaka needles plate models, for test 2 (top), test 3 (middle) and test 4 (bottom).

each of the three models in the parameter estimation sequence then provides a means of comparison with the assumption that each of the models may be better suited to accurately predicting the physical properties of the FGM under certain conditions. The three models for the property variations and the estimates for the actual volume fraction ratios of Ti to TiB reduced the number of variables the parameter estimation sequence needed to determine. It is possible that a more robust estimation sequence could be formulated that would directly estimate material properties in individual layers of the FGMs. For example, if the sequence were to directly determine the elastic modulus, Poisson's ratio, and density of each of the seven layers of the FGM, the sequence would need to determine 21 variables (three individual properties for each of the seven layers). If such a formulation could be successfully implemented, it would likely predict physical properties more accurately than those predicted using models that may or may not accurately represent physical properties under certain conditions. However, the increased fidelity of such a formulation would come at a significant increase in computational cost.

7. Conclusions

The *major contribution* of this work is a property estimation sequence that can be applied to virtually any two-phase FGM plate system under impact loading where strain data has been experimentally collected over the course of an impact event. Each of the four *key objectives* necessary to construct and validate the property estimation sequence were realized and discussed at length: (a) obtain an analytical model that reasonably approximates the conditions and results of a series of FGM plate impact tests; (b) construct a finite element model that can be used to study the FGM plate impact experiments; (c) outline the parameter estimation framework that determines FGM properties from impact data using the analytical and finite element models of the tests; and (d) correlate the FEM and experimental results using the estimated FGM properties in the finite element models for the plate specimens. The sequence ties experimental, analytical, and computational data from FGM plate impact events together and poses the estimation sequence as a sophisticated minimization problem. The property estimation sequence was effectively demonstrated using a Ti-TiB FGM system and would be, in theory, extendable to practically any two-phased FGM system.

As a final note, the material properties determined in this study were assumed to be *rate-independent*. Given the relatively low-velocity impacts in the FGM plate tests and the fact that the plates behaved elastic to failure, the rate-independent assumption used here is likely sufficient. In high-velocity impact tests, generally rate effects become very important to the constitutive models of the system of interest. The property estimation sequence discussed here could be modified to study such problems, however the objective function and material property parameters would have to take a different form.

Acknowledgements

The views expressed in this article are those of the authors and do not reflect the official policy or position of the United States Air Force, Department of Defense, or the U.S. Government. This work was primarily funded by the Air Force Research Laboratory, Air Vehicles Directorate, Structural Science Center (AFRL/RBS); and the Dayton Area Graduate Studies Institute (DAGSI) under the AFRL/DAGSI Ohio Student-Faculty Research Fellowship Program.

References

- [Arora 1989] J. S. Arora, *Introduction to optimum design*, McGraw-Hill, New York, 1989.
- [Atri et al. 1999] R. R. Atri, K. S. Ravichandran, and S. K. Jha, “Elastic properties of in-situ processed Ti-TiB composites measured by impulse excitation of vibration”, *Mater. Sci. Eng. A* **271**:1-2 (1999), 150–159.
- [BAE 2007] Correspondence with BAE Systems sales engineer Greg Nelson, April 2007.
- [Banks-Sills et al. 2002] L. Banks-Sills, R. Eliasi, and Y. Berlin, “Modeling of functionally graded materials in dynamic analyses”, *Compos. B Eng.* **33**:1 (2002), 7–15.
- [Benveniste 1987] Y. Benveniste, “A new approach to the application of Mori-Tanaka’s theory in composite materials”, *Mech. Mater.* **6**:2 (1987), 147–157.
- [Berryman 1980a] J. G. Berryman, “Long-wavelength propagation in composite elastic media, I: spherical inclusions”, *J. Acoust. Soc. Am.* **68**:6 (1980), 1809–1819.
- [Berryman 1980b] J. G. Berryman, “Long-wavelength propagation in composite elastic media, II: ellipsoidal inclusions”, *J. Acoust. Soc. Am.* **68**:6 (1980), 1820–1831.
- [Birman and Byrd 2007] V. Birman and L. W. Byrd, “Modeling and analysis of functionally graded materials and structures”, *Appl. Mech. Rev. (ASME)* **60**:5 (2007), 195–216.
- [Box and Behnken 1960] G. E. P. Box and D. W. Behnken, “Some new three level designs for the study of quantitative variables”, *Technometrics* **2** (1960), 455–475.
- [Bruck 2000] H. A. Bruck, “A one-dimensional model for designing functionally graded materials to manage stress waves”, *Int. J. Solids Struct.* **37**:44 (2000), 6383–6395.
- [Daniel and Ishai 2006] I. M. Daniel and O. Ishai, *Engineering mechanics of composite materials*, 2nd ed., Oxford University Press, New York, 2006.
- [Dennis Jr. and Schnabel 1983] J. E. Dennis Jr. and R. B. Schnabel, *Numerical methods for unconstrained optimization and nonlinear equations*, Prentice Hall, Englewood Cliffs, NJ, 1983.
- [Goldsmith 1960] W. Goldsmith, *Impact: the theory and physical behaviour of colliding solids*, Edward Arnold, London, 1960.
- [Gong et al. 1999] S. W. Gong, K. Y. Lam, and J. N. Reddy, “The elastic response of functionally graded cylindrical shells to low-velocity impact”, *Int. J. Impact Eng.* **22**:4 (1999), 397–417.
- [Haftka et al. 1990] R. T. Haftka, Z. Gurdal, and M. P. Kamat, *Elements of structural optimization*, 2nd ed., Kluwer, Boston, 1990.
- [Hill 1965] R. Hill, “A self-consistent mechanics of composite materials”, *J. Mech. Phys. Solids* **13**:4 (1965), 213–222.
- [Hill and Lin 2002] M. R. Hill and W. Lin, “Residual stress measurement in a ceramic-metallic graded material”, *J. Eng. Mater. Technol. (ASME)* **124**:2 (2002), 185–191.
- [Larson 2008] R. A. Larson, “A novel method for characterizing the impact response of functionally graded plates”, technical report DS/ENY/08-06, Air Force Institute of Technology, 2008, Available at <http://www.stormingmedia.us/10/1096/A109684.html>.
- [Larson et al. 2009] R. A. Larson, A. N. Palazotto, and H. E. Gardenier, “Impact response of Ti-TiB monolithic and functionally graded composite plates”, *AIAA J.* **47**:3 (March 2009), 676–691.
- [Lawson and Erjavec 2001] J. Lawson and J. Erjavec, *Modern statistics for engineering and quality improvement*, Duxbury/Thomas Learning, Pacific Grove, CA, 2001.
- [Li et al. 2001] Y. Li, K. T. Ramesh, and E. S. C. Chin, “Dynamic characterization of layered and graded structures under impulsive loading”, *Int. J. Solids Struct.* **38**:34-35 (2001), 6045–6061.
- [Loy et al. 1999] C. T. Loy, K. Y. Lam, and J. N. Reddy, “Vibration of functionally graded cylindrical shells”, *Int. J. Mech. Sci.* **41**:3 (1999), 309–324.
- [Mori and Tanaka 1973] T. Mori and K. Tanaka, “Average stress in matrix and average elastic energy of materials with misfitting inclusions”, *Acta Metall.* **21**:5 (1973), 571–574.
- [Myers and Montgomery 1995] R. H. Myers and D. C. Montgomery, *Response surface methodology: process and product optimization using designed experiments*, Wiley, New York, 1995.

- [Oberg et al. 2000] E. Oberg, F. D. Jones, H. L. Horton, and H. H. Ryffel, *Machinery's handbook*, 26th ed., Industrial Press, New York, 2000.
- [Panda and Ravichandran 2003] K. B. Panda and K. S. Ravichandran, "Synthesis of ductile titanium-titanium boride (Ti-TiB) composites with a beta-titanium matrix: the nature of TiB formation and composite properties", *Metall. Mater. Trans. A* **34**:6 (2003), 1371–1385.
- [Panda and Ravichandran 2006] K. B. Panda and K. S. Ravichandran, "First principles determination of elastic constants and chemical bonding of titanium boride (TiB) on the basis of density functional theory", *Acta Mater.* **54**:6 (2006), 1641–1657.
- [Pradhan et al. 2000] S. C. Pradhan, C. T. Loy, K. Y. Lam, and J. N. Reddy, "Vibration characteristics of functionally graded cylindrical shells under various boundary conditions", *Appl. Acoust.* **61**:1 (2000), 111–129.
- [Prakash and Ganapathi 2006] T. Prakash and M. Ganapathi, "Asymmetric flexural vibration and thermoelastic stability of FGM circular plates using finite element method", *Compos. B Eng.* **37**:7-8 (2006), 642–649.
- [Ravichandran et al. 2004] K. S. Ravichandran, K. B. Panda, and S. S. Sahay, "TiB_w-reinforced Ti composites: processing, properties, application prospects, and research needs", *J. Minerals Metals Mat. Soc.* **56**:5 (2004), 42–48.
- [Reddy 2000] J. N. Reddy, "Analysis of functionally graded plates", *Int. J. Numer. Methods Eng.* **47**:1-3 (2000), 663–684.
- [Reddy and Cheng 2001] J. N. Reddy and Z.-Q. Cheng, "Three-dimensional thermomechanical deformations of functionally graded rectangular plates", *Eur. J. Mech. A Solids* **20**:5 (2001), 841–855.
- [Reddy and Cheng 2002] J. N. Reddy and Z.-Q. Cheng, "Frequency correspondence between membranes and functionally graded spherical shallow shells of polygonal planform", *Int. J. Mech. Sci.* **44**:5 (2002), 967–985.
- [Reddy et al. 1999] J. N. Reddy, C. M. Wang, and S. Kitipornchai, "Axisymmetric bending of functionally graded circular and annular plates", *Eur. J. Mech. A Solids* **18**:2 (1999), 185–199.
- [Sahay et al. 1999] S. S. Sahay, K. S. Ravichandran, R. Atri, B. Chen, and J. Rubin, "Evolution of microstructure and phases in situ processed Ti-TiB composites containing high volume fractions of TiB whiskers", *J. Mater. Res.* **14**:11 (1999), 4214–4223.
- [Suresh and Mortensen 1998] S. Suresh and A. Mortensen, *Fundamentals of functionally graded materials: processing and thermomechanical behaviour of graded metals and metal-ceramic composites*, IOM Communications, London, 1998.
- [Ugural 1999] A. C. Ugural, *Stresses in plates and shells*, 2nd ed., McGraw-Hill, Boston, 1999.
- [Vel and Batra 2002] S. S. Vel and R. C. Batra, "Exact solution for thermoelastic deformations of functionally graded thick rectangular plates", *AIAA J.* **40**:7 (2002), 1421–1433.
- [Westergaard 1926] H. M. Westergaard, "Stresses in concrete pavements computed by theoretical analysis", *Public Roads—U.S. Dept. of Agriculture* **7**:2 (1926), 25–35.
- [Woo and Meguid 2001] J. Woo and S. A. Meguid, "Nonlinear analysis of functionally graded plates and shallow shells", *Int. J. Solids Struct.* **38**:42-43 (2001), 7409–7421.
- [Yang and Shen 2001] J. Yang and H.-S. Shen, "Dynamic response of initially stressed functionally graded rectangular thin plates", *Compos. Struct.* **54**:4 (2001), 497–508.
- [Yang and Shen 2002] J. Yang and H.-S. Shen, "Vibration characteristics and transient response of shear-deformable functionally graded plates in thermal environments", *J. Sound Vib.* **255**:3 (2002), 579–602.
- [Zukas et al. 1982] J. A. Zukas, T. Nicholas, H. F. Swift, L. B. Greszczuk, and D. R. Curran, *Impact dynamics*, Wiley, New York, 1982.

Received 4 Dec 2008. Revised 16 Mar 2009. Accepted 13 Apr 2009.

REID A. LARSON: reid.larson@afit.edu

Air Force Institute of Technology, 2950 Hobson Way, Wright-Patterson AFB, OH 45433, United States

ANTHONY N. PALAZOTTO: anthony.palazotto@afit.edu

Air Force Institute of Technology, 2950 Hobson Way, Wright-Patterson AFB, OH 45433, United States

A HIGH-ORDER THEORY FOR CYLINDRICAL SANDWICH SHELLS WITH FLEXIBLE CORES

RENFU LI AND GEORGE KARDOMATEAS

This paper presents a nonlinear high-order theory for cylindrical sandwich shells with flexible cores, extending a previously presented high-order theory for sandwich plates. The outer and inner faces are assumed to be relatively thin compared to the core and the effects from the core compressibility are addressed in the solution by incorporating the extended nonlinear core theory into the constitutive relations of the cylindrical shells. The governing equations and boundary conditions for the cylindrical shells are derived using a variational principle. Numerical results are presented for the cases where the two faces and the core are made of orthotropic materials. These results show that this model could capture the nonlinearity in the transverse stress distribution in the core of the cylindrical sandwich shell. Numerical results are presented on the details of the stress and displacement profiles for a cylindrical sandwich shell under localized external pressure. This study could have significance for the optimal design of advanced cylindrical sandwich shells.

1. Introduction

Unique properties such as high stiffness/weight and strength/weight ratios present increasing promise for applications of cylindrical sandwich shells in aerospace and marine vehicles, such as aircraft fuselage sections, rockets and submarine hulls. A cylindrical sandwich shell consists of outer and inner stiff thin faces made either from homogeneous metallic materials or composite laminates, separated by a thick core of soft foam or honeycomb. In the analysis of the sandwich construction, it is routinely assumed that the face sheets carry the in-plane and bending loadings and the core transmits the transverse normal and shear loads [Plantema 1966; Vinson 1999]. These classical theories also consider the transverse displacement of the core to be the same as the displacements of the middle surface of the two face sheets. The variation in thickness (compressibility) of the core is often neglected.

However, recent studies show that the core could experience significant changes in thickness [Liang et al. 2007; Nemat-Nasser et al. 2007; Li et al. 2008]. As a consequence, there is an increasing concern on the influence of core compressibility on the behavior of sandwich structures. Efforts to address this issue are demonstrated through the formulation of various advanced high-order sandwich models in the literature [Frostig et al. 1992; Pai and Palazotto 2001; Hohe and Librescu 2003; Li and Kardomateas 2008]. Models considering the core compressibility may not only give a more accurate solution to simpler problems, but may also help to analytically address some otherwise difficult problems such as debond behavior [Li et al. 2001], shock wave propagation and energy absorption in sandwich structures.

In previous work, we derived a high-order sandwich plate theory [Li and Kardomateas 2008], in which the transverse displacement of the core is no longer assumed a constant, but it is a fourth order function

Keywords: composite sandwich shells, compressibility, high-order theory, external pressure.

of the transverse coordinate. The in-plane displacements vary as fifth order functions of the transverse coordinate. The current paper presents an adaptation of this nonlinear high-order core model to the configuration of cylindrical sandwich shells. The derivation procedure of this theory is similar to the one in [Li and Kardomateas 2008] but accommodated to the specific geometry of cylindrical sandwich shells. In the development of the advanced cylindrical sandwich shell model, the following assumptions have been made:

- (1) The face sheets satisfy the Kirchhoff–Love assumptions and their thicknesses are small compared with the overall thickness of the sandwich section. The transverse displacements in the faces do not vary through the thickness. In the current paper, the two face sheets are considered to have identical thickness.
- (2) The core is compressible in the transverse direction, that is, its thickness may change.
- (3) The bonding between the face sheets and the core is assumed perfect.

The paper is organized as follows: We first extend the high-order sandwich plate compressible core theory to the cylindrical sandwich shell. In the derivation, the cylindrical coordinate system (x, s, z) is introduced and located at the middle plane of the core or the face sheets. The transverse displacement of the initial mid-plane is considered as an unknown function of the coordinates (x, s) . The axial, circumferential and transverse displacements in the core are then expressed as functions in terms of the displacements of the two face sheets and the displacement of the core initial mid-plane. The displacement continuity conditions along the interface between the face sheet and the core are employed. We then formulate the governing equations, boundary conditions, and solution procedure for cylindrical sandwich shells. As a representative, the equations for an orthotropic sandwich shell are studied in detail. Next, the numerical results for a typical cylindrical sandwich shell with three orthotropic phases (two face sheets and a core) are presented. Finally, we draw some conclusions and suggestions on future work.

2. Extension of high-order sandwich plate theory to shells

Let a coordinate system (x, s, z) be located at the middle plane of the face sheets or the core with x in the axial direction, s in the circumferential direction, and z in the outward normal direction (Figure 1), and (u, v, w) be the corresponding displacements. R_i and R_o are the radii of the middle surface of the inner and outer face, respectively; L is the shell length; the outer and inner faces are assumed to have an identical thickness, h_f , and the core thickness is h_c . Also set $R = (R_o + R_i)/2$.

2A. Displacement field representation. In the classical sandwich model, the compressibility of the core in the thickness direction is ignored. This may give a good approximation in simple and preliminary studies. However, in many more demanding cases, such as a sandwich structure subject to blast/impact loading, consideration of the transverse compressibility of the core may be needed. In the high-order core theory proposed in [Li and Kardomateas 2008], the transverse displacement in the core $(-h_c/2 \leq z \leq h_c/2)$ is in the form

$$w^c(x, s, z) = \left(1 - \frac{2z^2}{h_c^2} - \frac{8z^4}{h_c^4}\right)w_0^c(x, s) + \left(\frac{2z^2}{h_c^2} + \frac{8z^4}{h_c^4}\right)w(x, s) - \left(\frac{z}{h_c} + \frac{4z^3}{h_c^3}\right)\bar{w}(x, s), \quad (1)$$

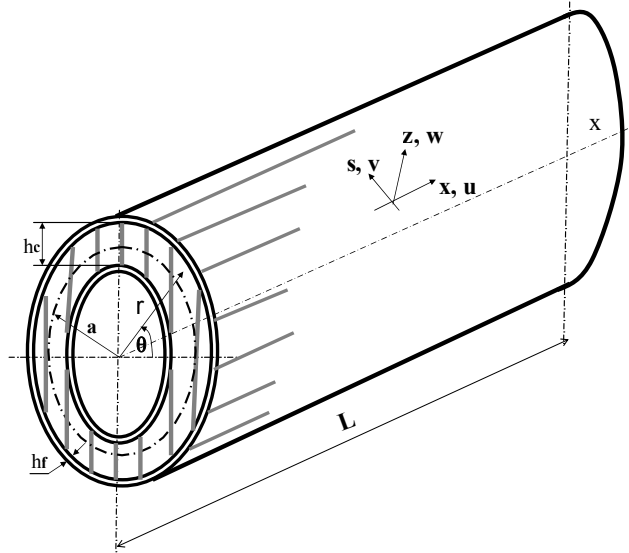


Figure 1. A cylindrical sandwich shell.

and the in-plane displacements in the core are in the form

$$\begin{aligned}
 u^c(x, s, z) &= u(x, s) - \frac{z}{h_c/2} \bar{u}(x, s) + z \frac{h_f}{h_c} w_{,x}^c(x, s, z), \\
 v^c(x, s, z) &= v(x, s) - \frac{z}{h_c/2} \bar{v}(x, s) + z \frac{h_f}{h_c} w_{,y}^c(x, s, z),
 \end{aligned}
 \tag{2}$$

In these equations, $w_0^c(x, s)$ is the transverse displacement of the middle surface of the core; $w(x, s)$ is the average of the displacements of top face sheet, $w^t(x, s)$ and bottom face sheet, $w^b(x, s)$; and $\bar{w}(x, s)$ is half of the difference of these displacements. Similar definitions hold for the corresponding in-plane displacements.

This high-order core theory could be extended to other geometric configurations such as shapes with curvature, provided the thickness of the face sheets is small compared to the total thickness of the sandwich structure. In this work, it will be extended to cylindrical sandwich shells with orthotropic phases. The thin face sheets of the shell satisfy the Kirchhoff–Love assumptions. Therefore, setting $h = (h_c + h_f)/2$, one has for the displacements in the outer face, $-(h_c/2 + h_f) \leq z \leq -h_c/2$, the expressions

$$\begin{aligned}
 u^t(x, s, z) &= u_0^t(x, s) - (z + h)w_{,x}^t(x, s), \\
 v^t(x, s, z) &= v_0^t(x, s) - (z + h)w_{,s}^t(x, s), \\
 w^t(x, s, z) &= w^t(x, s),
 \end{aligned}
 \tag{3}$$

and for the and displacements in the inner face, $h_c/2 \leq z \leq h_c/2 + h_f$,

$$\begin{aligned}
 u^b(x, s, z) &= u_0^b(x, s) - (z - h)w_{,x}^b(x, s), \\
 v^b(x, s, z) &= v_0^b(x, s) - (z - h)w_{,s}^b(x, s), \\
 w^b(x, s, z) &= w^b(x, s).
 \end{aligned}
 \tag{4}$$

In order to take the core compressibility into account, nonlinear models can be proposed. The one proposed here satisfies all the displacement continuity conditions along the interface between the core and the face sheets, as shown in [Li and Kardomateas 2008].

2B. Strain-displacement relation. For thin face sheets, one can obtain the strain tensor at a point in the outer face sheet of the cylindrical sandwich shell as

$$[\epsilon^t] = \begin{pmatrix} \epsilon_x^t \\ \epsilon_s^t \\ \gamma_{xs}^t \end{pmatrix} = \begin{pmatrix} \epsilon_{0x}^t \\ \epsilon_{0s}^t \\ \gamma_{0xs}^t \end{pmatrix} + (z+h)[\kappa^t] = \begin{pmatrix} u_{0,x}^t \\ v_{0,s}^t + w^t/R_o \\ u_{0,s}^t + v_{0,x}^t \end{pmatrix} + (z+h)[\kappa^t]. \tag{5}$$

A similar expression holds for the strain tensor in the inner face,

$$[\epsilon^b] = \begin{pmatrix} \epsilon_x^b \\ \epsilon_s^b \\ \gamma_{xs}^b \end{pmatrix} = \begin{pmatrix} \epsilon_{0x}^b \\ \epsilon_{0s}^b \\ \gamma_{0xs}^b \end{pmatrix} + (z-h)[\kappa^b] = \begin{pmatrix} u_{0,x}^b \\ v_{0,s}^b + w^b/R_i \\ u_{0,s}^b + v_{0,x}^b \end{pmatrix} + (z-h)[\kappa^b]. \tag{6}$$

In these equations,

$$[\kappa^{t,b}] = \begin{pmatrix} \kappa_x^{t,b} \\ \kappa_s^{t,b} \\ \kappa_{xs}^{t,b} \end{pmatrix} = \begin{pmatrix} -w_{,xx}^{t,b} \\ -w_{,ss}^{t,b} \\ -2w_{,xs}^{t,b} \end{pmatrix}. \tag{7}$$

The core is considered undergoing large rotation with small displacements and its in-plane strains could be neglected. Therefore, one can derive the strain-displacement relations of the core from equations (1) and (2) as follows:

$$\begin{aligned} \epsilon_z^c &= \left(-\frac{1}{2h_c} + \frac{2z}{h_c^2} - \frac{6z^2}{h_c^3} + \frac{16z^3}{h_c^4}\right)w^t(x,s) - \left(\frac{4z}{h_c^2} + \frac{32z^3}{h_c^4}\right)w_0^c(x,s) + \left(\frac{1}{2h_c} + \frac{2z}{h_c^2} + \frac{6z^2}{h_c^3} + \frac{16z^3}{h_c^4}\right)w^b(x,s), \\ \gamma_{xz}^c &= -\frac{2}{h_c}\bar{u}(x,s) + \eta_1(z)w_{,x}^t(x,s) + \eta_2(z)w_{0,x}^c(x,s) + \eta_3(z)w_{,x}^b(x,s), \\ \gamma_{sz}^c &= -\frac{2}{h_c}\bar{v}(x,s) + \eta_1(z)w_{,s}^t(x,s) + \eta_2(z)w_{0,s}^c(x,s) + \eta_3(z)w_{,s}^b(x,s) - \frac{v^c}{r}, \end{aligned} \tag{8}$$

in which $R - h_c/2 \leq r \leq R + h_c/2$ and

$$\begin{aligned} \eta_1(z) &= -\left(\frac{1}{2} + \frac{h_f}{h_c}\right)\frac{z}{h_c} + \left(1 + 3\frac{h_f}{h_c}\right)\frac{z^2}{h_c^2} - 2\left(1 + 4\frac{h_f}{h_c}\right)\frac{z^3}{h_c^3} + 4\left(1 + 5\frac{h_f}{h_c}\right)\frac{z^4}{h_c^4}, \\ \eta_2(z) &= \left(1 + \frac{h_f}{h_c}\right) - 2\left(1 + \frac{3h_f}{h_c}\right)\frac{z^2}{h_c^2} - 8\left(1 + \frac{5h_f}{h_c}\right)\frac{z^4}{h_c^4}, \\ \eta_3(z) &= \left(\frac{1}{2} + \frac{h_f}{h_c}\right)\frac{z}{h_c} + \left(1 + 3\frac{h_f}{h_c}\right)\frac{z^2}{h_c^2} + 2\left(1 + 4\frac{h_f}{h_c}\right)\frac{z^3}{h_c^3} + 4\left(1 + 5\frac{h_f}{h_c}\right)\frac{z^4}{h_c^4}. \end{aligned} \tag{9}$$

2C. Constitutive relation. The face sheets of the shell are made of orthotropic laminated composites and the core is also orthotropic. The stress-strain relationship for any layer of the faces reads as

$$\begin{pmatrix} \sigma_x \\ \sigma_s \\ \tau_{xs} \end{pmatrix} = \begin{pmatrix} Q_{11} & Q_{12} & Q_{16} \\ Q_{12} & Q_{22} & Q_{26} \\ Q_{16} & Q_{26} & Q_{66} \end{pmatrix} \begin{pmatrix} \epsilon_x \\ \epsilon_s \\ \gamma_{xs} \end{pmatrix}, \quad \text{or} \quad [\sigma] = [Q][\epsilon], \quad (10)$$

where the Q_{ij} , for $i, j = 1, 2, 6$, are the reduced stiffness coefficients. The stress-strain relations for the orthotropic core are written as

$$\sigma_z^c = E^c \epsilon_z^c, \quad \tau_{xz} = G_{xz}^c \gamma_{xz}^c, \quad \tau_{sz} = G_{sz}^c \gamma_{sz}^c. \quad (11)$$

Here, we define the resultants for the outer face sheet of the sandwich shell by

$$\begin{aligned} [N^t] &= \begin{pmatrix} N_x^t \\ N_s^t \\ N_{xs}^t \end{pmatrix} = \int_{-(h_c/2+h_f)}^{-h_c/2} [\sigma^t] dz = \int_{-(h_c/2+h_f)}^{-h_c/2} [Q^t][\epsilon^t] dz = [A][\epsilon_0^t] + [B][\kappa^t], \\ [M^t] &= \begin{pmatrix} M_x^t \\ M_s^t \\ M_{xs}^t \end{pmatrix} = \int_{-(h_c/2+h_f)}^{-h_c/2} [\sigma^t]_z dz = [B][\epsilon_0^t] + [D][\kappa^t], \end{aligned} \quad (12)$$

in which the stiffness coefficients are defined as

$$[\hat{A}_{ij}^t, \hat{B}_{ij}^t, \hat{D}_{ij}^t] = \int_{-(h_c/2+h_f)}^{-h_c/2} Q_{ij}^t [1, (z+h), (z+h)^2] dz. \quad (13)$$

Applying a similar procedure, one can obtain the expressions for the resultants in the inner face sheet.

3. Equilibrium equations and boundary conditions

The cylindrical sandwich shell is assumed subject to external and internal pressure $q^{t,b}(x, s)$. Let U denote the strain energy and W the work of external forces. The variational principle (equivalent to a virtual displacement approach) states that

$$\delta(U - W) = 0, \quad (14)$$

in which

$$\begin{aligned} \delta U &= \int_0^L \oint \left(\int_{-h_c/2-h_f}^{-h_c/2} (\sigma_x^t \delta \epsilon_x^t + \sigma_s^t \delta \epsilon_s^t + \tau_{xs}^t \delta \gamma_{xs}^t)(R_o + z) dz \right. \\ &\quad + \int_{-h_c/2}^{h_c/2} (\sigma_z^c \delta \epsilon_z^c + \tau_{xz}^c \delta \gamma_{xz}^c + \tau_{sz}^c \delta \gamma_{sz}^c)(R + z) dz \\ &\quad \left. + \int_{h_c/2}^{h_c/2+h_f} (\sigma_x^b \delta \epsilon_x^b + \sigma_s^b \delta \epsilon_s^b + \tau_{xs}^b \delta \gamma_{xs}^b)(R_i + z) dz \right) d\theta dx, \\ \delta W &= \int_0^L \oint q^{t,b}(x, s) \delta w^{t,b} ds dx + \int_0^L \oint N_x(x, s) \delta u ds dx. \end{aligned} \quad (15)$$

We now introduce the notation

$$\alpha = \frac{h_f}{h_c} \quad \text{and} \quad \beta = \frac{h_c}{R}.$$

For the thin face sheets of $R_i + z \cong R_i$, $R_o + z \cong R_o$ and $\beta \ll 1$, one can obtain the equilibrium equations and boundary conditions by substituting the stress strain relations (10)–(11) strain-displacement relations (5)–(9) and the displacement representation equations (1)–(4) into (15), then into (14) and employing integration by parts. For the outer face sheet this results in the governing equations

$$\delta u_0^t : -N_{x,x}^t - \frac{1}{R_o} N_{x\theta,\theta}^t + G_{xz}^c \left(\frac{4}{\beta} (u_0^t - u_0^b) - \frac{\zeta_1}{\beta} R w_{,x}^t - \frac{22}{15} R w_{o,x}^c - \frac{\bar{\zeta}_1}{\beta} R w_{,x}^b \right) = 0,$$

$$\delta v_0^t : -N_{x\theta,x}^t - \frac{1}{R_o} N_{\theta,\theta}^t + G_{sz}^c (\zeta_6 v_0^t - \zeta_7 v_0^b + \zeta_8 w_{,\theta}^t + \zeta_9 w_{0,\theta}^c + \zeta_{10} w_{,\theta}^b) = 0,$$

$$\begin{aligned} \delta w_0^t : & - \left(M_{x,xx}^t + \frac{2}{R_o} M_{x\theta,x\theta}^t + \frac{1}{R_o^2} M_{\theta,\theta\theta}^t - \frac{1}{R_o} N_x^t \right) + E_z^c \left(\frac{61 + 23\beta}{21\beta} w^t + \frac{358 + 115\beta}{105\beta} w_0^c + \frac{53}{105\beta} w^b \right) \\ & + \zeta_1 R G_{xz}^c (u_{0,x}^t - u_{0,x}^b) + G_{sz}^c (\zeta_{11} v_{0,\theta}^t - \bar{\zeta}_{11} v_{0,\theta}^b) - \zeta_2 R^2 G_{xz}^c w_{,xx}^t - \zeta_{12} G_{sz}^c w_{,\theta\theta}^t \\ & - \zeta_3 R^2 G_{xz}^c w_{0,xx}^c - \zeta_{13} G_{sz}^c w_{0,\theta\theta}^c - \zeta_4 R^2 G_{xz}^c w_{,xx}^b - \zeta_{14} G_{sz}^c w_{,\theta\theta}^b - Q_o(x, \theta, t) = 0. \end{aligned}$$

For the compressive core:

$$\begin{aligned} \delta w_0^c : & E_z^c \left(\frac{358 + 115\beta}{105\beta} w^t + \frac{716}{105\beta} w_0^c + \frac{358 - 115\beta}{105\beta} w^b \right) \\ & + \frac{22}{15} G_{xz}^c (u_{0,x}^t - u_{0,x}^b) + G_{sz}^c (\zeta_{11}^c v_{0,\theta}^t - \bar{\zeta}_{11}^c v_{0,\theta}^b) - \zeta_3 R^2 G_{xz}^c w_{,xx}^t - \zeta_{12}^c G_{sz}^c w_{,\theta\theta}^t \\ & - \zeta_5 R^2 G_{xz}^c w_{0,xx}^c - \zeta_{13}^c G_{sz}^c w_{0,\theta\theta}^c - \bar{\zeta}_3 R^2 G_{xz}^c w_{,xx}^b - \zeta_{14}^c G_{sz}^c w_{,\theta\theta}^b = 0. \end{aligned}$$

For the inner face sheet:

$$\delta u_0^b : -N_{x,x}^b - \frac{1}{R_i} N_{\theta,\theta}^b - G_{xz}^c \left(\frac{4}{\beta} (u_0^t - u_0^b) - \frac{\zeta_1}{\beta} R w_{,x}^t - \frac{22}{15} R w_{0,x}^c - \frac{\bar{\zeta}_1}{\beta} R w_{,x}^b \right) = 0,$$

$$\delta v_0^b : -N_{x\theta,x}^b - \frac{1}{R_i} N_{\theta,\theta}^b - G_{sz}^c (\zeta_7 v_0^t - \bar{\zeta}_6 v_0^b - \bar{\zeta}_8 w_{,\theta}^t - \bar{\zeta}_9 w_{0,\theta}^c - \bar{\zeta}_{10} w_{,\theta}^b) = 0,$$

$$\begin{aligned} \delta w_0^b : & - \left(M_{x,xx}^b + \frac{2}{R_i} M_{x\theta,x\theta}^b + \frac{1}{R_i^2} M_{\theta,\theta\theta}^b - \frac{1}{R_i} N_x^b \right) + E_z^c \left(\frac{53}{105\beta} w^t + \frac{358 - 115\beta}{105\beta} w_0^c + \frac{61 - 23\beta}{21\beta} w^b \right) \\ & + \bar{\zeta}_1 R G_{xz}^c (u_{0,x}^t - u_{0,x}^b) + G_{sz}^c (\zeta_{11}^b v_{0,\theta}^t - \bar{\zeta}_{11}^b v_{0,\theta}^b) - \zeta_4 R^2 G_{xz}^c w_{,xx}^t - \zeta_{12}^b G_{sz}^c w_{,\theta\theta}^t \\ & - \bar{\zeta}_3 R^2 G_{xz}^c w_{0,xx}^c - \zeta_{13}^b G_{sz}^c w_{0,\theta\theta}^c - \bar{\zeta}_2 R^2 G_{xz}^c w_{,xx}^b - \zeta_{14}^b G_{sz}^c w_{,\theta\theta}^b - Q_i(x, \theta, t) = 0. \end{aligned}$$

The constants ζ_i and $\zeta_i^{t,c,b}$, for $i = 1, 2, \dots, 14$, in these equations are functions of β and α and are listed in the [Appendix](#).

The corresponding boundary conditions at $x = 0, L$ are

$$u_0^t = \tilde{u}^t \quad \text{or} \quad N_x^t = \tilde{N}_x^t,$$

$$w^t = \tilde{w}^t \quad \text{or}$$

$$N_x^t w_{,x}^t + M_{x,x}^t + N_{x\theta}^t w_{,y}^t + 2M_{x\theta,x}^t + G_{xz}^c (\zeta_1 R(u_0^b - u_0^t) + \zeta_2 R^2 w_{,x}^t + \zeta_2 R^2 w_{0,x}^c + \zeta_4 R^2 w_{,x}^b) = \tilde{Q}_x^t,$$

$$w_{,x}^t = \tilde{w}_{,x}^t \quad \text{or} \quad M_x^t = \tilde{M}_x^t,$$

$$w_0^c = \tilde{w}_0^c \quad \text{or} \quad \frac{22}{15} R(u_0^b - u_0^t) + \zeta_3 R^2 w_{,x}^t + \zeta_5 R^2 w_{0,x}^c + \bar{\zeta}_3 R^2 w_{,x}^b = \tilde{Q}_c,$$

$$u_0^b = \tilde{u}^b \quad \text{or} \quad N_x^b = \tilde{N}_x^b,$$

$$w^b = \tilde{w}^b \quad \text{or}$$

$$N_x^b w_{,x}^b + M_{x,x}^b + N_{xy}^b w_{,y}^b + 2M_{x\theta,x}^b + G_{xz}^c (\bar{\zeta}_1 R(u_0^b - u_0^t) + \zeta_4 R^2 w_{,x}^t + \bar{\zeta}_3 R^2 w_{0,x}^c + \bar{\zeta}_2 R^2 w_{,x}^b) = \tilde{Q}_x^t,$$

$$w_{,x}^b = \tilde{w}_{,x}^b \quad \text{or} \quad M_x^b = \tilde{M}_x^b,$$

where the superscript $\tilde{}$ denotes the known external boundary values. At $\theta = 0$ and 2π , continuity conditions hold.

For the sandwich shell made out of orthotropic materials, the governing equations for the outer face sheet can be rewritten as

$$\begin{aligned} \left(A_{11}^t \frac{\partial^2}{\partial x^2} + \frac{A_{66}^t}{R_o^2} \frac{\partial^2}{\partial \theta^2} - \frac{4G_{xz}^c}{\beta} \right) u_0^t + \frac{A_{12}^t + A_{66}^t}{R_o} \frac{\partial^2 v_0^t}{\partial x \partial \theta} + \left(\frac{\zeta_1}{\beta} R G_{xz}^c + \frac{A_{12}^t}{R_o} \right) w_{,x}^t \\ + \frac{22}{15} R G_{xz}^c w_{0,x}^c + \frac{4G_{xz}^c}{\beta} u_0^b + \frac{\bar{\zeta}_1}{\beta} G_{xz}^c R w_{,x}^b = 0, \end{aligned} \quad (16)$$

$$\begin{aligned} \frac{A_{21}^t + A_{66}^t}{R_o} \frac{\partial^2 u_0^t}{\partial x \partial \theta} + \left(A_{66}^t \frac{\partial^2}{\partial x^2} + \frac{A_{22}^t}{R_o^2} \frac{\partial^2}{\partial \theta^2} - \zeta_6 G_{sz}^c \right) v_0^t + \left(\frac{A_{22}^t}{R_o^2} - \zeta_8 G_{sz}^c \right) w_{,\theta}^t \\ - \zeta_9 G_{sz}^c w_{0,\theta}^c + \zeta_7 G_{sz}^c v_0^b - \zeta_{10} G_{sz}^c w_{,\theta}^b = 0, \end{aligned} \quad (17)$$

$$\begin{aligned} \left(D_{11}^t \frac{\partial^4}{\partial x^4} + 2 \frac{D_{12}^t + 2D_{66}^t}{R_o^2} \frac{\partial^4}{\partial x^2 \partial \theta^2} + \frac{D_{22}^t}{R_o^4} \frac{\partial^4}{\partial \theta^4} + \frac{(61+23\beta)E_z^c}{21\beta} - \zeta_2 R^2 G_{xz}^c \frac{\partial^2}{\partial x^2} - \zeta_{12}^t G_{sz}^c \frac{\partial^2}{\partial \theta^2} + \frac{A_{12}^t}{R_o^2} \right) w^t \\ + \frac{A_{11}^t}{R_o} \frac{\partial u_0^t}{\partial x} + \zeta_1 R G_{xz}^c \frac{\partial}{\partial x} (u_0^t - u_0^b) + \left(\frac{(358+115\beta)E_z^c}{105\beta} - \zeta_3 R^2 G_{xz}^c \frac{\partial^2}{\partial x^2} - \zeta_{13}^t G_{sz}^c \frac{\partial^2}{\partial \theta^2} \right) w_0^c \\ + \frac{A_{12}^t}{R_o^2} \frac{\partial v_0^t}{\partial \theta} + G_{sz}^c \frac{\partial}{\partial \theta} (\zeta_{11}^t v_0^t - \bar{\zeta}_{11}^t v_0^b) + \left(\frac{53E_z^c}{105\beta} - \zeta_4 R^2 G_{xz}^c \frac{\partial^2}{\partial x^2} - \zeta_{14}^t G_{sz}^c \frac{\partial^2}{\partial \theta^2} \right) w^b = Q_o(x, \theta). \end{aligned} \quad (18)$$

Similarly, the equation for the core can be recast as

$$\begin{aligned} \frac{22}{15} G_{xz}^c u_{0,x}^t + G_{sz}^c \zeta_{11}^c v_{0,\theta}^t + \left(\frac{(358+115\beta)E_z^c}{105\beta} - \zeta_3 R^2 G_{xz}^c \frac{\partial^2}{\partial x^2} - \zeta_{12}^c G_{sz}^c \frac{\partial^2}{\partial \theta^2} \right) w^t \\ + \left(\frac{716E_z^c}{105\beta} - \zeta_5 R^2 G_{xz}^c \frac{\partial^2}{\partial x^2} - \zeta_{13}^c G_{sz}^c \frac{\partial^2}{\partial \theta^2} \right) w_0^c - \frac{22}{15} G_{xz}^c u_{0,x}^b - \bar{\zeta}_{11}^c G_{sz}^c v_{0,\theta}^b \\ + \left(\frac{(358-115\beta)E_z^c}{105\beta} - \bar{\zeta}_3 R^2 G_{xz}^c \frac{\partial^2}{\partial x^2} - \zeta_{14}^c G_{sz}^c \frac{\partial^2}{\partial \theta^2} \right) w^b = 0. \end{aligned} \quad (19)$$

Finally, for the inner face sheet:

$$\left(A_{11}^b \frac{\partial^2}{\partial x^2} + \frac{\hat{A}_{66}^b}{R_i^2} \frac{\partial^2}{\partial \theta^2} - \frac{4G_{xz}^c}{\beta} \right) u_0^b + \frac{A_{12}^b + A_{66}^b}{R_i} \frac{\partial^2 v_0^b}{\partial x \partial \theta} + \left(\frac{\bar{\zeta}_1}{\beta} R G_{xz}^c + \frac{A_{12}^b}{R_i} \right) w_{,x}^b + \frac{22}{15} R G_{xz}^c w_{0,x}^c + \frac{4G_{xz}^c}{\beta} u_0^t + G_{xz}^c \frac{\zeta_1}{\beta} R w_{,x}^t = 0, \quad (20)$$

$$\frac{A_{21}^b + A_{66}^b}{R_i} \frac{\partial^2 u_0^b}{\partial x \partial \theta} + \left(A_{66}^b \frac{\partial^2}{\partial x^2} + \frac{A_{22}^b}{R_i^2} \frac{\partial^2}{\partial \theta^2} - \bar{\zeta}_6 G_{sz}^c \right) v_0^b - \left(\bar{\beta}_{10} G_{sz}^c - \frac{A_{22}^b}{R_i^2} \right) w_{,\theta}^b - \bar{\zeta}_9 G_{sz}^c w_{0,\theta}^c + \zeta_7 G_{sz}^c v_0^t - \bar{\zeta}_8 G_{sz}^c w_{,\theta}^t = 0, \quad (21)$$

$$\left[D_{11}^b \frac{\partial^4}{\partial x^4} + 2 \frac{D_{12}^b + 2D_{66}^b}{R_i^2} \frac{\partial^4}{\partial x^2 \partial \theta^2} + \frac{D_{22}^b}{R_i^4} \frac{\partial^4}{\partial \theta^4} + \frac{(61-23\beta)E_z^c}{21\beta} - \left(\bar{\zeta}_2 R^2 G_{xz}^c \frac{\partial^2}{\partial x^2} + \zeta_{14}^b G_{sz}^c \frac{\partial^2}{\partial \theta^2} \right) + \frac{A_{12}^b}{R_i^2} \right] w^b + \bar{\zeta}_1 R G_{xz}^c \frac{\partial}{\partial x} (u_0^t - u_0^b) + \frac{A_{11}^b}{R_o} \frac{\partial u_0^b}{\partial x} + \left(\frac{(358-115\beta)E_z^c}{105\beta} - \bar{\beta}_3 R^2 G_{xz}^c \frac{\partial^2}{\partial x^2} - \zeta_{13}^b G_{sz}^c \frac{\partial^2}{\partial \theta^2} \right) w_0^c + \frac{A_{12}^b}{R_i^2} \frac{\partial v_0^b}{\partial \theta} + G_{sz}^c \frac{\partial}{\partial \theta} (\zeta_{11}^b v_0^t - \bar{\zeta}_{11}^b v_0^b) + \left(\frac{53E_z^c}{105\beta} - \zeta_4 R^2 G_{xz}^c \frac{\partial^2}{\partial x^2} - \zeta_{12}^b G_{sz}^c \frac{\partial^2}{\partial \theta^2} \right) w^t = Q_i(x, \theta, t). \quad (22)$$

It should be noted that since this new core theory is a three-dimensional approximation model for the core (but more efficient than a complete three-dimensional elasticity approach), none of the existing shell theories could produce identical governing equations.

4. A cylindrical sandwich shell under external pressure

In this section the solution procedure for the response of sandwich shells will be demonstrated through the study of simply supported cylindrical shell under external pressure. The boundary conditions are

$$w^t = 0, \quad w^c = 0, \quad w^b = 0; \quad M_x^t = 0, \quad M_x^b = 0, \quad \text{for } x = 0, L.$$

and $v_0^t, w^t, w^c, v_0^b, w^b, M_{yy}^t$ and M_{yy}^b are continuous at $\theta = 0, 2\pi$. As such, the displacements can be set in the form

$$\begin{aligned} u_0^t &= \sum_{\substack{m=0 \\ n=0}}^{M,N} U_{mn}^t \cos \frac{m\pi x}{L} \cos n\theta, & u_0^b &= \sum_{\substack{m=0 \\ n=0}}^{M,N} U_{mn}^b \cos \frac{m\pi x}{L} \cos n\theta, \\ v_0^t &= \sum_{\substack{m=0 \\ n=0}}^{M,N} V_{mn}^t \sin \frac{m\pi x}{L} \sin n\theta, & v_0^b &= \sum_{\substack{m=0 \\ n=0}}^{M,N} V_{mn}^b \sin \frac{m\pi x}{L} \sin n\theta, \\ w^t &= \sum_{\substack{m=0 \\ n=0}}^{M,N} W_{mn}^t \sin \frac{m\pi x}{L} \cos n\theta, & w^b &= \sum_{\substack{m=0 \\ n=0}}^{M,N} W_{mn}^b \sin \frac{m\pi x}{L} \cos n\theta, & w^c &= \sum_{\substack{m=0 \\ n=0}}^{M,N} W_{mn}^c \sin \frac{m\pi x}{L} \cos n\theta, \end{aligned} \quad (23)$$

where $U_{mn}^t, V_{mn}^t, W_{mn}^t, W_{mn}^c, U_{mn}^b, V_{mn}^b$ and W_{mn}^b are constants to be determined. The applied external and internal loading $Q_o(x, \theta)$ and $Q_i(x, \theta)$ can be, respectively, expressed in the form

$$Q_o(x, \theta) = \sum_{\substack{m=0 \\ n=0}}^{M,N} \hat{Q}_{mn}^o \sin \frac{m\pi x}{L} \cos n\theta, \quad Q_i(x, \theta) = \sum_{\substack{m=0 \\ n=0}}^{M,N} \hat{Q}_{mn}^i \sin \frac{m\pi x}{L} \cos n\theta, \quad (24)$$

where $0 \leq \theta \leq 2\pi$ and the coefficients are defined for $m = 0, \dots, M$ and $n = 0, \dots, N$ as

$$\hat{Q}_{mn}^o = \frac{2}{a\pi} \int_0^L \int_0^\Theta Q_o(x, \theta) dx d\theta, \quad \hat{Q}_{mn}^i = \frac{2}{a\pi} \int_0^L \int_0^\Theta Q_i(x, \theta) dx d\theta. \quad (25)$$

Substituting equations (23)–(25) into the governing equations (16)–(22), one can obtain a set of equations in matrix form:

$$[K^{MN}]U_{mn} = F_{mn}, \quad (26)$$

where the displacement vector U_{mn} is defined as $U_{mn} = [U_{mn}^t, V_{mn}^t, W_{mn}^t, W_{mn}^c, U_{mn}^b, V_{mn}^b, W_{mn}^b]^T$ and the loading vector F_{mn} as $[0.0, 0.0, \hat{Q}_{mn}^o, 0.0, 0.0, 0.0, \hat{Q}_{mn}^i]^T$. The $[K^{MN}]$ is a 7×7 matrix, whose entries are given on the next page. Once the applied loading is given, the displacements can be found by solving (26) for each pair (m, n) until the solutions in form of (23) converge as m and n increase.

Results for a cylindrical sandwich shell under localized external pressure. Assume that a constant pressure loading is applied on a portion of the outer face sheet:

$$p(x, \theta) = p_0, \quad 0 \leq x \leq a, \quad -\frac{\pi}{4} \leq \theta \leq \frac{\pi}{4}.$$

From equations (24) and (25) one can obtain the following loading in the transformed space for $m = 1, 2, 3, \dots$:

$$Q_{m0} = \frac{2}{m\pi} p_0 \sin^2 \frac{m\pi}{2}, \quad Q_{mn} = \frac{8}{mn\pi^2} p_0 \sin^2 \frac{m\pi}{2} \sin \frac{n\pi}{4} \quad n = 1, 2, 3, \dots$$

The relationship for the Poisson’s ratio, $\nu_{ij} = \nu_{ji} E_i / E_j$, will be applied since the sandwich structure consists of orthotropic phases. In the following study, we set the radius of the core middle plane, $R = 0.8$ m. Its core thickness is $h_c = \beta R$ with $\beta = 1/10$. The thickness of two face sheets is the same, $h_f = \alpha h_c$, with $\alpha = 1/20$. The length of the sandwich shell is set as $L = 1.5$ m. The face sheets of this cylindrical sandwich shell have the following elastic constants (in GPa): $E_1^f = 40.0, E_2^f = 10.0, E_3^f = 10.0, G_{12}^f = 4.50, G_{23}^f = 3.50, G_{31}^f = 4.50$; Poisson’s ratios: $\nu_{12}^f = 0.065, \nu_{31}^f = 0.26, \nu_{23}^f = 0.40$. The core is made of orthotropic honeycomb material with elastic constants reading as (in GPa): $E_1^c = E_2^c = 0.032, E_3^c = E_z^c = 0.30, G_{12}^c = 0.013, G_{31}^c = 0.048, G_{23}^c = 0.048$; Poisson’s ratios: $\nu_{12}^c = \nu_{31}^c = \nu_{32}^c = 0.25$.

In the computation of results, $M = 16$ and $N = 10$ in equations (23) is required for the numerical convergence. The displacements are normalized by $p_0 h_{tot} / (E_f)$, where h_{tot} is the total thickness of the shell; the stress normalized by p_0 in the following study. Figure 2 plots the normalized mid-plane displacements in the outer face sheet, core and inner face sheet as a function of x at $\theta = 0$. One can readily see that the displacements in the three phases of the cylindrical shell are not identical, implying that the current theory can capture the compressibility of the core in the cylindrical sandwich shells. It can also be seen that the displacement difference in magnitude between the outer face and the core mid-plane is

$$\begin{aligned}
 & 11 -\hat{A}_{11}^t \left(\frac{m\pi}{a}\right)^2 - \hat{A}_{66}^t \left(\frac{n}{R_o}\right)^2 - G_{xz}^c/\alpha \quad 12 -(\hat{A}_{12}^t + \hat{A}_{66}^t) \frac{m\pi}{a} \frac{n}{R_o} \quad 13 -(\hat{A}_{12}^t/R_o + \beta_0 R G_{xz}^c) \frac{m\pi}{a} \\
 & \quad 14 -\frac{11}{15} G_{xz}^c \frac{m\pi}{a} \quad 15 G_{xz}^c/\alpha \quad 16 0 \quad 17 -\beta_1 G_{xz}^c R \frac{m\pi}{a} \quad 21 -(\hat{A}_{21}^t + \hat{A}_{66}^t) \frac{m\pi}{a} \frac{n}{R_o} \\
 & \quad 22 -\hat{A}_{66}^t \left(\frac{m\pi}{a}\right)^2 - \hat{A}_{22}^t \left(\frac{n}{R_o}\right)^2 + \beta_2 G_{sz}^c \quad 23 (\hat{A}_{22}^t/R_o^2 + \frac{2+\alpha}{2-\alpha} \beta_4 G_{sz}^c) n \quad 24 (2+\alpha) \beta_5 G_{sz}^c n \\
 & \quad 25 0 \quad 26 -\beta_3 G_{sz}^c \quad 27 \beta_4 G_{sz}^c n \quad 31 -R\beta_6 G_{xz}^c \frac{m\pi}{a} \quad 32 \beta_4 \frac{2+\alpha}{2-\alpha} G_{sz}^c n \\
 & 33 \hat{D}_{111}^t \left(\frac{m\pi}{a}\right)^4 + 2 \frac{\hat{D}_{112}^t + 2\hat{D}_{166}^t}{R_o^2} \left(\frac{m\pi}{a}\right)^2 n^2 + \frac{\hat{D}_{122}^t}{R_o^4} n^4 + \frac{(61-23\alpha)E_z^c}{21\alpha} + \beta_7 G_{xz}^c \left(\frac{m\pi}{a}\right)^2 + \beta_8 G_{sz}^c n^2 \\
 & 34 \hat{D}_{211}^t \left(\frac{m\pi}{a}\right)^4 + 2 \frac{\hat{D}_{212}^t + 2\hat{D}_{266}^t}{R_o^2} \left(\frac{m\pi}{a}\right)^2 n^2 + \frac{\hat{D}_{222}^t}{R_o^4} n^4 - \frac{(358-115\alpha)E_z^c}{105\alpha} + \left(\beta_9 G_{xz}^c \frac{m\pi}{a}\right)^2 + \beta_{10} G_{sz}^c n^2 \\
 & \quad 35 R\beta_6 G_{xz}^c \frac{m\pi}{a} \quad 36 -\beta_4 \frac{2+\alpha}{2-\alpha} G_{sz}^c n \\
 & 37 \hat{D}_{311}^t \left(\frac{m\pi}{a}\right)^4 + 2 \frac{\hat{D}_{312}^t + 2\hat{D}_{366}^t}{R_o^2} \left(\frac{m\pi}{a}\right)^2 n^2 + \frac{\hat{D}_{322}^t}{R_o^4} n^4 + \frac{53E_z^c}{105} - \beta_{11} G_{xz}^c \left(\frac{m\pi}{a}\right)^2 - \beta_{12} G_{sz}^c n^2 \\
 & 41 -\frac{11}{15} G_{xz}^c \frac{m\pi}{a} \quad 42 -G_{sz}^c (2+\alpha) \beta_5 n \quad 43 -\left(\frac{(358-115\alpha)E_z^c}{105\alpha} - \beta_9 G_{xz}^c \left(\frac{m\pi}{a}\right)^2 - \beta_{10} G_{sz}^c n^2\right) \\
 & \quad 44 \frac{716E_z^c}{105\alpha} + \beta_{13} G_{xz}^c \left(\frac{m\pi}{a}\right)^2 - \beta_{14} G_{sz}^c n^2 \quad 45 \frac{11}{15} G_{xz}^c \frac{m\pi}{a} \quad 46 (2-\alpha) G_{sz}^c \beta_5 n \\
 & 47 -\frac{(358+115\alpha)E_z^c}{105\alpha} - \beta_{15} G_{xz}^c \left(\frac{m\pi}{a}\right)^2 - \beta_{16} G_{sz}^c n^2 \quad 51 G_{xz}^c/\alpha \quad 52 0 \quad 53 \beta_0 G_{xz}^c R \frac{m\pi}{a} \\
 & \quad 54 \frac{11}{15} G_{xz}^c \frac{m\pi}{a} \quad 55 -\hat{A}_{11}^b \left(\frac{m\pi}{a}\right)^2 - \hat{A}_{66}^b \left(\frac{n}{R_i}\right)^2 - G_{xz}^c/\alpha \quad 56 -(\hat{A}_{12}^b + \hat{A}_{56}^b) \frac{m\pi}{a} \frac{n}{R_i} \\
 & \quad 57 (\beta_1 R G_{xz}^c) \frac{m\pi}{a} - \hat{A}_{12}^b/R_o \quad 61 0 \quad 62 -\beta_3 G_{sz}^c n \quad 63 \beta_4 G_{sz}^c n \quad 64 (2-\alpha) \beta_5 G_{sz}^c n \\
 & 65 -(\hat{A}_{21}^t + \hat{A}_{66}^t) \frac{m\pi}{a} \frac{n}{R_i} \quad 66 \hat{A}_{66}^b \left(\frac{m\pi}{a}\right)^2 + \hat{A}_{22}^b \left(\frac{n}{R_i}\right)^2 + \beta_2 G_{sz}^c \quad 67 \left(\frac{\hat{A}_{22}^b}{R_i^2} - \frac{2-\alpha}{2+\alpha} \beta_4 G_{sz}^c\right) n \\
 & \quad 71 -R\beta_1 G_{xz}^c \frac{m\pi}{a} \quad 72 -\beta_4 G_{sz}^c n \\
 & 73 \hat{D}_{111}^b \left(\frac{m\pi}{a}\right)^4 + 2 \frac{\hat{D}_{112}^b + 2\hat{D}_{166}^b}{R_i^2} \left(\frac{m\pi}{a}\right)^2 n^2 + \frac{\hat{D}_{122}^b}{R_i^4} n^4 + \frac{53E_z^c}{105} - \beta_{11} G_{xz}^c \left(\frac{m\pi}{a}\right)^2 - \beta_{12} G_{sz}^c n^2 \\
 & 74 \hat{D}_{211}^b \left(\frac{m\pi}{a}\right)^4 + 2 \frac{\hat{D}_{212}^b + 2\hat{D}_{266}^b}{R_i^2} \left(\frac{m\pi}{a}\right)^2 n^2 + \frac{\hat{D}_{222}^b}{R_i^4} n^4 - \frac{(358+115\alpha)E_z^c}{105\alpha} + \beta_{15} G_{xz}^c \left(\frac{m\pi}{a}\right)^2 + \beta_{16} G_{sz}^c n^2 \\
 & \quad 75 R\beta_1 G_{xz}^c \frac{m\pi}{a} \quad 76 -\beta_4 \frac{2-\alpha}{2+\alpha} G_{sz}^c n \\
 & 77 \hat{D}_{311}^b \left(\frac{m\pi}{a}\right)^4 + 2 \frac{\hat{D}_{312}^b + 2\hat{D}_{366}^b}{R_i^2} \left(\frac{m\pi}{a}\right)^2 n^2 + \frac{\hat{D}_{322}^b}{R_i^4} n^4 + \frac{(61+23\alpha)E_z^c}{21\alpha} + \beta_{17} G_{xz}^c \left(\frac{m\pi}{a}\right)^2 + \beta_{18} G_{sz}^c n^2
 \end{aligned}$$

Table 1. Matrix $[K^{MN}]$ in (26). The number 12 introduces the entry $M = 1, N = 2$, etc.

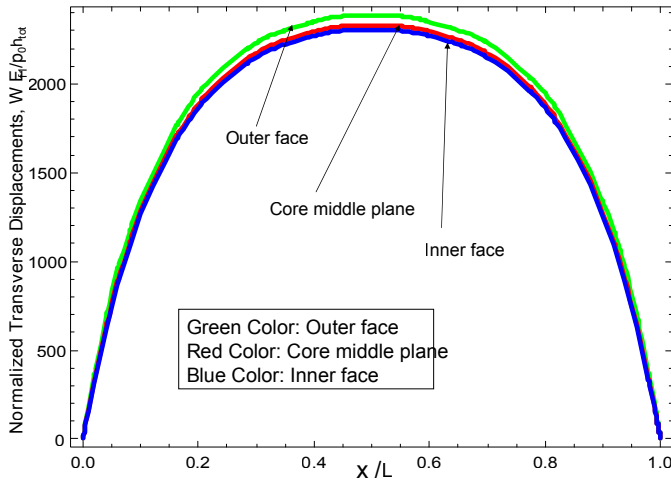


Figure 2. Mid-plane transverse displacement in the outer face sheet, core and inner face sheet as a function of x at $\theta = 0$.

larger than that between the core mid-plane and the inner face sheet. This observation demonstrates that the radial displacement in the core is a nonlinear function with respect to the radial coordinate.

Figure 3 presents the cross-sectional shapes of the outer face sheet mid-plane cut through $x = L/6$, $L/4$ and $L/2$. The undeformed shape is also plotted as a reference. It can be seen that the cross-section deforms the most from its original shape at the middle of the cylindrical shell in the axial direction ($x = L/2$), in particular within the region $-\pi/4 \leq \theta \leq \pi/4$ of each cross section where the loading is applied.

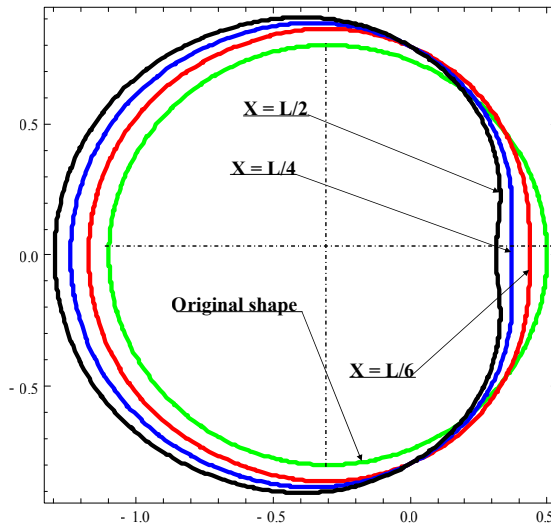


Figure 3. The deformed cross-sectional shape of the mid-plane in the outer face sheet at $x = L/6$, $L/4$ and $L/2$, along with the undeformed cross-sectional shape.

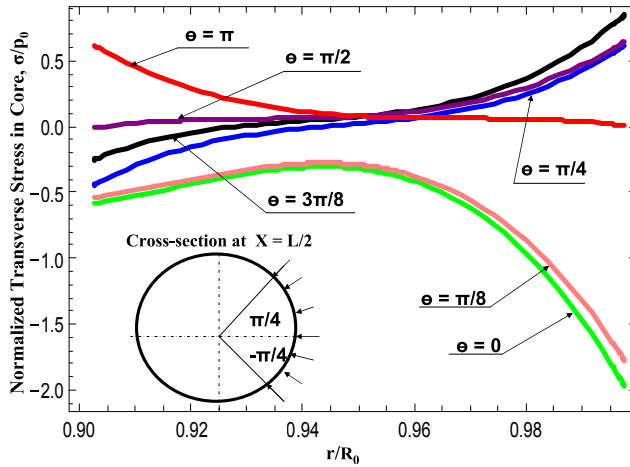


Figure 4. Variation of transverse stress through the core of the shell for various θ .

We also investigated the transverse (radial) stress distribution in the core of the sandwich shell, one of the most interesting issues in sandwich structural studies. The results are plotted in Figures 4 and 5 (where + denotes expansion pressure and – compressive pressure). Figure 4 shows the transverse stress for the cross-section $x = L/2$ at different θ . We see that the stress varies with θ from completely compressive (at $\theta = 0$) to completely expansive pressure (at $\theta = \pi$). The maximum stress in magnitude happens along the interface between the core and the outer face sheet on which the loading is applied. This maximum stress is compressive. The maximum expansion stress happens at $\theta = \pi/2$, also at the interface between the core the outer face sheet. This suggests that these could be the possible positions for damage initiation — useful knowledge for the optimal design of cylindrical sandwich shells.

The variation of the transverse stresses at $\theta = 0$ for different cross-sections is presented in Figure 5. The results show that the maximum compressive stress for each cross-section occurs along the interface

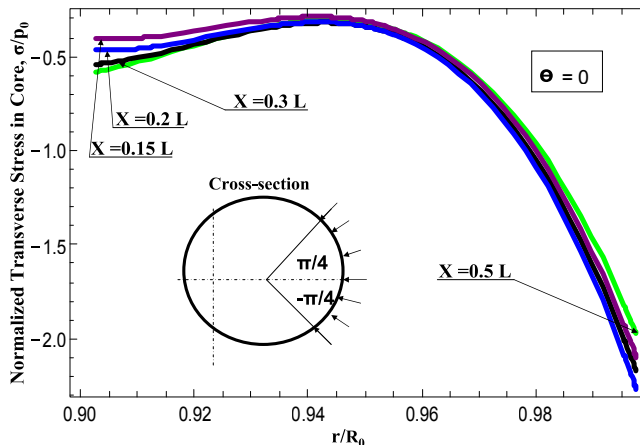


Figure 5. Cross-sectional shape of the mid-plane of the outer face sheet for various x .

between the outer face sheet and the core. Another interesting observation in this study is that the global maximum compressive stress (of 2.2662) is found around $(x = 0.2L, \theta = 0)$, not at $(x = 0.5L, \theta = 0)$, where the transverse compressive stress is 1.98787. If one uses the value at $(x = 0.5L, \theta = 0)$ as the design criterion, it could yield 12% error. This approximation may be acceptable in some preliminary designs. For an accurate design, one may have to find out the exact global maximum compressive and expansion stresses. Therefore, the study in this work can provide useful guidelines for the design of advanced cylindrical sandwich shells.

5. Conclusions

We have developed an analytical solution for a cylindrical sandwich shell with flexible core. A nonlinear high order model for cylindrical sandwich shells is formulated by extending our previous work on sandwich plates. The governing equations and boundary conditions thus derived have the compressibility of the core included. The solution procedure for an orthotropic sandwich cylindrical shell is studied in detail. Numerical results for external pressure loading exerted on a portion of the outer face sheet are presented. The observations from the numerical results suggest the following conclusions:

- (1) The mid-plane displacements of the outer face sheet, the core and the inner face sheet are not identical.
- (2) The transverse displacement distribution in the core through its thickness is a nonlinear function of the radial coordinate.
- (3) The maximum stress in magnitude occurs at the interface between the core and the face sheets on which the loading is applied.
- (4) The present nonlinear model is able to capture the nonlinear stress and displacement profiles and predict the global maximum stress and its location. Therefore, this study can have significance for the design of advanced cylindrical sandwich shells.

Acknowledgments

The financial support of the Office of Naval Research, Grant N00014-07-10373, and the interest and encouragement of the Grant Monitor, Dr. Y. D. S. Rajapakse, are gratefully acknowledged.

Appendix: Constants appearing in the governing equations (page 1458)

When constants are given together, separated by commas, the upper signs correspond to the symbol(s) before the comma and the lower signs to the symbol(s) after the comma.

$$\zeta_1, \bar{\zeta}_1 = (8\beta + 30\alpha\beta \pm 4\beta^2 \pm 11\alpha\beta^2)/30,$$

$$\zeta_2, \bar{\zeta}_2 = (116\beta + 746\alpha\beta + 1235\alpha^2\beta \pm 47\beta^2 \pm 315\alpha\beta^2 \pm 517\alpha^2\beta^2)/1260,$$

$$\zeta_3, \bar{\zeta}_3 = (74\beta + 74\alpha\beta - 766\alpha^2\beta \pm 37\beta^2 \mp 286\alpha^2\beta^2)/1260,$$

$$\zeta_4 = (-22\beta - 22\alpha\beta + 161\alpha^2\beta)/1260, \quad \zeta_5 = (776\beta + 776\alpha\beta + 1532\alpha^2\beta)/1260,$$

$$\zeta_6, \bar{\zeta}_6 = \frac{1}{4\beta^2} \left[\pm 16\beta^2 + (4 \mp \beta)^2 \log \frac{2+\beta}{2-\beta} \right], \quad \zeta_7 = \frac{1}{4\beta^2} \left[(16 - \beta^2) \log \frac{2+\beta}{2-\beta} \right],$$

$$\zeta_8, \zeta_{11}^t = \mp \frac{1}{60(2+\beta)\beta^5} \left[2\beta [2(240-60\beta+20\beta^2-5\beta^3-4\beta^4+13\beta^5) + \alpha(9120-1080\beta+220\beta^2+180\beta^3-216\beta^4+137\beta^5)] \right. \\ \left. - 15[64-16\beta-4\beta^4+\beta^5+2\alpha(608-72\beta-36\beta^2+18\beta^3-23\beta^4+3\beta^5)] \log \frac{2+\beta}{2-\beta} \right],$$

$$\bar{\zeta}_8 = \bar{\zeta}_{11}^t = \frac{1}{60(2+\beta)\beta^5} \left[2\beta [2(240+60\beta+20\beta^2+5\beta^3-4\beta^4+3\beta^5) + \alpha(9120+2520\beta+580\beta^2+300\beta^3-96\beta^4+47\beta^5)] \right. \\ \left. + 15(2+\beta)[-32+8\beta-4\beta^2+2\beta^3+\beta^4+2\alpha(-304+68\beta-28\beta^2+11\beta^3+3\beta^4)] \log \frac{2+\beta}{2-\beta} \right],$$

$$\zeta_9, \zeta_{11}^c = \pm \frac{1}{30\beta^5} \left[8\beta [60-15\beta+20\beta^2-5\beta^3-11\beta^4+\alpha(720-150\beta+180\beta^2-35\beta^3-11\beta^4)] \right. \\ \left. - 15[32-8\beta+8\beta^2-2\beta^3-4\beta^4+\beta^5+2\alpha(192-40\beta+32\beta^2-6\beta^3-8\beta^4+\beta^5)] \log \frac{2+\beta}{2-\beta} \right],$$

$$\bar{\zeta}_9 = \bar{\zeta}_{11}^c = \frac{1}{30\beta^5} \left[8\beta [-60-15\beta-20\beta^2-5\beta^3+11\beta^4+\alpha(-720-150\beta-180\beta^2-35\beta^3+11\beta^4)] \right. \\ \left. + 15[32+8\beta+8\beta^2+2\beta^3-4\beta^4-\beta^5+2\alpha(192+40\beta+32\beta^2+6\beta^3-8\beta^4-\beta^5)] \log \frac{2+\beta}{2-\beta} \right],$$

$$\zeta_{10}, \zeta_{11}^b = \pm \frac{1}{60(2-\beta)\beta^5} \left[2\beta [2(-240+60\beta-20\beta^2+5\beta^3+4\beta^4+3\beta^5) + \alpha(-9120+2520\beta-580\beta^2+300\beta^3+96\beta^4+47\beta^5)] \right. \\ \left. + 15[64-16\beta-4\beta^4+\beta^5+2\alpha(608-168\beta-12\beta^2-6\beta^3-17\beta^4+3\beta^5)] \log \frac{2+\beta}{2-\beta} \right],$$

$$\bar{\zeta}_{10} = \bar{\zeta}_{11}^b = \frac{-1}{60(2-\beta)\beta^5} \left[2\beta [2(-240-60\beta-20\beta^2-5\beta^3+4\beta^4+13\beta^5) + \alpha(-9120-1080\beta-220\beta^2+180\beta^3+216\beta^4+137\beta^5)] \right. \\ \left. + 15(2-\beta)[32+24\beta+12\beta^2+6\beta^3+\beta^4+2\alpha(304+188\beta+76\beta^2+29\beta^3+3\beta^4)] \log \frac{2+\beta}{2-\beta} \right],$$

$$\zeta_{12}^t, \zeta_{14}^b = \frac{1}{420(2\pm\beta)^2\beta^8} \left[4\beta [-6720-560\beta^2+756\beta^4+55\beta^6+20\beta^8\pm 23\beta^9] \right. \\ \left. + 7\alpha^2(-369600\mp 73920\beta+160\beta^2\mp 18640\beta^3+17700\beta^4\pm 1576\beta^5 \right. \\ \left. - 188\beta^6\pm 484\beta^7-97\beta^8\pm 91\beta^9) \right. \\ \left. + \alpha(-309120\mp 33600\beta-8960\beta^2\mp 11200\beta^3+23576\beta^4\pm 980\beta^5 \right. \\ \left. + 640\beta^6\pm 520\beta^7-30\beta^8\pm 243\beta^9) \right. \\ \left. + 105(2\pm\beta)^2[(8\mp 4\beta+2\beta^2\mp \beta^3)^2+4\alpha(736\mp 656\beta+432\beta^2\mp 248\beta^3+78\beta^4\mp 21\beta^5+4\beta^6) \right. \\ \left. + 4\alpha^2(6160\mp 4928\beta+2872\beta^2\mp 1432\beta^3+385\beta^4\mp 86\beta^5+13\beta^6)] \log \frac{2+\beta}{2-\beta} \right],$$

$$\zeta_{12}^b, \zeta_{14}^t = \frac{-1}{420(4-\beta^2)\beta^8} \left[4\beta [6720+560\beta^2-756\beta^4-55\beta^6+26\beta^8] \right. \\ \left. + 7\alpha^2(369600-4480\beta^2-20220\beta^4-316\beta^6+89\beta^8) \right. \\ \left. + \alpha(309120+8960\beta^2-23576\beta^4-640\beta^6+286\beta^8) \right. \\ \left. - 105(\beta^2-4)[(\beta^2-4)(4+\beta^2)^2+8\alpha(-368-72\beta^2+13\beta^4+2\beta^6) \right. \\ \left. + 4\alpha^2(-6160-952\beta^2+127\beta^4+13\beta^6)] \log \frac{2+\beta}{2-\beta} \right],$$

$$\left. \begin{matrix} \zeta_{12}^c, \zeta_{13}^t \\ \zeta_{13}^b, \zeta_{14}^c \end{matrix} \right\} = \frac{1}{210(2 \pm \beta)\beta^8} \left[2\beta [6720 + 2240\beta^2 - 1036\beta^4 - 174\beta^6 + 47\beta^8 \right. \\ \left. + \alpha^2(1680000 \pm 154560\beta + 318080\beta^2 \pm 73360\beta^3 - 87640\beta^4 \pm 3192\beta^5 \right. \\ \left. - 6624\beta^6 \mp 684\beta^7 + 103\beta^8) \right. \\ \left. + \alpha(248640 \pm 13440\beta + 62720\beta^2 \pm 7840\beta^3 - 23212\beta^4 \mp 112\beta^5 - 2350\beta^6 \right. \\ \left. \mp 376\beta^7 + 235\beta^8) \right] \\ - 105[(4 - \beta^2)^2(8 + 6\beta^2 + \beta^4) \\ + 4\alpha^2(8000 \pm 736\beta + 848\beta^2 \pm 288\beta^3 - 588\beta^4 \mp 18\beta^5 - 11\beta^6 \mp 7\beta^7 + 4\beta^8) \\ + \alpha(4736 \pm 256\beta + 800\beta^2 \pm 128\beta^3 - 568\beta^4 \mp 16\beta^5 - 18\beta^6 \mp 8\beta^7 + 9\beta^8)] \log \frac{2+\beta}{2-\beta}, \\ \zeta_{13}^c = \frac{1}{105\beta^8} \left[4\beta [-1680 - 980\beta^2 + 224\beta^4 + 117\beta^6 + 14\alpha(-3360 - 1600\beta^2 + 208\beta^4 + 81\beta^6) \right. \\ \left. + \alpha^2(-268800 - 105560\beta^2 + 5040\beta^4 + 1843\beta^6)] \right. \\ \left. + 105[(-8 - 2\beta^2 + \beta^4)^2 + 4\alpha^2(2560 + 792\beta^2 - 146\beta^4 - 21\beta^6 + \beta^8) \right. \\ \left. + 4\alpha(448 + 176\beta^2 - 48\beta^4 - 10\beta^6 + \beta^8)] \log \frac{2+\beta}{2-\beta} \right],$$

References

- [Frostig et al. 1992] Y. Frostig, M. Baruch, O. Vilnay, and I. Sheinman, “High-order theory for sandwich-beam behavior with transversely flexible core”, *J. Eng. Mech. (ASCE)* **118**:5 (1992), 1026–1043.
- [Hohe and Librescu 2003] J. Hohe and L. Librescu, “A nonlinear theory for doubly curved anisotropic sandwich shells with transversely compressible core”, *Int. J. Solids Struct.* **40**:5 (2003), 1059–1088.
- [Li and Kardomateas 2008] R. Li and G. A. Kardomateas, “Nonlinear high-order core theory for sandwich plates with orthotropic phases”, *AIAA J.* **46**:11 (2008), 2926–2934.
- [Li et al. 2001] R. Li, Y. Frostig, and G. A. Kardomateas, “Nonlinear high-order response of imperfect sandwich beams with delaminated faces”, *AIAA J.* **39**:9 (2001), 1782–1787.
- [Li et al. 2008] R. Li, G. A. Kardomateas, and G. J. Simitse, “Nonlinear response of a shallow sandwich shell with compressible core to blast loading”, *J. Appl. Mech. (ASME)* **75**:6 (2008), #061023.
- [Liang et al. 2007] Y. Liang, A. V. Spuskanyuk, S. E. Flores, D. R. Hayhurst, J. W. Hutchinson, R. M. McMeeking, and A. G. Evans, “The response of metallic sandwich panels to water blast”, *J. Appl. Mech. (ASME)* **74**:1 (2007), 81–99.
- [Nemat-Nasser et al. 2007] S. Nemat-Nasser, W. J. Kang, J. D. McGee, W.-G. Guo, and J. B. Isaacs, “Experimental investigation of energy-absorption characteristics of components of sandwich structures”, *Int. J. Impact Eng.* **34**:6 (2007), 1119–1146.
- [Pai and Palazotto 2001] P. F. Pai and A. N. Palazotto, “A higher-order sandwich plate theory accounting for 3-D stresses”, *Int. J. Solids Struct.* **38**:30–31 (2001), 5045–5062.
- [Plantema 1966] F. J. Plantema, *Sandwich construction*, Wiley, New York, 1966.
- [Vinson 1999] J. R. Vinson, *The behavior of sandwich structures of isotropic and composite materials*, Technomic, Lancaster, PA, 1999.

Received 17 May 2009. Revised 23 Jun 2009. Accepted 9 Jul 2009.

RENFU LI: renfu.li@mail.hust.edu.cn

Department of Aerospace Engineering, Georgia Institute of Technology, Atlanta, GA 30332-0150, United States

Current address: School of Energy and Power Engineering, HuaZhong University of Science and Technology, Wuhan 430074, China

GEORGE KARDOMATEAS: george.kardomateas@aerospace.gatech.edu

Department of Aerospace Engineering, Georgia Institute of Technology, Atlanta, GA 30332-0150, United States

FAILURE INVESTIGATION OF DEBONDED SANDWICH COLUMNS: AN EXPERIMENTAL AND NUMERICAL STUDY

RAMIN MOSLEMIAN, CHRISTIAN BERGGREEN, LEIF A. CARLSSON AND FRANCIS AVILES

Failure of compression loaded sandwich columns with an implanted through-width face/core debond is examined. Compression tests were conducted on sandwich columns containing implemented face/core debonds. The strains and out-of-plane displacements of the debonded region were monitored using the digital image correlation technique. Finite element analysis and linear elastic fracture mechanics were employed to predict the critical instability load and compression strength of the columns. Energy release rate and mode mixity were determined and compared to fracture toughness data obtained from TSD (tilted sandwich debond) tests, predicting propagation loads. Instability loads of the columns were determined from the out-of-plane displacements using the Southwell method. The finite element estimates of debond propagation and instability loads are in overall agreement with experimental results. The proximity of the debond propagation loads and the instability loads shows the importance of instability in connection with the debond propagation of sandwich columns.

1. Introduction

A sandwich panel consists of two strong and stiff face sheets bonded to a core of low density. The face sheets in the sandwich resist in-plane and bending loads. The core separates the face sheets to increase the bending rigidity and strength of the panel and transfers shear forces between the face sheets [Zenkert 1997]. It is recognized that the bond between the face sheets and core is a potential weak link in a sandwich structure [Shivakumar et al. 2005; Xie and Vizzini 2005; Chen and Bai 2002; Avery and Sankar 2000; Veedu and Carlsson 2005]. A crucial problem arises when bonding between the face sheets and core is not adequate or absent (debonding) as a result of manufacturing flaws or damage inflicted during service, such as impact or blast situations. The behavior of sandwich structures containing imperfections or interfacial cracks subjected to in-plane loading has been investigated to a certain extent. Hohe and Becker [2001] conducted an analytical investigation to study the effect of intrinsic microscopic face-core debonds. Kardomateas and Huang [2003] studied buckling and post-buckling behavior of debonded sandwich beams through a perturbation procedure based on nonlinear beam equations. Sankar and Narayan [2001] studied the compressive behavior of debonded sandwich columns by testing and numerical analysis. Most of their columns failed by buckling of the debonded face sheet. Vadakke and Carlsson [2004] similarly studied the compression failure of sandwich columns with a face/core debond. They investigated the effect of core density and debond length on compressive strength of sandwich columns. Results of their experiments showed that failure occurred by buckling of the debonded face sheet, followed by rapid debond growth towards the ends of the specimen. They also showed that the compression strength of the sandwich columns decreases significantly with increasing

Keywords: sandwich structures, columns, debond damages, buckling, fracture mechanics, compressive strength.

debond size. Furthermore, columns with high-density cores experienced less strength reduction at any given debond size. Østergaard [2008] used a cohesive zone model for debonded columns and investigated the relation between global buckling behavior and cohesive layer properties. The study showed that the compression strength reduction caused by a debond can be explained by two mechanisms: First from the interaction of local debond and global column buckling and secondly from the development of a damage zone at the debond crack tip. Only a few works have in detail assessed determination of fracture parameters like energy release rate, phase angle and debond propagation in composite and sandwich structures subjected to in-plane loading [Sallam and Simitzes 1985; Avilés and Carlsson 2007; Nøkkentved et al. 2005; Berggreen and Simonsen 2005]. The first of these papers presented a one dimensional model to estimate the delamination buckling load and ultimate load-carrying capacity of axially loaded composite plates, while the other three focused on sandwich panels containing two-dimensional embedded debonds. Important insight can be gained from detailed fracture analysis of a column with a through-width debond which has not been thoroughly examined in the literature. The failure analysis of such columns is the objective of the present paper.

2. Column test specimen and test set-up

Sandwich panels consisting of 2 mm thick plain weave E-glass/epoxy face sheets over 50 mm thick Divinycell H45, H100, and H200 PVC foam cores were manufactured using vacuum assisted resin transfer molding and cured at room temperature. A face/core debond was defined by inserting strips of Teflon film, 30 μm thick, between face and core at desired locations in the panels. The widths of the Teflon strip were 25.4, 38.1, and 50.8 mm. The width defines the length of the debond in the column specimens subsequently cut from the panels. It was observed that the single Teflon layer insert used to define the face/core debond did not perfectly release the bond between the face and core. To achieve a nonsticking, traction-free debond in the specimens, the debond was mechanically released by wedging knives with very thin blades (0.35 and 0.43 mm thick). The width and length of the columns were 38 and 153 mm respectively.

Figure 1 shows a column specimen cut from a panel. A test rig was designed and manufactured for axial compression testing of the columns; see Figure 2, left. The test rig includes four 25 mm diameter

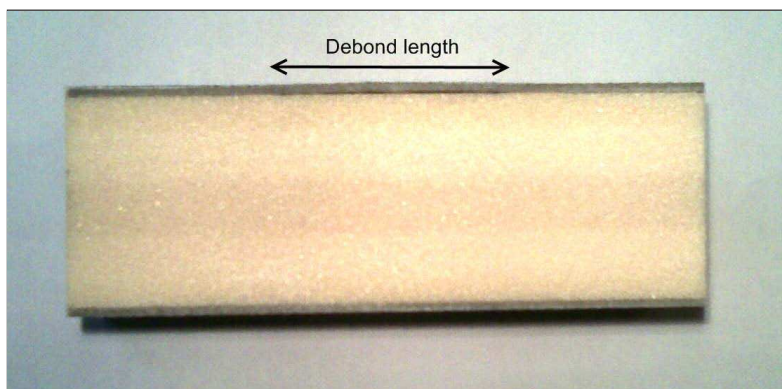


Figure 1. A column test specimen with H100 core and 38.1 mm debond.

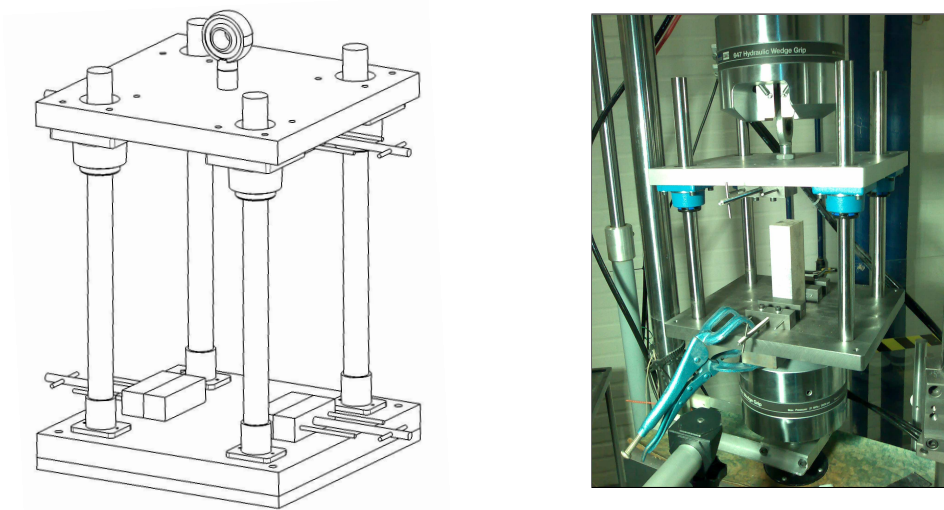


Figure 2. Left: Schematic representation of the compression test fixture. Right: View of actual test set-up.

solid steel rods to maintain alignment of the upper and lower plates of the test rig during compressive loading. Linear bearings were attached to the upper plate to minimize friction. Steel clamps of 80 mm width were attached to the upper and lower plates of the fixture to clamp the columns. The test rig was inserted into an MTS 810 100 kN capacity servo-hydraulic universal testing machine; see Figure 2, right. A 2-megapixel digital image correlation measurement system (ARAMIS 2M) was used to monitor three-dimensional surface displacements and surface strains during the experiments. Testing of the columns was conducted using ramp displacement control with a piston loading rate of 0.5 mm/min. A sample rate of one image per second was used in the DIC (digital image correlation) measurements. Three replicate tests were conducted for each specimen configuration.

Material properties are listed in Table 1. Those of the face sheets, assumed in-plane isotropic, were determined by tensile tests based on the ASTM standard D3039. The compression strength of the face sheets was measured on laminate specimens cut from the actual sandwich face sheet using the ASTM standard IITRI (D3410) test fixture. Three replicate specimens were used. Core material properties were obtained from the manufacturer [DIAB].

Material	E (MPa)	G (MPa)	ν	σ_{\max} (MPa)		G_{IC} (J/m ²)
				tensile	compression	
Face: E-glass/epoxy	10360	3816	0.31	168	95.4	N/A
Core: H45	50	15	0.33		0.6	150
Core: H100	135	35	0.33		2	310
Core: H200	240	85	0.33		4.8	625

Table 1. Face and core material properties and fracture toughness [DIAB; Viana and Carlsson 2002]. E = Young's modulus; G = shear modulus; ν = Poisson's ratio; σ_{\max} = material strength; G_{IC} = mode I fracture toughness.

3. Column specimen test results

Figure 3 shows typical load versus axial displacement and load versus out-of-plane displacement curves for columns with a 50.8 mm debond and H45, H100, and H200 cores. The out-of-plane deflection refers to the center of the debond. The plot on the left shows that the columns respond in a fairly linear fashion after the initial stiffening region until collapse. The one on the right shows that the out-of-plane deflection increases slowly with increasing load until the maximum load. It will later be shown that the point of maximum load corresponds to the onset of debond propagation. It is also seen in Figure 3, right, that the critical load at propagation increases as the core density is increased.

Figure 4 shows DIC images of out-of-plane displacement in a column with H45 core and a 50.8 mm debond just before and after debond propagation. During the compression tests the DIC measurements

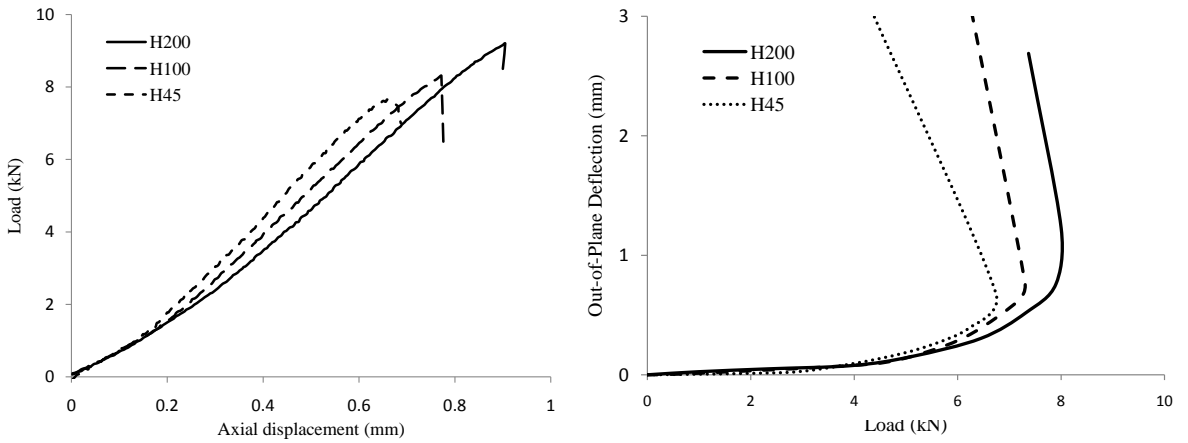


Figure 3. Load versus axial displacement (left) and out-of-plane deflection at the debond center versus load (right) for columns with 50.8 mm debond length.

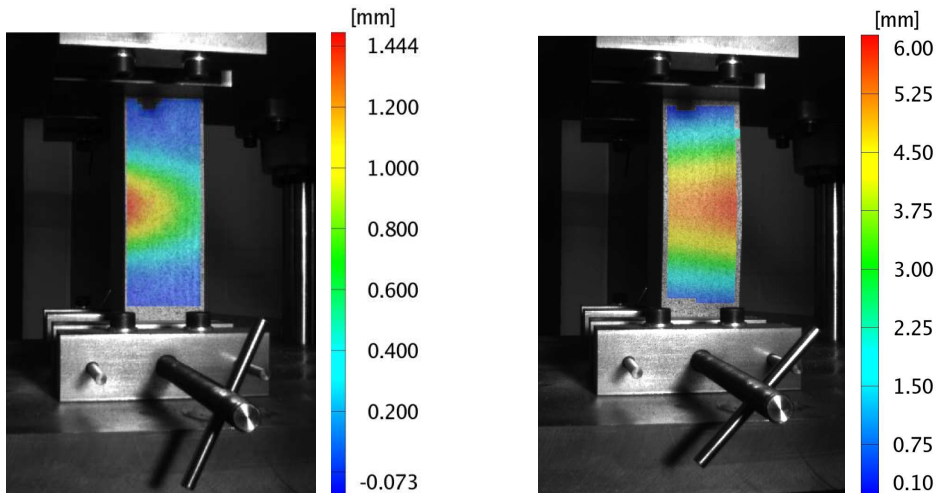


Figure 4. Debond opening prior to propagation (left) and after propagation (right) for a column with H100 core and 50.8 mm debond length from DIC measurements.

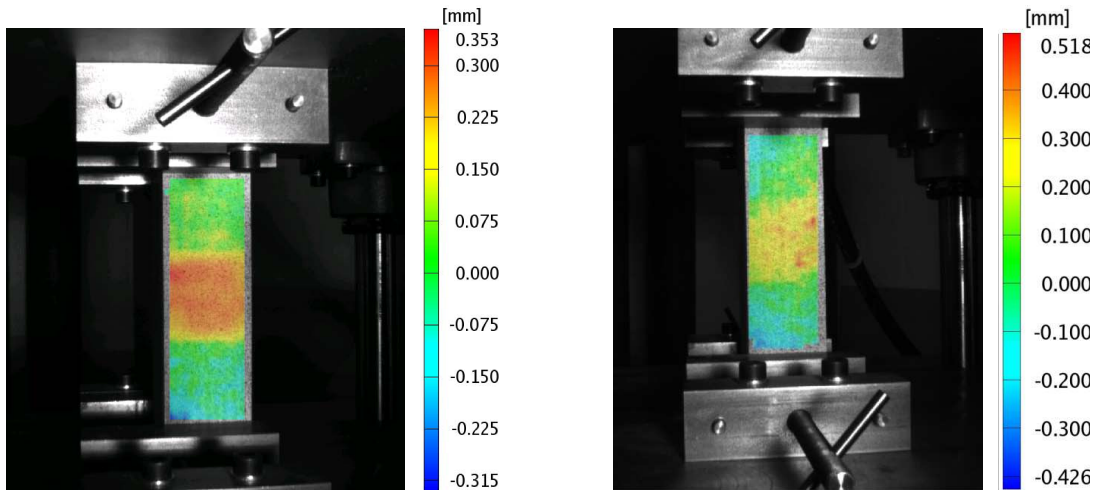


Figure 5. Initial imperfections in columns with H100 core and 50.8 mm debond length, where the debond was released using a thin blade (0.35 mm; left) and a thicker one (0.43 mm; right).

revealed that opening of the debond was not perfectly symmetric, as seen in [Figure 4](#). This can be attributed to a slight misalignment of the fibers in the face sheets and lack of perfectly uniform load introduction at the ends of the columns.

[Figure 5](#) shows DIC images of initial out-of-plane imperfection of two columns with H100 core and a 50.8 mm debond, released using the thin (0.35 mm) and thicker (0.43 mm) blades respectively. The initial imperfection amplitudes are approximately 0.25 and 0.51 mm. A Photron APX-RS high-speed camera was used to track the debond propagation at a frame rate of 1000 images per second. [Figure 6](#), left,

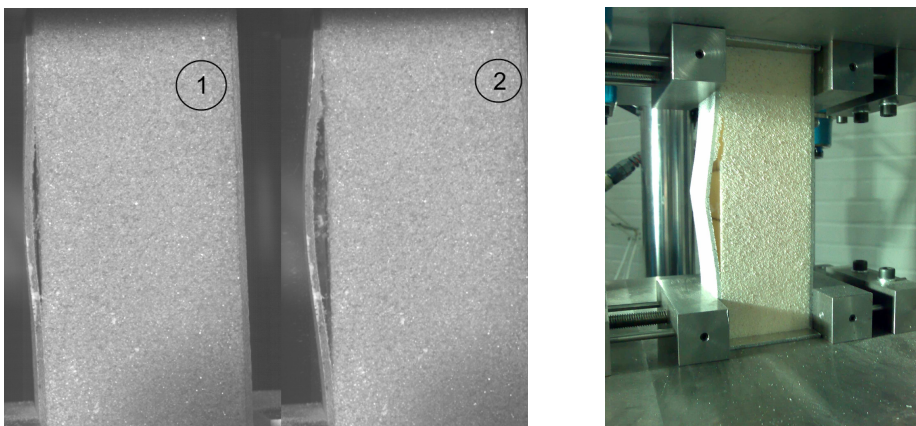


Figure 6. Left: High speed images showing the debond in a column with H45 core and 50.8 mm debond length 1 ms before propagation (1) and right after propagation has taken place (2). Right: Crack kinking into the core in a column with H100 core and 25.4 mm debond length.

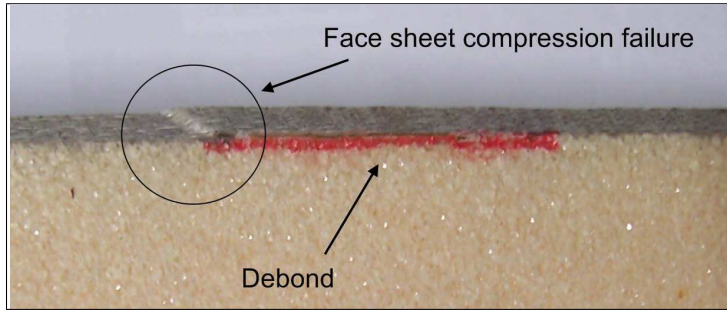


Figure 7. Face compression failure in a column specimen with H200 core and 25.4 mm debond.

shows the debond 1 ms before and right after the debond propagation. A slight opening of the debond can be seen before propagation. Slight crack kinking into the core, resulting in the crack propagating just beneath the interface on the core side, was observed in most of the column specimens with an H45 core. Some specimens with an H100 core displayed this failure mode as well; see [Figure 6](#), right.

The fracture toughness of the H45 core (150 J/m^2 ; see [Table 2](#) on page 1476) is likely less than that of the face/core interface, which could explain the observed crack propagation path. A detailed kinking analysis, similar to what is presented in [[Li and Carlsson 1999](#); [Berggreen et al. 2007](#)], must be carried out to investigate this further. This is however out of the scope of this paper.

All columns with H200 core and 25.4 mm debond length failed by compression failure of the face sheet above the debond location; see [Figure 7](#). This can be explained by the proximity between the debond propagation load of the debonded face sheet and the compression failure load of the face sheet which can be calculated from the compressive strength (see [Table 1](#)) and cross section area of the face sheet. Face compression failure was also observed for one of the columns with H100 core and 25.4 mm debond length. The H200 column specimens with 38.1 and 50.8 mm debond failed by debond propagation. No kinking was observed in these specimens, resulting in crack propagation directly in the face/core glue interface. Additionally the observed crack propagation rate was less for the H200 specimens, indicating a tough interface. The average failure loads are listed in [Table 5](#) on page 1484.

4. Characterization of face/core interface fracture resistance

The aim of this section is to determine the fracture toughness of the interface at a phase angle identical to the one in the column specimens at the onset of crack propagation. The fracture toughness will be used later to determine the crack propagation load in the column specimens using the finite element method. A modified version of the tilted sandwich debond specimen [[Li and Carlsson 1999](#); 2001; [Berggreen and Carlsson 2008](#)], shown in [Figure 8](#), was used to determine the fracture toughness of the interface. [Berggreen and Carlsson \[2008\]](#) showed that reinforcing the top face by a stiff metal plate considerably increases the shear loading and thus the range of phase angles. Finite element analysis of the modified TSD specimen was carried out to determine the appropriate tilt angle to match the phase angles for the tested columns.

A two-dimensional finite element model with a highly refined mesh in the crack tip region, element size of $3.33 \mu\text{m}$, was developed in ANSYS version 11 [[ANSYS](#)], using 8 node isoparametric elements

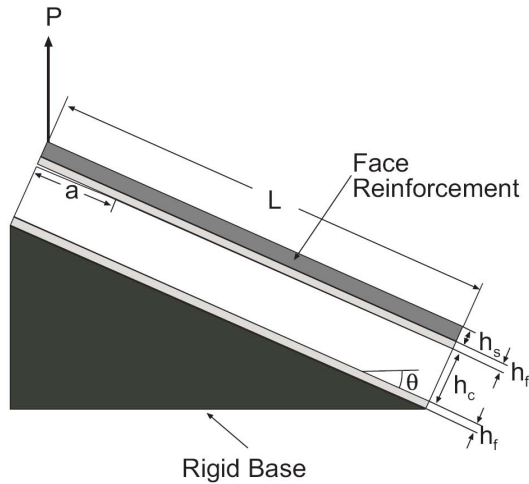


Figure 8. Schematic representation of the modified TSD specimen.

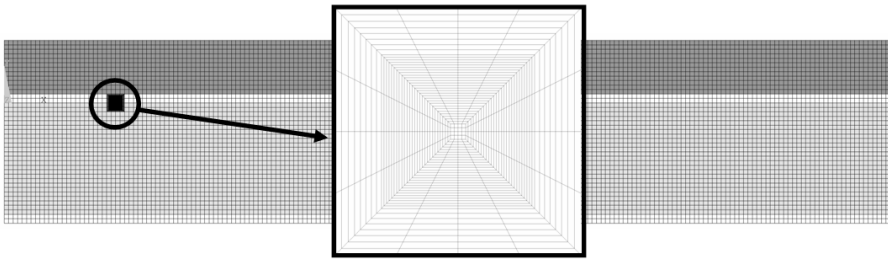


Figure 9. Finite element mesh used in analysis of the modified TSD specimen with near tip mesh refinement. The smallest element size is $3.33 \mu\text{m}$.

(PLANE82), see Figure 9. Energy release rate (G) and phase angle (ψ) were determined from relative nodal pair displacements along the crack flanks obtained from the finite element analysis using the CSDE method outlined in [Berggreen and Simonsen 2005; Berggreen et al. 2007]. The energy release rate and the phase angle are given by (see [Hutchinson and Suo 1992])

$$G = \frac{\pi(1+4\varepsilon^2)}{8H_{11}x} \left(\frac{H_{11}}{H_{22}} \delta_y^2 + \delta_x^2 \right), \quad \psi_K = \tan^{-1} \sqrt{\frac{H_{22}}{H_{11}} \frac{\delta_x}{\delta_y}} - \varepsilon \ln \frac{x}{h} + \tan^{-1}(2\varepsilon), \quad (1)$$

where δ_y and δ_x are the opening and sliding relative displacement of the crack flanks, while H_{11} , H_{22} and the oscillatory index ε are bimaterial constants determined from the elastic stiffnesses of the face and core (see sidebar on next page). Moreover, h is the characteristic length of the crack problem; it has no direct physical meaning; it is chosen here arbitrarily as the thickness of the face sheet. Further details concerning the FE model can be found in [Berggreen and Carlsson 2008].

The phase angle of each column specimen was extracted at a load corresponding to the onset of debond propagation using finite element modeling (to be presented below). The extracted phase angles were exploited in finite element models of the TSD specimens to determine the matching tilt angle at a

	Core	H45	H100	H200
Initial crack length	50 mm	63.5 mm	63.5 mm	
Phase angle	-24 deg	-29 deg	-37 deg	
Tilt angle (θ)	55 deg	60 deg	70 deg	

Table 2. Dimensions and tilt angle of TSD specimens.

crack length of 50 mm for specimens with H45 core and 63.5 mm for specimens with H100 and H200 cores. The face sheets were 1.5 mm thick, and the core thickness was 25 mm. A 12.7 mm thick steel bar of the same width (25.4 mm) and length (180 mm) as the sandwich specimen was used to reinforce the loaded face sheet. Material properties of the face sheets and cores in the TSD-specimens are identical to those of the columns specimens. The resulting specifications for the TSD specimen including the calibrated tilt angle are given in [Table 2](#).

TSD specimens 180 mm long and 25.4 mm wide were cut from panels prepared with one face sheet only. [Figure 10](#) shows the TSD test set-up with an H100 sandwich specimen tilted 60°. The bottom core surface of the specimen was bonded to a steel plate bolt connected to the test rig. Prior to bonding, the bonding surfaces were thoroughly sanded and cleaned with acetone to promote adhesion. Hysol EA-9309 aerospace epoxy paste adhesive was used for bonding. The steel bar contained a through-width hole near the end to allow pin load application. All tests were conducted at a rate of 1 mm/min, and three replicate specimens were tested.

[Figure 11](#) shows typical load versus displacement curves for TSD specimens with H45, H100, and H200 foam cores. The load-displacement plots are fairly linear until the point of crack propagation, where the load suddenly drops. The load required to propagate the crack significantly increases as the core density is increased. Compared to conventional TSD specimens without steel reinforcement [[Li and Carlsson 2001](#)], substantially larger loads are required to generate crack growth in the steel reinforced

Oscillatory index ϵ and bimaterial constants

Equations (1) use bimaterial constants H_{11} and H_{22} defined in terms of the material compliances by

$$H_{11} = [2n\lambda^{1/4}\sqrt{S_{11}S_{22}}]_1 + [2n\lambda^{1/4}\sqrt{S_{11}S_{22}}]_2, \quad H_{22} = [2n\lambda^{-1/4}\sqrt{S_{11}S_{22}}]_1 + [2n\lambda^{-1/4}\sqrt{S_{11}S_{22}}]_2,$$

where $\lambda = S_{11}/S_{22}$ and $n = \sqrt{(1+\rho)/2}$, $\rho = \frac{1}{2}(2S_{12}+S_{66})/\sqrt{S_{11}S_{22}}$, are nondimensional orthotropic constants given in terms of the elements S_{11} and S_{22} of the compliance matrix. The compliance elements for plane stress conditions are given by $S_{11} = 1/E_1$, $S_{12} = S_{21} = -\nu_{12}/E_1 = -\nu_{21}/E_2$, $S_{22} = 1/E_2$, $S_{66} = 1/G_{12}$. For plane strain conditions, $S_{ij}^* = S_{ij} - (S_{i3}S_{j3}/S_{33})$.

Equations (1) also contain the oscillatory index

$$\epsilon = \frac{1}{2\pi} \ln \frac{1-\beta}{1+\beta},$$

where $\beta = \frac{[S_{12} + \sqrt{S_{11}S_{22}}]_2 - [S_{12} + \sqrt{S_{11}S_{22}}]_1}{\sqrt{H_{11}H_{22}}}$. For details, see [[Berggreen et al. 2007](#)].

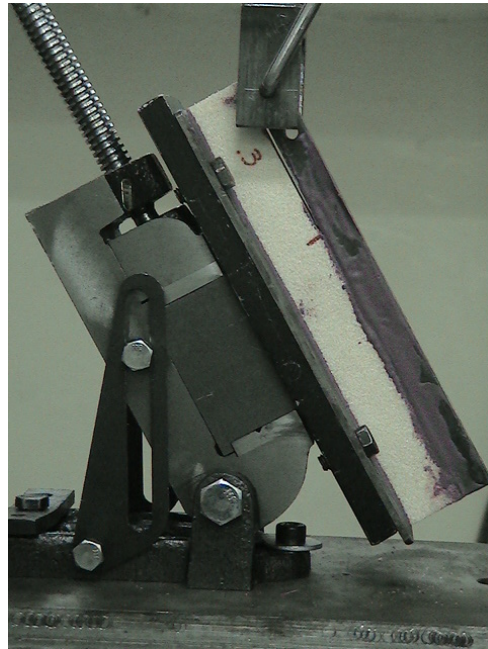


Figure 10. Modified TSD test set-up.

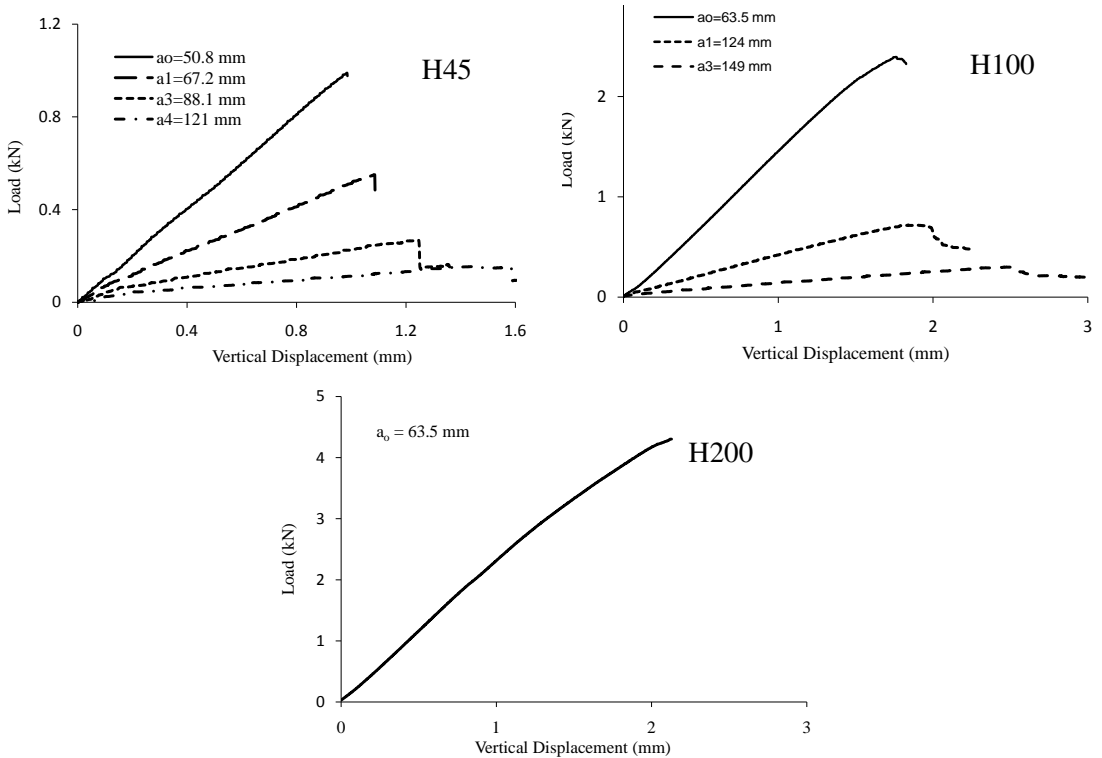


Figure 11. Load versus vertical displacement diagram for TSD specimens.

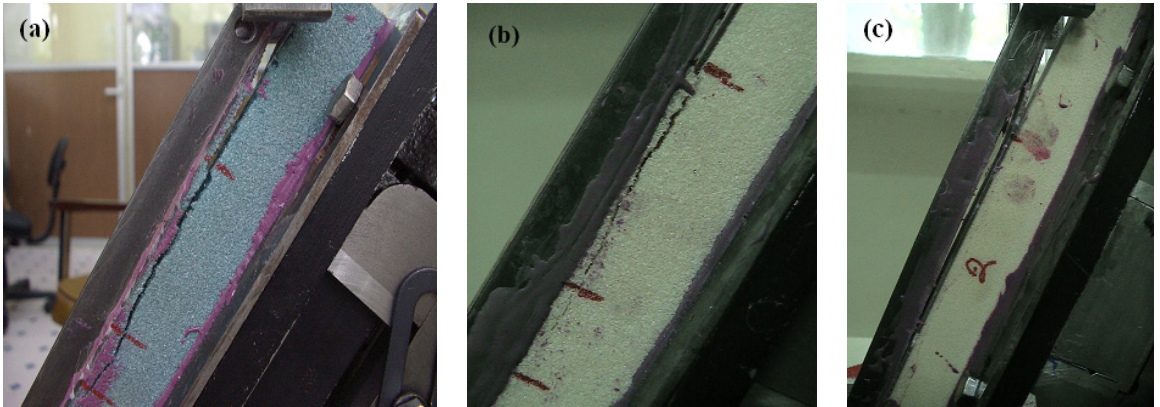


Figure 12. Crack propagation behavior in TSD specimens: (a) H45; (b) H100; (c) H200.

specimens as a result of the large bending and shear stiffnesses of the steel reinforced upper face sheet. The crack propagation behavior for the H45 specimens was rather unstable with the crack suddenly growing 25–50 mm at each crack increment which allowed only about three crack increments before the crack reached more than 70% of the total specimen length at which point the test was stopped. For the specimens with an H45 foam core, the crack propagated on the core side beneath the face/core interface, see [Figure 12\(a\)](#). This is consistent with the observations from the column tests and the previous observations of crack path behavior for low density foam cores [[Li and Carlsson 1999](#)]. For specimens with an H100 core, unstable crack growth was more pronounced with the crack growing about 50 mm at each increment which allowed only two crack increments before the crack reached 70% of the specimen length. For the H100 specimens the crack location was again beneath the face/core interface, but now slightly closer to the face sheet just below the resin rich layer on the core side, see [Figure 12\(b\)](#). The H200 specimens failed at considerably higher loads (> 4 kN) by sudden delamination between the plies of the upper face sheet causing a large unstable crack which reached almost to the end of the specimen in one crack increment, see [Figure 12\(c\)](#).

Given such an unstable crack growth behavior with a few crack increments per specimen, the use of standard data reduction methods such as *compliance calibration* or *modified beam theory* becomes questionable for this test. Thus, fracture toughness of the face/core interface was determined from finite element analysis of the TSD specimen with the critical load as input. The calculated fracture toughness values and phase angles are listed in [Table 3](#).

TSD specimen	Phase angle	Fracture toughness
H45	−24 deg	176 ± 35 J/m ²
H100	−29 deg	672 ± 69 J/m ²
H200	−37 deg	—

Table 3. Calculated phase angle and fracture toughness at measured fracture load.

For the H200 specimens kinking of the crack into the face sheet occurred and the fracture toughness of the face/core interface could thus not be determined. Consequently, it was not possible to predict the face/core debond propagation load for the columns with an H200 core.

5. Finite element model of column specimens

Finite element modeling of the column specimen employed the commercial finite element code, ANSYS version 11 [ANSYS]. Because of material, geometrical and loading symmetries, only the upper half symmetry section of the column geometry was modeled; see Figure 13. The columns were assumed to contain an initial imperfection in the form of a one half wave eigen-mode shape, determined from eigen-buckling analysis. Overlapping of crack flanks was avoided by use of contact elements (CONTACT173 and TARGET170), and displacement controlled geometrical nonlinear analysis was conducted. To simulate the boundary conditions in the experimental set-up, nodes at the top side of the columns, in contact with the top ending platen of the test rig, were displaced uniformly in the direction of loading. Furthermore the nodes in contact with the lateral clamp surfaces were constrained to have zero lateral displacement. Symmetry boundary conditions were applied at the symmetry plane. Hence, displacements of the nodes on the symmetry plane were assumed to be zero in the loading direction; see again Figure 13. Due to the need of a high mesh density at the crack front when performing the fracture mechanics analysis, a submodeling technique was developed, where displacements calculated on the cut boundaries of the global model with a coarse mesh were specified as boundary conditions for the submodel. Submodeling is based on Saint-Venant's principle, which states that if an actual distribution of forces is replaced by a statically equivalent system, the distributions of stresses and strains are altered only near the regions of load application. The approach assumes that stress concentration around the crack tip is highly localized. Therefore, if the boundaries of the submodel are sufficiently far away from the crack tip, reasonably accurate results can be obtained in the submodel. Interpolated displacement results at the

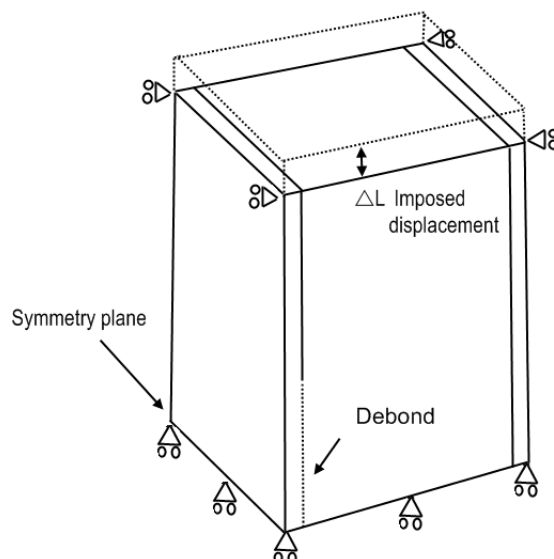


Figure 13. Applied boundary conditions on the finite element model of the columns.

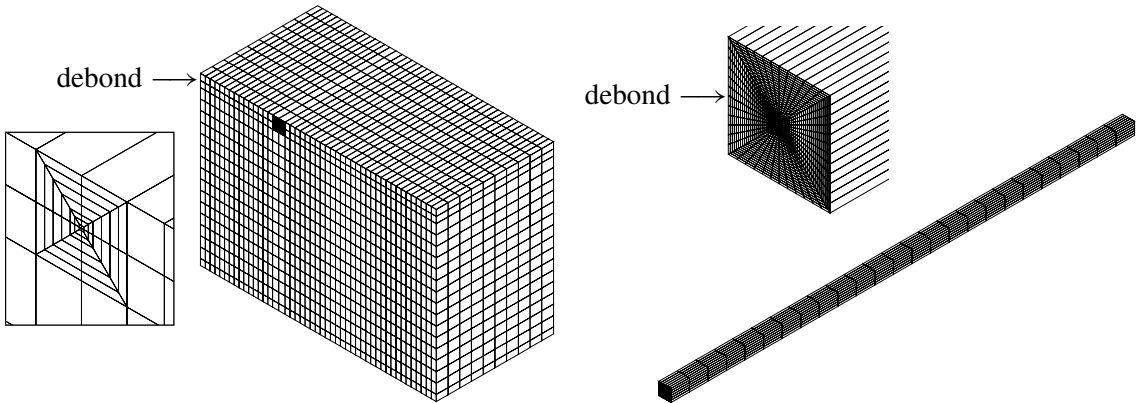


Figure 14. Finite element models. Left: half-model showing the mesh in the global model. The smallest element size is 0.2 mm. Right: submodel showing the refined mesh. Element size close to the crack tip is 10 μm .

cut boundaries in the global model were used as boundary conditions in the submodel at different load steps. Twenty-node isoparametric elements (solid 95) were used in the finite element model. The finite element model and submodel are shown in Figure 14. In the global model and submodel, the size of elements along the crack flanks near the crack tip are 0.2 and 0.01 mm, respectively. Energy release rate (given by the expression for G on page 1475) and mode-mixity are determined based on relative nodal pair displacements along the crack flanks obtained from the finite element analysis. The CSDE method [Berggreen and Simonsen 2005] and the mode-mixity formulation (expression for ψ_K on page 1475) were used.

6. Comparison of numerical and experimental results

Results from the experimental testing and numerical modeling presented above are compared. Three issues are addressed: the effect of imperfections on the instability behavior, the through-width variation of energy release rate and mode-mixity, and the influence of imperfections on debond propagation.

To examine the effect of initial imperfection on the instability behavior of the specimens, columns with initial imperfection amplitudes of 0.1, 0.2, and 0.4 mm were analyzed numerically and compared with test results. The columns tested had on average an imperfection magnitude of 0.2 mm. Figure 15 shows the deformed shape of a debonded sandwich column with H100 core containing a 50.8 mm face/core debond and 0.2 mm initial imperfection amplitude. The imperfection resembles a half-sine wave with the maximum deflection at the center consistent with DIC measurements described above. Figure 16 shows load versus out-of-plane deflection for columns with H100 core and 25.4, 38.1, and 50.8 mm debonds determined from numerical analysis at imperfection amplitudes of 0.1, 0.2, and 0.4 mm and testing (two or three replicates are shown). The numerical and test results show that the debond opening initially increases slowly with increasing load, but then increases rapidly as the maximum load is approached. At the maximum load, which corresponds to the onset of propagation, the load decreases due to the displacement controlled loading and debond propagation resulting in increased compliance, while the out-of-plane displacement of the debonded face rapidly increases. The load reduction is shown only

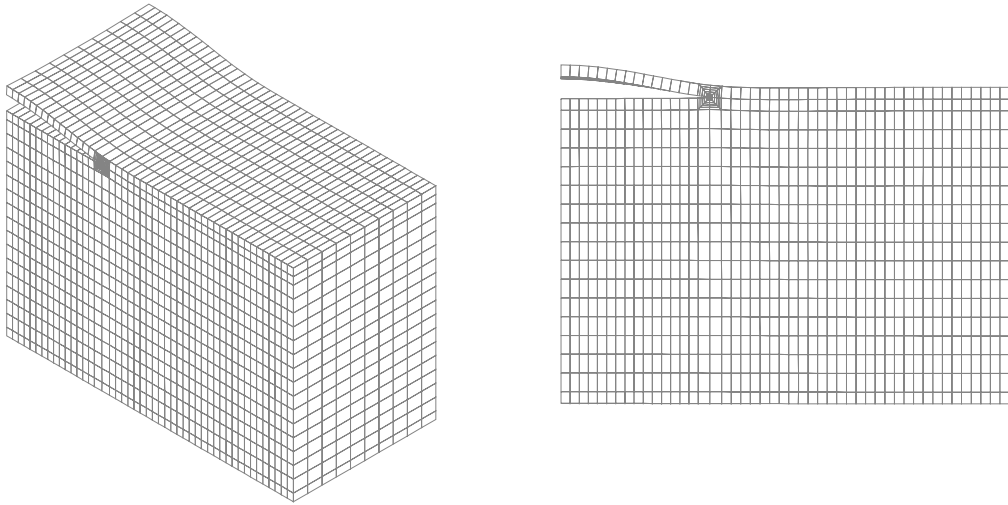


Figure 15. Deformed shape of a column with H100 core containing a 50.8 mm face/core debond after local buckling of the debonded face sheet.

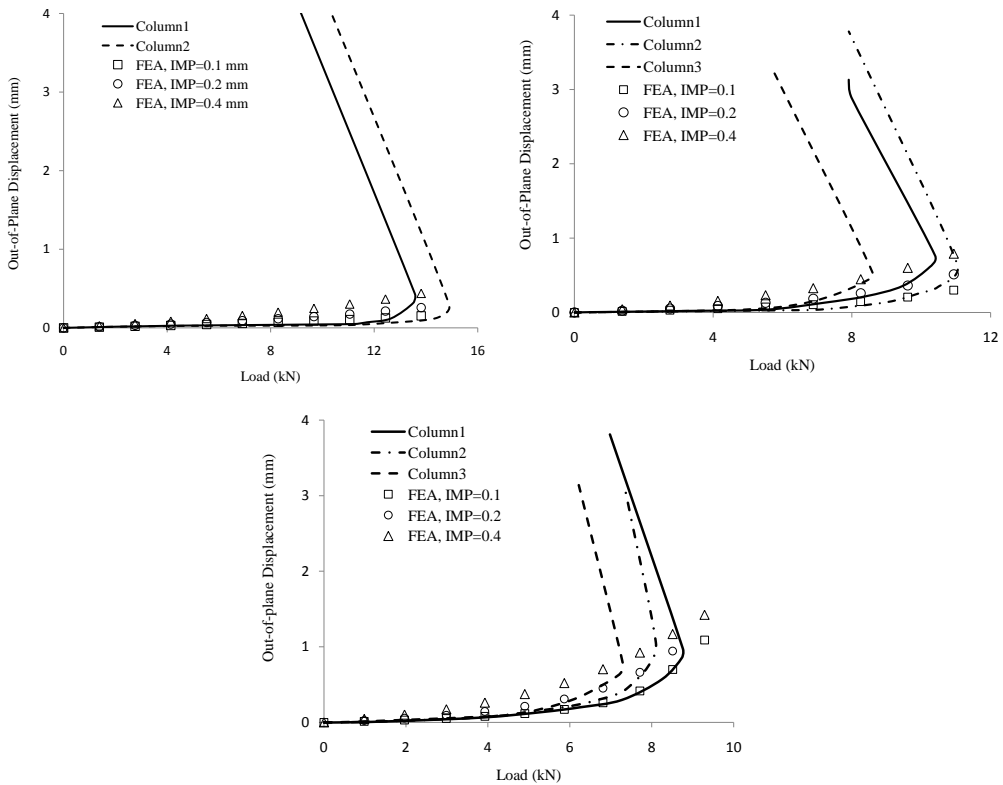


Figure 16. Finite element and experimental results for out-of-plane versus load diagram for columns with H100 core and (a) 25.4 mm debond, (b) 38.1 mm debond, (c) 50.8 mm debond. The average initial imperfection magnitude in the tested columns is 0.2 mm.

Core	Experiment			FE Analysis		
	Debond length			Debond length		
	25.4 mm	38.1 mm	50.8 mm	25.4 mm	38.1 mm	50.8 mm
H45	12.9 ± 1.5	10.1 ± 1.1	6.1 ± 0.9	14.1	8.5	5.6
H100	14.8 ± 0.8	10.5 ± 1.7	8.7 ± 0.6	15.2	11.6	8.8
H200	–	13.0 ± 1.2	8.5 ± 0.3	–	13.8	9.0

Table 4. Instability loads, in kN, determined from Southwell plots applied to experimental and finite element results, using a 0.2 mm initial imperfection.

for the experimental results, as only initiation of debond propagation is modeled numerically (no crack propagation algorithms are implemented in the finite element model). It can be seen that the initial imperfection magnitude does not influence the out-of-plane deflection of the columns very much.

A bifurcation instability of the debonded face sheet is not observed before the propagation point. Evidently the presence of initial imperfection transforms the behavior of the debonded face sheet into compression loading of a curved column. The failure load is found from fracture mechanics analysis, when the crack tip loading reaches the fracture toughness.

Because of the imperfection present in the debonded face sheet, the critical instability load was extracted from both experimental and finite element results applying the Southwell method. This is a graphical method which estimates the instability load of imperfect structural columns. Southwell [1932] showed that the deflection, δ , at the center of an imperfect column, loaded by a load P , is given by

$$\delta - P_{cr} \frac{\delta}{P} + \alpha = 0, \quad (2)$$

where P_{cr} is the buckling load and α is proportional to the initial imperfection (δ_0). By plotting δ versus δ/P , the instability load P_{cr} can be determined by the slope of the line (designated the Southwell-plot method).

Numerical and experimental results are compared in terms of instability load values listed in Table 4. For the finite element analysis results, a 0.2 mm initial imperfection was selected which is consistent with experimental values. From the results listed in Table 4, it can be seen that experimental and numerical instability loads are in good agreement. Further, it can be seen that the instability load drops significantly as the debond length increases which is well-known for any buckling problem.

Energy release rate and mode-mixity were determined across the width of the columns. Generally it is assumed that the edges of the columns are under plane stress and the interior is in plane strain. Thus, in the analysis of energy release rate and phase angle a plane stress formulation was adopted for nodes on the specimen edges and a plane strain formulation for the interior points.

Figure 17 depicts the distributions of energy release rate normalized with the interface fracture toughness, G_c , and phase angle across the width of a column with H45 core and 50.8 mm debond. Similar results were obtained for columns with other core materials and debond lengths. The graphs shows the classical thumb-nail distribution of the energy release rate, normalized with fracture toughness of the interface, increasing from the edges towards the center of the specimen. The phase angle also displays a maximum in the interior. The magnitude of the phase angle, however, is minimum in the interior meaning

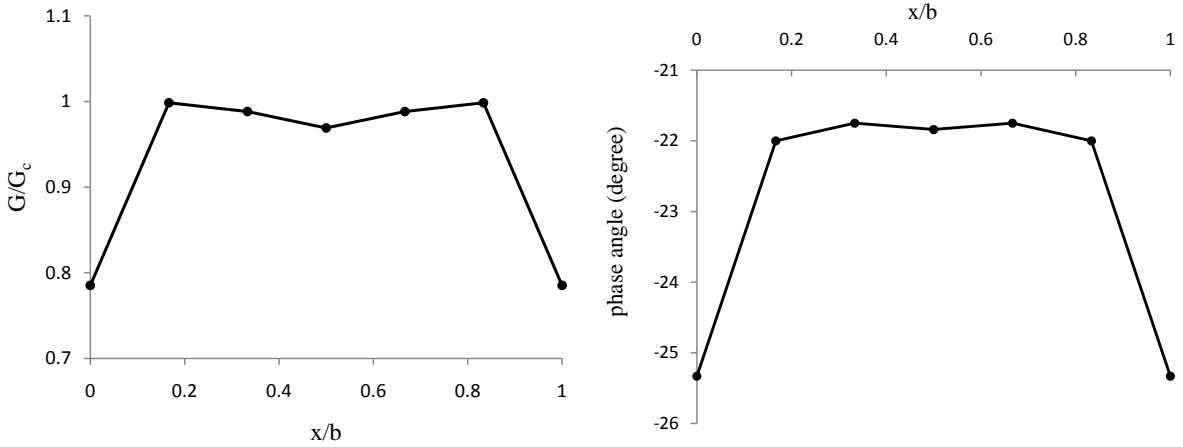


Figure 17. Distribution of energy release rate (left) and phase angle (right) across the column width for a column with H100 core and 50.8 mm debond.

that the loading in the center is more mode *I* dominated than the edges. Based on the results shown in Figure 17 the debond propagation is expected to initiate in the interior. Thus, in the debond propagation analysis, the plane strain formulation in the center of the specimen was employed.

Figure 18 shows energy release rate and mode-mixity in terms of phase angle versus load for columns with a 50.8 mm debond and H45, H100, and H200 cores. The first graph shows that *G* increases significantly at a certain load regime which can be associated with the opening of the debond. The fracture toughness values shown in the graph were determined with the TSD tests described in Section 4. The reduction of phase angle as the load increases, displayed in the second graph, shows that the crack tip loading becomes more shear dominated at high loads.

To investigate the influence of the initial imperfection on *G* and ψ , columns with H100 core and 38.1 mm debond with initial imperfection magnitudes of 0.1, 0.2, and 0.5 mm were analyzed. Figure 19

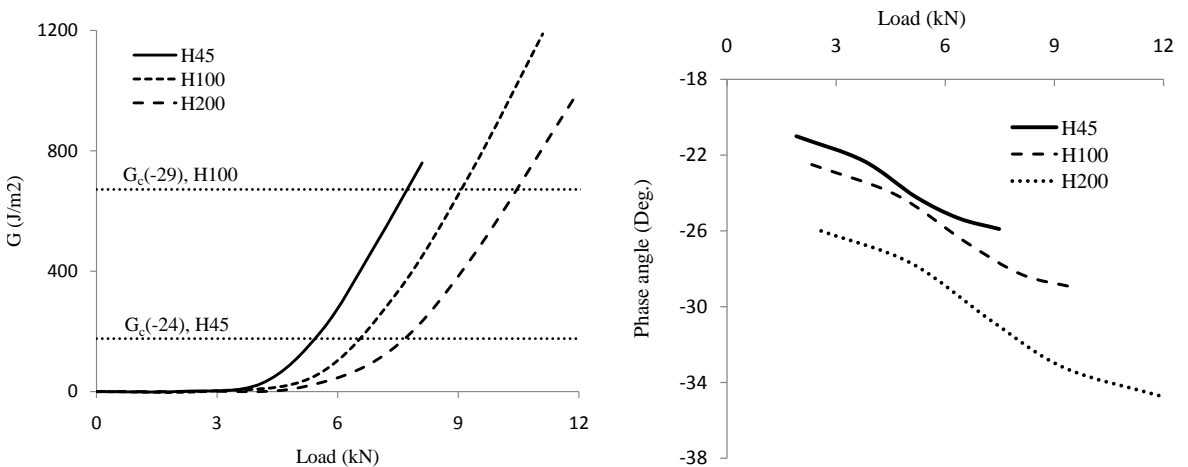


Figure 18. Energy release rate (left) and phase angle (right) versus load for columns with a 50.8 mm debond and H45, H100 and H200 cores.

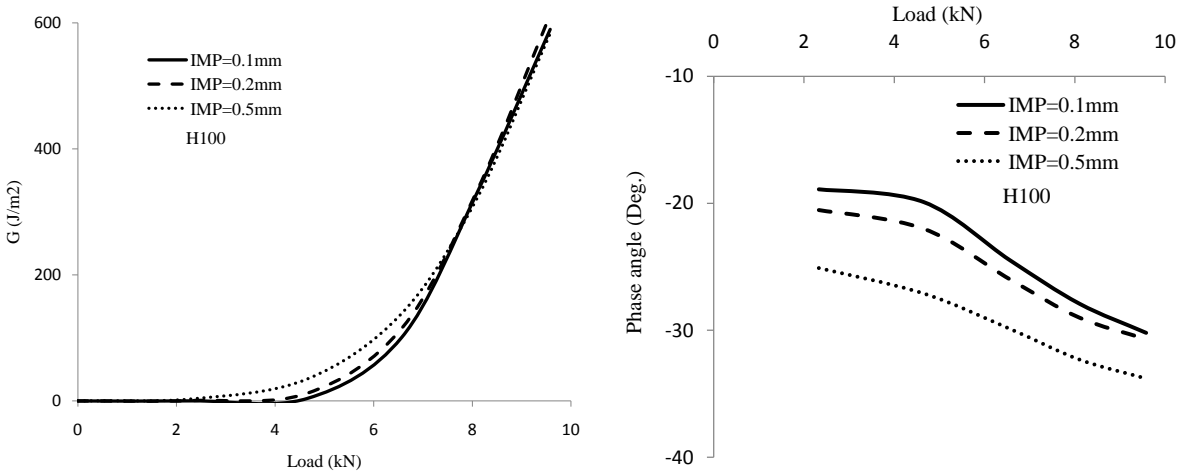


Figure 19. Energy release rate (left) and phase angle (right) versus load for a column with H100 core and 38.1 mm debond with different initial imperfection magnitudes.

shows G and ψ versus load for these columns. In the first graph it can be seen that G is not highly sensitive to the initial imperfection magnitude. The phase angle, shown in the second graph, is sensitive to the initial imperfection at small loads, but appears to converge to a value about -30° at higher loads indicating that the mode-mixity is less influenced by initial imperfection at higher loads.

The crack propagation load was estimated using fracture toughness data from the TSD tests. Energy release rate and mode-mixity in terms of phase angle were determined in the interior (center) of the columns. Table 5 lists numerically predicted and experimentally determined propagation loads (the maximum load in the load versus axial displacement diagrams of Figure 3, left) for the debonded columns.

The FEA predictions of debond propagation loads agree reasonably with the experimentally measured ones. It is clearly observed that the debond propagation load in the debonded columns decreases as the debond length increases. Furthermore the propagation load increases with increased core density as a result of the increasing fracture resistance with core density. However, some inconsistencies can be seen in experimental results. For example the measured debond propagation loads for columns with H100 and H200 cores, and 50.8 mm debond length are almost identical. These inconsistencies could be attributed to the local material distortions at the crack tip caused by the use of a blade to release the face/core debond and the resin rich area at the tip of the insert film. The proximity of the debond propagation loads and the instability loads in Tables 4 and 5 show that the local instability load could be used as

Core	Experiment			FE Analysis		
	Debond length			Debond length		
	25.4 mm	38.1 mm	50.8 mm	25.4 mm	38.1 mm	50.8 mm
H45	13.5 ± 1	9.8 ± 1.4	6.3 ± 1.1	10.6	7.1	5.4
H100	13.8 ± 0.9	10 ± 1.2	8 ± 0.9	16.8	11.2	9.1
H200	–	12.3 ± 1.7	8.1 ± 1.2	–	–	–

Table 5. Debond propagation loads, in kN: numerical predictions and experimental values.

a measure of debonded column strength for this particular column case. This is however not a general conclusion valid for all debonded column cases where other failure mechanisms, such as compression failure, occur prior to local buckling instability.

7. Conclusions

The compressive failure mechanism of foam cored sandwich columns containing a face-to-core debond was experimentally and numerically investigated. Sandwich columns with glass/epoxy face sheets and H45, H100, and H200 PVC foam cores were tested in a specially designed test rig. Most of the columns with H200 core and some columns with H100 failed by debond propagation at the face/core interface towards the column ends. Bifurcation type buckling instability of the debonded face sheet was not observed before the debond propagation initiated. It is believed that the initial imperfections are mostly responsible for this behavior which is similar to compression loading of a curved beam.

Slight kinking of the debond into the core was another failure mechanism which occurred in columns with a low density H45 core. Compression failure of the face sheet occurred in all specimens with H200 cores and a 25.4 mm debond which can be explained by the proximity between the debond propagation and the compression failure load of the face sheet.

Instability and crack propagation loads of the columns were predicted based on geometrically non-linear finite element analysis and linear elastic fracture mechanics. Testing of modified TSD specimens was conducted to measure the fracture toughness of the interface at the calculated phase angles for the column specimens associated with the debond propagation. Comparison of the measured out-of-plane deflection, instability, and debond propagation loads from experiments and finite element analyses showed fair agreement. For most of the investigated column specimens, it was shown that the instability and debond propagation loads are very reasonable estimates of the ultimate failure load, unless the other failure mechanisms occur prior to buckling instability.

Acknowledgements

This work has been partially performed within the context of the Network of Excellence on Marine Structures (MARSTRUCT) partially funded by the European Union through the Growth Programme under contract TNE3-CT-2003-506141.

The supply of core materials from DIAB (USA) through Chris Kilbourn and James Jones, the manufacturing of sandwich panels and test specimens by Justin Stewart, Department of Ocean Engineering, Florida Atlantic University, and testing done by Alejandro May at CICY are highly appreciated. The support from the Otto Mønstedts Foundation for a guest professorship for Leif A. Carlsson at the Technical University of Denmark is likewise highly appreciated.

References

- [ANSYS] ANSYS, www.ansys.com.
- [Avery and Sankar 2000] J. L. Avery, III and B. V. Sankar, "Compressive failure of sandwich beams with debonded face-sheets", *J. Compos. Mater.* **34**:14 (2000), 1176–1199.
- [Avilés and Carlsson 2007] F. Avilés and L. A. Carlsson, "Post-buckling and debond propagation in sandwich panels subject to in-plane compression", *Eng. Fract. Mech.* **74**:5 (2007), 794–806.

- [Berggreen and Carlsson 2008] C. Berggreen and L. A. Carlsson, “Fracture mechanics analysis of a modified TSD specimen”, pp. 173–185 in *Proceedings of the 8th International Conference on Sandwich Structures (ICSS8)* (Porto, 2008), vol. 1, edited by A. J. M. Ferreira, Faculty of Engineering, University of Porto, Porto, 2008. A full-length version of this paper will appear under the title “A modified TSD specimen for fracture toughness characterization: Fracture mechanics analysis and design” in *J. Compos. Mater.* (2010).
- [Berggreen and Simonsen 2005] C. Berggreen and B. C. Simonsen, “Non-uniform compressive strength of debonded sandwich panels, II: Fracture mechanics investigation”, *J. Sandw. Struct. Mater.* **7**:6 (2005), 483–517.
- [Berggreen et al. 2007] C. Berggreen, B. C. Simonsen, and K. K. Borum, “Experimental and numerical study of interface crack propagation in foam-cored sandwich beams”, *J. Compos. Mater.* **41**:4 (2007), 493–520.
- [Chen and Bai 2002] H. Chen and R. Bai, “Postbuckling behavior of face/core debonded composite sandwich plate considering matrix crack and contact effect”, *Compos. Struct.* **57**:1–4 (2002), 305–313.
- [DIAB] DIAB, “Divinycell technical data”, www.diabgroup.com.
- [Hohe and Becker 2001] J. Hohe and W. Becker, “Assessment of the delamination hazard of the core face sheet bond in structural sandwich panels”, *Int. J. Fract.* **109**:4 (2001), 413–432.
- [Hutchinson and Suo 1992] J. W. Hutchinson and Z. Suo, “Mixed mode cracking in layered materials”, *Adv. Appl. Mech.* **29** (1992), 63–191.
- [Kardomateas and Huang 2003] G. A. Kardomateas and H. Huang, “The initial post-buckling behavior of face-sheet delaminations in sandwich composites”, *J. Appl. Mech. (ASME)* **70**:2 (2003), 191–199.
- [Li and Carlsson 1999] X. Li and L. A. Carlsson, “The tilted sandwich debond (TSD) specimen for face/core interface fracture characterization”, *J. Sandw. Struct. Mater.* **1**:1 (1999), 60–75.
- [Li and Carlsson 2001] X. Li and L. A. Carlsson, “Fracture mechanics analysis of tilted sandwich debond (TSD) specimen”, *J. Compos. Mater.* **35**:23 (2001), 2145–2168.
- [Nøkkentved et al. 2005] A. Nøkkentved, C. Lundgaard-Larsen, and C. Berggreen, “Non-uniform compressive strength of debonded sandwich panels, I: experimental investigation”, *J. Sandw. Struct. Mater.* **7**:6 (2005), 461–482.
- [Østergaard 2008] R. C. Østergaard, “Buckling driven debonding in sandwich columns”, *Int. J. Solids Struct.* **45**:5 (2008), 1264–1282.
- [Sallam and Simiteses 1985] S. Sallam and G. J. Simiteses, “Delamination buckling and growth of flat, cross-ply laminates”, *Compos. Struct.* **4**:4 (1985), 361–381.
- [Sankar and Narayan 2001] B. V. Sankar and M. Narayan, “Finite element analysis of debonded sandwich beams under axial compression”, *J. Sandw. Struct. Mater.* **3**:3 (2001), 197–219.
- [Shivakumar et al. 2005] K. N. Shivakumar, H. Chen, and S. A. Smith, “An evaluation of data reduction methods for opening mode fracture toughness of sandwich panels”, *J. Sandw. Struct. Mater.* **7**:1 (2005), 77–90.
- [Southwell 1932] R. V. Southwell, “On the analysis of experimental observations in problems of elastic stability”, *Proc. R. Soc. Lond. A* **135**:828 (1932), 601–616.
- [Vadakke and Carlsson 2004] V. Vadakke and L. A. Carlsson, “Experimental investigation of compression failure of sandwich specimens with face/core debond”, *Compos. B Eng.* **35**:6–8 (2004), 583–590.
- [Veedu and Carlsson 2005] V. P. Veedu and L. A. Carlsson, “Finite-element buckling analysis of sandwich columns containing a face/core debond”, *Compos. Struct.* **69**:2 (2005), 143–148.
- [Viana and Carlsson 2002] G. M. Viana and L. A. Carlsson, “Mechanical properties and fracture characterization of cross-linked PVC foams”, *J. Sandw. Struct. Mater.* **4**:2 (2002), 99–113.
- [Xie and Vizzini 2005] Z. Xie and A. J. Vizzini, “Damage propagation in a composite sandwich panel subjected to increasing uniaxial compression after low-velocity impact”, *J. Sandw. Struct. Mater.* **7**:4 (2005), 269–288.
- [Zenkert 1997] D. Zenkert, *An introduction to sandwich construction*, EMAS, London, 1997.

RAMIN MOSLEMIAN: rmo@mek.dtu.dk

*Department of Mechanical Engineering, Technical University of Denmark, Nils Koppels Allé, Building 403,
2800 Kongens Lyngby, Denmark*

CHRISTIAN BERGGREEN: cbe@mek.dtu.dk

*Department of Mechanical Engineering, Technical University of Denmark, Nils Koppels Allé, Building 403,
2800 Kongens Lyngby, Denmark*

LEIF A. CARLSSON: carlsson@fau.edu

Department of Mechanical Engineering, Florida Atlantic University, 777 Glades Road, Boca Raton, FL 33431, United States

FRANCIS AVILES: faviles@cicy.mx

*Centro de Investigación Científica de Yucatán, A.C. Unidad de Materiales, Calle 43, No. 103, Colonia Chuburná de Hidalgo,
CP 97200 Mérida, Yucatán, Mexico*

COUPLED FINITE ELEMENT FOR THE NONLINEAR DYNAMIC RESPONSE OF ACTIVE PIEZOELECTRIC PLATES UNDER THERMOELECTROMECHANICAL LOADS

DIMITRIS VARELIS AND DIMITRIS SARAVANOS

A theoretical framework is presented for analyzing the coupled nonlinear dynamic behavior of laminated piezoelectric composite plates subject to high thermoelectromechanical loadings. It incorporates coupling between mechanical, electric, and thermal governing equations and encompass geometric non-linearity effects due to large displacements and rotations. The mixed-field shear-layerwise plate laminate theory formulation is considered, thus degenerating the 3D electromechanical field to 2D nodal variables, and an eight-node coupled nonlinear plate element is developed. The discrete coupled nonlinear dynamic equations of motion are formulated, linearized, and numerically solved at each time step using the implicit Newmark scheme with a Newton–Raphson technique. Validation and evaluation cases on active laminated beams demonstrate the accuracy of the method and its robust capability to effectively predict the nonlinear dynamic response under time-dependent combined mechanical, thermal, and piezoelectric actuator loads. The results illustrate the capability of the method to simulate large amplitude vibrations and dynamic buckling phenomena in active piezocomposite plates. The influence of loading rates on the nonlinear dynamic structural response is also quantified. Additional numerical cases demonstrate the complex dynamic interactions between electrical, mechanical, and thermal buckling loads.

1. Introduction

In the last decade a substantial amount has been published addressing the nonlinear static response of laminated beams, plates, and shells with attached piezoelectric devices subjected to thermoelectromechanical loads. The reported works implement various types of external loads, kinematic assumptions, and numerical methods to solve the resultant nonlinear equations. [Tzou and Zhou \[1997\]](#) reported theoretical work on the dynamics, electromechanical coupling, and control of thermal buckling of a nonlinear piezoelectric laminated circular plate with an initial large deformation, [Bao et al. \[1998\]](#) analyzed nonlinear piezothermoelastic laminated beams, and [Oh et al. \[2001\]](#) studied thermopiezoelectric phenomena of active laminated plates. [Wang et al. \[2004\]](#) analyzed adaptive structures involving large imposed deformation. [Ahmad et al. \[2004\]](#) formulated a nonlinear model of a smart beam using general electrothermoelastic relations. In [\[Varelis and Saravanos 2004\]](#) the present authors demonstrated the prebuckling and postbuckling response of piezoelectric plates solving the static coupled nonlinear equations, and in [\[Varelis and Saravanos 2008\]](#) we developed a coupled nonlinear shell element for the prediction of stable and unstable deflection paths of piezolaminated shells subject to thermoelectromechanical loads, and also demonstrated the capability of piezoelectric shells to induce large deflections through active snap-through buckling.

Keywords: adaptive structures, composite, piezoelectric, actuators, sensors, finite element, nonlinear dynamics, vibration, geometric nonlinearity, thermal, buckling.

Additional reported works addressed the nonlinear dynamic behavior of piezolaminated plates and beams limited, however, to small amplitude free vibrations. Lee and Lee [1997] investigated the linearized vibration behavior of unstiffened and stiffened thermally postbuckled anisotropic plates, Singha et al. [2006] predicted the vibration characteristics of thermally stressed skew plates, and Park and Kim [2006] investigated small amplitude vibration behavior of simply supported FGM plates with temperature dependent materials in prebuckling and postbuckling state. Oh et al. [2000] presented an uncoupled layerwise theory to quantify the influence of buckling and postbuckling on natural frequencies. In [Varelis and Saravanos 2006] we reported on a coupled nonlinear finite element for the prediction of small amplitude free vibrations of piezocomposite beams and plates subjected to large deflections and initial stresses and quantified the advantages of the coupled formulation; a strong relation between modal frequencies and the ongoing buckling prediction was also postulated.

Very little work has been reported on the nonlinear dynamic response of adaptive piezoelectric structures for large loads and deflection amplitudes. Gao and Shen [2003] adopted first-order shear deformation theory for analyzing the geometrical nonlinear transient vibration response of plates and their control. Yi et al. [2000] applied solid elements to perform geometrically nonlinear analysis of surface bonded piezoelectric sensor wafers on plates and shells. Mukherjee and Chaudhuri [2005] developed a finite element for piezolaminated beams using an uncoupled approach for the prediction of sensory voltage in polyvinylidene fluoride (PVDF) bimorph cantilever beams vibrating at large amplitudes. Lentzen et al. [2007] worked on the control of the nonlinear vibration of piezoelectric beams under transverse load. Oh [2005] developed a finite plate element encompassing an uncoupled layerwise theory considering snap-through piezoelectric behavior.

The current paper presents a nonlinear coupled thermopiezoelectric plate theory and a finite element for laminated piezoelectric plates undergoing large displacements and rotations, for predicting the nonlinear dynamic response of adaptive plates exposed to dynamic thermal, electrical, and mechanical loads. The coupled nonlinear governing equations for piezolaminates are first formulated using the mixed-field shear-layerwise kinematic assumptions [Varelis and Saravanos 2008]. Generalized governing equations are formulated combining the Green–Lagrange nonlinear strains, with the kinematic assumptions of the mixed-field shear-layerwise shell laminate theory and linear thermopiezoelectric constitutive equations, including rotational inertia effects. Based on the previous generalized mechanics, a local finite element approximation is formulated and an eight-node nonlinear thermopiezoelectric plate element is developed. Finally, the discrete nonlinear coupled dynamic equations of motion are solved at each time step using the Newmark time integration in combination with a Newton–Raphson technique. Validation cases verify the present model, and various numerical examples evaluate the capability of the present method to predict the oncoming dynamic instability of smart beams under various combinations of dynamic mechanical, electric, and thermal loads.

2. Piezoelectric laminated shells

The case of a piezoelectric laminate plate is considered, consisting of an arbitrary configuration of linear piezoelectric layers or composite plies. The material of each ply of the piezoelectric laminate is assumed to remain within the range of linear piezoelectricity,

$$\sigma_i = C_{ij}^{E,T} S_j - e_{ik}^T E_k - \lambda_{im}^{E,T} \theta_m, \quad D_l = e_{lj}^T S_j + \varepsilon_{lk}^{S,T} E_k + p_{lm}^T \theta_m, \quad (1)$$

where $i, j = 1, \dots, 6$ and $k, l = 1, \dots, 3$; σ_i and S_i denote the mechanical stresses and Green's engineering strains in extended vectorial notation, C_{ij} is the elastic stiffness tensor, e_{ik} is the piezoelectric tensor, E_k is the electric field vector, λ_{im} is the thermal expansion tensor, $\theta_m = \Delta T = T - T_o$ is the temperature difference between the current temperature T and the thermally stress-free reference temperature T_o , D_l is the electric displacement vector, ε_{lk} is the electric permittivity tensor, and p_{lm} is the pyroelectric tensor. Superscript E, S, T represent constant voltage, strain, and temperature conditions, respectively.

The first shear deformation theory for the elastic displacements in combination with a layerwise linear field assumption for the electric potential and temperature are implemented, in the context of the mixed-field kinematic assumptions. Geometric nonlinear effects are usually realized in flexible structures which do not exhibit significant shear deformable effects, and vice versa; therefore, the consideration of shear deformation mainly aims to improve to the robustness of the linear part of the solution at plates of higher thickness aspect ratios.

The mechanical strains, the electric and thermal field components through the thickness of the laminate take the form

$$S_i = S_i^o + zk_i^o + S_{Li} \quad (i = 1, 2, 6), \quad S_{sj} = S_{sj}^o \quad (j = 4, 5), \quad (2)$$

where S_i^o and S_{sj}^o are the midsurface in-plane and shear strains respectively, k_i^o are the midsurface curvatures, and S_{Li} the resultant nonlinear mechanical strains described with respect to midsurface parameters:

$$S_{L1} = \frac{1}{2} w_{,x}^o{}^2, \quad S_{L2} = \frac{1}{2} w_{,y}^o{}^2, \quad S_{L6} = w_{,x}^o w_{,y}^o. \quad (3)$$

The generalized electric fields are

$$E_i(x, y, z, t) = \sum_{i=1}^m E_i^m(x, y, t) \Psi^m(z) \quad (i = 1, 2), \quad E_3(x, y, z, t) = \sum_{i=1}^m E_3^m(x, y, t) \Psi_{,z}^m(z). \quad (4)$$

The generalized thermal field is

$$\Theta(x, y, z, t) = \sum_{m=1}^N \Theta^m(x, y, t) \Psi^m(z), \quad (5)$$

where N indicates the number of discrete layers which may subdivide the laminate, E^m and Θ^m are the generalized electric and thermal fields at the m discrete layer, $\Psi^m(\zeta)$ are linear interpolation functions, and N is the number of discrete layers.

2.1. Generalized dynamic equations of motion in variational form. Since the present formulation refers to dynamic generalized equations, the estimation of the latter from a known equilibrium configuration at discrete time t to the next equilibrium state in discrete time $t + \Delta t$ is required. Through the use of the divergence theorem and neglecting the damping effects, the generalized imbalances between external and internal mechanical forces and electric charges, away from the equilibrium denoted by the vectors Ψ_u and Ψ_e , can be expressed at time t over the volume of the piezoelectric laminated plate, in an equivalent variational form:

$$\begin{aligned} \delta u^T {}^t\Psi_u &= - \int_V \delta {}^tS^T {}^t\sigma dV + \int_V \delta u^T {}^t b dV - \int_V \delta u^T \rho {}^t\ddot{u} dV + \int_{\Gamma_r} \delta u^T {}^t\bar{\tau} d\Gamma, \\ \delta \phi^T {}^t\Psi_e &= - \int_V \delta {}^tE^T {}^t\mathcal{D} dV + \int_{\Gamma_q} \delta \phi^T {}^t\bar{q} d\Gamma, \end{aligned} \quad (6)$$

where tS and ${}^t\sigma$ are the total Green–Lagrange strain tensor and second Piola–Kirchhoff stress tensor respectively, tb are the body forces, $\rho {}^t\ddot{u}$ indicate the inertia body forces, ${}^t\tau$ are the surface tractions on the bounding surface Γ_τ , tq is the electrical charge applied on the terminal bounding surface Γ_q , an overbar indicates surface quantities, and V represents the whole laminated plate volume including all passive and active piezoelectric layers.

Substituting Equations (1)–(5) into (6), integrating over the thickness coordinate ζ and collecting the mechanical, electric, and thermal field state variables, the following generalized equations of motion result, which express the electromechanical equilibrium of the laminate at time step t :

$$\begin{aligned} \delta^t u^T {}^t\Psi_u = & - \int_{A_o} \left(\delta^t S^{oT} [A] {}^tS^o + \delta^t S^{oT} [B] {}^tk^o + \delta^t k^{oT} [B] {}^tS^o + \delta^t k^{oT} [D] {}^tk^o + \delta^t S_s^{oT} [A_s] {}^tS_s^o \right. \\ & + \delta^t S^{LT} [A] {}^tS^o + \delta^t S^{LT} [A] {}^tS^L + \delta^t S^{LT} [B] {}^tk^o + \delta^t S^{oT} [A] {}^tS^L + \delta^t k^{oT} [B] {}^tS^L + \sum_m \delta^t S^{oT} [\bar{E}^m] {}^tE^m \\ & + \sum_m \delta^t k^{oT} [\hat{E}^m] {}^tE^m + \sum_m \delta^t S^{LT} [\bar{E}^m] {}^tE^m + \sum_m \delta^t S^{oT} [\bar{\Theta}^m] {}^t\Theta^m + \sum_m \delta^t k^{oT} [\hat{\Theta}^m] {}^t\Theta^m \\ & \left. + \sum_m \delta^t S^{LT} [\bar{\Theta}^m] {}^t\Theta^m \right) dA + \int_{A_o} (\delta^t u^T b^A + \delta^t \beta^T b^B) dA + \int_{\Gamma_\tau} \delta^t \bar{u}^T t_\tau d\Gamma, \end{aligned} \tag{7}$$

$$\begin{aligned} \delta^t \phi^T {}^t\Psi_e = & - \int_{A_o} \left(\sum_m \delta^t E^{mT} [\bar{E}^m] {}^tS^o + \sum_m \delta^t E^{mT} [\bar{E}^m] {}^tk^o + \sum_m \delta^t E^{mT} [\bar{E}^m] {}^tS^L \right. \\ & \left. + \sum_{mn} \delta^t E^{mT} [G^{mn}] {}^tE^n + \sum_{mn} \delta^t E^{mT} [T^{mn}] {}^t\Theta^n \right) dA + \int_{\Gamma_q} \delta \overline{\phi^t q} d\Gamma, \quad m, n = 1, \dots, N, \end{aligned}$$

where $[A]$, $[B]$, $[D]$, and $[A_s]$ are the extensional, coupling, flexural, and shear stiffness matrices; E^m overbar and overhat are the equivalent extensional and flexural piezoelectric coefficients; $[\bar{\Theta}^m]$ and $[\hat{\Theta}^m]$ are the in-plane and out-of-plane laminate thermal expansion matrices; and G^{mn} are the generalized electric permittivity matrices.

3. Finite element methodology

In order to solve the above generalized nonlinear variational equation (7), the finite element methodology is adopted. The multifield state variables are approximated on the reference midplane A_o with local interpolation functions, taking the form

$$\begin{aligned} u_j^o(x, y, t) = & \sum_{i=1}^M u_j^{oi}(t) P^i(x, y) \quad (j = 1, 2, 3), \quad \beta_j^o(x, y, t) = \sum_{i=1}^M \beta_j^i(t) P^i(x, y) \quad (j = 1, 2), \\ \phi^m(x, y, t) = & \sum_{i=1}^M \phi^{mi}(t) P^i(x, y) \quad \text{and} \quad \theta^m(x, y, t) = \sum_{i=1}^M \theta^{mi}(t) P^i(x, y) \quad (m = 1, \dots, N), \end{aligned} \tag{8}$$

where N indicates the number of discrete layers which subdivide the laminate, M the number of element nodes, and P denotes local C_o continuous interpolation functions.

3.1. Generalized dynamic equations of motion in variational form. Substituting (8) into (7) and collecting the common nodal displacement, electric potential, and temperature terms, the following coupled

system of nonlinear equations of motion is ultimately derived for time t :

$$\begin{aligned} {}^t\Psi_u(u, \varphi) &= [M]{}^t\ddot{u} + [K_{uu}(u, \varphi)]{}^t u + [K_{ue}(u, \varphi)]{}^t \varphi + [K_{u\theta}(u, \varphi)]{}^t \theta - {}^t R = 0, \\ {}^t\Psi_e(u, \varphi) &= [K_{eu}(u, \varphi)]{}^t u + [K_{ee}(u, \varphi)]{}^t \varphi + [K_{e\theta}(u, \varphi)]{}^t \theta - {}^t Q = 0, \end{aligned} \tag{9}$$

where ${}^t u$ and ${}^t \phi$ are the nodal displacement and electric potential vectors, respectively, and ${}^t \theta$ is the applied nodal temperature vector ${}^t \theta = \{ {}^t \theta^A \}$; ${}^t R$ and ${}^t Q$ are the externally applied mechanical loads and charge vectors at time t , respectively. The electric potential vector ${}^t \phi$ encompasses both applied and free electric potential terms, that is

$${}^t \phi = \begin{bmatrix} {}^t \phi^A \\ {}^t \phi^S \end{bmatrix},$$

where ${}^t \phi^A$ is the externally applied nodal electric potential at the actuators and ${}^t \phi^S$ is the induced unknown electric potential at nodes with prescribed electric displacement. In a smart piezoelectric plate, the electric potential vectors ϕ^A and ϕ^S correspond to actuators and sensors respectively, moreover, in case of an adaptive structure they may be further connected through a proper controller; however, in this study no feedback from sensors to actuators is considered. At mechanical and electrical equilibrium, where ${}^t\Psi_u = 0$ and ${}^t\Psi_e = 0$, equations (9) represent the discrete system of nonlinear equilibrium equations and the electric potential ϕ^S together with the free displacement nodal vector u represents the unknowns of the nonlinear system. The availability of active and sensory electric potential in combination with the nonlinear system (9), reflects the capability of the present model to be interfaced in future studies through a nonlinear controller. The matrices $[K]$ with subscripts uu , ue , ee , $u\theta$, and $e\theta$ indicate the actual stiffness, piezoelectric, electric permittivity, thermal expansion, and pyroelectric matrices respectively, including linear and nonlinear terms:

$$\begin{aligned} [K_{uu}(u, \phi)] &= [K_{uu}^o] + [K_{uu}^L] = [K_{uu}^o] + [P_1(u)] + [P_2(u^2)], \\ [K_{ue}(u, \phi)] &= [K_{ue}^o] + [K_{ue}^L] = [K_{ue}^o] + [P_3(u)], \\ [K_{eu}(u, \phi)] &= [K_{eu}^o] + [K_{eu}^L] = [K_{eu}^o] + [P_4(u)], \\ [K_{ee}(u, \phi)] &= [K_{ee}^o]. \end{aligned} \tag{10}$$

3.2. Solution scheme for coupled nonlinear equations. Let us assume that an equilibrium between internal and external mechanical forces and electric charges has been predicted for the configuration at time t , yielding ${}^t\Psi_u = 0$ and ${}^t\Psi_e = 0$. Assuming also that external forces and charges are applied incrementally at discrete time steps, such that ${}^{t+\Delta t}R = {}^t R + \Delta R$ and ${}^{t+\Delta t}Q = {}^t Q + \Delta Q$, we are looking to predict the next equilibrium state at time $t + \Delta t$, which will satisfy the equilibrium equations ${}^{t+\Delta t}\Psi_u = 0$ and ${}^{t+\Delta t}\Psi_e = 0$. The resulting global set of generalized equations of motion are solved in time, using Newmark’s time integration method.

Since the imbalance forces and charges ${}^{t+\Delta t}\Psi_u(u, \phi)$ and ${}^{t+\Delta t}\Psi_e(u, \phi)$ depend nonlinearly on the nodal point displacements and electric potentials, convergence can’t be directly achieved at each time step. Thus, the Newton–Raphson iterative technique is adopted in order to solve the generalized nonlinear dynamic equations at each iteration, shown analytically below for the k -th iteration into the configuration

time $t + \Delta t$:

$$\begin{aligned} {}^{t+\Delta t}\bar{K}_{uu}(u^{k-1}, \phi^{k-1})\Delta u^k + {}^{t+\Delta t}\bar{K}_{ue}(u^{k-1}, \phi^{k-1})\Delta \phi^k &= -{}^{t+\Delta t}\Psi_u(u^{k-1}, \phi^{k-1}), \\ {}^{t+\Delta t}\bar{K}_{eu}(u^{k-1}, \phi^{k-1})\Delta u^k + {}^{t+\Delta t}\bar{K}_{ee}(u^{k-1}, \phi^{k-1})\Delta \phi^k &= -{}^{t+\Delta t}\Psi_e(u^{k-1}, \phi^{k-1}). \end{aligned} \tag{11}$$

In the above system of equations, the overbar indicates tangential structural, piezoelectric, and permittivity matrices which encompass the following matrix terms:

$$\begin{aligned} [\bar{K}_{uu}(u, \phi)] &= \frac{4}{\Delta t^2}[M] + [\bar{K}_{uu}^o] + [\bar{K}_{uu}^\sigma] + [\bar{P}_1(u)] + [\bar{P}_2(u^2)], \\ [\bar{K}_{ue}(u, \phi)] &= [\bar{K}_{ue}^o] + [\bar{K}_{ue}^L] = [\bar{K}_{ue}^o] + [\bar{P}_3(u)], \\ [\bar{K}_{eu}(u, \phi)] &= [\bar{K}_{eu}^o] + [\bar{K}_{eu}^L] = [\bar{K}_{eu}^o] + [\bar{P}_4(u)], \\ [\bar{K}_{ee}(u, \phi)] &= [\bar{K}_{ee}^o]. \end{aligned} \tag{12}$$

The updated displacement, velocity, acceleration, and electric potential vectors are expressed below:

$$\begin{aligned} {}^{t+\Delta t}u^{(k)} &= {}^{t+\Delta t}u^{(k-1)} + \Delta u^{(k)}, \\ {}^{t+\Delta t}\dot{u}^{(k)} &= \frac{4}{\Delta t^2}({}^{t+\Delta t}u^{(k-1)} - {}^t u) - \frac{4}{\Delta t} {}^t \dot{u} - {}^t \ddot{u}, \\ {}^{t+\Delta t}\phi^{(k)} &= {}^{t+\Delta t}\phi^{(k-1)} + \Delta \phi^{(k)}, \end{aligned} \tag{13}$$

where ${}^t u$, ${}^t \dot{u}$, and ${}^t \ddot{u}$ are the converged values at time step t related to the respective values at step $t + \Delta t$ as follows: ${}^t u = {}^{t+\Delta t}u^{(0)}$, ${}^t \dot{u} = {}^{t+\Delta t}\dot{u}^{(0)}$, and ${}^t \ddot{u} = {}^{t+\Delta t}\ddot{u}^{(0)}$.

4. Numerical results

Validation and novel evaluation cases of the developed FE model are presented, for various active piezoelectric laminated beams and plates under combined thermoelectromechanical dynamic loading conditions. The considered materials were aluminum, graphite-epoxy, PVDF piezopolymer, and PZT5 piezoceramic, the properties of which are shown in [Table 1](#).

5. Validation cases

5.1. Mechanical buckling of a cantilever bimorph beam under ramp loading. In the present numerical case the lateral nonlinear dynamic response of a PVDF [p/p] bimorph cantilever beam was examined. The beam was 100 mm long and 5 mm wide and the thickness of the PVDF layer was 0.5 mm. A ramp point load of 0.005 N was applied in the transverse direction at the middle of the tip along with a constant uniform axial mechanical load. Closed circuit electric conditions were considered at each piezoelectric layer. [Figure 1](#) shows the transverse deflection amplitude on the tip versus time, when a compressive axial load is applied. Obviously the displacement amplitude increases as the axial compressive load approaches the critical value $F_{cr} = 0.204$ N, due to softening effects. Also the curves corresponding to higher compressive loads exhibit a higher vibration period due again to the reduction of stiffness. Conversely, [Figure 2](#) illustrates the tip vibration of the beam subject to a tensile axial load and shows an amplitude reduction with a simultaneous vibration period reduction due to stiffening effects produced by

Property	Gr/epoxy	Al	PZT-5	PVDF	Property	Gr/epoxy	Al	PZT-5	PVDF
Elastic properties (10^9 Pa)					Electric permittivity (10^{-9} F/m)				
E_{11}	132.4	66	62	2	ϵ_{11}	0.031	0.026	23	0.1
E_{22}	10.8	66	62	2	ϵ_{22}	0.026	0.026	23	0.1
E_{33}	10.8	66	62	2	ϵ_{33}	0.026	0.026	24	0.1
G_{23}	3.6	27	23.6	0.77	Thermal expansion coefficient (10^{-6} / $^{\circ}$ C)				
G_{13}	5.6	27	23.6	0.77	α_{11}	-0.9	24	1.1	42
G_{12}	5.6	27	18	0.77	α_{22}	27	24	1.1	42
ν_{12}	0.24	0.3	0.31	0.29	Pyroelectric constant (10^{-3} / m^2 $^{\circ}$ C)				
ν_{13}	0.24	0.3	0.31	0.29	p_{11}	0	0	-0.2	0.05
ν_{23}	0.49	0.3	0.31	0.29	p_{22}	0	0	-0.2	0.05
Piezoelectric coefficients (10^{-12} m/V)					p_{33}	0	0	-0.2	0.05
d_{31}	0	0	-220	-16					
d_{32}	0	0	-220	-16					
d_{24}	0	0	670	33					
d_{15}	0	0	670	33					

Table 1. Material properties. All E and G values in units of GPa.

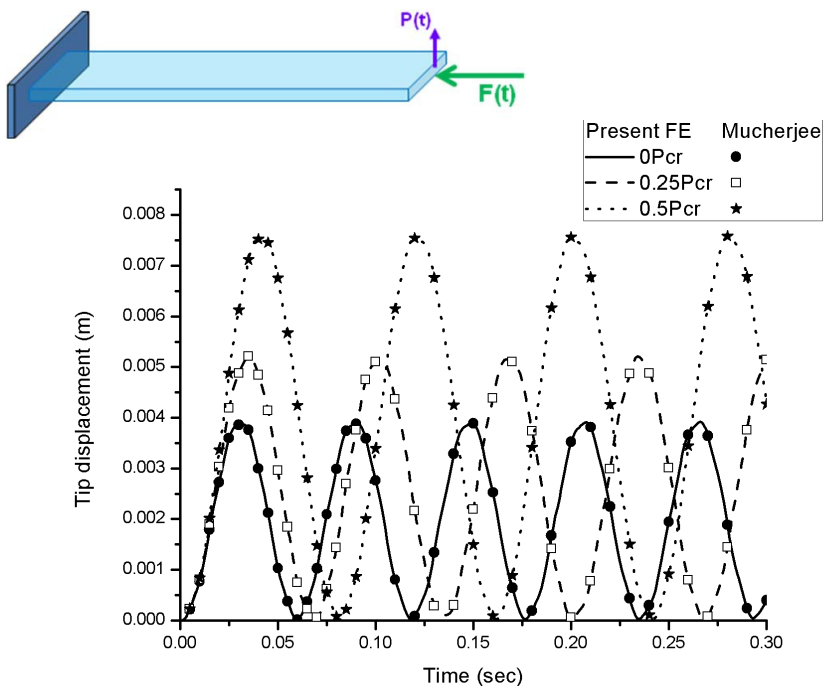


Figure 1. Tip dynamic displacement of a bimorph [PVDF/PVDF] cantilever beam induced by a combined step in-plane compressive and ramp transverse load applied at the tip of the beam.

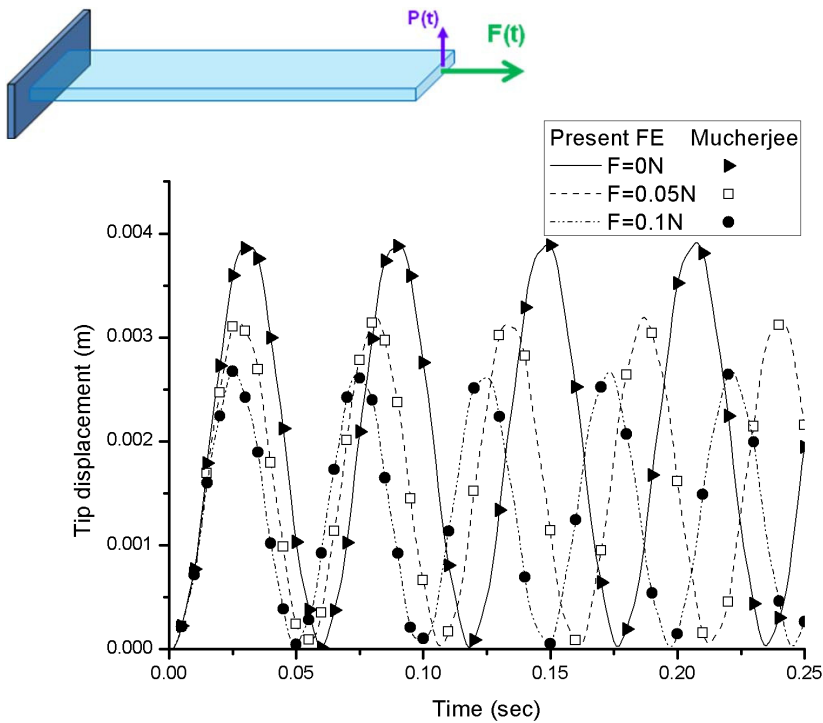


Figure 2. Tip dynamic displacement of a bimorph [PVDF/PVDF] cantilever beam induced by a combined ramp transverse and step in-plane tensile mechanical load applied at the tip of the beam.

the axial tensile load. Finally, the results are in excellent agreement with those reported by [Mukherjee and Chaudhuri \[2005\]](#) who used a beam finite element based on uncoupled laminate theory.

5.2. Fully simply-supported square plate under pulse loading. In the second validation case, the dynamic response of a fully simply supported square $2.438 \text{ m} \times 2.438 \text{ m}$ aluminum plate, with thickness 6.35 mm was investigated. A uniform pressure pulse load $P = 47.84 \text{ Pa}$ was applied on the plate. An 8×8 element mesh model was used. [Figure 3](#) shows the dynamic response of the plate under various pulse load values. The results reveal the nonlinear dependence between applied load and vibration amplitude and period due to membrane effects. The predicted results are in excellent agreement with those reported by [Gao and Shen \[2003\]](#), who used an uncoupled piezoelectric laminate theory and a four node plate finite element. Overall, the current method has accurately predicted the nonlinear dynamic response of flexible structures including the onset of dynamic mechanical buckling, as well as the stiffening effects due to tensile axial loads.

6. Numerical examples

6.1. Mechanical buckling of a cantilever bimorph beam under various ramp loads. The nonlinear dynamic response of a cantilever [PVDF/PVDF] beam, having the same geometric dimensions with that of the first validation case is further studied. Three compressive ramp loads with identical maximum

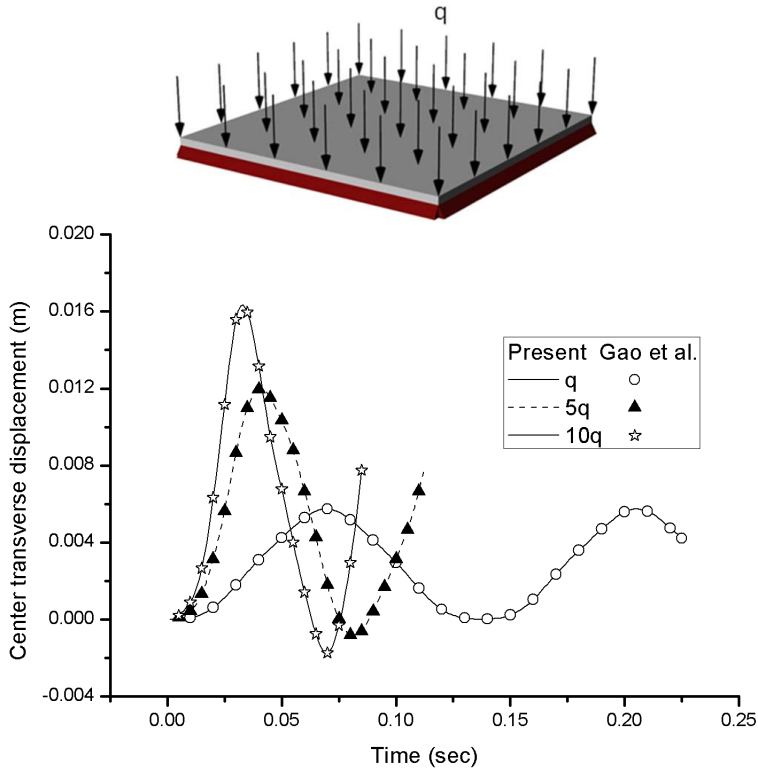


Figure 3. Central dynamic transverse deflection of a square simply-supported aluminum plate loaded under various uniform step pressures.

values $F_{\max} = 1.1F_{\text{cr}}$ ($F_{\text{cr}} = 0.204 \text{ N}$), were progressively applied at the tip of the beam however, at different rates (see Figure 4a). A step of low uniform pressure (0.5 Pa) was applied on the beam at $t = 0 \text{ sec}$ in order to induce an eccentricity and a stable buckling path (see Figure 4a). Figure 4b shows the transverse displacement at the tip of the beam versus the time for the various ramp load rates. Clearly all three curves show a rapid increase of the dynamic tip deflection near the corresponding buckling load step, which however occurs at different times for each loading rate, with the high-rate ramp load reaching the critical buckling load faster, and so forth. Yet, the rate of loading is predicted to have a drastic effect on the resultant maximum dynamic tip deflection. Apparently, in the high-rate ramp load inertial forces also play a dominant role in the dynamic buckling of the beam, and vice versa. The predicted results show the capability of the method to predict the onset of dynamic buckling under various dynamic loads.

6.2. Active thermopiezoelectric buckling of a simply-supported composite beam. The nonlinear dynamic response of a simply-supported $[p/0/90/45/-45]_s$ graphite/epoxy beam with continuous piezoelectric layers attached on the upper and lower surface is predicted. The length and the width of the beam were 200 mm and 20 mm, respectively; the thicknesses of the composite plies and piezoelectric layers were $h_l = h_p = 0.1 \text{ mm}$. The beam is loaded by a time step of uniform temperature load ΔT applied at $t = 0 \text{ sec}$, and a ramp piezoelectric load with rate $dV/dt = 600 \text{ V/sec}$, induced by unidirectional electric fields imposed by equal but opposite in polarity electric potential values applied on the outer terminals of

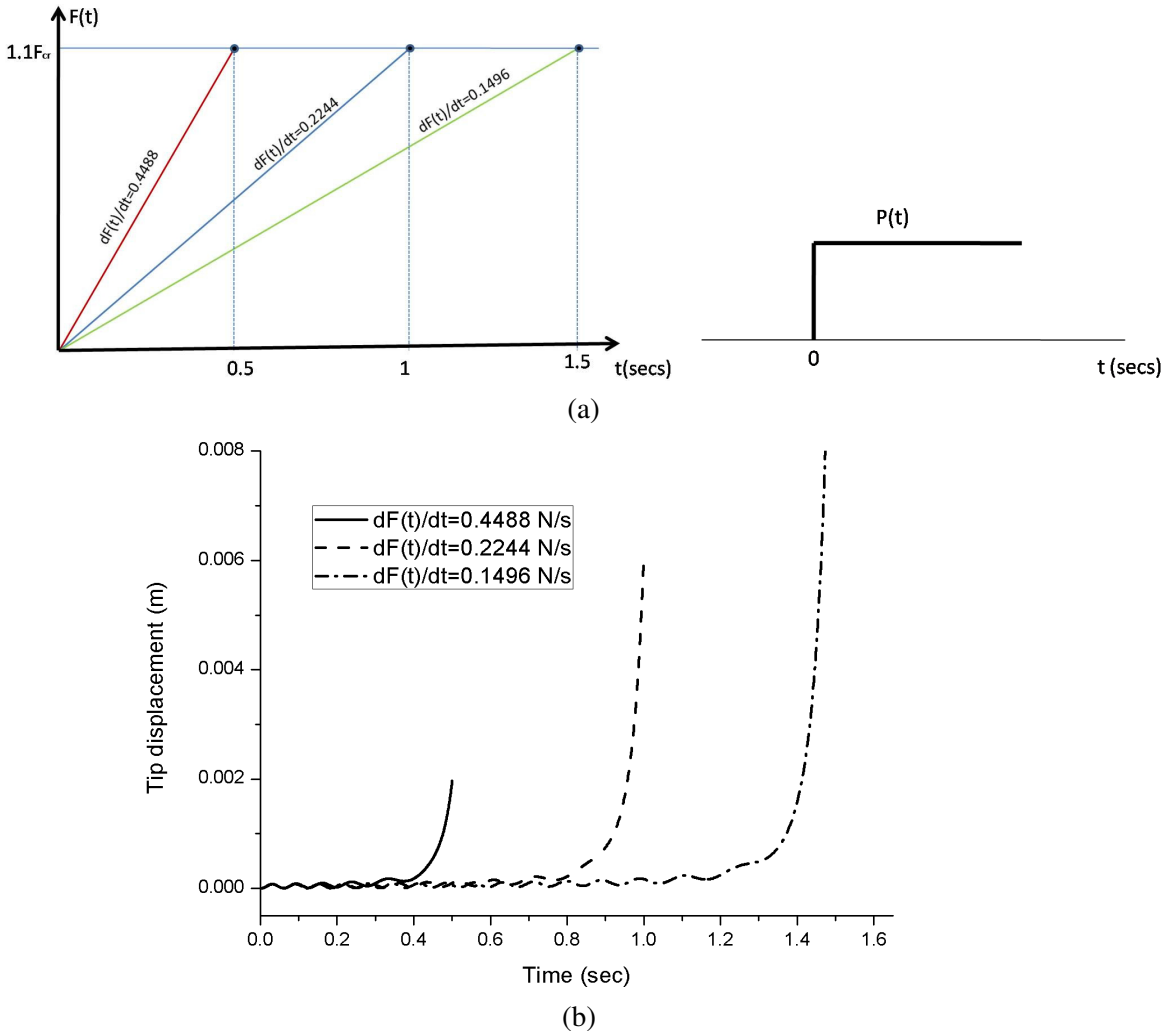


Figure 4. Effect of the rate of an in-plane compressive ramp force on the onset of dynamic buckling of a bimorph [PVDF/PVDF] cantilever beam. (a) Time dependence of applied loads and (b) predicted transverse tip displacement.

the piezoactuators (see Figure 5a). An imperfection induced by a time step of very low constant uniform pressure (1 Pa) was considered to stimulate the onset of a stable buckling path (see Figure 5a). Figure 5b shows the predicted center transverse displacement of the beam versus time. Both thermal load and electric fields induce in-plane compressive stresses in the beam. The beam buckles under the piezoelectric load alone ($\Delta T = 0^\circ\text{C}$), but the simultaneous application of the thermal load effectively causes the shifting of the stable equilibrium trajectory. The underlying vibration on the buckling trajectory is caused by the lateral force and near and beyond the critical electric potential the vibration amplitude reaches higher values due to the initiation of dynamic buckling. The results show the inherent capability of the present method to simulate the combined dynamic thermoelectric buckling of flexible piezocomposite structures.

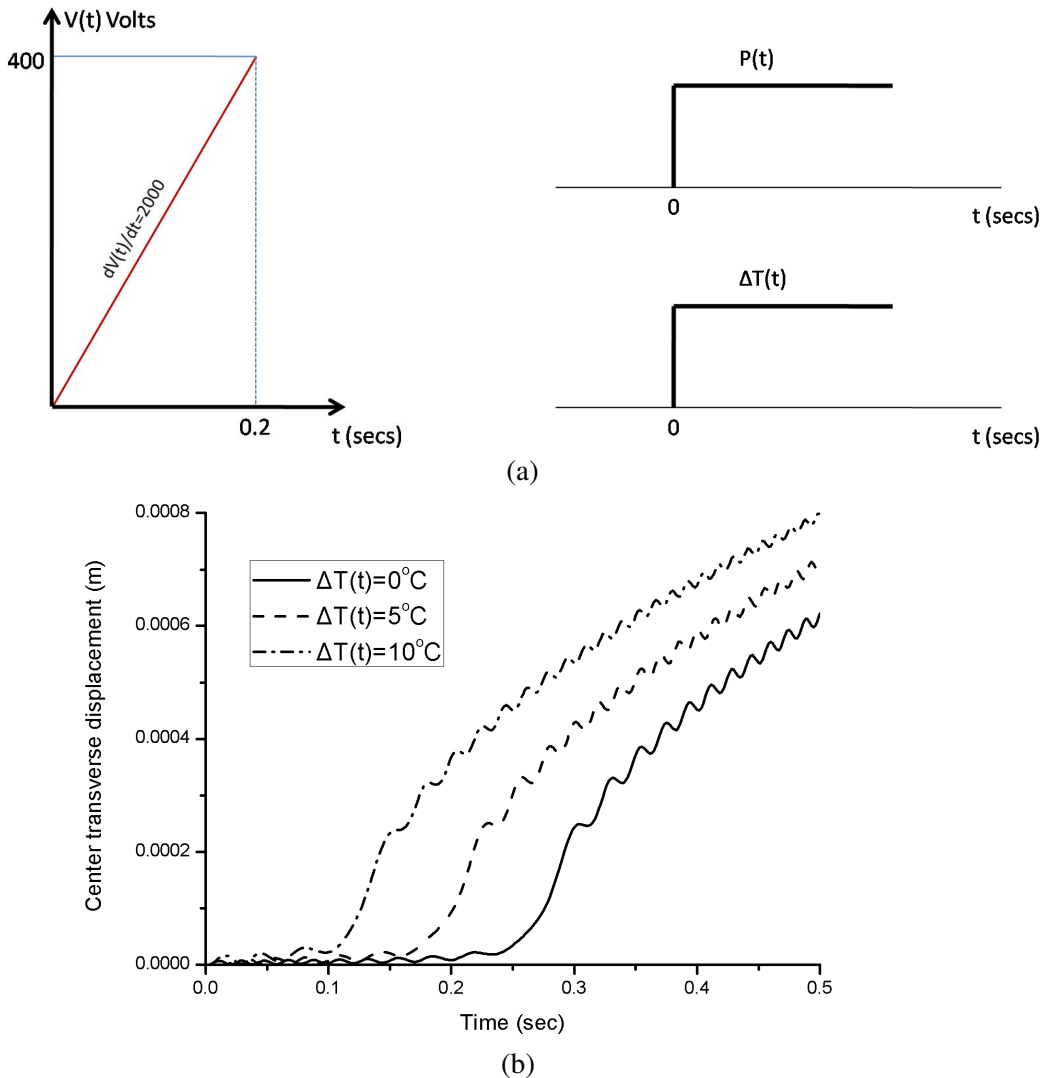


Figure 5. Dynamic buckling response of a simply-supported active $[p/0/90/45/-45]_s$ beam under combined uniform in-plane piezoelectric, in-plane thermal, and off-plane pressure loads. (a) Time dependence of applied electric field, temperature, and uniform pressure; and (b) predicted transverse deflection at center.

6.3. Laminated active beam under electromechanical bending load. In the present case, the bending response of a simply-supported active $[p/0/90/45/-45]_s$ gr-epoxy beam subject to combination of dynamic electromechanical loads is simulated. The geometric dimensions of the beam are the same as those of the previous example. A time step of uniform pressure (200 Pa) was applied on the beam at $t = 0$ sec (see Figure 6a). A uniform and equal in value and polarity ramp electric potential was also imposed on the outer terminals at each piezoelectric layer at $t = 0$ sec, while their inner terminals remained grounded, such that distributed piezoelectric bending moment was progressively induced on

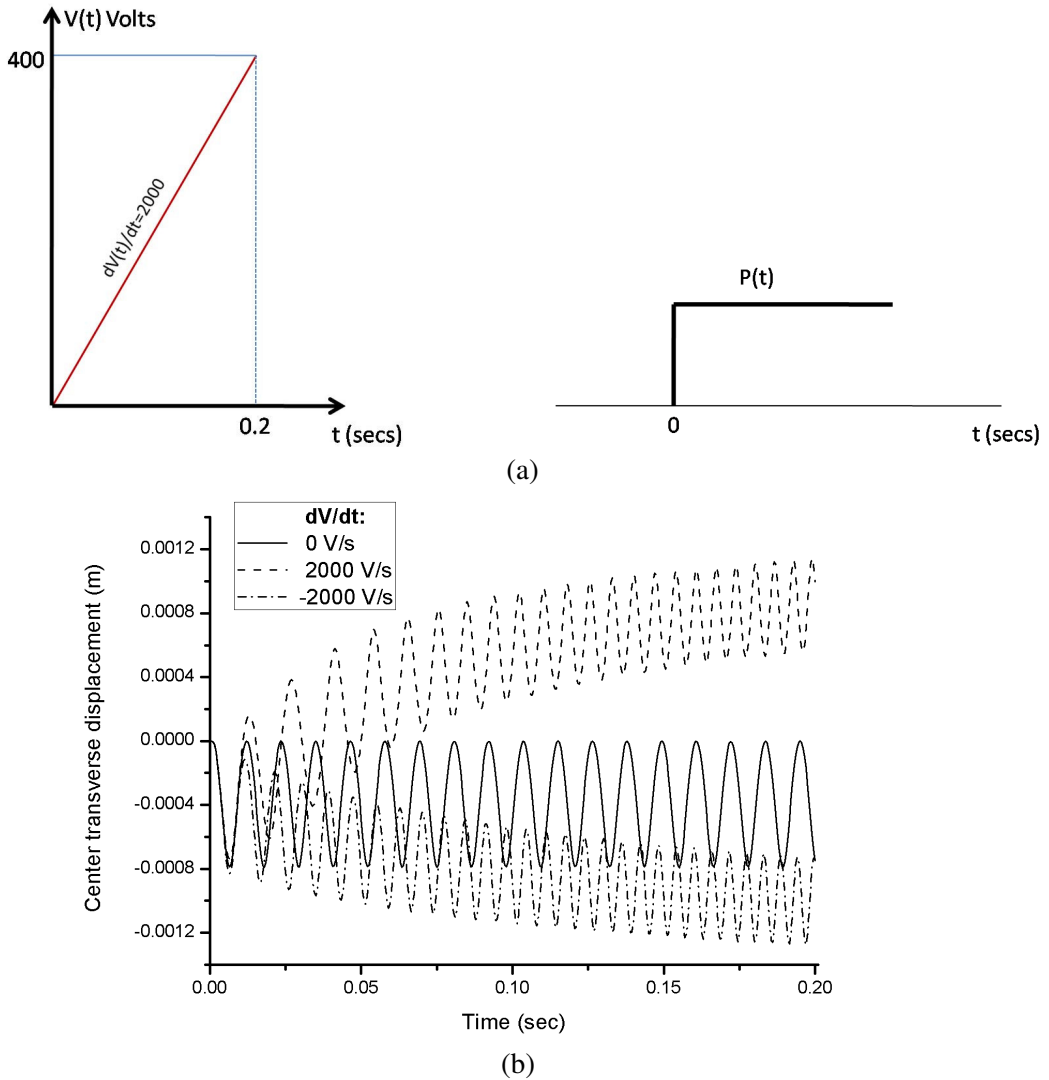


Figure 6. Bending of a simply-supported active $[p/0/90/45/-45]_s$ beam under a combined bending piezoelectric load with a uniform pressure. (a) Time dependence of applied loads, and (b) transverse deflection at center.

the beam (see Figure 6a). Figure 6b shows the predicted transverse displacement at midspan versus time for three cases of ramp electric loads: $V_{\max} = 0$ V, $dV/dt = 0$ V/sec; $V_{\max} = 400$ V, $dV/dt = 2000$ V/sec; and $V_{\max} = -400$ V, $dV/dt = -2000$ V/sec. The free vibration is caused mainly by the applied time step of uniform pressure. The curves corresponding to positive and negative electric potential, show great differences in the vibratory response and the underlying average displacement, indicating strong nonlinearity in the respective response.

6.4. Active buckling of simply-supported composite beam under combined thermopiezoelectric loading. The dynamic response of a simply-supported $[p/0/90/45/-45]_s$ gr-epoxy beam with continuous

piezoelectric actuators attached on the upper and lower surface is predicted. The length and the width of the beam were 200 mm and 20 mm, respectively; the thicknesses of the composite plies and piezoelectric layers were $h_l = h_p = 0.1$ mm. The beam is loaded by a step of uniform temperature thermal load ΔT , a ramp piezoelectric load ($V_{\max} = 2V_{cr}$, $dV/dt = 110$ V/sec), inducing unidirectional electric fields in the piezoactuators through the application of equal but opposite electric potential values on their outer terminals, and a time step of very low constant uniform pressure (3 Pa), all applied at $t = 0$ sec (see Figure 7a). Both the thermal and the piezoelectric loading induce in-plane compressive stresses in the beam. The predicted thermal and electric potential critical values were $\Delta T_{cr} = 18^\circ\text{C}$ and $V_{cr} = 54$ V respectively. Figures 7b and 7c show the predicted dynamic center transverse displacement of the beam

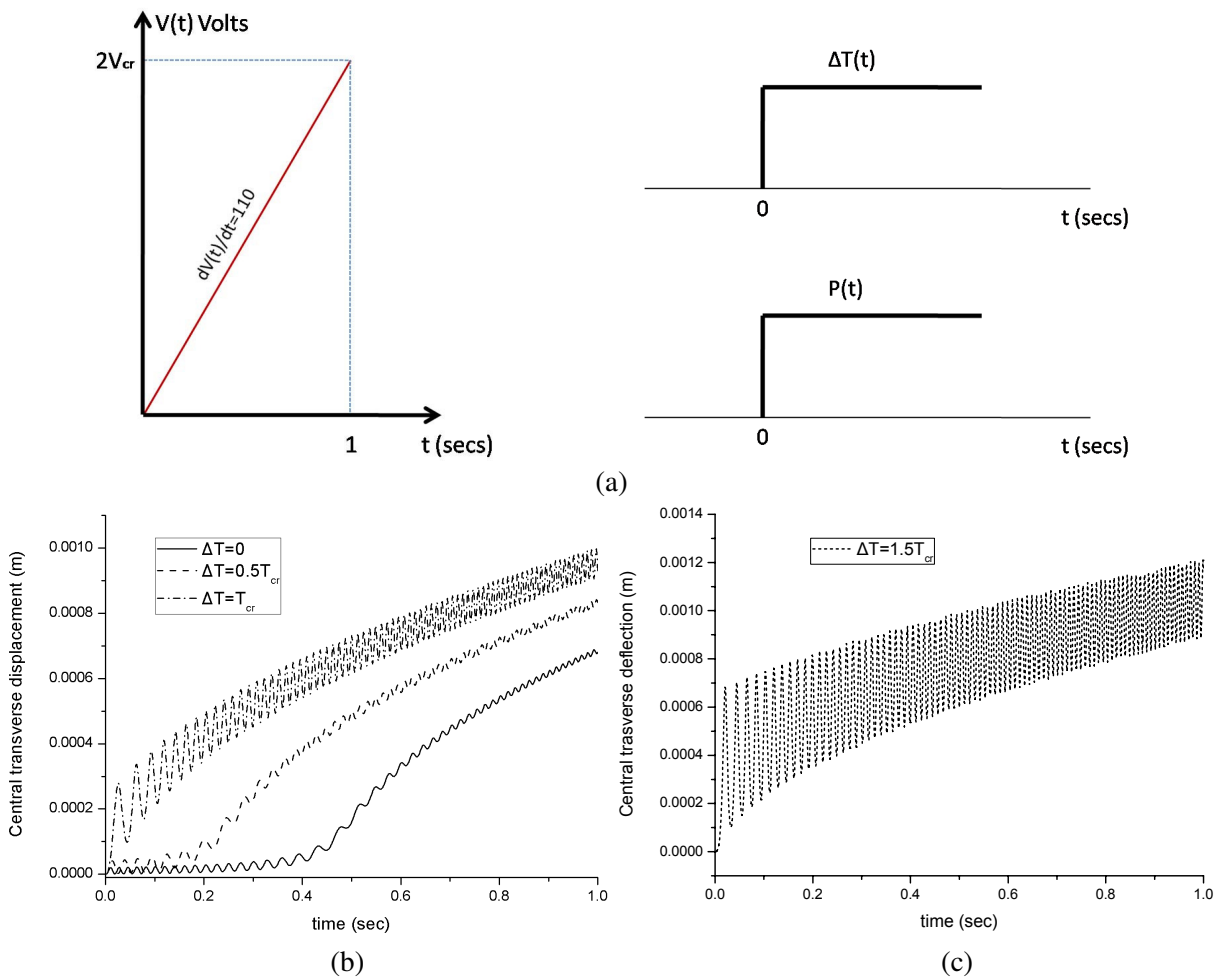


Figure 7. Dynamic thermopiezoelectric buckling of a simply-supported active $[p/0/90/45/-45]_s$ beam under combined compressive in-plane piezoelectric and thermal loading and small uniform pressure (a) time dependence of applied loads; (b) and (c) predicted center deflection for various thermal load values.

versus time for thermal load values. Without thermal buckling load ($\Delta T = 0^\circ\text{C}$) the beam enters in the pure piezoelectric buckling under compressive stresses caused by the piezoelectric actuators. All other trajectories are the result of combined application of various temperature loads ΔT and approach earlier the onset of buckling due to additional compressive thermal stresses. Obviously, for $\Delta T = T_{cr}$ and $1.5T_{cr}$, the beam buckles first thermally and due to the loss of its out-of-plane stiffness vibrates under much higher amplitudes. Again, the results show the inherent capability of the present method to simulate the combined dynamic thermoelectric buckling of flexible piezocomposite structures.

7. Summary and conclusions

A theoretical framework and a finite element methodology were presented, to predict the coupled nonlinear dynamic response of active laminated piezoelectric beams and plates exposed to dynamic thermoelectromechanical fields. The mechanics uses the mixed-field shear-layerwise laminate kinematic assumptions and encompasses the geometric nonlinearity due to large displacements and rotations. An eight-node nonlinear coupled plate element was developed. The coupled generalized nonlinear dynamic equations of motion were formulated, linearized, and solved using the Newton–Raphson technique in combination with the Newmark time integration method.

Validations and evaluation cases of laminated beams and plates subject to high in-plane and out-of-plane dynamic loads demonstrated the capability of the present method to accurately and robustly predict their nonlinear dynamic response. Moreover they quantified the complex and highly nonlinear dynamic response of active structures.

The obtained numerical results illustrate the tendency of active plate beams to exhibit substantially different behavior under dynamic loads than static buckling. In this context, the rates of applied loads drastically affect the dynamic buckling trajectory, and vibrations may coexist which change the amplitude and frequency near critical loads. Thermal loads may significantly influence the highly nonlinear response of piezocomposite beams shifting the stable equilibrium trajectory due to additional compressive/tensile thermal stresses. The possibility of actively inducing large vibration amplitudes by combining steady external mechanical or thermal loads with proper dynamic electric potential input on the actuators was also quantified.

References

- [Ahmad et al. 2004] S. N. Ahmad, C. S. Upadhyay, and C. Venkatesan, “Linear and nonlinear analysis of a smart beam using general electrothermoelastic formulation”, *AIAA J.* **42**:4 (2004), 840–849.
- [Bao et al. 1998] Y. Bao, H. S. Tzou, and V. B. Venkayya, “Analysis of non-linear piezothermoelastic laminated beams with electric and temperature effects”, *J. Sound Vib.* **209**:3 (1998), 505–518.
- [Gao and Shen 2003] J.-X. Gao and Y.-P. Shen, “Active control of geometrically nonlinear transient vibration of composite plates with piezoelectric actuators”, *J. Sound Vib.* **264**:4 (2003), 911–928.
- [Lee and Lee 1997] D.-M. Lee and I. Lee, “Vibration behaviors of thermally postbuckled anisotropic plates using first-order shear deformable plate theory”, *Comput. Struct.* **63**:3 (1997), 371–378.
- [Lentzen et al. 2007] S. Lentzen, P. Klosowski, and R. Schmidt, “Geometrically nonlinear finite element simulation of smart piezolaminated plates and shells”, *Smart Mater. Struct.* **16**:6 (2007), 2265–2274.
- [Mukherjee and Chaudhuri 2005] A. Mukherjee and A. S. Chaudhuri, “Nonlinear dynamic response of piezolaminated smart beams”, *Comput. Struct.* **83**:15–16 (2005), 1298–1304.

- [Oh 2005] I.-K. Oh, “Thermopiezoelastic nonlinear dynamics of active piezolaminated plates”, *Smart Mater. Struct.* **14**:4 (2005), 823–834.
- [Oh et al. 2000] I.-K. Oh, J.-H. Han, and I. Lee, “Postbuckling and vibration characteristics of piezolaminated composite plate subject to thermo-piezoelectric loads”, *J. Sound Vib.* **233**:1 (2000), 19–40.
- [Oh et al. 2001] I.-K. Oh, J.-H. Han, and I. Lee, “Thermopiezoelastic snapping of piezolaminated plates using layerwise nonlinear finite elements”, *AIAA J.* **39**:6 (2001), 1188–1198.
- [Park and Kim 2006] J.-S. Park and J.-H. Kim, “Thermal postbuckling and vibration analyses of functionally graded plates”, *J. Sound Vib.* **289**:1–2 (2006), 77–93.
- [Singha et al. 2006] M. K. Singha, L. S. Ramachandra, and J. N. Bandyopadhyay, “Vibration behavior of thermally stressed composite skew plate”, *J. Sound Vib.* **296**:4–5 (2006), 1093–1102.
- [Tzou and Zhou 1997] H. S. Tzou and Y. H. Zhou, “Nonlinear piezothermoelasticity and multi-field actuations, 2: Control of nonlinear deflection, buckling and dynamics”, *J. Vib. Acoust. (ASME)* **119**:3 (1997), 382–389.
- [Varelis and Saravanos 2004] D. Varelis and D. A. Saravanos, “Coupled buckling and postbuckling analysis of active laminated piezoelectric composite plates”, *Int. J. Solids Struct.* **41**:5–6 (2004), 1519–1538.
- [Varelis and Saravanos 2006] D. Varelis and D. A. Saravanos, “Small-amplitude free-vibration analysis of piezoelectric composite plates subject to large deflections and initial stresses”, *J. Vib. Acoust. (ASME)* **128**:1 (2006), 41–49.
- [Varelis and Saravanos 2008] D. Varelis and D. A. Saravanos, “Non-linear coupled multi-field mechanics and finite element for active multi-stable thermal piezoelectric shells”, *Int. J. Numer. Methods Eng.* **76**:1 (2008), 84–107.
- [Wang et al. 2004] D. W. Wang, H. S. Tzou, and H.-J. Lee, “Control of nonlinear electro/elastic beam and plate system: finite element formulation and analysis”, *J. Vib. Acoust. (ASME)* **126**:1 (2004), 63–70.
- [Yi et al. 2000] S. Yi, S. F. Ling, and M. Ying, “Large deformation finite element analyses of composite structures integrated with piezoelectric sensors and actuators”, *Finite Elem. Anal. Des.* **35**:1 (2000), 1–15.

Received 6 Jul 2009. Revised 26 Aug 2009. Accepted 4 Sep 2009.

DIMITRIS VARELIS: barell@mech.upatras.gr

Applied Mechanics Section, Department of Mechanical Engineering and Aeronautics, University of Patras, 26500 Patras, Greece

DIMITRIS SARAVANOS: saravanos@mech.upatras.gr

Applied Mechanics Section, Department of Mechanical Engineering and Aeronautics, University of Patras, 26500 Patras, Greece

SUBMISSION GUIDELINES

ORIGINALITY

Authors may submit manuscripts in PDF format on-line. Submission of a manuscript acknowledges that the manuscript is *original and has neither previously, nor simultaneously, in whole or in part, been submitted elsewhere*. Information regarding the preparation of manuscripts is provided below. Correspondence by email is requested for convenience and speed. For further information, consult the web site at <http://www.jomms.org> or write to

jomms.steele@stanford.edu

LANGUAGE

Manuscripts must be in English. A brief abstract of about 150 words or less must be included. The abstract should be self-contained and not make any reference to the bibliography. Also required are keywords and subject classification for the article, and, for each author, postal address, affiliation (if appropriate), and email address if available. A home-page URL is optional.

FORMAT

Authors are encouraged to use \LaTeX and the standard article class, but submissions in other varieties of \TeX , and, exceptionally in other formats, are acceptable. Electronic submissions are strongly encouraged in PDF format only; after the refereeing process we will ask you to submit all source material.

REFERENCES

Bibliographical references should be listed alphabetically at the end of the paper and include the title of the article. All references in the bibliography should be cited in the text. The use of \BIBTeX is preferred but not required. Tags will be converted to the house format (see a current issue for examples), however, in the manuscript, the citation should be by first author's last name and year of publication, e.g. "as shown by Kramer, et al. (1994)". Links will be provided to all literature with known web locations and authors are encouraged to provide their own links on top of the ones provided by the editorial process.

FIGURES

Figures prepared electronically should be submitted in Encapsulated PostScript (EPS) or in a form that can be converted to EPS, such as GnuPlot, Maple, or Mathematica. Many drawing tools such as Adobe Illustrator and Aldus FreeHand can produce EPS output. Figures containing bitmaps should be generated at the highest possible resolution. If there is doubt whether a particular figure is in an acceptable format, the authors should check with production by sending an email to

production@mathscipub.org

Each figure should be captioned and numbered so that it can float. Small figures occupying no more than three lines of vertical space can be kept in the text ("the curve looks like this:"). It is acceptable to submit a manuscript with all figures at the end, if their placement is specified in the text by comments such as "Place Figure 1 here". The same considerations apply to tables.

WHITE SPACE

Forced line breaks or page breaks should not be inserted in the document. There is no point in your trying to optimize line and page breaks in the original manuscript. The manuscript will be reformatted to use the journal's preferred fonts and layout.

PROOFS

Page proofs will be made available to authors (or to the designated corresponding author) at a web site in PDF format. Failure to acknowledge the receipt of proofs or to return corrections within the requested deadline may cause publication to be postponed.

Journal of Mechanics of Materials and Structures

Volume 4, Nº 7-8 September 2009

Special issue dedicated to George J. Simites

- Dedication** GEORGE KARDOMATEAS and VICTOR BIRMAN 1185
- Buckling and postbuckling behavior of laminated composite stringer stiffened curved panels under axial compression: Experiments and design guidelines**
HAIM ABRAMOVICH and TANCHUM WELLER 1187
- Effect of elastic or shape memory alloy particles on the properties of fiber-reinforced composites** VICTOR BIRMAN 1209
- On the detachment of patched panels under thermomechanical loading**
WILLIAM J. BOTTEGA and PAMELA M. CARABETTA 1227
- Exponential solutions for a longitudinally vibrating inhomogeneous rod**
IVO CALIÒ and ISAAC ELISHAKOFF 1251
- Stability studies for curved beams** CHONG-SEOK CHANG and DEWEY H. HODGES 1257
- Influence of core properties on the failure of composite sandwich beams** ISAAC M. DANIEL 1271
- Nonlinear behavior of thermally loaded curved sandwich panels with a transversely flexible core**
YEOSHUA FROSTIG and OLE THOMSEN 1287
- Determination of offshore spar stochastic structural response accounting for nonlinear stiffness and radiation damping effects** RUPAK GHOSH and POL D. SPANOS 1327
- The elusive and fickle viscoelastic Poisson's ratio and its relation to the elastic-viscoelastic correspondence principle**
HARRY H. HILTON 1341
- Dynamic buckling of a beam on a nonlinear elastic foundation under step loading**
MAHMOOD JABAREEN and IZHAK SHEINMAN 1365
- Direct damage-controlled design of plane steel moment-resisting frames using static inelastic analysis**
G. S. KAMARIS, G. D. HATZIGEORGIOU and D. E. BESKOS 1375
- Nonlinear flutter instability of thin damped plates: a solution by the analog equation method**
JOHN T. KATSIKADELIS and NICK G. BABOUSKOS 1395
- The effect of infinitesimal damping on nonconservative divergence instability systems**
ANTHONY N. KOUNADIS 1415
- Property estimation in FGM plates subject to low-velocity impact loading**
REID A. LARSON and ANTHONY N. PALAZOTTO 1429
- A high-order theory for cylindrical sandwich shells with flexible cores**
RENFU LI and GEORGE KARDOMATEAS 1453
- Failure investigation of debonded sandwich columns: An experimental and numerical study**
R. MOSLEMIAN, C. BERGGREEN, L. A. CARLSSON and F. AVILES 1469
- Coupled finite element for the nonlinear dynamic response of active piezoelectric plates under thermoelectromechanical loads** DIMITRIS VARELIS and DIMITRIS SARAVANOS 1489